

5-1-2015

Effect of Void Geometry on Strength, Stiffness, and Failure Modes of Rock-like Materials

Omed Yousif

University of Nevada, Las Vegas, yousifo@unlv.nevada.edu

Follow this and additional works at: <https://digitalscholarship.unlv.edu/thesesdissertations>



Part of the [Civil Engineering Commons](#)

Repository Citation

Yousif, Omed, "Effect of Void Geometry on Strength, Stiffness, and Failure Modes of Rock-like Materials" (2015). *UNLV Theses, Dissertations, Professional Papers, and Capstones*. 2450.

<https://digitalscholarship.unlv.edu/thesesdissertations/2450>

This Dissertation is protected by copyright and/or related rights. It has been brought to you by Digital Scholarship@UNLV with permission from the rights-holder(s). You are free to use this Dissertation in any way that is permitted by the copyright and related rights legislation that applies to your use. For other uses you need to obtain permission from the rights-holder(s) directly, unless additional rights are indicated by a Creative Commons license in the record and/or on the work itself.

This Dissertation has been accepted for inclusion in UNLV Theses, Dissertations, Professional Papers, and Capstones by an authorized administrator of Digital Scholarship@UNLV. For more information, please contact digitalscholarship@unlv.edu.

**EFFECT OF VOID GEOMETRY ON STRENGTH, STIFFNESS, AND FAILURE
MODES OF ROCK-LIKE MATERIALS**

By

Omed Yousif

Bachelor of Science in Civil Engineering
Salahaddin University, Hawler, Iraq
1997

Master of Science in Hydraulic Engineering
University of Sulaimani, Sulaimani, Iraq
2003

A dissertation submitted in partial fulfillment
of the requirements for the

Doctor of Philosophy - Civil and Environmental Engineering

Department of Civil and Environmental Engineering and Construction
Howard R. Hughes College of Engineering
The Graduate College

University of Nevada, Las Vegas
May 2015

Copyright by Omed Yousif, 2015

All Rights Reserved

We recommend the dissertation prepared under our supervision by

Omed Yousif

entitled

Effect of Void Geometry on Strength, Stiffness, and Failure Modes of Rock-like Materials

is approved in partial fulfillment of the requirements for the degree of

Doctor of Philosophy in Engineering - Civil and Environmental Engineering

Department of Civil and Environmental Engineering and Construction

Moses Karakouzian, Ph.D., Committee Chair

Samaan Ladkany, Ph.D., Committee Member

Douglas Rigby, Ph.D., Committee Member

Mohamed Kaseko, Ph.D., Committee Member

Vernon Hodge, Ph.D., Graduate College Representative

Kathryn Hausbeck Korgan, Ph.D., Interim Dean of the Graduate College

May 2015

ABSTRACT

Effect of Void Geometry on Strength, Stiffness, and Failure Modes of Rock-like Materials

By

Omed Yousif

Dr. Moses Karakouzian, Examination Committee Chair
Professor of Civil and Environmental Engineering and Construction
University of Nevada, Las Vegas

The host rock of portion of the first proposed high-level nuclear waste repository in the United States of America (Yucca Mountain, Nevada) is tuff rock that contains voids (lithophysae) with different shapes, sizes, and distributions. The existence of these voids can cause a dramatic change in the rock's mechanical properties such as uniaxial compressive strength, UCS , and Young's modulus, E . Accordingly, in an experimental program, the effects of void existence on the engineering properties of the tuff rocks was explored in a work of US Department of Energy conducted in the Department of Civil and Environmental Engineering and Construction of the University of Nevada at Las Vegas (UNLV); Project Activity Task ORD-FY04-013. Since it was difficult to test actual rock specimens, due to heterogeneity, break down during coring and sampling, and impossibility of controlling shape, size and distribution of voids in actual specimens of tuff rock, rock-like material (Hydro-StoneTB[®]), instead, was used in the experimental program. The experimental works consisted of laboratory testing on rock-like material (Hydro-StoneTB[®]) cubes under uniaxial compression. To obtain porous cubes with different void geometries, cubes with open ended longitudinal openings having different cross sections (circular, square, and diamond), different sizes (uniform large, medium,

and small, and mixed voids), and different distributions (patterns A, B, and C) were made and tested under uniaxial compression. Fifty two porous specimens were made. Each porous specimen, porous cube, was produced in triplicate. Ten solid cubes were also cast to represent analog material with zero void porosity. The total number of experiments, including the ten solid cubes, was one hundred sixty six, 166, cubes.

This study attempted to characterize the effects of void porosity on compressive strength and elastic modulus more definitively through considering the other factors in data analysis and sought for more effective relationships between them using the experimental results of Project Activity Task ORD-FY04-013. In addition, the experimental results were used to validate a numerical analysis carried out using a discontinuous computer program; Universal Distinct Element Codes - UDEC. Furthermore, another numerical analysis was performed to study the effect of void geometry on mechanical properties more systematically.

The results showed that not-only the porosity but also the void geometry can affect the strength and deformability of rock-like materials. Void shape, void orientation, and void spatial distribution are partially responsible for the scattering in the mechanical property values as a function of void porosity. In addition, the results of the numerical simulations using UDEC software displayed consistent trends in Hydro-StoneTB® uniaxial strength and deformation as a function of void porosity. Furthermore, the two-dimensional numerical results can be transferred to three-dimensional experimental results through a power correlation.

ACKNOWLEDGEMENTS

Foremost, I want to express my deepest gratitude and sincere appreciation to my advisor, Professor Dr. Moses Karakouzian, for his valuable guidance, support, and encouragement throughout my PHD study. I would also like to express my best gratitude and appreciation to Dr. Douglas Rigby for his time, advice, and encouragement in this study. Word can't describe my appreciations for both Professor Dr. Moses Karakouzian and Dr. Douglas Rigby for their contributions to complete this study. Special thanks to Professor Dr. Samaan Ladkany for his useful suggestions. I extend my thanks and appreciations to my thesis committee members, Associate Professor Dr. Mohamed Kaseko and Professor Dr. Vernon Hodge for inspiring me to finish this study.

This thesis is dedicated to:

- My parents and my siblings.
- Wshyar and Hawkar.
- Bahman Hama Ameen Mustafa and Falah Murad Khan Shakarm.

TABLE OF CONTENTS

ABSTRACT.....	iii
ACKNOWLEDGEMENTS.....	v
LIST OF TABLES.....	x
LIST OF FIGURES.....	xii
CHAPTER ONE <i>INTRODUCTION</i>	1
1.1 General	1
1.2 Tuff Rock at Yucca Mountain.....	2
1.3 Rock-like Materials	4
1.4 Study Objectives	5
1.5 Dissertation Outline.....	6
CHAPTER TWO <i>LITERATURE RIVIEW</i>	8
2.1 Introduction	8
2.2 Actual Rock Samples	8
2.2.1 Tuff Rock.....	8
2.2.2 Basalt	23
2.2.3 Chalks	27
2.3 Rock-like Materials.....	28
2.4 Relationship between Voids and Failure Modes.....	43
2.5 Summary of the Literature Review	45
CHAPTER THREE <i>MECHANICAL CHARACTERIZATION OF BRITTLE MATERIALS</i>	47
3.1 Introduction	47
3.2 Failure in Materials	48
3.3 Brittle Materials.....	48
3.4 Strength and Failure of Brittle Materials.....	49
3.5 Failure Criteria of Brittle Materials.....	50
3.5.1 Maximum Principle Stress Theory (Rankine, Lamé', Clapeyron - 1858).....	51

3.5.3 Coulomb-Mohr Theory.....	55
3.5.4 Griffith’s Criterion of Tensile Failure (1921).....	59
3.6 Fracture Mechanics	63
3.6.1 Stress Concentration in Brittle Materials.....	64
3.6.2 The Stress Field near a Crack Tip	66
3.6.3 Stress Concentration in a Plate containing a Circular Hole.....	70
3.7 Failure Criteria for Rocks.....	71
3.7.1 Griffith criterion (1921).....	73
3.7.2 Mohr-Coulomb criterion.....	74
3.7.3 Hoek-Brown criterion (2002)	76
3.8 Failure Modes of Brittle Materials in General	77
3.9 Failure Modes of Brittle Porous Solids under Compression Stress	79
CHAPTER FOUR <i>ANALYSIS OF THE EXPERIMENTAL RESULTS</i>	82
4.1 Introduction	82
4.2 Material and Specimens	83
4.3 Laboratory Experiments	87
4.4 Analysis of Experimental Results	88
4.4.1 Effects of Void Porosity	94
4.4.2 Void Geometry Characterizations	96
4.4.5 Alternative Methods to Explore the Effects of Void Geometry.....	112
4.4.6 Correlation between Uniaxial Compression and Young’s Modulus	124
4.5 Failure Modes of Hydro-StoneTB [®] Cubes.....	127
4.5.1 Porous Cubes Containing Circular Voids.....	127
4.5.2 Porous Cubes Containing Non-circular Voids	130
CHAPTER FIVE <i>NUMERICAL ANALYSIS TO SIMULATE THE EXPERIMENTAL TESTS</i>	134
5.1 Introduction	134
5.2 Numerical Analysis	134
5.2.1 Continuous Numerical Models.....	135
5.2.2 Discontinuous Numerical Models	136
5.2.3 Differences between Numerical Models	136

5.3 Discrete Element Method (DEM)	137
5.4 Universal Distinct Element Code (UDEC)	139
5.5 UDEC Model Description.....	142
5.6 UDEC Model Calibration.....	144
5.6.1 Calibrated Material Properties.....	145
5.6.2 Deformation Calibration.....	147
5.6.3 Strength Calibration.....	148
5.6.4 Numerical Simulations for Porous Cubes	150
5.7 Results and Discussions	150
5.7.1 Numerical Simulations for Models Containing Circular Holes	151
5.7.2 Numerical Simulations for Models Containing Non-Circular Holes	164
5.7.3 Numerical Simulations for All Experimental Tests – All Cubes	173
5.8 Numerical versus Experimental Results	177
5.9 Three-Dimensional versus Two-Dimensional	200
CHAPTER SIX <i>NUMERICAL SIMULATIONS TO GENERATE NEW MODELS CONTAINING VOIDS WITH DIFFERENT SHAPES, SIZES, AND DISTRIBUTIONS</i>	211
6.1 Introduction	211
6.2 Generate Models to Study the Effects of Void Shape on the Mechanical Properties of Rock-like Material	211
6.3 Numerical Simulations to Study the Effects of Void Orientations on the Mechanical Properties of Rock-like Material	221
6.4 Numerical Simulations to Validate the Effects of Void Geometry on the Mechanical Properties	234
CHAPTER SEVEN <i>CONCLUSIONS AND RECOMMENDATIONS</i>	245
7.1 Conclusions	245
7.1.1 Conclusions for the Experimental Results.....	245
7.1.2 Conclusions from the Numerical Results	247
7.2 Recommendations	250
APPENDIX (I) <i>LABROTARY TEST DATA</i>	252
APPENDIX (II) <i>UDEC CALIBRATION</i>	271

APPENDIX (III) <i>NUMERICAL SIMULATIONS FOR HYDRO-STONETB[®] CUBES AND THEIR STRESS-STRAIN CURVES</i>	278
APPENDIX (IV) <i>NUMERICAL MODELS AND THEIR STRESS-STRAIN CURVES</i> ..	297
BIBLIOGRAPHY.....	311
VITA.....	319

LIST OF TABLES

Table (4.1) Porous and Solid Cubes - Specimens with Unisize Circular Voids	85
Table (4.2) Porous and Solid Cubes - Specimens with Mixed Circular Voids.....	86
Table (4.3) Specimens with Square and Diamond Voids	86
Table (4.4) Experimental Results for Cubes Containing Unisize Circular Voids	90
Table (4.5) Experimental Results for Cubes Containing Mixed Circular Voids	91
Table (4.6) Experimental Results for Cubes Containing Square or Diamond.....	91
Table (4.7) Normalized Results for Cubes Containing Unisize Circular Voids.....	92
Table (4.8) Normalized Results for Cubes Containing Mixed Circular Voids.....	93
Table (4.9) Normalized Results for Cubes Containing Square or Diamond Voids.....	93
Table (4.10) Bridge, Side distances, and Top Distances of Unisize Circular Voids	107
Table (4.11) Bridge, Side distances, and Top Distances of Mixed Circular Voids	108
Table (4.12) Bridge, Side distances, and Top Distances of Unisize Non-Circular Voids – Square and Diamond Voids	108
Table (4.13) Total Width of Solid Columns for Cubes Containing Unisize Circular Voids	118
Table (4.14) Total Width of Solid Columns for Cubes Containing Mixed Circular Voids	119
Table (4.15) Total Width of Solid Columns for Cubes Containing Unisize	119
Table (5.1) UDEC Input Data for Hydro-StoneTB [®] Specimens	150
Table (5.2) Numerical Results for the Models Containing Circular Voids – Unisize Voids	163
Table (5.3) Numerical Results for the Models Containing Circular Voids – Mixed Voids	164
Table (5.4) Numerical Results for the Models Containing Non-Circular Voids – Square and Diamond Voids	172
Table (5.5) Numerical and Experimental Results for the Models Containing Unisize Circular Voids.....	196
Table (5.6) Numerical to Experimental Ratios for Models Containing Unisize Circular Voids.....	197
Table (5.7) Numerical and Experimental Results for Models Containing Models Containing Circular Voids with Mixed Sizes	198
Table (5.8) Numerical to Experimental Ratios for Models Containing Circular Voids with Mixed Sizes.....	198
Table (5.9) Numerical and Experimental Results for Models Containing Non-Circular Voids (Square and Diamond).....	199
Table (5.10) Numerical to Experimental Ratios for Models Containing Non-Circular Voids (Square and Diamond).....	199
Table (5.11) Ratios of Numerical <i>UCS</i> to Experimental <i>UCS</i> for All Numerical	200
Table (5.12) Ratios of Numerical <i>E</i> to Experimental <i>E</i> for All Numerical Models	200

Table (6.1) Numerical Models to Simulate the Effects of Void Shapes.....	212
Table (6.2) Numerical Models Containing Unisize Large Voids with Different Shapes	217
Table (6.3) Differences in <i>UCS</i> and <i>E</i> for Numerical Models Containing Large Voids	217
Table (6.4) Numerical Models Containing Unisize Voids with Different Orientations.	223
Table (6.5) Numerical Results for Models Containing Unisize Large Voids.....	226
Table (6.6) Numerical Results for Models Containing Unisize Small Voids.....	227
Table (6.7) Total Width of Solid Columns for Models Containing Large Unisize Voids	239
Table (6.8) Total Width od Solid Columns for Models Containing Unisize Small Voids	240
Table (I-A1) EXPERIMENTAL RESULTS OF TESTED CUBES	252
Table (I-A2) EXPERIMENTAL RESULTS OF TESTED CUBES	253
Table (I-A3) EXPERIMENTAL RESULTS OF TESTED CUBES	254
Table (I-A4) EXPERIMENTAL RESULTS OF TESTED CUBES	255
Table (I-A5) EXPERIMENTAL RESULTS OF TESTED CUBES	256
Table (II-1) MATERIAL PROPERTIES USED IN THE MODEL CALIBRATION...	271
Table (II-2) MATERIAL PROPERTIES USED IN THE MODEL CALIBRATION...	272
Table (II-3) MATERIAL PROPERTIES USED IN THE MODEL CALIBRATION...	273
Table (II-4) NUMERICAL RESULTS FOR SIMULATED MODELS IN THE CALIBRATION PROCESS	274
Table (II-5) NUMERICAL RESULTS FOR SIMULATED MODELS IN THE CALIBRATION PROCESS	275

LIST OF FIGURES

Figure (1.1) Photographs of Lithophase-rich Tuff from Yucca Mountain	4
Figure (2.1) Uniaxial Compressive Strength for Saturated Specimens of Topopah Spring Tuff (samples with 50.8 mm or smaller in diameter) (Rigby 2004).....	15
Figure (2.2) Young’s Modulus for Saturated Specimens of Topopah Spring Tuff (samples with 50.8 mm or smaller in diameter) (Rigby 2004)	15
Figure (2.3) Photograph of the Large (267 mm) Diameter Cores from Busted Butte Samples (Rigby 2004).....	16
Figure (2.4) Correlation between Uniaxial Compressive Strength of Tuff and the Porosity (Small and Large-Diameter Cores of Topopah Spring Tuff) (Rigby 2004)	16
Figure (2.5) Correlation between Young’s Modulus of Tuff and the Porosity (Small and Large-Diameter Cores of Topopah Spring Tuff) (Rigby 2004).....	17
Figure (2.6) Correlation between Uniaxial Compressive Strength of Tuff and the Porosity (Large-Diameter Cores of Topopah Spring Tuff) (Rigby 2004)	17
Figure (2.7) Correlation between Young’s Modulus of Tuff and the Porosity (Large-Diameter Cores of Topopah Spring Tuff) (Rigby 2004)	18
Figure (2.8) Correlation between Uniaxial Compressive Strength and the Young’s Modulus Large-Diameter Cores of Topopah Spring Tuff (Rigby 2004).....	18
Figure (2.9) Comparison of UDEC Numerical Models to Experimental Tests on Lithophysal Tuff Regarding Uniaxial Compressive Strength (UCS) (Christianson et al. 2006)	19
Figure (2.10) Comparison of UDEC Numerical Models to Experimental Tests on Lithophysal Tuff Regarding Young’s Modulus (E) (Christianson et al. 2006).....	19
Figure (2.12) Correlation between Mechanical Properties of Tuff and the Total Porosity (Avar 2002).....	20
Figure (2.11) Photograph of Some Tuff Specimens Tested by Avar (2002).....	20
Figure (2.13) Photograph Some Tuff Specimens Tested by Hudyma et al. (2004).....	21
Figure (2.14) Correlation between UCS versus the total Porosity (Hudyma et al. 2004)	21
Figure (2.15) Photograph of Large-Diameter Cores of Tuff; (a) Samples before testing, and (b) Samples during testing (Costin et al. 2009)	22
Figure (2.16) Correlation between Uniaxial Compressive Strength and the approximate (total) Porosity (Costin et al. 1999).....	22
Figure (2.17) Correlation between Uniaxial Compressive Strength and Young’s Modulus (Costin et al. 2009).....	23
Figure (2.18a, b, & c) Photograph Samples of Vesicular Basalt Tested by	25
Figure (2.19) Correlation between Uniaxial Compressive Strength of Vesicular Basalt and the actual Porosity (Al-Harthi et al. 1999).....	26
Figure (2.20) Correlation between Young’s Modulus, E , of Vesicular Basalt and the actual Porosity (Al-Harthi et al. 1999).....	26

Figure (2.21) Correlation between Uniaxial Compressive Strength of Chalk and Porosity (Palchik and Hatzor 2004)	28
Figure (2.22) Normalized Young's Modulus versus Total Porosity for Urethane Cubes for both Experimental Tests and Numerical Models (Avar 2002).	35
Figure (2.23) Normalized Young's Modulus versus Total Porosity for Plaster Specimens Containing Cylindrical Tubes for both Experimental Tests and Numerical Models (Avar 2002).	36
Figure (2.24) Uniaxial Compressive Strength (σ_c) versus Total Porosity for Plaster Cubes Containing either Randomly Distributed Cylindrical Tubes or Uniform Distributed Cylindrical Tubes (Avar 2002).	36
Figure (2.25) Young's Modulus versus Total Porosity for Plaster Cubes Containing either Randomly Distributed Cylindrical Tubes or Uniform Distributed Cylindrical Tubes (Avar 2002).	37
Figure (2.26) Uniaxial Compressive Strength (σ_c) versus Total Porosity for Plaster Cubes Containing either Cylindrical Tubes or Styrofoam Inclusions (Avar 2002).	37
Figure (2.27) Young's Modulus versus Total Porosity for Plaster Cubes Containing either Cylindrical Tubes or Styrofoam Inclusions (Avar 2002).	38
Figure (2.28) Correlation between Uniaxial Compressive Strength and Porosity (Hudyma 2004).	38
Figure (2.29) Correlation between Normalized Uniaxial Compressive Strength and Porosity (Erfourth 2006).	39
Figure (2.30) Correlation between Normalized Uniaxial Compressive Strength and Porosity (Erfourth 2006).	39
Figure (2.31) Correlation between Elastic Modulus with Porosity (Erfourth 2006).	40
Figure (2.32) Correlation between Young's Modulus and Porosity	40
Figure (2.33) Correlation between Normalized Uniaxial Compressive Strength with Porosity for both Numerical Models and Experimental Tests (Erfourth (2006).	41
Figure (2.34) Correlation between Young's Modulus with Porosity for both Numerical Models and Experimental Tests (Erfourth (2006).	41
Figure (2.35) Correlation between Normalized Uniaxial Compressive Strength and Porosity (Rigby 2007).	42
Figure (2.36) Correlation between Normalized Young's Modulus and Porosity (Rigby 2007).	42
Figure (2.37) Correlation between Ultimate Tensile Strength and Porosity for both Numerical Models and Experimental Tests (Nott 2009).	43
Figure (2.38) Failure Modes-Cylindrical Plaster Specimens (Hudyma et al. 2004).	44
Figure (2.39a, b, & c) Failure Modes Cubic Plaster Specimens - Jespersen et al. (2010)	45
Figure (3.1a & b) Typical stress-strain curves for (a) brittle material and, (b) ductile material	49
Figure (3.2) Maximum Principle Stress failure criterion.	53

Figure (3.3) Mohr’s Theory (a) Mohr’s circles of stress; (b) Mohr’s envelopes (Ugural and Fenster 2012).....	55
Figure (3.4) Coulomb–Mohr criterion	59
Figure(3.5) A plate of thickness t containing a crack of length $2a$. (a) Unloaded condition, (b) and (c) Loaded conditions (Meyers and Chawla 2009).	63
Figure (3.6) “Lines of force” in a bar with (a) a sharp crack and, (b) a side notch. (Meyers and Chawla 2009).	65
Figure (3.7) Elliptical hole in a flat plate (Anderson 1995).....	66
Figure (3.8) The three modes of fracture. (a) Mode I: opening mode. (b) Mode II: sliding mode. (c) Mode III: tearing mode (Meyers and Chawla 2009).	68
Figure (3.9) Infinite, homogeneous, elastic plate containing a through-the-thickness central crack of length $2a$, subjected to a tensile stress σ (Meyers and Chawla 2009).....	69
Figure (3.10) Stress distribution in a large plate containing a circular hole (Meyers and Chawla 2009).	71
Figure (3.11) Mohr_Coulomb criterion (a) Shear failure on plane ab, (b) Strength envelope in terms of shear and normal stresses (Brady and Brown 2006).....	75
Figure (3.12) Coulomb strength envelopes with a tensile cut-off T_o (Brady and Brown 2006).	76
Figure (3.13) Failure Modes and Stress- Strain Curves for Porous Solids.....	80
Figure (4.1) Location of First Void; Patterns A, B, and C for Circular Voids, and Patterns A and B for Non-circular Voids.....	87
Figure (4.2) Normalized Uniaxial Strength versus Void Porosity for Cubes with Voids Having Different Size, Shape and Distribution	95
Figure (4.3) Normalized Deformation versus Void Porosity for Cubes with Voids Having Different Size, Shape and Distribution	96
Figure (4.4) Normalized Uniaxial Compression versus Void Porosity for Cubes Containing Unisize Circular Voids.....	97
Figure (4.5) Normalized Deformation versus Void Porosity for Cubes.....	98
Figure (4.6) Normalized Uniaxial Compression versus Void Porosity for Cubes	98
Figure (4.0.7) Normalized Deformation versus Void Porosity for Cubes.....	99
Figure (4.0.8) Normalized Uniaxial Compression versus Void Porosity for Cubes	99
Figure (4.9) Normalized Deformation versus Void Porosity for Cubes.....	100
Figure (4.10) Normalized Uniaxial Compression versus Void Porosity for Cubes	102
Figure (4.11) Normalized Deformation versus Void Porosity for Cubes.....	102
Figure (4.12) Bridge distances, B_r , Side distances, S , and Top distances, T , for Hydro-StoneTB [®] cubes	104
Figure (4.13) Normalized Uniaxial Compression versus Normalized Bridge Distance.	109
Figure (4.14) Normalized Deformation versus Normalized Bridge Distance	109
Figure (4.15) Normalized Uniaxial Compression versus Normalized Side Distance	110
Figure (4.16) Normalized Deformation versus Normalized Side Distance.....	110

Figure (4.17) Normalized Uniaxial Compression versus Normalized Top Distance	111
Figure (4.18) Normalized Deformation versus Normalized Top Distance.....	111
Figure (4.19) Total Width of Solid Columns for Porous Specimens.....	113
Figure (4.20) Normalized Uniaxial Compression versus Total Width of Solid Columns for Cubes with Voids Having Different Size, Shape and Distribution	120
Figure (4.21) Normalized Deformation versus Total Width of Solid Columns for Cubes with Voids Having Different Size, Shape and Distribution.....	120
Figure (4.22) Normalized Uniaxial Compression versus Normalized Total Width of Solid Columns for Cubes with Voids Having Different Size, Shape and Distribution.....	121
Figure (4.23) Normalized Deformation versus Normalized Total Width of Solid Columns for Cubes with Voids Having Different Size, Shape and Distribution	121
Figure (4.24) Normalized Uniaxial Compression versus Normalized Total Width of Solid Columns for Cubes with Voids Having Different Size, Shape and Distribution.....	122
Figure (4.25) Normalized Deformation versus Normalized Total Width of Solid Columns	122
Figure (4.26) Normalized Uniaxial Compression versus Normalized Total Width of Solid Columns and Void Porosity for Cubes with Voids Having Different Size, Shape and Distribution	123
Figure (4.27) Normalized Deformation versus Normalized Total Width of Solid Columns and Void Porosity for Cubes with Voids Having Different Size, Shape and Distribution	123
Figure (4.28) Uniaxial Compression versus Deformation for Cubes with Voids.....	125
Figure (4.29) Uniaxial Compression versus Deformation and Void Porosity for Cubes with Voids Having Different Size, Shape and Distribution.....	126
Figure (4.30) Uniaxial Compression versus Deformation, Void Porosity, and Total Width of Solid Columns for Cubes with Voids Having Different Size, Shape and Distribution	126
Figure (4.31) Photographs of Tested Cubes Containing Large Unisize Circular Voids	128
Figure (4.32) Photographs of Tested Cubes Containing Medium Unisize Circular Voids	129
Figure (4.33) Photographs of Tested Cubes Containing Small Unisize Circular Voids	129
Figure (4.34) Photographs of Tested Cubes Containing Mixed Circular Voids.....	129
Figure (4.35) Photographs of Tested Cubes Containing Large Unisize Circular Voids	130
Figure (4.36) Photographs of Tested Cubes Containing Circular Voids	130
Figure (4.37) Photographs of Tested Cubes Containing Large Unisize Square Voids ..	131
Figure (4.38) Photographs of Tested Cubes Containing Small Unisize Square Voids ..	132
Figure (4.39) Photographs of Tested Cubes Containing Large Unisize Diamond Voids	132
Figure (4.40) Photographs of Tested Cubes Containing Small Unisize Diamond Voids	132
Figure (4.41) Photographs of Tested Cubes Containing Unisize Non-circular Voids ...	133

Figure (5.1) Material Representation in UDEC Models Using Voronoi Tessellation Joint Generator (BSC 2003)	144
Figure (5.2) Compressive Strength versus Void Porosity for Numerical Models Containing Circular Voids – Both Unisize and Mixed Voids	154
Figure (5.3) Deformation versus Void Porosity for Numerical Models Containing Circular Voids– Both Unisize and Mixed Voids	154
Figure (5.4) Compressive Strength versus Void Porosity for Numerical Models Containing Circular Voids – Large Unisize Voids	155
Figure (5.5) Compressive Strength versus Void Porosity for Numerical Models Containing Circular Voids – Medium Unisize Voids.....	155
Figure (5.6) Compressive Strength versus Void Porosity for Numerical Models Containing Circular Voids – Small Unisize Voids	156
Figure (5.7) Compressive Strength versus Void Porosity for Numerical Models Containing Circular Voids – Mixed Voids	156
Figure (5.8) Deformation versus Void Porosity for Numerical Models Containing Circular Voids – Large Unisize Voids.....	157
Figure (5.9) Deformation versus Void Porosity for Numerical Models Containing Circular Voids – Medium Unisize Voids.....	157
Figure (5.10) Deformation versus Void Porosity for Numerical Models Containing Circular Voids – Small Unisize Voids.....	158
Figure (5.11) Deformation versus Void Porosity for Numerical Models Containing Circular Voids –Mixed Voids	158
Figure (5.12) Compressive Strength versus Void Porosity for Numerical Models Containing Circular Voids – Both Unisize and Mixed Voids	159
Figure (5.13) Deformation versus Void Porosity for Numerical Models Containing Circular Voids– Both Unisize and Mixed Voids	159
Figure (5.14) Compressive Strength versus Void Porosity for Numerical Models Containing Circular Voids– Some Unisize and All Mixed Voids	160
Figure (5.15) Deformation versus Void Porosity for Numerical Models Containing Circular Voids– Some Unisize and All Mixed Voids.....	160
Figure (5.16) Compressive Strength versus Deformation for Numerical Models Containing Circular Voids	161
Figure (5.17) Compressive Strength versus Deformation for Numerical Models Containing Circular Voids – All Circular Voids	161
Figure (5.18) Compressive Strength versus Deformation for Numerical Models Containing Circular Voids – Some Unisize and All Mixed Voids	162
Figure (5.19) Compressive Strength versus Void Porosity for Numerical Models Containing Square Voids	166
Figure (5.20) Compressive Strength versus Void Porosity for Numerical Models Containing Diamond Voids	166

Figure (5.21) Deformation versus Void Porosity for Numerical Models Containing Square Voids	167
Figure (5.22) Deformation versus Void Porosity for Numerical Models Containing Diamond Voids	167
Figure (5.23) Compressive Strength versus Void Porosity for Numerical Models Containing Large Non-Circular Voids – Both Square and Diamond Voids	168
Figure (5.24) Compressive Strength versus Void Porosity for Numerical Models Containing Small Non-Circular Voids – Both Square and Diamond Voids	168
Figure (5.25) Compressive Strength versus Void Porosity for Numerical Models Containing Non-Circular Voids – Both Square and Diamond Voids.....	169
Figure (5.26) Deformation versus Void Porosity for Numerical Models Containing	169
Figure (5.27) Deformation versus Void Porosity for Numerical Models Containing	170
Figure (5.28) Deformation versus Void Porosity for Numerical Models Containing Non-Circular Voids – Both Square and Diamond Voids.....	170
Figure (5.29) Compressive Strength versus Deformation for Numerical Models Containing Square Voids	171
Figure (5.30) Compressive Strength versus Deformation for Numerical Models Containing Diamond Voids	171
Figure (5.31) Compressive Strength versus Deformation for Numerical Models Containing Non-Circular Voids – Both Square and Diamond Voids.....	172
Figure (5.32) Compressive Strength versus Void Porosity for Numerical Models with Voids Having Different Size, Shape and Distribution.....	175
Figure (5.33) Deformation versus Void Porosity for Numerical Models with Voids Having Different Size, Shape and Distribution	175
Figure (5.34) Compressive Strength versus Deformation for Numerical Models with Voids Having Different Size, Shape and Distribution.....	176
Figure (5.35) Compressive Strength versus Deformation for Numerical Models with Voids Having Different Size, Shape and Distribution.....	176
Figure (5.36) Compressive Strength versus Void Porosity for Specimens Containing..	180
Figure (5.37) Compressive Strength versus Void Porosity for Specimens Containing..	180
Figure (5.38) Compressive Strength versus Void Porosity for Specimens Containing..	181
Figure (5.39) Compressive Strength versus Void Porosity for Specimens Containing..	181
Figure (5.40) Compressive Strength versus Void Porosity for Specimens Containing..	182
Figure (5.41) Deformation versus Void Porosity for Specimens Containing Unisize ...	182
Figure (5.42) Deformation versus Void Porosity for Specimens Containing Unisize ...	183
Figure (5.43) Deformation versus Void Porosity for Specimens Containing Unisize ...	183
Figure (5.44) Deformation versus Void Porosity for Specimens Containing Unisize ...	184
Figure (5.45) Deformation versus Void Porosity for Specimens Containing Unisize ...	184
Figure (5.46) Compressive Strength versus Void Porosity for Specimens Containing..	185
Figure (5.47) Compressive Strength versus Void Porosity for Specimens Containing..	185

Figure (5.48) Compressive Strength versus Void Porosity for Specimens Containing..	186
Figure (5.49) Compressive Strength versus Void Porosity for Specimens Containing..	186
Figure (5.50) Compressive Strength versus Void Porosity for Specimens Containing..	187
Figure (5.51) Compressive Strength versus Void Porosity for Specimens Containing..	187
Figure (5.52) Deformation versus Void Porosity for Specimens Containing.....	188
Figure (5.53) Deformation versus Void Porosity for Specimens Containing.....	188
Figure (5.54) Deformation versus Void Porosity for Specimens Containing.....	189
Figure (5.55) Deformation versus Void Porosity for Specimens Containing.....	189
Figure (5.56) Deformation versus Void Porosity for Specimens Containing.....	190
Figure (5.57) Deformation versus Void Porosity for Specimens Containing.....	190
Figure (5.58) Compressive Strength versus Void Porosity for Specimens Containing..	191
Figure (5.59) Deformation versus Void Porosity for Specimens Containing.....	191
Figure (5.60) Compressive Strength versus Void Porosity for Specimens with Voids Having Different Size, Shape and Spatial Distributions.....	192
Figure (5.61) Deformation versus Void Porosity for Specimens with Voids Having Different Size, Shape and Spatial Distributions	192
Figure (5.62) Compressive Strength versus Deformation for Specimens with Voids Having Different Size, Shape and Spatial Distributions.....	193
Figure (5.63) Ratios of Numerical Strength to Experimental Strength for.....	193
Figure (5.64) Ratios of Numerical Strength to Experimental Strength for.....	194
Figure (5.65) Ratios of Numerical Deformation to Experimental Deformation	194
Figure (5.66) Ratios of Numerical Deformation to Experimental Deformation	195
Figure (5.67) Experimental <i>UCS</i> versus Numerical <i>UCS</i> for Specimens.....	206
Figure (5.68) Experimental <i>UCS</i> versus Numerical <i>UCS</i> for Specimens.....	206
Figure (5.69) Experimental <i>UCS</i> versus Numerical <i>UCS</i> for Specimens.....	207
Figure (5.70) Experimental <i>UCS</i> versus Numerical <i>UCS</i> for Specimens Containing	207
Figure (5.71) Experimental <i>UCS</i> versus Numerical <i>UCS</i> for Specimens Containing	208
Figure (5.72) Experimental <i>E</i> versus Numerical <i>E</i> for Specimens Containing Voids....	208
Figure (5.73) Experimental <i>E</i> versus Numerical <i>E</i> for Specimens Containing Voids with Different Geometry – All Voids except Large Unisize Circular Voids.....	209
Figure (5.74) Experimental Experimental <i>E</i> versus Numerical <i>E</i> for Specimens Containing Non-Circular Unisize Voids with Different Geometry	209
Figure (5.75) Experimental <i>E</i> versus Numerical <i>E</i> for Specimens Containing Voids....	210
Figure (5.76) Experimental <i>E</i> versus Numerical <i>E</i> for Specimens Containing Voids....	210
Figure (6.1) Numerical Models to Simulate the Effects of Void Shapes – Large Size ..	213
Figure (6.2) Numerical Models to Simulate the Effects of Void Shapes – Small Size ..	214
Figure (6.3) Compression Strength versus Void Porosity for Numerical Models.....	218
Figure (6.4) Compression Strength versus Void Porosity for Numerical Models.....	218
Figure (6.5) Deformation versus Void Porosity for Numerical Models.....	219
Figure (6.6) Deformation versus Void Porosity for Numerical Models.....	219

Figure (6.7) Differences in Uniaxial Compression versus Void Porosity for Numerical Models Containing Unisize Voids – Both Large and Small Sizes	220
Figure (6.8) Differences in Deformation versus Void Porosity for Numerical	220
Figure (6.9) Compression Strength versus Deformation for Numerical Models Containing Unisize Voids – Both Large and Small Sizes	221
Figure (6.10) Numerical Models to Simulate the Effects of Void Orientation–Large Size	222
Figure (6.11) Compression Strength versus Void Porosity for Numerical.....	228
Figure (6.12) Compression Strength versus Void Porosity for Numerical.....	228
Figure (6.13) Deformation versus Void Porosity for Numerical Models.....	229
Figure (5.14) Deformation versus Void Porosity for Numerical Models.....	229
Figure (6.15) Compressive Strength versus Void Porosity for Numerical.....	230
Figure (6.16) Compressive Strength versus Void Porosity for Numerical.....	230
Figure (6.17) Deformation versus Void Porosity for Numerical Models.....	231
Figure (6.18) Deformation versus Void Porosity for Numerical Models.....	231
Figure (6.19) Compressive Strength versus Void Porosity for Numerical.....	232
Figure (6.20) Compressive Strength versus Void Porosity for Numerical.....	232
Figure (6.21) Deformation versus Void Porosity for Numerical Models.....	233
Figure (6.22) Deformation versus Void Porosity for Numerical Models.....	233
Figure (6.23) Total Width of Solid Columns (W) for Numerical Models Containing Six Large Unisize Voids	238
Figure (6.24) Normalized UCS versus Void Porosity for All Numerical Models.....	241
Figure (6.25) Normalized E versus Void Porosity for All Numerical Models.....	241
Figure (6.26) Normalized UCS versus Normalized Total Width of Solid Columns	242
Figure (6.27) Normalized E versus Normalized Total Width of Solid Columns	242
Figure (6.28) Normalized UCS versus Void Porosity versus and Normalized Total	243
Figure (6.29) Normalized E versus Void Porosity versus and Normalized Total	243
Figure (6.30) Compressive Strength versus Void Porosity and Deformation for.....	244
Figure (6.31) Compressive Strength versus Void Porosity, Deformation, and	244
Figure (I.1) Photographs of Tested Porous and Solid Cubes.....	257
Figure (II.1) COMPRESSION STRESS-STRAIN CURVE FOR THE CALIBRATED MODEL	276
Figure (II.2) POST-FAILURE MODE (IN COMPRESSION) FOR THE CALIBRATED MODEL	276
Figure(II.3) TENSION STRESS-STRAIN CURVE FOR THE CALIBRATED MODEL	277
Figure (II.4) POST-FAILURE MODE (IN TENSION) FOR THE CALIBRATED MODEL	277
Figure (III.1) Numerical Simulations for Hydro-StonTB [®] Cubes and Their Stress-Strain Curves - PA-UCL2-1	278

Figure (IV.1) Numerical Models and their Stress-Strain Curves - PA-UCL1..... 297

CHAPTER ONE INTRODUCTION

1.1 General

Existence of voids and cavities, specific type of discontinuities in rocks, can cause a dramatic change in mechanical properties of the rock. For instance, an increase in void porosity, ratio of volume of voids and cavities to the total volume of the rock, leads to a reduction in rock uniaxial compressive strength, *UCS*, and Young's modulus, *E*, (Dunn et al., 1973; Price 1983; Price et al., 1985; Logan 1987; Vernik et al., 1993; Avar 2002; BSC 2003; Price 2004; Hudyma et al., 2004; Costin et al., 2009). Since the pores and cavities are appearing in different sizes, the porosity is generally classified into two types; microporosity and macroporosity (Avar et al., 2003; Hudmya et al., 2004; Jespersen et al., 2010). The microporosity is created by micropores between rock minerals, or grains. The macroporosity, also void porosity, on the other hand, is created by larger pores (macropores) that are visible to the unaided eye such as large cavities, vugs and vesicles.

In rock mechanics, the effects of microporosity on the mechanical properties of rocks is usually ignored; it is assumed that microscopic porosity is uniformly distributed within the rock matrix, or laboratory specimens, and therefore, the rocks can be classified as intact rocks (Avar 2002). On the contrary, macroporosity has important roles on the rock's engineering behavior, and accordingly, its effects have been studied in different types of rocks such as basalt (Al-Harhi et al., 1999), chalk (Palchik and Hatzor 2004), and tuff (Price 1983; Tillerson, and Nimick 1984; Price et al., 1985 & 1994; Schultz and Li 1995; Avar 2002; BSC 2003; Price 2004; Hudyma et al., 2004; Costin et al., 2009). However, due to Yucca Mountain in Nevada, USA, which is the nation's first proposed

high-level nuclear waste repository, more attention has been given to tuff rock (BSC 2003; Rigby 2004).

1.2 Tuff Rock at Yucca Mountain

The host rock of portions of the first proposed high-level nuclear waste repository in the United States of America (Yucca Mountain, Nevada) is tuff rock; both lithophysal and nonlithophysal tuff (BSC 2003). Lithophysal tuff rock is pyroclastic volcanic rock (igneous rock) formed by welding of falling volcanic ash and has composition of high-silica rhyolite, contains wide range of lithophysae in sizes and shapes as shown in Figure (1.1) (Avar 2002; BSC 2003; Hudyma et al., 2004). Lithophysae are hollow, bubble like cavities formed by trapped pockets of gas within the volcanic ash (Avar 2002; BSC 2003). Their sizes are typically ranging from millimeters to decameter. The largest measured Lithophyse at Yucca Mountain, however, is 1.8 m across (BSC 2003). In many tuff rocks, a thin layer of vapor-phase minerals is coating the inner faces of the lithophysae. The coating layers are called rims and/or spots, and their thickness is less than few millimeters (BSC 2003). Accordingly, lithostratigraphic features in the tuff rocks of the Yucca Mountain are matrix-groundmass, the phase altered material around the lithophysal cavities (rims or spots), and the cavities (lithophysae) themselves (Price et al., 1985; BSC 2003). The matrix-groundmass consists of solid minerals that contain intergranular spaces (pores).

Non-lithophysal tuff rock, on the other hand, is fine-grained, densely welded, low porosity, strong volcanic rock that contains limited numbers of lithophysae, rims, and spots (BSC 2003).

In the reports and studies related to Yucca Mountain, the tuff porosity of Yucca Mountain is generally divided into four types; groundmass matrix porosity, rim and spot porosity, lithophysal porosity, and total porosity (Price 1983; Price et al., 1985; Avar 2002; BSC 2003). However, according to BSC (2003), it is the total porosity that plays an important role in assessing the mechanical properties of lithophysal tuff rocks.

The porosity of matrix groundmass consists of pores smaller than 2 micrometer, and its value for the Topopah Spring Tuff is about 10 percent; ranging from 8 to 13 percent (BSC 2003). The porosity of the rim and spot is typically ranging from 20 to 40 percent with 30 percent average (BSC 2003; Rigby 2004). The lithophysal porosity consists of pores vary in size from one millimeter to larger than a meter, and its value varies from 3 to 35 percent with 15 percent average (Rigby 2004). The summation of the above porosities is called total porosity. The total porosities can be calculated by several ways as follows:

- 1- Drying the tuff samples to determine the dry unit weight and then pulverizing them to find the specific gravity and using them in this equation $n(\%) = [(1 - (\gamma_d / G_s \gamma_w))]$ (Avar 2002). The specific gravity, G_s , is found from the ratio of weight of a particular volume of pulverized tuff to the weight of an equal volume of distilled water in accordance to ASTM D854. The dry unit weight, γ_d , is determined by using total volume of a specimen and its weight.
- 2- By saturating the specimen and the determining the volume of water that occupies the pores (BSC 2003).
- 3- By an approximation method using point counting and planimetric analysis (Price et al., 1985).



Figure (1.1) Photographs of Lithophysae-rich Tuff from Yucca Mountain (Rigby 2004; Nott 2009)

1.3 Rock-like Materials

Due to heterogeneity, breaking down during coring and sampling, and impossibility of controlling shape, size and distribution of voids, it is difficult to sample and test actual specimens; especially lithophysae-rich tuff (Rigby 2004; Erfourth 2006; Rigby 2007). Therefore, rock like material, instead, has been used to explore the effects of void porosity on the engineering properties of the rocks. It is quick, easy, and controllable. The majority of the specimens of the rock-like, analog, material specimens have been made of either plaster of Paris (gypsum plaster), or Hydro-StoneTB[®] (Avar 2002; Hudyma et al., 2004; Erfourth 2006; Rigby 2007). The Hydro-StoneTB[®] is a powdered mixture of plaster of Paris (more than 90% by weight), Portland cement (less than 5%), and sand (less than 5%) (Chawla 2007; Nott 2009).

However, the Hydro-StoneTB[®] is better analog material compared to the plaster of Paris regarding the lithophysal tuffs from Topopah Spring formation (Rigby 2007).

The average values of Young's modulus (E) and the uniaxial compressive strength (UCS) of plaster of Paris are about 3.1 GPa (Avar et al., 2003) and 11 MPa (Hydyma et al., 2004) respectively. These average values are very far from those of the lithophysal tuffs from Topopah Spring formation at Yucca Mountain; the average values of Young's Modulus and the uniaxial compressive strength of the lithophysal tuffs, from Topopah Spring formation at Yucca Mountain, are about 20 GPa and 60 MPa respectively (Rigby 2004). Therefore, in an attempt, Rigby (2007) adopted the Hydro-StoneTB[®] as a new rock like material to simulate the lithophysal tuffs from Topopah Spring formation at Yucca Mountain. From uniaxial compression tests carried out on cubical specimens (152 mm on a side), made of Hydro-StoneTB[®], Rigby (2007) obtained an average Young's modulus of 16 GPa and a strength of 55 MPa. It was also found that the brittle behavior of Hydro-StoneTB[®] was similar to those estimated for solid Yucca Mountain lithophysal tuff.

1.4 Study Objectives

The previous studies show that the higher void porosity leads to lower strength and stiffness of rock-like materials. However, the correlations between the mechanical properties of the rock-like materials with void porosity are not very clear and well-established. It is believed that, besides the void porosity, other geometric factors, such as void shape, void size, and void spatial distributions can affect the relationships between the engineering properties and void porosity. Identifying the significance of those factors will enhance insight into the effects of void geometry on engineering properties.

This study attempts to characterize the effects of void porosity on compressive strength and elastic models more definitively through considering the other factors in data analysis and seeks for more effective relationships between them. In addition, new numerical models generating to study the effects of void geometry on engineering properties of rock-like materials more thoroughly. The methodology of this study composed of three main parts. The first part comprises presenting and analyzing data obtained from the work conducted under Cooperative Agreement No. DEFC28-04RW12232 between the U. S. Department of Energy and the Nevada System of Higher Education (NSHE). For the second part, the experimental test data in the first part are used to validate numerical models of rock-like material using a discontinuum computer program; Universal Distinct Element Codes - UDEC. In the third phase, another numerical analysis will be performed to study the effect of void geometry on mechanical properties more systematically.

1.5 Dissertation Outline

The outline of this dissertation is as follows

- Chapter 2 reviews the experimental and numerical studies those carried out on both actual rocks and rock-like material specimens to investigate the effects of void porosity on strength and deformation properties and crack patterns.
- Chapter 3 presents a general description on the mechanical characterization of brittle materials generally and rocks particularly; it is concerning with the mechanical characterization of brittle, homogenous, and isotropic materials, including rocks, under static load.

- In Chapter 4, the results of experimental tests carried out on cubes made of rock-like material containing voids with different shape, size, and distribution are analyzed in order to obtain mathematical models describing the variation of strength and deformation properties with porosity. In addition, the effects of porosity on failure crack patterns of the cubic specimens are addressed.
- Chapter 5 represents numerical analysis to simulate the experimental tests in Chapter 4.
- Chapter 6 represents a new set of numerical models in order to study the mechanical behavior of the analog material under compression considering new void shapes, void orientations, and voids distribution.
- Finally, the conclusions and recommendations are given in Chapter 7.

CHAPTER TWO *LITERATURE RIVIEW*

2.1 Introduction

To quantify the effects of void porosity, macroporosity, on rock engineering behaviors, several studies have been carried out on both actual rock samples and rock-like materials. However, in general, the studies are very few in number and so far limited to three rock types; basalt (Al-Harathi et al., 1999), chalk (Palchik and Hatzor 2004), and tuff (Price 1983; Tillerson and Nimick 1984; Price et al., 1985 & 1994; Schultz and Li 1995; Avar 2002; BSC 2003; Price 2004; Rigby 2004; Hudyma et al., 2004; Costin et al., 2009). For the reasons mentioned in the previous chapter, it is difficult to sample and test actual rock specimens. Therefore, rock like material, instead, has been used to explore the effects of void porosity on the engineering properties of the rocks. The majority of the specimens were made of either plaster of Paris (Gypsum plaster) or Hydro-StoneTB® (Avar 2002; Hudyma et al., 2004; Erfourth 2006; Rigby 2007; Nott 2009; Jespersen et al. 2010).

2.2 Actual Rock Samples

2.2.1 Tuff Rock

To assess mineability and stability of underground openings in the Yucca Mountain, and to explore the effects of lithophysae presence, the mechanical properties of tuff rock was intensively studied in the Yucca Mountain Project. Therefore, adequate experimental data are available on tuff rock obtained from several studies carried out by Sandia National Laboratories, in association with the Yucca Mountain project. However,

the sizes of the tested samples in the above researches were mainly 50.8 mm or smaller in diameter with length to diameter ratio of approximately 2.0. The experimental data on the small diameter samples (25 mm to 50 mm) are described in the BSC (2003), and additional analysis is presented in Rigby (2004). The results showed a sharp decline in both elastic modulus and compressive strength with increasing porosity, see Figures (2.1) and (2.2). However, the data showed a very large scattering in both tuff's compressive strength and elastic modulus. Part of the scatterings might be due to the specimen size (Rigby 2004). According to Rigby (2004), due to small specimen size, the total porosity of these samples, typically ranged from 8 to 19 percent, captures only small amounts of lithophysae; the total porosity of the small samples was primarily composed of matrix porosity, with additional porosity, of course, contributed by small amounts of rims, spots, and lithophysae. Therefore, the results may not precisely represent the actual strength or elastic properties of the lithophysal tuff rock; the results may be biased and not indicative. Accordingly, this section is only considering the studies in which tuff specimens with diameter (or side dimension) greater than 50.8mm have been tested.

In an experimental program to study the mechanical properties of Yucca Mountain's tuff, Price et al. (1985) tested ten large-diameter cores of lithophysal tuff rock (266.7 mm in diameter and 533.4 mm in length) recovered from outcrops of Busted Butte (Nevada Test Site at Yucca Mountain). The tuff specimens were first water saturated, shown in Figure (2.3), and then tested under uniaxial compression at room temperature (23° C). The specimens had total porosities ranging from 30.9% to 40% with an average of 35.2%. The total porosities, summations of large lithophysal cavities (under several centimeter), small pores (under 0.2 mm), and intergranular pores (1-2 micrometer) in

vapor-phase-altered zones around lithophysae, and submicroscopic intergranular pores in the devitrified matrix, were measured using point counting and planimetric analysis. From the results, since the specimen's porosities were distributed in a narrow range, a conclusive relationship between mechanical properties (uniaxial compressive strength and Young's modulus) and the total porosity was not obtained. However, when the results were supplemented by previous testing by Price (1983) on saturated small specimens of tuff (25.4 mm in diameter and 50.8 mm in length), the results showed that, for the corresponding porosities, the strength of the large lithophysal specimens were lower and Young's moduli were higher than those of small size specimens as shown in Figures (2.4) and (2.5). They contributed these findings, lower strength and higher Young's modulus, to the existing of large pores in the large samples; smaller pores in the small size samples led to stiffer system, smaller short-term built-up of pore pressure, and more homogeneity compared to the large samples.

In 2002, to study the mechanical properties of lithophysal tuff rocks using large size samples, thirteen large-diameter core specimens having 290 mm diameter with a length to diameter of 1.7 or greater (a length of at least 304 mm) were recovered from repository host horizon at Yucca Mountain. All thirteen specimens, four saturated and nine room dried, were tested under uniaxial compression at room temperature (24° C) (discussed in Price 2004 and Rigby 2004). The lithophysal porosities, ranging from 11.9% to 30.3%, were found by conducting four vertical line surveys down the length of each specimen. The total porosities, ranging from 25.6% to 51.7%. were estimated by summing: (1) matrix porosity, (2) rims and spots porosity, and (3) lithophysal porosity. The results were supplemented by previous testing by Price et al. (1985) on ten saturated

large-diameter specimens of tuff (266.7 mm in diameter and 533.4 mm in length). From the high scatter results, it can be seen that the uniaxial compressive strength and Young's modulus (E) decrease exponentially with increasing void porosity for both room dry and saturated sample conditions as shown in Figures (2.6) and (2.7). However, the saturated sample conditions showed lower strength compared to the room dry sample conditions. The result yielded the following best fit-regressions:

$$\text{Room Dry, UCS(MPa)} = 39.235e^{-0.032*Porosity (\%)} \quad R^2 = 0.43 \quad \dots (2.1)$$

$$\text{Saturated, UCS(MPa)} = 28.473e^{-0.0383*Porosity (\%)} \quad R^2 = 0.282 \quad \dots (2.2)$$

$$\text{Room Dry, E (GPa)} = 33.452e^{-0.0593(Porosity,\%)} \quad R^2 = 0.69 \quad \dots (2.3)$$

$$\text{Saturated, E (GPa)} = 27.405e^{-0.0497*Porosity (\%)} \quad R^2 = 0.156 \quad \dots (2.4)$$

In addition, the results showed an increase in uniaxial compressive strength with an increase in the Young's modulus following a linear law, see Figures (2.8), as follows:

$$\text{Room Dry, UCS(MPa)} = 0.9832 * E (GPa) + 10.593 \quad R^2 = 0.587 \quad \dots (2.5)$$

$$\text{Saturated, UCS(MPa)} = 0.6625 * E (GPa) + 67239 \quad R^2 = 0.556 \quad \dots (2.6)$$

Furthermore, in an numerical analysis, Christianson et al. (2006) used the aforementioned experimental results (results of experimental tests on large-diameter core specimens having either 267 mm diameter or 290 mm diameter) to verify their numerical simulations. In the numerical analysis, universal distinct element code (UDEC) software was used to general 1 m x 1 m plain strain models. The material in the models was

described by randomized Voronoi tessellation technique. In this technique, Voronoi tessellation, the model material is represented by an assemblage of small discrete blocks (or sub-blocks or grains – having average dimension of 17 mm) by which the realistic crack initiation and propagation can be achieved. To generate lithophysal cavities in the numerical models, 90-mm diameter holes were cut into the solid models with three different hole configurations. By the three different hole configurations, three different porosity, 10, 17, and 24%, were obtained. The numerical results were consistent with the experimental results in both strength and deformation as shown in Figures (2.9) and (2.10); both compressive strengths and Young’s modulus of the numerical models decreased exponentially with increasing porosity in the same trend of the experimental tests. The best fit regressions are:

$$\text{Numerical } UCS, q(MPa) = 51.648e^{-6.202*Porosity (\%)} \quad R^2 = 0.9344 \quad \dots(2.7)$$

$$\text{Numerical } E, (GPa) = 19.68 * e^{-3.1677*Porosity (\%)} \quad R^2 = 0.9344 \quad \dots(2.8)$$

In an experimental program to study the effects of porosity on the mechanical properties of tuff for his dissertation, Avar (2002), tested ten cubes (approximately 150 mm per side) of lithophysae-rich tuff cut from blocks recovery from Busted Butte, Fran Ridge and Sandia Quarry near Yucca Mountain on the Nevada Test Site. Several plaster samples were also tested in the same experimental program. The ten tuff specimens, had total (bulk) porosities ranging from 12.2 to 32.9%, and were tested dry at room temperature under uniaxial compression. The tuff specimen total porosities, %, were calculated using this equation:

$$Total\ porosity, \% = \left[\left(1 - \frac{\gamma_d}{G_s \gamma_w} \right) \right] \quad \dots (2.9)$$

where G_s is specific gravity, γ_d is dry unit weight, and γ_w is water unit weight. The specific gravity, G_s , was found from the ratio of weight of a particular volume of pulverized tuff to the weight of an equal volume of distilled water in accordance to ASTM D854. The dry unit weight of the tuff, γ_d , was determined by using total volume of a specimen and its weight. Figure (2.11) shows some of the tuff specimens used in this study. The results showed that both compressive strengths and deformation decreased with increasing porosity, see Figures (2.12a & b), giving linear relationship as shown below:

$$UCS, (Psi) = -372.6 * Porosity (\%) + 14025 \quad R^2 = 0.76 \quad \dots (2.10)$$

$$E, (Ksi) = -44.616 * Porosity (\%) + 1699.4 \quad R^2 = 0.77 \quad \dots (2.11)$$

Hudyma et al. (2004) tested several cubic specimens of tuff to explore the effects of lithophysae on compressive strength. The tuff samples, cut from outcrops of Topopah Spring Tuff at Yucca Mountain, had approximately 100 mm per side (as shown in Figure (2.13)) and total porosities ranging from 17 to 49%. The tuff specimen total porosities were calculated using the same method as Avar (2002); using this equation $[(1 - (\gamma_d / G_s \gamma_w))]$ in accordance with ASTM D854 (2002). Similarly, the specific gravity, G_s , was found from the ratio of weight of a particular volume of pulverized tuff to the weight of an equal volume of distilled water. The dry unit weight, γ_d , was determined by using total

volume of a specimen and its weight. By incorporating this data with previous tests carried out by Price et al. (1985), Martin et al. (1994, 1995), and Avar (2002), a wide range of porosities, from approximately 12 to 49%, were covered. The very scattering results gave a logarithmic relationship between uniaxial compression strength and porosity, see Figure (2.14), as follows:

$$UCS, (MPa) = -49.36 * \ln Porosity (\%) + 189.35 \quad R^2 = 0.62 \quad \dots (2.12)$$

In a more recent study, to characterize mechanical behaviors of the, Costin et al. (2009) tested several large cores of lithophysal tuff recovered from outcrops at Yucca Mountain nearby Busted Butte lithophysal rock units. To achieve the goals of the study, and considering the compatibility between size distribution of lithophysae (25-75 mm) with core sizes, and adopting the length to diameter ratio of ≥ 2 , tuff specimens having approximately 300 mm diameter to 600 mm in length were cored and tested under uniaxial compression, see Figure (2.15a & b). The samples were tested either at room temperature, for both saturated and room dry conditions, or at 200 °C (room dry only). The total porosity, which includes the porosity of the matrix material, the phase altered material around the lithophysal cavities, and the cavities themselves, were found to be between 35 to about 50 percents for samples tested at room temperature; both room dried and saturated. The result showed that uniaxial compressive strength of the high lithophysal tuff was inversely proportional to the porosity and directly proportional to the elastic modulus as can be seen from Figures (2.16) and (2.17)). However, no relationship was given.

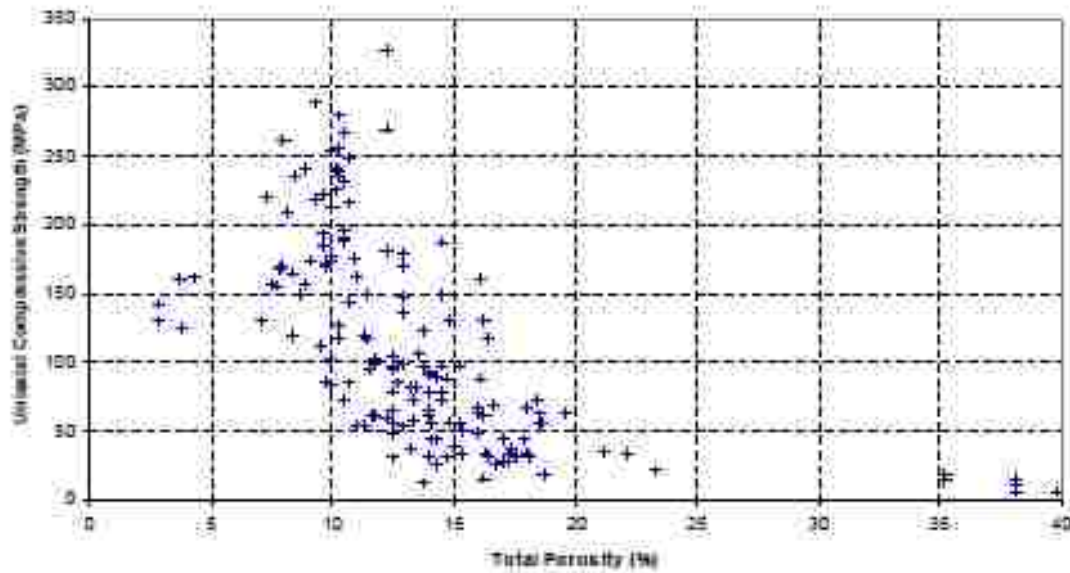


Figure (2.1) Uniaxial Compressive Strength for Saturated Specimens of Topopah Spring Tuff (samples with 50.8 mm or smaller in diameter) (Rigby 2004)

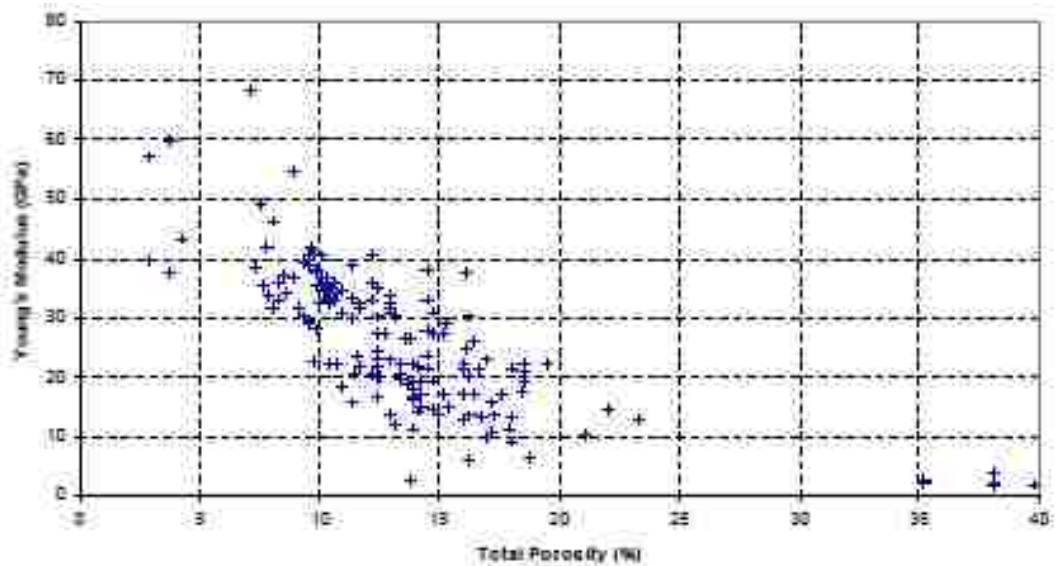


Figure (2.2) Young's Modulus for Saturated Specimens of Topopah Spring Tuff (samples with 50.8 mm or smaller in diameter) (Rigby 2004)



Figure (2.3) Photograph of the Large (267 mm) Diameter Cores from Busted Butte Samples (Rigby 2004)

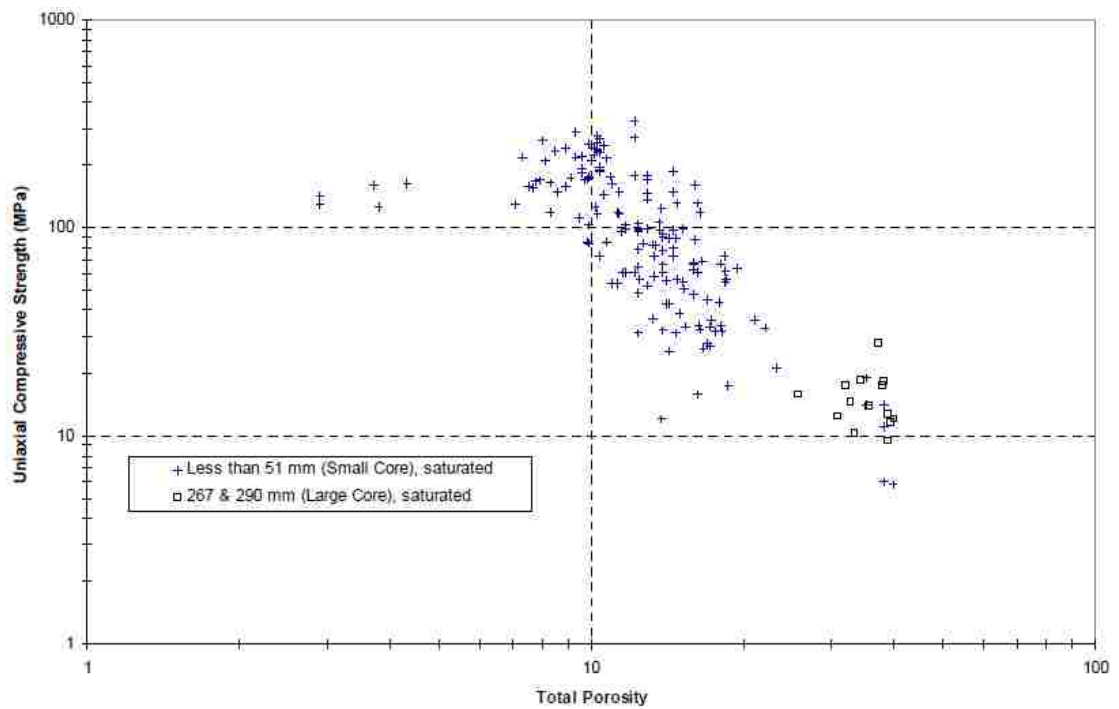


Figure (2.4) Correlation between Uniaxial Compressive Strength of Tuff and the Porosity (Small and Large-Diameter Cores of Topopah Spring Tuff) (Rigby 2004)

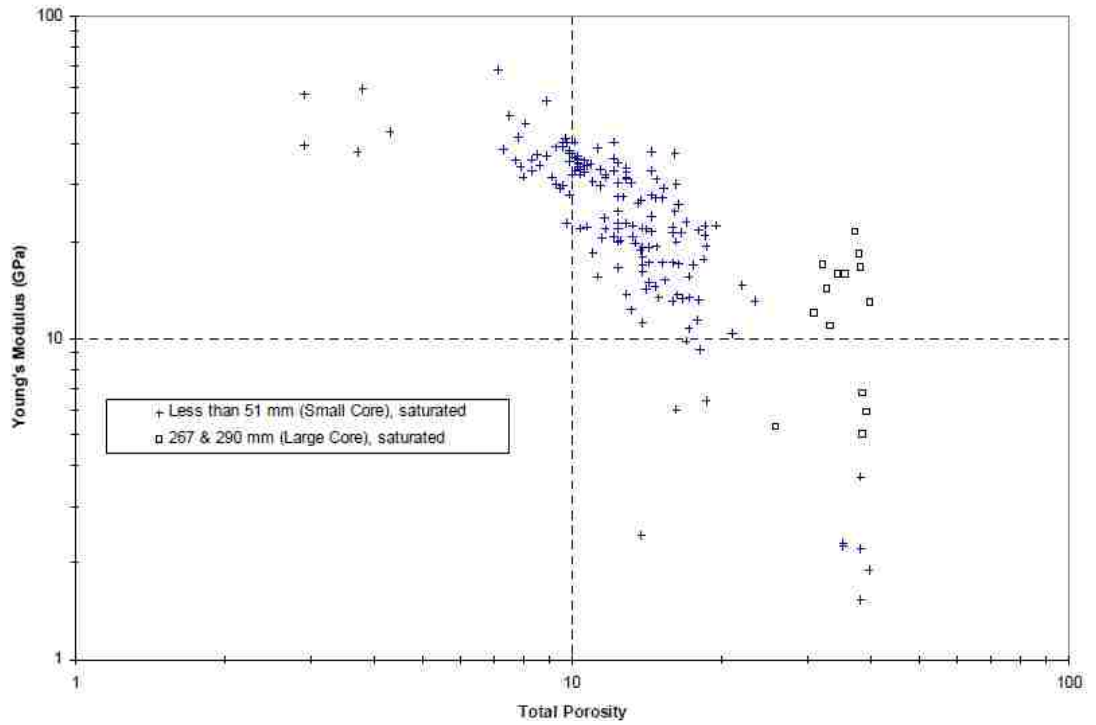


Figure (2.5) Correlation between Young's Modulus of Tuff and the Porosity (Small and Large-Diameter Cores of Topopah Spring Tuff) (Rigby 2004)

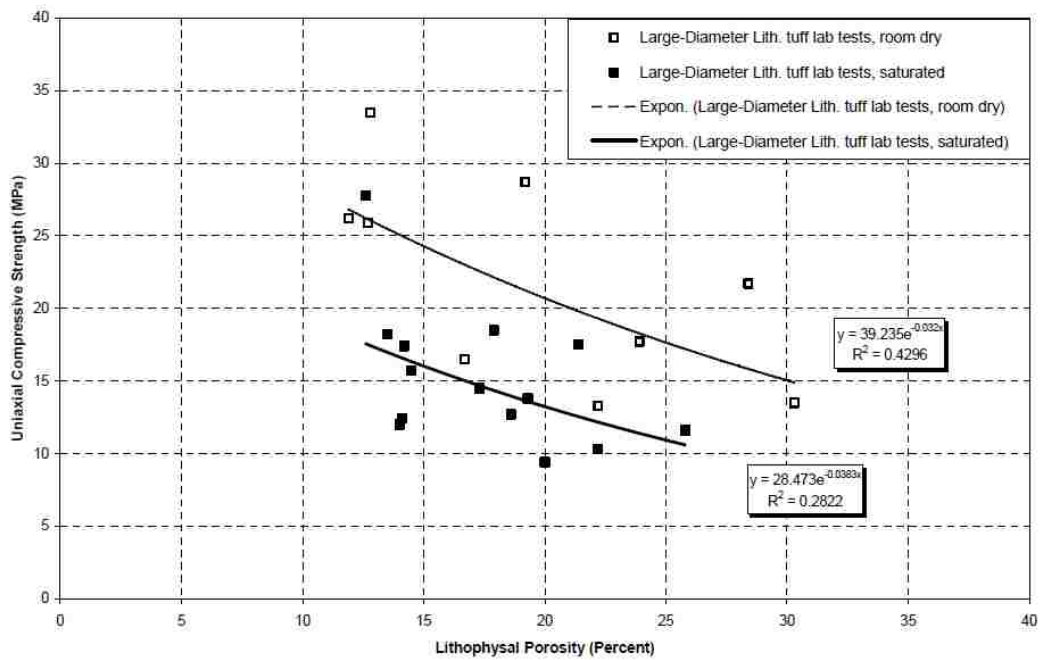


Figure (2.6) Correlation between Uniaxial Compressive Strength of Tuff and the Porosity (Large-Diameter Cores of Topopah Spring Tuff) (Rigby 2004)

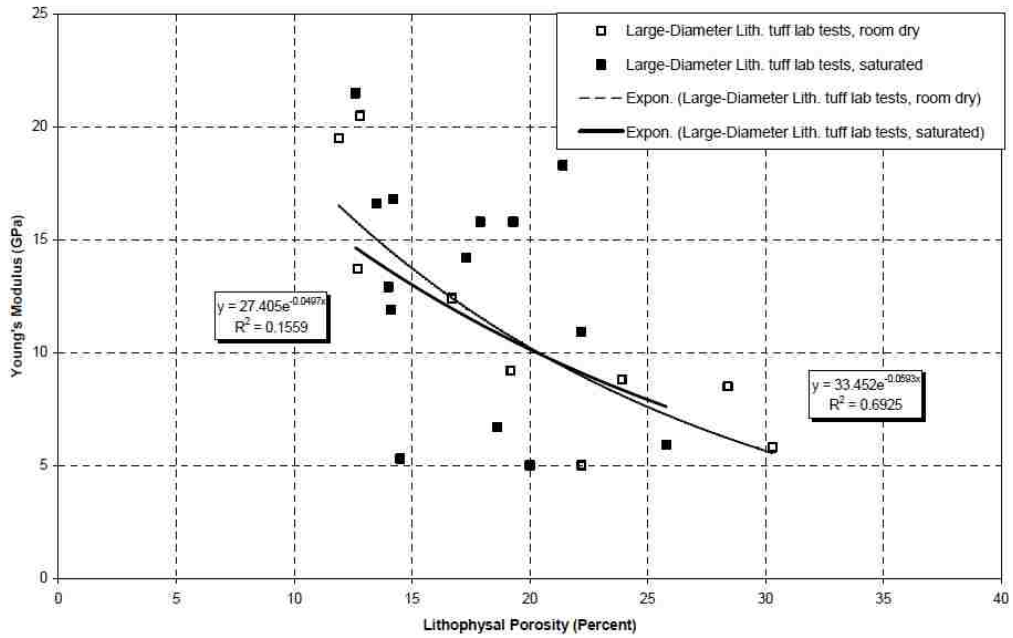


Figure (2.7) Correlation between Young's Modulus of Tuff and the Porosity (Large-Diameter Cores of Topopah Spring Tuff) (Rigby 2004)

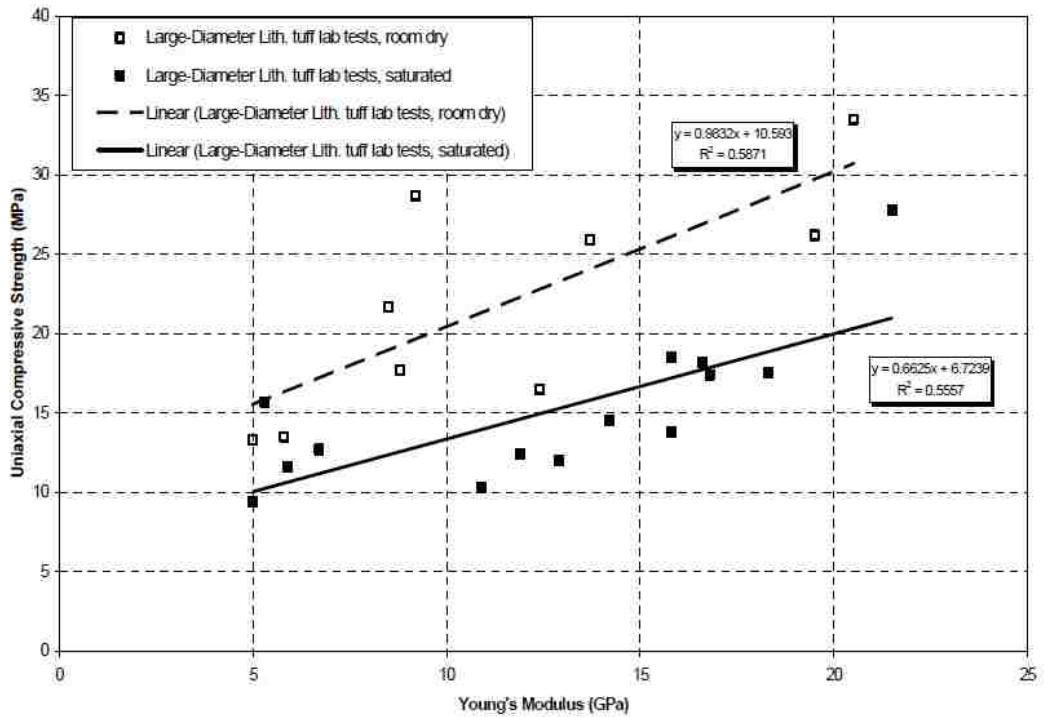


Figure (2.8) Correlation between Uniaxial Compressive Strength and the Young's Modulus Large-Diameter Cores of Topopah Spring Tuff (Rigby 2004)

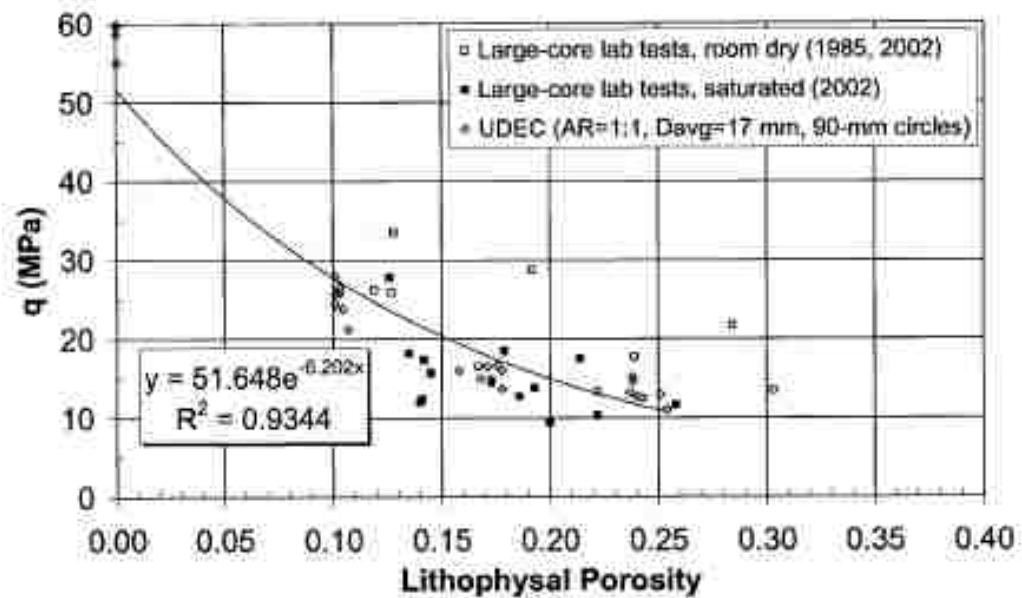


Figure (2.9) Comparison of UDEC Numerical Models to Experimental Tests on Lithophysal Tuff Regarding Uniaxial Compressive Strength (UCS) (Christianson et al., 2006)

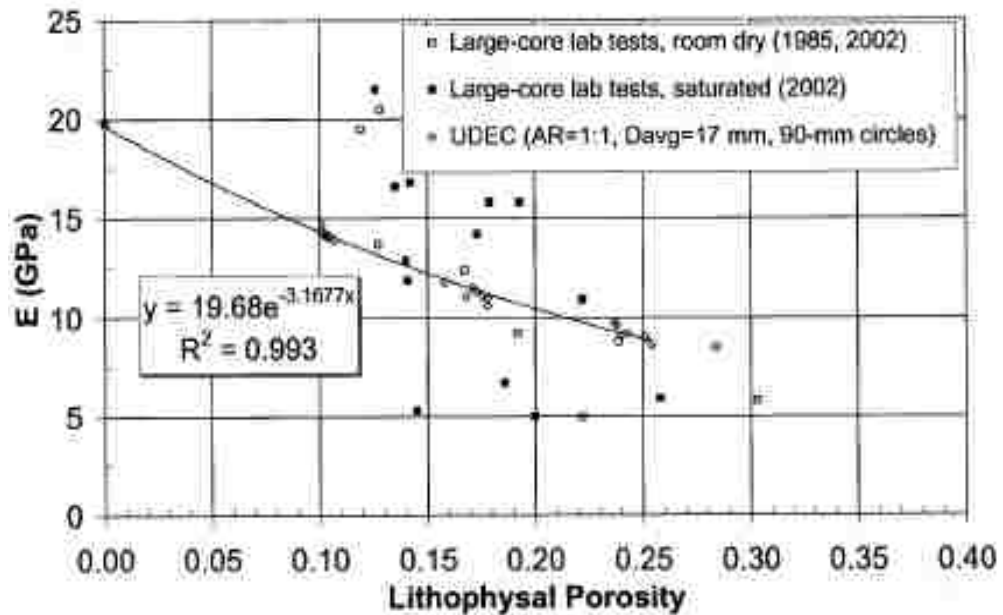


Figure (2.10) Comparison of UDEC Numerical Models to Experimental Tests on Lithophysal Tuff Regarding Young's Modulus (E) (Christianson et al., 2006)

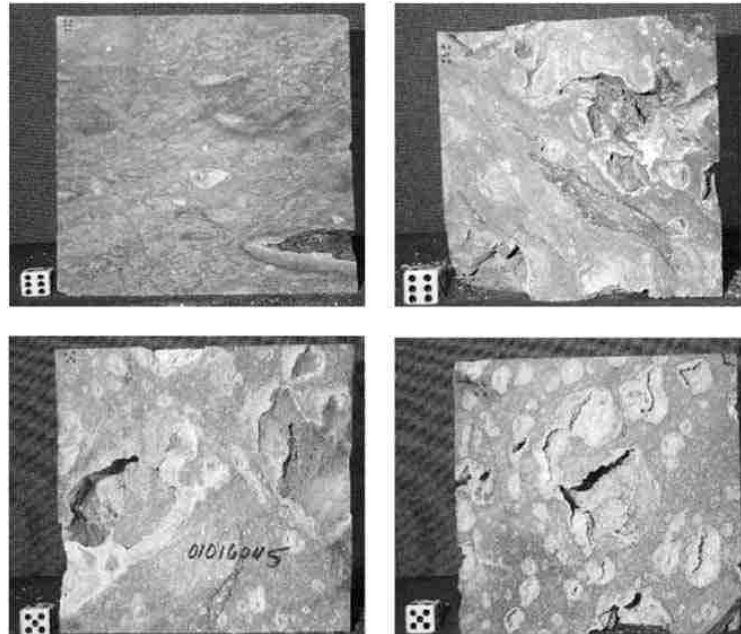


Figure (2.11) Photograph of Some Tuff Specimens Tested by Avar (2002)

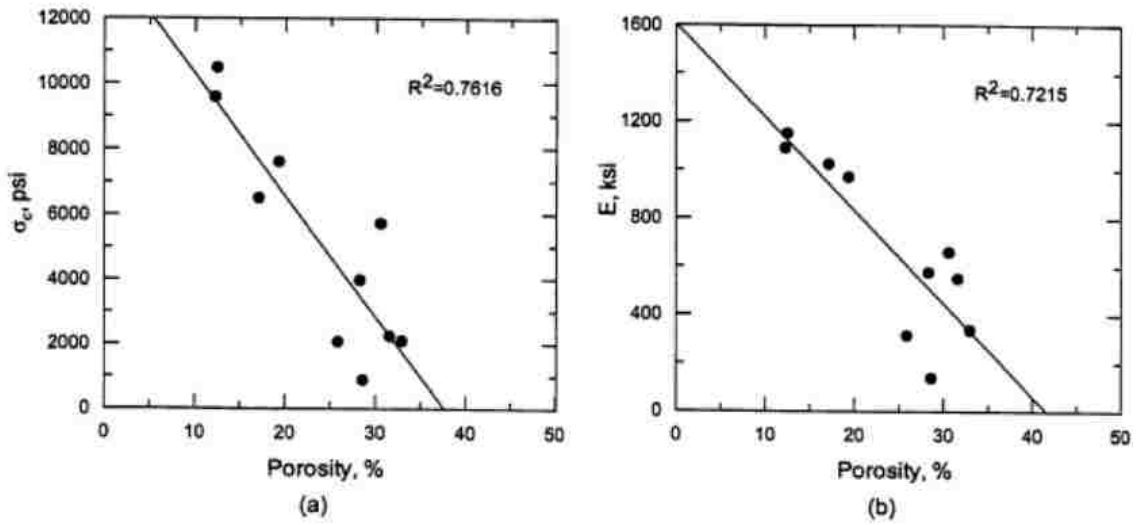


Figure (2.12) Correlation between Mechanical Properties of Tuff and the Total Porosity (Avar 2002)



Figure(2.13) Photograph Some Tuff Specimens Tested by Hudyma et al. (2004)

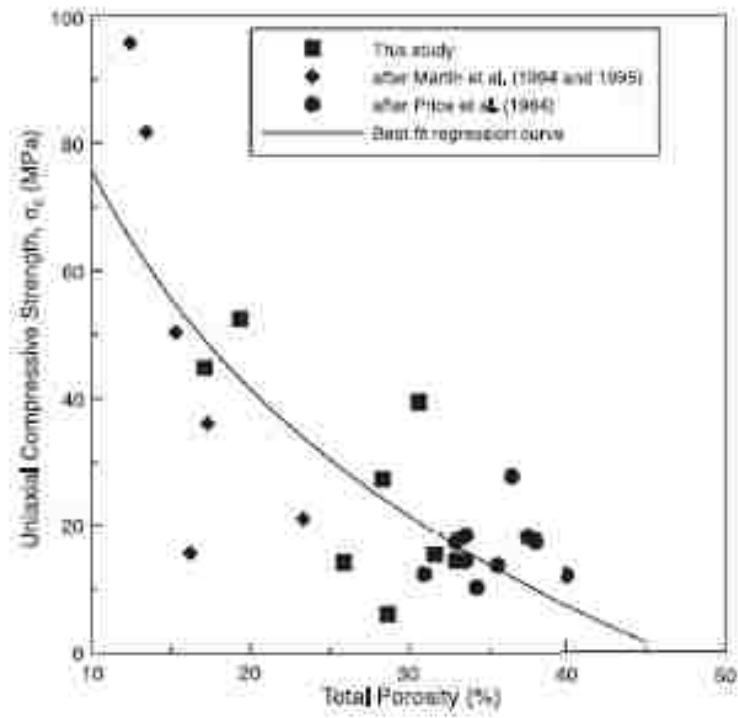


Figure (2.14) Correlation between UCS versus the total Porosity (Hudyma et al., 2004)

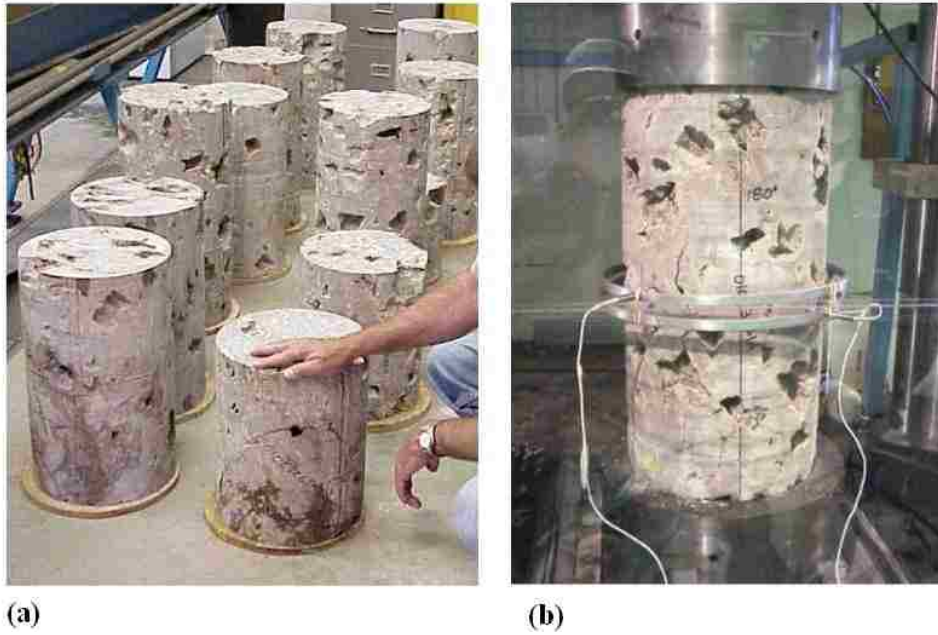


Figure (2.15) Photograph of Large-Diameter Cores of Tuff; **(a)** Samples before testing, and **(b)** Samples during testing (Costin et al., 2009)

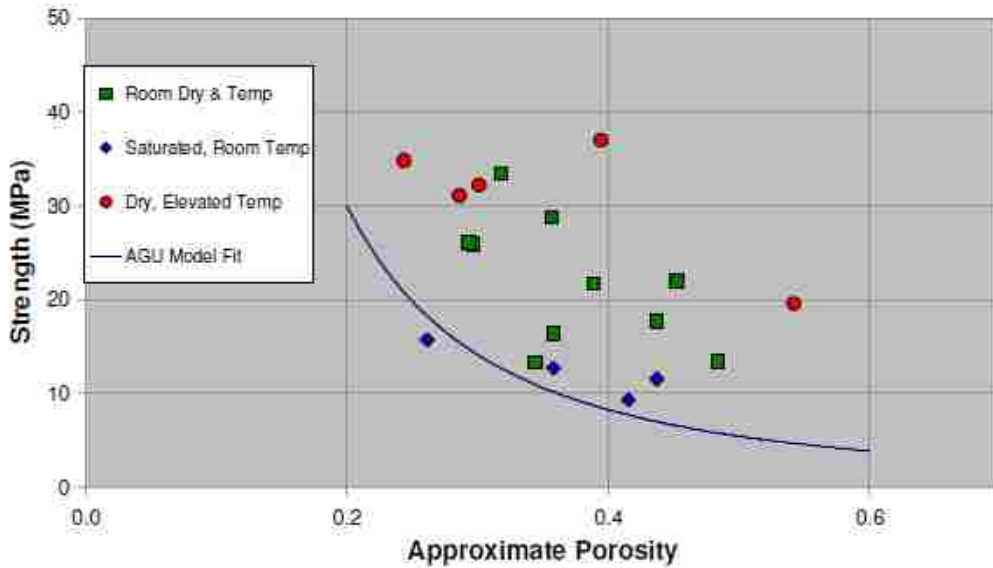


Figure (2.16) Correlation between Uniaxial Compressive Strength and the approximate (total) Porosity (Costin et al., 2009)

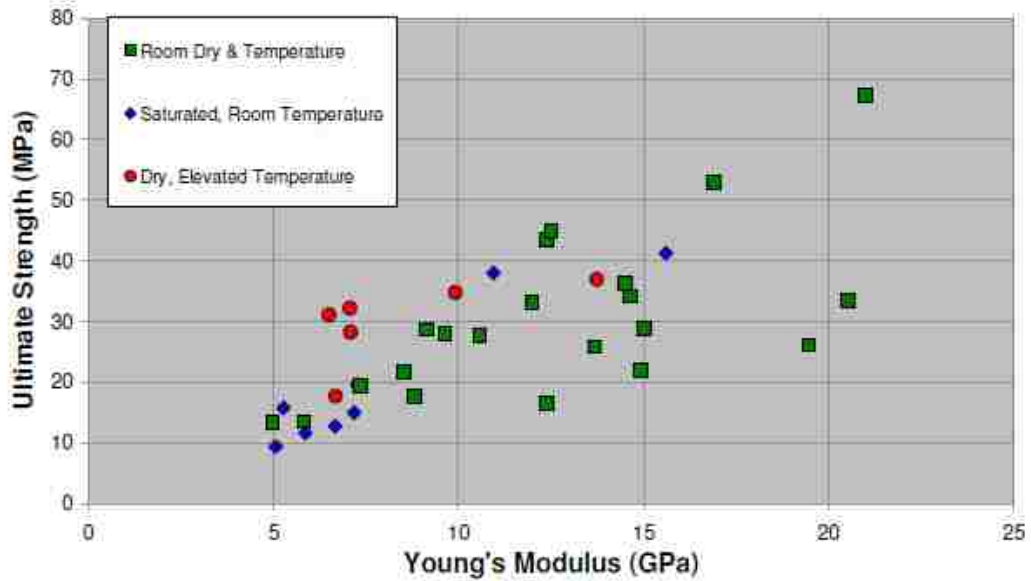


Figure (2.17) Correlation between Uniaxial Compressive Strength and Young's Modulus (Costin et al., 2009)

2.2.2 Basalt

The variations of mechanical properties of vascular basalt due to porosity changing were investigated experimentally by Al-Harhi et al. (1999). The vesicles in the basalt were non-connected pores, spherical to irregular in shapes, with sporadic to densely spatial distribution (Fig. 2.18a). Their sizes (diameter) range from a fraction of a millimeter to few centimeters (Fig. 2.18b & c). The vesicle porosities (from about 0 to about 65%) were found using two methods; image analysis technique (on thin cross-section of basalts) and weight and volume correlations. Both dynamic and static properties of vesicular basalt were explored. For the dynamic properties, the effects of vesicle porosity on both dynamic modulus of elasticity and dynamic Poisson's ration were explored using non-destructive technique of sonic pulse velocity measurement for the specimens. Regarding the static properties (uniaxial compression, static modulus of

elasticity, and static Poisson's ratio), the same basalt specimens used in the dynamic properties study were tested under uniaxial compression to find the variation of strength and deformation of the basalt with vesicle porosity. It was found that the static property estimations can be done with higher confidence compared to dynamic property estimation. According to the results, proposed in two part correlations as shown in Figure (2.19), a sharp reduction in both UCS and modulus of elasticity was observed until a porosity value of 20% reached. For the porosity > 20%, a relatively mild reduction was obtained. The correlations between both UCS and modulus of elasticity with vesicle porosity were good. For the UCS, the two-part correlations were linear, and the correlations were as follows

$$\text{For Porosity} \leq 20 \quad \mathbf{UCS} \text{ (MPa)} = 274 - 8.51 * \text{Porosity}(\%) \quad R^2 = 0.98 \quad \dots \text{ (2.13)}$$

$$\text{For Porosity} > 20 \quad \mathbf{UCS} \text{ (MPa)} = 104 - 1.01 * \text{Porosity}(\%) \quad R^2 = 0.96 \quad \dots \text{ (2.14)}$$

For the modulus of elasticity, Young's Modulus (E), the correlations was initially logarithmic and then linear, see Figure (2.20). The best-fit regression equations were as follows

$$\text{For Porosity} \leq 20 \quad \mathbf{E} \text{ (GPa)} = 75.7 - 9.38 * \ln \text{Porosity}(\%) \quad R^2 = 0.95 \quad \dots \text{ (2.15)}$$

$$\text{For Porosity} > 0 \quad \mathbf{E} \text{ (GPa)} = 48.4 - 0.675 * \text{Porosity}(\%) \quad R^2 = 0.95 \quad \dots \text{ (2.16)}$$

Regarding the Poisson's ratio, it increased as the porosity increased linearly until a porosity value of 20%, and became more or less constant for porosity values > 20%. The best-fit regression equations are:

$$\text{For Porosity} \leq 20 \quad \nu = 0.189 - 0.002 * \text{Porosity}(\%) \quad R^2 = 0.96 \quad \dots (2.17)$$

$$\text{For Porosity} > 20 \quad \nu = 0.235 \quad R^2 = 0.003 \quad \dots (2.18)$$

Although supported by several previous researchers such as Kelsall et al. (1986) and Tugrul and Gurpinar (1997), the results, except the second part of Poisson's ratio, showed good relationships (see the correlation coefficients) and well defined which are rare in researches in rock mechanics field. No explanations are given by the researches. In addition, the effects of vesicle shapes and vesicle spatial distributions have not been addressed.

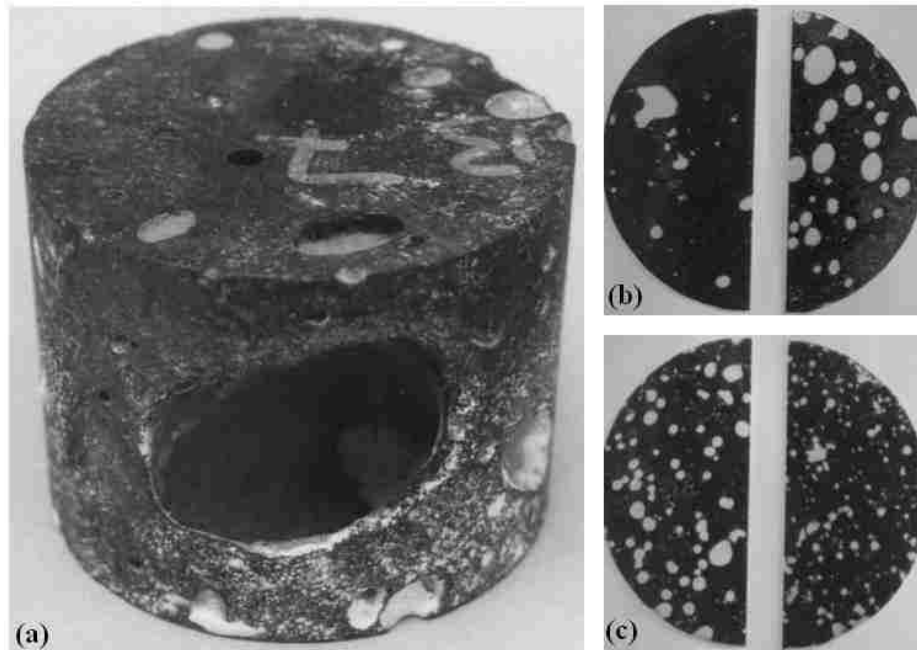


Figure (2.18a, b, & c) Photograph Samples of Vesicular Basalt Tested by Al-Harhi et al. (1999).

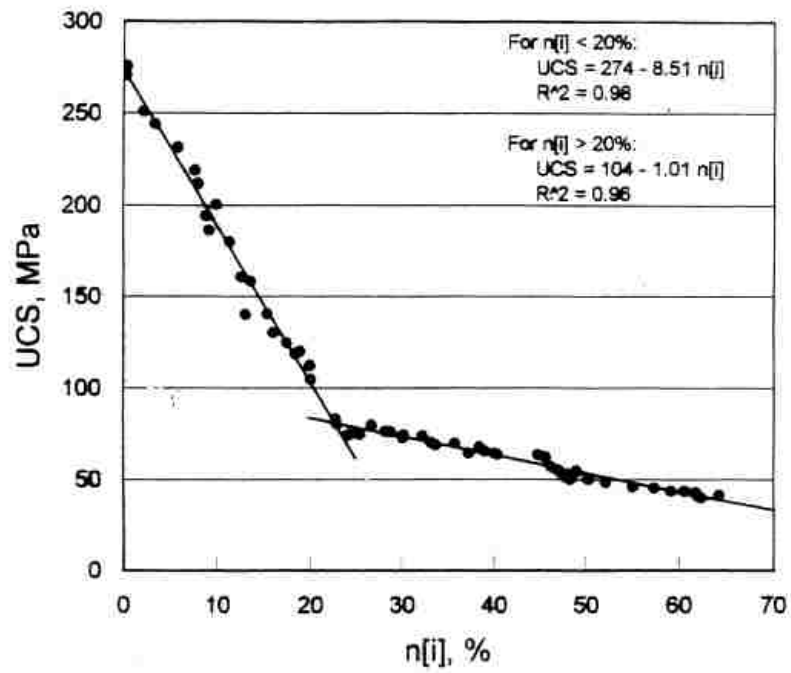


Figure (2.19) Correlation between Uniaxial Compressive Strength of Vesicular Basalt and the actual Porosity (Al-Harhi et al., 1999).

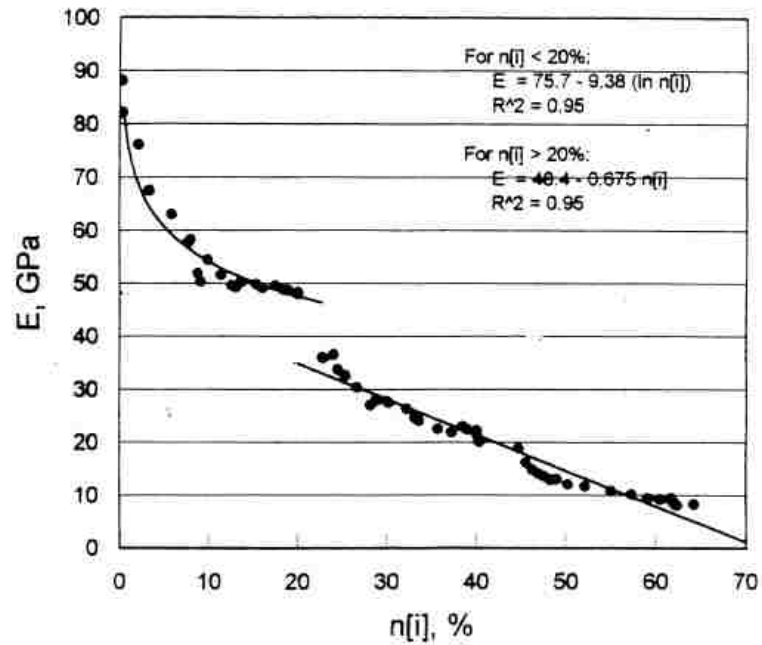


Figure (2.20) Correlation between Young's Modulus, E , of Vesicular Basalt and the actual Porosity (Al-Harhi et al., 1999).

2.2.3 Chalks

To study the effect of porosity on strength of very porous chalks, Palchik and Hatzor (2004) tested twelve cylindrical specimens under uniaxial compression. The specimens, 52mm in diameter with length to diameter ratio of approximately 2.0, were taken from Adulam formation in Israel having total porosity ranging from 19% to 32%. The chalk specimen total porosities were calculated using the same method as Avar (2002); using this equation $n = [(1 - (\gamma_d / G_s \gamma_w))]$. However, the specific gravity, G_s , was first assumed to be 2.7 and then validated by using Helium porosimeter. In the porosity validation, a very good linear correlation ($R^2 = 0.99$) between the calculated (assuming $G_s = 2.7$) and measured porosity values was obtained. No information about pore size and distribution is given. Returning to the previous discussion regarding tuff samples, test results with small size samples are not indicative, however, the uniaxial compression test results showed a decrease in compressive strength (uniaxial compressive strength - UCS) with an increase in the porosity following an exponential law. Figure (2.21) shows the result of the twelve tested samples. The best fit-regression equation is:

$$UCS(MPa) = 273.15 e^{-0.076 * Porosity (\%)} \quad R^2 = 0.87 \quad \dots (2.19)$$

The effect of porosity on the Young's modulus is not addressed.

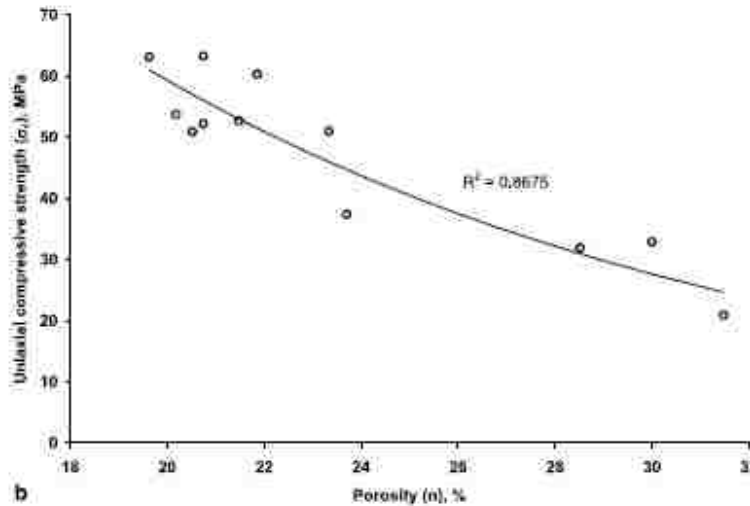


Figure (2.21) Correlation between Uniaxial Compressive Strength of Chalk and Porosity (Palchik and Hatzor 2004)

2.3 Rock-like Materials

Until nowadays, few studies have been carried out to explore the effects of void porosity on the engineering properties of the rocks using rock-like materials. In this section, most of them will be reviewed.

Avar (2002) studied the influence of void porosity on the mechanical behavior of rock-like materials (gypsum plaster and urethane) both experimentally and numerically. The plaster cubes, 150 mm on side and contained either open ended cylindrical tubes or spherical Styrofoam inclusions were tested under uniaxial compression loads. The open ended cylindrical tubes, with diameters ranging from 6.4 mm to 108.7 mm giving porosities ranging from 4.9 to 44.2%, were distributed either uniformly or randomly throughout the cubes. While the spherical cavities, ranging from 25.4 mm to 101.6 mm in diameter giving porosities ranging from 8 to 40%, were distributed randomly only. The

urethane cubes (with 150 mm per side) contained open ended cylindrical tubes distributed uniformly only, and tested under biaxial compression loads. The urethane is a rubber type material produced under a controlled environment and used in this study in order to explore the effects of porosity on the elastic properties of elastic materials. Regarding the numerical analysis, two-dimensional finite difference FLAC software was used to simulate both the urethane cubes and the plaster cubes containing open ended cylindrical tubes. Both numerical analysis and experimental testing showed a very good correlation; the numerical normalized Young's modulus decreased exponentially with increasing porosity like those of the experimental tests on the urethane cube as shown in Figure (2.22) and the following two equations

$$\left(\frac{E}{E_o}\right)_{Experimental} = e^{-0.023*Porosity(\%)} \quad R^2 = 0.9664 \quad \dots (2.20)$$

$$\left(\frac{E}{E_o}\right)_{Numerical} = e^{-0.0215*Porosity(\%)} \quad R^2 = 0.9899 \quad \dots (2.21)$$

For the plaster cubes contained open ended tubes, the numerical results overestimated the Young's modulus as shown in Figure (2.23). This was attributed to either modeling a three-dimensional material in two dimensions, or ignoring the effect of friction between the steel platen and the plaster cubes, or both. Regarding the experimental tests on the plaster cubes contained open ended tubes, the results showed that the plaster cubes contained uniformly distributed open ended tubes had higher compressive strength and Young's modulus compared to those plaster cubes contained randomly distributed open ended tubes. This was attributed to existing larger plaster columns between the uniformly distributed holes; larger bridge distances between the holes. Figures (2.24) and (2.25) show the experimental results for plaster cubes. It was also concluded that, since its

mechanical properties closer to the ones of lithophysal tuffs, the gypsum plaster was better analog material to simulate lithophysal tuff rocks compared with urethane. However, the Hydro-StoneTB® is better analog material than both (Rigby 2007). Regarding the experimental tests on the plaster cubes contained spherical Styrofoam inclusions, the results gave higher strength and stiffness compared to those contained open ended cylindrical tubes, see Figures (2.26) and (2.27). This was attributed to the effect of hole shape; spherical Styrofoam inclusions are localized inside the cube and don't cross them from one side to the other like the open ended tubes. This will leave a solid zone which in turn leads to stronger and stiffer material. Regardless of distribution of voids in the cubes, the following correlation were obtained from the data in Tables (6.2) and (7.6) in the author's dissertation.

$$\text{Cubes with sphers, } \mathbf{UCS}, (Psi) = 1775.9 * e^{-0.04*Porosity(\%)} \quad R^2 = 0.85 \quad \dots (2.22)$$

$$\text{Cubes with sphers, } \mathbf{E}, (Ksi) = 444 * e^{-0.03*Porosity(\%)} \quad R^2 = 0.82 \quad \dots (2.23)$$

$$\text{Cubes with tubes, } \mathbf{UCS}, (Psi) = 1439.2 * e^{-0.049*Porosity(\%)} \quad R^2 = 0.71 \quad \dots (2.24)$$

$$\text{Cubes with tubes, } \mathbf{E}, (Ksi) = 438.6 * e^{-0.042*Porosity(\%)} \quad R^2 = 0.823 \quad \dots (2.25)$$

In an experimental study carried out by Hudyma et al. (2004), thirty four plaster specimens, both cubical and cylindrical, were tested under uniaxial compression loading to mimic tests on lithophysal tuff rocks. The cubic plaster specimens tested in this study, fourteen cubes, contained spherical Styrofoam inclusions ranging from 25.4 to 102 mm in diameter, and having void porosity (macroporosity) starting from 5 to 35%. The twenty cylindrical specimens (50.8 x 101.6 mm) contained either spherical Styrofoam inclusions

(ranging from 6 to 8 mm diameter and having porosity from 7.4% to 37.6%) or ellipsoidal air injected bubble (having narrow porosity range from 4% to 7.8%). Regardless of specimen shape, the wide spreading results displayed non-linear (exponential) reduction in UCS data with increasing porosity giving the following equation:

$$UCS, \sigma_c, (MPa) = 12.618e^{-0.0415*Porosity(\%)} \quad R^2 = 0.8 \quad \dots (2.26)$$

No clear effects of void shapes on the mechanical behavior of the analog materials were adopted. However, as can be seen from Figure (2.28), the specimens containing regular voids, specimens contain Styrofoam inclusions, are more uniformly distributed around the regression curve comparing to the specimens containing irregular air injected bubbles.

Erfourth (2006) studied the mechanical behaviors of rock-like material under uniaxial compression both experimentally and numerically. In the experimental tests, different size cylinders of plaster of Paris (95 samples) containing spherical Styrofoam inclusions (3, 12.7, and 25.4 mm in diameter, and having porosity from 0 to 30%) were cast and tested under compression. Regarding the spherical Styrofoam inclusions of 3 and 12.7 mm in diameter, the cylinder size was 50.8x101.6 mm. While, for the spherical Styrofoam inclusions of 25.4 mm in diameter, two different sizes of cylinder were used; 76.2x152.4 mm and 101.6x203.2 mm. For the numerical analysis, the experimental specimens were modeled in Itasca's FLAC3D (finite different method) using linear-elastic material model to investigate the stiffness and Mohr-Coulomb material model to investigate the strength. The results had high scattering for both strength and elastic modulus with average correlation coefficients. The results of normalized uniaxial

compressive strength displayed a mediocre (exponential) relationship, see Figure (2.29), giving the following equation:

$$\text{Normalized UCS} = 0.9464 * e^{-0.04\text{Porosity}(\%)} \quad R^2 = 0.67 \quad \dots (2.27)$$

In addition, from Figure (2.30), it can be seen that the specimens containing small spherical Styrofoam inclusions, 3 mm in diameter, gave higher strength but lower correlation coefficients compared to the specimens containing larger spherical Styrofoam inclusions, 12.7 mm or 25.4 mm in diameter. This attributed partly to sample preparing deficiency; specimens containing uniformly distributed small voids (3 mm) was problematic. For the elastic properties, the data showed that the Young's modulus decreased linearly with porosity increasing as shown in Figure (2.31). However, void size had less effect on Young's modulus, see Figure (2.32); therefore, they did not give a very good relationship as shown below:

$$E \text{ (GPa)} = -56.482 * \text{Porosity}(\%) + 3563.8 \quad R^2 = 0.44 \quad \dots (2.28)$$

This was attributed to the sensitivity of the Young's modulus with respect to the variations of void size and distribution. This attribution was supported by the numerical analysis; since the void size and distribution can be controlled in the numerical analysis more effectively than in the experimental tests, the numerical Young's modulus data showed less scattering, see Figure (2.33). In general, the numerical results for both elastic modulus and strength followed trends similar to those of the experimental results; see

Figures (2.33) and (2.34). However, the scattering was higher for the uniaxial compressive strength, *UCS*.

In an attempt to study the influence of void geometry on engineering properties of lithophysal tuff using rock-like material, Rigby (2007) tested fifty two Hydro-StoneTB[®] cubes contained open ended longitudinal openings (voids) with different sizes, shapes, and distributions. The research was a part of the Cooperative Agreement No. DEFC28-04RW12232 between the U. S. Department of Energy and the Nevada System of Higher Education (NSHE). Cubes (15 cm per side) contained three different shapes of voids (circular, square, and diamond) arranged in different void pattern types, three patterns for circular voids (A, B, and C) and two void patterns for each of the square and diamond voids (A and B), were tested under uniaxial compression. Different patterns represented different randomly generated void geometries. Regarding the void sizes, the circular openings had three different diameter, 12.7 mm, 21.8 mm, and 31.1 mm, while both square and diamond voids had two different sizes; large (15.6 mm on side) and small (22 mm on side). In addition to the cubes contained unisize circular voids, cubes contained mixed circular voids were also tested. The void porosities were ranging from 5% to 20%. The high scatter results displayed that the uniaxial compressive strength and Young's modulus decreased linearly with increasing void porosity as shown in Figures (2.35) and (2.36). The results are also discussed in Chawla (2007). The best fit-regression equations for normalized values are

$$\text{Normalized } UCS = -0.02 * \text{Porosity}(\%) + 0.57 \quad R^2 = 0.68 \quad \dots (2.29)$$

$$\text{Normalized } E = -0.01 * \text{Porosity}(\%) + 0.78 \quad R^2 = 0.36 \quad \dots (2.30)$$

The results did not show any dependency of Young's modulus on void size shape (at similar values of porosity), but a slight to moderate correlation between strength and void shape and size. However, diamond and large size voids led to the highest reduction in the uniaxial compressive strength. This was attributed to the likeliness of shape and size dependency on both orientation of the voids and average bridge length (distances between voids). The three different void patters did not show significant differences in the Hydro-StoneTB[®] properties; the Young's modulus and strength values for each of the three patterns yielded similar results. No explanation has been mentioned regarding ineffectual of the void patterns on the mechanical properties of Hydro-StoneTB[®].

In a more recent attempt, Nott (2009) studied the effects of void porosity on tensile strength of rock-like material, Hydro-StoneTB[®], both experimentally and numerically. In the experimental part, both direct and indirect methods were used to find the rock-like material tensile strength. Since the direct method (Dog Bone specimens with 100 by 100 mm cross section) was not successful in evaluating the tensile strength, only indirect method, Brazilian tests, were used to find the tensile strength of the rock-like material and its variation with regard to void porosity changes. For the Brazilian tests, twenty porous discs (101.6 mm in diameter and 50.8 mm long specimens) contained holes (open ended tubes) were tested under compression; indirect method. Holes with different sizes (17.9 mm and 25.4 mm) and number (2, 4, and 8 holes to provide different porosities ranging from 6.2 to 18.7%) were distributed throughout the disks. In the numerical analysis, discs in the Brazilian tests were modeled in UDEC software using plain strain assumption. The results showed that the tensile strength

decreased with increasing porosity, and the numerical results were consistent with the experimental results as shown in Figure (2.37); both numerical analysis and experimental results followed power law:

$$(UTS)_{Experimental}(Psi) = 954.1 * (Porosity(\%))^{-0.8026} \quad R^2 = 0.993 \quad \dots (2.31)$$

$$(UTS)_{Experimental}(Psi) = 357.73 * (Porosity(\%))^{-0.583} \quad R^2 = 0.96 \quad \dots (2.32)$$

In addition, it was found that that the UDEC software can successfully predict the cracking patterns of the experimental test specimens.

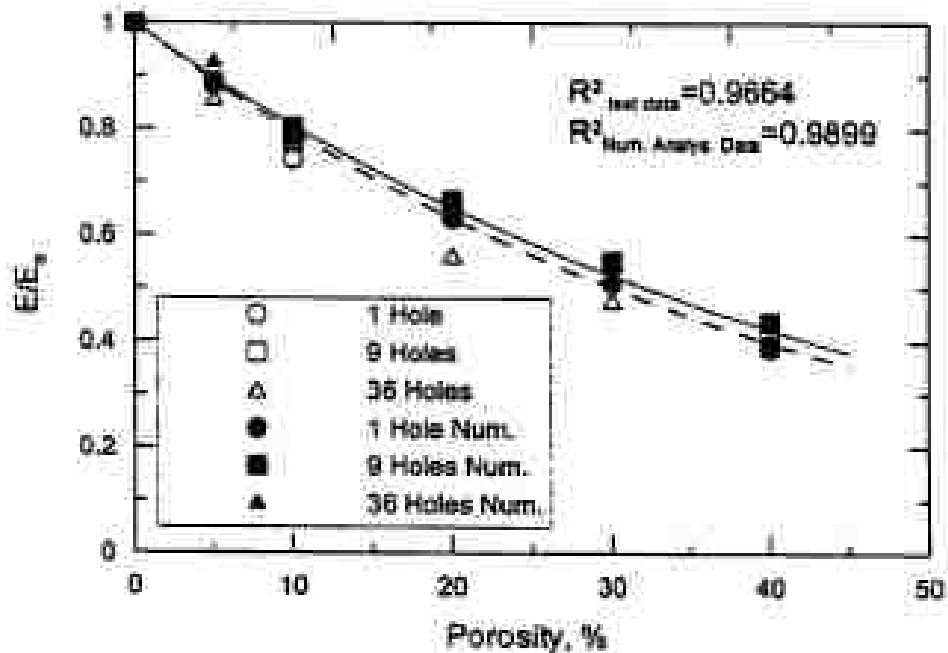


Figure (2.22) Normalized Young's Modulus versus Total Porosity for Urethane Cubes for both Experimental Tests and Numerical Models (Avar 2002).

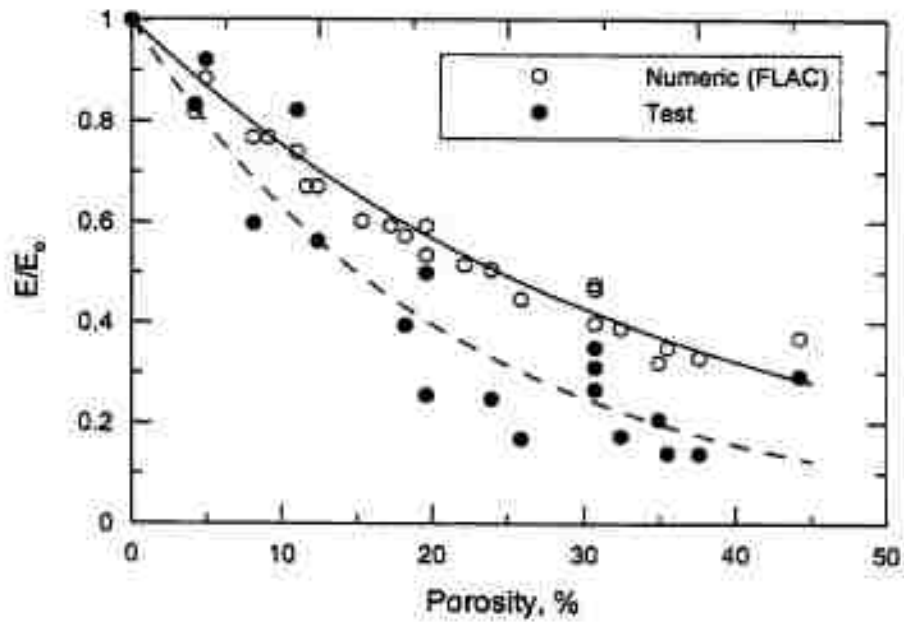


Figure (2.23) Normalized Young's Modulus versus Total Porosity for Plaster Specimens Containing Cylindrical Tubes for both Experimental Tests and Numerical Models (Avar 2002).

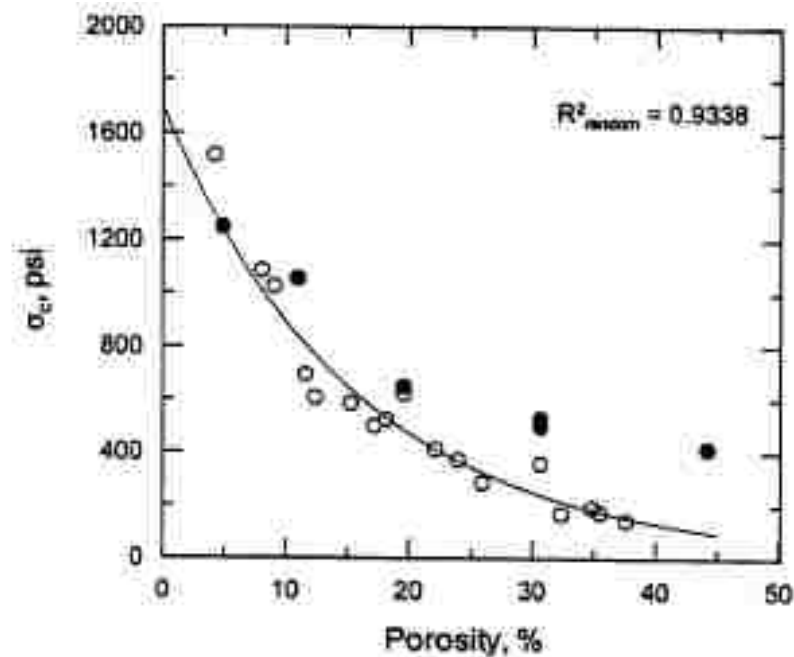


Figure (2.24) Uniaxial Compressive Strength (σ_c) versus Total Porosity for Plaster Cubes Containing either Randomly Distributed Cylindrical Tubes or Uniform Distributed Cylindrical Tubes (Avar 2002).

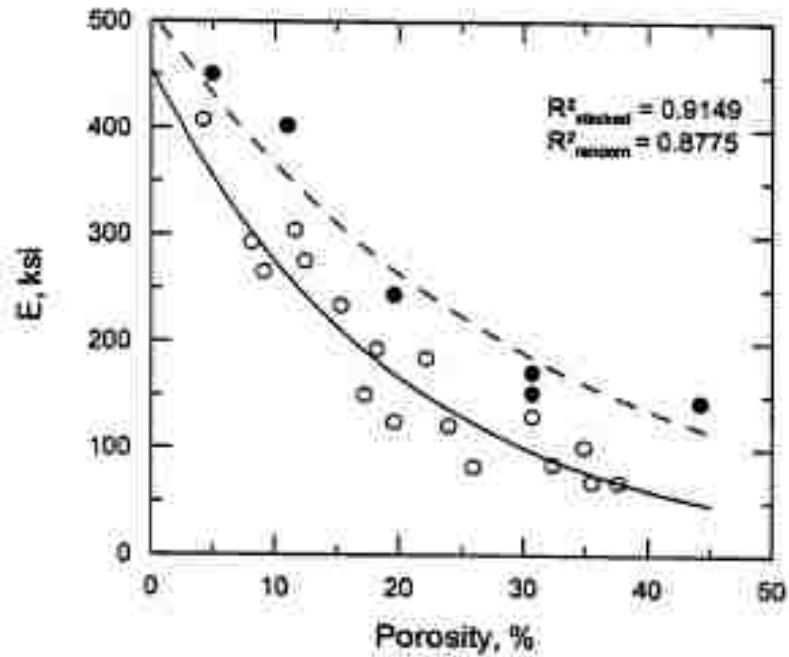


Figure (2.25) Young's Modulus versus Total Porosity for Plaster Cubes Containing either Randomly Distributed Cylindrical Tubes or Uniform Distributed Cylindrical Tubes (Avar 2002).

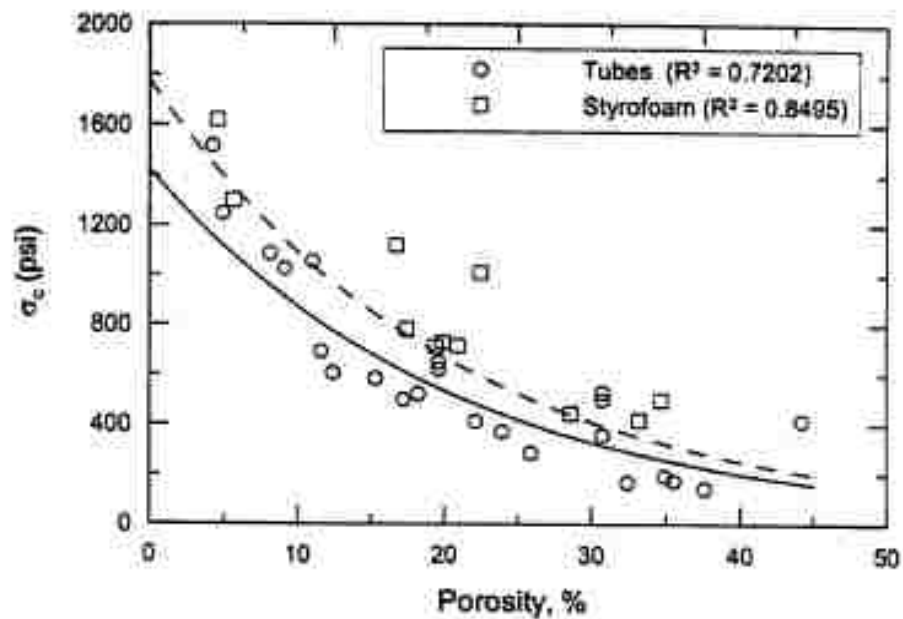


Figure (2.26) Uniaxial Compressive Strength (σ_c) versus Total Porosity for Plaster Cubes Containing either Cylindrical Tubes or Styrofoam Inclusions (Avar 2002).

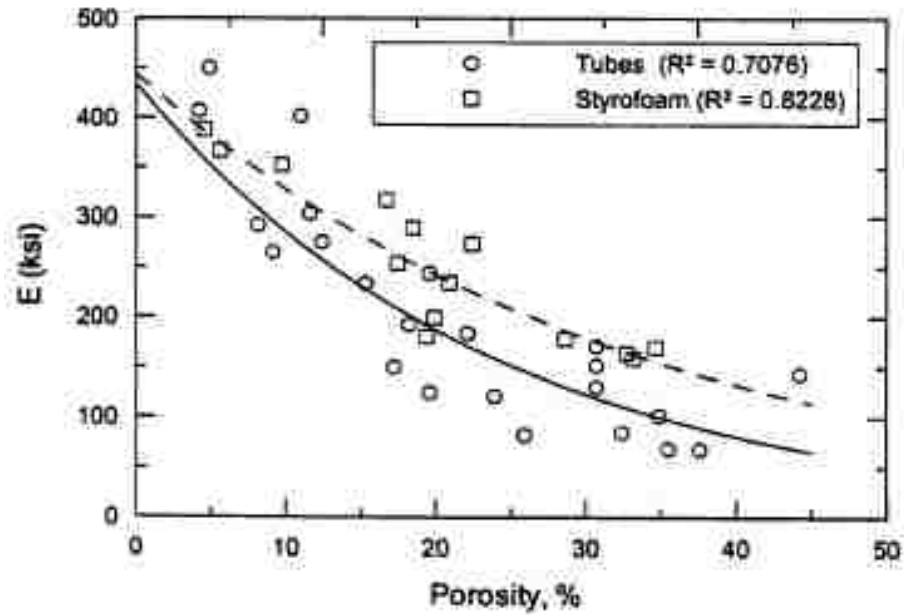


Figure (2.27) Young's Modulus versus Total Porosity for Plaster Cubes Containing either Cylindrical Tubes or Styrofoam Inclusions (Avar 2002).

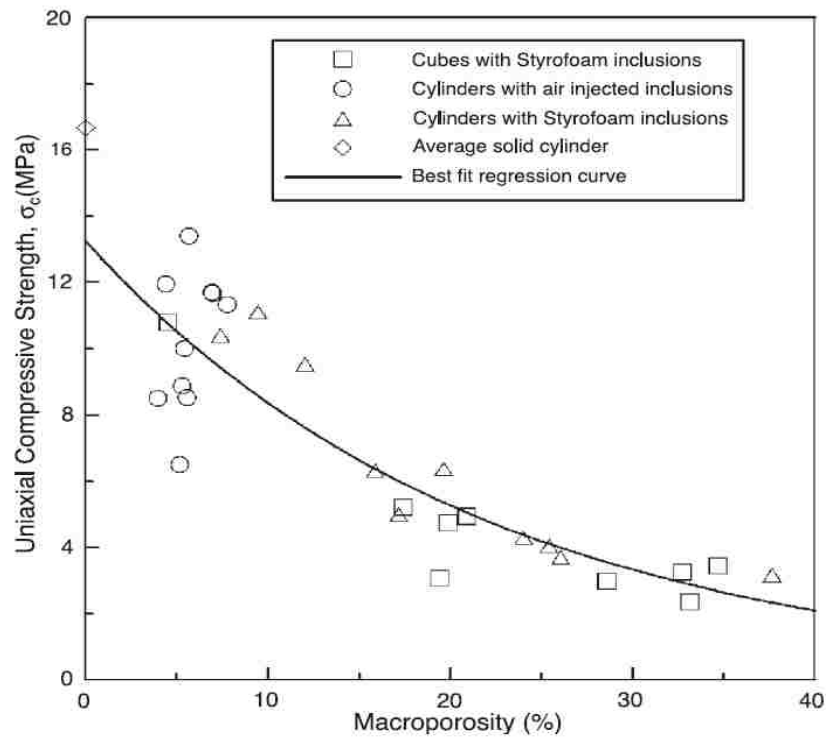


Figure (2.28) Correlation between Uniaxial Compressive Strength and Porosity (Hudyma et al., 2004).

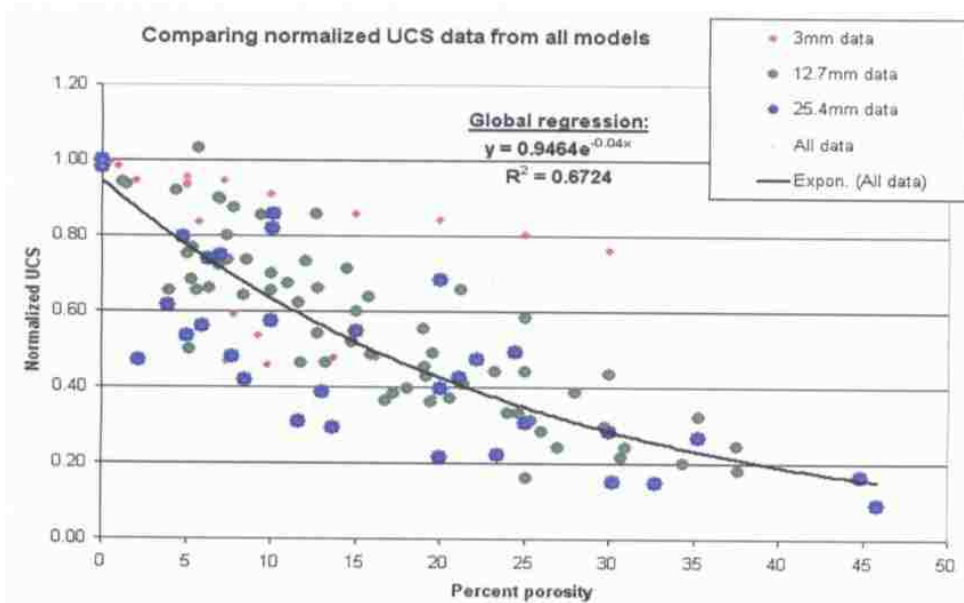


Figure (2.29) Correlation between Normalized Uniaxial Compressive Strength and Porosity (Erfourth 2006).

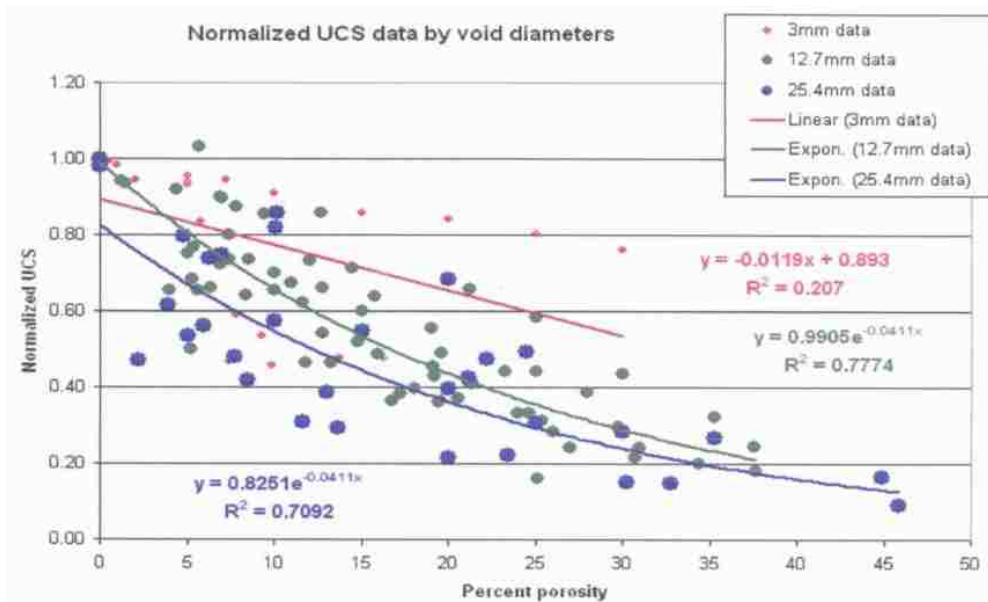


Figure (2.30) Correlation between Normalized Uniaxial Compressive Strength and Porosity (Erfourth 2006).

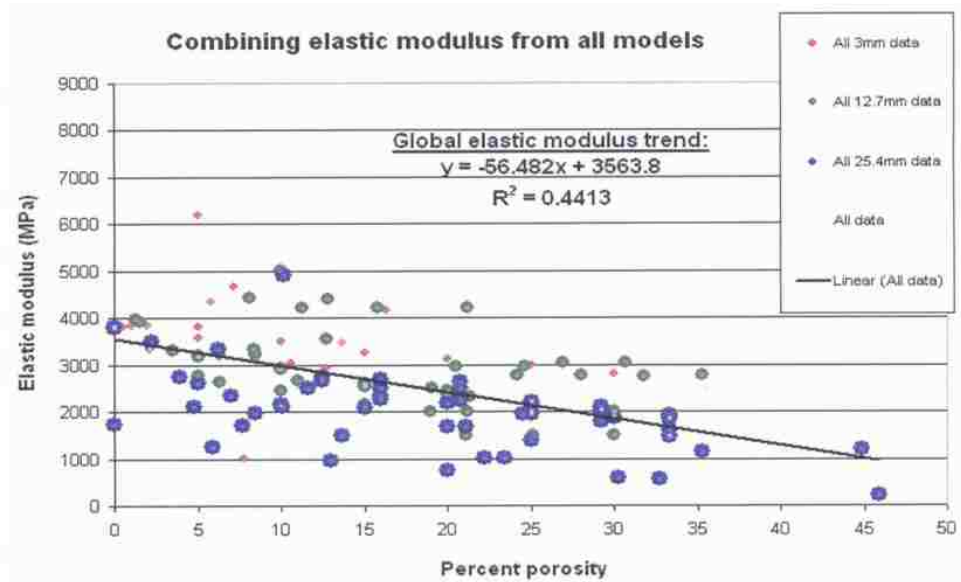


Figure (2.31) Correlation between Elastic Modulus with Porosity (Erfourth 2006).

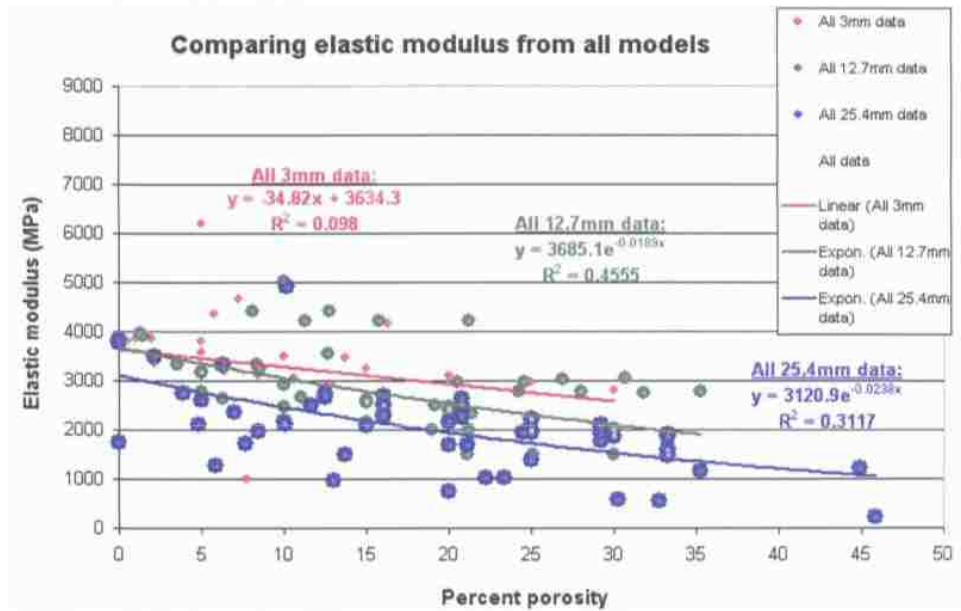


Figure (2.32) Correlation between Young's Modulus and Porosity (Erfourth 2006).

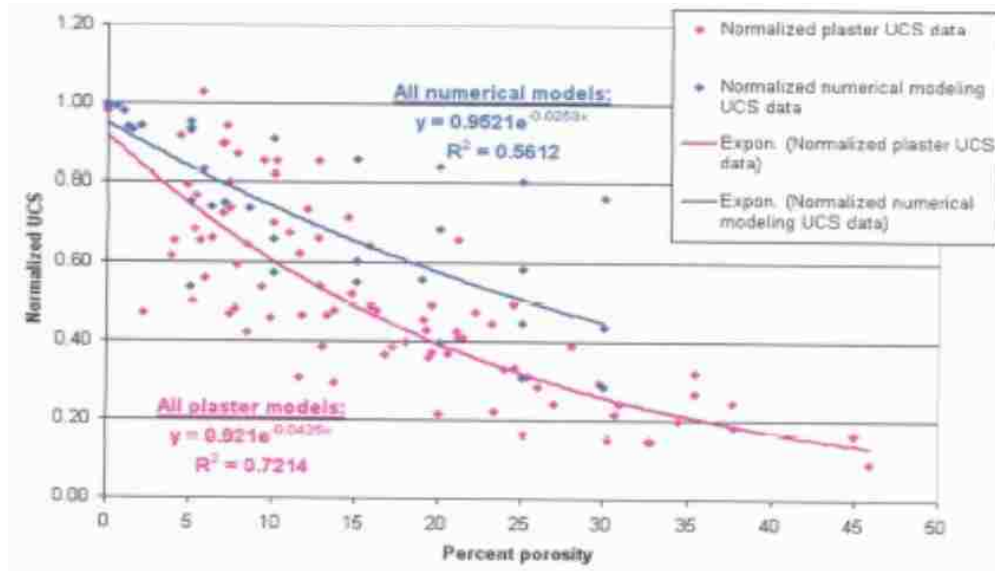


Figure (2.33) Correlation between Normalized Uniaxial Compressive Strength with Porosity for both Numerical Models and Experimental Tests (Erfourth 2006).

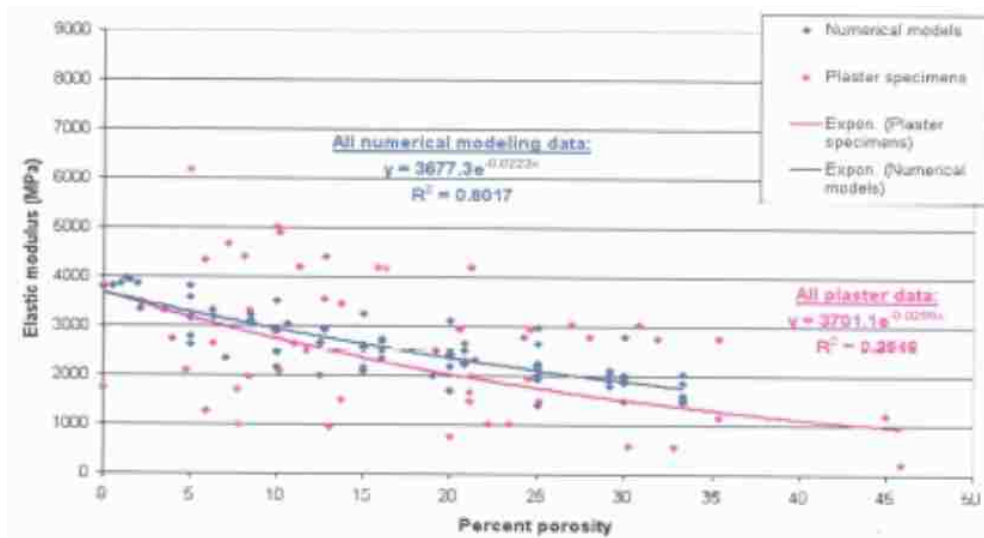


Figure (2.34) Correlation between Young's Modulus with Porosity for both Numerical Models and Experimental Tests (Erfourth 2006).

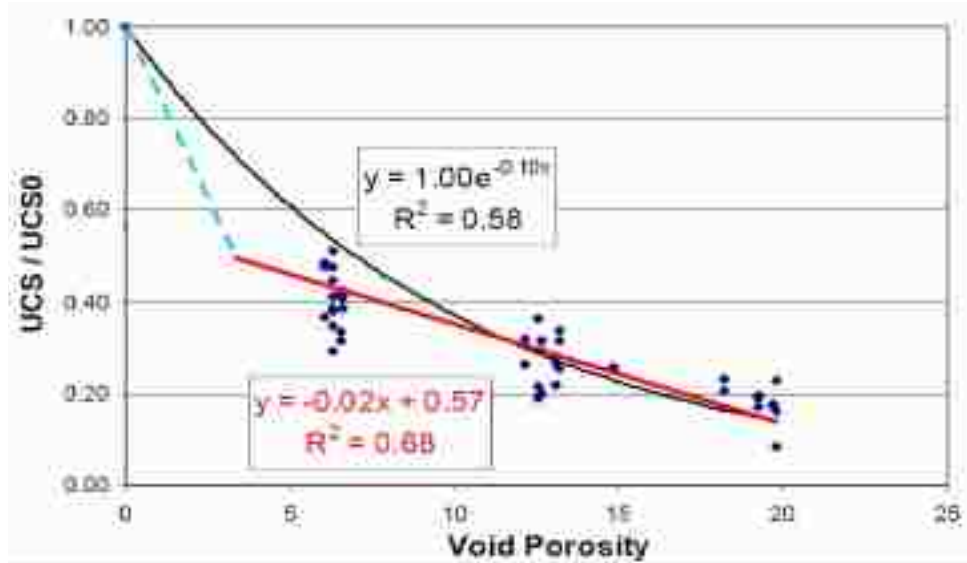


Figure (2.35) Correlation between Normalized Uniaxial Compressive Strength and Porosity (Rigby 2007).

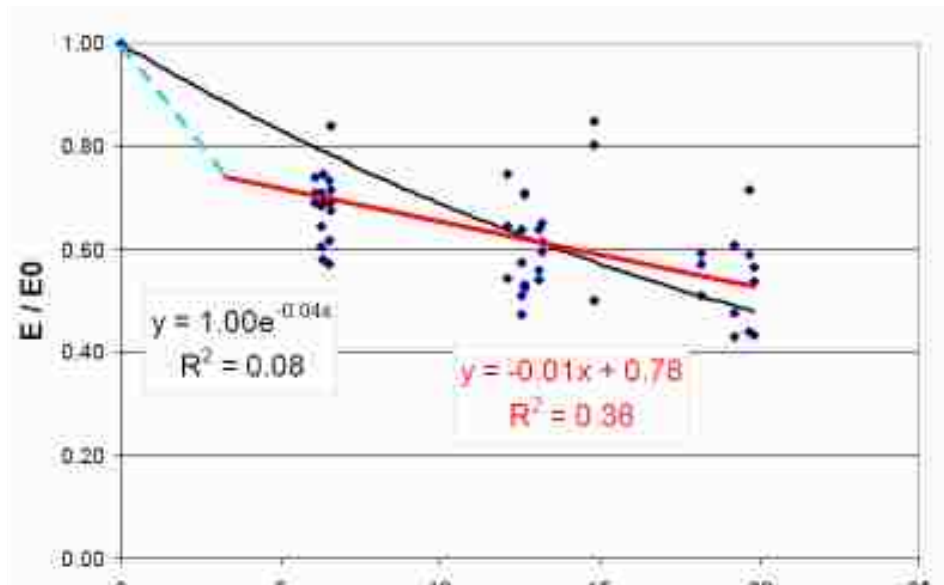


Figure (2.36) Correlation between Normalized Young's Modulus and Porosity (Rigby 2007).

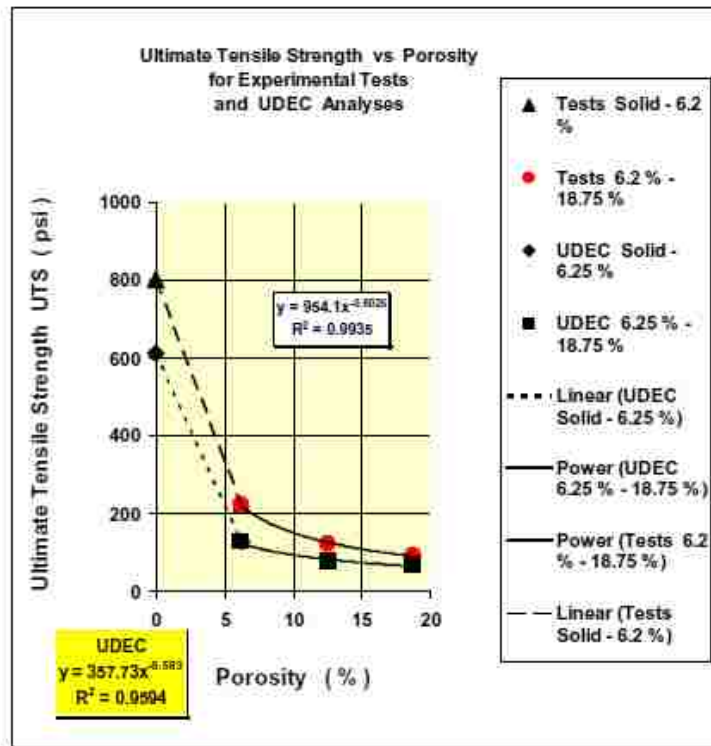


Figure (2.37) Correlation between Ultimate Tensile Strength and Porosity for both Numerical Models and Experimental Tests (Nott 2009).

2.4 Relationship between Voids and Failure Modes

Depending on the expected in-situ stress-state conditions such as uniaxial and triaxial compressive loading, failure modes of materials are necessary and helpful to evaluate the behaviors of geo-structures or/and their foundations under different loading conditions. Regarding geo-engineering materials containing substantial volume of cavities, studying failure modes are even more important due to the detrimental effects of the voids on the geo-materials' mechanical behavior. Uniaxial compression testing of rock-like materials with varying porosity may provide useful information regarding the effects of porosity on the rock failure modes. Previous studies indicate that failure modes

of rock-like materials are influenced by void porosity and void geometry (bridge distances exclusively).

Hudyma et al. (2004) identified four failure modes for the cylindrical plaster specimens as shown in Figure (2.38); spalling for void porosity range 0 – 5%, axial splitting for void porosity range 5 – 10%, shear failure for void porosity range 10 – 20%, and web failure for void porosity $\geq 20\%$. However, they did not find a strong relationship between failure modes and porosity for the cubic specimens; the specimens failed via a combination of the four failure modes occurred in the cylindrical specimens.

Jespersen et al. (2010) concluded that, as bridge distance increases from 0.5 to 1.5 void diameters, the dominant failure mode is tensile failure (vertical to sub-vertical tension fractures oriented approximately parallel to the applied axial load), see Figure (2.39a). At a bridge distance of 1.5 void diameters, the dominant failure mode is shear failure as shown in Figure (2.39b). At bridge distances greater than 1.5 void diameters, the dominant failure mode returns to tensile failure as shown in Figure (2.39c). In sum, according to previous research, the failure modes depend primarily on porosity and bridge distance.





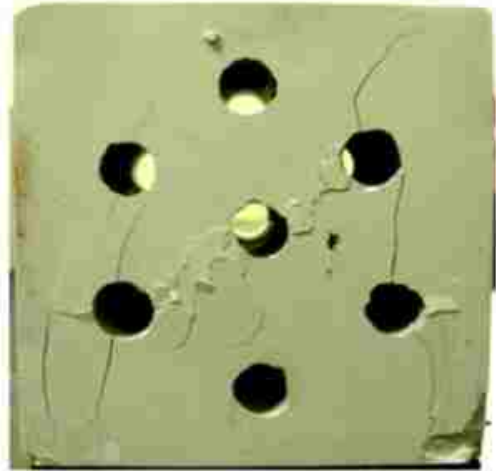
Failure Mode				
	a	b	c	d
	Spalling	Axial Splitting	Shear Failure	Web Failure
Macroporosity Range	0 – 5%	5 – 10%	10 – 20%	> 20%

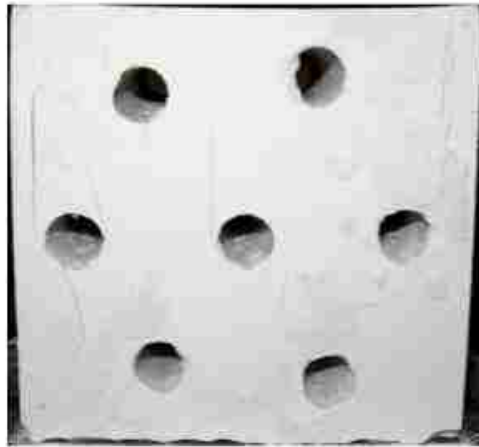
Figure (2.38) Failure Modes-Cylindrical Plaster Specimens (Hudyma et al. 2004).



a- Tension Failure
(Vertical to sub-vertical fractures)



b- Shear Failure



c- Tension Failure

Figure (2.39a, b, & c) Failure Modes Cubic Plaster Specimens - Jespersen et al. (2010)

More details on the influences of voids on crack patterns and failure modes in rocks and rock-like materials are discussed in Chapter 3 (sections 3.8 and 3.9) and Chapter 4 (section 4.5).

2.5 Summary of the Literature Review

From the literature review, although the results show that the uniaxial compressive strength and elastic modulus of rocks and rock-like materials decrease while

void porosity increases, the general relationships between them are poorly defined and unclear, and the data have high scatter (low to moderate coefficient of determination). The effects of void size, void shapes, void orientation, and void spatial distributions have not been explored clearly. In addition, almost all the correlations regarding the effects of void porosity on the mechanical behaviors of rocks and rock-like materials are solely drawn between the mechanical properties, mostly *UCS* and *E*, and the void porosity. In other words, the effects of void size, void shape, void orientation, and void spatial distributions have not been addressed in the correlations. It is believed that, besides the porosity, those factors (void size, void shapes, and void orientation, and void spatial distributions) are important as well.

This study aims to address the void size, void shapes, and void orientation, and void spatial distributions and weigh their effects on the mechanical properties of rock-like materials. It intends to find a better correlation between the mechanical properties, *UCS* and *E*, of rock-like materials and void porosity considering the aforementioned factors; it searches to see if the aforementioned factors can reduce the data scattering, in other words increase the coefficients of determination of the correlations. In addition, since the influences of void porosity and geometry on failure modes of rock-like material have been addressed by very few researchers (only two researches so far), more attention about the subject will be helpful in evaluating the geo-structures or/and their foundations under different loading conditions. Accordingly this study also aims to explore the effects of void existences on the crack pattern and failure modes in rock-like materials.

CHAPTER THREE *MECHANICAL CHARACTERIZATION OF BRITTLE MATERIALS*

3.1 Introduction

Matter, any physical substance surrounds us, becomes material if used or/and processed by humans (Meyers and Chawla 2009). For instance, rock naturally is a matter, but it becomes a material when used by humans as a construction material such as stones in masonry or aggregate in concrete. Materials have different properties such as physical properties, chemical properties, and mechanical properties. Hence, they exhibit different behaviors under given condition. However, in engineering, it is the mechanical properties which are essentially important for design purposes (Singh and Dwivedi 2009).

Mechanical properties of materials are those which describe the material behavior under external loads such as strength, elasticity, rigidity (stiffness) plasticity, ductility, brittleness, impact strength, hardness, and toughness (Meyers and Chawla 2009). They depend on the bond forces between the materials' crystal structure and flaws (imperfections) within the crystal and among the crystals (Singh and Dwivedi 2009). Mechanical properties are corner stone of mechanical characterization of materials.

The mechanical characterization of materials means studying the deformation and cracking of materials under external loads which is vital for preventing failure of materials in service (Meyers and Chawla 2009). Since rocks, including lithophysal tuff, are typically considered as brittle material, this chapter is concerned with the mechanical characterization of brittle materials under static load.

3.2 Failure in Materials

Failure in term of material behaviors has various definitions such as (1) the process by which the behavior of material changes from one state to another ((Bieniawski et al., 1961; Andreev 1995), and (2) an irreversible alteration in the microstructure of the material responding to excessive loads or deformations which leads to a change in the normal material constitutive behavior (Kelly 2013). According to the most of failure theories, failure occurs when some physical variable such as stress, strain, or energy reaches a critical value. Regarding the stresses, the critical value might be the maximum principal stress, the maximum shear stress or some more complicated function of the stress components (Kelly 2013). Basing on various factors such as composition, aging, and temperature, the mechanisms of failure of materials can generally be classified into two main failure fashions, ductile and brittle (Runesson 2006; Pytel and Kiusalaas 2012; Ugural and Fenster 2012). However, the differentiation between the two mechanisms is not an easy process; to view a material as being either ductile or brittle (Christensen 2005).

3.3 Brittle Materials

Brittle materials, also called non-ductile materials, are typically those materials which can not undergo considerable permanent deformation prior to failure ($\epsilon < 0.05$) and do not exhibit an identifiable yielding (Norton 1997; Kelly 2013). Some examples of brittle materials are concrete, rock, cast iron, and glass. Ductile materials are those can undergo a considerable of permanent deformation ($\epsilon \geq 0.05$) before failure occurs and exhibit identifiable yielding (yield strength) before failing (Kelly 2013). Examples of

these materials are mild steel, aluminum, copper, and lead. Figure (3.1) show typical stress-strain curves (σ - ϵ curve) for both brittle and ductile materials.

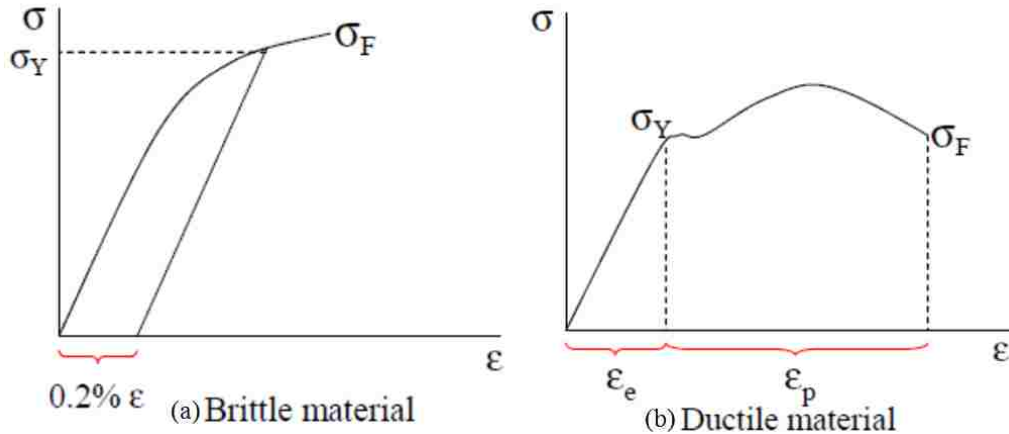


Figure (3.1a &b) Typical stress-strain curves for (a) brittle material and, (b) ductile material

3.4 Strength and Failure of Brittle Materials

Brittle materials should not be considered as weak materials. They just have little or no plasticity; the strain is mainly elastic strain as shown in Figure (3.1a). The stress at which failure occurs is called failure stress (fracture stress) and is usually symbolized by σ_F , see Figure (3.1a). However, if the yield point is required in brittle materials, the offset method is typically used (Pytel and Kiusalaas 2012). In this method, a line at a prescribed offset strain, usually 0.2% ($\epsilon = 0.002$) of the stress-strain curve, is drawn parallel to the initial tangent. The intersecting point between this line and the stress-strain curve is considered as the yield point; see Figure (3.1a). Regarding the ductile materials, the stress at which the stress-strain curve becomes almost horizontal is considered as the yield point, and is usually symbolized by σ_Y as shown in Figure (3.1b). In addition, the strain in

ductile materials has two parts; elastic strain (ϵ_e) and plastic strain (ϵ_p), Figure (3.1b). The failure stress in ductile material is called ultimate stress (rupture stress) and is usually symbolize by σ_F , see Figure (3.1a).

Depending on their compressive, tensile, and shear strengths, brittle materials can be divided into two types; even and uneven materials (Norton 1997). The even brittle materials are those have equal compressive and tensile strength. The uneven brittle materials are those have different strength for both compressive and tensile stresses; compressive strength is higher than tensile strength. In addition, uneven brittle materials are those which have greater shear strength compared to their tensile strength; their shear strength is falling between their compressive and tensile strength (Norton 1997). Accordingly, concrete, soil, and rock, are uneven brittle materials.

Regarding failure, brittle materials are usually fractured with clean breaks at failure (Norton 1997; Kelly 2013). According to Ugural and Fenster (2012), fracture means creating new surfaces within the material under stress; separating into two or more parts. Fractures are commonly occurring through the grains and termed as transcrystalline failure (Ugural and Fenster 2012). They will be created due to normal tensile stress alone if the materials are under tension forces, while in the materials under compression stress, the fractures will be created due to some combination of normal compressive stress and shear stress (Norton 1998).

3.5 Failure Criteria of Brittle Materials

The main objective of computing and understanding of stresses is to predict if a given material will fail under a given external load; to predict strength value of the

material. In some cases the stress conditions are very complex and the aforementioned objective difficult to obtain. Therefore, failure data obtained from simple experimental tests, uniaxial tensile or compressive tests, are used instead to predict strength of the material under complex stress system; to check if it is fail or not. By this, a formula or an equation is obtained to predict the failure, strength value, of the material under all combination of stresses which is called material failure criteria or theories of failure. These theories, failure criteria of materials, are classified into two main groups; one for those materials fail by fracturing (brittle materials), and the other for those materials yielding (ductile materials) (Pytel and Kiusalaas 2012).

Although, there are no universal failure criteria to correlate failure in a simple test with failure due to complex stress condition, there are several theories that work well enough for certain materials (Pytel and Kiusalaas 2012). Regarding brittle materials, the most accepted theories of failure, failure criteria, are Maximum Principle Stress theory, Mohr's theory, Coulomb-Mohr theory, and Griffith's theory (Sandhu 1972; Hertzberg 1996; Norton 1997; Gordon 2003; Meyers and Chawla 2009; Pytel and Kiusalaas 2012; Ugural and Fenster 2012; Kelly 2013).

3.5.1 Maximum Principle Stress Theory (Rankine, Lamé, Clapeyron - 1858)

The oldest, simplest too, but least accurate theory of failure of brittle materials is the maximum principle stress theory which credited to W. J. M. Rankine (1820–1872). It assumes that an element of a stressed body fails by fracture when the largest tensile principle stress exceeds the elastic limit in a simple tension test like uniaxial tension test (Sandhu 1972; Hearn 2001; Pytel and Kiusalaas 2012; Ugural and Fenster 2012).

In other words, according to the maximum principle stress theory any one of the principle stresses reaches the ultimate strength of the brittle material ($\sigma_1 = \sigma_u$, or $\sigma_2 = \sigma_u$, or $\sigma_3 = \sigma_u$) failure should be occurred. Thus

$$(\sigma_1^2 - \sigma_u^2) * (\sigma_2^2 - \sigma_u^2) * (\sigma_3^2 - \sigma_u^2) = 0 \quad \dots (3.1)$$

where $\sigma_1, \sigma_2, \sigma_3$ are principle stresses and σ_u is the ultimate (failure) stress in a simple tension or compression test. Accordingly, the failure criterion according to the maximum principle stress theory is:

$$\frac{\sigma_1}{\sigma_u} = \mp 1 \quad or \quad \frac{\sigma_2}{\sigma_u} = \mp 1 \quad or \quad \frac{\sigma_3}{\sigma_u} = \mp 1 \quad \dots (3.2)$$

Graphical representation for Eq. (3.2), in three-dimensional stress, will be a cubic surface spaced symmetrically about the origin of coordinates for even brittle materials (Sandhu 1972). For uneven brittle materials, the cubic surface will be spaced asymmetrically about the origin of coordinates. For two-dimensional stress ($\sigma_3 = 0$), plane stress condition, the failure criterion for even materials is:

$$\frac{\sigma_1}{\sigma_u} = \mp 1 \quad or \quad \frac{\sigma_2}{\sigma_u} = \mp 1 \quad \dots (3.3)$$

For uneven brittle material, since the ultimate stress (σ_u) is not the same in both tension and compression, the failure criterion for uneven materials will be:

$$\frac{\sigma_1}{\sigma_{ut}} = +1 \quad or \quad \frac{\sigma_2}{\sigma_{ut}} = +1 \quad or \quad \frac{\sigma_1}{\sigma_{uc}} = -1 \quad or \quad \frac{\sigma_2}{\sigma_{uc}} = -1 \quad \dots (3.4)$$

where σ_{ut} is the materials' ultimate tensile strength, and σ_{uc} is the materials' ultimate compressive strength.

Graphical representation for Eq. (3.4) is shown in Figure (3.2). The failure criterion is represented by the outline of the shaded squares and rectangles. Any point, which corresponds to the principal stresses in the materials, lying on or extending the

shaded area represent failure. However, if it falls inside the shaded area, the material will be in fail condition (Pytel and Kiusalaas 2012; Ugural and Fenster 2012).

When the maximum principle stress theory is using to predict the failure in brittle materials, the following notes should be borne in mind (Sandhu 1972; Hearn 2001):

- 1- For a case in which σ_3 is compression and both σ_1 and σ_2 are tension stresses, according to the maximum principle stress theory, failure can occur when the minimum principle stress σ_3 reaches the value of the elastic limit stress in compression, σ_{uc} , even if the elastic limit stress in tension, σ_{ut} , has not been reached (Hearn 2001). Therefore, one criterion will be:

$$\frac{\sigma_3}{\sigma_{uc}} = -1 \quad \dots (3.5)$$

- 2- For a case in which $\sigma_1 = \sigma_2 = \sigma_3 = \sigma_u$, failure should not be expected; it rather causes a volume change only (Sandhu 1972).

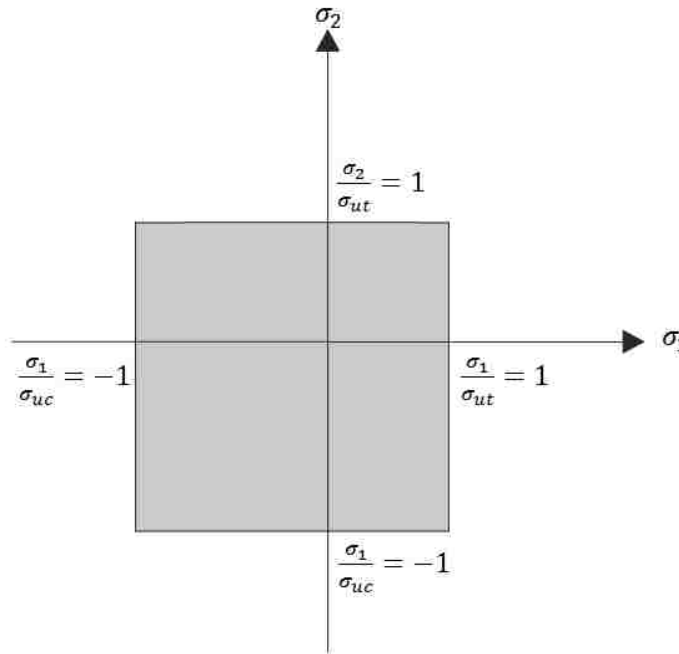


Figure (3.2) Maximum Principle Stress failure criterion.

3.5.2 Mohr's Theory (1900)

To predict fractures in uneven brittle materials, the Mohr's theory of failure is considered as an accepted failure criterion (Norton 1998; Pytel and Kiusalaas 2012; Ugural and Fenster 2012). The theory can be applied using well-known Mohr's circles of stress incorporating with the results of simple tests such as uniaxial loading tests (Norton 1997; Pytel and Kiusalaas 2012; Ugural and Fenster 2012). Two Mohr's circles can be drawn using the ultimate tensile stress, as the maximum principle stress in tension, $(\sigma_{ult})_t$, and the ultimate compressive stress, as the maximum principle stress in compression $(\sigma_{ult})_c$. And then by drawing two lines that are tangent to the circles, the failure envelope for Mohr's theory can be obtained, see Figure (3.3). The Mohr's theory predicts failure if the Mohr's circle of any state of stress in the material tangent to, or extends beyond the failure envelop (Pytel and Kiusalaas 2012).

From Figure (3.3a), between points *A* and *B*, the *maximum* and *minimum* principal stresses, there are unlimited vertical lines like *PC* line which represent the states of stress on planes with the same normal stress but different shear stress. According to Mohr's theory, the weakest plane of all planes carrying the same normal stress in the material is the plane which has maximum shear stress; point *P* in Figure (3.3a) (Sandhu 1972; Pytel and Kiusalaas 2012; Ugural and Fenster 2012). In this theory the effect of the intermediate principle stress, due to its negligible effects on the failure stress, is not considered.

From Figure (3.3b), if besides ultimate tensile stress (simple tension) and ultimate compressive stress (simple compression), the ultimate shear stress obtained from torsion is too used to construct the failure envelope for Mohr's theory, a new failure envelope

will be constructed, and the theory becomes modified Mohr's theory (Pytel and Kiusalaas 2012; Ugural and Fenster 2012). The tangent lines to the three circles, AB and A'B', are now the failure envelopes; Mohr's envelopes.

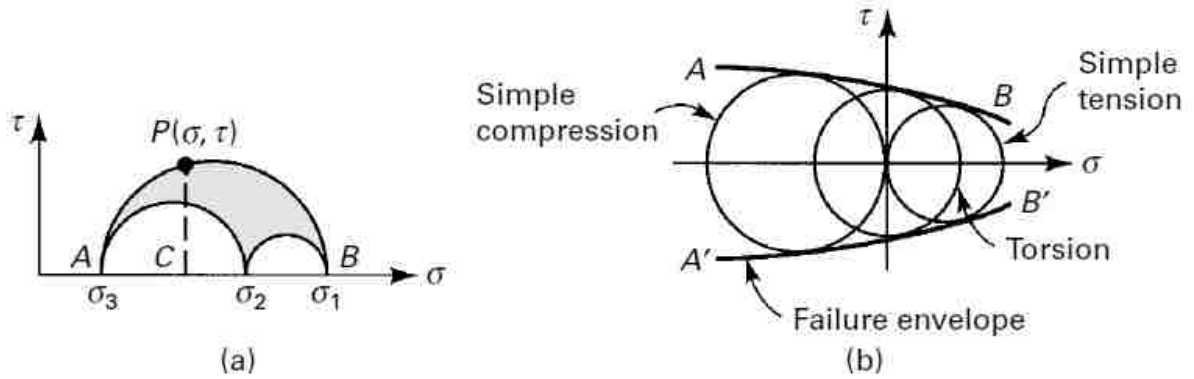


Figure (3.3) Mohr's Theory (a) Mohr's circles of stress; (b) Mohr's envelopes (Ugural and Fenster 2012)

3.5.3 Coulomb-Mohr Theory

The Coulomb-Mohr theory, also called internal friction theory and established in 1900, assumes that fracture occurs in materials when the ultimate normal stress, tensile or compressive, reaches a corresponding critical value; strength of the material in tension or compression. It is a modification of the maximum principle stress theory with considering that the maximum shearing stress in frictional materials is depending on internal friction of the material (Ugural and Fenster 2012). In addition, the effect of the intermediate principle stress is not considered in this theory too.

Coulomb, in 1773, hypothesized that failure occurs on a plane within a material when the shearing stress is equal to the sum of the cohesive strength and frictional strength (Sandhu 1972). This can be written as follow

$$\tau = c + \mu\sigma \quad \dots (3.6)$$

where τ is shear stress along the plane, σ is normal stress on the plane, c is cohesive strength of the plane, and μ is coefficient of friction of the plane. The plane is also called failure plane.

Ugural and Fenster (2012) rewrote Eq. (3.6) as follow

$$\tau = b + a\sigma \quad \dots (3.7)$$

Note that a and b are corresponding to cohesive strength, c , and coefficient of friction, μ , respectively; material properties. Bearing in mind the assumption that the failure is not affected by the intermediate principle stress, the maximum shear stress and the corresponding normal stress can be written in terms of the principle stress as follows (Ugural and Fenster 2012):

$$\frac{\text{Principle } \sigma_{max} - \text{Principle } \sigma_{min}}{2} = b + a * \frac{\text{Principle } \sigma_{max} + \text{Principle } \sigma_{min}}{2} \quad \dots (3.8)$$

To obtain Coulomb-Mohr criterion in plane stress condition, four combinations of stresses (cases) should be considered (Ugural and Fenster 2012); Case I (both σ_1 and σ_2 are tensile – first quadrant), Case II (σ_1 is compressive and σ_2 is tensile - second quadrant), Case III (both σ_1 and σ_2 are compressive – third quadrant), and Case IV (σ_1 is tensile and σ_2 is compressive - fourth quadrant).

Case I (both σ_1 and σ_2 are tensile – first quadrant): In this case of biaxial tension, both σ_1 and σ_2 have the same sign on σ_1, σ_2 plane ($\sigma_1 > 0, \sigma_2 > 0$), the σ_3 , becomes the minor principle stress ($\sigma_3 = 0$). Therefore, Eq. (3.8) becomes:

$$\begin{aligned} \tau &= \frac{\text{Maximum Principle Stress} - \text{Minimum Principle Stress}}{2} \\ &= \frac{(\sigma_{1or2}) - (\sigma_3)}{2} = \frac{(\sigma_{1or2}) - 0}{2} = \left(\frac{\sigma_1}{2}\right) \text{ or } \left(\frac{\sigma_2}{2}\right) \quad \dots (3.9) \end{aligned}$$

Furthermore, since neither σ_1 nor σ_2 can be higher than the material's ultimate tensile strength (σ_{ut}), hence, the failure criterion for **Case I** will be (Ugural and Fenster 2012)

$$\frac{\sigma_1}{\sigma_{ut}} = 1 \quad \text{or} \quad \frac{\sigma_2}{\sigma_{ut}} = 1 \quad \dots (3.10)$$

Case II (σ_1 is compressive and σ_2 is tensile - second quadrant): When σ_1 and σ_2 are of opposite sign on σ_1, σ_2 plane ($\sigma_1 < 0, \sigma_2 > 0$), instead of σ_3 ($\sigma_3 = 0$), the σ_1 becomes the minor principle stress. Therefore, Eq. (3.8) becomes:

$$\frac{\sigma_2 - \sigma_1}{2} = b + a * \left(\frac{\sigma_2 + \sigma_1}{2} \right) \quad \dots (3.11)$$

In addition, to find the values of a and b , the following conditions should be considered:

$$\sigma_1 = -\sigma_{uc} \quad \text{when} \quad \sigma_2 = 0 \quad \dots (3.12a)$$

$$\sigma_2 = \sigma_{ut} \quad \text{when} \quad \sigma_1 = 0 \quad \dots (3.12b)$$

Combining Eqs. (3.12a&b) with Eqs (3.11), we obtain

$$a = \frac{\sigma_{ut} - \sigma_{uc}}{\sigma_{uc} + \sigma_{ut}}, \quad b = \frac{\sigma_{ut} * \sigma_{uc}}{\sigma_{uc} + \sigma_{ut}} \quad \dots (3.13)$$

Substitute Eq. (3.13) into Eq. (3.11), the following failure criterion is obtained for **Case II**:

$$\frac{\sigma_1}{\sigma_{uc}} - \frac{\sigma_2}{\sigma_{ut}} = -1 \quad \dots (3.14)$$

Case III (both σ_1 and σ_2 are compressive – third quadrant): In this biaxial compression case, like **Case I**, both σ_1 and σ_2 have the same sign on σ_1, σ_2 plane ($\sigma_1 < 0, \sigma_2 < 0$). However, here the σ_3 ($\sigma_3 = 0$) becomes the major principle stress. Therefore, Eq. (3.8) becomes:

$$\begin{aligned} \tau &= \frac{\text{Maximum Principle Stress} - \text{Minimum Principle Stress}}{2} \\ &= \frac{(\sigma_3) - (\sigma_{1or2})}{2} = \frac{0 - (\sigma_{1or2})}{2} = \left(\frac{-\sigma_1}{2} \right) \quad \text{or} \quad \left(\frac{-\sigma_2}{2} \right) \quad \dots (3.15) \end{aligned}$$

Again, noting that σ_1 and σ_2 cannot be higher than the material's ultimate tensile strength (σ_{uc}). Hence, for Case III ($\sigma_1 > \sigma_2$ and $\sigma_2 > \sigma_1$), the failure criterion is (Ugural and Fenster 2012)

$$\frac{\sigma_1}{\sigma_{uc}} = -1 \quad \text{or} \quad \frac{\sigma_2}{\sigma_{uc}} = -1 \quad \dots (3.16)$$

Case IV (σ_1 is tensile and σ_2 is compressive - fourth quadrant): When σ_1 and σ_2 are of opposite sign on σ_1, σ_2 plane ($\sigma_1 > 0, \sigma_2 < 0$), instead of σ_3 ($\sigma_3 = 0$), the σ_2 becomes the minor principle stress. Therefore, Eq. (3.8) becomes:

$$\frac{\sigma_1 - \sigma_2}{2} = b + a * \left(\frac{\sigma_1 + \sigma_2}{2} \right) \quad \dots (3.17)$$

In addition, to find the values of a and b , the following conditions should be concerned:

$$\sigma_1 = \sigma_{ut} \quad \text{when} \quad \sigma_2 = 0 \quad \dots (3.18a)$$

$$\sigma_2 = -\sigma_{uc} \quad \text{when} \quad \sigma_1 = 0 \quad \dots (3.18b)$$

Combining Eqs. (3.18a & b) with Eqs (3.8), we obtain

$$a = \frac{\sigma_{ut} - \sigma_{uc}}{\sigma_{ut} + \sigma_{uc}}, \quad b = \frac{\sigma_{ut} * \sigma_{uc}}{\sigma_{ut} + \sigma_{uc}} \quad \dots (3.19)$$

Substitute Eq. (3.19) into Eq. (3.17), the following failure criterion is obtained:

$$\frac{\sigma_1}{\sigma_{ut}} - \frac{\sigma_2}{\sigma_{uc}} = 1 \quad \dots (3.20)$$

The graphical representation of the Coulomb–Mohr theory can be obtained through plotting the expressions in Eqs. (3.10), (3.14), (3.16), and (3.20) for the all four cases as shown in Figure (3.4). The Coulomb-Mohr theory predicts failure if any state of stress in the material lay on, or extends beyond the shaded area in Figure (3.4). Regarding pure shear, point a in Figure (3.4) represents the boundary point.

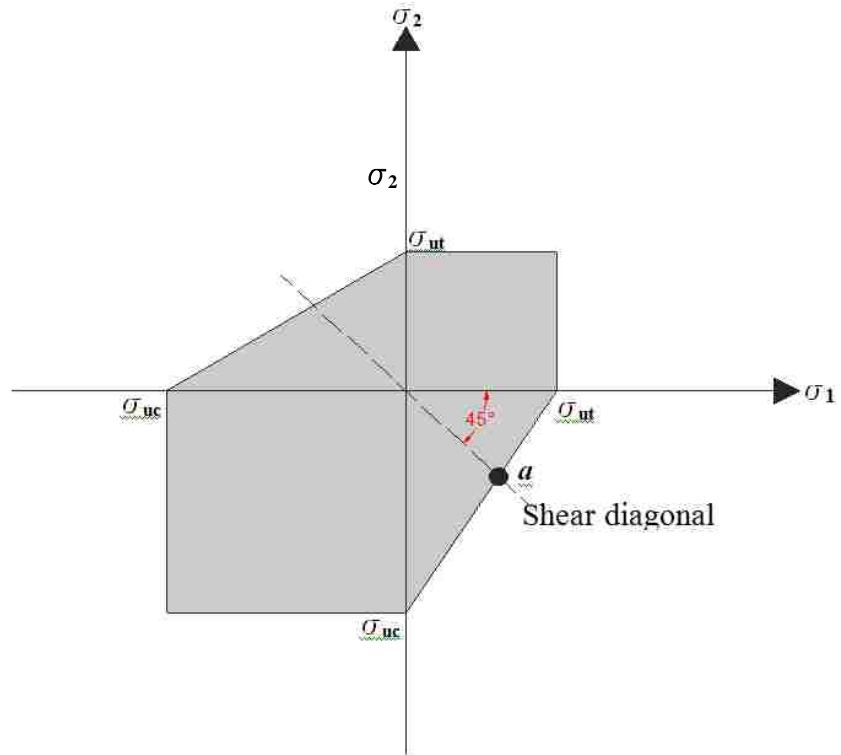


Figure (3.4) Coulomb–Mohr criterion

3.5.4 Griffith’s Criterion of Tensile Failure (1921)

Theoretically, strength of any substance comes from the bonds between the substance’s molecules (cohesive forces between atoms of the substance) (Jumikis 1983; Franklin and Dusseault 1989), and it is about ten percent of the Young’s modulus, $0.1 E$ (Anderson 1995; Meyers and Chawla 2009). However, in reality, due to existence of natural flaws (microfractures) in almost all materials, it is well known that the true strength is usually lower than the theoretical strength. This observation led Griffith to adopt a new criterion to predict failure rupture in brittle materials that has later become

one of the most famous theories in materials science (Jumikis 1983; Franklin and Dusseault 1989; Roylance 2001).

Griffith elucidated that the difference between the theoretical and the actual strength is due to the natural defects (thin flat, narrow, elliptical uniform microcracks, also called Griffith's cracks) in brittle materials which act as stress riser which in turn act as strength reducer; stress concentrations at the crack tips lead to lower the fracture strength of the materials (Jumikis 1983; Franklin and Dusseault 1989; Roylance 2001). According to Griffith theory, using the Minimum Strain Energy theorem, crack propagation occurs when the released elastic strain energy is at least equal to the energy required to generate new crack surfaces.

Consider an infinite plate with t thickness containing a crack with length of $2a$ (Figure (3.5a)). When the crack is introduced into the unstressed plate, an increase in the surface energy is produced due to creating two new crack surfaces. Accordingly, the increased surface energy equals (Meyers and Chawla 2009):

$$\text{Increased surface energy} = 2at (2\gamma_s) \quad \dots (3.21)$$

where γ_s is the specific surface energy, i.e., the energy per unit area.

When the plate is subjected to a tensile stress, σ , through the remote ends as shown in Figure (3.5b), the crack opens up and the stored elastic energy is released. According to Meyers and Chawla (2009), for an infinite plate with t thickness containing a crack (Figure (3.5b)), the released elastic energy is approximately equal to the shaded area in Figures (3.5b & c). Recalling that the elastic energy per unit volume for a stressed solid body is equal to half of the area under the linear part of a stress-strain curve, $\sigma^2/2E$, the released total strain energy can be found from multiplying the elastic energy per unit

volume by the volume over which elastic energy is released (or $2 \pi a^2 t$ - the volume of the shaded ellipse in Figures (3.5b & c)). Thus

$$\text{Total strain energy released} = \frac{\pi \sigma^2 a^2 t}{E} \quad \dots (3.22)$$

The difference between the total strain energy released due to the stress and the increased surface energy due to the crack introduction into the plate is equal to the change in potential energy of the plate, U , and can be found by subtracting Eq. (3.22) from Eq. (3.21), or

$$U = 2at (2\gamma_s) - \frac{\pi \sigma^2 a^2 t}{E} \quad \dots (3.23)$$

The maximum stress at which the crack is still stable and does not propagate (equilibrium condition) can be found by equating to zero the first derivative of Eq. (3.23) with respect to the crack length. Thus

$$\sigma_{max} = \sqrt{\frac{2E\gamma_s}{\pi a}} \quad \dots (3.24)$$

Accordingly, Griffith obtained his failure criterion from Eq. (3.24) by assuming that the maximum stress is the stress required for crack propagation (failure stress) as follows

$$\text{For plane stress} \quad \sigma_{failure} = \sqrt{\frac{2E\gamma_s}{\pi a}} \quad \dots (3.25)$$

$$\text{For plane strain} \quad \sigma_{failure} = \sqrt{\frac{2E\gamma_s}{(1 - \nu^2)\pi a}} \quad \dots (3.26)$$

where σ_f is the applied stress, a is half the crack length, E is the modulus of elasticity of the material, γ_s is the specific surface energy, ν is the Poisson's ratio.

Griffith failure criterion was originally adopted for ideally brittle material (glass rods - very brittle material) (Jumikis 1983; Franklin and Dusseault 1989; Roylance 2001). However, there are some brittle materials which not ideally brittle and normally undergo plastic deformation prior to failure (fracture); plastic deformation in the material near the crack tip (blunting of the crack tip) causes energy dissipation which in turn leads to an increase in the fracture stress; relaxing stress concentration by increasing the radius of curvature of the crack at its tip (Roylance 2001; Meyers and Chawla 2009). Accordingly, the Griffith's equation was modified by Irwin and Orowan to be suitable for non-ideal brittle materials by including the plastic work, γ_p , into the total elastic surface energy necessary for extending the crack wall. The Griffith's equation can then be rewritten as follows (Roylance 2001; Meyers and Chawla 2009)

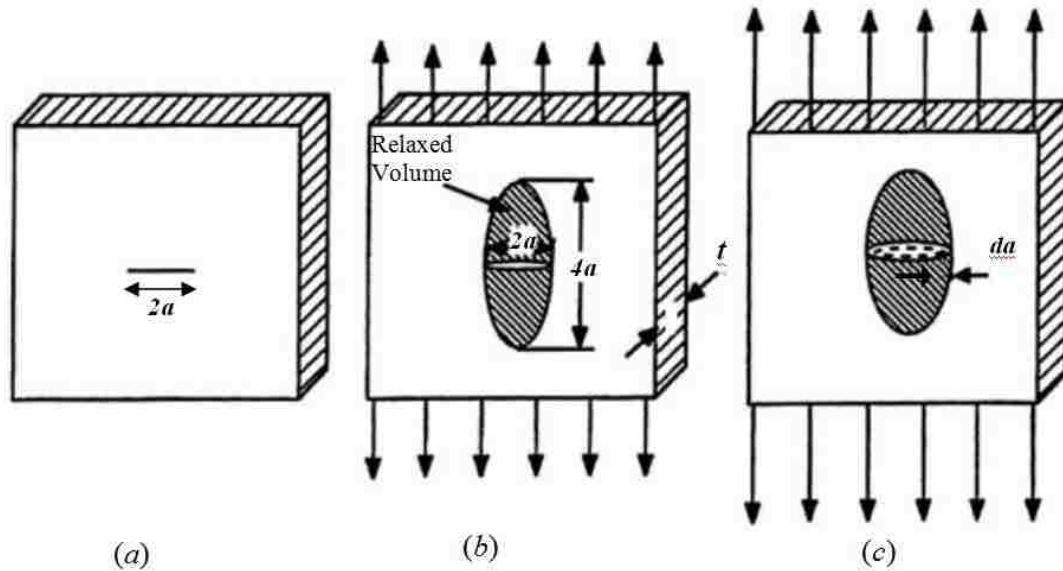
$$\text{For plane stress} \quad \sigma_{failure} = \sqrt{\frac{2E(\gamma_s + \gamma_p)}{\pi a}} \quad \dots (3.27)$$

$$\text{For plane strain} \quad \sigma_{failure} = \sqrt{\frac{2E(\gamma_s + \gamma_p)}{(1 - \nu^2)\pi a}} \quad \dots (3.28)$$

where γ_p is plastic work. Since the γ_s is relatively small compared to plastic work γ_p ($\gamma_s = 0.1\gamma_p$) (Meyers and Chawla 2009), the Eqs. (3.27) and (3.28) can be rewritten as follows:

$$\text{For plane stress} \quad \sigma_{failure} \cong \sqrt{\frac{2E(\gamma_p)}{\pi a}} \quad \dots (3.29)$$

$$\text{For plane strain} \quad \sigma_{failure} \cong \sqrt{\frac{2E(\gamma_p)}{(1 - \nu^2)\pi a}} \quad \dots (3.30)$$



Figure(3.5) A plate of thickness t containing a crack of length $2a$. (a) Unloaded condition, (b) and (c) Loaded conditions (Meyers and Chawla 2009).

3.6 Fracture Mechanics

An existing crack within a material may stay intact under a given condition of loading and environment (Roesler et al., 2007). These types of crack are called stationary cracks (or non-propagating cracks). If the loading and environment conditions are changed, the crack size may change too; the crack may extend and propagate. The branch of mechanics which deals with the conditions of loading and environments which causes an existing crack to extend to a critical size at which an instant fracture occurs is called fracture mechanics (Roesler et al., 2007; Ugural and Fenster 2012). Regarding brittle materials, fracture mechanics deals with the conditions of loading and environments under which the existing crack extends rapidly to a critical value at which an instant failure appears (Ugural 2004; Roesler et al., 2007; Ugural and Fenster 2012).

3.6.1 Stress Concentration in Brittle Materials

It is well known that the fracture in brittle materials is connected to high local stresses and strains over a very small area in the immediate vicinity of geometrical irregularities (defects) such as cracks, sharp corners, fillets, notches and holes (Roylance 2001; Gordon 2003; Meyers and Chawla 2009; Pytel and Kiusalaas 2012; Ugural and Fenster 2012). These defects, both natural and artificial, may raise the stresses around their immediate surrounding area to a level much higher than the material capacity even when the stresses in the parts away from the defects are low and safe (Gordon 2003; Meyers and Chawla 2009). The condition which produces the high local stresses is called stress concentration, and it is the primary cause of failure in brittle material (Ugural 2004). Hence, knowing the amount and distribution of these stresses and strains around the geometrical irregularities in brittle materials is vital for design engineers.

Consider a thin plate contains a notch or a sharp crack, Fig. (3.6a & b), subjected to tensile stress through the remote ends; ends far away from the notch or the crack. As shown in the figure, the black lines, lines of forces which represent the in-plane stresses produced by the uniform tensile stress, are distributed uniformly at the ends of the plate and clustering near the tip of the notch, or the crack. This leads to concentrating more force lines in a smaller area near the crack or notch tip which in turns leads to produce high local stresses; stress.

In fracture mechanics, this high localized stress, stress concentration, is connected to the nominal stress by a geometric (or theoretical) factor that called stress concentration factor (Ugural 2004). The stress concentration factor, typically denoted by K_t , is the ratio of the maximum stress at the flaw immediate vicinity to the nominal stress (Ugural

2004). The nominal stress is the stress that would occur in the same material if it was free from flaws (ideal material), of course under the same loading condition; stress σ .

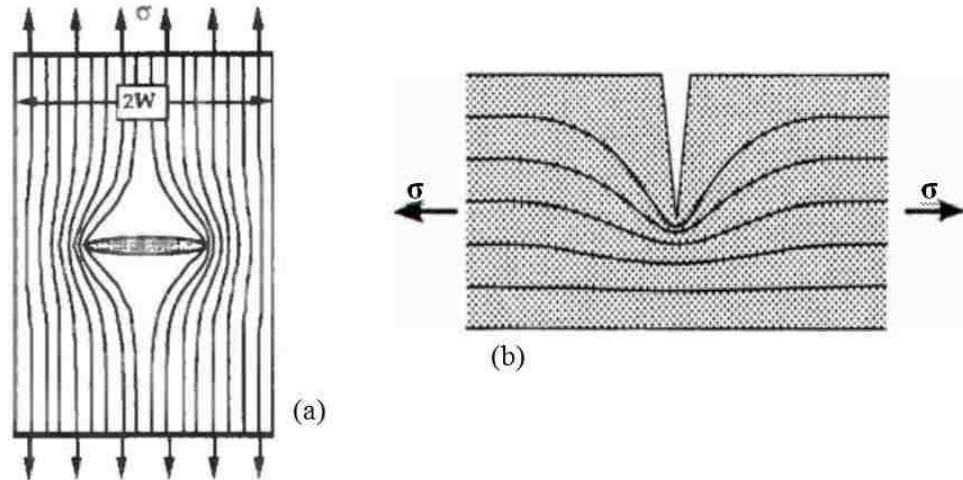


Figure (3.6) “Lines of force” in a bar with (a) a sharp crack and, (b) a side notch. (Meyers and Chawla 2009).

Inglis (1913) was the first who provided a formula to describe the stress concentration due to flaws through analyzing a flat plate containing an elliptical hole ($2a$ long by $2b$ wide) subjected to uniform stresses (σ) as shown in Figure (3.7) (Anderson 1995). Inglis found that, when the ratio a/b increases (elliptical hole changes to a sharp crack), the stress at the leading edge of the hole becomes extremely large (Anderson 1995; Meyers and Chawla 2009). Accordingly, the maximum stress occurs at the ends of the leading edge of the elliptical hole, point A in Figure (3.7), and its value is given in the following formula.

$$\sigma_{max} = \sigma_A = \sigma \left(1 + 2\sqrt{\frac{a}{\rho}} \right) \quad \dots (3.31)$$

where ρ is the radius of curvature of the leading edge of the elliptical hole.

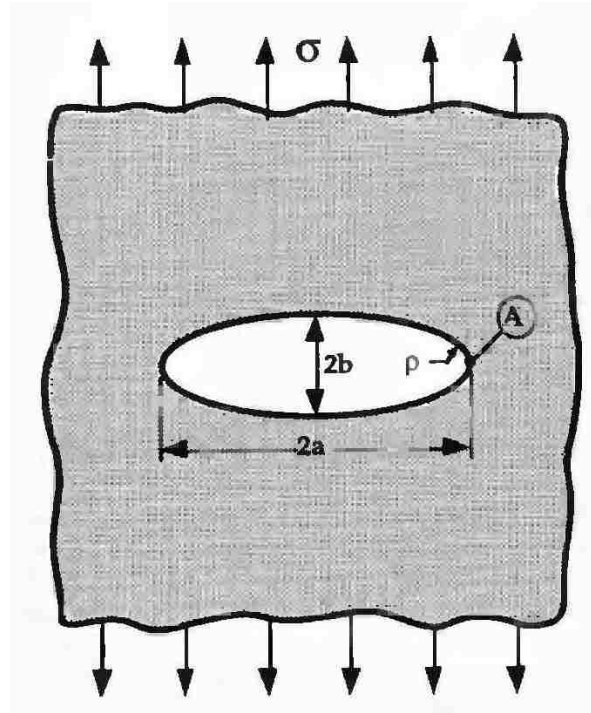


Figure (3.7) Elliptical hole in a flat plate (Anderson 1995).

5.6.2 The Stress Field near a Crack Tip

From Eq. (3.31), when the radius of curvature (ρ) approaches zero (such as in a sharp crack), the stress at the ends of the leading edge of the crack, crack tips, approaches infinity. This is called stress singularity, and always exists in isotropic, linearly elastic materials under condition of plane strain or plane stress (Hutchinson 1983; Roesler et al., 2007). Basing on this, stress singularity existing near the crack tip which is one of the basic hypotheses of linear elastic fracture mechanics as well, the general form of stress singularity can be represented as follow (Hutchinson 1983; Anderson 1995):

$$\sigma_{ij} = \frac{K}{\sqrt{2\pi r}} f_{ij}(\theta) \quad \dots (3.32)$$

where K is the amplitude of singularity and called stress intensity factor, f_{ij} are dimensionless functions, or θ -variation (Hutchinson 1983), r is polar coordinate and should be smaller than the crack size, or crack length (Meyers and Chawla 2009). Both K and f_{ij} are describing the stress distribution around the crack tip, and they depend on the types of loading which the crack can experience; crack deformations (Hutchinson 1983; Anderson 1995; Meyers and Chawla 2009). Although the stress singularity in Eq. (3.32) is for two dimensional elastic materials, the K and f_{ij} are the same for all cracks in two- or three-dimensional elastic materials (Meyers and Chawla 2009).

In fracture mechanics, three different modes in which a crack in a solid can be stressed have been distinguished as illustrated in Figure (3.8); Mode I, Mode II, and Mode III (Broek 1986; Anderson 1995; Ugural and Fenster 2012; Meyers and Chawla 2009). The first mode, Mode I (see Figure (3.8a)), has tensile stress normal to the crack plane tends to open the crack and called opening mode. The Mode II (see Figure (3.8b)) has in-plane shear stress tends to slide one face of the crack on the other face and called sliding mode. The third mode, Mode III (see Figure (3.8c)), has out-of-plane shear tends to tear the crack, through sliding it transversely, and called tearing mode or transverse shear mode. A crack can be stressed in any one of these modes (Anderson 1995). However, a combination of two or three modes can also occur (Anderson 1995; Roesler et al., 2007).

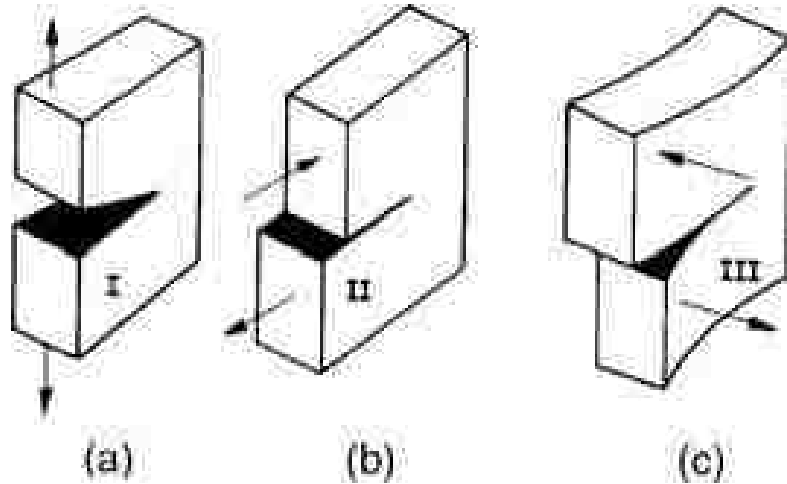


Figure (3.8) The three modes of fracture. (a) Mode I: opening mode. (b) Mode II: sliding mode. (c) Mode III: tearing mode (Meyers and Chawla 2009).

The stress components, their derivations are attributed to Westergaard 1939, corresponding to the crack modes are given below (see Figure (3.9)) (Meyers and Chawla 2009):

MODE I:

$$\begin{bmatrix} \sigma_{11} \\ \sigma_{22} \\ \sigma_{12} \end{bmatrix} = \frac{K_I}{\sqrt{2\pi r}} * \cos \frac{\theta}{2} * \begin{bmatrix} 1 & -\sin \frac{\theta}{2} & \sin \frac{3\theta}{2} \\ 1 & \sin \frac{\theta}{2} & \sin \frac{3\theta}{2} \\ \sin \frac{\theta}{2} & \cos \frac{3\theta}{2} \end{bmatrix} \quad \dots (3.33)$$

$$\sigma_{13} = \sigma_{23} = 0, \quad \sigma_{33} = \nu(\sigma_{11} + \sigma_{22}) \text{ (plane strain)}, \sigma_{33} = 0 \text{ (plane stress)}$$

MODE II:

$$\begin{bmatrix} \sigma_{11} \\ \sigma_{22} \\ \sigma_{12} \end{bmatrix} = \frac{K_{II}}{\sqrt{2\pi r}} * \begin{bmatrix} -\sin \frac{\theta}{2} & \left(2 \cos \frac{\theta}{2} * \cos \frac{3\theta}{2}\right) \\ \sin \frac{\theta}{2} & \cos \frac{\theta}{2} \cos \frac{3\theta}{2} \\ -\cos \frac{\theta}{2} & \left(1 - \sin \frac{\theta}{2} * \sin \frac{3\theta}{2}\right) \end{bmatrix} \quad \dots (3.34)$$

$$\sigma_{13} = \sigma_{23} = 0, \quad \sigma_{33} = \nu(\sigma_{11} + \sigma_{22}) \text{ (plane strain)}, \sigma_{33} = 0 \text{ (plane stress)}$$

MODE III:

$$\begin{bmatrix} \sigma_{13} \\ \sigma_{23} \end{bmatrix} = \frac{K_{III}}{2\pi r} * \begin{bmatrix} -\sin \frac{\theta}{2} \\ \cos \frac{\theta}{2} \end{bmatrix} \quad \dots (3.35)$$

$$\sigma_{11} = \sigma_{22} = \sigma_{33} = \sigma_{12} = 0$$

For anisotropic materials, the above expressions must be modified to permit the asymmetry of stress at the crack tip (Meyers and Chawla 2009).

The stress intensity factor, K , has a critical value, designated as K_c , and known as fracture toughness. The critical (or maximum) stress intensity factor, K_c , is the force necessary to extend a crack; when the K reaches K_c , the existing cracks will start to propagate and therefore, K_c , is called fracture toughness (Hutchinson 1983; Ugural and Fenster 2012).

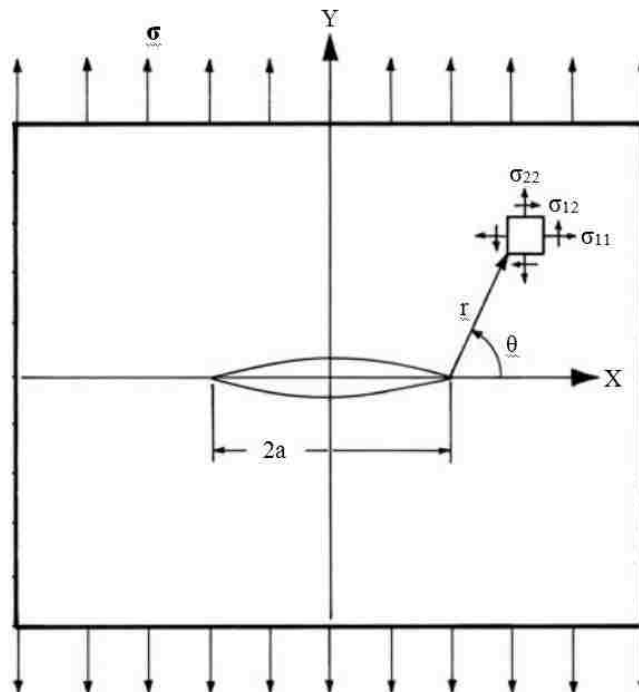


Figure (3.9) Infinite, homogeneous, elastic plate containing a through-the-thickness central crack of length $2a$, subjected to a tensile stress σ (Meyers and Chawla 2009).

3.6.3 Stress Concentration in a Plate containing a Circular Hole

The tangential and radial stresses in a large plate containing a circular hole at the center and subjected to uniaxial load, Figure (3.10), can be expressed in polar coordinate as follows (Timoshenko and Goodier 1951):

$$\sigma_{rr} = \frac{\sigma}{2} \left(1 - \frac{a^2}{r^2} \right) + \frac{\sigma}{2} \left(1 + 3 \frac{a^4}{r^4} - 4 \frac{a^2}{r^2} \right) \cos 2\theta \quad \dots (3.36)$$

$$\sigma_{\theta\theta} = \frac{\sigma}{2} \left(1 + \frac{a^2}{r^2} \right) - \frac{\sigma}{2} \left(1 + 3 \frac{a^4}{r^4} \right) \cos 2\theta \quad \dots (3.37)$$

$$\sigma_{r\theta} = -\frac{\sigma}{2} \left(1 - 3 \frac{a^4}{r^4} + 2 \frac{a^2}{r^2} \right) \sin 2\theta \quad \dots (3.38)$$

where σ is the uniform stress applied at the ends of the plate, a is the radius of the hole, and r is the radial coordinate (distance from the center of the hole).

According to the above equations, the maximum tangential stress, $\sigma_{\theta\theta}$, occurs at a point where $r = a$ and $\theta = \pi/2$ (and $\theta = 3\pi/2$), point A in Figure (3.3), and equals threefold of the applied uniaxial stress, σ . Accordingly the stress concentration factor, K_t , is equal to 3; $\sigma_{\theta\theta}/\sigma = 3$. However, the stress concentration factor, K_t , depending on the plate thickness, plate lateral dimension, D , as well as the ratio of the hole diameter ($2a$) to the plate lateral dimension (D) which changes from about zero to close to unity, the stress concentration factor decreases from 3 to 2.2 (Meyers and Chawla 2009). Note that the radial and shear stress at any point on the periphery of the hole are equal to zero; $\sigma_{rr} = \sigma_{r\theta}$

= 0 for all points located on the hole's circumference. Furthermore, at the points where $r = a$ and $\theta = 0$ (and $\theta = \pi$), north and south poles, an opposite stress to the applied stress at the ends of the plate will be produced; if the applied stress at the ends of the plate is compression, the produced stresses at the north and south poles will be tension. Thus

$$\text{For } r = a \text{ and } \theta = 0 \text{ (and } \theta = \pi), \quad \sigma_{rr} = \sigma_{r\theta} = 0, \text{ and } \sigma_{\theta\theta} = -\sigma$$

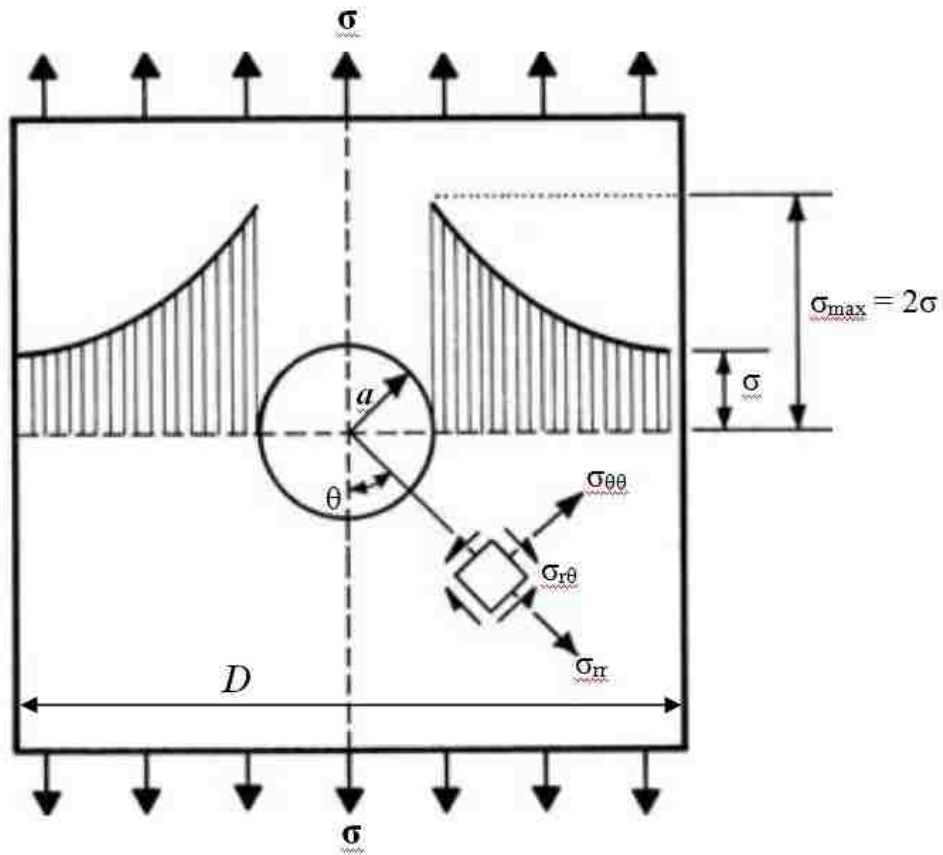


Figure (3.10) Stress distribution in a large plate containing a circular hole (Meyers and Chawla 2009).

3.7 Failure Criteria for Rocks

Rocks are actually quasibrittle materials (Anderson 1995). Under high confining pressures and temperatures, rocks may exhibit ductile behavior; yielding and deforming

plastically before failure, while, under normal temperature and pressure, they are considered as brittle materials, and fracture at or very near to the proportional limit of elasticity; their plastic deformation, if any, is relatively very small (Jumikis 1983; Franklin and Dusseault 1989).

Strength of rocks is regarded as the stress needed to cause failure at a given environmental condition; in another word, it is regarded as the resistance of rocks to external applied loads, (Jumikis 1983). The most two important types of failure in rocks are fracture (brittle fracture) and rupture ((Bieniawski et al., 1961)). Fracture is regarded as a process by which creating new crack surfaces or/and extending the existing cracks ((Bieniawski et al., 1961)). It means a complete loss of cohesion across the surface of failure which is well connected to the initiation and propagation of cracks caused by stresses (tensile stresses) (Andreev 1995). Very good definition for the two failure mechanisms can be found in Bieniawski et al. (1961) as follow:

*“.....**Fracture** is the failure process by which new surfaces in the form of cracks are formed in a material or existing crack surfaces are extended. Various stages of fracture may be visualized, namely, fracture initiation, fracture propagation (stable and unstable) and strength failure. **Rupture** is the failure process by which a structure (e.g. a rock specimen) disintegrates into two or more pieces”*

Rock failure criterion is an equation, or formula, that used to predict the strength value of rock under all combination of multiaxial stresses ((Bieniawski et al., 1961; Jumikis 1983; Franklin and Dusseault 1989; Andreev 1995). This is usually done through comparing the produced stresses with a critical (strength) value obtained from a simple

test such as the uniaxial tensile or compressive test; if the stresses reached that critical value, the failure should be occurred (Bieniawski et al., 1961).

Although earlier attempts to find the failure criteria of rocks, brittle materials in general, were mainly theoretical and evolved from Griffith's crack theory (Franklin and Dusseault 1989), the most used failure criteria in practice are empirical criteria such as Fairhurst criterion (1964), Hobb's criterion (1970), Franklin's criterion (1971), Bieniawski criterion (1974), Yudhbir criterion (1983), Johnston criterion (1985), Sheorey criterion (1989), Yoshida criterion (1990), Ramamurthy criterion (1993), Hoek and Brown criterion (2002), and Mogi criterion (2007). This is due to the fact that the theoretical attempts were not fit the experimental data particularly well. The theoretical criteria are Griffith and Mohr-coulomb criteria (Franklin and Dusseault 1989). However, the most accepted and widely used theoretical and empirical strength criteria for both intact rock and rock masses are Mohr-Coulomb criterion and Hoek-Brown criterion (Franklin 1989: Hoek and Brown 2002).

3.7.1 Griffith criterion (1921).

Basing on the energy instability concept mentioned in his criterion of tensile failure (1921), Griffith (1924) extended his theory and stated that fracture of brittle, isotropic, and elastic material, initiated due to presence of micro-cracks and flaws, can propagate and lead to tensile failure through producing stress concentration around the tips of the defects even under compressive stress conditions (Norton 1997). Griffith criterion was originally adopted for purely brittle material, glass, and then later expanded

to other brittle materials such as rock (Norton 1997; Brady and Brown 2006). It can be expressed in terms of principle stress as follow

$$(\sigma_1 - \sigma_3)^2 = 8T(\sigma_1 + \sigma_3) \quad \text{for } \sigma_1 + 3\sigma_3 \geq 0 \quad \dots (3.39)$$

$$\sigma_3 = T \quad \text{for } \sigma_1 + 3\sigma_3 < 0 \quad \dots (3.40)$$

where T is the uniaxial tensile strength of intact rock.

Griffith theory does not provide a very good model with regarding to the experimental tests of rocks under multiaxial compression (Brady and Brown 2006). Therefore, it has been modified by several researchers. One of them is Murrell (1966) (Brady and Brown 2006). In terms of shear stress, τ , and the normal stress, σ_n , acting on the plane containing the major axis of the crack, Murrell (1966) modified Griffith criterion and expressed as follow (Brady and Brown 2006)

$$\tau^2 = 8T(2T + \sigma_n) \quad \dots (3.41)$$

However, the Murrell's modification is only valid for the condition in which the uniaxial compressive strength is eight times the uniaxial tensile strength. Note that, Murrell equation is the same as Mohr's envelop equation.

3.7.2 Mohr-Coulomb criterion.

This criterion was based on the assumption that there will be a plane in rock and soil, called critical plane, on which the material shear strength will be first reached as the peak stress, σ_1 , is increased, see Figure (3.11a) (Brady and Brown 2006). The critical plane, β , can found through constructing the Mohr circle as shown in Figure (3.11b). Accordingly, in principle stress coordinate, assuming that the intermediate stresses has

not effects on the failure criteria, the Mohr-Coulomb criterion for rocks can be expressed by the following equation:

$$\sigma_1 = \frac{2c \cos \phi + \sigma_3(1 + \sin \phi)}{1 - \sin \phi} \quad \dots (3.42)$$

where c = cohesion and ϕ = angle of internal friction.

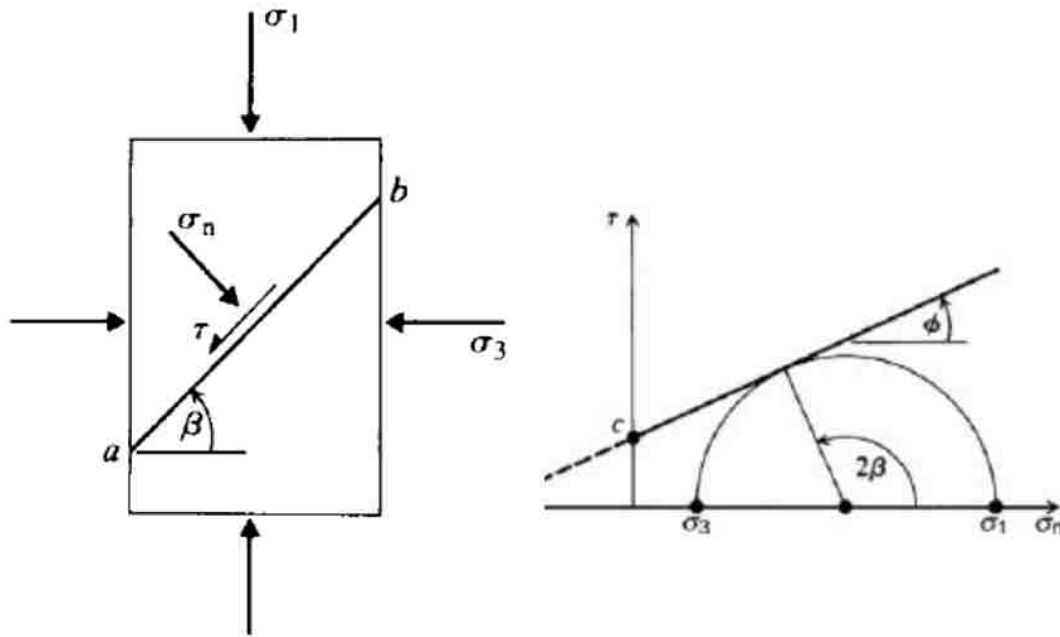


Figure (3.11) Mohr_Coulomb criterion (a) Shear failure on plane ab, (b) Strength envelope in terms of shear and normal stresses (Brady and Brown 2006).

For $\sigma_3 = 0$, uniaxial compressive strength can be related to c and ϕ as follows

$$\text{uniaxial compressive strength, } \sigma_c = \frac{2c \cos \phi}{1 - \sin \phi} \quad \dots (3.43)$$

For $\sigma_1 = 0$, uniaxial tensile strength can be related to c and ϕ as follows

$$\text{uniaxial tensile strength, } \sigma_t = -\sigma_3 = \frac{2c \cos \phi}{1 + \sin \phi} \quad \dots (3.44)$$

The determination of a satisfied value of the uniaxial tensile strength of rock, σ_t , is full of difficulty because the results from Eq. (3.44) are generally higher than the measured values from the experimental tests (Brady and Brown 2006). Therefore, a selected value of uniaxial tensile stress, called tensile cutoff and designated by T_o , is usually applied as shown in Figure (3.12). However, for practical purpose, it is better to put tensile cutoff to zero.

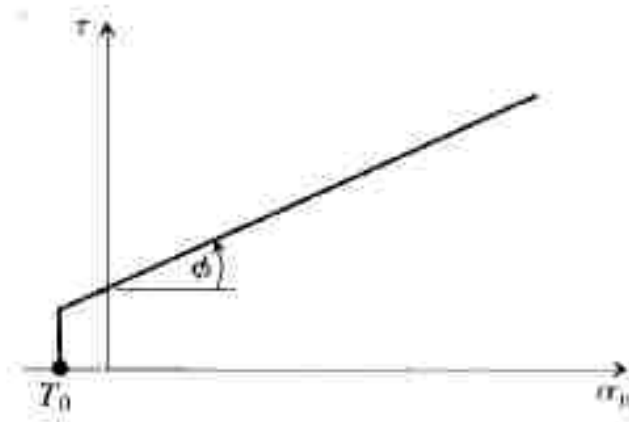


Figure (3.12) Coulomb strength envelopes with a tensile cut-off T_o (Brady and Brown 2006).

According to Brady and Brown (2006), the Mohr-Coulomb criterion is not preferred for intact rock to obtain the peak strength. However, it is very helpful in obtaining the residual shear strength of materials and the shear strength of discontinuities in rocks.

3.7.3 Hoek-Brown criterion (2002)

A widely accepted failure criterion, applied in a large number of projects around the world, was derived by Hoek and Brown (1980) to describe the characterizations for

both intact rocks and rock masses. It is considered as the most important criterion which has a high capability of describing both intact rock and rock masses behaviors. The criterion was first developed for intact rocks and then modified to describe the characteristics of joints in rock masses (Hoek and Brown 2002). Its generalized form is expressed as:

$$\sigma'_1 = \sigma'_3 + \sigma_{ci} \left(m_b \frac{\sigma'_3}{\sigma_{ci}} + s \right)^a \quad \dots (3.45)$$

$$m_b = m_i e^{\left(\frac{GSI-100}{28-14D} \right)} \quad \dots (3.46)$$

$$s = e^{\left(\frac{GSI-100}{9-3D} \right)} \quad \dots (3.47)$$

$$a = \frac{1}{2} + \frac{1}{6} \left(e^{\frac{-GSI}{15}} - e^{\frac{-20}{3}} \right) \quad \dots (3.48)$$

where σ_{ci} is uniaxial compressive strength of intact rock, m_i , s , and a are material constants; m_i is a intact rock and s and a are for the rock mass. D is disturbance factor; disturbances come from blast damage and stress relaxation. The values of D are changes from zero for undisturbed in situ rock masses to 1 for very disturbed rock masses. And GSI is the Geological Strength Index which describes both rock mass's structure and surface condition (Hoek and Brown 2002).

3.8 Failure Modes of Brittle Materials in General

The mechanical behaviors of brittle materials, such as rock and concrete, are mainly affected by pressure (confining stress), strain rate, temperature, and pore fluid pressure (Horri and Nemat-Nasser 1986). However, under a certain temperature (low temperature) and above a certain strain rate, the confining pressure is the main controlling factor for dry materials. Regarding failure under compression, solids made of brittle

materials fail by a process of progressive microfracture (Sammis and Ashby 1986). Flaws or stress concentrations within the solids, such as pores, inclusions, and small cracks (often grain-sized cracks left by its earlier thermal or mechanical history), initiate individual microcracks. These microcracks within the solids propagate in a direction approximately parallel to the largest principal compressive stress until they coalesce to form one of several types of failure modes. Basing on a long list of previous works, Horri and Nemat-Nasser (1986) identified three main failure modes for brittle materials under compression with low temperature and rate-independent process (loading) as follows:

- 1- Axial splitting at zero lateral confining pressure, or uniaxial compression test. Under uniaxial compression loading, microscopic cracks initiate at the vicinity of the flaws. Accordingly macrocracks may extend in the direction of axial compression which in turn leads to the axial splitting.
- 2- Faulting or macroscopic shear failure at low to moderate confining pressure. For low to moderate confining pressure, a narrow region of high microcrack density will be formed. At the axial stress close to the ultimate strength, the region is finally forming a fault plane.
- 3- Ductile flow or cataclastic flow at large confining pressure. For this failure mode, the formation of the narrow region of high microcrack density is suppressed by the high confining pressure. Accordingly, depending on the material (types of rocks) and the temperature and pressure level, either ductile flow or cataclastic flow will be formed. The ductile flow is produced by plastic deformation throughout the sample, while the cataclastic flow is characterized by distributed microcracking.

Since the compressive strength of brittle materials increases with confining pressure increasing, the uniaxial compressive strength can be taken as a good measure of minimum strength of brittle materials under compression. Accordingly the failure modes of brittle material under uniaxial compression can be helpful in designing engineering structures safely and economically (Maji 2011).

3.9 Failure Modes of Brittle Porous Solids under Compression Stress

For porous solids made of brittle materials, when they are loaded in compression, the individual microcracks initiate at the pore peripheries. These microcracks propagate and coalesce to form a failure mode depending on the confining stress. Sammis and Ashby (1986) identified three main types of failure modes under compression for brittle porous solids as shown in Figure (3.13):

- 1- Axial splitting or vertical slabbing: Under uniaxial compression loading, microcracks initiate, propagate and finally coalesce to form contiguous vertical failure planes as shown in Figure (3.13a).
- 2- At low to intermediate confining pressures, failure appears as a shear fault, or as a shear band as shown in Figure (3.13b). The inclination of the shear band changes with the confining pressure. It is often following a simple Coulomb failure criterion.
- 3- At high confining pressures, the sample deforms in a pseudo-ductile mode; many, short, homogeneously distributed, microfractures will be formed at large-scale deformation as shown in Figure (3.13c).

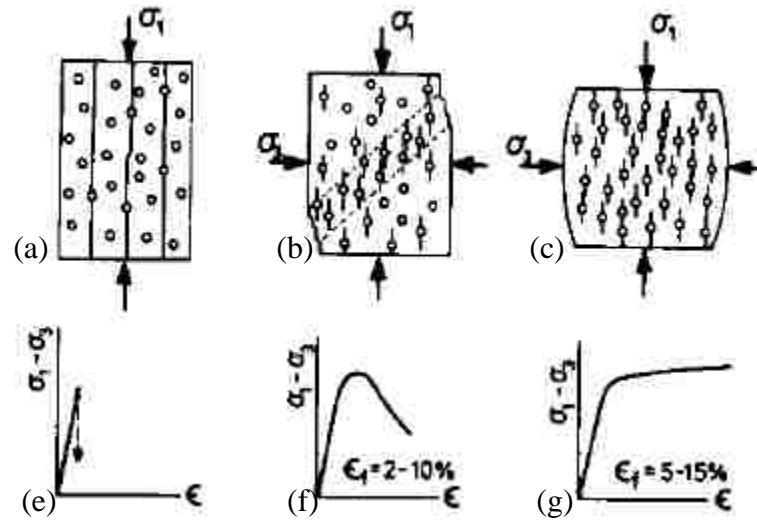


Figure (3.13) Failure Modes and Stress- Strain Curves for Porous Solids (Sammis and Ashby 1986)

From the stress- strain curves, for porous solids with zero confining pressure, the axial-stress-axial-strain curve will be composed of a peak stress followed by a very sharp descending portion. They show a zero hardening beyond the peak stress, see the stress-strain curve shown in Figure (3.13e). The hardening beyond the peak stress increases with increasing confining pressure as shown in Figures (3.13f & g). Eventually, at high confining pressure, the portion of the axial-stress-axial-strain curve, after peak stress, starts to ascend and transits gradually from brittle to ductile stress-strain curve; see the stress-strain curve in Figure (3.13g). At this stage several short, homogenously distributed, microfractures will be formed throughout the sample.

In addition, according to Hudyma et al. (2004) and Jespersen et al. (2010), for porous solids under uniaxial compression, the failure modes are mainly depending on void porosity and bridge distances. Accordingly, they identified three main failure modes; axial splitting (or tensile failure), shear failure, and web failure. For void porosity

$\leq 10\%$, and for bridge distances from 0.5 to 1.5 void diameters, the dominant failure mode was axial splitting (vertical to sub-vertical tension fractures oriented approximately parallel to the applied axial load), see Figures (2.38) and (2.39a) in Chapter Two. For void porosity range 10 – 20%, and for bridge distance of 1.5 void diameters, the dominant failure mode was shear failure as shown in Figures (2.38) and (2.39b). Finally, according to Hudyma et al. (2004), the dominant failure mode was web failure for void porosity $\geq 20\%$, see Figure (2.38). However, at bridge distances greater than 1.5 void diameters, the dominant failure mode returns to tensile failure as shown in Figure (2.39c).

CHAPTER FOUR ANALYSIS OF THE EXPERIMENTAL RESULTS

4.1 Introduction

In this chapter, the data from the work of Project Activity Task ORD-FY04-013, conducted under Cooperative Agreement No. DEFC28-04RW12232 between the U.S. Department of Energy and the Nevada System of Higher Education (NSHE), are analyzed to explore the effects of void geometry, besides porosity, on the mechanical properties of rock-like material (analog material). The main purpose of the work of Project Activity Task ORD-FY04-013 was to study the effects of void porosity and void geometry on the mechanical behavior of lithophysal-rich tuff from the Topopah Spring formation at Yucca Mountain using rock-like material (analog material).

Since until nowadays, the effects of void size, void shape, void orientation, and void spatial distributions on the mechanical properties of rock-like materials have not been addressed in the correlations between the mechanical behaviors of rock-like materials (UCS and E) and void porosity, this chapter aims to find a hypothesis, or hypotheses, that can consider the effects of those factors using the data obtained from the experimental tests carried out in the work mentioned above. In addition, the influences of void existence on failure modes of Hydro-StoneTB[®] cubes are explored to obtain a better insight into the influences of void existences on the crack patterns and failure modes for rocks and rock-like materials.

4.2 Material and Specimens

Due to the reasons mentioned in Chapter One, it is impracticable to obtain actual specimens to quantify the mechanical behaviors of the Topopah Spring formation at Yucca Mountain under uniaxial compression. Therefore, Hydro-StoneTB[®], instead, was used as the rock-like material in the Project Activity Task ORD-FY04-013. To achieve the goals of the Project Activity Task ORD-FY04-013, the Hydro-StoneTB[®] was cast into 152.4x152.4x152.4 mm cubes to produce porous and solid specimens. Fifty two porous specimens were made. Each porous specimen, porous cube, was produced in triplicate. Ten solid cubes were also cast to represent rock-like material with zero void porosity. The total number of experiments, including the ten solid cubes, was one hundred sixty six, 166, cubes.

Due to its easy reproductive ability, cubical shape was selected for the experimental specimens in the Project Activity Task ORD-FY04-013. Furthermore, to compare the experimental results with those of two-dimensional plane strain numerical models, open ended longitudinal openings were used to represent the voids in the porous cubes. However, cubes with longitudinal openings cannot be considered as an exact two-dimensional plane strain models; they lie somewhere between plane strain (infinite length holes) and plane stress (thin plate) assumptions (Rigby 2007). To obtain porous cubes with different void geometries, cubes with open ended longitudinal openings having different cross sectional shape (circular, square, and diamond), different sizes (unsize large, medium, and small), and different void distributions (patterns A, B, and C) were made and tested under uniaxial compression. Tables (4.1) to (4.3) show void porosities and characterizations of void geometry for the porous cubes.

The diameters of the unisize circular openings were 31.14 mm (large), 22.1 mm (medium), and 12.78 mm (small) as shown in Table (4.1). For the samples with mixed voids, the three diameters (large, medium, and small) were mixed in each specimen, see Table (4.2). For the samples with non-circular voids, square and diamond voids, the side lengths of both square and diamond openings were 15.6 mm (small voids) and 22 mm (large void) as shown in Table (4.3). The three void patterns (A, B, and C) were generated depending on the location of the first void. Putting the origin of x-y axis at the center of the cubes, the locations of the first void for the patterns A, B, and C were selected to be at (0, 0), (-38.1, -38.1), and (-53.98, -53.98) respectively as shown in Figure (4.1). The locations of the remained voids in each cube were randomly generated by Itasca Consulting Group, Inc. personnel, in 2004, basing on the following two conditions (1) Void overlapping should not be allowed and (2) The number of voids should not exceed thirty three voids.

Table (4.1) Porous and Solid Cubes - Specimens with Unisize Circular Voids

Description of Voids		Number of Voids	Void Porosity (n), %	Sample Pattern	Number of Samples Tested	
Void Size						
Unisize Circular Voids	Large (L)	31.14 mm	2	6.56	A	3
					B	3
					C	3
		31.14 mm	4	13.12	A	3
					B	3
					C	3
		31.14 mm	6	19.68	A	3
					B	3
					C	3
	Medium (M)	22.1 mm	4	6.61	A	3
					B	3
					C	3
		22.1 mm	8	13.21	A	3
					B	3
					C	3
		22.1 mm	12	19.82	A	3
					B	3
					C	3
	Small (S)	12.78 mm	11	6.07	A	3
					B	3
					C	3
12.78 mm		22	12.14	A	3	
				B	3	
				C	3	
12.78 mm		33	18.22	A	3	
				B	3	
				C	3	
Total Number of Cubes					81	

Table (4.2) Porous and Solid Cubes - Specimens with Mixed Circular Voids

Description of Voids	Size of Voids, mm	Number of Voids	Void Porosity, <i>n</i> , %	Sample Pattern	Number of Cubes Tested
Mixed Circular Voids	12.78 – 31.14 (1L, 1M, 3S)	5	6.59	A	3
				B	3
				C	3
	12.8 – 31.14 (2L, 3M, 6S)	11	14.83	A	3
				B	3
				C	3
	12.78 – 31.14 (2L, 5M, 8S)	15	19.24	A	3
				B	3
				C	3
Total Number of Cubes					27

Table (4.3) Specimens with Square and Diamond Voids

Description of Voids	Side Length of Voids, mm	Number of Voids	Void Porosity, <i>n</i> , %	Sample Pattern	Number of Cubes Tested
Large Diamond Voids (L)	22.05	3	6.28	A	3
				B	3
	22.05	6	12.56	A	3
				B	3
Small Diamond Voids (S)	15.65	6	6.32	A	3
				B	3
	15.65	12	12.65	A	3
				B	3
Large Square Voids (L)	22.05	3	6.28	A	3
				B	3
	22.05	6	12.56	A	3
				B	3
Small Square Voids (S)	15.65	6	6.32	A	3
				B	3
	15.65	12	12.65	A	3
				B	3
Total Number of Cubes					48

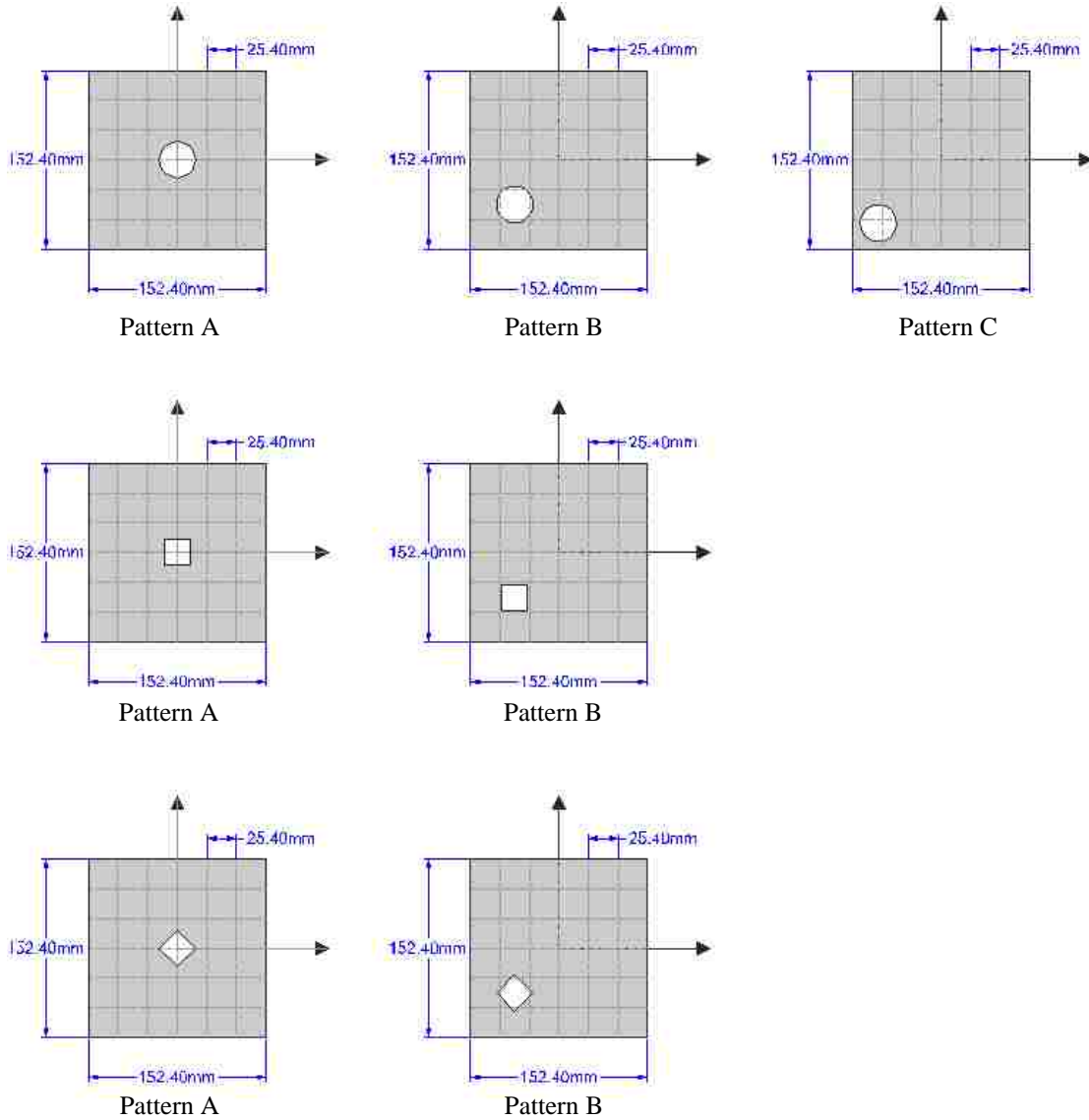


Figure (4.1) Location of First Void; Patterns A, B, and C for Circular Voids, and Patterns A and B for Non-circular Voids

4.3 Laboratory Experiments

The cubical specimens, both solid and porous cubes, were tested in a large Instron 600RD load frame, hydraulically driven, with a load capacity of 3000 kN (600 kips) and the strain rate of about 3×10^{-5} at the Nevada Department of Transportation (NDOT)

materials lab facility in Las Vegas. The Instron load cell force measurement accuracy is $\pm 0.2\%$ of its full-scale output. The axial and lateral displacement transducers (LVDTs) were Daytronic ± 0.1 inches full-scale LVDTs and each had accuracy within $\pm 0.5\%$. The uniaxial compressive strength (*UCS*) and Young's Modulus (*E*) were calculated for each specimen from the stress-strain curve of uniaxial compression test as follows:

- 1- The peak load divided by the original cube surface area (152.4x152.4 mm) was taken as the ultimate strength; the uniaxial compressive strength:

$$\text{Uniaxial Compressive Strength (UCS)} = \frac{\text{Peak Load}}{\text{Area of the Cube}} \quad \dots (4.1)$$

- 2- The modulus of elasticity of the cubes, Secant Young's Modulus, was found from the stress-strain curve plotted for each specimen by taking the ratio of the difference between 50% of the uniaxial compressive strength and 25% of the uniaxial compressive strength to the difference of their corresponding strains as shown in the following equation:

$$\text{Young's Modulus (E)} = \frac{50\% \text{ of UCS} - 25\% \text{ of UCS}}{\text{Strain}_{50\% \text{ of UCS}} - \text{Strain}_{25\% \text{ of UCS}}} \quad \dots (4.2)$$

4.4 Analysis of Experimental Results

In order to obtain high-quality data analysis, the data should be cleansed searching for anomalies (incomplete, or incorrect, data) and checking the data precision (accuracy). Searching for anomalies was done through comparing the existing data to the

data in the original documents which were kept in Soil Mechanics Laboratory at UNLV. Regarding the data accuracy, British Standards (BS 1881: 1983) was used to check the precision data. According to the British Standards (BS 1881: Part 116: 1983), the precision data for measurements of the compressive strength of hardened concrete can be expressed as percentage of the mean of the cube strengths whose differences are not higher than 9%. Since the specimens in Project Activity Task ORD-FY04-013 were tested in triplicate, any cube strength value differs from the mean value by more than 9% is not considered in this analysis. The average values of the experimental results are shown in Tables (4.4) to (4.6). All laboratory test results and the photographs of all tested cubes are shown in Appendix (I). The codes used to name the specimens are in accordance with their void pattern name, void type, void size, and number of voids as follows:

- 1- PA, PB, and PC are patterns A, B, and C respectively (Figure 4.1).
- 2- U = Unisize (all voids have the same size), UX = Mixed (different size voids).
- 3- C = Circular, Sq = Square, and Dm = Diamond.
- 4- L = Large, M = Medium, and S = Small.
- 5- The numbers affixed to the end (2, 3, 4, 6, 8, 11, 12, 22, and 33) indicate the number of voids. and
- 6- The letters affixed to the end of the specimen name (A, B, and C) indicate the number of specimen in the three specimens of the same sample pattern.

The experimental test results in the Project Activity Task ORD-FY04-013 are used to explore the effects of voids on uniaxial compressive strength, elastic modulus, and failure modes of rock-like material. The normalized values are used to generalize the results. The normalization is accomplished by dividing the values of the porous cube's

mechanical properties by the average value of the solid specimen's mechanical properties. Tables (4.7) to (4.9) show the normalized results of the experimental results.

Table (4.4) Experimental Results for Cubes Containing Unisize Circular Voids

Sample Name	Porosity (<i>n</i>)	Uniaxial Compressive Strength, <i>UCS</i>	Young's Modulus, <i>E</i> (25-50%)
	%	MPa	GPa
PA-UCL2-A&B	6.56	19.31	9.36
PA-UCL2-C	6.56	16.62	8.65
PB-UCL2	6.56	17.31	11.74
PC-UCL2	6.56	24.61	9.86
PA-UCL4-A	13.12	18.20	9.66
PA-UCL4-B	13.12	14.27	8.56
PA-UCL4-C	13.12	13.51	8.55
PB-UCL4	13.12	11.55	8.68
PC-UCL4	13.12	16.27	11.27
PA-UCL6	19.68	9.84	6.69
PB-UCL6	19.68	9.63	7.47
PC-UCL6	19.68	9.65	7.54
PA-UCM4	6.61	22.57	12.08
PB-UCM4	6.61	21.48	10.91
PC-UCM4	6.61	24.55	13.42
PA-UCM8	13.21	18.66	7.92
PB-UCM8	13.21	17.34	10.07
PC-UCM8	13.21	13.24	11.85
PA-UCM12	19.82	12.53	8.61
PB-UCM12	19.82	9.41	9.03
PC-UCM12	19.82	5.55	7.57
PA-UCS11	6.07	26.27	11.58
PB-UCS11	6.07	26.74	10.67
PC-UCS11	6.07	21.65	11.38
PA-UCS22	12.14	15.72	9.49
PB-UCS22	12.14	17.56	8.72
PC-UCS22	12.14	16.75	12.09
PA-UCS33	18.22	11.35	8.19
PB-UCS33	18.22	13.27	9.19
PC-UCS33	18.22	10.09	7.44

Table (4.5) Experimental Results for Cubes Containing Mixed Circular Voids

Sample Name	Porosity (<i>n</i>)	Uniaxial Compressive Strength, <i>UCS</i>	Young's Modulus, <i>E</i> (25-50%)
	%	MPa	GPa
PA-UXCL1M1S3	6.59	23.44	11.08
PB-UXCL1M1S3	6.59	23.96	10.85
PC-UXCL1M1S3	6.59	21.19	9.88
PA-UXCL2M3S6	14.83	13.93	7.99
PB-UXCL2M3S6	14.83	13.79	8.18
PC-UXCL2M3S6	14.83	14.69	9.47
PA-UXCL2M5S8	19.24	11.79	7.10
PB-UXCL2M5S8	19.24	10.43	8.30
PC-UXCL2M5S8	19.24	8.20	7.24

Table (4.6) Experimental Results for Cubes Containing Square or Diamond Voids

Sample Name	Porosity (<i>n</i>)	Uniaxial Compressive Strength, <i>UCS</i>	Young's Modulus, <i>E</i> (25-50%)
	%	MPa	GPa
PA-USqL3	6.28	20.98	10.19
PB-USqL3	6.28	28.27	11.34
PA-USqL6	12.56	16.2	10.98
PB-USqL6	12.56	20.02	8.18
PA-USqM6	6.32	26.20	11.11
PB-USqM6	6.32	26.52	10.36
PA-USqM12	12.65	17.37	10.56
PB-USqM12	12.65	16.18	7.73
PA-UDmL3	6.28	16.06	10.32
PB-UDmL3	6.28	22.80	11.50
PA-UDmL6	12.56	11.88	8.95
PB-UDmL6	12.56	10.55	10.02
PA-UDmM6	6.32	19.21	11.71
PB-UDmM6	6.32	22.58	11.22
PA-UDmM12	12.65	11.01	9.26
PB-UDmM12	12.65	16.93	10.72

Table (4.7) Normalized Results for Cubes Containing Unisize Circular Voids

Sample Name	Porosity (<i>n</i>)	Normalized <i>UCS</i>	Normalized <i>E</i> (25-50%)
	%		
PA-UCL2-A&B	6.56	0.351	0.585
PA-UCL2-C	6.56	0.302	0.541
PB-UCL2	6.56	0.315	0.734
PC-UCL2	6.56	0.447	0.616
PA-UCL4-A	13.12	0.331	0.604
PA-UCL4-B	13.12	0.259	0.535
PA-UCL4-C	13.12	0.246	0.534
PB-UCL4	13.12	0.210	0.543
PC-UCL4	13.12	0.296	0.704
PA-UCL6	19.68	0.179	0.418
PB-UCL6	19.68	0.175	0.467
PC-UCL6	19.68	0.175	0.471
PA-UCM4	6.61	0.410	0.755
PB-UCM4	6.61	0.391	0.682
PC-UCM4	6.61	0.446	0.839
PA-UCM8	13.21	0.339	0.495
PB-UCM8	13.21	0.315	0.629
PC-UCM8	13.21	0.241	0.741
PA-UCM12	19.82	0.228	0.538
PB-UCM12	19.82	0.171	0.564
PC-UCM12	19.82	0.101	0.473
PA-UCS11	6.07	0.478	0.724
PB-UCS11	6.07	0.486	0.667
PC-UCS11	6.07	0.394	0.711
PA-UCS22	12.14	0.286	0.593
PB-UCS22	12.14	0.319	0.545
PC-UCS22	12.14	0.305	0.756
PA-UCS33	18.22	0.206	0.512
PB-UCS33	18.22	0.241	0.574
PC-UCS33	18.22	0.183	0.465

Table (4.8) Normalized Results for Cubes Containing Mixed Circular Voids

Sample Name	Porosity (<i>n</i>)	Normalized <i>UCS</i>	Normalized <i>E</i> (25-50%)
	%		
PA-UXCL1M1S3	6.59	0.426	0.693
B-UXCL1M1S3	6.59	0.436	0.678
PC-UXCL1M1S3	6.59	0.385	0.618
PA-UXCL2M3S6	14.83	0.253	0.499
PB-UXCL2M3S6	14.83	0.251	0.511
PC-UXCL2M3S6	14.83	0.267	0.592
PA-UXCL2M5S8	19.24	0.214	0.444
PB-UXCL2M5S8	19.24	0.190	0.519
PC-UXCL2M5S8	19.24	0.149	0.453

Table (4.9) Normalized Results for Cubes Containing Square or Diamond Voids

Sample Name	Porosity (<i>n</i>)	Normalized Experimental <i>UCS</i>	Normalized Experimental <i>E</i> (25-50%)
	%		
PA-USqL3	6.28	0.381	0.637
PB-USqL3	6.28	0.514	0.709
PA-USqL6	12.56	0.294	0.686
PB-USqL6	12.56	0.364	0.511
PA-USqM6	6.32	0.476	0.694
PB-USqM6	6.32	0.482	0.648
PA-USqM12	12.65	0.316	0.660
PB-USqM12	12.65	0.294	0.483
PA-UDmL3	6.28	0.292	0.645
PB-UDmL3	6.28	0.414	0.719
PA-UDmL6	12.56	0.216	0.559
PB-UDmL6	12.56	0.192	0.626
PA-UDmM6	6.32	0.349	0.732
PB-UDmM6	6.32	0.410	0.701
PA-UDmM12	12.65	0.200	0.579
PB-UDmM12	12.65	0.308	0.670

4.4.1 Effects of Void Porosity

The results of uniaxial compressive strength and Young's modulus for experimental results are plotted as a function of void porosity in Figures (4.2) and (4.3). According to the results, for the void porosity ranging between 6.28% and 19.82%, regardless of the void size, void distribution, and void uniformity, the normalized experimental results showed increases in both normalized UCS and E with decreasing porosity. However, the coefficient of determination for uniaxial compressive strength ($R^2 = 0.729$) is higher than that for the Young's modulus ($R^2 = 0.5364$). The results showed power trend with increasing porosity for both uniaxial compressive strength and Young's Modulus. The relationships can be represented best by the following equations:

$$\text{Normalized } UCS = 0.0631 * ((porosity)^{-1})^{0.6849} \quad R^2 = 0.729 \quad \dots (4.3)$$

$$\text{Normalized } E = 0.324 * ((porosity)^{-1})^{0.2753} \quad R^2 = 0.5364 \quad \dots (4.4)$$

From Figures (4.2) and (4.3) and Tables (4.4) to (4.6), for similar void porosity, the results showed different values for both UCS and E . However, the differences for UCS are smaller than those for E . For similar void porosities, 6.5%, 12.6%, and 19.6%, some cubes had very low uniaxial strength (16.06 MPa, 10.55 MPa, and 5.55 MPa for void porosities of 6.5%, 12.6% and 19.6% respectively), while the others had very high uniaxial strength (28.27 MPa, 20.02 MPa, and 12.53 MPa for void porosities of 6.5%, 12.6% and 19.6% respectively). Accordingly, the percentages of the maximum differences in UCS values were 76%, 89.6%, and 126% for void porosities 6.5%, 12.6% and 19.6% respectively. There are also several cubes that their strength values are located between the lowest and the highest strengths.

Similarly, some cubes gave smaller Young's Modulus (8.65 GPa, 7.73 GPa, and 6.69 GPa for void porosities of 6.5%, 12.6% and 19.6% respectively) compared to some other cubes which gave larger Young's Modulus (13.42 GPa, 10.56 GPa, and 8.61 GPa for void porosities of 6.5%, 12.6% and 19.6% respectively). Accordingly, the percentages of the maximum differences in E values were 55.6%, 36.6%, and 28.6% for void porosities 6.5%, 12.6% and 19.6% respectively. Of course, there are also several cubes that their Young's Modulus values are located between the lowest and the highest values. These differences can be partly attributed to the experimental uncertainties, while, the other part of the differences might be due to the effects of void geometry. In the next sections, the contributions of void geometry in the differences in both UCS and E are explored.

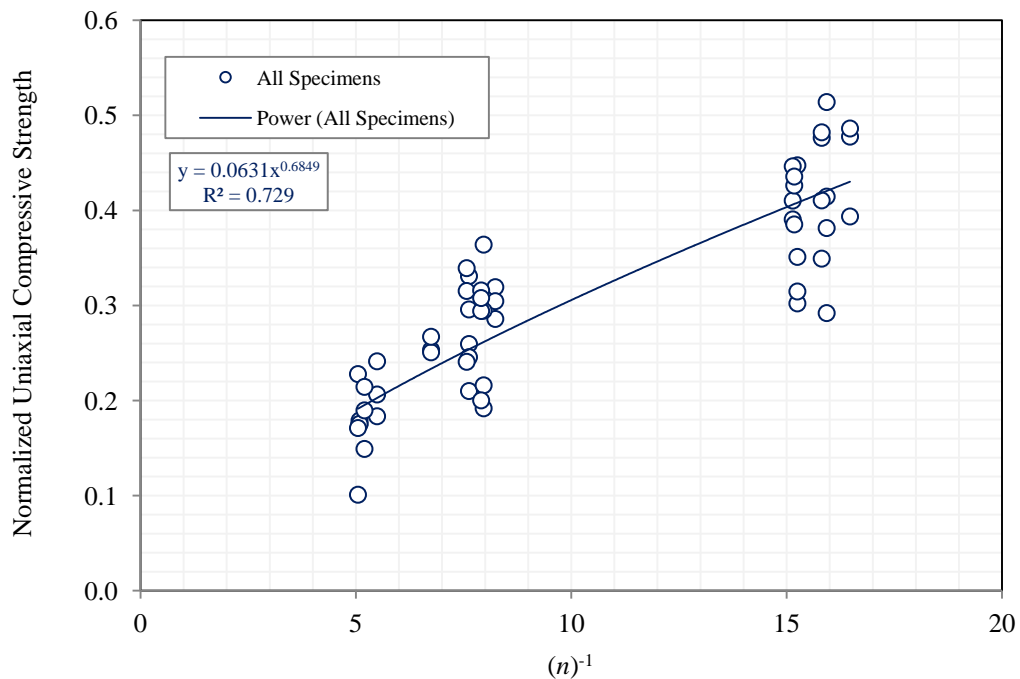


Figure (4.2) Normalized Uniaxial Strength versus Void Porosity for Cubes with Voids Having Different Size, Shape and Distribution

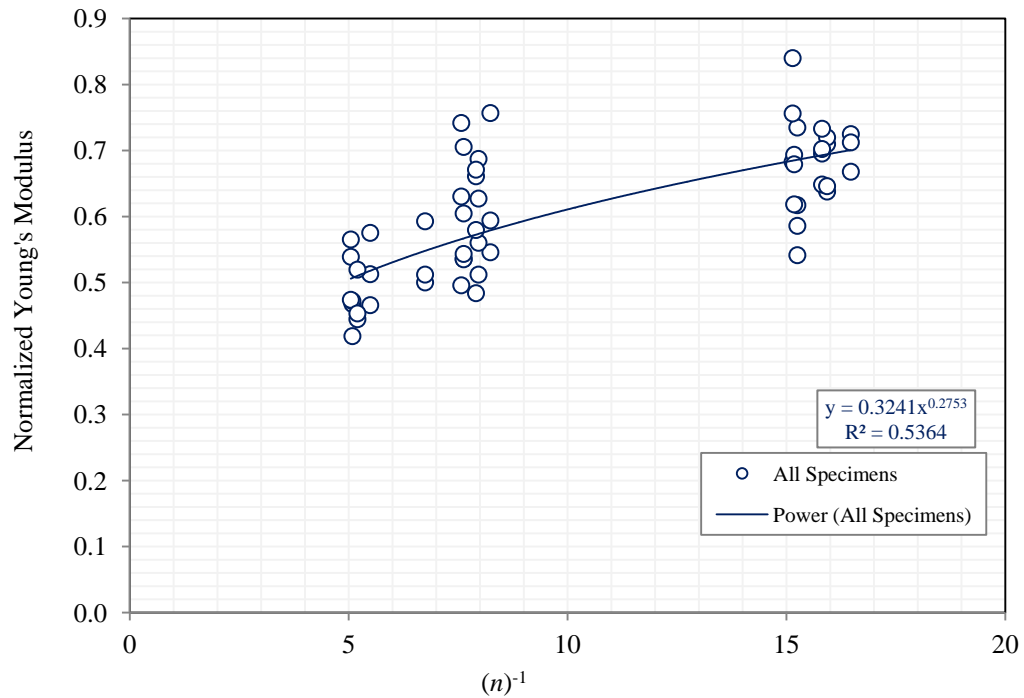


Figure (4.3) Normalized Deformation versus Void Porosity for Cubes with Voids Having Different Size, Shape and Distribution

4.4.2 Void Geometry Characterizations

Void geometry comprises void size, void shape, void orientation, and void geometrical distributions. The void geometrical distributions, spatial distributions of voids, mean spatial frequency of void occurrence in a porous medium. They are typically controlled by void positions with respect to the boundaries (edges of the specimens).

The experimental results from the work in Project Activity Task ORD-FY04-013 are used to check the effects of void geometry on the mechanical properties the rock-like material.

4.4.2.1 Effects of Void Size

The results of uniaxial compressive strength and Young's modulus for cubes containing unisize circular voids are plotted as a function of void porosity in Figures (4.4) to (4.9). The three different sizes of circular voids (large size - 31.14 mm, medium size - 22.1 mm, and small size - 12.78 mm) showed similar changes in values of both normalized *UCS* and *E* with void porosity changing as shown in Figures (4.4) and (4.5). Figures (4.6) to (4.9) show the experimental results for cubes containing unisize square voids or unisize diamond voids. Similarly, the two different sizes of voids (large size - 22.05x22.05 mm, and small size - 15.65x15.65 mm) gave similar changes in both normalized *UCS* and *E* with void porosity changing. Accordingly, the different void sizes studied in this experimental program did not show discernible effects on the mechanical properties of the Hydro-StoneTB[®].

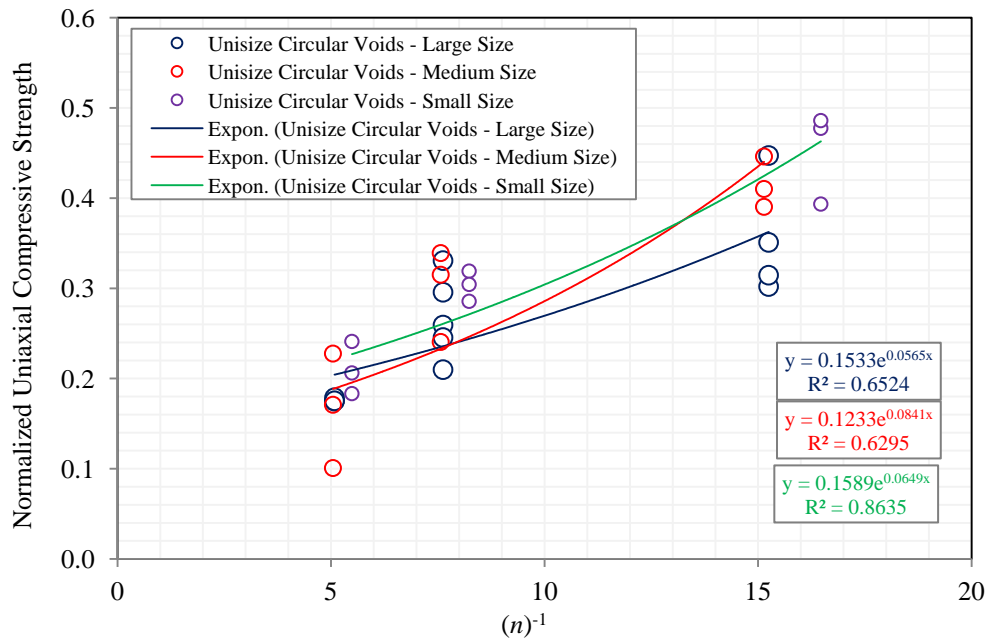


Figure (4.4) Normalized Uniaxial Compression versus Void Porosity for Cubes Containing Unisize Circular Voids

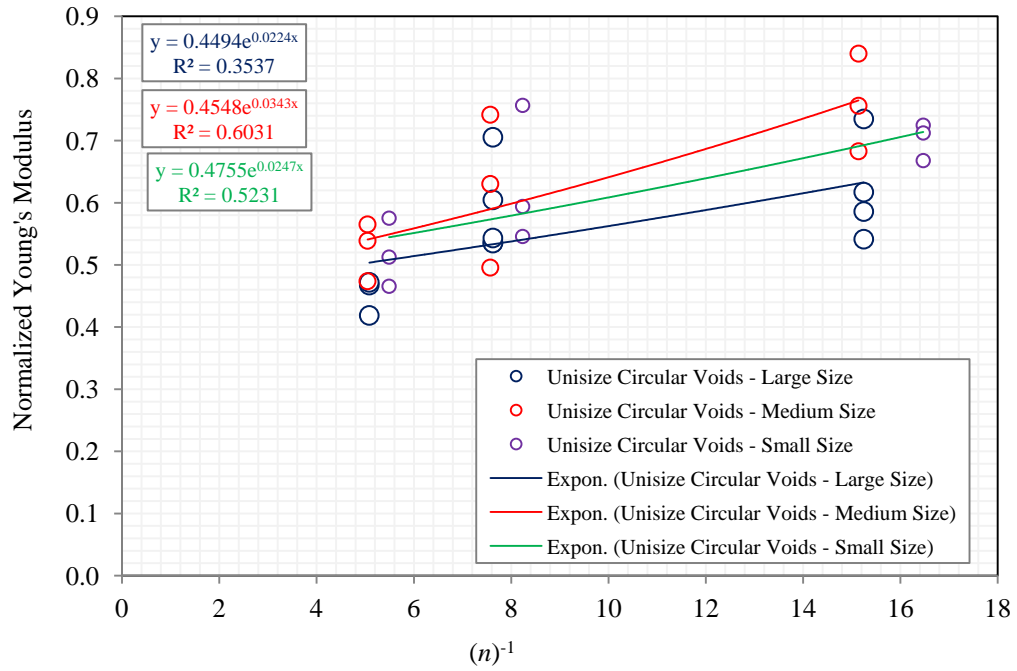


Figure (4.5) Normalized Deformation versus Void Porosity for Cubes Containing Unisize Circular Voids

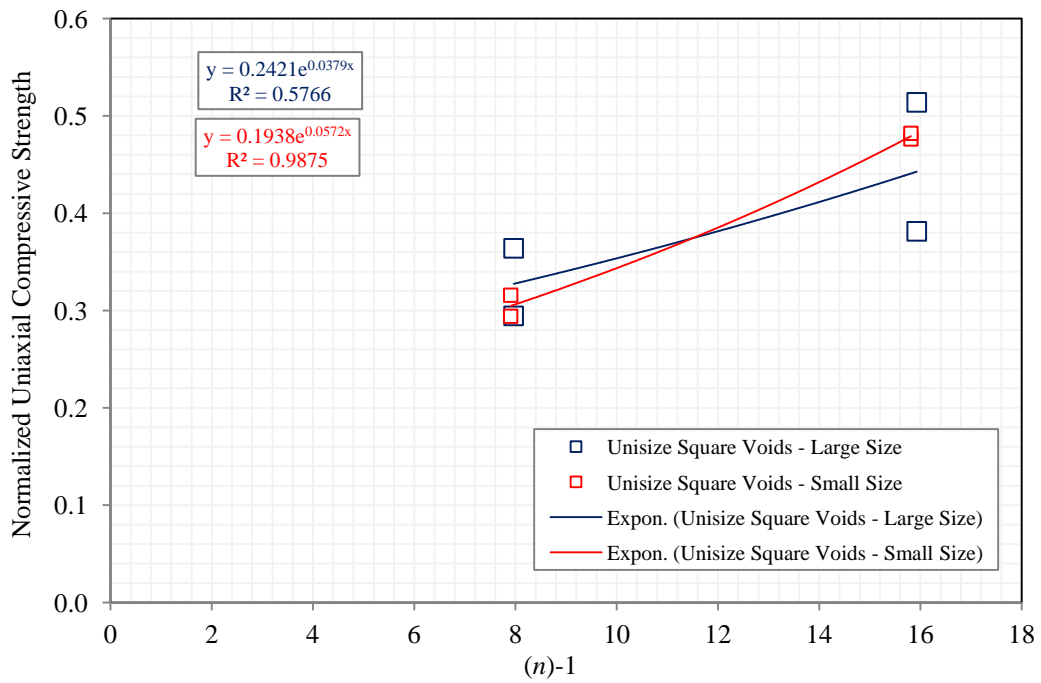


Figure (4.6) Normalized Uniaxial Compression versus Void Porosity for Cubes Containing Unisize Square Voids

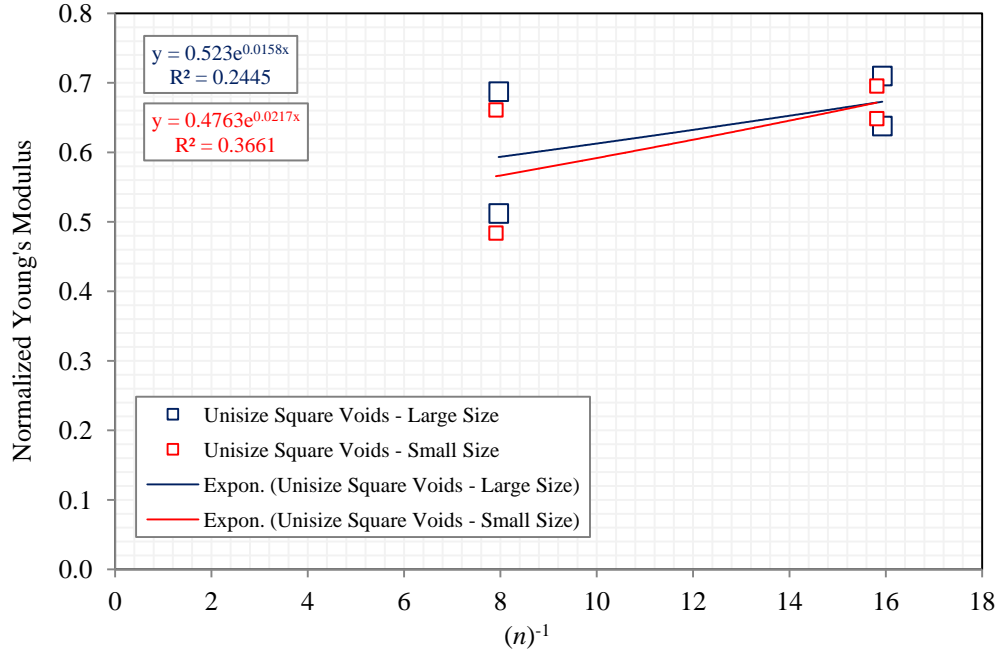


Figure (4.0.7) Normalized Deformation versus Void Porosity for Cubes Containing Unisize Square Voids

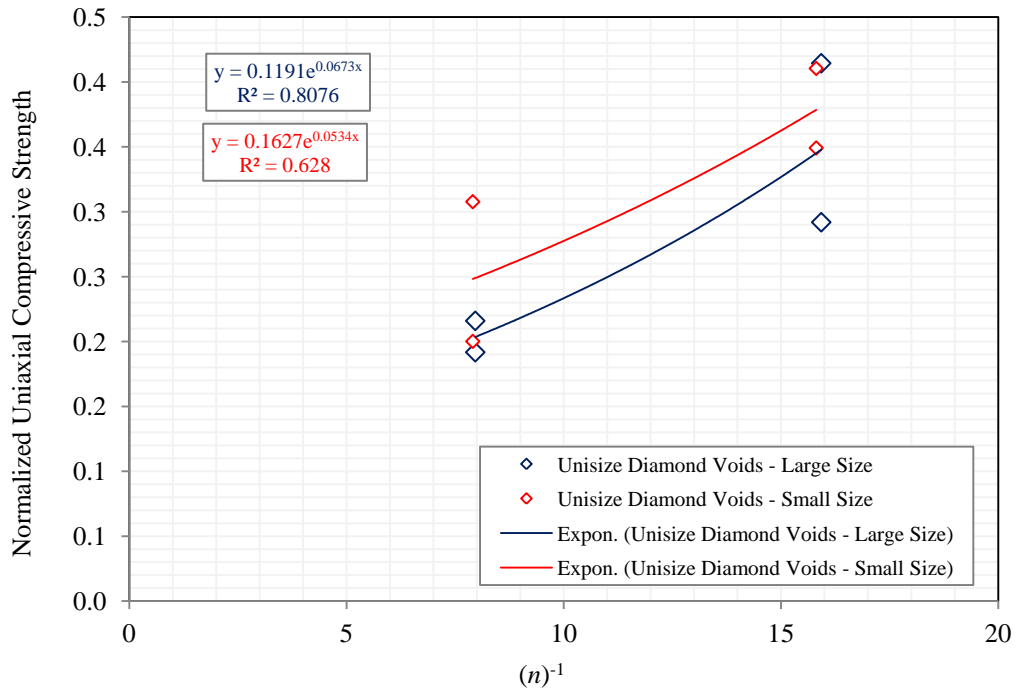


Figure (4.0.8) Normalized Uniaxial Compression versus Void Porosity for Cubes Containing Unisize Diamond Voids

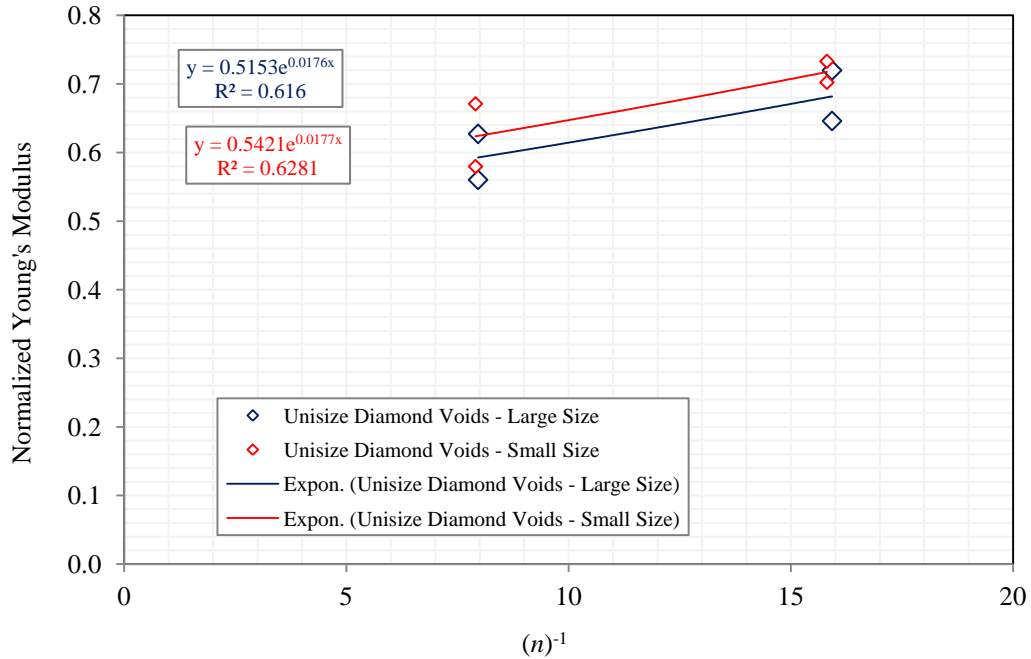


Figure (4.9) Normalized Deformation versus Void Porosity for Cubes Containing Unisize Diamond Voids

4.4.2.2 Effects of Void Shape

Both circular and non-circular voids (square and diamond voids) were created in the cubic specimens tested in Project Activity Task ORD-FY04-013. Since, for the same void porosity, the size and distribution of circular voids were different from those of non-circular voids, the results are not comparable to find the effect of void shapes on the mechanical properties of the rock-like material. Regarding the models containing non-circular voids (square and diamond voids), although the size and distribution of the voids are alike for the same void porosity, the diamond voids are just the square voids rotated by 45 degree (they are square voids with different orientation). Therefore, the two non-circular voids cannot be considered as voids with two different shapes. However, the results of cubes containing non-circular voids can be used to explore the effects of void

orientation on the mechanical properties of the rock like material. Accordingly, the results of uniaxial compressive strength and Young's modulus for cubes containing either unisize square or unisize diamond voids are plotted as a function of void porosity in Figures (4.10) and (4.11). According to the results, the following observations can be discussed:

- 1- The experimental results showed increases in both *UCS* and *E* of Hydro-StoneTB[®] cubes with decreasing void porosity following power trends.
- 2- From Figures (4.10), regardless of the void size (large and small size voids), and void distribution (patterns A and B), the cubes containing square voids showed slightly higher *UCS* compared to the cubes containing diamond voids (square voids rotated by 45 degree). On average, the cubes containing square voids gave higher strength by 9% compared to the cubes containing square voids rotated by 45 degree; the differences ranging between -1.36% to 17.2%.
- 3- From Figure (4.11), the results for models having similar porosity showed similar changes in *E* regardless of the void size (large and small size voids), void distribution (patterns A and B) and void orientations.

Accordingly, rotating square voids by 45 degree led to a reduction in the uniaxial compressive strength by 9% on average. This might due to larger void width for diamond shapes compared to square voids; the void dimension perpendicular to the maximum compression stress is larger for diamond square which in turn may lead to lesser strength. However, the effect of void orientation on Young's modulus was insignificant.

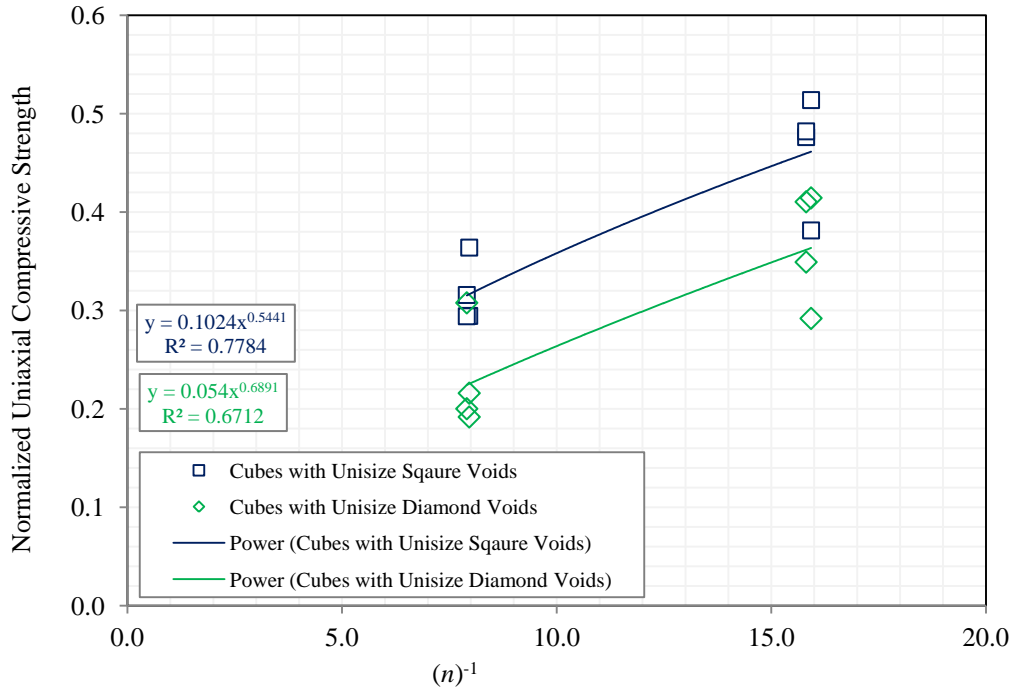


Figure (4.10) Normalized Uniaxial Compression versus Void Porosity for Cubes Containing Non-circular Voids

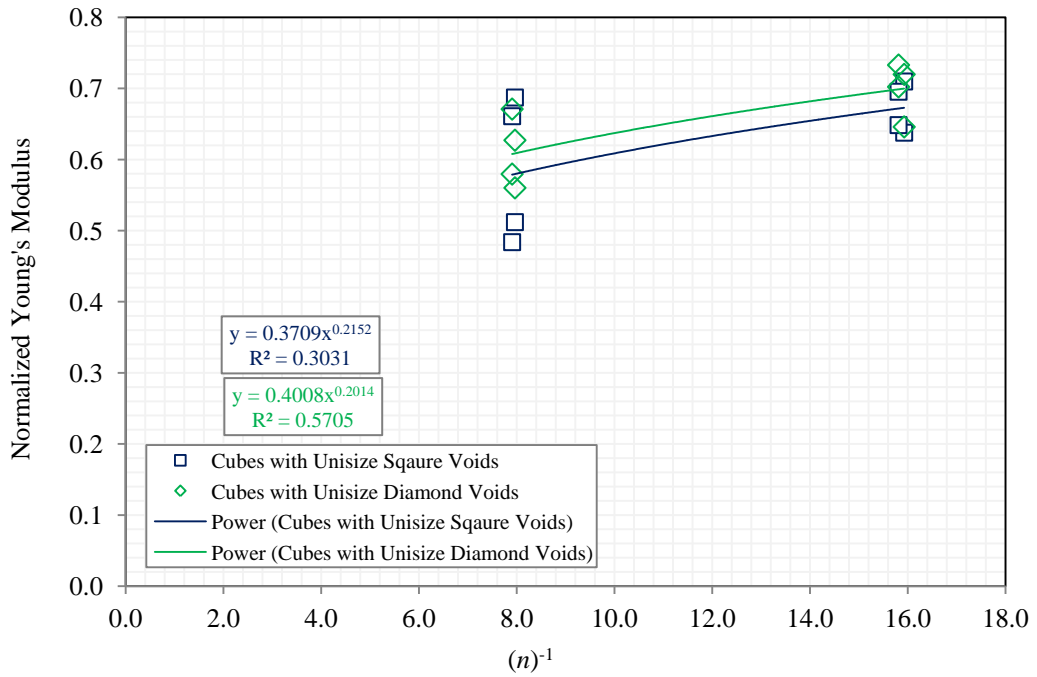


Figure (4.11) Normalized Deformation versus Void Porosity for Cubes Containing Non-circular Voids

4.4.2.3 Effects of Void Spatial Distributions

For cubic porous specimens containing open-ended longitudinal openings, the spatial distributions of voids are specified by choosing the distances between the voids and the cube edges (edge distances). The edge distance is usually composed of two parts; side distance (shortest distance between the void periphery and the vertical sides of the cube) and top (or bottom) distance (shortest distance between the void periphery and either top or bottom edge of the cube). For the same porosity, different spatial distributions of voids can be obtained by different combination of side distances and top distances. This can lead to porous cubes having the same void porosity, number of voids, and void sizes but different bridge distances. The bridge distance is the shortest distance between two adjacent voids. Therefore, the void spatial distribution can be defined as the combination of side distances, top distances and bridge distance. Figure (4.12) shows an example on how to measure the side distances, top distances and bridge distances for voids within porous cubes.

The experimental results from the work in Project Activity Task ORD-FY04-013 showed different values for both UCS and E at almost the same void porosity; see Figures (4.2) and (4.3). These differences can be partly due to the effects of void geometry. Since the different void sizes and void shapes did not show distinct effects on the mechanical properties of Hydro-StoneTB[®], see Figures (4.4) to (4.11), the remained factor in the void geometry characterizations is the void spatial distribution. In addition, although the results were are not very conclusive, Jespersen et al. (2010) found that the mechanical properties of rock-like material changes with bridge distances changing. One reason of

obtaining inconclusive results by Jespersen et al. (2010) might be due to not considering the effects of side distances and top distances when the bridge distances changed.

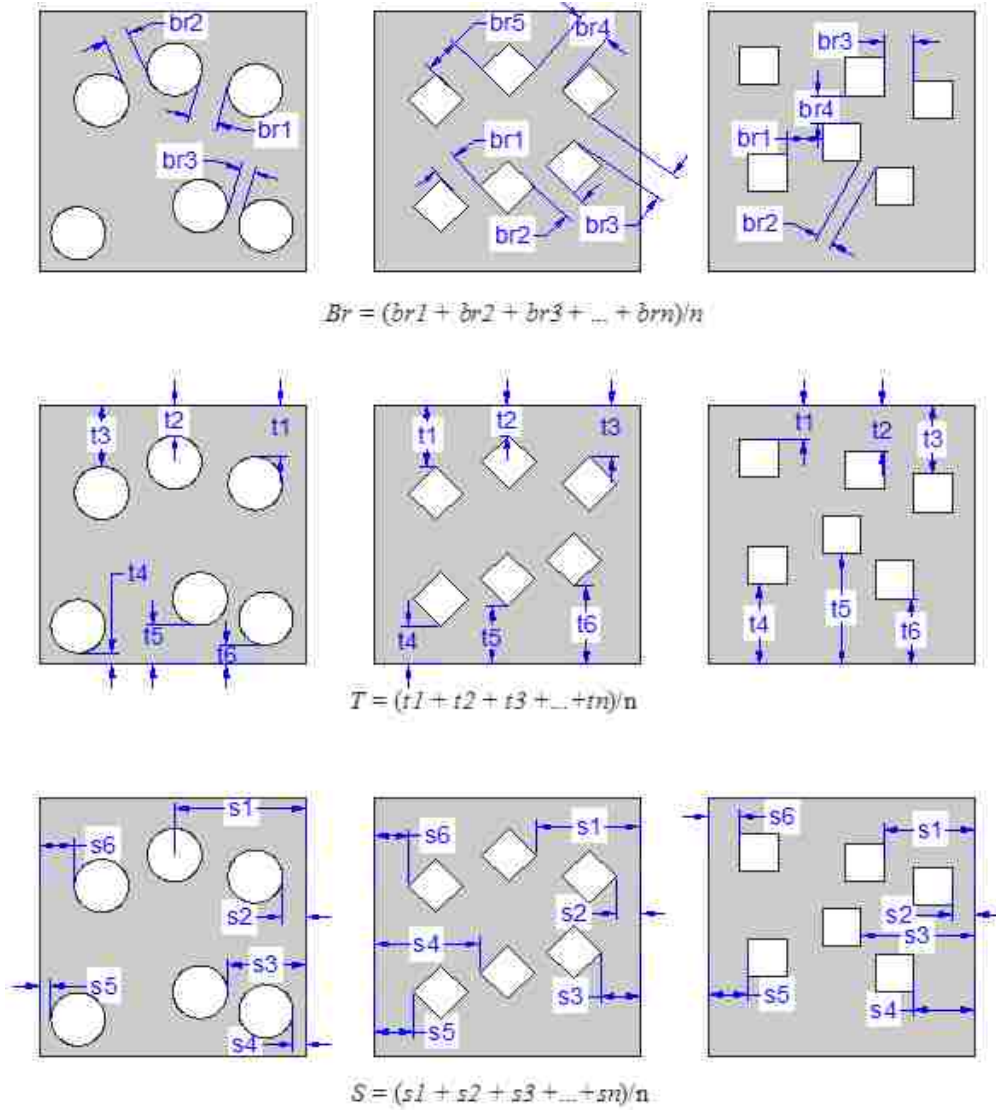


Figure (4.12) Bridge distances, B_r , Side distances, S , and Top distances, T , for Hydro-StoneTB[®] cubes

Accordingly, it can be assumed that the mechanical properties of rock-like material containing voids is a function of void porosity, n , (or void size, D , and the number of

voids) and bridge distance, b_r (or side distance, s , and top distances, t). This can be written mathematically as follows:

$$\text{Normalized Uniaxial Compressive Strength} = f(n^{-1}, b_r, s, t) \quad \dots (4.5)$$

$$\text{Normalized Young's Modulus} = f(n^{-1}, b_r, s, t) \quad \dots (4.6)$$

The experimental results from the work in Project Activity Task ORD-FY04-013 are used to check the validation of the above mathematic expressions; Eqs. (4.5) and (4.6).

4.4.2.4 Effects of Bridge, Side and Top distances

The sketches of the cubes tested in Project Activity Task ORD-FY04-013 were redrawn in AutoCAD program, and from them the void bridge distances, b_r , side distances, s , and top distances, t , for each cube were measured. Tables (4.10) to (4.12) show the measured distances for all specimens. However, the bridge distances larger than the void diameter, D , (or side length for the square voids or diagonal length for the diamond voids - see Figure (4.12) were not considered. According to Timoshenko and Goodier (1951), when a large plate containing a circular hole at the center is subjected to uniaxial compression stress, the maximum compression stress produced on the periphery of the hole and equals to threefold of the applied uniaxial stress reduces to the normal value of the applied compression stress (1.074 of the applied uniaxial compression stress) at a distance equals to one hole's diameter. Accordingly, based on Timoshenko and Goodier (1951), the bridge distances larger than the D were disregarded. Finally, the average values of bridge distances, B_r , side distances, S , and top distances, T , for each cube were obtained as shown in Figure (4.12).

The results of uniaxial compressive strength and Young's modulus for experimental results are plotted as a function of the distances (bridge, side and top) as shown in Figures (4.13) to (4.18). The normalized values of the distances were also used to generalize the results. The normalized bridge distances were obtained by dividing average values of bridge distances between every two adjacent voids by the void diameter for circular voids, or side length for the square voids, or diagonal length for the diamond voids. Regarding both top and side distances, the normalized distances were obtained by dividing the average value of the shortest top (or the shortest side) distances by the half of the specimen size ($152.4/2 = 76.2$ mm). Since the specimens were tested by loading them from both sides (top and bottom), the effective specimen size should be measured from the middle of the specimen to the top, or the bottom. Therefore, the effective size of the specimens is the actual size of the specimens divided by two; $152.4/2 = 76.2$ mm. Similarly, for the side distances, the effective specimen size should be measured from a vertical line passes through the middle of the specimens. Accordingly, the maximum top and side distances should be less than or equal to half of the actual specimen size minus the void diameter (or side length for the square voids or diagonal length for the diamond voids) as shown in Figure (4.12).

From the results, as can be seen in Figures (4.13) to (4.18), the normalized average values of bridge, side, and top distances show weak correlations with the mechanical properties of Hydro-StoneTB® cubes. From Figures (4.13) to (4.16), both bridge distances and side distances showed poor correlations with the mechanical properties; for the bridge distances the values of R^2 are 0.42 and 0.1636 for *UCS* and *E* respectively; while for the side distances the values of R^2 are 0.2794 and 0.1 for *UCS* and

E respectively. The top distances did not show any correlation with the mechanical properties of the Hydro-StoneTB® cubes; the values of R^2 are zero, see Figures (4.17) and (4.18). The correlations for all of them followed linear trend.

Table (4.10) Bridge, Side distances, and Top Distances of Unisize Circular Voids

Sample Name	Average Bridge Distances (B_r)	Average Top Distances (T)	Average Side Distances (S)
	mm	mm	Mm
PA-UCL2-A&B	31.14	30.31	37.08
PA-UCL2-C	31.14	30.32	37.09
PB-UCL2	9.42	28.33	41.38
PC-UCL2	31.14	12.45	33.03
PA-UCL4-A	12.18	30.63	38.33
PA-UCL4-B	12.18	38.33	30.63
PA-UCL4-C	12.18	38.33	30.63
PB-UCL4	8.69	34.75	31.38
PC-UCL4	16.72	17.93	31.70
PA-UCL6	17.81	22.55	29.71
PB-UCL6	12.63	31.33	33.03
PC-UCL6	13.18	31.48	25.61
PA-UCM4	18.22	42.85	35.15
PB-UCM4	17.79	39.27	35.90
PC-UCM4	20.50	24.12	35.53
PA-UCM8	16.77	39.76	37.71
PB-UCM8	16.55	35.78	36.53
PC-UCM8	11.09	31.82	34.38
PA-UCM12	13.50	31.70	32.82
PB-UCM12	12.28	36.06	31.02
PC-UCM12	9.55	34.69	28.53
PA-UCS11	12.78	38.43	39.29
PB-UCS11	12.78	41.10	37.70
PC-UCS11	12.78	36.79	35.68
PA-UCS22	9.08	38.89	38.66
PB-UCS22	8.23	29.65	37.29
PC-UCS22	8.81	37.63	37.68
PA-UCS33	8.49	34.70	34.51
PB-UCS33	9.01	35.30	36.49
PC-UCS33	8.79	36.03	36.13

Table (4.11) Bridge, Side distances, and Top Distances of Mixed Circular Voids

Sample Name	Average Bridge Distances (B _r)	Average Top Distances (T)	Average Side Distances (S)
	mm	mm	Mm
PA-UXCL1M1S3	21.36	71.82	32.59
PB-UXCL1M1S3	17.79	74.84	37.86
PC-UXCL1M1S3	28.02	67.00	35.25
PA-UXCL2M3S6	18.07	62.41	35.49
PB-UXCL2M3S6	18.91	69.38	38.16
PC-UXCL2M3S6	18.91	63.23	34.27
PA-UXCL2M5S8	16.63	52.65	34.80
PB-UXCL2M5S8	15.90	70.61	37.48
PC-UXCL2M5S8	16.27	69.67	38.23

Table (4.12) Bridge, Side distances, and Top Distances of Unisize Non-Circular Voids – Square and Diamond Voids

Sample Name	Average Bridge Distances (B _r)	Average Top Distances (T)	Average Side Distances (S)
	mm	mm	Mm
PA-USqL3	22.05	35.29	44.70
PB-USqL3	22.05	26.31	39.51
PA-USqL6	20.55	39.91	34.27
PB-USqL6	22.05	35.88	37.58
PA-USqM6	16.01	43.11	37.47
PB-USqM6	17.22	39.08	40.78
PA-USqM12	10.58	34.93	36.05
PB-USqM12	13.02	39.28	34.25
PA-UDmL3	21.24	39.75	30.73
PB-UDmL3	19.67	21.75	34.94
PA-UDmL6	20.95	35.35	29.70
PB-UDmL6	31.18	31.31	33.41
PA-UDmM6	21.37	39.88	34.23
PB-UDmM6	16.46	35.84	37.53
PA-UDmM12	15.49	32.81	32.20
PB-UDmM12	15.56	31.01	36.04

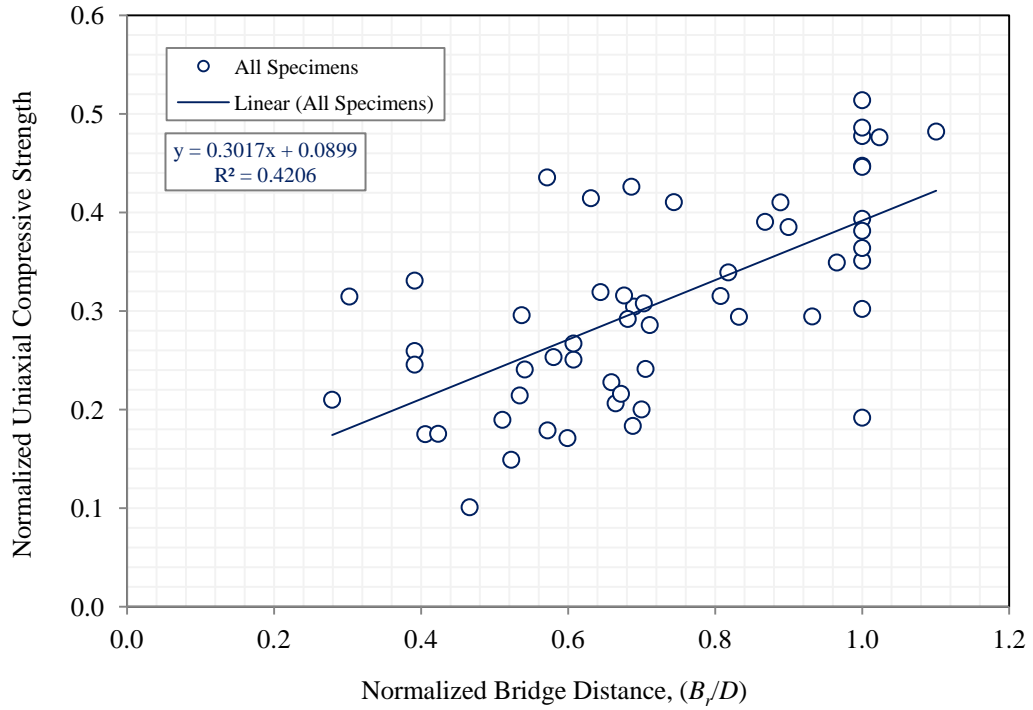


Figure (4.13) Normalized Uniaxial Compression versus Normalized Bridge Distance for Cubes with Voids Having Different Size, Shape and Distribution

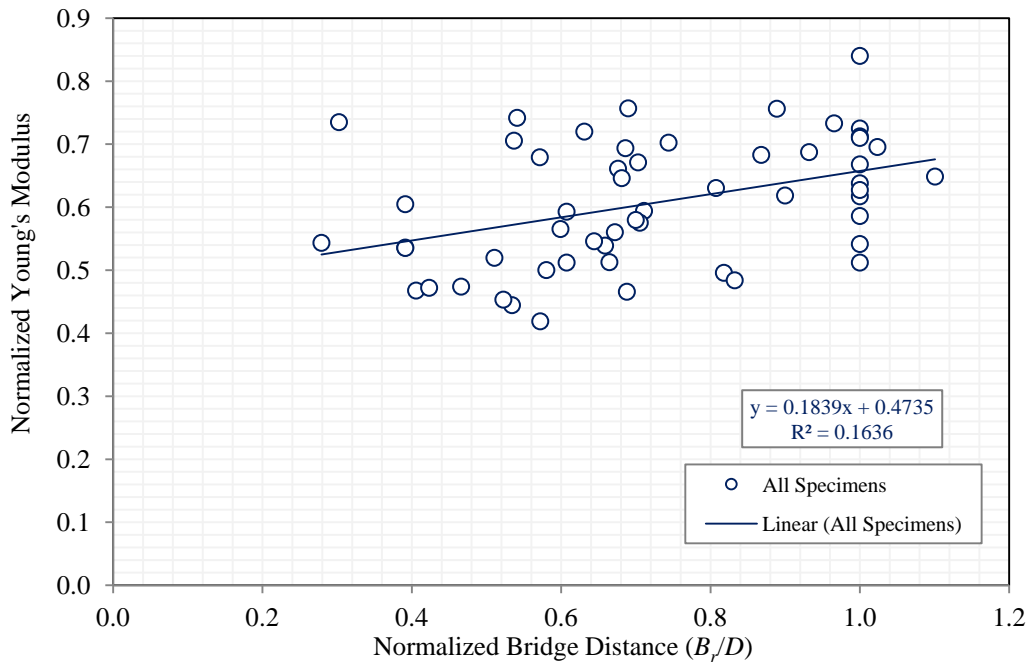


Figure (4.14) Normalized Deformation versus Normalized Bridge Distance for Cubes with Voids Having Different Size, Shape and Distribution

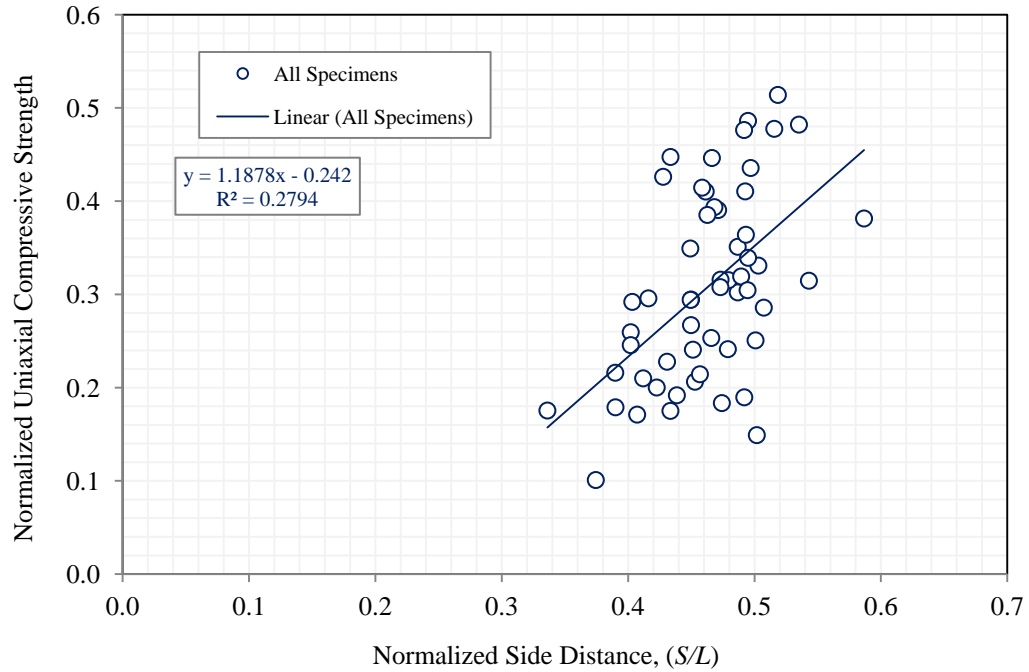


Figure (4.15) Normalized Uniaxial Compression versus Normalized Side Distance for Cubes with Voids Having Different Size, Shape and Distribution

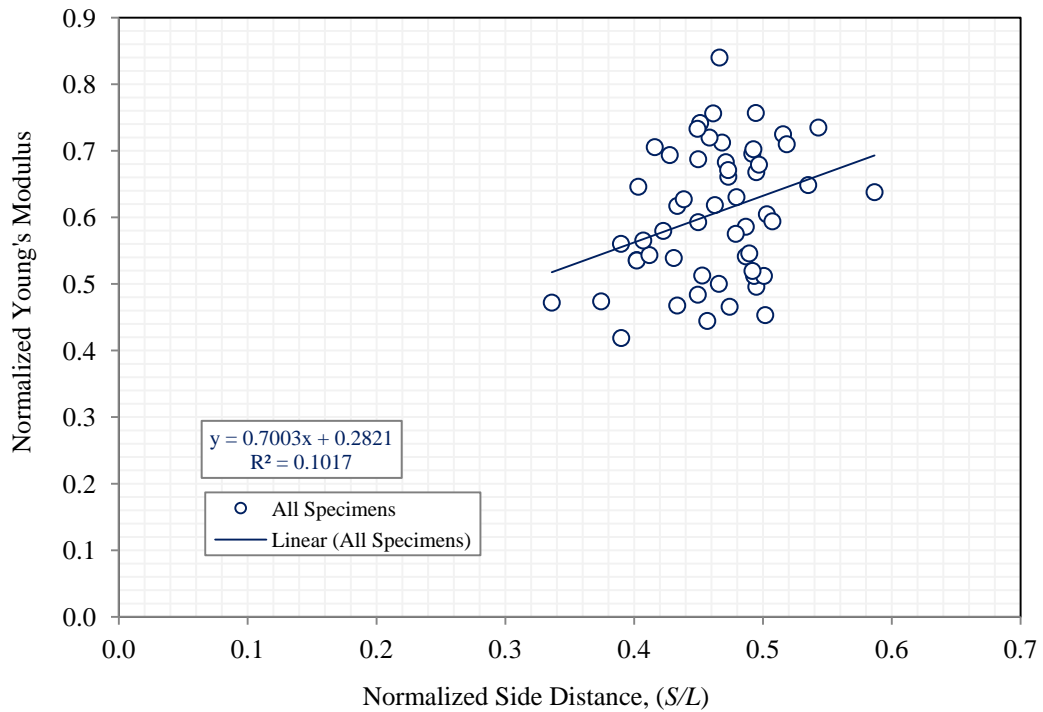


Figure (4.16) Normalized Deformation versus Normalized Side Distance for Cubes with Voids Having Different Size, Shape and Distribution

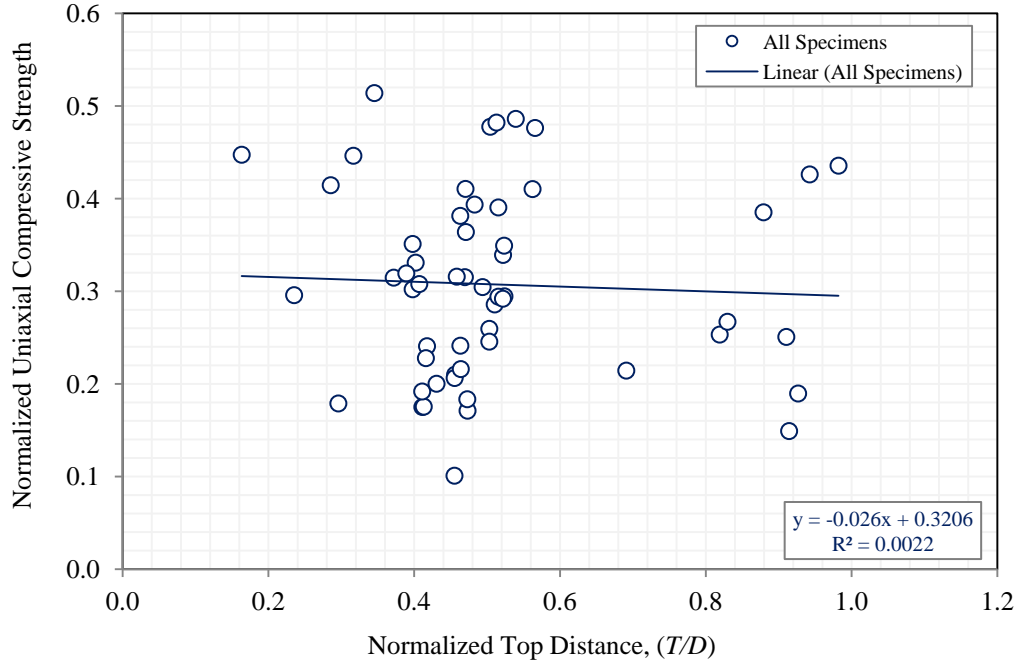


Figure (4.17) Normalized Uniaxial Compression versus Normalized Top Distance for Cubes with Voids Having Different Size, Shape and Distribution

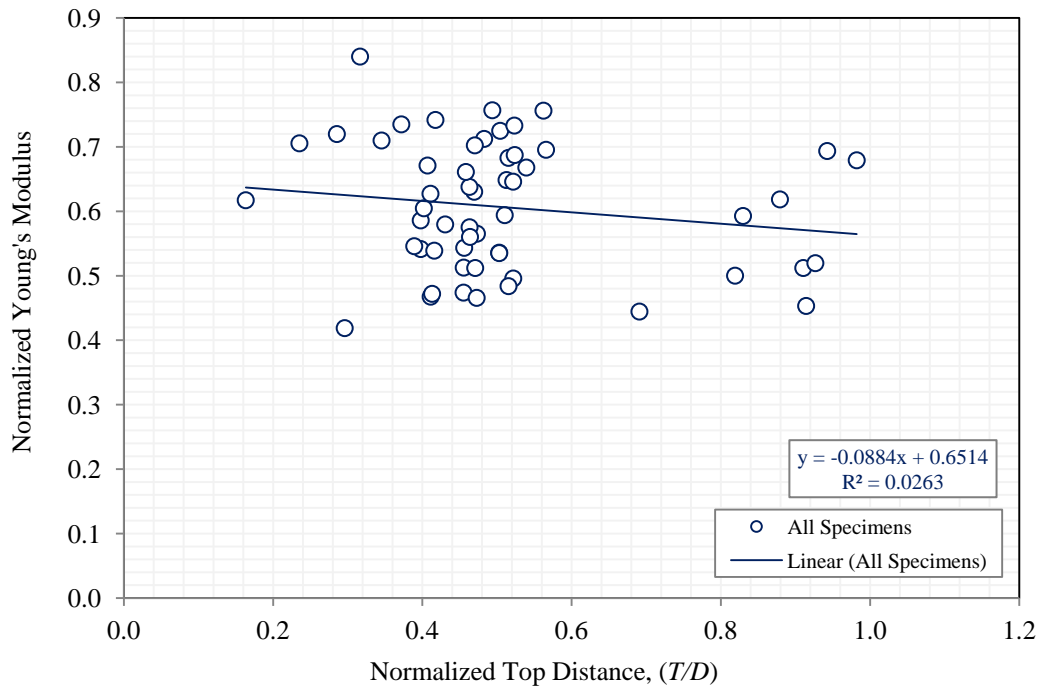


Figure (4.18) Normalized Deformation versus Normalized Top Distance for Cubes with Voids Having Different Size, Shape and Distribution

4.4.5 Alternative Methods to Explore the Effects of Void Geometry

According to Sammis and Ashby (1986), the brittle porous solids under uniaxial compression fail due to microcracks initiated at the void peripheries and propagated and finally coalesced to form contiguous vertical failure planes (see Figure (3.13)). In addition, according to Timoshenko and Goodier (1951), when a large plate containing a circular hole at the center is subjected to uniaxial compression stress, the maximum compression stress occurs at a point on the periphery of the hole and equals threefold of the applied uniaxial stress. At a distance equals to one hole's diameter from the hole periphery, the maximum compression stress reduces to the normal value (1.074 of the applied uniaxial stress); from Eq. (3.37) in Chapter Three. Accordingly, it can be concluded that when a porous specimen is subjected to uniaxial stress, the produced stresses within the sample are concentrated at the immediate vicinities of the voids in the porous specimens. Therefore, those zones next to the voids are critical parts in the porous materials. Basing on the aforementioned paragraphs, the porous cubes can be assumed to be composed of two types of vertical columns; porous columns those solid parts of the cubes containing voids and solid columns immediately next to the porous columns as shown in Figure (4.19). Furthermore, it can be assumed that the total strength of the porous comes from the summation of the strength of the individual columns.

Since the vertical columns in the porous cubes are two types, porous columns and solid columns as shown in Figure (4.19), shaded part and colored part, the ultimate strength of the porous specimens should come largely from the solid columns. Basing on the assumption, the porous specimens having larger solid parts ($W = w_1 + w_2 + w_3 + \dots$) should give higher ultimate strength. In other words, for the same void porosity of a

porous specimen, the void geometry that gives larger solid parts, wider solid columns, should give higher ultimate strength compared to that gives smaller solid parts.

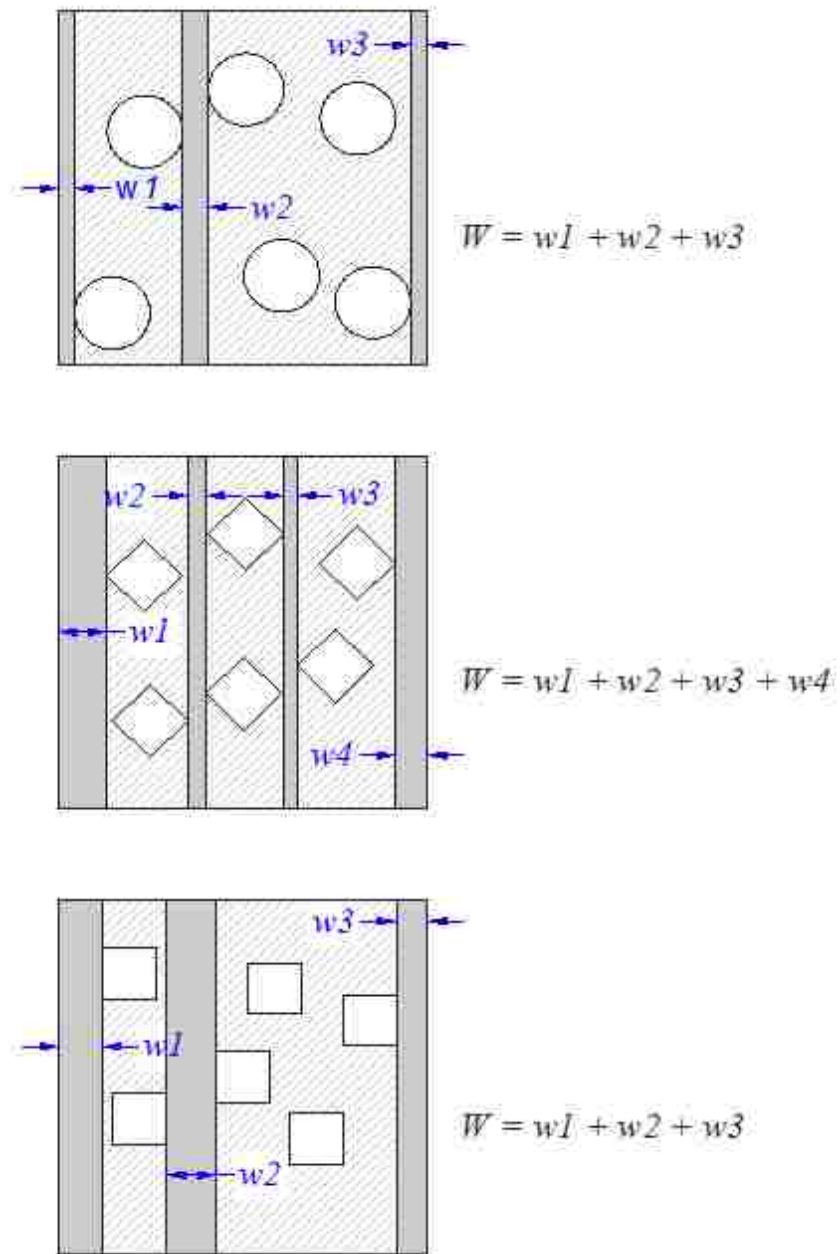


Figure (4.19) Total Width of Solid Columns for Porous Specimens

Accordingly, the Eqs. (4.5) and (4.6) can be rewritten mathematically as follows:

$$\text{Normalized Uniaxial Compressive Strength} = f(n^{-1}, W) \quad \dots (4.7)$$

$$\text{Normalized Young's Modulus} = f(n^{-1}, W) \quad \dots (4.8)$$

The above expressions can be rewritten as follows:

$$\frac{(UCS)_{\text{Porous}}}{(UCS)_{\text{Solid}}} \propto \left(\frac{W}{n}\right) \quad \dots (4.9)$$

$$\frac{(E)_{\text{Porous}}}{(E)_{\text{Solid}}} \propto \left(\frac{W}{n}\right) \quad \dots (4.10)$$

Where

$(UCS)_{\text{Porous}}$ = uniaxial compressive strength of porous cubes,

$(UCS)_{\text{Solid}}$ = uniaxial compressive strength of solid cubes,

$(E)_{\text{Porous}}$ = Young's modulus of porous cubes,

$(E)_{\text{Solid}}$ = Young's modulus of solid cubes..

n = void porosity, and

W = total width of solid columns

One problem in the above expressions is that for the porous specimens having zero W , the strength and Young's modulus reduce to zero which is physically incorrect. This can be solved by normalizing the total width of solid columns (W) through replacing it by $[(W + (0.01 * D)) / (0.01 * D)]$. The D is void diameter for circular voids, side length for square voids, and diagonal length for the diamond voids, see Figure (4.19). Accordingly, the above expression can be rewritten as follows:

$$\frac{(UCS)_{\text{Porous}}}{(UCS)_{\text{Solid}}} \propto \left[\frac{\left(\frac{W + 0.01D}{0.01D}\right)}{n} \right] \quad \dots (4.11)$$

$$\frac{(E)_{\text{Porous}}}{(E)_{\text{Solid}}} \propto \left[\frac{\left(\frac{W + 0.01D}{0.01D} \right)}{n} \right] \quad \dots (4.12)$$

To validate the above expressions, Eqs. (4.11) and (4.12), the experimental results from the work in Project Activity Task ORD-FY04-013 were used. Accordingly, the total width of solid columns (W) for each cube was measured as shown in Tables (4.13) to (4.15). Finally, the results of uniaxial compressive strength and Young's modulus for experimental results are plotted as a function of void porosity, total width of solid columns (W), and void size as shown in Figures (4.20) to (4.27). From the results, the following observations can be discussed:

- 1- From Figure (4.20), the relationship of normalized UCS with the total width of solid columns (W) showed a good agreement, and followed a moderate power trend with $R^2 = 0.5$. The value of UCS increased when the value of W increasing, and accordingly, this can be considered as a response of the hypothesis of using the total width of solid columns to represent the effects of void geometry on the strength of the Hydro-StoneTB[®] cubes. Regarding the deformation, however, the relationship of normalized E with the total width of solid columns (W) did not show a good correlation; showed a weak power correlation with $R^2 = 0.26$, see Figure (4.21). This may be due to the fact that the used methods to measure the strains in the experimental tests on porous cubes (uniaxial compression tests) are not adequate; especially in measuring the lateral displacements. This opinion is supported by the numerical analysis in Chapter 5; the numerical results gave a very decent correlation between E

and void porosity ($R^2 = 0.9292$), see Figure (5.61). It is also supported by the numerical results in Christianson et al. (2006) and Erfourth (2006).

- 2- From Figures (4.22) to (4.25), the relationships of normalized UCS and E with normalized total width of solid columns (W) using D (void diameter or side length) showed better correlations, and followed good power trends. The value of R^2 increased from 0.5 to 0.79 for UCS , and from 0.26 to 0.41 for E .
- 3- From Figures (4.26) and (4.27), the mathematical expressions in Eqs. (4.11) and (4.12) showed very good agreements. Regarding the strength, UCS , using the expressions in Eqs. (4.11), the relationship gave a very good correlation following a very decent power trend and the value of R^2 increased from 0.5 to 0.84. For the deformation, E , using the expressions in Eqs. (4.12), the relationship gave better correlation following a moderate power trend and the value of R^2 increased from 0.41 to 0.51. The mathematical expressions in equations Eqs. (4.11) and (4.12) can be represented best by the following equations:

$$\frac{(UCS)_{\text{Porous}}}{(UCS)_{\text{Solid}}} = 0.1019 * \left[\frac{W + 0.01 * D}{0.01 * D * n} \right]^{0.3536} \quad R^2 = 0.8412 \quad \dots (4.13)$$

$$\frac{(E)_{\text{Porous}}}{(E)_{\text{Solid}}} = 0.7292 * \left[\frac{W + 0.01 * D}{0.01 * D * n} \right]^{0.1613} \quad R^2 = 0.509 \quad \dots (4.14)$$

- 4- From Figure (4.26), using the mathematical expression in Eq. (4.11), the hypothesis of using the total width of solid columns (W) to express the effects of void geometry on mechanical properties improved the correlations between

the uniaxial compressive strength of Hydro-StoneTB[®] and void geometry. The percentage of the maximum difference in *UCS* value, 126% - see Figure (4.2), reduced to 57%; reduced to less than half. In addition, the coefficient of determination for uniaxial compressive strength increased from $R^2 = 0.729$ to $R^2 = 0.8412$.

- 5- From Figure (4.27) using the mathematical expression in Eq. (4.12), the Young's modulus did not show any distinct response; on the contrary, the coefficient of determination reduced from $R^2 = 0.5364$ to $R^2 = 0.508$. However, the percentage of the maximum difference in *E* value, 55.6% - see Figure (4.3), reduced to 46%; reduced by about 17%. This might be due to the fact of using inadequate method to measure strains in the experimental tests.

Table (4.13) Total Width of Solid Columns for Cubes Containing Unisize Circular Voids

Sample Name	Total Width of Solid Columns (<i>W</i>), mm							
	<i>w</i> ₁	<i>w</i> ₂	<i>w</i> ₃	<i>w</i> ₄	<i>w</i> ₅	<i>w</i> ₆	<i>w</i> ₇	<i>W</i>
PA-UCL2-1	13.54	60.63	15.95					90.12
PA-UCL2-2	13.63	60.63	15.95					90.21
PB-UCL2	7.37	60.22	22.53					90.12
PC-UCL2	6.65	59.41	24.05					90.11
PA-UCL4-1	13.26	34.04	16.23					63.53
PA-UCL4-2	11.46	30.33	13.54					55.33
PA-UCL4-3	11.46	30.33	13.54					55.33
PB-UCL4	6.45	22.63	7.37	20.14				56.59
PC-UCL4	0.36	24.05	6.65	13.23				44.29
PA-UCL6	8.33	13.54	11.46					33.33
PB-UCL6	5.64	20.14	7.37	13.23				46.38
PC-UCL6	0.36	10.57	6.65	7.04				24.62
PA-UCM4	8.2	34.85	18.06	20.5				81.61
PB-UCM4	15.49	27.15	16.41	24.66				83.71
PC-UCM4	9.4	33.1	11.18	17.75				71.43
PA-UCM8	10.87	18.15	12.85					41.87
PB-UCM8	6.86	24.66	11.56	16.41				59.49
PC-UCM8	11.19	22.76	14.02					47.97
PA-UCM12	12.85	18.06						30.91
PB-UCM12	8.15	8.56						16.71
PC-UCM12	3.56	5.36						8.92
PA-UCS11	0.43	22.72	1.81	4.52	17.51	5.61	4.32	56.92
PB-UCS11	1.42	13.22	12.81	1.54	1.93			30.92
PC-UCS11	1.91	15.84	10.02	3.53	4.7	2.9	2.42	41.32
PA-UCS22	0.74	11.82	9.61	2.11				24.28
PB-UCS22	1.12	13.22	12.81					27.15
PC-UCS22	2.51	10.02	6.52					19.05
PA-UCS33	2.51	6.82	6.52					15.85
PB-UCS33	8.22	8.7						16.92
PC-UCS33	6.41	6.52						12.93

Table (4.14) Total Width of Solid Columns for Cubes Containing Mixed Circular Voids

Sample Name	Total Width of Solid Columns (<i>W</i>), mm							
	<i>w</i> ₁	<i>w</i> ₂	<i>w</i> ₃	<i>w</i> ₄	<i>w</i> ₅	<i>w</i> ₆	<i>w</i> ₇	<i>W</i>
PA-UXCL1M1S3	8.34	20.47	9.22	18.06	17.51			73.60
PB-UXCL1M1S3	5.31	27.42	26.14	22.53				81.40
PC-UXCL1M1S3	6.65	24.27	22.42	18.72				72.06
PA-UXCL2M3S6	12.81	16.23						29.04
PB-UXCL2M3S6	7.37	22.53	16.22	10.97				57.09
PC-UXCL2M3S6	0.37	18.68	13.22	6.65				38.92
PA-UXCL2M5S8	11.82	13.6						25.42
PB-UXCL2M5S8	1.25	11.56	11.32	3.24				27.37
PC-UXCL2M5S8	5.57	13.22	6.65					25.44

Table (4.15) Total Width of Solid Columns for Cubes Containing Unisize Non-circular Voids – Square and Diamond Voids

Sample Name	Total Width of Solid Columns (<i>W</i>), mm							
	<i>w</i> ₁	<i>w</i> ₂	<i>w</i> ₃	<i>w</i> ₄	<i>w</i> ₅	<i>w</i> ₆	<i>w</i> ₇	<i>W</i>
PA-USqL3	20.82	46.96	22.31					90.09
PB-USqL3	16.87	40.87	27.08					84.82
PA-USqL6	12.88	20.55	18.12					51.55
PB-USqL6	14.73	24.69	16.46	17.78				73.66
PA-USqM6	1.45	26.95	6.35	16.08	21.32			72.15
PB-USqM6	20.98	30.28	21.13	22.86				72.39
PA-USqM12	1.45	21.29	1.65	16.08	2.47			42.94
PB-USqM12	11.38	11.79						23.17
PA-UDmL3	11.42	60.61	13.56					85.59
PB-UDmL3	7.73	36.3	22.51					66.54
PA-UDmL6	8.31	13.56	11.42					33.29
PB-UDmL6	5.62	20.12	13.23	7.35				46.32
PA-UDmM6	12.84	20.47	18.08					51.39
PB-UDmM6	15.46	24.65	17.74	16.38				74.23
PA-UDmM12	8.14	8.93						17.07
PB-UDmM12	2.13	21.04	11.56	9.36				44.09

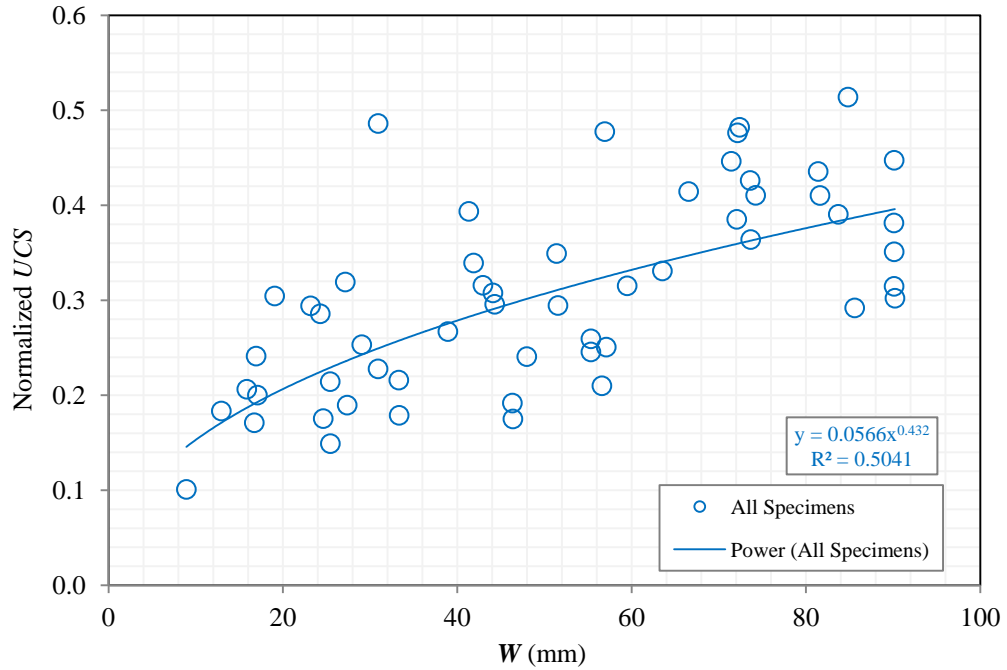


Figure (4.20) Normalized Uniaxial Compression versus Total Width of Solid Columns for Cubes with Voids Having Different Size, Shape and Distribution

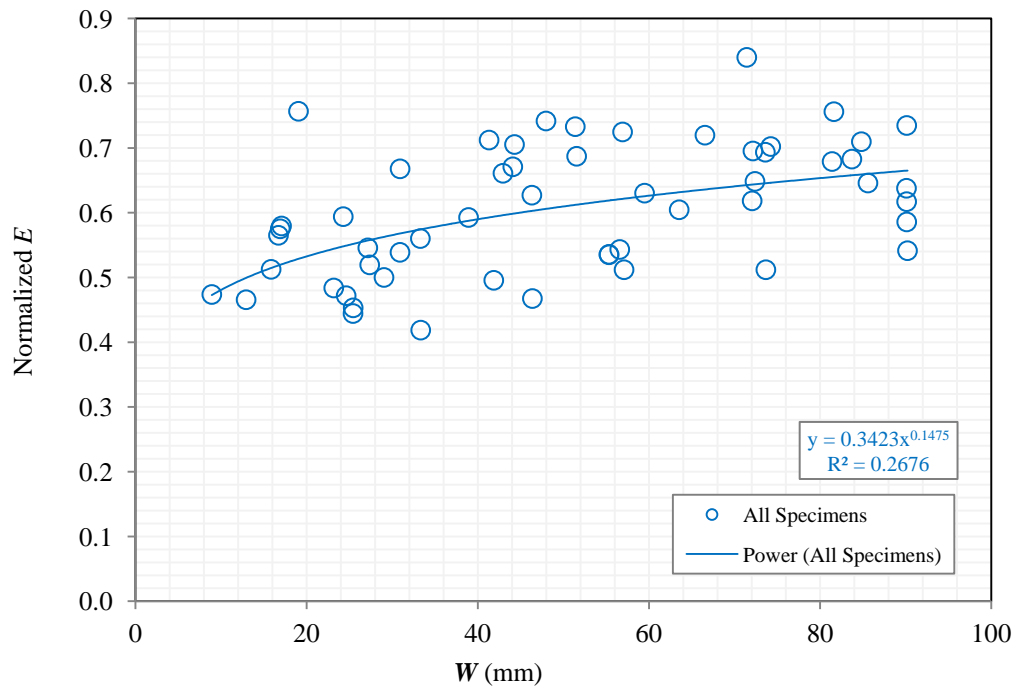


Figure (4.21) Normalized Deformation versus Total Width of Solid Columns for Cubes with Voids Having Different Size, Shape and Distribution

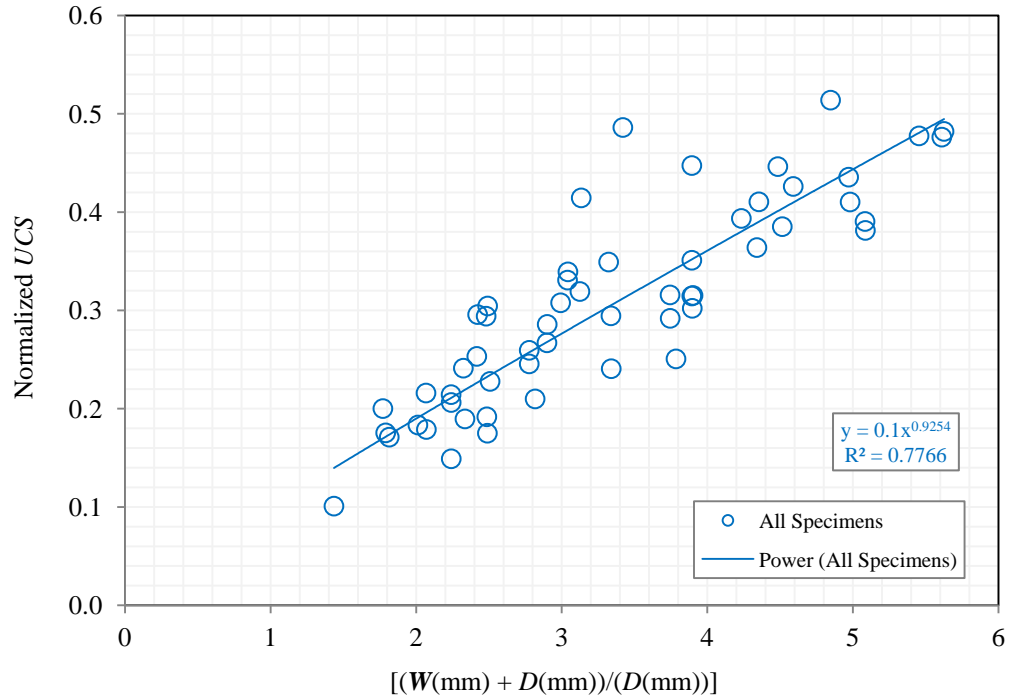


Figure (4.22) Normalized Uniaxial Compression versus Normalized Total Width of Solid Columns for Cubes with Voids Having Different Size, Shape and Distribution

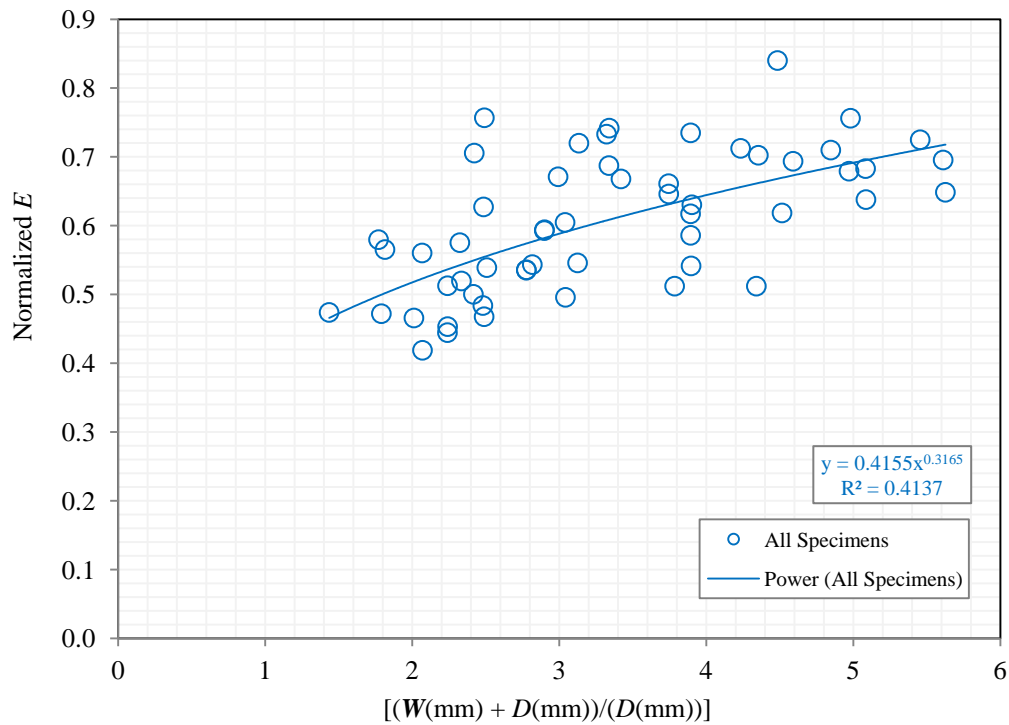


Figure (4.23) Normalized Deformation versus Normalized Total Width of Solid Columns for Cubes with Voids Having Different Size, Shape and Distribution

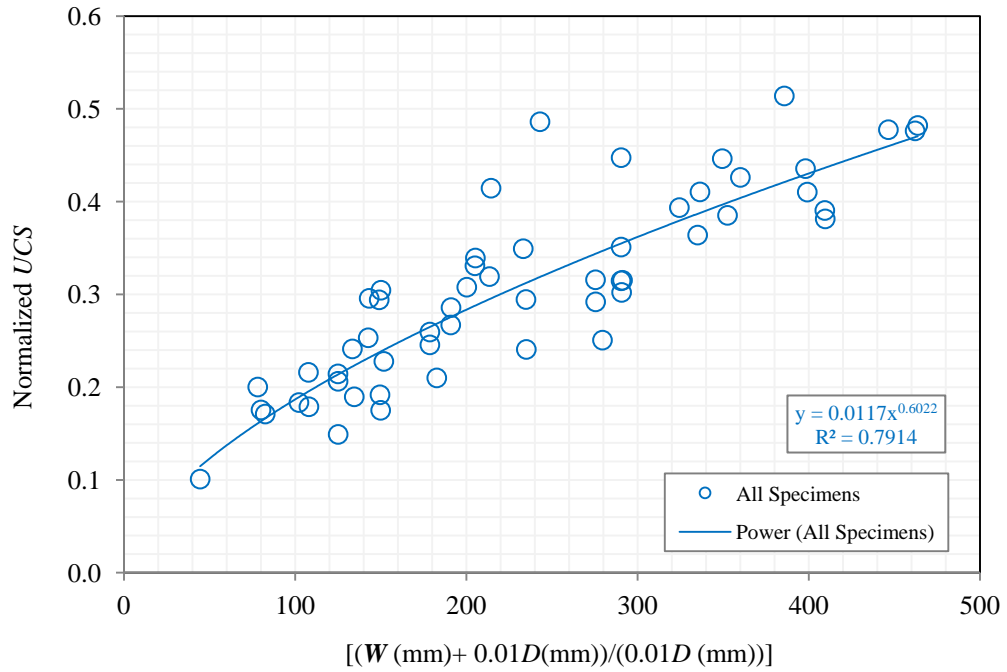


Figure (4.24) Normalized Uniaxial Compression versus Normalized Total Width of Solid Columns for Cubes with Voids Having Different Size, Shape and Distribution

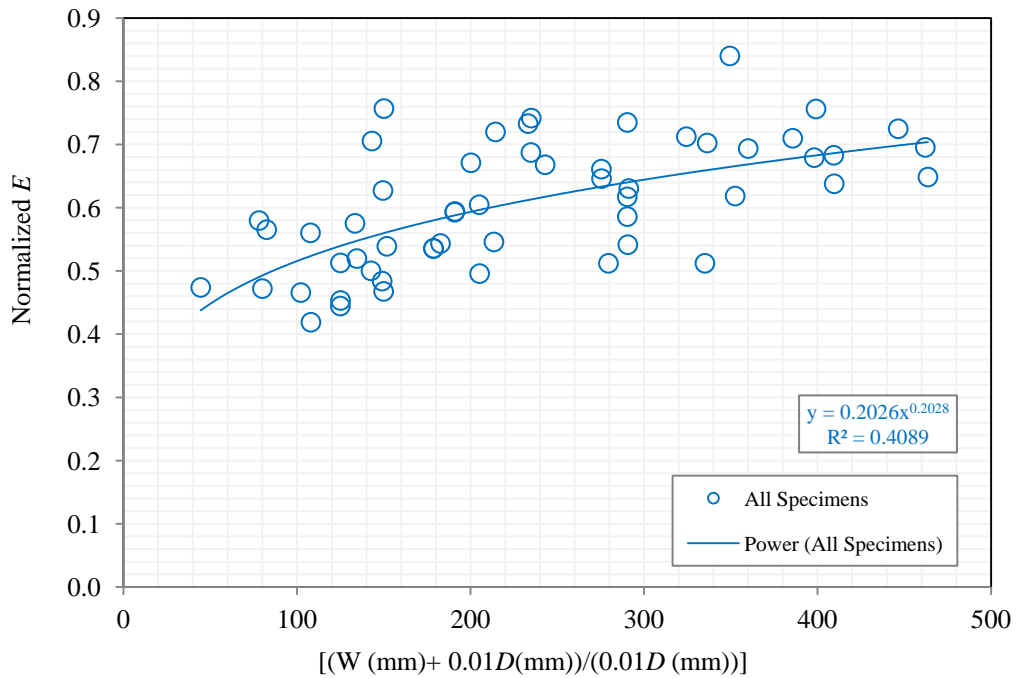


Figure (4.25) Normalized Deformation versus Normalized Total Width of Solid Columns for Cubes with Voids Having Different Size, Shape and Distribution

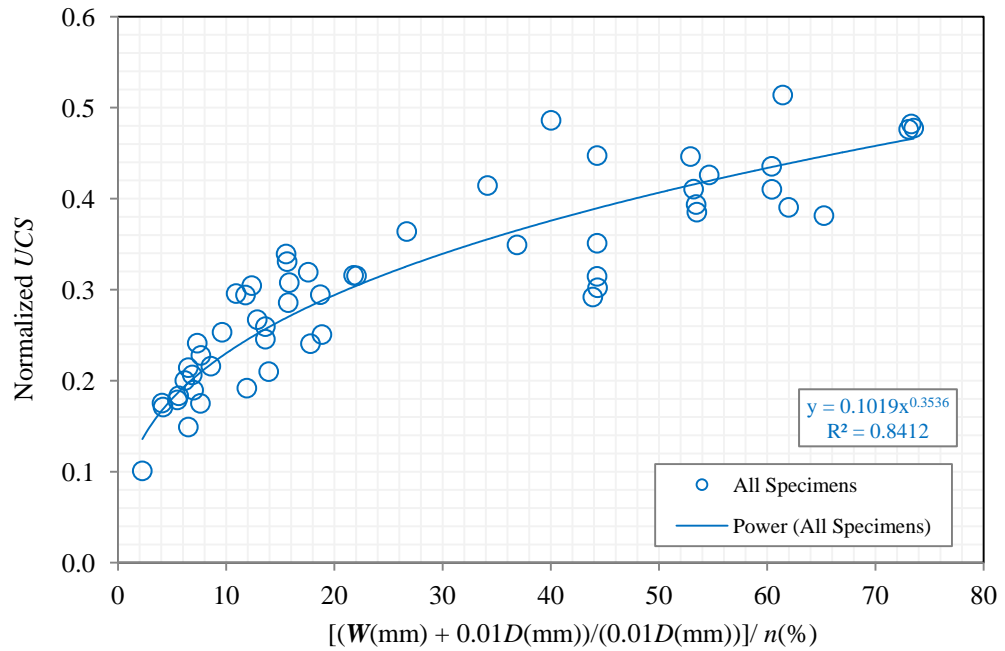


Figure (4.26) Normalized Uniaxial Compression versus Normalized Total Width of Solid Columns and Void Porosity for Cubes with Voids Having Different Size, Shape and Distribution

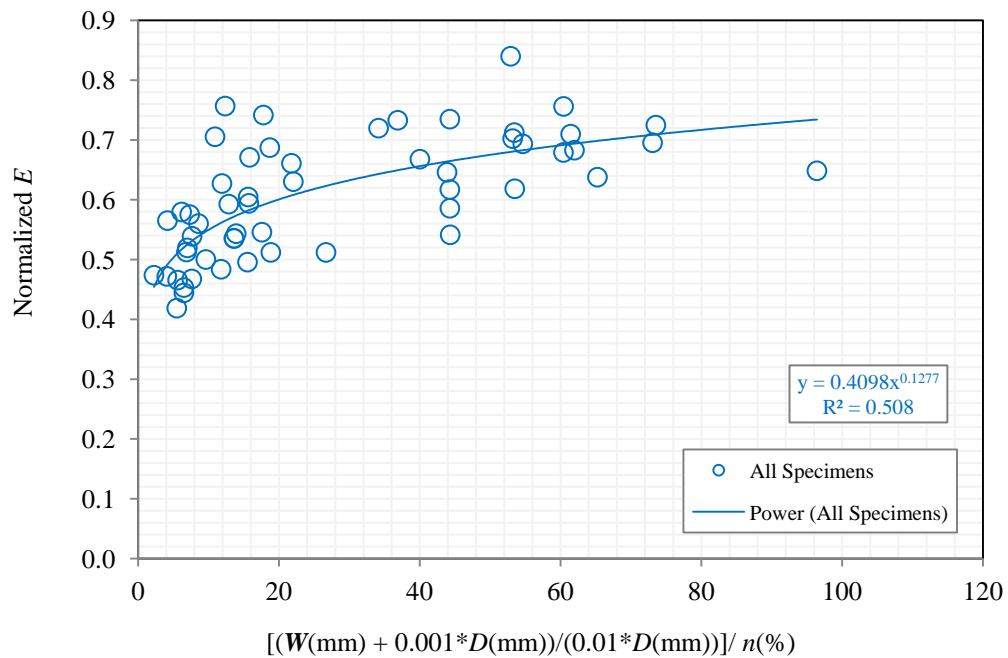


Figure (4.27) Normalized Deformation versus Normalized Total Width of Solid Columns and Void Porosity for Cubes with Voids Having Different Size, Shape and Distribution

4.4.6 Correlation between Uniaxial Compression and Young's Modulus

According to Palchik (1999) and Chawla (2007), uniaxial compressive strength (*UCS*) of porous rock and rock-like materials is inversely proportional to the porosity (*n*) and directly proportional to the elastic modulus (Young's Modulus – *E*). This can be mathematically written as follow:

$$(UCS)_{\text{Porous}} \propto \frac{E}{n} \quad \dots (4.15)$$

Considering Eqs. (4.11), the above expression can be rewritten as follows:

$$(UCS)_{\text{Porous}} \propto \left[\frac{E * \left(\frac{W + 0.01D}{0.01D} \right)}{n} \right] \quad \dots (4.16)$$

The test data obtained from the work of Project Activity Task ORD-FY04-013 were used to validate the above expression, Eqs. (4.16). Accordingly, the results of uniaxial compressive strength of the experimental tests are plotted as a function of Young's modulus (*E*), void porosity (*n*), total width of solid columns (*W*), and void size (*D*) as shown in Figures (4.28) to (4.30). According to the figures, for the void porosity ranging from 6.28% to 19.82%, the following results were observed:

- 1- The uniaxial compressive strength (*UCS*) of Hydro-StoneTB[®] is inversely proportional to the void porosity (see Figure 4.2) and directly proportional to *E* (see Figure (4.28)). The correlation is followed decent power trend as shown in figure (4.29).

2- Considering the total width of solid columns (W) to express the effects of void spatial distribution on mechanical properties led to improve the correlations between the uniaxial compressive strength of Hydro-StoneTB[®] with void geometry and Young's Modulus. The relationships can be represented best by the following power equation:

$$(UCS)_{\text{Porous}} = 3.1475 * \left[\frac{100 * W + D}{D * n} \right]^{0.3111} \quad R^2 = 0.8525 \quad \dots (4.13)$$

Accordingly, considering total width of solid columns (W) to express the effects of void spatial distribution on mechanical properties led to better correlations between the uniaxial compressive strength of Hydro-StoneTB[®] and Young's Modulus. The coefficient of determination increased from $R^2 = 0.7424$ to $R^2 = 0.8525$.

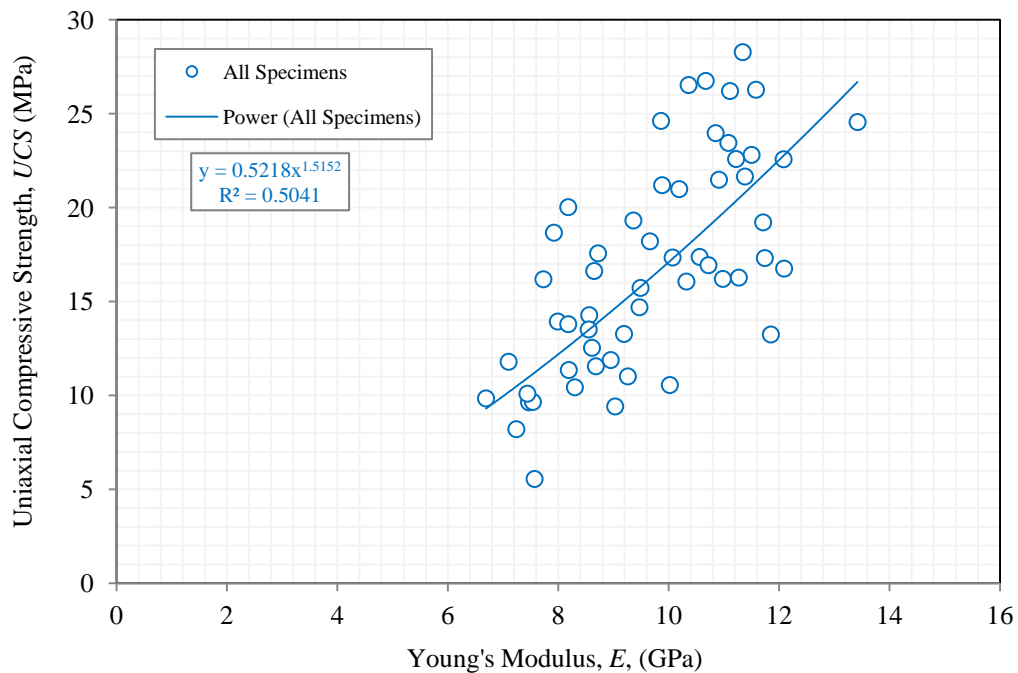


Figure (4.28) Uniaxial Compression versus Deformation for Cubes with Voids Having Different Size, Shape and Distribution

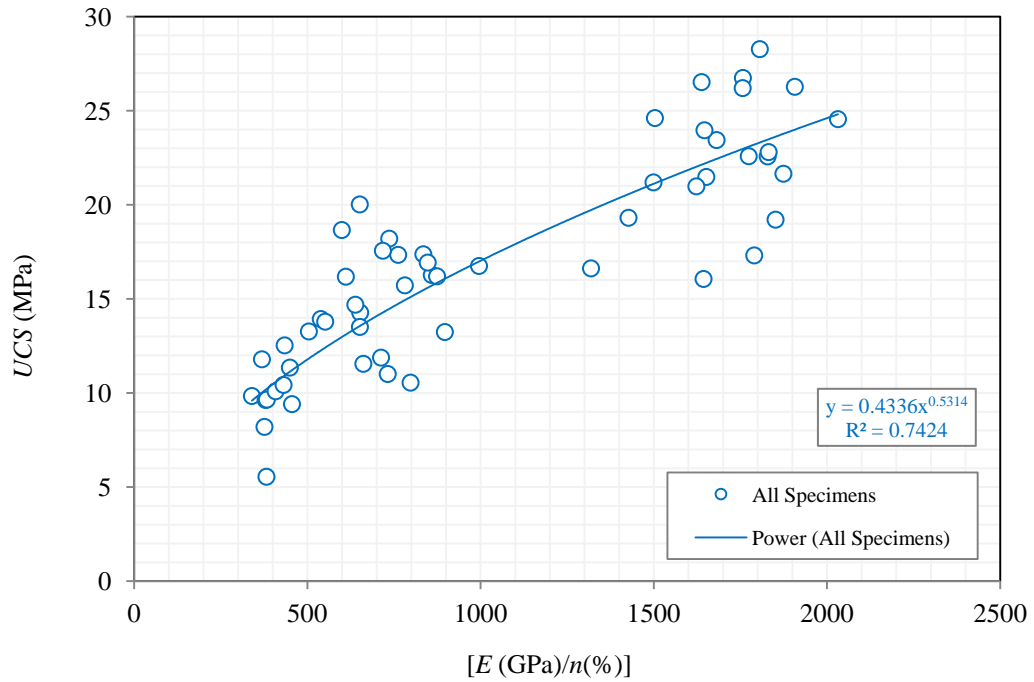


Figure (4.29) Uniaxial Compression versus Deformation and Void Porosity for Cubes with Voids Having Different Size, Shape and Distribution

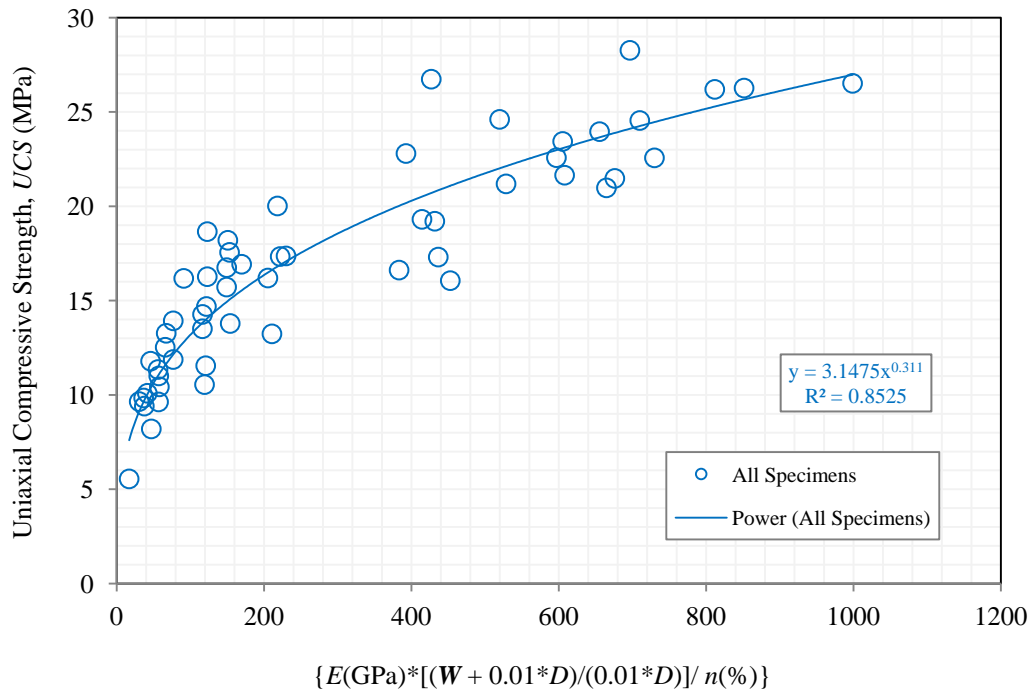


Figure (4.30) Uniaxial Compression versus Deformation, Void Porosity, and Total Width of Solid Columns for Cubes with Voids Having Different Size, Shape and Distribution

4.5 Failure Modes of Hydro-StoneTB[®] Cubes.

At the end of each experiment in Project Activity Task ORD-FY04-013, the tested cube was photographed from both front and back. From the photographs, the dominate failure mode is tension (axial) failure mode. However, depending on bridge distances, side distances, and alignment of voids with nearby voids, some cubes showed shear failure mode as well.

4.5.1 Porous Cubes Containing Circular Voids

The photographs for porous cubes containing circular voids with different void size and distribution are shown in Appendix (I). In general, regardless of void size and distribution and void porosity, the majority of the cracks were formed at the peripheries of the voids in the direction of vertical to sub-vertical; oriented approximately parallel to the applied axial compression. However, there are some horizontal cracks which connected the vertical to sub vertical cracks to the pore sides or sample side (surface). Furthermore, some cracks (vertical to sub-vertical) were formed in the solid parts of the cubes; between voids or/and between voids and the cube sides. Most of the cracks are extended to the sample surfaces in the direction of axial compression which in turn led to axial splitting; tension fractures.

From the Figures (4.31) to (4.34), for the porous cubes with circular voids having different void size (small, medium, and large), different void porosity (about 6%, about 13%, and about 20%), and different void distribution (Pattern A, B, and C), the crack pattern showed axial splitting (tension fractures or failure) as the dominant failure modes regardless of void porosity, void size, void uniformity, and void spatial distribution.

However, in some porous cubes there are some shear failure (inclined cracks) depending on the void alignments and bridge distances.

In general, the cracks were formed mainly at the void poles and intended to expand approximately parallel to the axial compression load. However, in some cubes depending on the distances between one void and the other voids located at the immediate vicinity of the void, cracks were formed horizontally or sub-horizontally between adjacent voids. In those cubes, when a crack passes vertically (or sub-vertically) between two voids, a horizontal crack was formed to connect that crack to the void side or the sample side. Finally, the coalescence of those cracks (horizontal (or sub-horizontal) and the vertical (or sub-vertical) cracks) formed an inclined crack that gave a failure mode similar to the shear failure mode as shown in Figures (4.35) and (4.36).

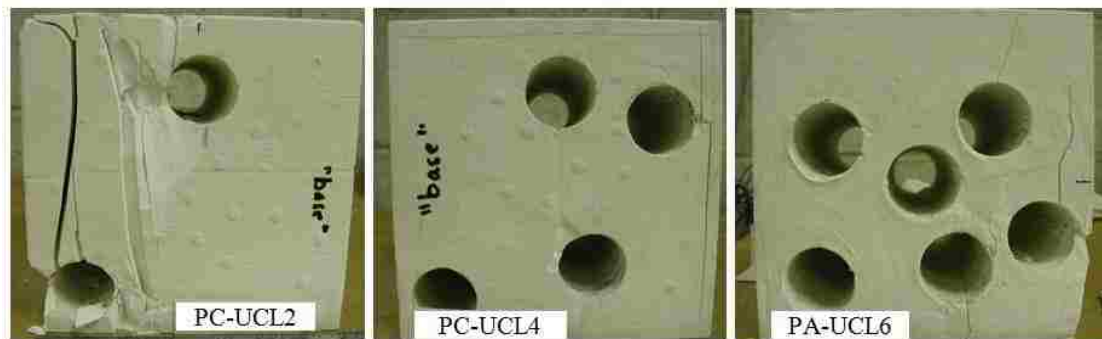


Figure (4.31) Photographs of Tested Cubes Containing Large Unisize Circular Voids

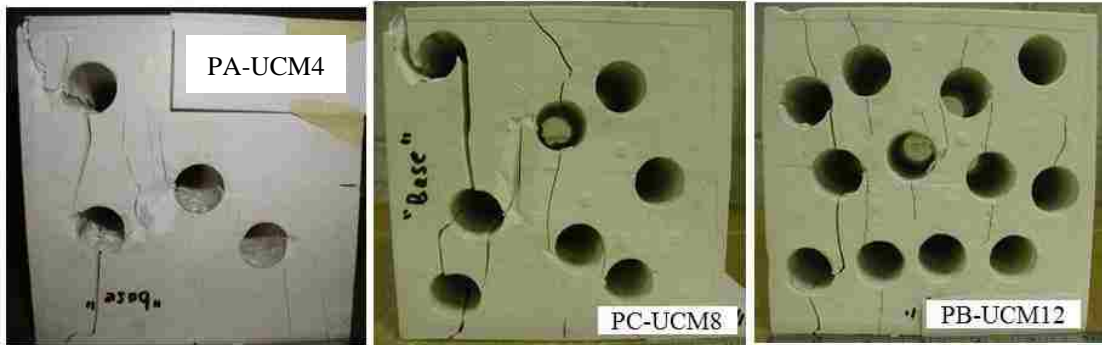


Figure (4.32) Photographs of Tested Cubes Containing Medium Unisize Circular Voids

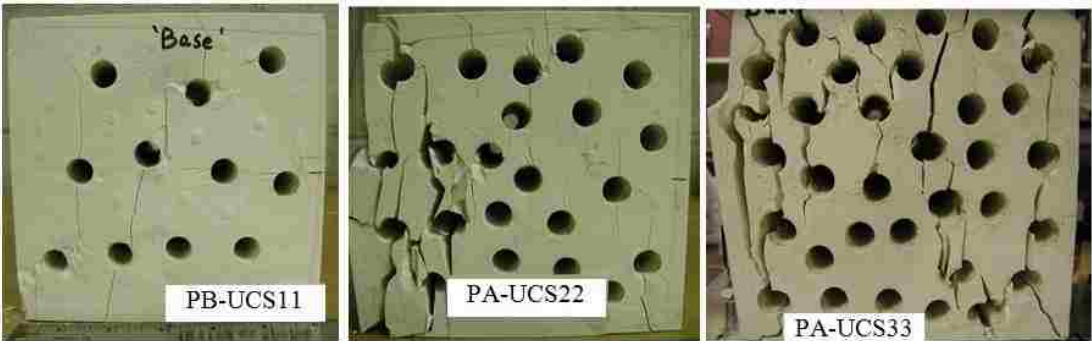


Figure (4.33) Photographs of Tested Cubes Containing Small Unisize Circular Voids

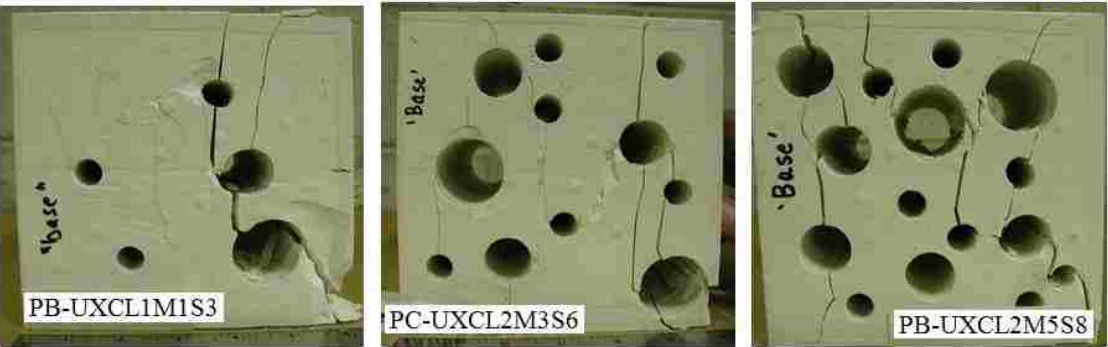


Figure (4.34) Photographs of Tested Cubes Containing Mixed Circular Voids

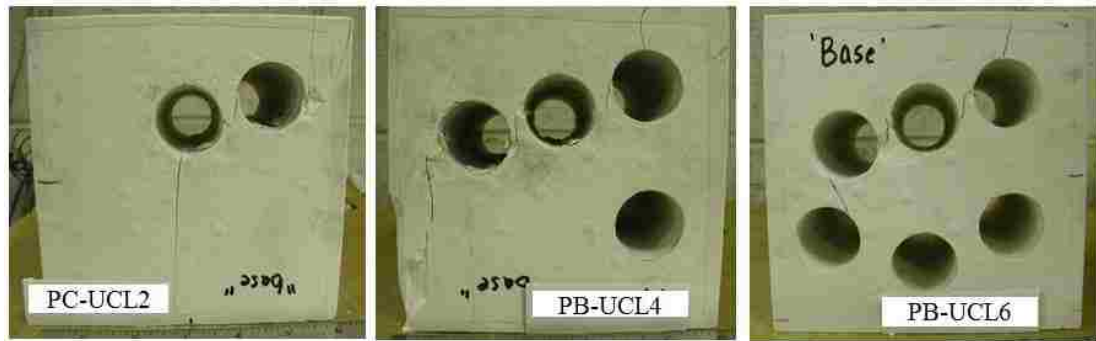


Figure (4.35) Photographs of Tested Cubes Containing Large Unisize Circular Voids

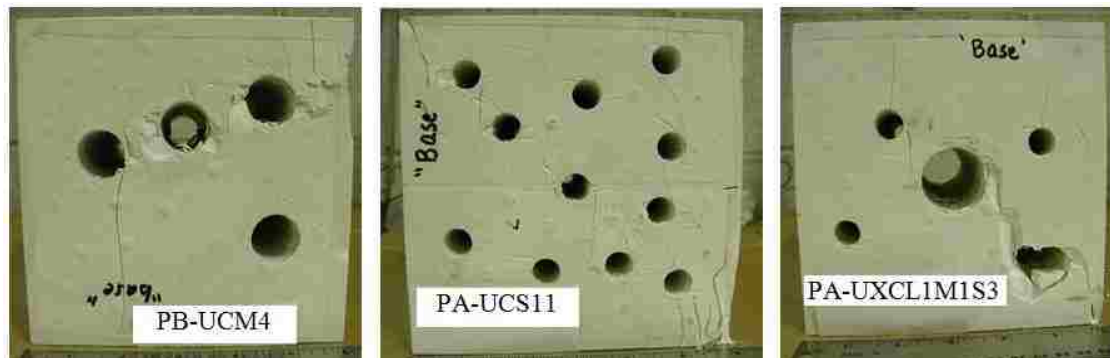


Figure (4.36) Photographs of Tested Cubes Containing Circular Voids

4.5.2 Porous Cubes Containing Non-circular Voids

For the porous cubes with either square voids or diamond voids having different void size (small and large), different void porosity (about 6% and about 13%), and different void distribution (Pattern A and B), the crack pattern showed axial splitting (tension fractures or failure) as the dominant failure modes similar to the cubes with circular voids as shown in Figures (4.37) to (4.40), see also Figures in Appendix (I). Most of the cracks were formed at the tips of the diamond voids in the direction approximately parallel to the applied axial compression. Some of these cracks are extended to the

sample surfaces, again in the direction of axial compression (vertical to sub-vertical), which in turn led to axial splitting; tension fractures. Some cracks (vertical to sub-vertical) were also formed in the solid parts of the cubes; between voids or/and between voids and the cube sides. In addition, there are some horizontal cracks which connected the vertical to sub vertical cracks to the void tips (or sides) or sample side (surface).

However, in each porous cube there are some shear failure (inclined cracks) depending on the void alignments and bridge distances. In general, due to stress concentration, the cracks were formed mainly at the void tips and intended to expand approximately parallel to the axial compression load, however, in some cubes cracks were formed between voids horizontally or sub-horizontally depending on the distances between one void and the other voids located at the immediate vicinity of the void. In those cubes, when a crack passes vertically (or sub-vertically) between two voids, a horizontal crack was formed to connect that crack to the void side or the sample side. In some cubes, the coalescence of those cracks (horizontal (or sub-horizontal) and the vertical (or sub-vertical) cracks) formed an inclined crack that gave a failure mode similar to the shear failure mode as shown in Figure (4.41).

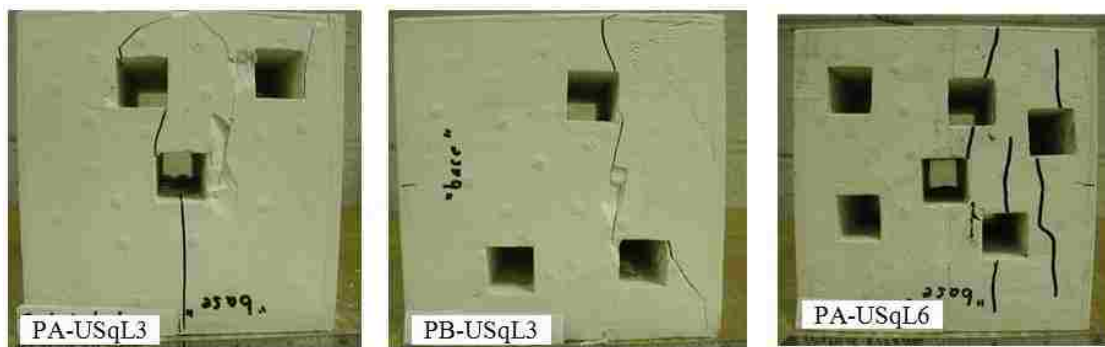


Figure (4.37) Photographs of Tested Cubes Containing Large Unisize Square Voids

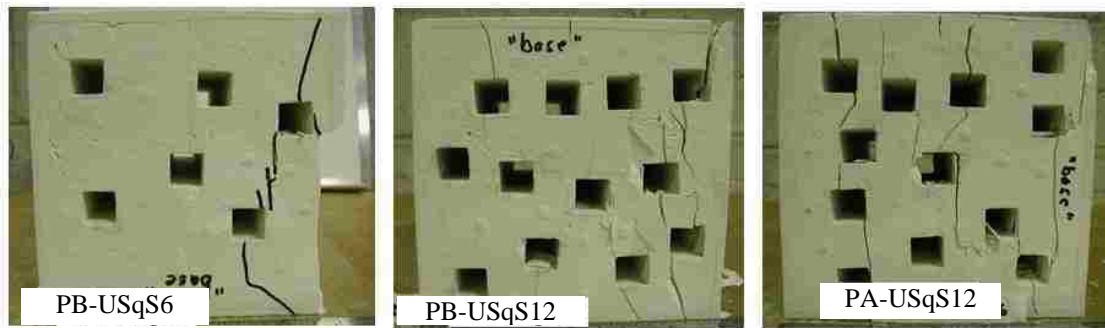


Figure (4.38) Photographs of Tested Cubes Containing Small Unisize Square Voids

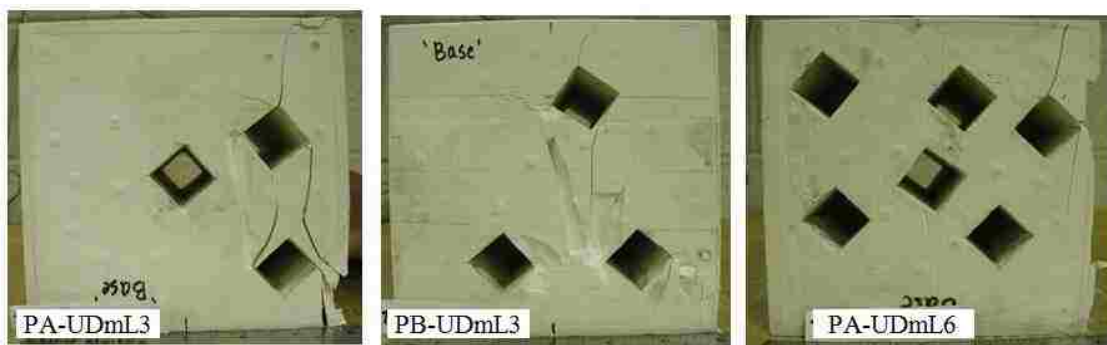


Figure (4.39) Photographs of Tested Cubes Containing Large Unisize Diamond Voids

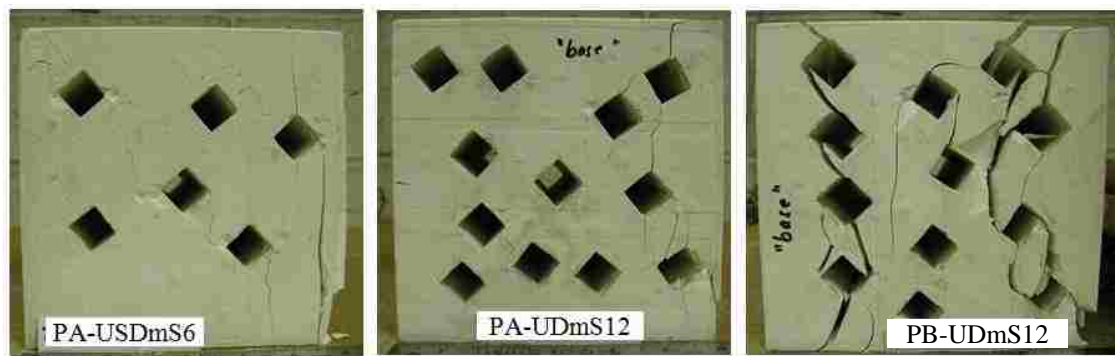


Figure (4.40) Photographs of Tested Cubes Containing Small Unisize Diamond Voids



Figure (4.41) Photographs of Tested Cubes Containing Unisize Non-circular Voids

From the photographs, it can be concluded that, due to stress concentration at the vicinity of the voids, the void existence produced tension stresses at the poles of the circular voids (or at the tips of non-circular voids) (Timoshenko and Goodier 1951). When the produced tension stresses exceed the material's tensile strength, cracks initiate at the poles (or tips) and then propagate vertically or sub-vertically in the direction parallel to the applied uniaxial loads if they are not interrupted or diverted by the other voids. These vertical to sub-vertical cracks will finally reach the top and bottom surfaces and divide the cubes into two or more vertical to sub-vertical columns. Accordingly, the tension failure modes dominate the failure modes in the cubes under uniaxial compression as suggested by Sammis and Ashby (1986)

CHAPTER FIVE *NUMERICAL ANALYSIS TO SIMULATE THE EXPERIMENTAL TESTS*

5.1 Introduction

Since the numerical analysis for the Hydro-StoneTB[®] cubes tested in the work of Project Activity Task ORD-FY04-013 (discussed in chapter four) has not been carried out, the experimental results can be used to validate numerical method (software). Furthermore, the results of the numerical analysis can be helpful in analyzing the experimental results. The UDEC program (version 3.1) is the software intended to be validated in this study. The UDEC codes to be used in this analysis are obtained from Software Configuration Management (SCM) in according with the AP-SI.1Q procedure. The program should be only used within the range of validation, as specified in the software qualification documentation (BSC 2003).

5.2 Numerical Analysis

In engineering, problems are typically solved by using either empirical or analytical methods (Scheldt 2002). In the empirical methods, the solution is usually done basing on experiment and comparison, while in the analytical methods, the problems are solved by either calculation or modeling (Scheldt 2002). In some engineering problems, the analytical solutions are represented by differential equations with a set of related boundary and initial conditions (Moaveni 2008). These differential equations are mathematical models and called governing equations. Due to the complexities embedded either in the equations themselves or in the boundary and initial conditions, or both, the

exact solutions of these differential equations are not achievable in many engineering problems (Moaveni 2008). Alternatively, numerical solutions, or numerical approximations, are used to deal with such problems. In general, there are two main numerical models in numerical analysis; continuous and discontinuous models (Scheldt 2002; Jing and Stephenson 2007).

5.2.1 Continuous Numerical Models

In continuous models, the material in the problem domain is assumed to be continuous throughout the physical processes; the material cannot be broken into pieces (Jing and Stephenson 2007). In other words, during the simulation process, the points which are originally in the vicinity of a certain point in the problem domain will stay in the same neighborhood. Regarding the problem domain contains fractures, continuous model assumes that the deformations along or across the fractures will be in the same order of magnitude as those of the solid matrix near the fractures (Jing and Stephenson 2007). This means, large-scale slide or opening of fractures is not allowed in the continuous models. Therefore, the continuous models are not suitable for engineering problems which contain fractures except those contain a small number of fractures experiencing small deformations. They are, however, most effective for problems of small deformation (strain) and linear constitutive material behavior (Jing and Stephenson 2007). The most universally used numerical methods for continuous models are the finite difference method (FDM), the finite element method (FEM) and the boundary element method (BEM) (Scheldt 2002; Jing and Stephenson 2007; Bobet 2010).

5.2.2 Discontinuous Numerical Models

For discontinuous models, the material in the problem domain is treated as an assemblage of independent units; a system of individual blocks interacting along their boundaries such as rock blocks, solid particles of granular materials, structural elements (Scheldt 2002; Jing and Stephenson 2007; Bobet 2010). The mechanical behavior of the discontinuous models is composed of two parts; behavior of the individual blocks and behavior of the boundaries (Cundall and Hart 1992). The discontinuous models are very effective for problems of large deformation (displacement rotation, slip, and strain) and nonlinear constitutive material behavior (Scheldt 2002; Jing and Stephenson 2007; Bobet 2010). Regarding the discontinuous models, there are several numerical methods; however, all of them are covered under a common adopted term called Discrete Element Method (DEM) (Cundall and Hart 1992; Jing and Stephenson 2007).

In addition to the aforementioned numerical methods, there are two other numerical methods which cannot be classified based on types of the numerical models. They are Meshless Methods (MM) and Artificial Neural Networks (ANN) (Bobet 2010).

5.2.3 Differences between Numerical Models

One of the essential differences between the numerical methods for continuous models (for example, FDM and FEM) and those for discontinuous models (DEM) is the unit system topology. The unit system topology, or the unit system identification, is the contact (or connectivity) patterns between individual units in the problem domain, or the system, which is the central computational issue of the Discrete Element Method (Jing and Stephenson 2007). In the numerical methods for continuous models, the topology is

assumed to be fixed throughout the simulation process (it is a fixed initial condition), while, it evolves with time and deformation process in the numerical methods for discontinuous models (Jing and Stephenson 2007). In other words, the Discrete Element Method has capability of detecting and updating of changeable contacts between the individual units as a result of their movements and deformations.

Another essential difference between the numerical methods for continuous models and those for discontinuous models is the rigid body mode of motion. In discontinuous models, the individual block displacements are much larger than the individual block continuous deformations when a large displacement occurs. While in the continuous models, since they are not producing strains in the elements, the element displacements are generally eliminated (Jing and Stephenson 2007). In other words, discontinuous models reflect more the individual unit displacement of the problem domain and continuous models reflect more the material deformation of the problem domains. This is because the individual blocks in the discontinuous models are free to move according to the force (or stress) constraints on their boundary contacts and other external loads according to the equations of motion which is contrary to continuous models in which the elements are not free to move, but are reserved within the same neighborhood of other elements by the displacement compatibility conditions.

5.3 Discrete Element Method (DEM)

Discrete element method (DEM) can be defined as any numerical method that has the following two capabilities (Cundall and Hart 1992): (1) permission of finite displacements and rotations of the individual units, including total separation of the units,

and (2) automatic recognition of the new formed contacts during simulation. And basing on the above definition, they, Cundall and Hart (1992), identified four main codes that comply with the above definition: *Distinct element programs*; *Modal methods*, *Discontinuous deformation analysis (DDA)*, and *Momentum-exchange methods*. The individual units in all four codes can be either rigid or deformable except for the *Momentum-exchange methods* (units are rigid only). The deformable means subdividing the individual units into finite difference zones. The contacts, boundaries between the individual units, are either rigid (*Distinct element programs* and *Modal methods*) or deformable (*DDA* and *Momentum-exchange methods*).

In addition, Bobet (2010) identified another method (or code) of DEM called Bonded Particle Model (BPM). In this method, BPM, the material in the discontinuous model is represented by an agglomerate of cemented grains (as discs in two dimensions or spheres in three dimensions). The grains are assumed to be rigid with a non-uniform distribution. They interact with each other through their contacts.

The numerical program used in the numerical analysis in this study, Universal Distinct Element Code (UDEC version 3.1), is described as a *Distinct element program* that uses an explicit time-marching scheme to solve the equations of motion of individual units directly (Itasca 2011, UDEC User's Guide). The explicit time-marching scheme means that unknown values of the variables in any individual unit in the problem are found from known values in the individual unit itself and the surrounding units as well. The individual units can be either rigid or deformable. The deformable means subdividing the individual units into finite difference zones.

The *Distinct element program* is based on Newton's second law, $F = ma$ (Scheldt 2002; Itasca 2011, UDEC User's Guide). It has many diverse applications in different engineering and science disciplines such as rock mechanics, soil mechanics, structural analysis, granular materials, fluid mechanics, ice mechanics, material processing, robot simulation, and computer animation (Jing and Stephenson 2007). It was originally created for representing a two-dimensional jointed rock mass. The formulation of *distinct element program* was initially presented by Cundall (1971). Its most developed version is embodied in a computer program called Three-Dimensional Distinct Element Code (3DEC) which has ability to simulate three-dimensional models (Itasca 2011, Theory and Background Manual).

5.4 Universal Distinct Element Code (UDEC)

The Universal Distinct Element Code (UDEC) is a two-dimensional numerical program that simulates the behavior of discontinuous geologic materials (such as rock mass or similar) under thermal, static, and dynamic loading using the distinct element method (Itasca Consulting Group 2002). It is well-suited program to simulate the large movements and deformations of a blocky system, using Lagrangian calculation scheme. In this program, UDEC, the problem domain is represented as an assemblage of individual units, also called discrete blocks, interacting along their boundaries. The boundaries are also called discontinuities. They, discontinuities, are treated as boundary condition along which large displacements and rotations of blocks are allowed (Itasca 2011, UDEC User's Guide). The relative motion of the discontinuities, in both the normal

and shear directions, is governed by linear or nonlinear force-displacement relations for movement.

Regarding the discrete blocks, they can be allowed to behave as either rigid or deformable blocks. The rigid block assumption is good for a physical system in which most of the deformation is accounted for by movement on discontinuities such as an unconfined assembly of rock blocks at a low stress level. One practical example is a shallow slope in well-jointed rock in which the deformation is mainly come from sliding and rotation of blocks, and from opening and interlocking of discontinuities. For the other physical systems, such as models in which high stress is expected, deformable block assumption is better one. In this assumption, UDEC automatically subdivides the discrete blocks into a mesh of finite-difference elements (triangular, constant-strain zones), and each element responds according to a prescribed linear or nonlinear stress-strain law (Itasca 2011, UDEC User's Guide). The zones can also follow an arbitrary, nonlinear constitutive law.

Accordingly, several built-in material constitutive models have been embedded in UDEC for both the discrete blocks and the discontinuities. The built-in constitutive models in UDEC range from linearly elastic models to highly nonlinear plastic models (Itasca 2011, UDEC Constitutive Models). They are grouped into two types; time-independent and time-dependent constitutive material models (creep) (Itasca 2011, UDEC Constitutive Models). The time-independent material models are fourteen models and arranged into three groups; null (one model), elastic (two models) and plastic model (eleven models) groups. The Null model group is used to represent material that is removed or excavated (to simulate voids, tunnels, for example). Some of the built-in

plastic constitutive models are Drucker-Prager model, Mohr-Coulomb model, Hoek-Brown model, and modified Hoek-Brown model. Regarding the time-dependent material models, eight creep models available in the creep model option for UDEC (Itasca 2011 - Creep Material Models).

UDEC is considered as a distinguished program due to its capability to address three most common difficulties in geomechanics; physical instability, path dependency of nonlinear materials, and implementation of extremely nonlinear constitutive models (Itasca, 2011, UDEC Constitutive Models). Physical instability can occur when softening behavior in the modeled material is expected; when the material fails, part of it accelerates and the stored energy is released as kinetic energy. Therefore, the numerical solution may fail to converge. For the second difficulty, path dependency of nonlinear materials, there are an infinite number of solutions that satisfy the equilibrium, compatibility and constitutive relations that describe the system. However, the numerical solution scheme should be able to accommodate different loading paths in order to apply the constitutive model properly; to find the “correct” solution. For the third difficulty, the nonlinearity of the stress-strain response, there are several forms of nonlinearity in geotechnical materials which should be accommodated in the numerical program such as nonlinear dependence of both the elastic stiffness and the strength envelope on the confining stress, and different post-failure response in the tensile, unconfined and confined regimes. UDEC has capability to overcome on the aforementioned three difficulties by using an explicit, dynamic solution scheme embedded in it (Itasca, 2011, UDEC Constitutive Models). In other words, first, since the inertial terms are included (kinetic energy is generated and dissipated), the numerical solution is stable (due to the

explicit, dynamic solution) even when the simulated geomechanical system is unstable. Second, the explicit, dynamic solution scheme has ability to follow the evolution of a geomechanical system in a realistic manner; since the full law of motion is embedded in it, the explicit, dynamic solution scheme can follow the physical path and evaluate the effect of the loading path on the constitutive response. Third, very nonlinear constitutive models can be complimented in UDEC because of the explicit, dynamic solution scheme; the field quantities at each element in the model, such as forces/stresses and velocities/displacements, can be isolated from one another during one calculation step in the general calculation sequence.

5.5 UDEC Model Description

The UDEC models are more realistic numerical models for studying the effects of voids on the mechanical behavior of rocks and rock-like material because of their ability to (1) represent physical voids in the material and (2) model complex failure mechanisms, such as fracture initiation and propagation between voids (Rigby 2004). The following two details can be helpful to explain why the UDEC models are more realistic in studying the mechanical behaviors of porous materials.

First, due to its capability of simulating crack initiation and propagation (fracturing) in the material when the stress exceeds strength, Voronoi tessellation joint generator embedded in UDEC is powerful tool to represent materials in numerical models (Itasca Consulting Group 2002). For numerical models using Voronoi tessellation joint generator, the material domain is divided into small elastic blocks (discrete blocks) that are attached together across their boundaries as shown in Figure (5.1) (Itasca Consulting

Group 2002; BSC 2003). For the plane-strain assumption in UDEC models, the blocks are considered to have an infinite depth. Regarding the discontinuities or joints, the contacts between the blocks, they are represented as liner interface contacts of finite length. The blocks, also called Voronoi blocks, are randomly-sized small polygons that can be uniformly distributed throughout the tessellation region by using Voronoi algorithm (Itasca 2011, UDEC User's Guide). In the Voronoi algorithm, movable points (also called seeds or interior points) are randomly distributed within the material domain. To obtain uniform sized Voronoi blocks, the seeds must be distributed more uniformly. Hence, an iteration procedure is used to move the seeds to an arrangement in which the distances between the seeds are approximately equal. The interior points (seeds) are then connected to create triangles. In the final step, all triangles that share a common side are bisected by drawing perpendicular lines to construct the Voronoi polygons (Itasca 2011, UDEC User's Guide). The necessity of having small, uniformly distributed blocks and block boundaries is to allow cracks to initiate and propagate (internal fracturing) and blocks to loosen and detach as the evolving stress state dictates. In other words, the block boundaries act as potential, or incipient, invisible fracture locations and become visible when the yielding begins (local failure for a given stress path) (BSC 2003).

Second, the UDEC has several constitutive models that can control the mechanical behaviors of the block boundaries, potential fracture locations (Itasca 2011, Theory and Background Manual; BSC 2003). Among them is Coulomb slip model with residual strength in which the most realistic behavior of physical joints can be modeled. In Coulomb slip model with residual strength one, the elastic behavior of potential fractures is controlled by constant normal and shear stiffness, and should be consistent

with the blocks elastic properties (Young's modulus and Poisson's ratio of the Voronoi blocks) (BSC 2003; BSC 2004). In addition, in this constitute model, it is allowed to the potential fracture to sustain a finite tensile stress, and its slip conditions is controlled by potential fracture's cohesion and friction angle prior to fail. If a potential fracture fails, either in tension or shear, tensile strength and cohesion are set to zero, whereas the friction angle is set to the residual value.

In sum, the UDEC models has a good ability to simulate the physics of deformation and fracture of a bonded granular matrix that contains void space of varying shape, size and porosity(Rigby 2004).

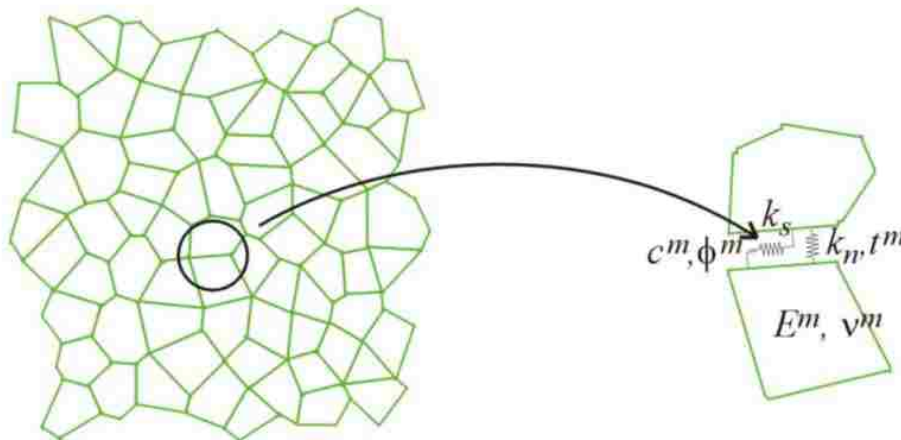


Figure (5.1) Material Representation in UDEC Models Using Voronoi Tessellation Joint Generator (BSC 2003)

5.6 UDEC Model Calibration

In order to represent the actual material used in the experimental tests in the UDEC models using Voronoi tessellation, the UDEC must be calibrated (BSC 2003). Calibration is usually done by matching the numerical model macro-behavior with the

one of the experimental test (BSC 2003). This can be done through adjusting the micro-properties of the numerical models until the macro properties of the two models (numerical and experimental obtained from the actual tests) are matched.

Calibration is a trial-and-error procedure with considering previous experience and some understating of the model mechanical behavior (BSC 2003; BSC 2004; Rigby 2004). Due to the high uncertainty in the material property database, assigning appropriate properties to the model material (calibration) is the most difficult part in the model generations (Itasca 2011, UDEC User's Guide).

5.6.1 Calibrated Material Properties

In the calibration, the loading and boundary conditions in the UDEC models should be similar to those in the experimental tests. Accordingly, those requirements were achieved by mimicking the idealized conditions assumed in uniaxial compression testing (two-dimensional plane strain); vertical translations along both bottom and top of the specimen in the y-directions are allowed by freeing gridpoints to move vertically. Furthermore, the gridpoints along the model's vertical sides are freed to move horizontally. The uniaxial compression test was simulated by applying a fixed velocity of 5×10^{-3} meter per second along the top and bottom rows of zones of the specimen. Stresses, strains and total unbalanced force will be monitored throughout the tests.

According to BSC (2003), the mechanical behaviors of UDEC models with Voronoi tessellation, using Mohr-Coulomb constitutive model for blocks and Coulomb slip model with residual strength for joints, are characterized by the followings parameters:

- 1- Size ratio between the models and the discrete blocks; numbers of the discrete blocks in the model.
- 2- Elastic properties of the discrete blocks; properties (E^m and ν^m , from Figure (5.1)).
- 3- Elastic properties of the discontinuities (normal stiffness, k_n , and shear stiffness, k_s , see Figure (5.1)).
- 4- Plastic properties of the discontinuities; strength properties (tensile strength, t^m , cohesion, c^m , and friction, ϕ^m , see Figure (5.1)).
- 5- Post failure plastic properties of the discontinuities. The strength properties of the discontinuities at the onset of yield are different from the initial, or original, values. They usually decrease to smaller value or zero.

As a result, the following parameters must be calibrated before starting the simulations using UDEC program: normal stiffness (k_n), shear stiffness (k_s), tensile strength (t^m), cohesion (c^m), and friction (ϕ^m) for the block boundaries (micro- joints between the Voronoi blocks), Young's modulus (E^m) and Poisson's ratio (ν^m) for the Voronoi blocks. However, since it is assumed that the material in the Voronoi blocks has isotropic behavior in elastic range, bulk modulus (K^m) and shear modulus (G^m) were used in UDEC rather than Young's modulus, (E^m) and Poisson's ratio (ν^m) (Itasca 2011, UDEC User's Guide). The elastic constants, K and G, can be obtained from the following equations:

$$K^m = \frac{E^m}{3(1 - 2\nu^m)} \quad \dots (5.1)$$

$$G^m = \frac{E^m}{2(1 + \nu^m)} \quad \dots (5.2)$$

According to the previous works in the literature (BSC 2003; Rigby 2004; BSC 2004), calibration for model deformability and strength can be carried out separately, and it is common to start with the model deformability (elastic properties). The model's deformation is controlled by the k_n , k_s , K^m and G^m , while the model's strength is controlled by c^m , ϕ^m , and t^m ; the compressive strength is controlled by c^m and ϕ^m , and the model's tensile strength is controlled by the t^m . (BSC 2003; Rigby (2004),

5.6.2 Deformation Calibration

UDEC's model elastic properties (E and ν) are functions of Voronoi block size and four micro-properties (k_n , k_s , K^m , and G^m) (BSC 2003). The Voronoi block size is usually determined based on observed fracture spacing and the condition that the ratio between the inclusion size (such as tunnel radius) and the block size is sufficiently large (>15 , see BSC 2004) (BSC 2003 and 2004; Rigby 2004). In this numerical analysis, since the Hydro-StoneTB[®] cubes tested in the actual tests were free from fractures and the smallest radius of the existing void (sizes) were extremely small compared to a actual tunnel radius, the first parameter mentioned in BSC (2003), size ratio between the models and the discrete blocks, has not been followed. Therefore, the minimum possible block size was considered; the model was subdivided into Voronoi blocks with average edge length of 3.5 mm (0.0035 m).

Regarding the micro-properties for the deformation calibration, the values shown in Table (5.1) were adopted considering the following:

- 1- The macro-elastic properties of the actual material used in the experimental tests were selected for the micro-elastic properties of the Voronoi blocks; $E^m = 16$ GPa

and $\nu^m = 0.28$. Rigby (2007) carried out several tests on the rock-like material, Hydro-StonTB[®] to find the macro-elastic properties. The tests were uniaxial compression tests on both cylindrical (50.8x101.6 mm) and cubic specimens (150 mm per side). Accordingly, the values $K^m = 12.1212$ GPa and $G^m = 6.25$ GPa were selected. The ratio of K^m/G^m is equal to 1.94.

- 2- According to the literature (BSC 2003 and 2004; Rigby 2004), it is desirable, from the perspective of convergence of the numerical model, to select a ratio of micro-joint stiffnesses (ratio of normal stiffness, k_n , to shear stiffness, k_s .) similar to the ratio of K^m/G^m . Accordingly, a value close to the ratio of K^m/G^m (1.94) was selected for the ratio of k_n/k_s (ratio of micro-joint stiffnesses); $k_n/k_s = 2$.
- 3- Finally, the appropriate macro deformability for the UDEC model was obtained by rescaling the elastic micro-joint stiffnesses; both normal stiffness, k_n , and shear stiffness, k_s .

5.6.3 Strength Calibration

Once the deformability calibration finished, the strength calibration was started by rescaling the plastic properties of the micro-joints (tensile strength, t^m , cohesion, c^m , and friction, ϕ^m) following these considerations:

- 1- According to the mechanical properties of materials, the macro tensile strength, t , is typically about 10 percent of the macro compressive strength; $t = 0.1 * 55 = 5.5$ MPa. In addition, Nott (2009) carried out several Brazilian tests on (101.6x50.8 mm) cylinders of Hydro-StoneTB[®], and found that the tensile strength of the Hydro-StoneTB[®] to be equal to 5.516 MPa (800 psi). Therefore, 5.516 MPa (about 10% of 55 MPa) was adopted as the macro tensile strength of the

numerical models. The micro-joint tensile strength, t^m , which gave the macro tensile strength, $t = 5.516$ MPa, was then obtained by rescaling the micro-joints in the UDEC models.

- 2- Since the micro-joint compressive strength is controlled by two parameters (c^m , and ϕ^m), the same macro compressive strength can be obtained by unlimited pairs of the compressive strength parameters. Accordingly, as shown in Appendix II, six pairs of the micro-joint compressive strength parameters were tested and one of them was selected basing on the failure mode; the micro-joint compressive strength parameters (c^m , and ϕ^m), which gave failure mode close to the experimental cube's failure mode was selected.
- 3- The common residual values for physical joints were selected for the UDEC models. According to Itasca's Theory and Background Manual (2011), usual residual values for tensile strength, t^m , cohesion, c^m , are zero for the cracks or joints at which failure has been occurred. For the friction angle (ϕ^m) of the micro-joints, the value started from 31° and softened in a brittle fashion to 11° after which no effect of residual angles was observed.
- 4- The full calibration for zero-porosity model was then achieved after simulating more than seventy models.

The numerical models simulated during the calibration processes to obtain the calibrated model are shown in Tables (II-A) and (II-B) in Appendix II. The stress-strain curves and failure mode for the calibrated model are also shown in Appendix II; Figure (II-A) and (II-B). The material properties for the calibrated model used as UDEC input data for Hydro-StoneTB[®] specimens are shown in Table (5.1).

Table (5.1) UDEC Input Data for Hydro-StoneTB[®] Specimens

Type	Description	Value	Units
Den	Density	1.7×10^{-3}	kg/m ³
K^m	Bulk Modulus	12.1212×10^9	Pa
G^m	Shear Modulus	6.25×10^9	Pa
jten, t^m	Tensile Strength of Micro-joints	16.072×10^6	Pa
jfric, ϕ^m	Friction Angle of Micro-joints	31	Degree
jcoh, C^m	Cohesion of Micro-joints	26.01735×10^6	Pa
resTen	Residual Tensile Strength of Micro-joints	0	Pa
resFric	Residual Friction Angle of Micro-joints	11	Degree
resCoh	Residual Cohesion of Micro-joints	0	Pa
k_n	Micro-joint Normal Stiffness	72728×10^9	Pa / m
k_s	Micro-joint Shear Stiffness	36364×10^{19}	Pa / m

5.6.4 Numerical Simulations for Porous Cubes

The UDEC model calibrated in the previous section was for solid, zero porosity samples at a uniaxial compressive strength of 55 MPa and a Young's modulus of 16 GPa. The porous samples can then be simulated through adding voids to the same calibrated solid model and test it under the same load condition as it was in the experimental tests. Accordingly, the 152.4 mm cubes tested in the Project Activity Task ORD-FY04-013 were simulated in UDEC under uniaxial compression loading as 152.4 mm squares with different void porosity, void shape, void size, and void distribution. The void sizes, void shapes, void spatial distributions, and void porosity were corresponding to those in the experimental tests.

5.7 Results and Discussions

Fifty five models, 52 squares with 152.4 mm per side, containing voids with different size, shape, distribution and uniformity were simulated in UDEC for this

numerical analysis. The simulated models and their corresponding stress-strain curves are shown in Appendix III. The peak value, ultimate strength, of the stress-strain curve was taken as the uniaxial compressive strength (*UCS*) each model. From the slope of a straight line drawn between 25% and 50% of the uniaxial compressive strength on the stress-strain curves, the secant Young's modulus (*E*) was obtained for each model. The results are also shown in tables and figures in this chapter.

For numerical models having void porosities ranging from 6% to 20%, regardless of the void size, void distribution, and void uniformity, the numerical results like the experimental results showed decreases in both *UCS* and *E* with increasing void porosity. However, there is relatively less scatter or overlap for the numerical results compared to the experimental ones. Accordingly, the coefficients of determination, R^2 , for both numerical *UCS* and *E* are higher than those for the experimental results.

5.7.1 Numerical Simulations for Models Containing Circular Holes

The results of *UCS* and *E* for the numerical models containing circular voids (both unisize and mixed) are plotted in Figures (5.2) to (5.18). The results are also shown in Tables (5.2) and (5.3). Basing on the numerical results, the following observations can be discussed:

- 1- For the void porosity ranging between 6% and 20%, regardless of the void size, void distribution, and void uniformity, the numerical results showed decreases in both *UCS* and *E* with increasing porosity. However, the coefficients of determination, R^2 , for Young's modulus are higher than those for the uniaxial compressive strength.

- 2- From Figures (5.2) and (5.3), regardless of the void size (large, medium, and small size voids), void distribution (patterns A, B, and C), and void uniformity (either unisize or mixed voids), the numerical models having similar porosity showed similar reduction in both UCS and E . The reductions followed exponential trends with higher coefficients of determination, R^2 , for E . The numerical results for UCS showed more scatterings than those for E .
- 3- Figures (5.4) to (5.11) show the relationships between UCS , and E with void porosity for models containing circular voids (either unisize voids or mixed voids) with different void distributions (void patterns). According to the figures, the numerical results showed similar reduction in both UCS and E with void porosity increasing. Accordingly, the different void distributions (patterns A, B, and C), did not show discernible effects on the mechanical properties of Hydro-StoneT^{B®}.
- 4- From Figures (5.12) and (5.13), after merging all the numerical results for the models containing circular voids (either unisize voids or mixed voids), the merged numerical results also showed exponential reductions with increasing porosity for both UCS and E . The relationship between both strength (UCS) and deformation (E) and void porosity can be represented best by equations as follows:

$$UCS(\text{MPa}) = 43.381 * e^{-0.045*(Porosity(\%))} \quad R^2 = 0.8595 \quad \dots (5.3)$$

$$E(\text{GPa}) = 16 * e^{-0.029*(Porosity(\%))} \quad R^2 = 0.9594 \quad \dots (5.4)$$

- 5- In order to check the validity of the ratio of void size to specimen size, all the numerical results for the models containing circular voids (either unisize voids or mixed voids) except the models containing large unisize circular voids are merged

and plotted as a function of void porosity in Figures (5.14) and (5.15). The merged numerical results similarly showed exponential decreases in both *UCS* and *E* with increasing void porosity. However, the coefficient of determinations, for both *UCS* and *E*, are slightly higher than those of all the numerical models including models containing large unisize circular voids. The relationship between both strength (*UCS*) and deformation (*E*) and void porosity can be represented best by exponential equations as follows:

$$UCS(\text{MPa}) = 43.992 * e^{-0.047*(Porosity(\%))} \quad R^2 = 0.8666 \quad \dots (5.5)$$

$$E(\text{GPa}) = 15.934 * e^{-0.028*(Porosity(\%))} \quad R^2 = 0.9868 \quad \dots (5.6)$$

This might be due to the ratio of the sample size (core diameter or cube length) to the inclusion size (grain or void diameter). According to ASTM D 45 43 (2001) and ISRM (1978), the ratio of the sample size (core diameter or cube length) should be at least six to ten times that of the inclusion size (grain or void diameter). For the Hydro-StoneTB[®] cubes, the ratio for the large voids (31.14 mm in diameter) is less than five (cube length is 15.24 mm).

- 6- The relationships between *UCS* and *E* are plotted in Figures (5.16) to (5.18). According to the figures, the uniaxial compressive strength increased with increasing deformation modulus (Young's modulus) following power trends. The merged results of numerical models containing both mixed and unisize voids except large unisize voids gave better correlation, and can be represented best by power equation as follows:

$$UCS(\text{MPa}) = 0.4249 * (E(\text{GPa}))^{1.678} \quad R^2 = 0.8943 \quad \dots (5.7)$$

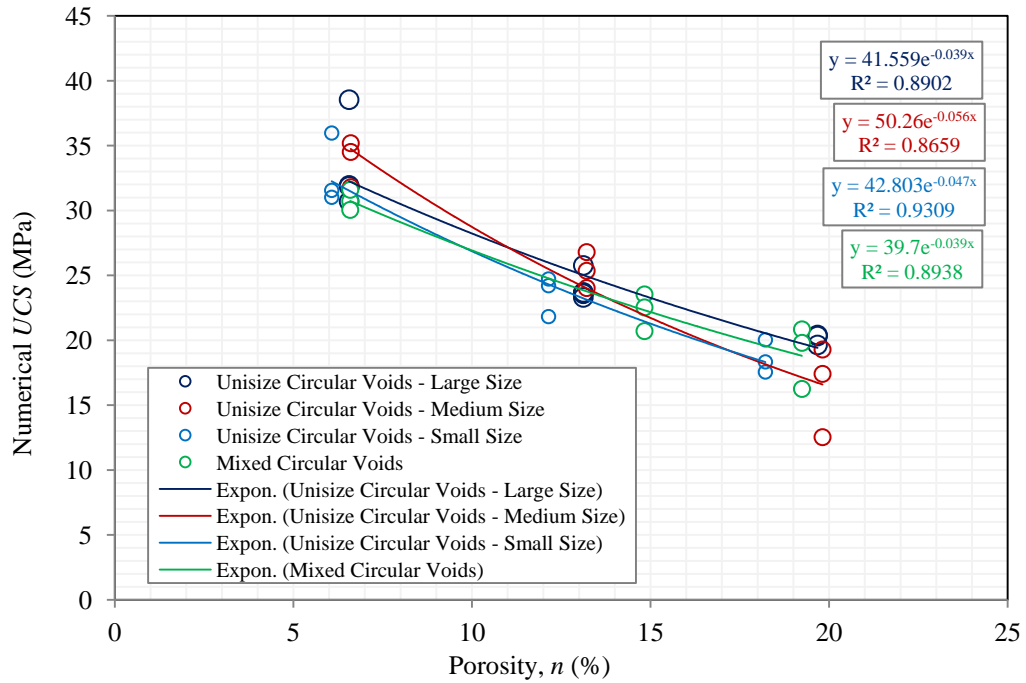


Figure (5.2) Compressive Strength versus Void Porosity for Numerical Models Containing Circular Voids – Both Unisize and Mixed Voids

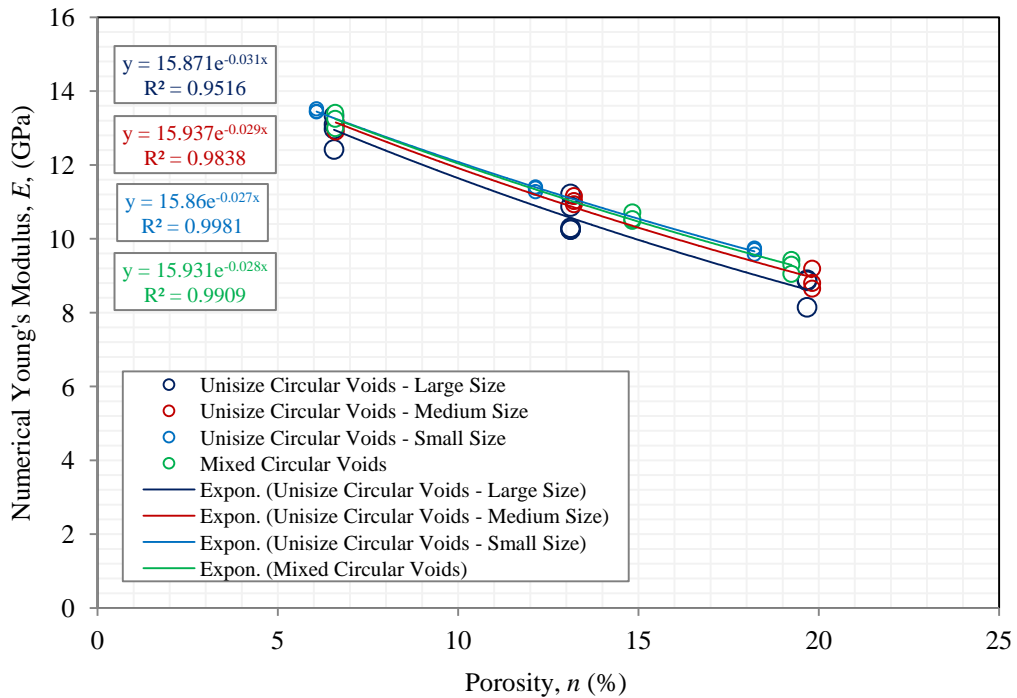


Figure (5.3) Deformation versus Void Porosity for Numerical Models Containing Circular Voids– Both Unisize and Mixed Voids

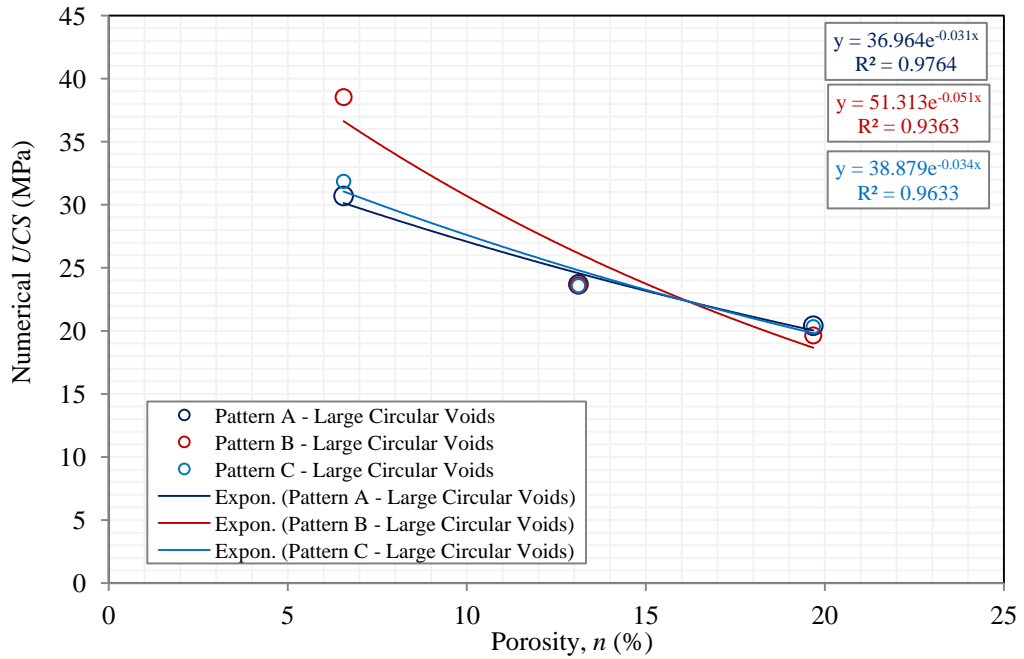


Figure (5.4) Compressive Strength versus Void Porosity for Numerical Models Containing Circular Voids – Large Unisize Voids

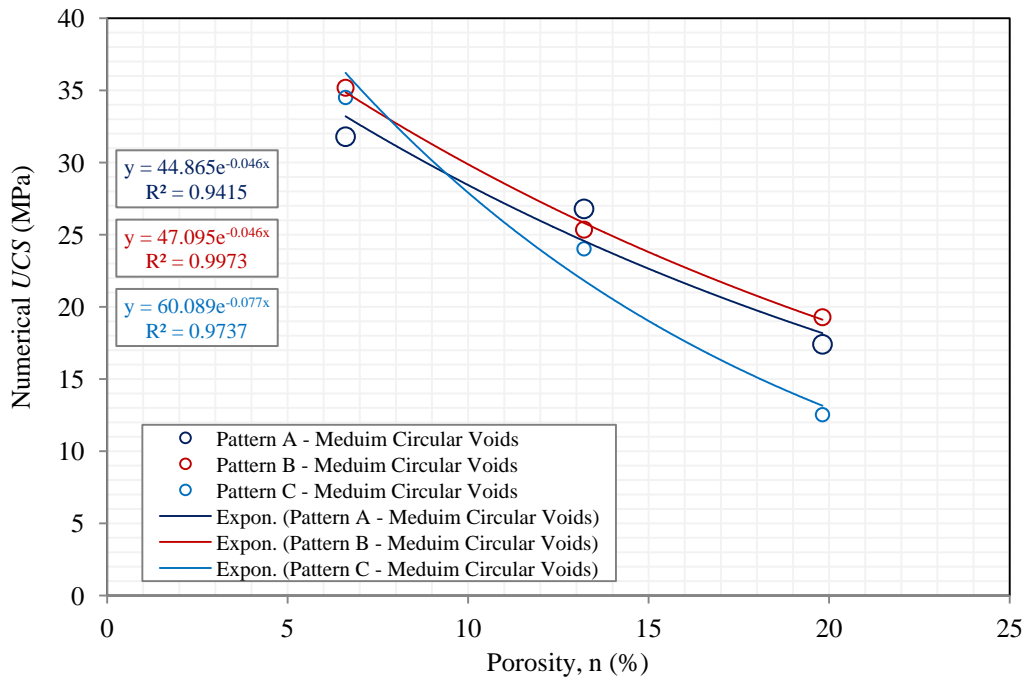


Figure (5.5) Compressive Strength versus Void Porosity for Numerical Models Containing Circular Voids – Medium Unisize Voids

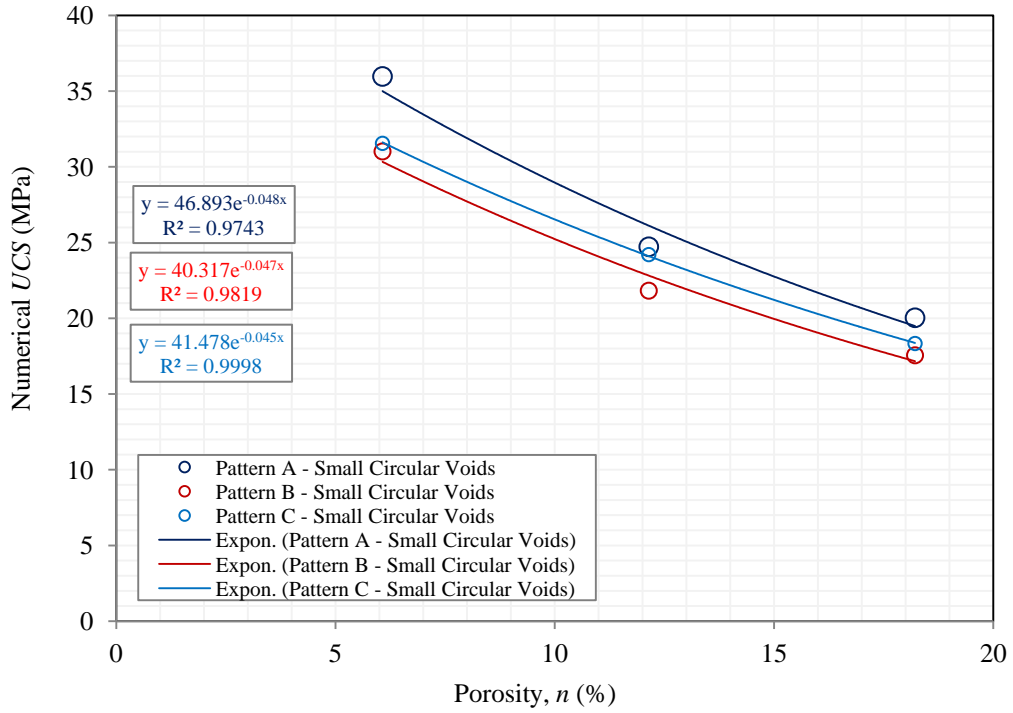


Figure (5.6) Compressive Strength versus Void Porosity for Numerical Models Containing Circular Voids – Small Unisize Voids

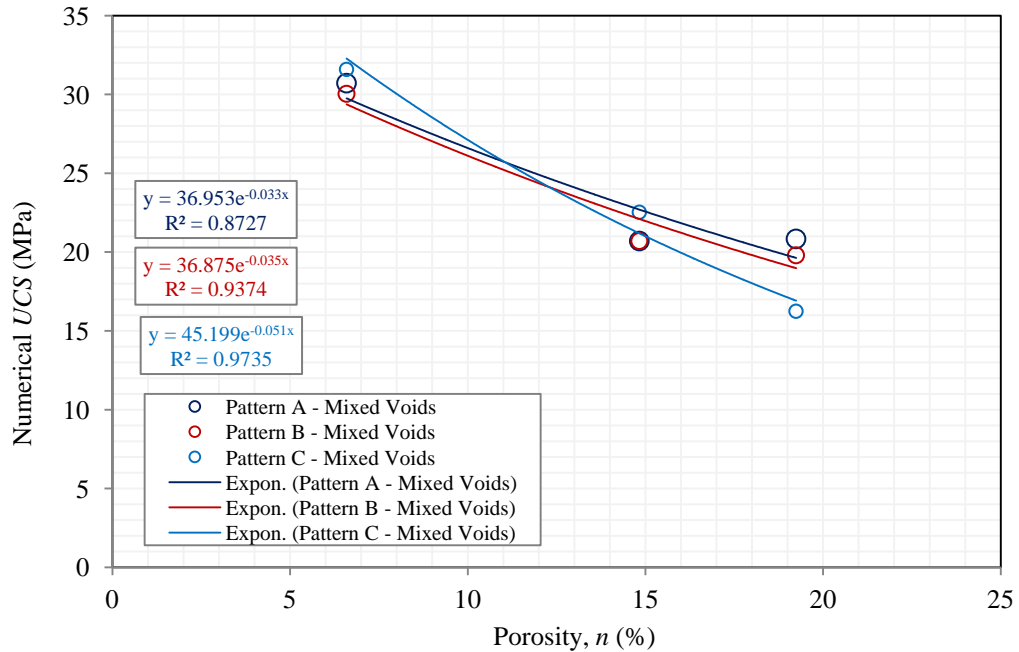


Figure (5.7) Compressive Strength versus Void Porosity for Numerical Models Containing Circular Voids – Mixed Voids

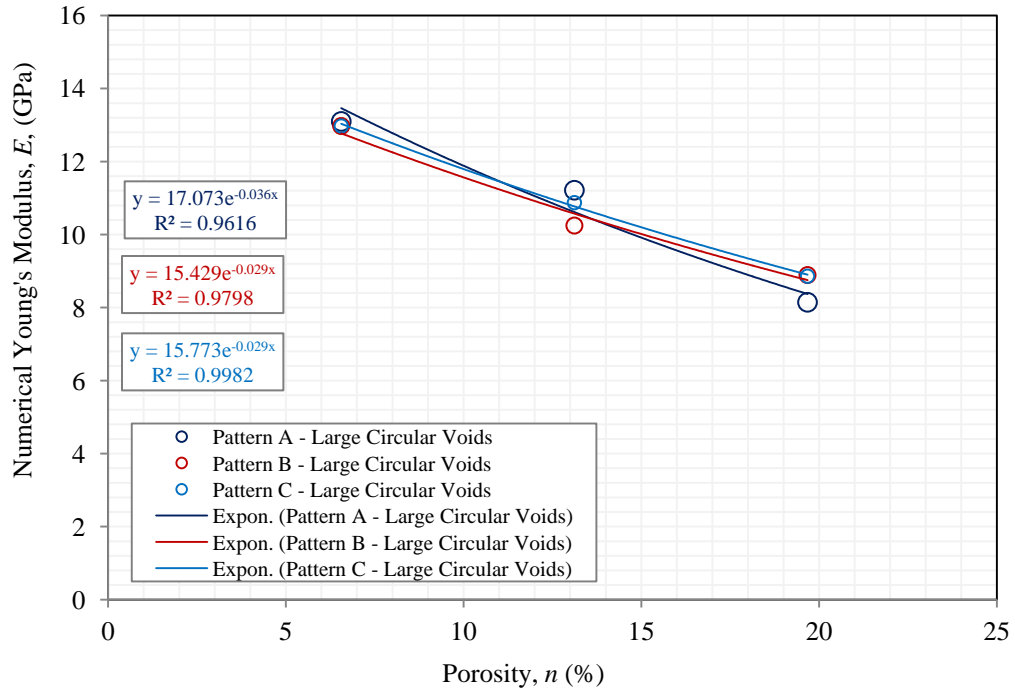


Figure (5.8) Deformation versus Void Porosity for Numerical Models Containing Circular Voids – Large Unisize Voids

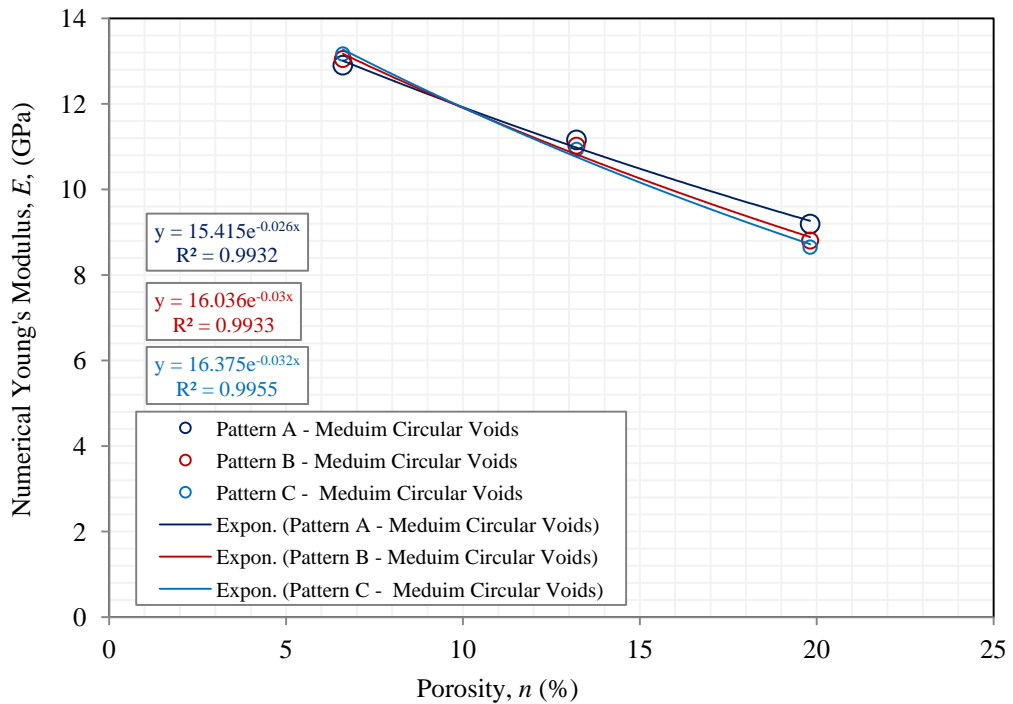


Figure (5.9) Deformation versus Void Porosity for Numerical Models Containing Circular Voids – Medium Unisize Voids

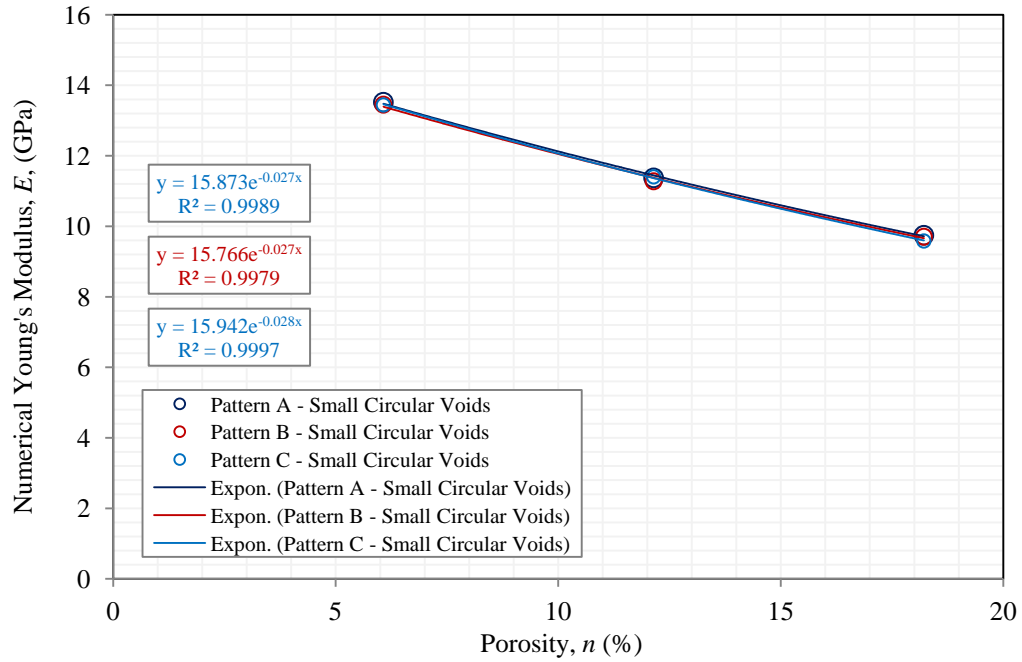


Figure (5.10) Deformation versus Void Porosity for Numerical Models Containing Circular Voids – Small Unisize Voids

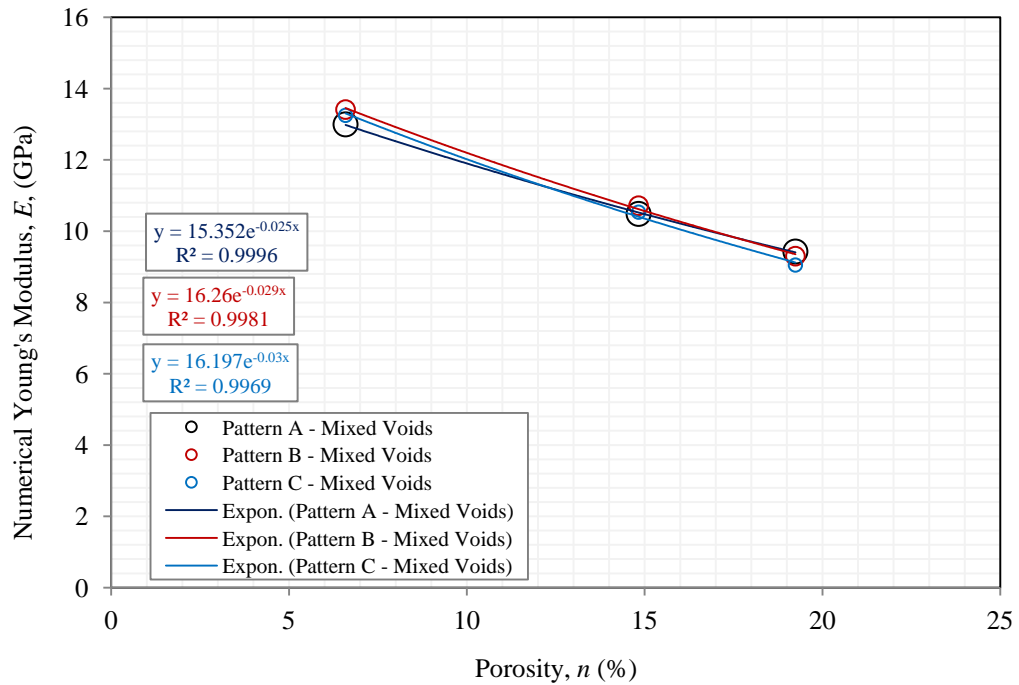


Figure (5.11) Deformation versus Void Porosity for Numerical Models Containing Circular Voids – Mixed Voids

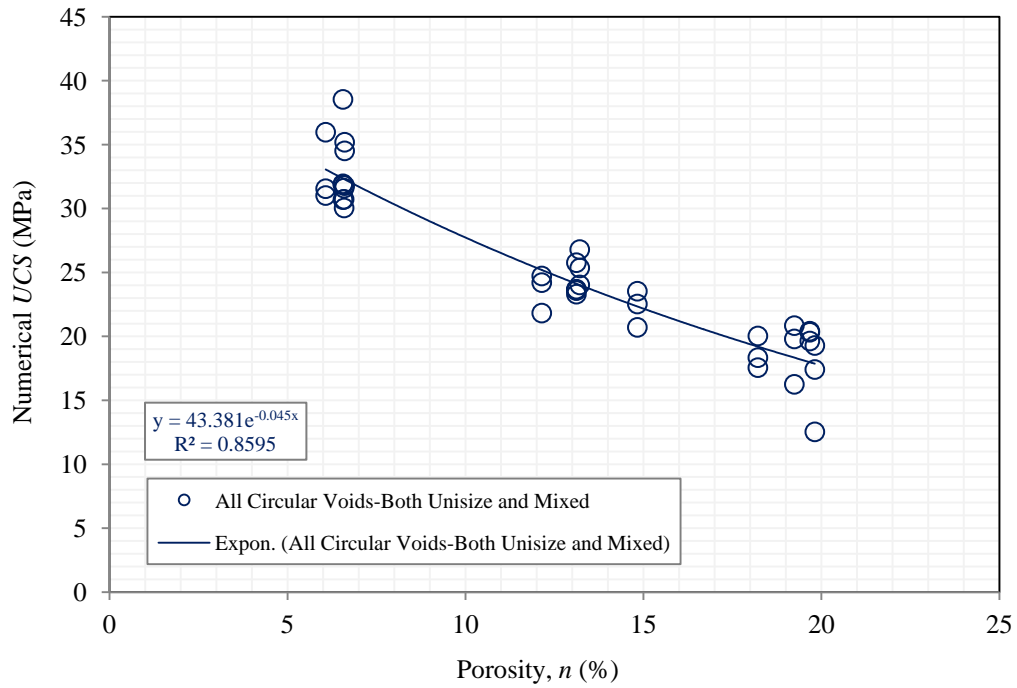


Figure (5.12) Compressive Strength versus Void Porosity for Numerical Models Containing Circular Voids – Both Unisize and Mixed Voids

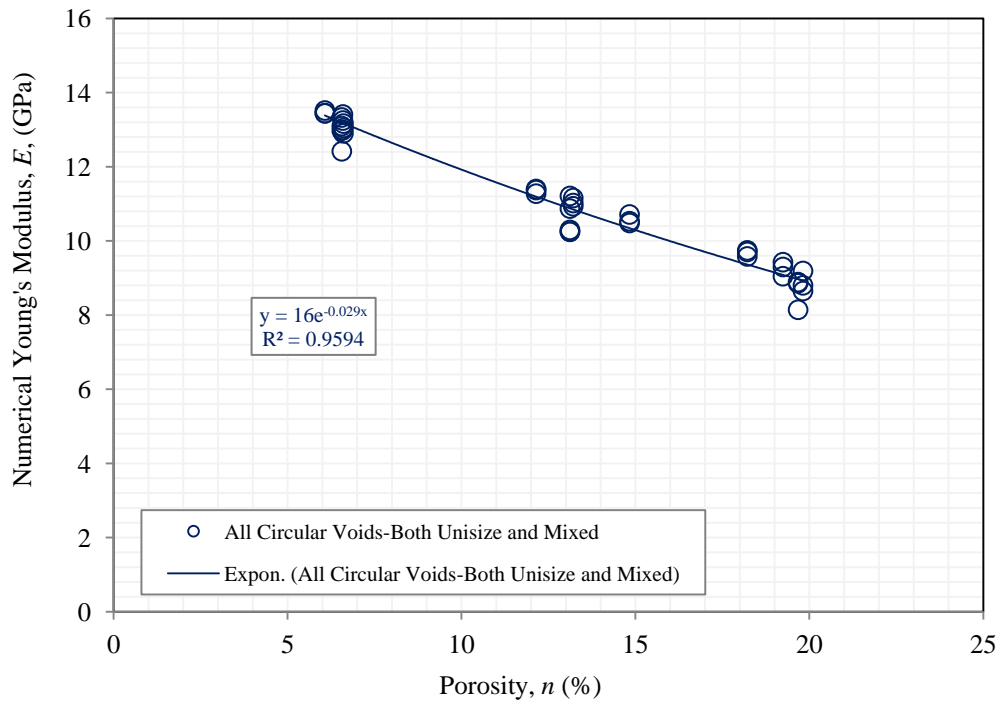


Figure (5.13) Deformation versus Void Porosity for Numerical Models Containing Circular Voids– Both Unisize and Mixed Voids

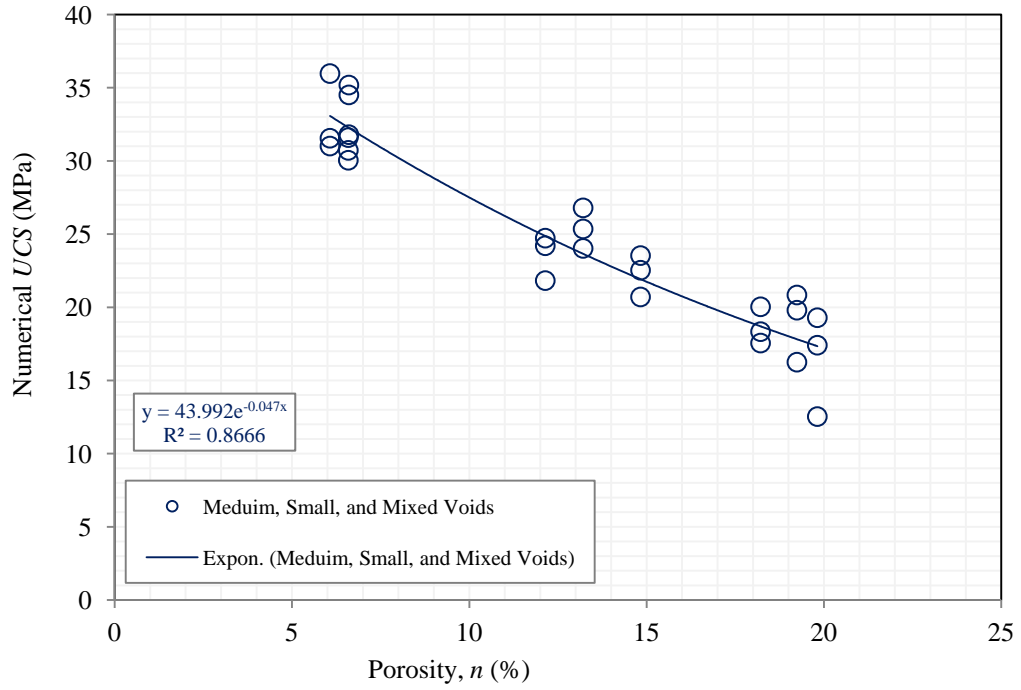


Figure (5.14) Compressive Strength versus Void Porosity for Numerical Models Containing Circular Voids– Some Unisize and All Mixed Voids

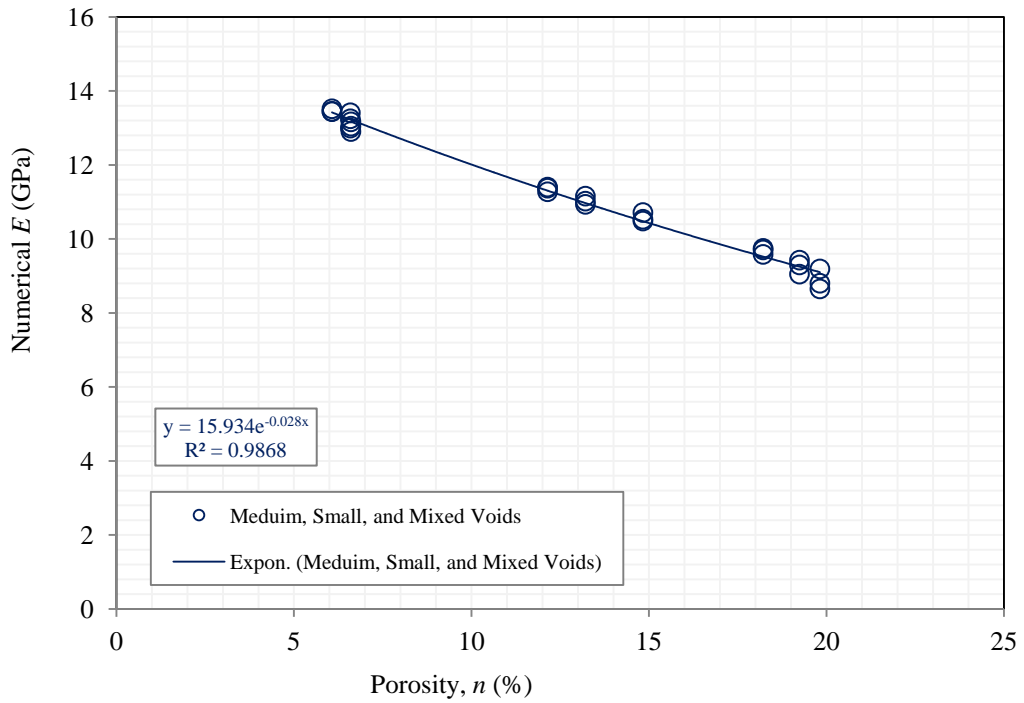


Figure (5.15) Deformation versus Void Porosity for Numerical Models Containing Circular Voids– Some Unisize and All Mixed Voids

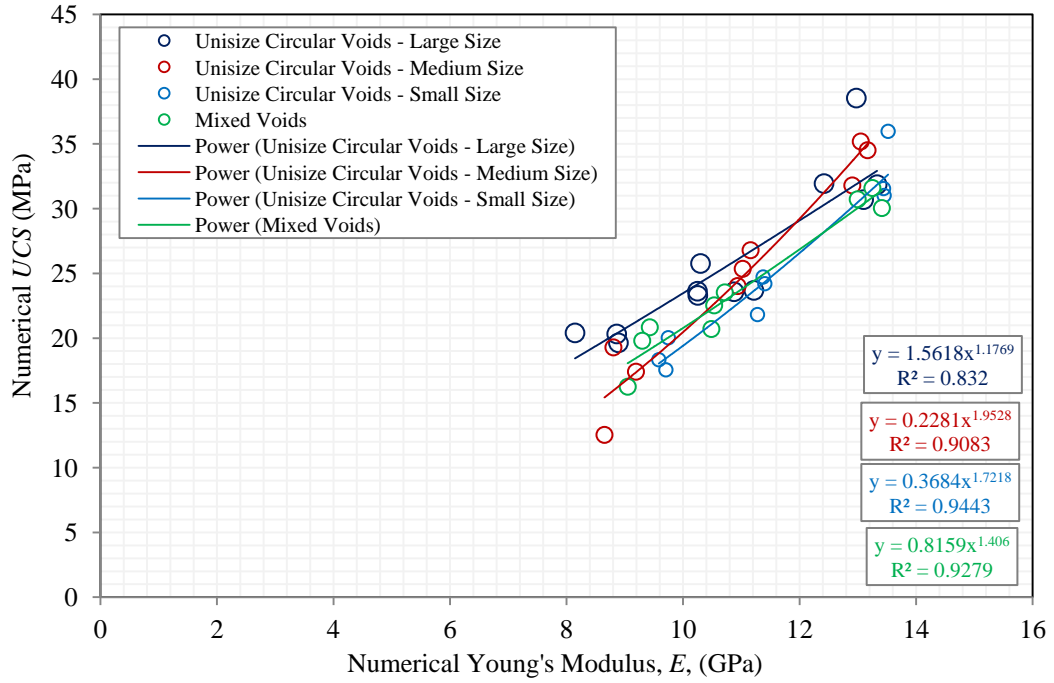


Figure (5.16) Compressive Strength versus Deformation for Numerical Models Containing Circular Voids

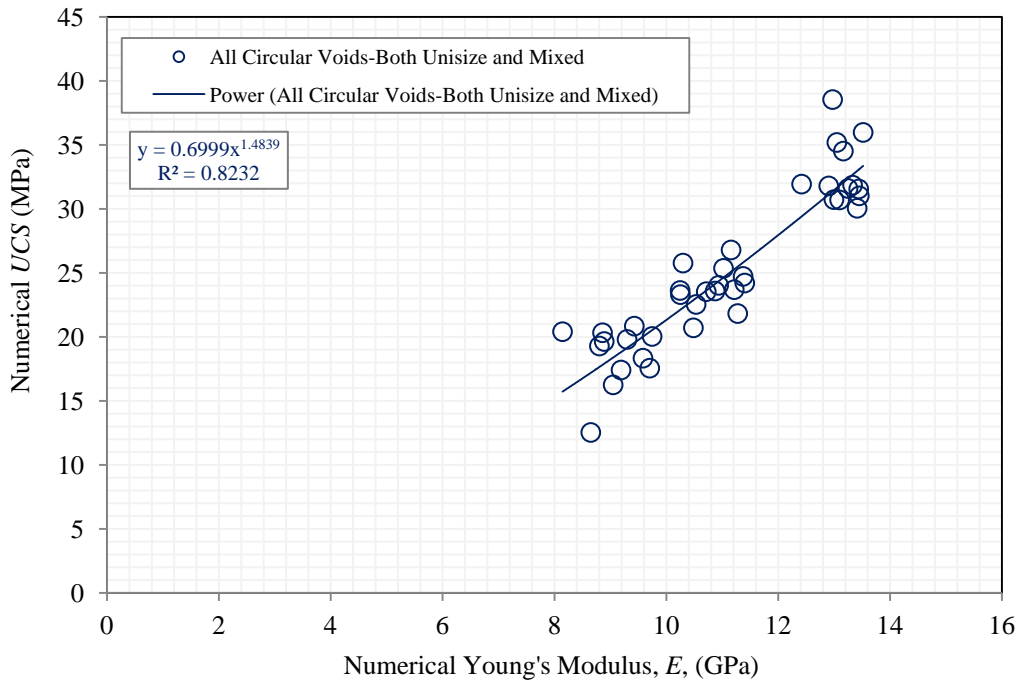


Figure (5.17) Compressive Strength versus Deformation for Numerical Models Containing Circular Voids – All Circular Voids

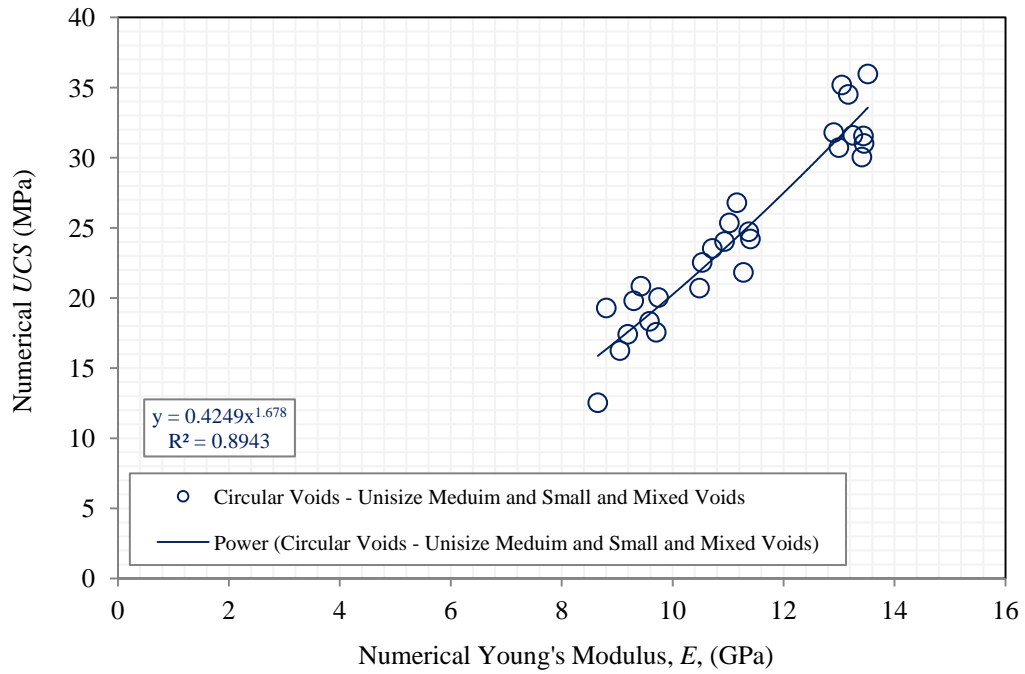


Figure (5.18) Compressive Strength versus Deformation for Numerical Models Containing Circular Voids – Some Unisize and All Mixed Voids

Table (5.2) Numerical Results for the Models Containing Circular Voids – Unisize Voids

Sample Name	Porosity (<i>n</i>)	Numerical <i>UCS</i>	Numerical <i>E</i> (25-50%)
	%	MPa	Gpa
PA-UCL2-1	6.56	30.695	13.099
PA-UCL2-2	6.56	31.934	12.419
PB-UCL2	6.56	38.537	12.973
PC-UCL2	6.56	31.852	13.331
PA-UCL4-1	13.12	23.689	11.215
PA-UCL4-2	13.12	23.301	10.252
PA-UCL4-3	13.12	25.765	10.299
PB-UCL4	13.12	23.623	10.247
PC-UCL4	13.12	23.583	10.874
PA-UCL6	19.68	20.406	8.145
PB-UCL6	19.68	19.638	8.890
PC-UCL6	19.68	20.323	8.860
PA-UCM4	6.61	31.792	12.904
PB-UCM4	6.61	35.185	13.049
PC-UCM4	6.61	34.512	13.166
PA-UCM8	13.21	26.791	11.158
PB-UCM8	13.21	25.354	11.023
PC-UCM8	13.21	24.024	10.936
PA-UCM12	19.82	17.409	9.191
PB-UCM12	19.82	19.287	8.804
PC-UCM12	19.82	12.533	8.650
PA-UCS11	6.07	35.969	13.519
PB-UCS11	6.07	31.017	13.450
PC-UCS11	6.07	31.552	13.440
PA-UCS22	12.14	24.724	11.373
PB-UCS22	12.14	21.823	11.276
PC-UCS22	12.14	24.205	11.403
PA-UCS33	18.22	20.033	9.746
PB-UCS33	18.22	17.555	9.704
PC-UCS33	18.22	18.335	9.583

Table (5.3) Numerical Results for the Models Containing Circular Voids – Mixed Voids

Sample Name	Porosity (<i>n</i>)	Numerical UCS	Numerical E (25-50%)
	%	MPa	Gpa
PA-UXCL1M1S3	6.59	30.721	12.997
PB-UXCL1M1S3	6.59	30.046	13.412
PC-UXCL1M1S3	6.59	31.594	13.249
PA-UXCL2M3S6	14.83	20.706	10.485
PB-UXCL2M3S6	14.83	23.533	10.715
PC-UXCL2M3S6	14.83	22.533	10.533
PA-UXCL2M5S8	19.24	20.840	9.428
PB-UXCL2M5S8	19.24	19.801	9.299
PC-UXCL2M5S8	19.24	16.250	9.050

5.7.2 Numerical Simulations for Models Containing Non-Circular Holes

The relationships between uniaxial strength, *UCS*, and deformation, *E*, for the numerical models containing non-circular voids (square and diamond voids) are plotted in Figures (5.19) to (5.31). The results are also shown in Table (5.4). According to the results, the following observations can be discussed:

- 1- The numerical results showed decreases in both *UCS* and *E* with increasing void porosity. The reductions followed exponential trend with high coefficients of determination, R^2 , for *E*.
- 2- From Figures (5.19) to (5.22), for models containing either square or diamond voids, regardless of the void size (large and medium size voids) and void distribution (patterns A and B), the numerical results for models having similar porosity showed similar linear reduction in both *UCS* and *E*. Hence, the used void size and void distributions did not show distinct effects on the mechanical properties of Hydro-StoneTB®.

- 3- From Figures (5.23) to (5.28), regardless of the void size (large and medium size voids), and void distribution (patterns A and B), the numerical models containing square voids showed slightly higher UCS and E compared to the numerical models containing diamond voids. This might due to smaller total width of solid columns, W , for the models containing diamond voids compared to those containing square voids. This may in turn lead to higher strength.
- 4- From Figures (5.25) and (5.28), after merging all the numerical results for the models containing non-circular voids (either square or diamond voids), the merged numerical results showed exponential reduction with increasing porosity for both UCS and E regardless of void size and void distribution. The relationship between both strength (UCS) and deformation (E) and void porosity can be represented best by the following equations:

$$\text{Square Voids ... } UCS_{(MPa)} = 46.758 * e^{-0.051*(Porosity(\%))} \quad R^2 = 0.8722 \quad \dots (5.8)$$

$$\text{Diamond Voids ... } UCS_{(MPa)} = 50.798 * e^{-0.072*(Porosity(\%))} \quad R^2 = 0.9359 \quad \dots (5.9)$$

$$\text{Square Voids ... } E_{(GPa)} = 16.46 * e^{-0.033*(Porosity(\%))} \quad R^2 = 0.9688 \quad \dots (5.10)$$

$$\text{Diamond Voids ... } E_{(GPa)} = 16.855 * e^{-0.036*(Porosity(\%))} \quad R^2 = 0.8984 \quad \dots (5.11)$$

- 5- The relationships between uniaxial compressive strength, UCS , and deformation, E , are plotted in Figures (5.29) to (5.31). According to the figures, the uniaxial compressive strength increases with increasing deformation modulus (Young's modulus). The relationships followed power trend and can be represented best by the following equations, from Figure (5.31):

$$\text{Square Voids ... } UCS_{(MPa)} = 0.7258(E(GPa))^{1.4811} \quad R^2 = 0.8379 \quad \dots (5.12)$$

$$\text{Diamond Voids ... } UCS_{(MPa)} = 0.3245 * (E(GPa))^{1.8063} \quad R^2 = 0.8618 \quad \dots (5.13)$$

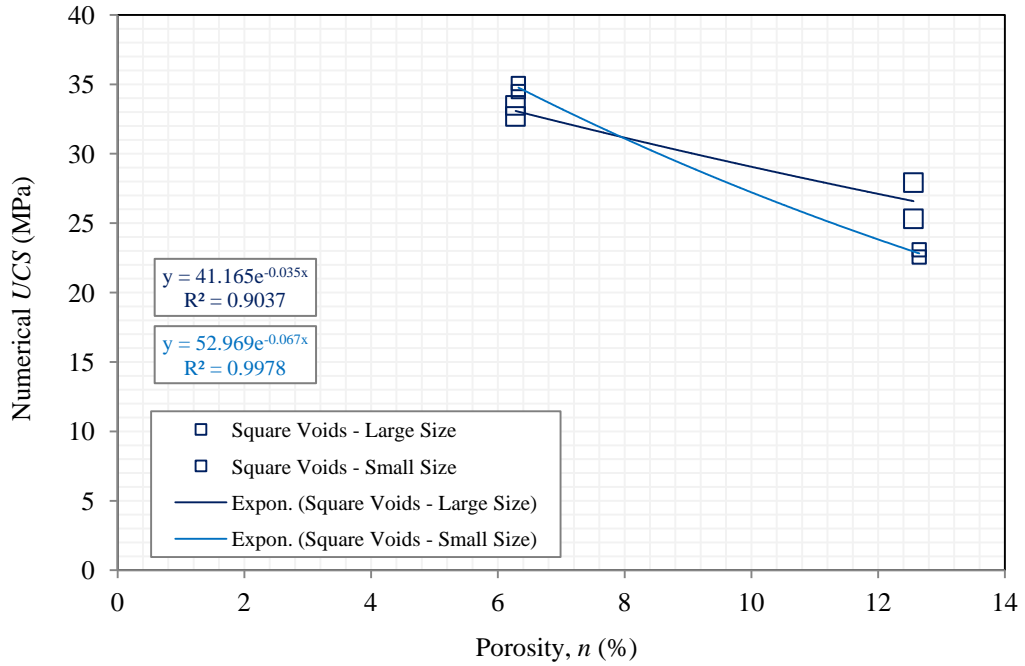


Figure (5.19) Compressive Strength versus Void Porosity for Numerical Models Containing Square Voids

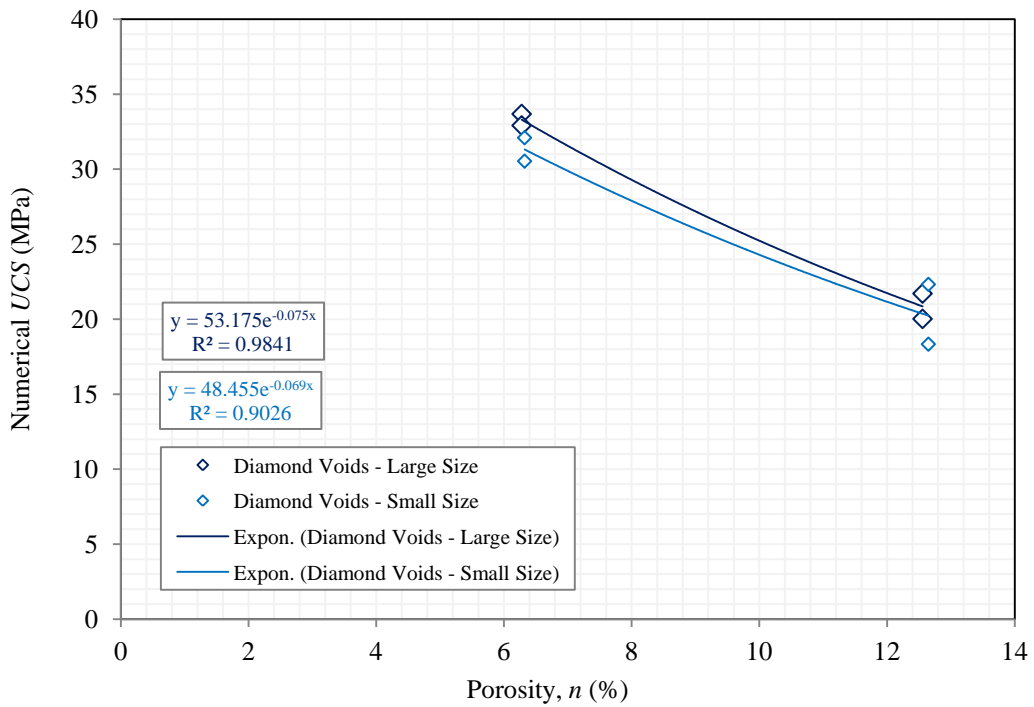


Figure (5.20) Compressive Strength versus Void Porosity for Numerical Models Containing Diamond Voids

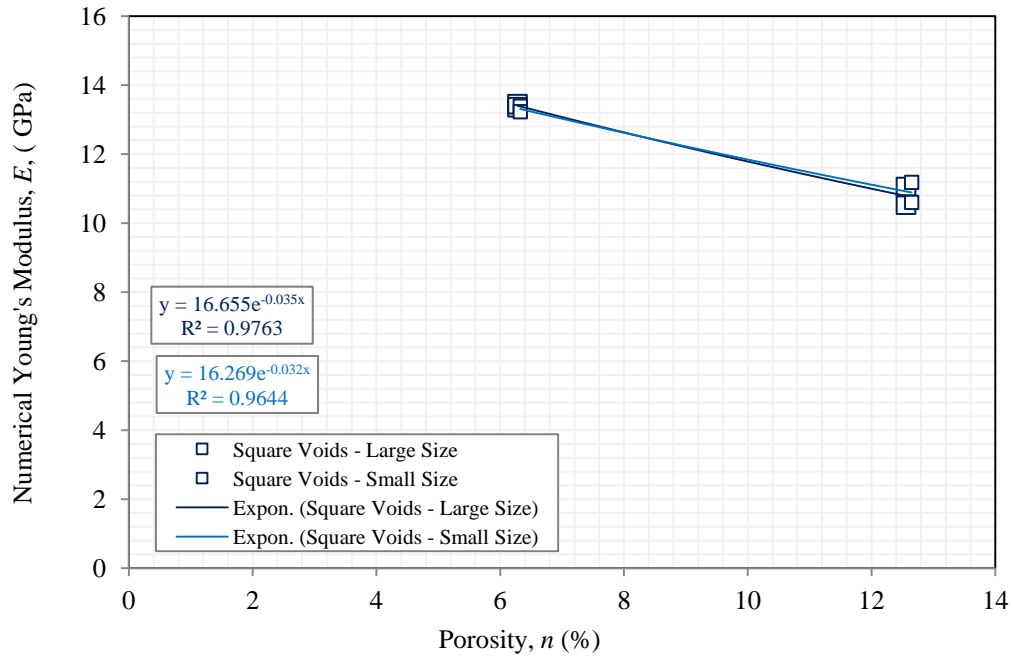


Figure (5.21) Deformation versus Void Porosity for Numerical Models Containing Square Voids

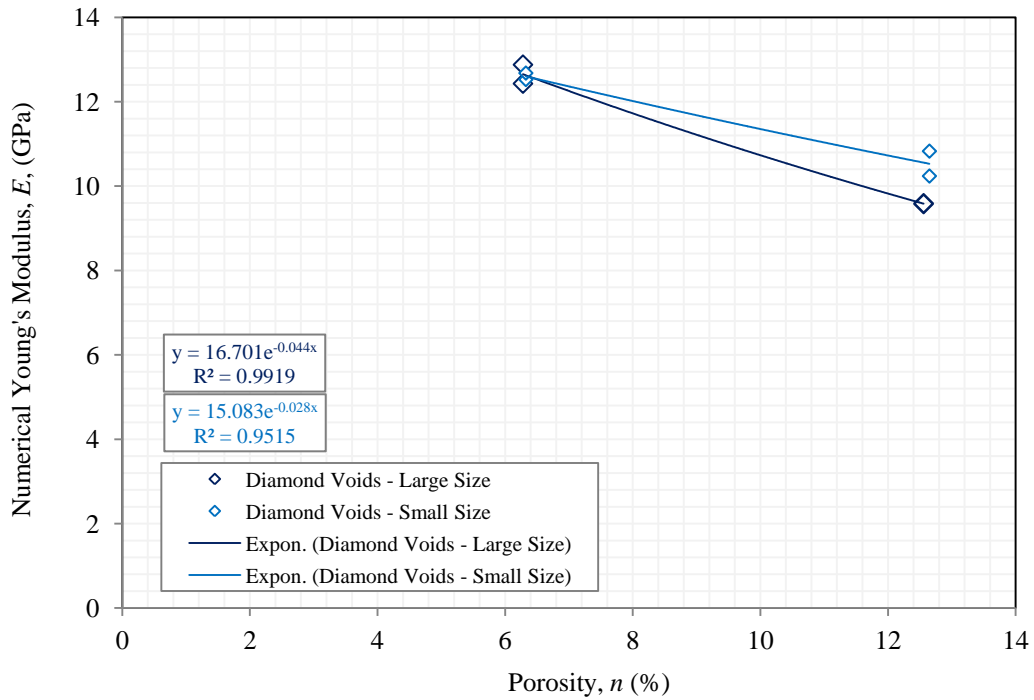


Figure (5.22) Deformation versus Void Porosity for Numerical Models Containing Diamond Voids

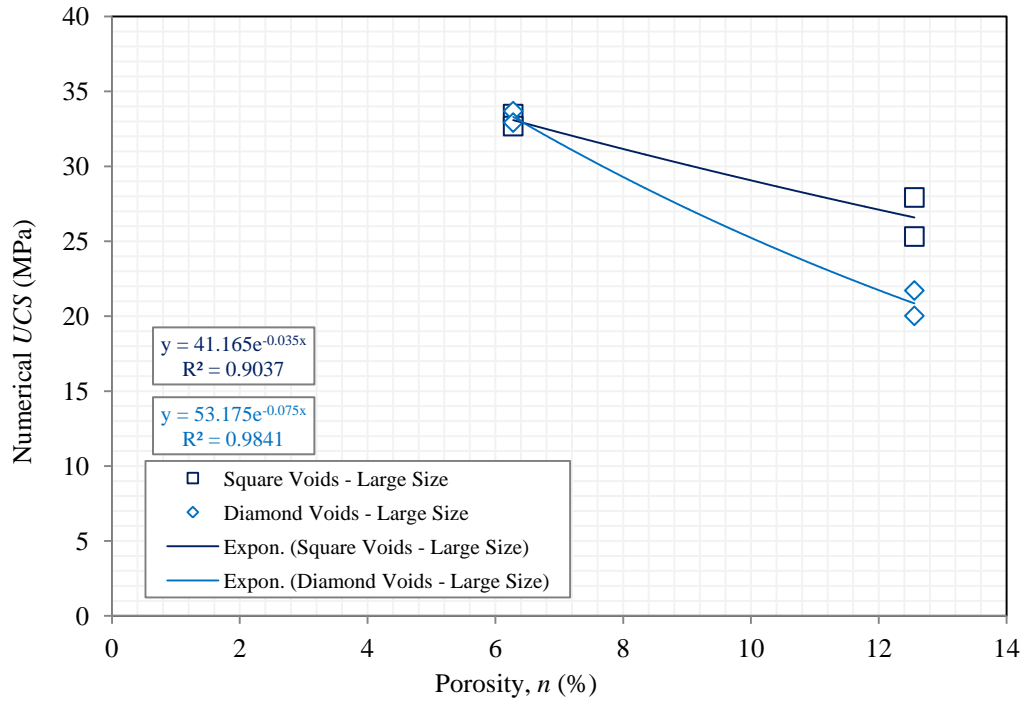


Figure (5.23) Compressive Strength versus Void Porosity for Numerical Models Containing Large Non-Circular Voids – Both Square and Diamond Voids

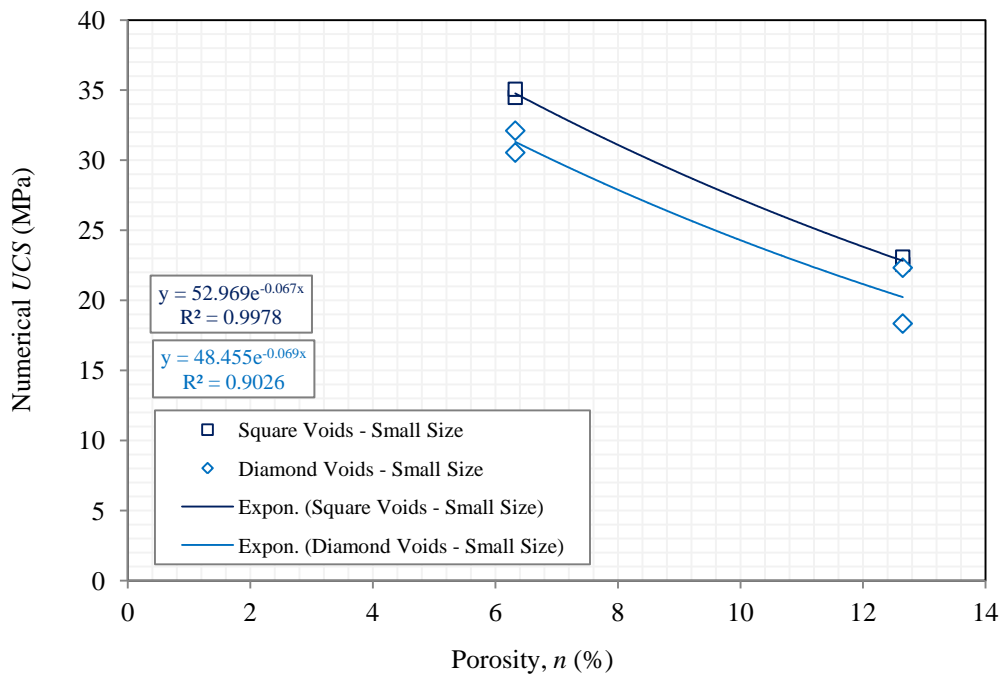


Figure (5.24) Compressive Strength versus Void Porosity for Numerical Models Containing Small Non-Circular Voids – Both Square and Diamond Voids

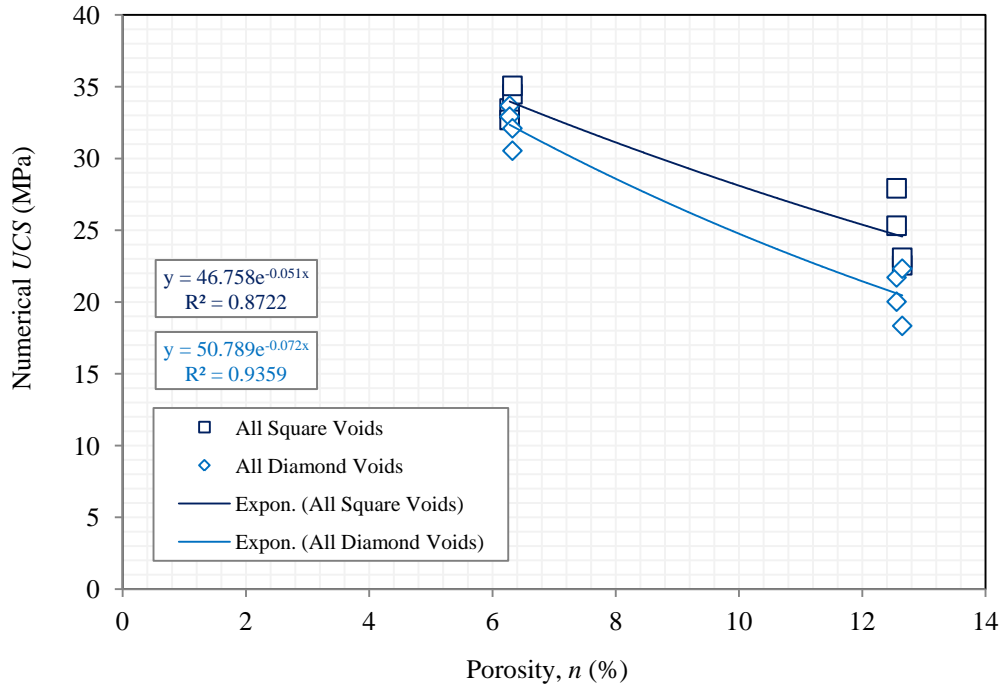


Figure (5.25) Compressive Strength versus Void Porosity for Numerical Models Containing Non-Circular Voids – Both Square and Diamond Voids

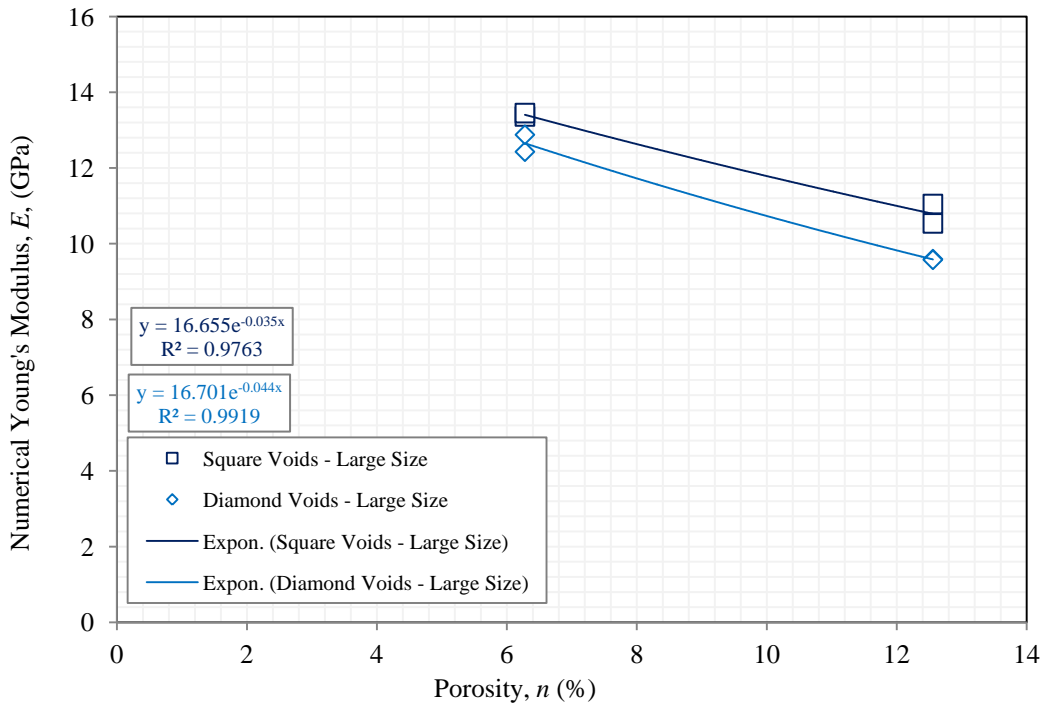


Figure (5.26) Deformation versus Void Porosity for Numerical Models Containing Large Non-Circular Voids – Both Square and Diamond Voids

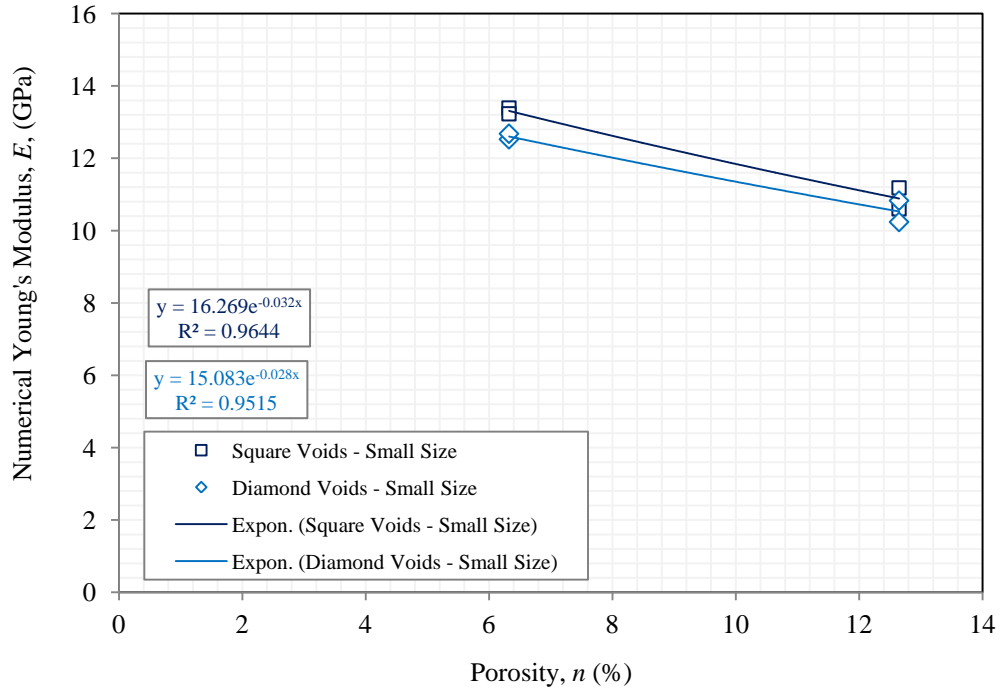


Figure (5.27) Deformation versus Void Porosity for Numerical Models Containing Small Non-Circular Voids – Both Square and Diamond Voids

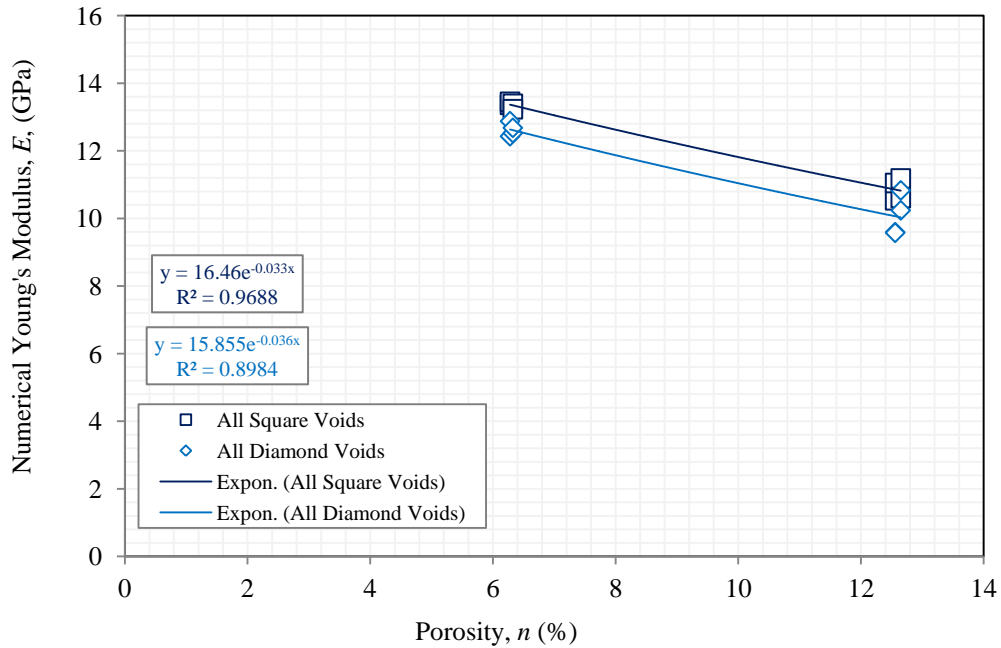


Figure (5.28) Deformation versus Void Porosity for Numerical Models Containing Non-Circular Voids – Both Square and Diamond Voids

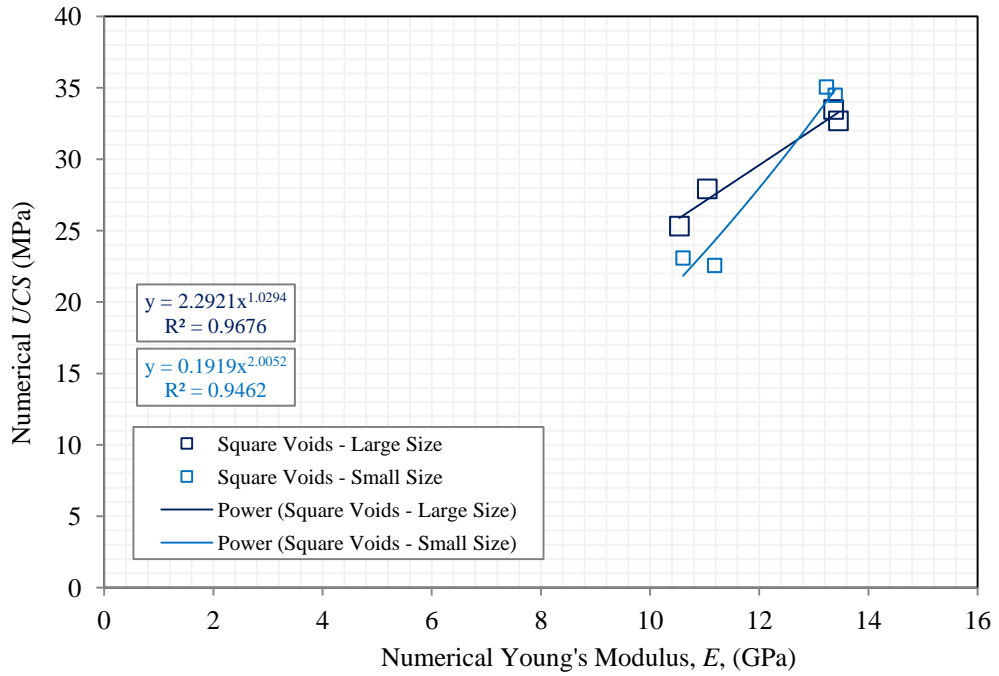


Figure (5.29) Compressive Strength versus Deformation for Numerical Models Containing Square Voids

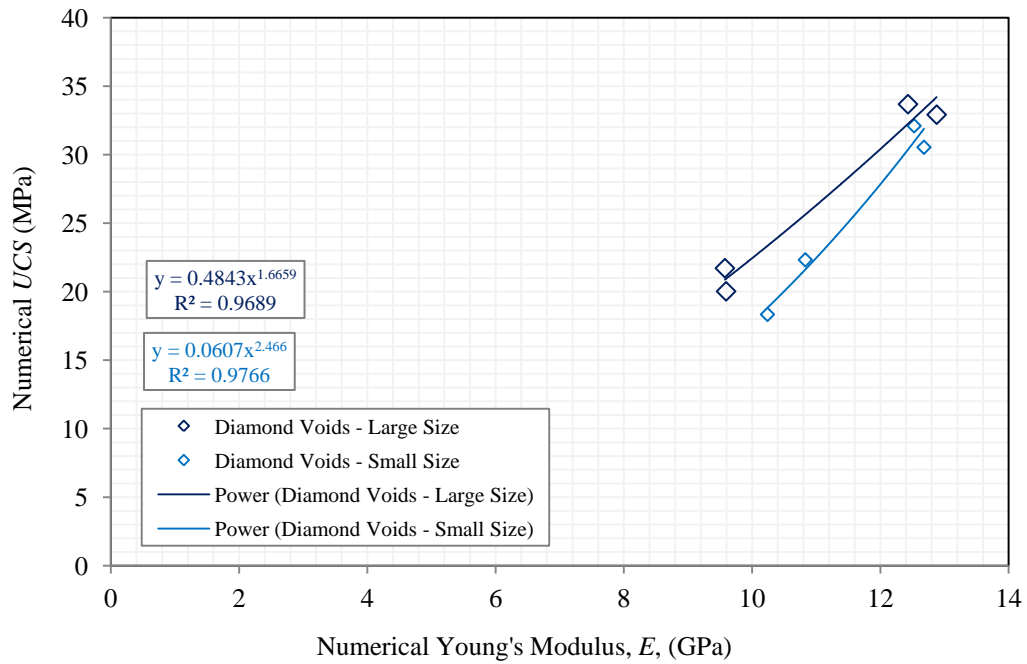


Figure (5.30) Compressive Strength versus Deformation for Numerical Models Containing Diamond Voids

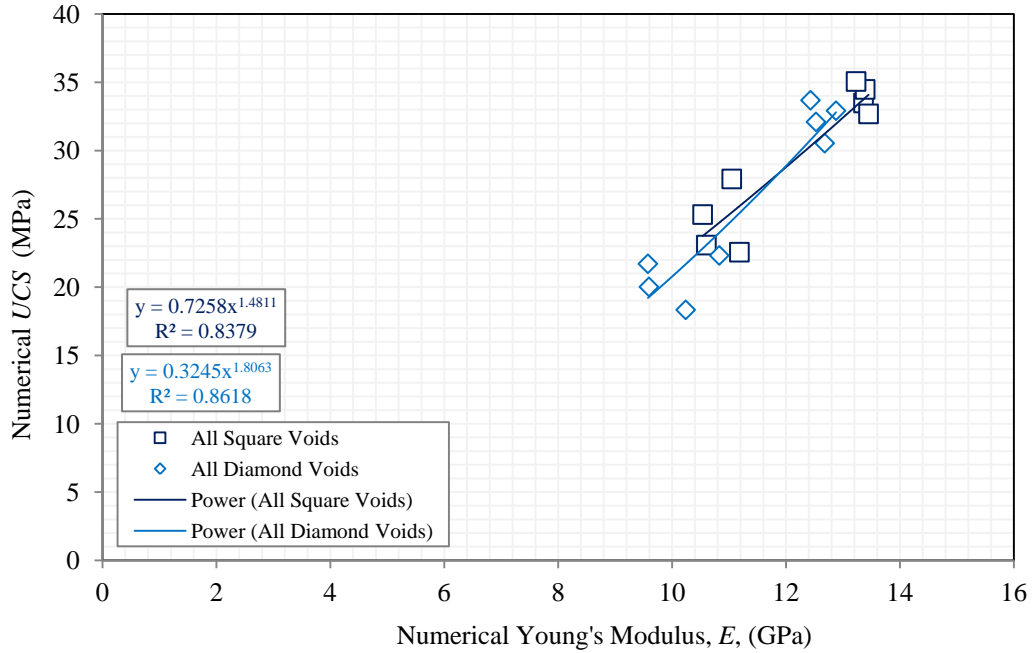


Figure (5.31) Compressive Strength versus Deformation for Numerical Models Containing Non-Circular Voids – Both Square and Diamond Voids

Table (5.4) Numerical Results for the Models Containing Non-Circular Voids – Square and Diamond Voids

Sample Name	Porosity (<i>n</i>)	Numerical UCS	Numerical <i>E</i> (25-50%)
	%	MPa	GPa
PA-USqL3	6.28	33.484	13.361
PB-USqL3	6.28	32.685	13.449
PA-USqL6	12.56	25.315	10.536
PB-USqL6	12.56	27.922	11.047
PA-USqM6	6.32	34.478	13.390
PB-USqM6	6.32	35.058	13.230
PA-USqM12	12.65	22.562	11.182
PB-USqM12	12.65	23.081	10.602
PA-UDmL3	6.28	33.683	12.430
PB-UDmL3	6.28	32.919	12.878
PA-UDmL6	12.56	20.024	9.593
PB-UDmL6	12.56	21.713	9.575
PA-UDmM6	6.32	32.102	12.526
PB-UDmM6	6.32	30.540	12.679
PA-UDmM12	12.65	18.338	10.239
PB-UDmM12	12.65	22.323	10.829

5.7.3 Numerical Simulations for All Experimental Tests – All Cubes

The numerical results for the models containing voids with different size (large, medium, and small), shape (circular, square, and diamond), distributions (pattern A, B, and C), and uniformity (unysize and mixed voids) are merged and plotted in Figures (5.32) to (5.37). According to the merged results, the following observations can be discussed:

- 1- From Figures (5.32) and (5.33), the numerical results showed decrease in both UCS and E with increasing void porosity. The relationship between both strength (UCS) and deformation (E) and void porosity can be represented best by power equations as follows:

$$UCS(\text{MPa}) = 85.092 * ((\text{Porosity}(\%))^{-1})^{0.511} \quad R^2 = 0.8432 \quad \dots (5.14)$$

$$E(\text{GPa}) = 23.732 * ((\text{Porosity}(\%))^{-1})^{0.3174} \quad R^2 = 0.9139 \quad \dots (5.15)$$

- 2- The relationships between UCS and E are plotted in Figures (5.34) and (5.35). According to the figures, the uniaxial compressive strength increased with increasing Young's modulus following power trend. For the merged results of numerical models containing both mixed and unysize voids except large unysize circular voids, the relationship between UCS and E can be represented best by power equation as follows:

$$UCS(\text{MPa}) = 40.65 * (E(\text{GPa}))^{1.7029} \quad R^2 = 0.8845 \quad \dots (5.16)$$

- 3- From Figures (5.2) and (5.32), the numerical strength results (numerical UCS) followed the same trends of the experimental strength results. However, the data scattering reduced and the coefficients of determination increased; the value of R^2 increased from 0.729 to 0.843. In addition, the percentages of the maximum

differences in *UCS* values reduced to 25.4%, 40%, and 62.8% for void porosities 6.5%, 12.6% and 19.6% respectively; the differences reduced by more than half. Accordingly, up to half of the differences in the experimental *UCS* values can be attributed to the uncertainties existing in the experimental uniaxial tests.

- 4- Similarly, from Figures (5.3) and (5.33), the numerical deformation results (numerical *E*) followed the same trends of the experimental deformation results. However, the data scattering tremendously reduced and the coefficients of determination increased very much; the value of R^2 increased from 0.5364 to 0.914. In addition, the percentages of the maximum differences in *E* values reduced to 8.1%, 16.7%, and 12.9% for void porosities 6.5%, 12.6% and 19.6% respectively; the differences reduced by more than half for void porosity equal to and greater than 12.6%, while for void porosities of 6.5%, the differences reduced by about 85%. This might be due to the efficiency of the strain measurement in the numerical simulation which in turn means that the method used to measure strains in the experimental tests were not adequate. Therefore, great care must be taken regarding strain measurement for uniaxial compression tests.
- 5- From the stress- strain curves shown in Appendix (II), the axial-stress-axial-strain curve for solid model is composed of a peak stress followed by a very sharp descending portion as suggested by Sammis and Ashby (1986), see Figure (II.1). However, the sharpness was reduced in the porous models regardless of void porosity, void orientation, and void special distribution, see the axial-stress-axial-strain curve in Appendix (III). Accordingly, the existence of voids could reduce the brittleness of rock-like materials.

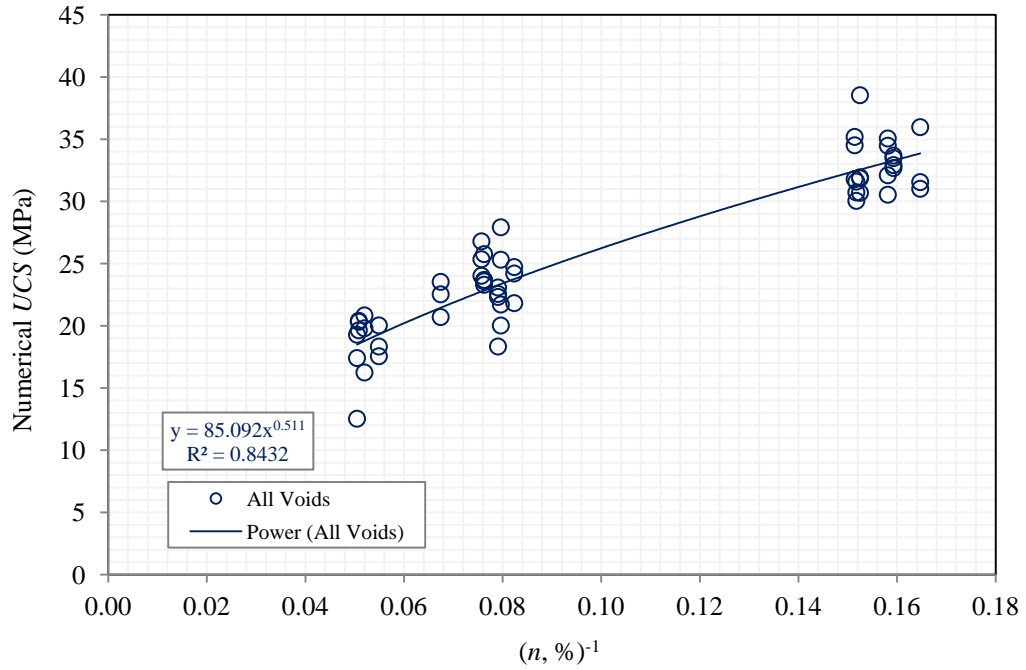


Figure (5.32) Compressive Strength versus Void Porosity for Numerical Models with Voids Having Different Size, Shape and Distribution

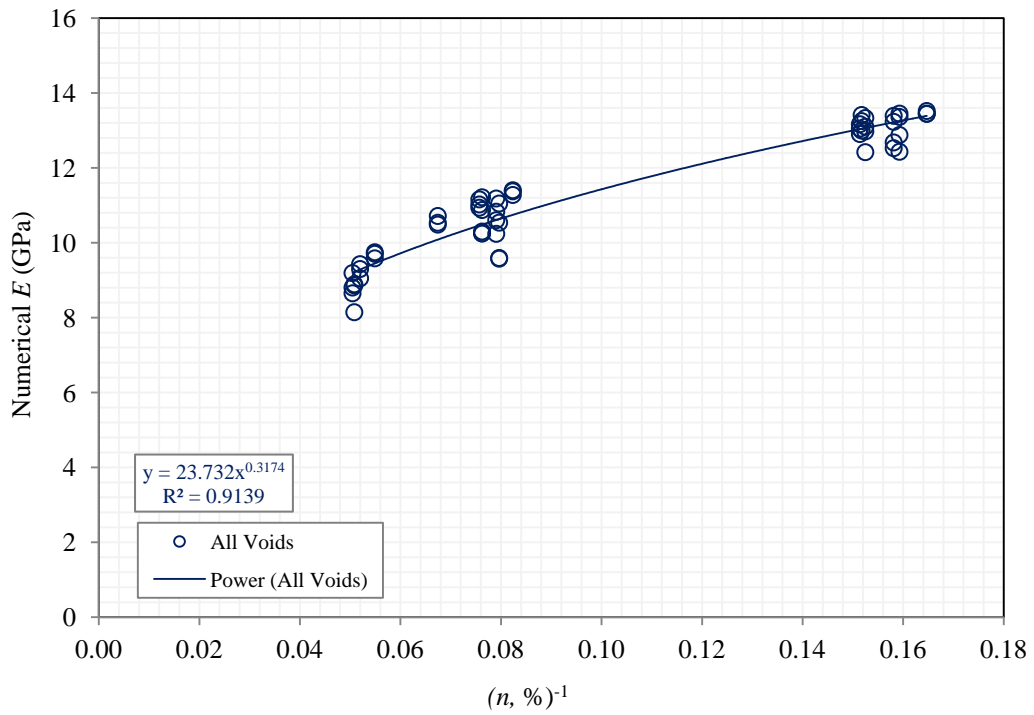


Figure (5.33) Deformation versus Void Porosity for Numerical Models with Voids Having Different Size, Shape and Distribution

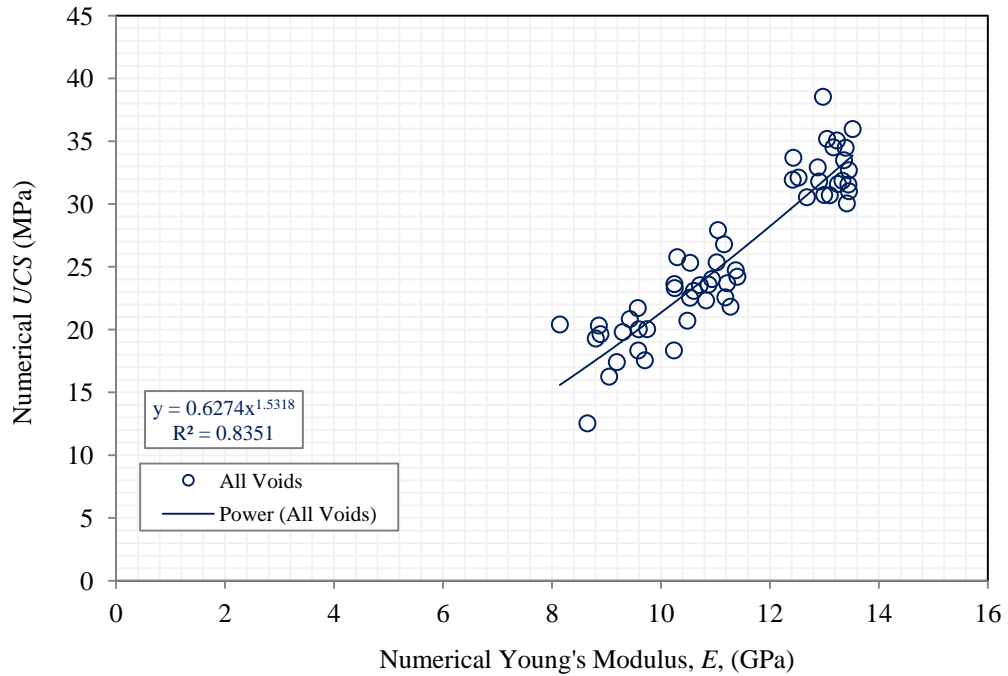


Figure (5.34) Compressive Strength versus Deformation for Numerical Models with Voids Having Different Size, Shape and Distribution

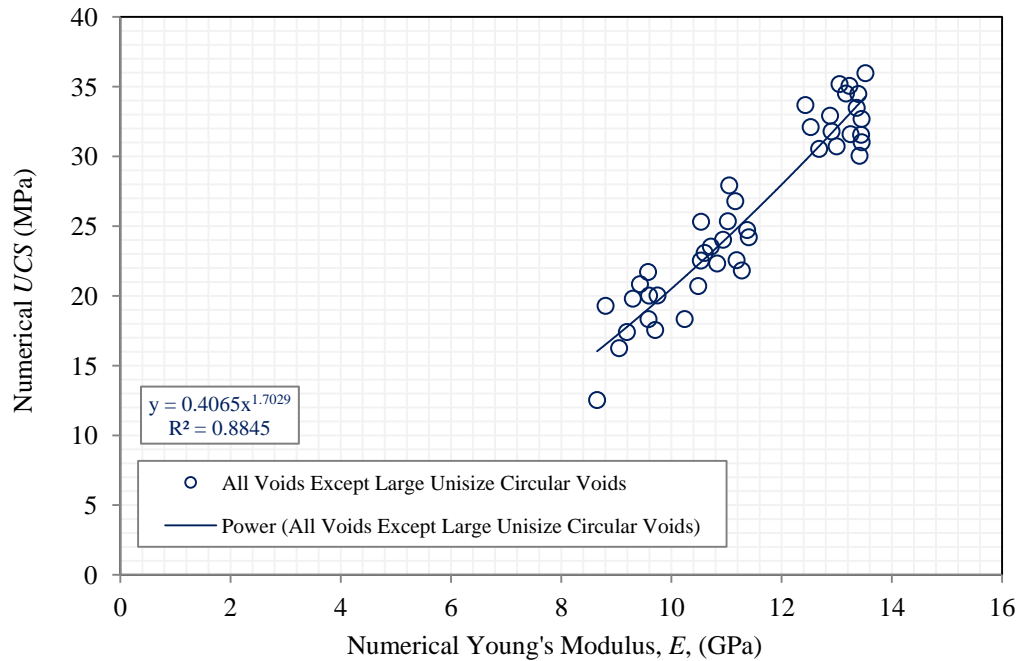


Figure (5.35) Compressive Strength versus Deformation for Numerical Models with Voids Having Different Size, Shape and Distribution

5.8 Numerical versus Experimental Results

In order to provide an understanding of the future usage and accuracy of UDEC as a modeling tool for porous materials, it will be helpful and useful to compare the result sets from both numerical and experimental analyses. Accordingly, the results of uniaxial compressive strength and Young's modulus for both numerical and experimental analyses are plotted as a function of void porosity in Figures (5.36) to (5.66). The results are also shown in Tables (5.5) to (5.12). According to the results, the following observations can be discussed:

- 1- From Figures (5.36) to (5.62), regardless of void geometry, the numerically calculated values of both UCS and E showed similar trends (logarithmic trend) to those obtained from the experimental compression tests on the Hydro-StoneTB[®] cubes. However, from Figures (5.60) and (5.61), the coefficients of determination for numerical results are much higher than those of the experimental results; for UCS , the R^2 increased from = 0.7577 to 0.8733, and for E , the R^2 increased from = 0.524 to 0.9292. Accordingly, it can be concluded that validation of the UDEC was successful.
- 2- In addition, the numerical relationship trend (power trend) between UCS and E , as shown in Figure (5.62), shows better correlation compared to the experimental relationship trend. From the figures, the coefficient of determination ($R^2 = 0.8351$) for numerical results is much higher than the one of the experimental results ($R^2 = 0.5041$).
- 3- As seen from the figures and tables, the numerically calculated values of both uniaxial compressive strength and Young's modulus overestimated the values

of experimental tests. The differences are attributed to either modeling a three-dimensional medium in two dimensions plane strain, or inability to model the friction between the steel platen and the Hydro-StoneTB[®] surfaces (top and bottom faces), or both (Avar 2002).

- 4- The overestimations are higher for uniaxial compressive strength compared to those of the deformation. The ratios of the numerical results to the experimental results ranged between 1.16 to 2.26 and 1.004 to 1.44 for uniaxial compressive strength and Young's modulus respectively; see Tables (5.6) and (5.8). Furthermore, the average of ratios of experimental values to numerical values for uniaxial compressive strength (1.642) is higher than those for Young's modulus (1.192).
- 5- As shown in Figures (5.36) to (5.38) and Table (5.11), the overestimations for models containing unisize circular voids increase with void size increasing. The average of ratios of experimental uniaxial strength to numerical uniaxial strength for models containing large voids (1.799) is higher than those of models containing medium voids (1.652) or small voids (1.462). However, as shown in Figures (5.41) to (5.43) and Table (5.12), the overestimations of deformation for models containing unisize circular voids did not show discernible differences. The dependence of the deformation overestimations on the void size is small. However, the average of ratios of experimental uniaxial strength to numerical uniaxial strength for models containing square voids (1.216) is higher than those of models containing diamond voids (1.084) or small voids (1.20).

- 6- The effect of void size on the overestimation is also true for the models containing non-circular voids, see Figures (5.46) to (5.51). For models containing square voids, from Table (5.11), the average of ratios of experimental uniaxial strength to numerical uniaxial strength for models containing large voids (1.428) is higher than those of models containing medium voids (1.343). For models containing diamond voids, from Table (5.11), the average of ratios of experimental uniaxial strength to numerical uniaxial strength for models containing large voids (1.823) is higher than those of models containing medium voids (1.503). Similarly, the dependence of the deformation overestimations on the void size is small as shown in Figures (5.54) to (5.57) and Table (5.12).
- 7- As shown in Figures (5.63) to (5.66), the dependency of the overestimations (the differences between the experimental and experimental values for both strength and deformation) on void porosity is very small. The ratio of the numerical deformation to the experimental deformation did not give any relationship with void porosity (see Figures (5.65) and (5.66)) while the values of the uniaxial compressive strength gave a very poor correlation (see Figures (5.63) and (5.64)).
- 8- Finally, from the numerical results shown in the figures and tables, it can be concluded that the experimental tests have been carried out with great cares and attentions; the standard procedures for the cube sampling, cube testing, and measuring of stress and strain values were followed with great cares and attentions.

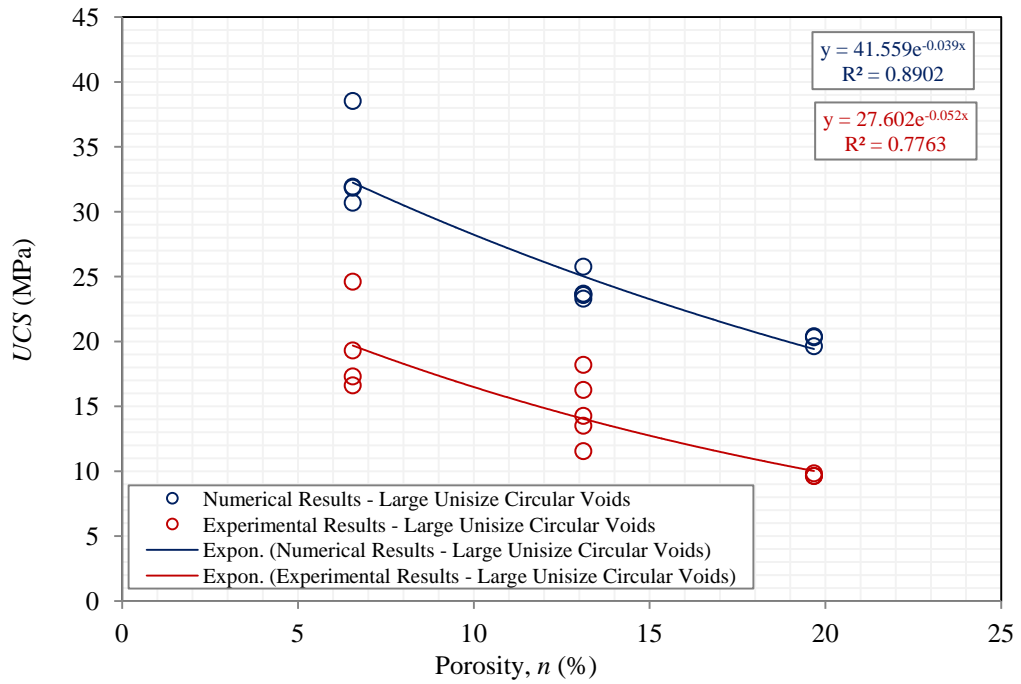


Figure (5.36) Compressive Strength versus Void Porosity for Specimens Containing Unisize Circular Voids – Large Size

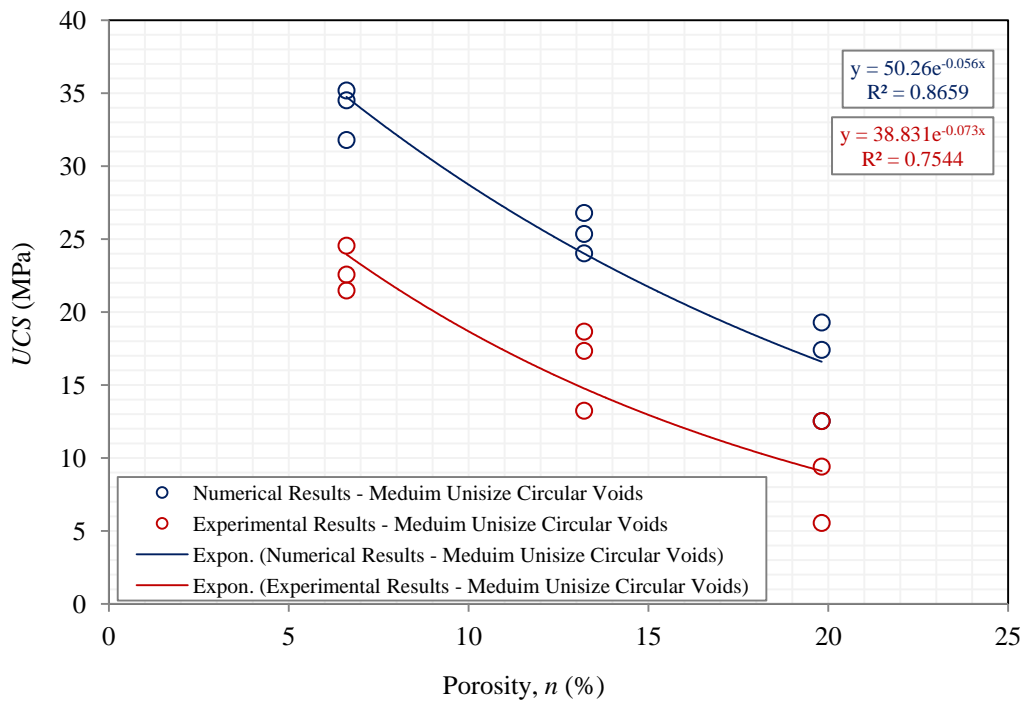


Figure (5.37) Compressive Strength versus Void Porosity for Specimens Containing Unisize Circular Voids – Medium Size

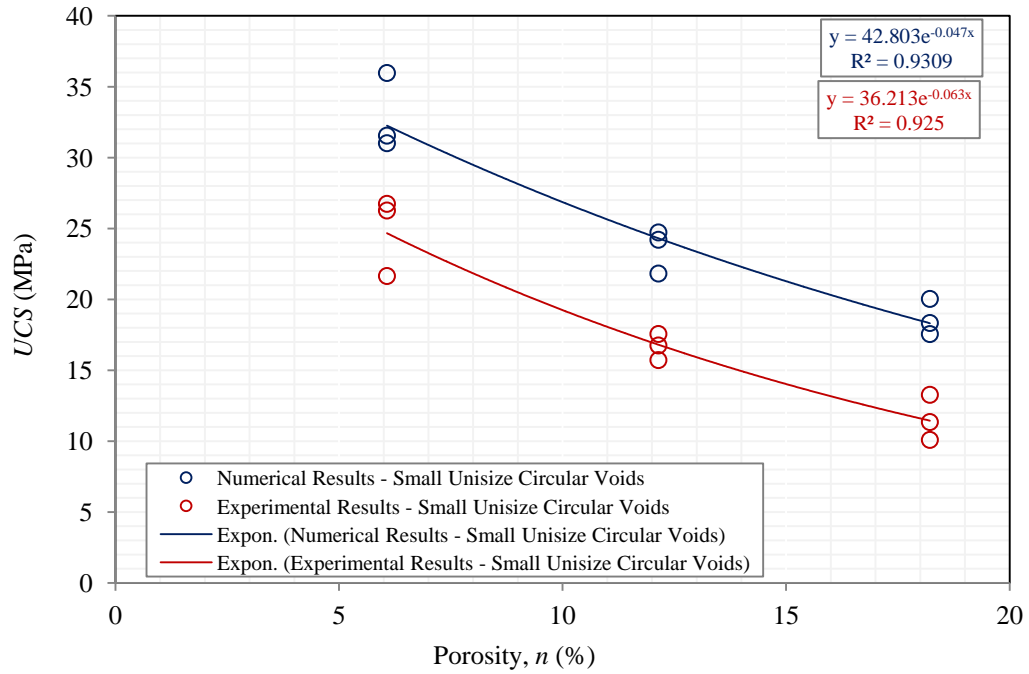


Figure (5.38) Compressive Strength versus Void Porosity for Specimens Containing Unisize Circular Voids – Small Size

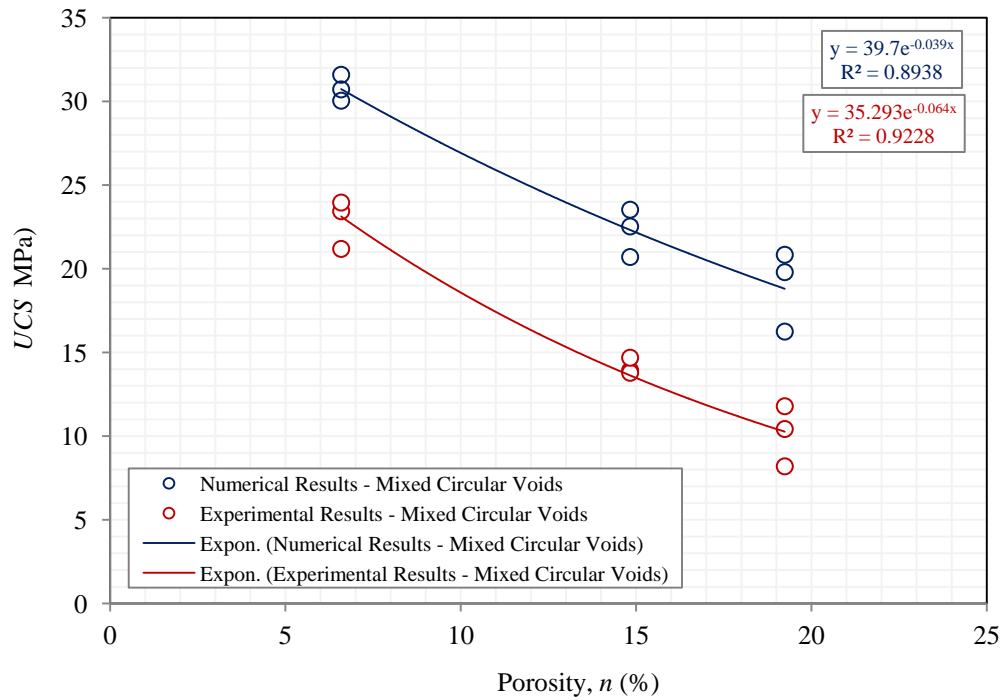


Figure (5.39) Compressive Strength versus Void Porosity for Specimens Containing Unisize Circular Voids – Mixed Size

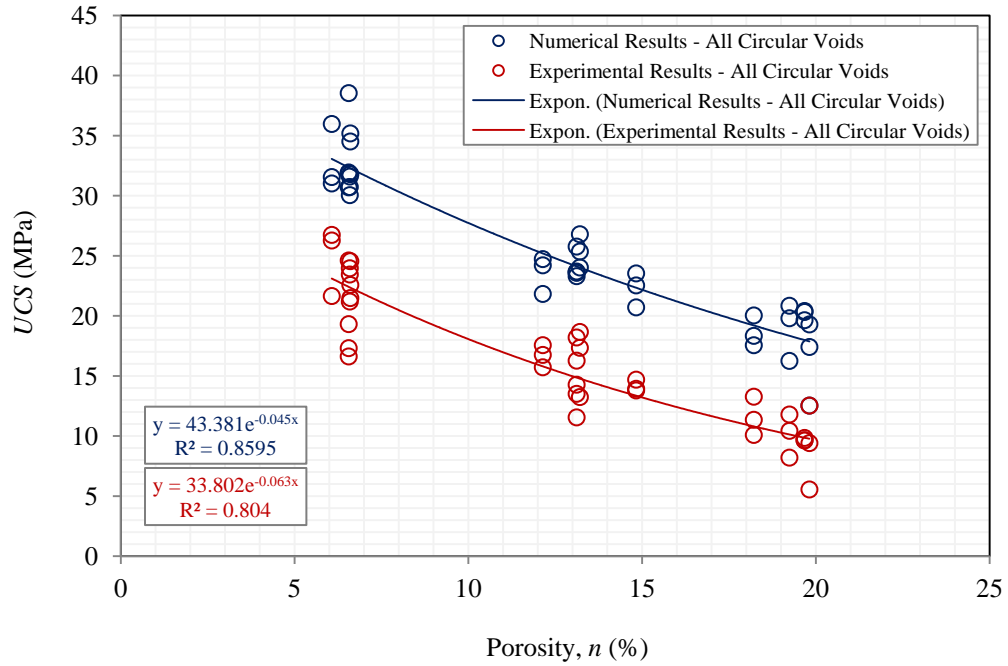


Figure (5.40) Compressive Strength versus Void Porosity for Specimens Containing Unisize Circular Voids – Both Unisize and Mixed Voids

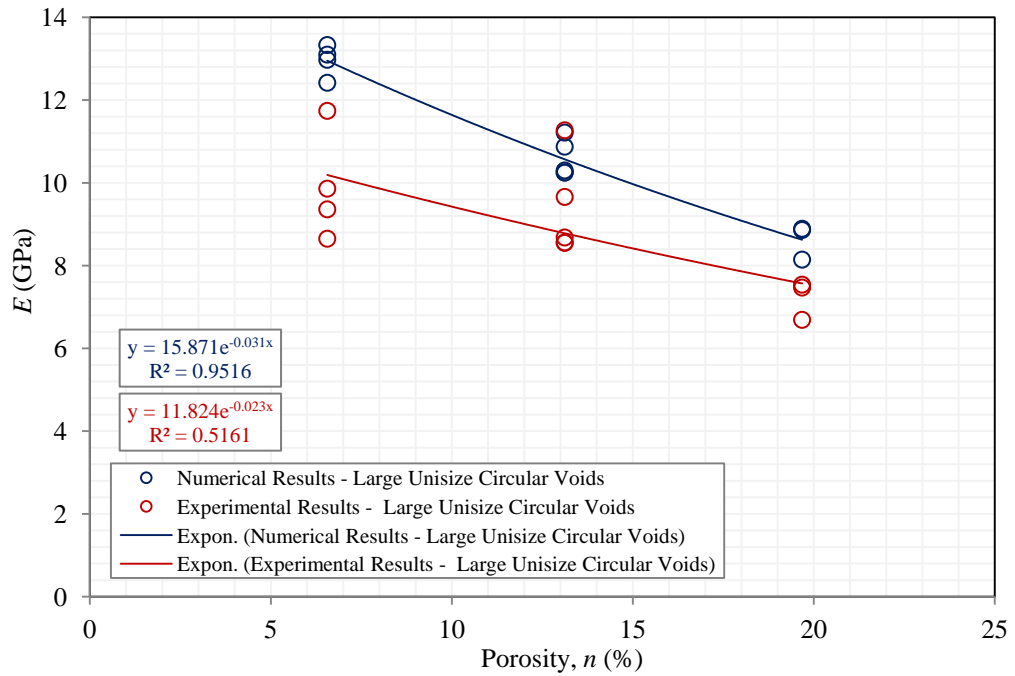


Figure (5.41) Deformation versus Void Porosity for Specimens Containing Unisize Circular Voids – Large Size

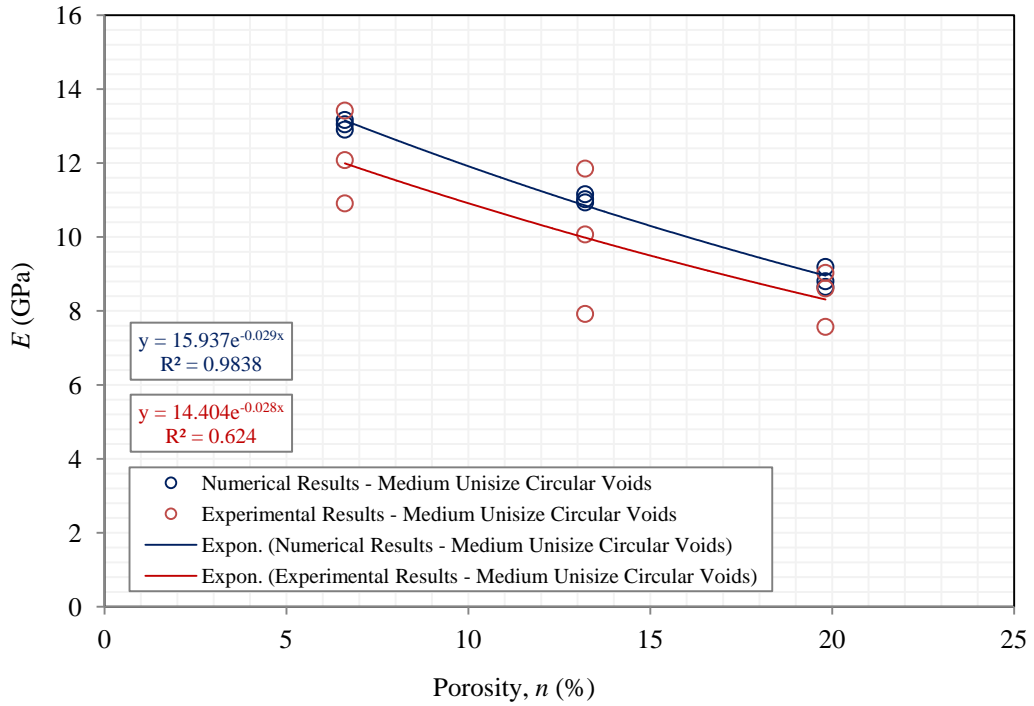


Figure (5.42) Deformation versus Void Porosity for Specimens Containing Unisize Circular Voids – Medium Size

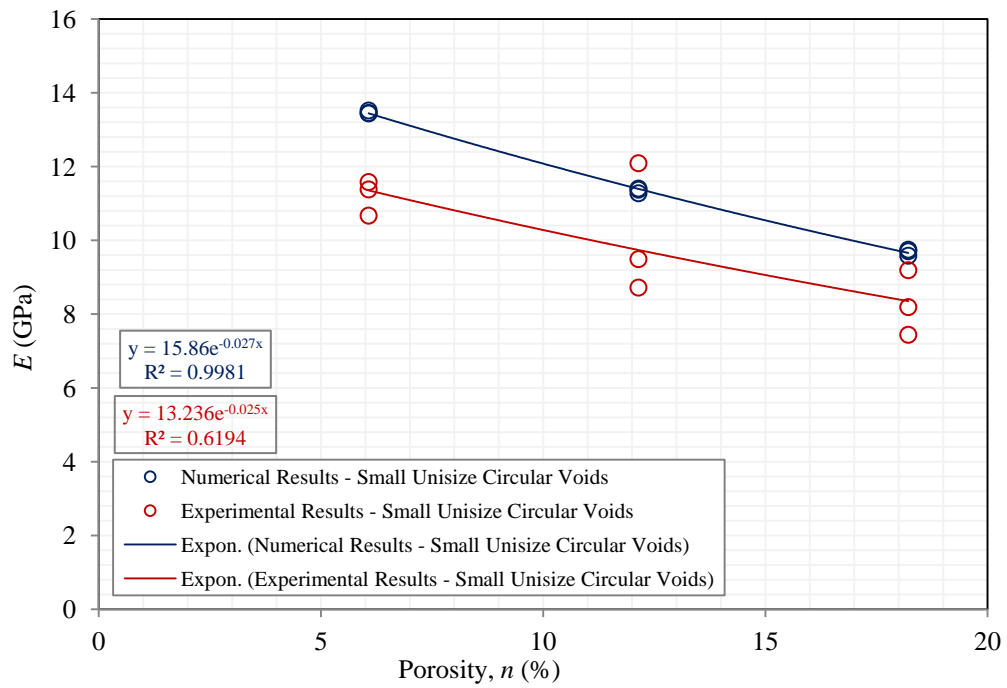


Figure (5.43) Deformation versus Void Porosity for Specimens Containing Unisize Circular Voids – Small Size

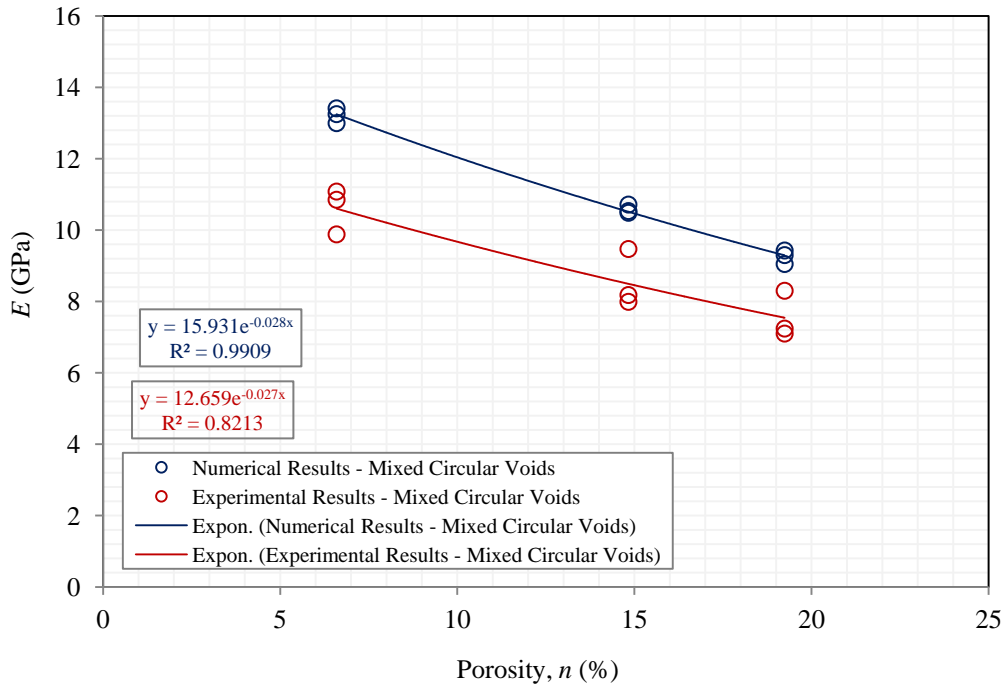


Figure (5.44) Deformation versus Void Porosity for Specimens Containing Unisize Circular Voids – Mixed Size

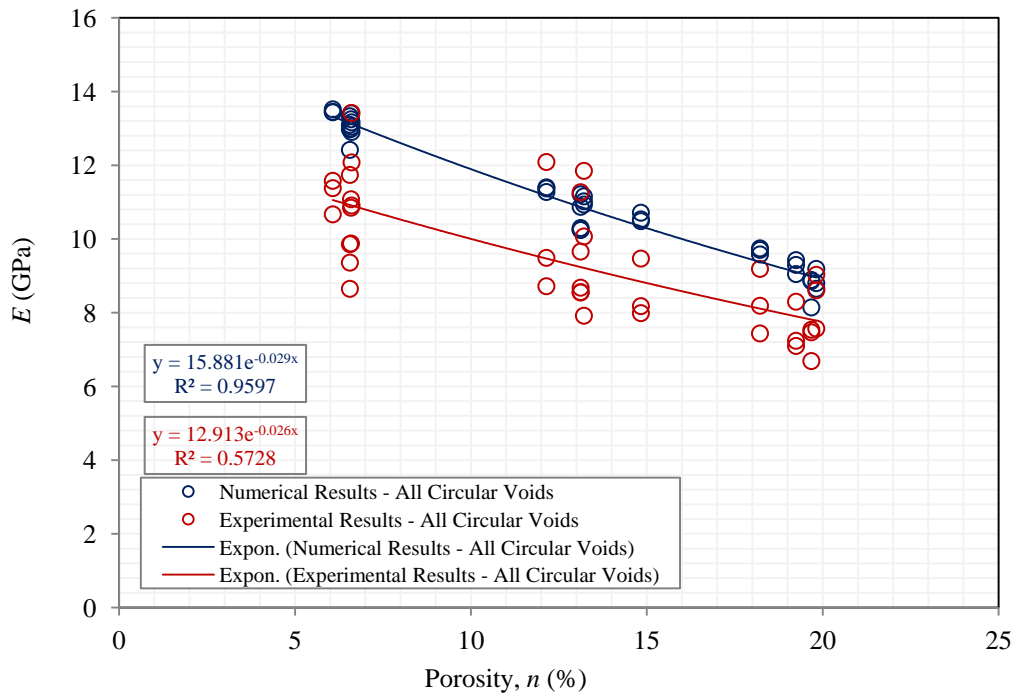


Figure (5.45) Deformation versus Void Porosity for Specimens Containing Unisize Circular Voids – Both Unisize and Mixed Voids

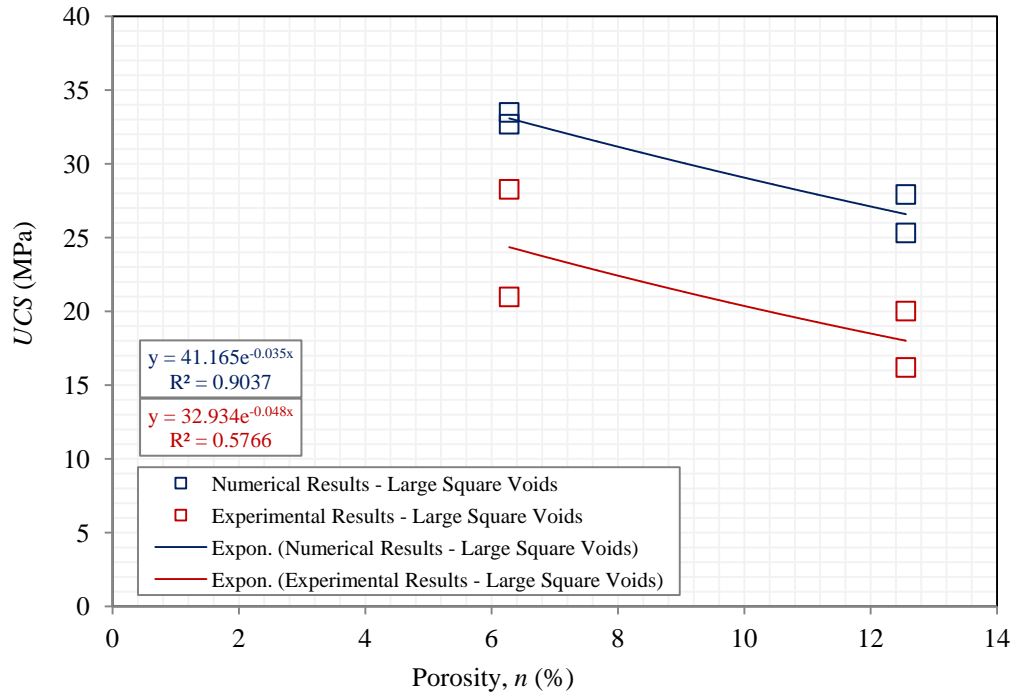


Figure (5.46) Compressive Strength versus Void Porosity for Specimens Containing Square Voids – Large Size

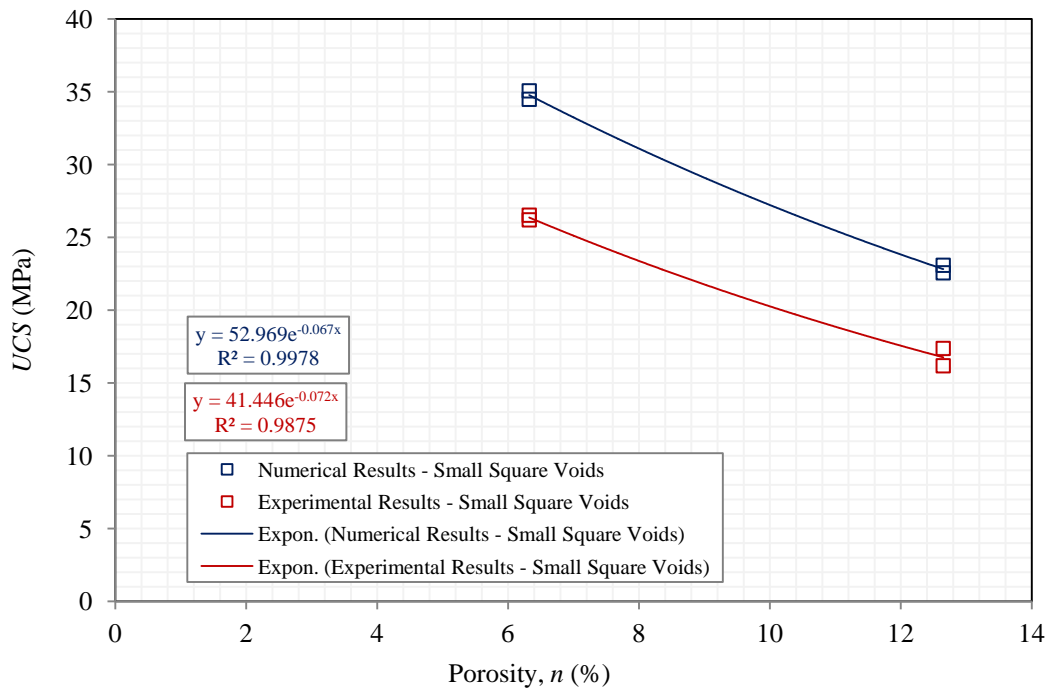


Figure (5.47) Compressive Strength versus Void Porosity for Specimens Containing Square Voids – Small Size

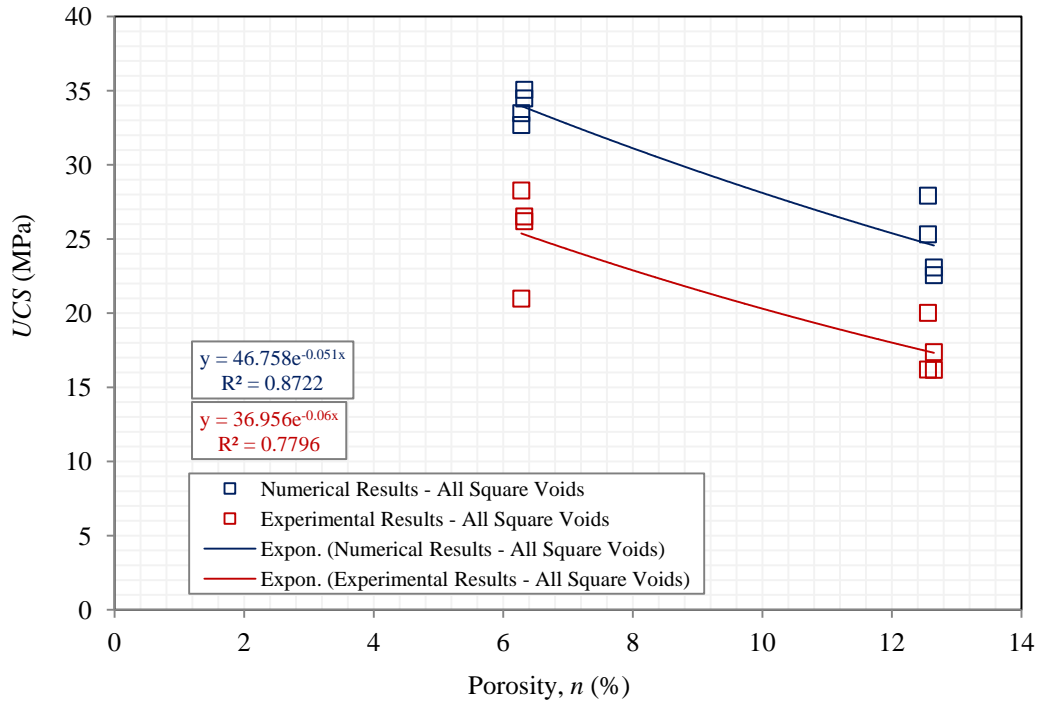


Figure (5.48) Compressive Strength versus Void Porosity for Specimens Containing Square Voids – Both Large and Small Sizes

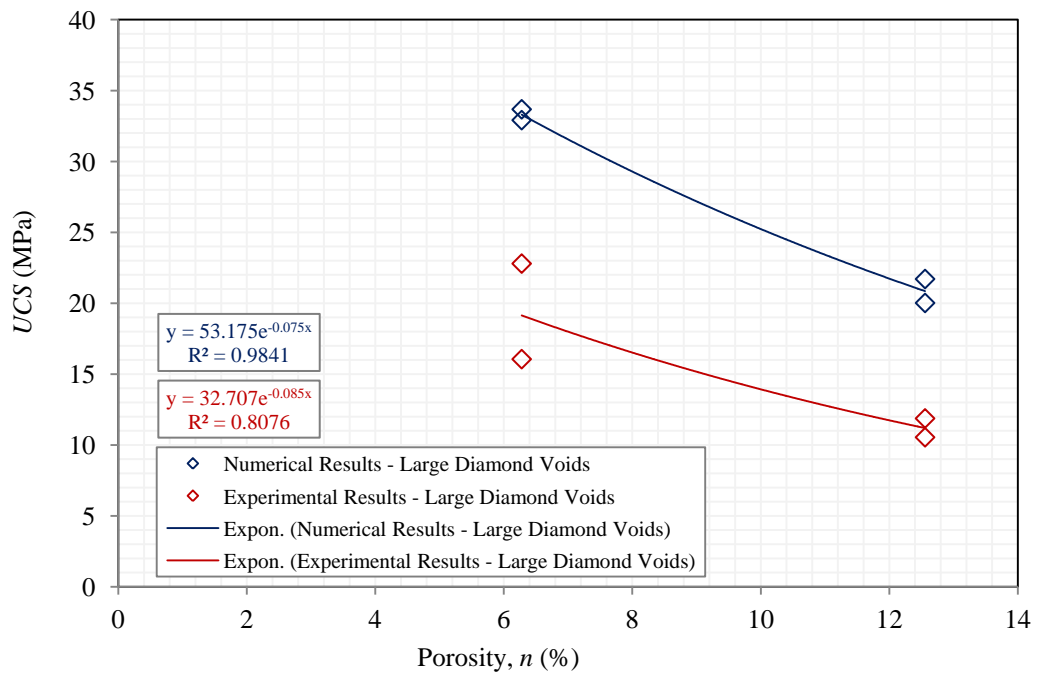


Figure (5.49) Compressive Strength versus Void Porosity for Specimens Containing Diamond Voids – Large Size

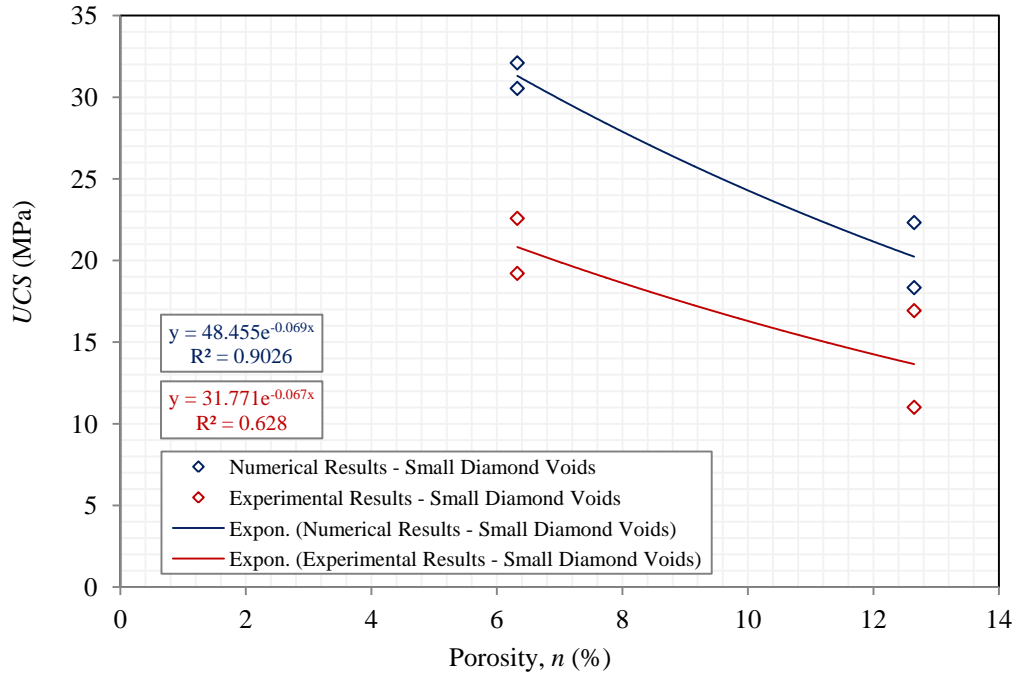


Figure (5.50) Compressive Strength versus Void Porosity for Specimens Containing Diamond Voids – Small Size

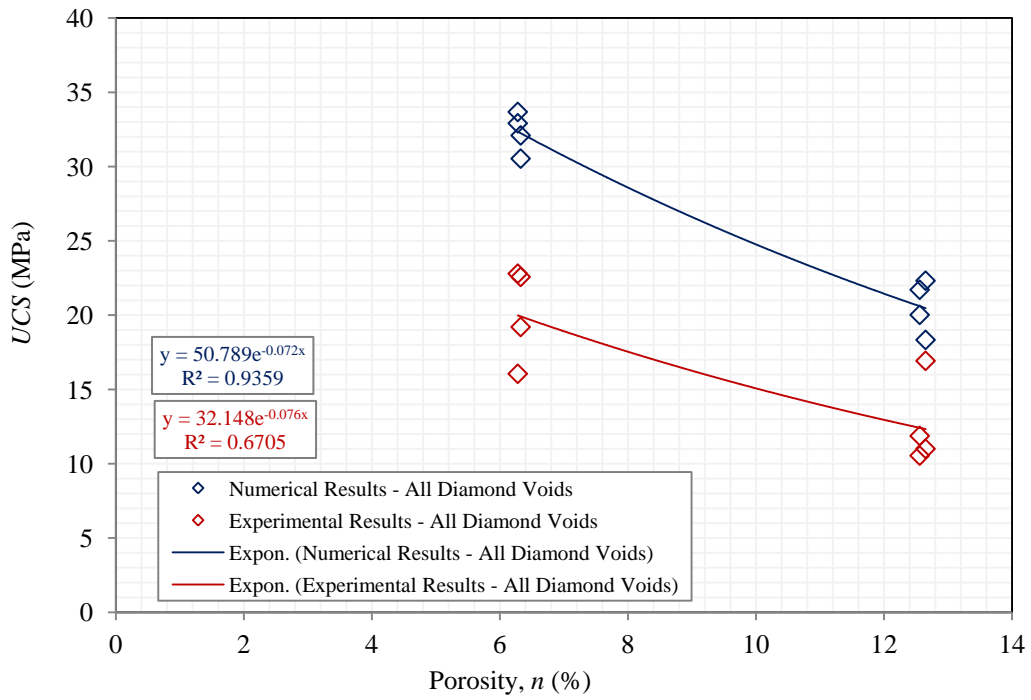


Figure (5.51) Compressive Strength versus Void Porosity for Specimens Containing Diamond Voids – Both Large and Small Sizes

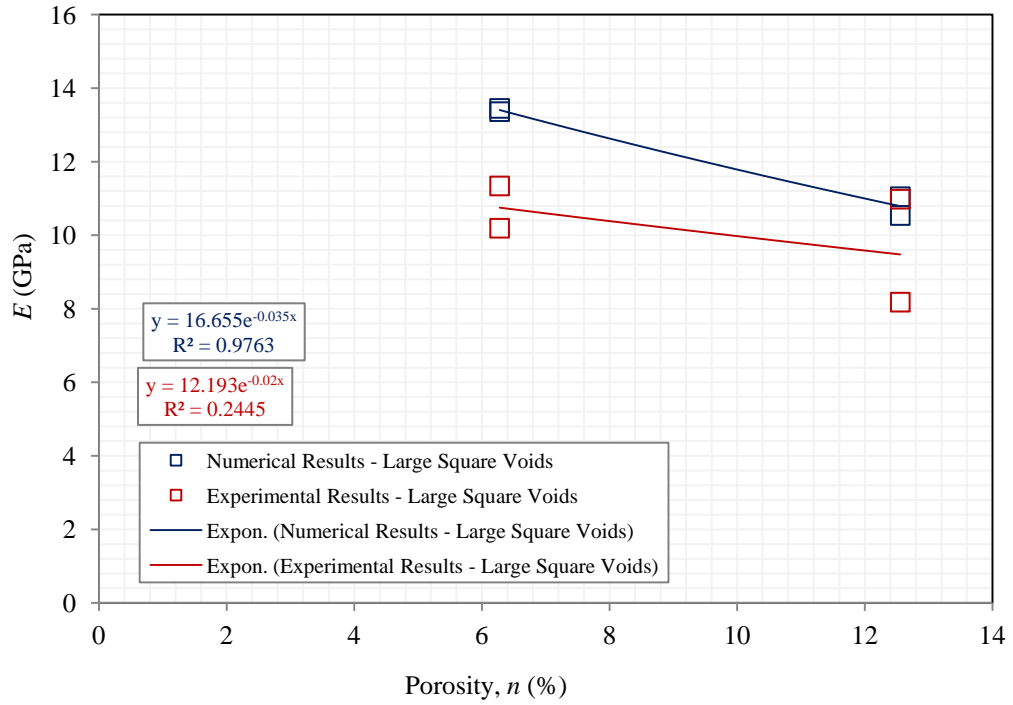


Figure (5.52) Deformation versus Void Porosity for Specimens Containing Square Voids – Large Size

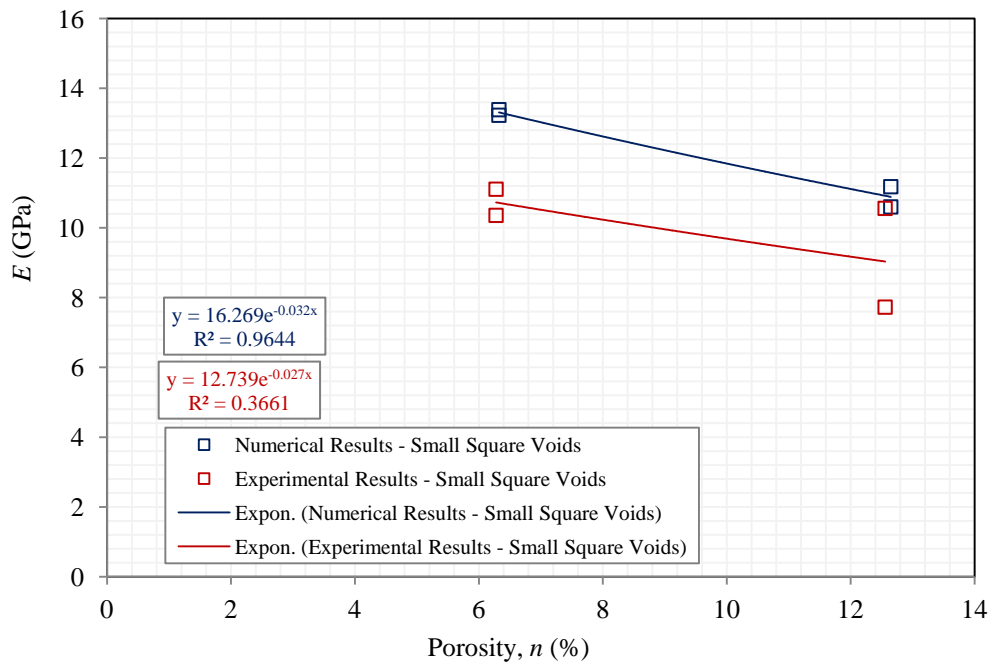


Figure (5.53) Deformation versus Void Porosity for Specimens Containing Square Voids – Small Size

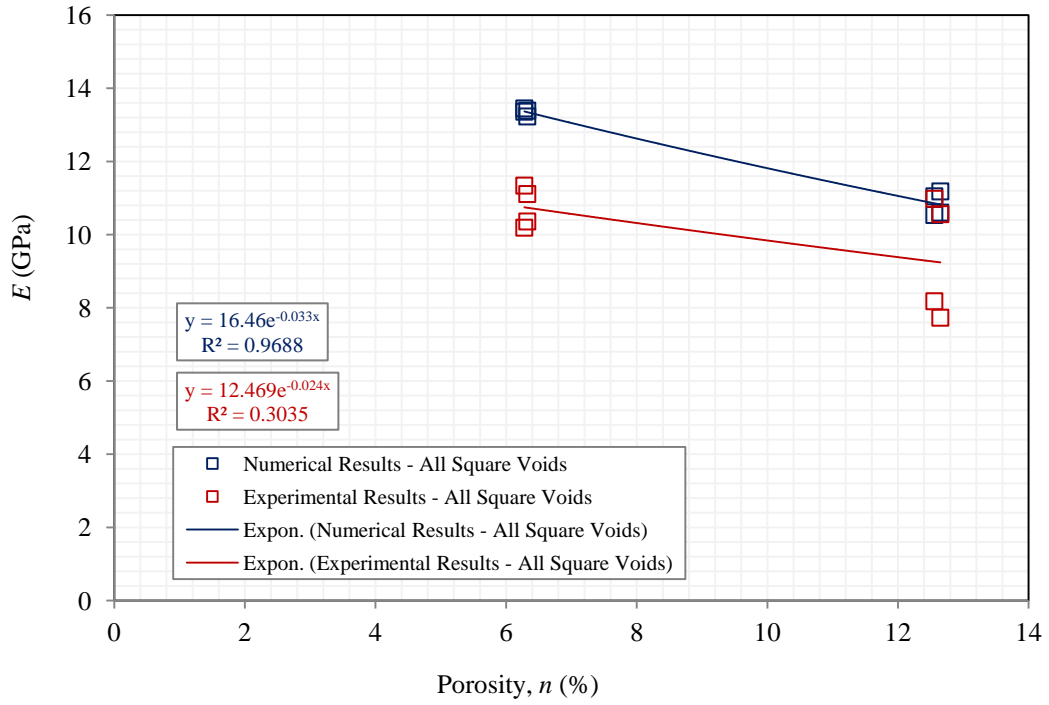


Figure (5.54) Deformation versus Void Porosity for Specimens Containing Square Voids – Both Large and Small Sizes

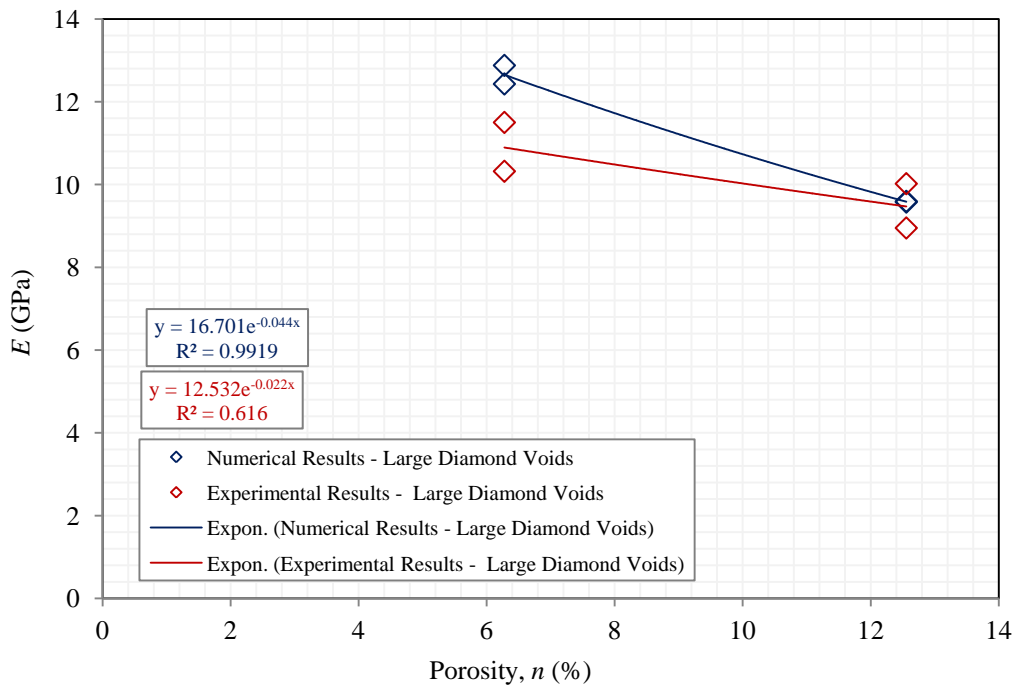


Figure (5.55) Deformation versus Void Porosity for Specimens Containing Diamond Voids – Large Size

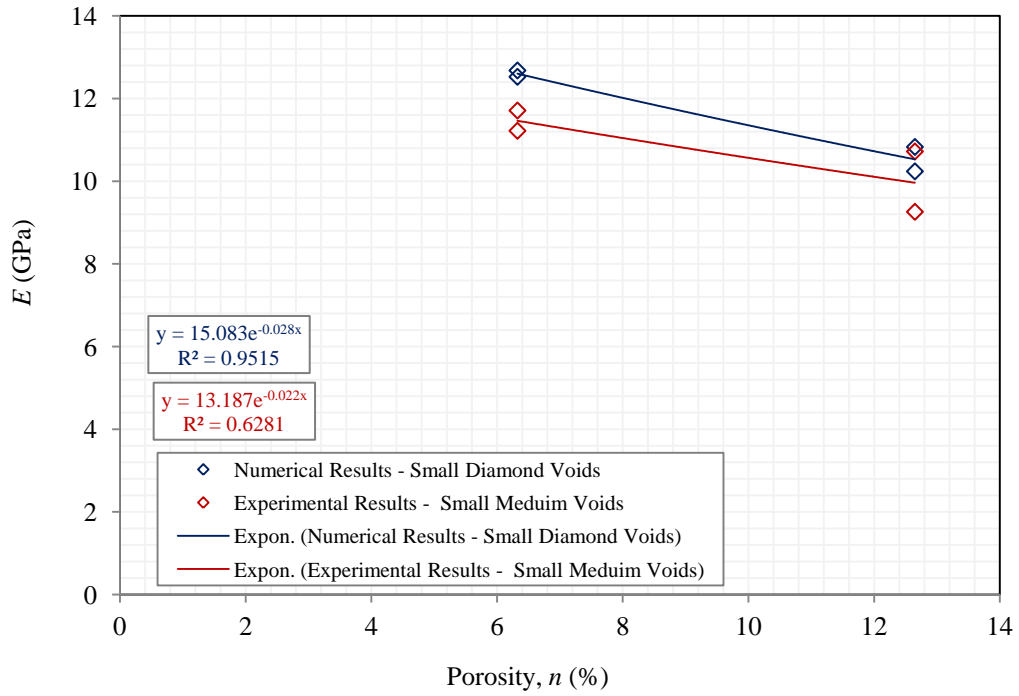


Figure (5.56) Deformation versus Void Porosity for Specimens Containing Diamond Voids – Small Size

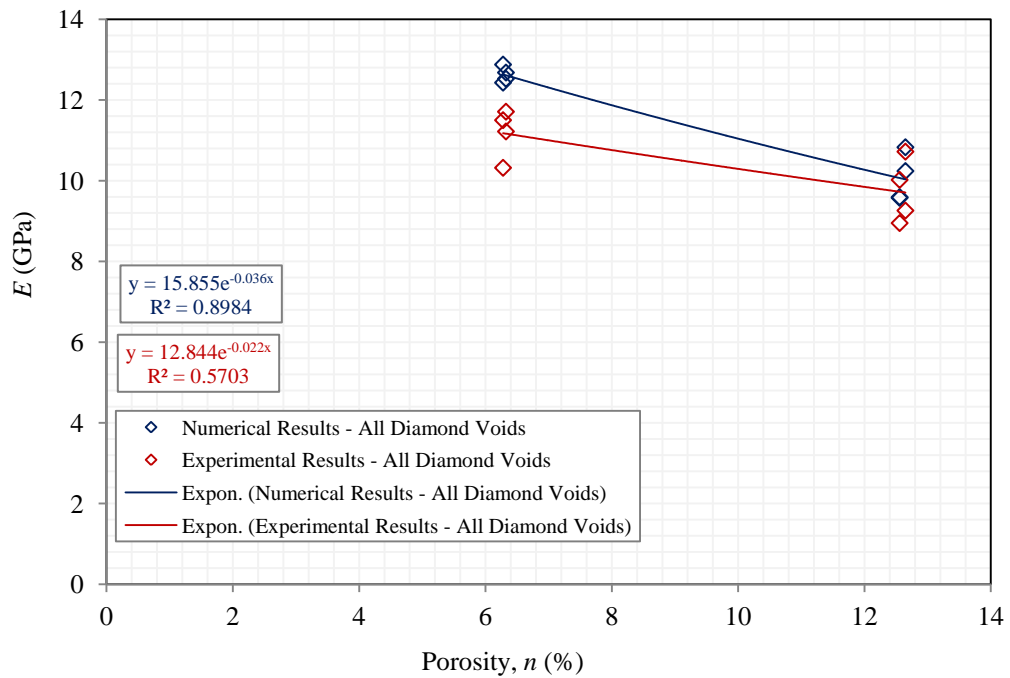


Figure (5.57) Deformation versus Void Porosity for Specimens Containing Diamond Voids – Both Large and Small Sizes

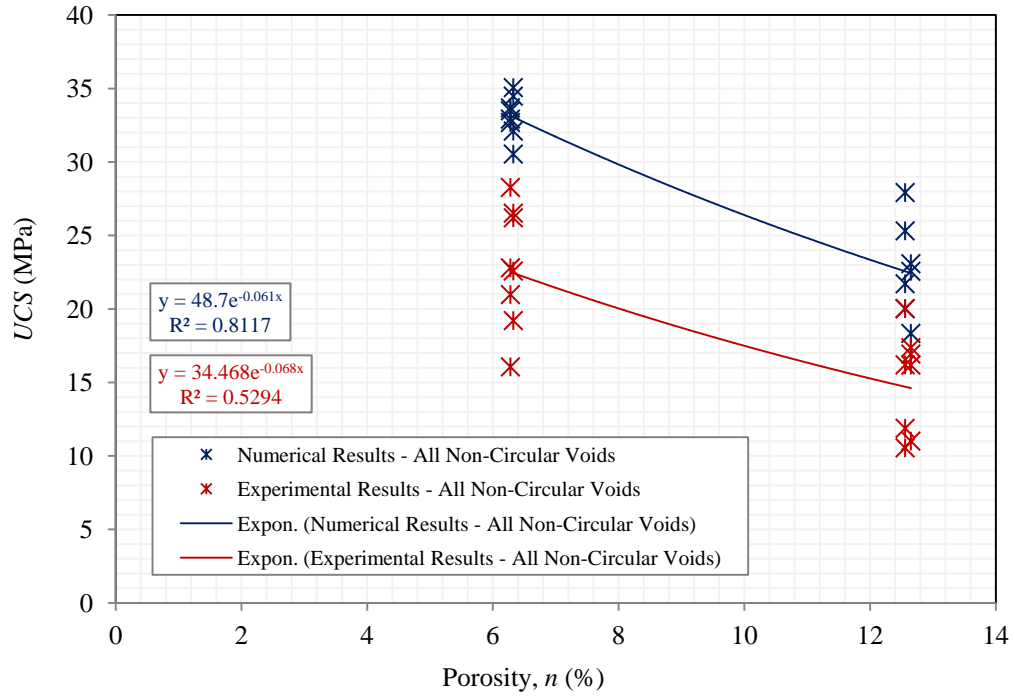


Figure (5.58) Compressive Strength versus Void Porosity for Specimens Containing Non-circular Voids – Both Square and Diamond Voids

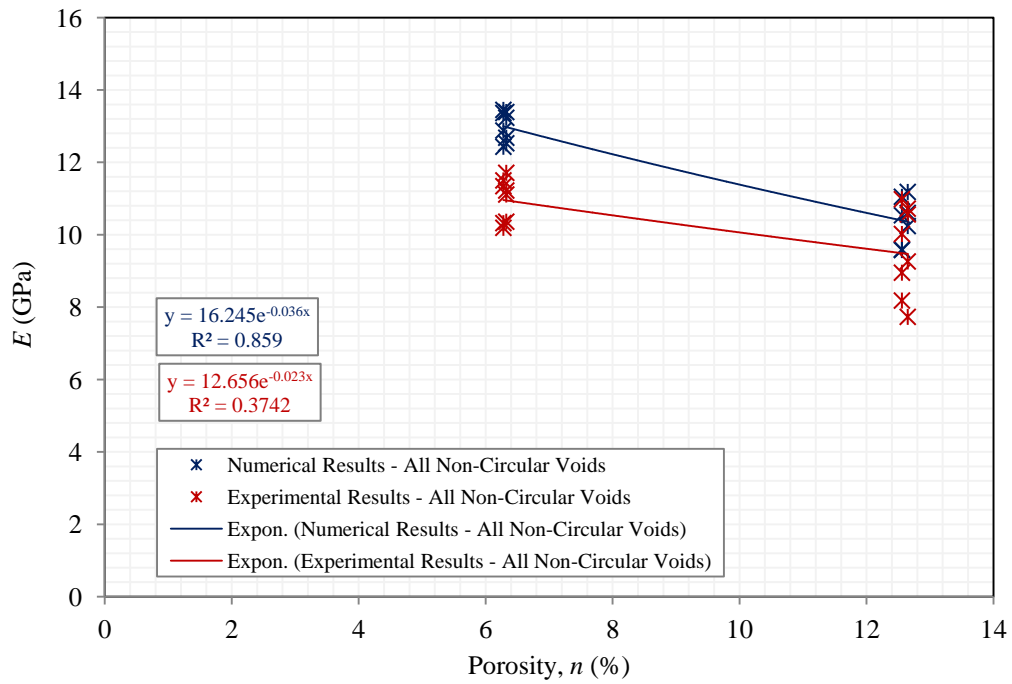


Figure (5.59) Deformation versus Void Porosity for Specimens Containing Non-circular Voids – Both Square and Diamond Voids

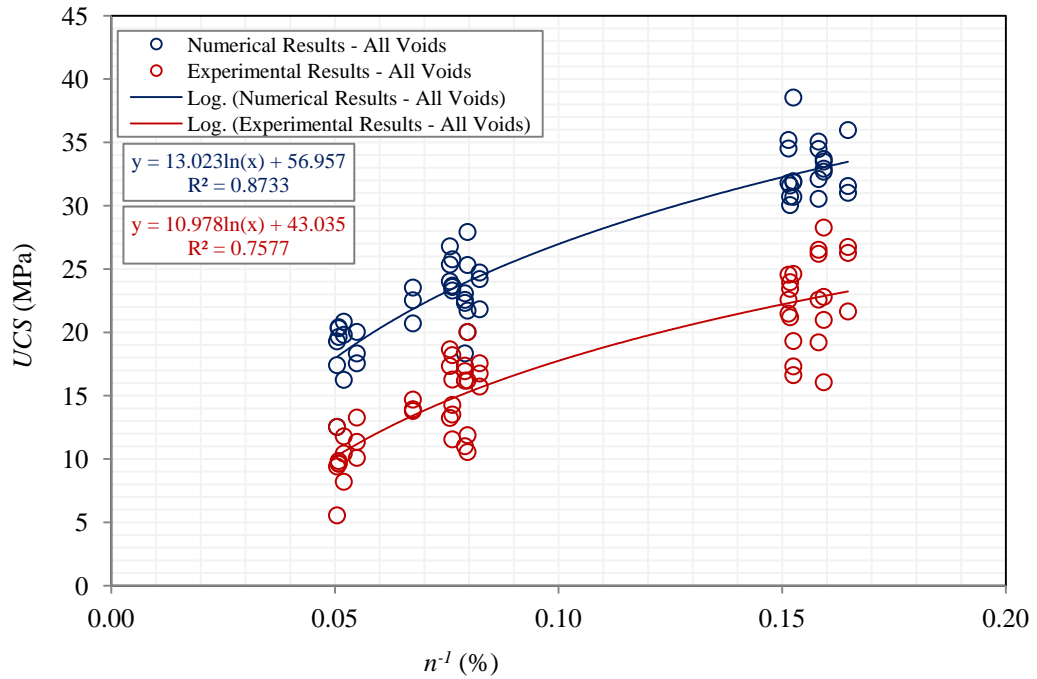


Figure (5.60) Compressive Strength versus Void Porosity for Specimens with Voids Having Different Size, Shape and Spatial Distributions

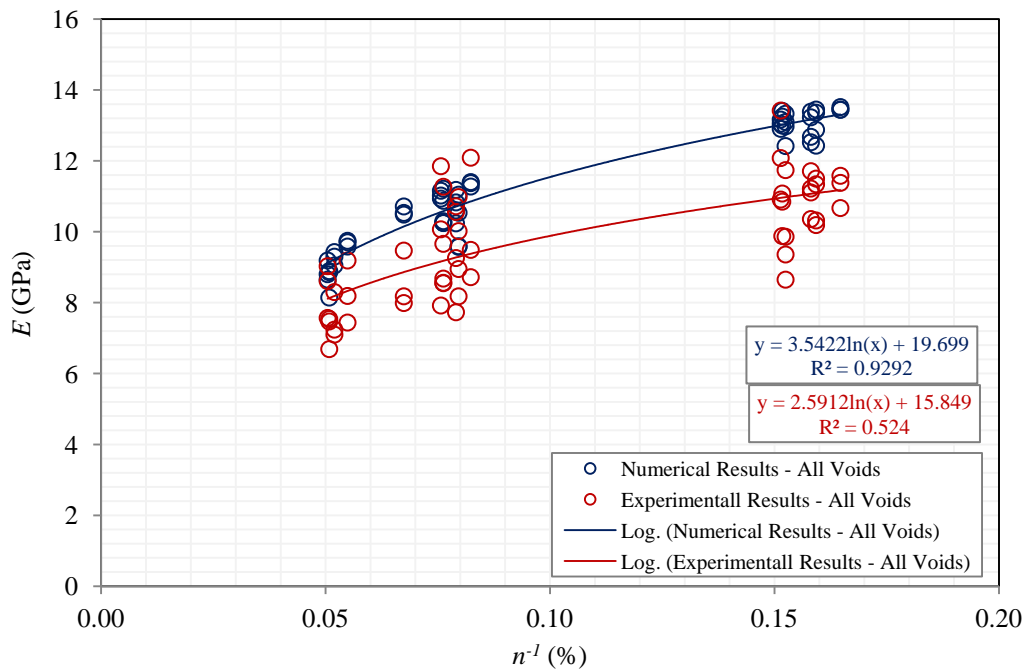


Figure (5.61) Deformation versus Void Porosity for Specimens with Voids Having Different Size, Shape and Spatial Distributions

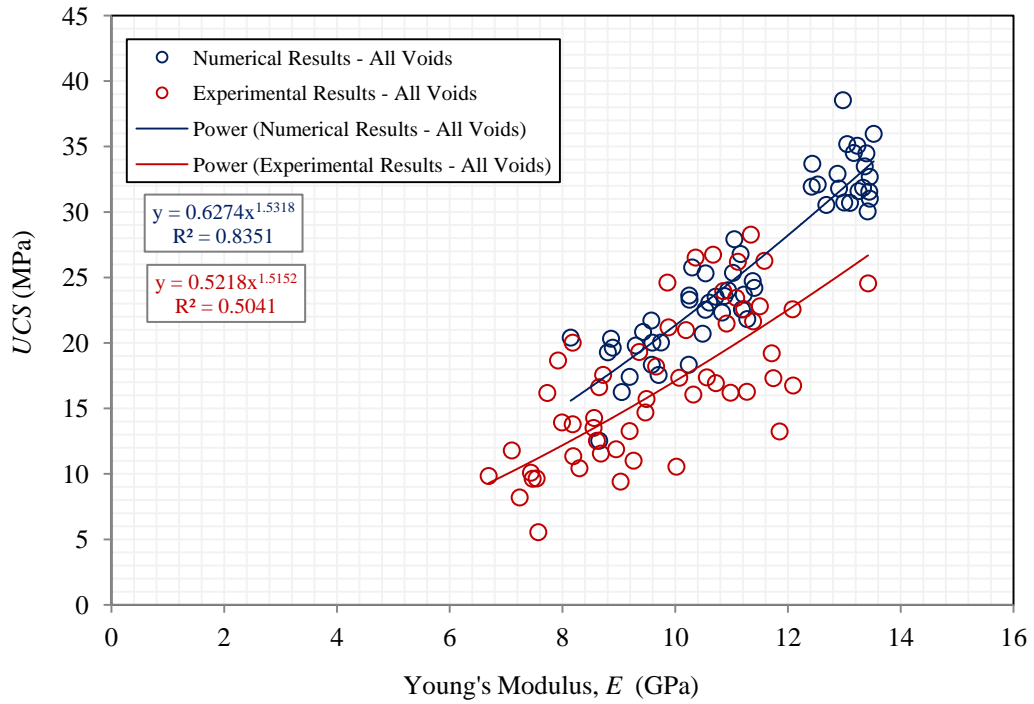


Figure (5.62) Compressive Strength versus Deformation for Specimens with Voids Having Different Size, Shape and Spatial Distributions

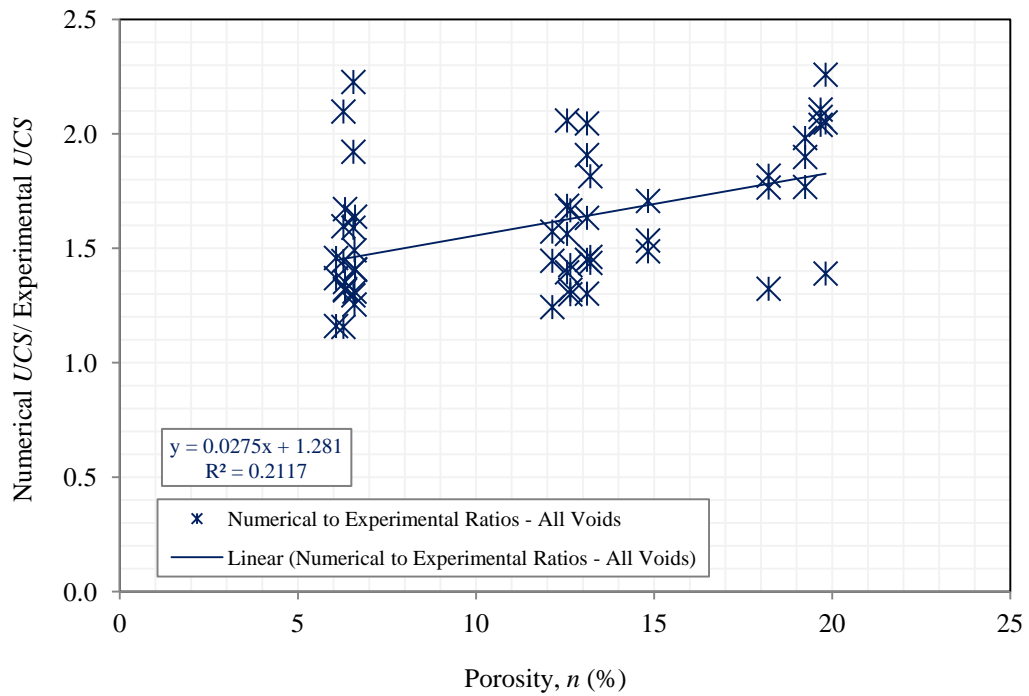


Figure (5.63) Ratios of Numerical Strength to Experimental Strength for All Numerical Models

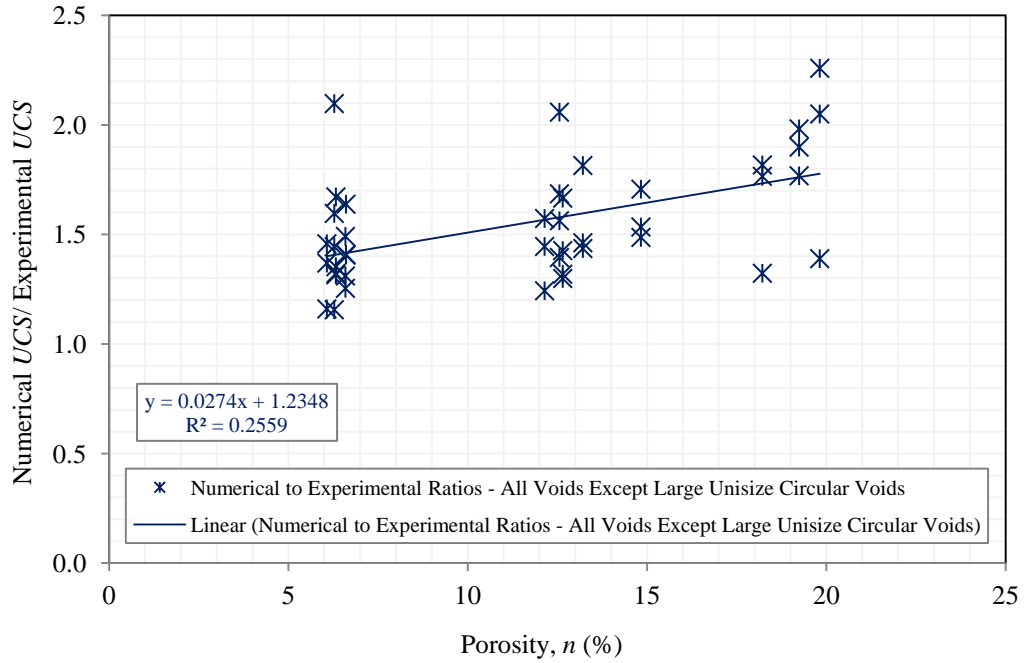


Figure (5.64) Ratios of Numerical Strength to Experimental Strength for All Numerical Models Except Those with Large Unisize Circular Voids

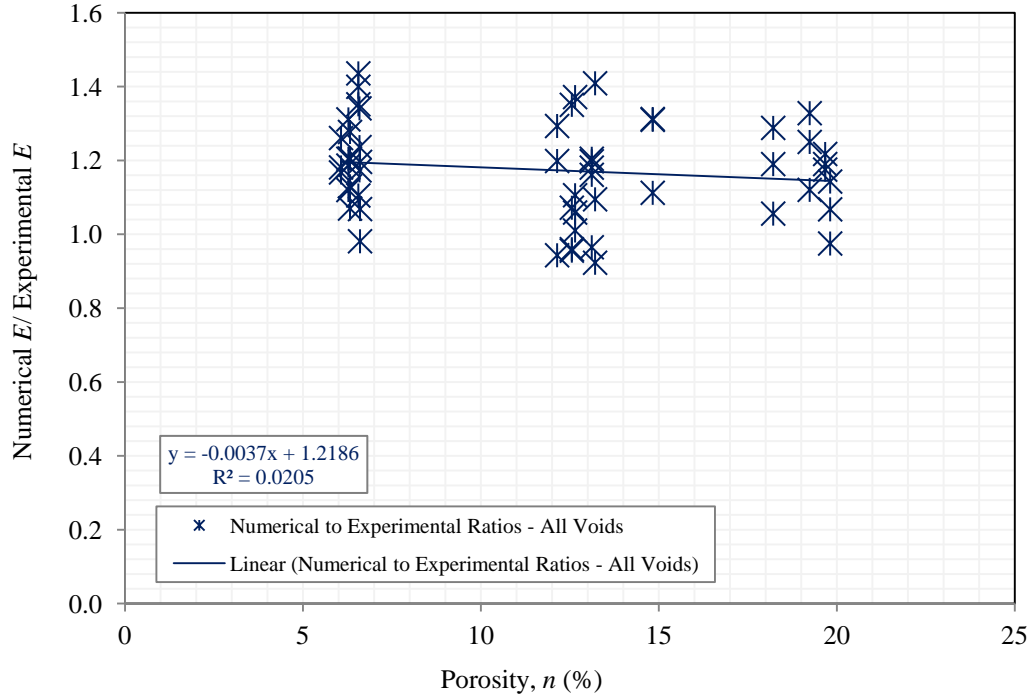


Figure (5.65) Ratios of Numerical Deformation to Experimental Deformation for All Numerical Models

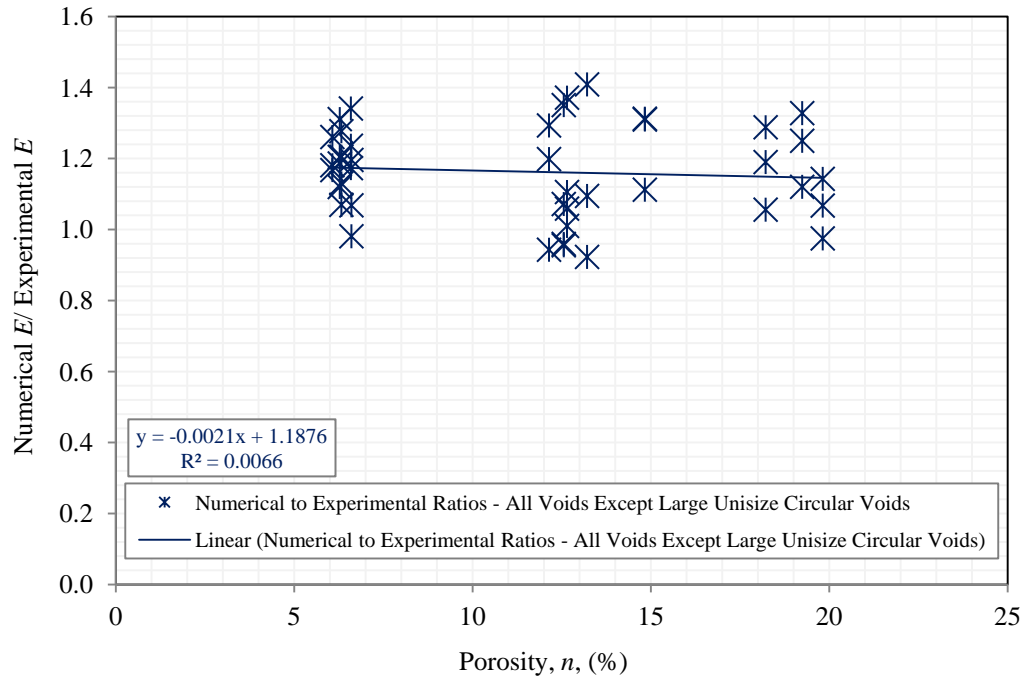


Figure (5.66) Ratios of Numerical Deformation to Experimental Deformation for All Numerical Models Except Those with Large Unisize Circular Voids

Table (5.5) Numerical and Experimental Results for the Models Containing Unisize Circular Voids

Sample Name	Porosity (n)	Experimental UCS	Numerical UCS	Experimental E (25-50%)	Numerical E (25-50%)
	%	MPa	MPa	GPa	GPa
PA-UCL2-1	6.56	19.31	30.695	9.36	13.099
PA-UCL2-2	6.56	16.62	31.934	8.65	12.419
PB-UCL2	6.56	17.31	38.537	11.74	12.973
PC-UCL2	6.56	24.61	31.852	9.86	13.331
PA-UCL4-1	13.12	18.20	23.689	9.66	11.215
PA-UCL4-2	13.12	14.27	23.301	8.56	10.252
PA-UCL4-3	13.12	13.51	25.765	8.55	10.299
PB-UCL4	13.12	11.55	23.623	8.68	10.247
PC-UCL4	13.12	16.27	23.583	11.27	10.874
PA-UCL6	19.68	9.84	20.406	6.69	8.145
PB-UCL6	19.68	9.63	19.638	7.47	8.890
PC-UCL6	19.68	9.65	20.323	7.54	8.860
PA-UCM4	6.61	22.57	31.792	12.08	12.904
PB-UCM4	6.61	21.48	35.185	10.91	13.049
PC-UCM4	6.61	24.55	34.512	13.42	13.166
PA-UCM8	13.21	18.66	26.791	7.92	11.158
PB-UCM8	13.21	17.34	25.354	10.07	11.023
PC-UCM8	13.21	13.24	24.024	11.85	10.936
PA-UCM12	19.82	12.53	17.409	8.61	9.191
PB-UCM12	19.82	9.41	19.287	9.03	8.804
PC-UCM12	19.82	5.55	12.533	7.57	8.650
PA-UCS11	6.07	26.27	35.969	11.58	13.519
PB-UCS11	6.07	26.74	31.017	10.67	13.450
PC-UCS11	6.07	21.65	31.552	11.38	13.440
PA-UCS22	12.14	15.72	24.724	9.49	11.373
PB-UCS22	12.14	17.56	21.823	8.72	11.276
PC-UCS22	12.14	16.75	24.205	12.09	11.403
PA-UCS33	18.22	11.35	20.033	8.19	9.746
PB-UCS33	18.22	13.27	17.555	9.19	9.704
PC-UCS33	18.22	10.09	18.335	7.44	9.583

Table (5.6) Numerical to Experimental Ratios for Models Containing Unisize Circular Voids

Sample Name	Porosity (n)	Numerical/Experimental Ratio	
	%	For UCS	For E
PA-UCL2-1	6.56	1.59	1.40
PA-UCL2-2	6.56	1.92	1.44
PB-UCL2	6.56	2.23	1.11
PC-UCL2	6.56	1.29	1.35
PA-UCL4-1	13.12	1.30	1.16
PA-UCL4-2	13.12	1.63	1.20
PA-UCL4-3	13.12	1.91	1.20
PB-UCL4	13.12	2.05	1.18
PC-UCL4	13.12	1.45	0.96
PA-UCL6	19.68	2.07	1.22
PB-UCL6	19.68	2.04	1.19
PC-UCL6	19.68	2.11	1.18
PA-UCM4	6.61	1.41	1.07
PB-UCM4	6.61	1.64	1.20
PC-UCM4	6.61	1.41	0.98
PA-UCM8	13.21	1.44	1.41
PB-UCM8	13.21	1.46	1.09
PC-UCM8	13.21	1.81	0.92
PA-UCM12	19.82	1.39	1.07
PB-UCM12	19.82	2.05	1.00
PC-UCM12	19.82	2.26	1.15
PA-UCS11	6.07	1.37	1.20
PB-UCS11	6.07	1.16	1.29
PC-UCS11	6.07	1.46	1.21
PA-UCS22	12.14	1.57	1.23
PB-UCS22	12.14	1.24	1.31
PC-UCS22	12.14	1.45	0.96
PA-UCS33	18.22	1.77	1.22
PB-UCS33	18.22	1.32	1.08
PC-UCS33	18.22	1.82	1.31

Table (5.7) Numerical and Experimental Results for Models Containing Models Containing Circular Voids with Mixed Sizes

Sample Name	Porosity (<i>n</i>)	Experime n. UCS	Numerical UCS	Experimen. E (25-50%)	Numerical E (25-50%)
	%	MPa	MPa	GPa	GPa
PA-UXCL1M1S3	6.59	23.44	30.721	11.08	12.997
PB-UXCL1M1S3	6.59	23.96	30.046	10.85	13.412
PC-UXCL1M1S3	6.59	21.19	31.594	9.88	13.249
PA-UXCL2M3S6	14.83	13.93	20.706	7.99	10.485
PB-UXCL2M3S6	14.83	13.79	23.533	8.18	10.715
PC-UXCL2M3S6	14.83	14.69	22.533	9.47	10.533
PA-UXCL2M5S8	19.24	11.79	20.840	7.10	9.428
PB-UXCL2M5S8	19.24	10.43	19.801	8.30	9.299
PC-UXCL2M5S8	19.24	8.20	16.250	7.24	9.050

Table (5.8) Numerical to Experimental Ratios for Models Containing Circular Voids with Mixed Sizes

Sample Name	Porosity (<i>n</i>)	Numerical/Experimental Ratio	
	%	For UCS	For <i>E</i>
PA-UXCL1M1S3	6.59	1.31	1.17
PB-UXCL1M1S3	6.59	1.25	1.24
PC-UXCL1M1S3	6.59	1.49	1.34
PA-UXCL2M3S6	14.83	1.49	1.31
PB-UXCL2M3S6	14.83	1.71	1.31
PC-UXCL2M3S6	14.83	1.53	1.11
PA-UXCL2M5S8	19.24	1.77	1.33
PB-UXCL2M5S8	19.24	1.90	1.12
PC-UXCL2M5S8	19.24	1.98	1.25

Table (5.9) Numerical and Experimental Results for Models Containing Non-Circular Voids (Square and Diamond)

Sample Name	Porosity	Experimental	Numerical	Experimental	Numerical E
	(n) %	UCS MPa	UCS MPa	E (25-50%) GPa	(25-50%) GPa
PA-USqL3	6.28	20.98	33.484	10.19	13.361
PB-USqL3	6.28	28.27	32.685	11.34	13.449
PA-USqL6	12.56	16.20	25.315	10.98	10.536
PB-USqL6	12.56	20.02	27.922	8.18	11.047
PA-USqM6	6.32	26.20	34.478	11.11	13.390
PB-USqM6	6.32	26.52	35.058	10.36	13.230
PA-USqM12	12.65	17.37	22.562	10.56	11.182
PB-USqM12	12.65	16.18	23.081	7.73	10.602
PA-UDmL3	6.28	16.06	33.683	10.32	12.430
PB-UDmL3	6.28	22.80	32.919	11.50	12.878
PA-UDmL6	12.56	11.88	20.024	8.95	9.593
PB-UDmL6	12.56	10.55	21.713	10.02	9.575
PA-UDmM6	6.32	19.21	32.102	11.71	12.526
PB-UDmM6	6.32	22.58	30.540	11.22	12.679
PA-UDmM12	12.65	11.01	18.338	9.26	10.239
PB-UDmM12	12.65	16.93	22.323	10.72	10.829

Table (5.10) Numerical to Experimental Ratios for Models Containing Non-Circular Voids (Square and Diamond)

Sample Name	Porosity	Numerical/Experimental Ratio	
	%	For UCS	For E
PA-USqL3	6.28	1.60	1.31
PB-USqL3	6.28	1.16	1.19
PA-USqL6	12.56	1.56	0.96
PB-USqL6	12.56	1.39	1.35
PA-USqM6	6.32	1.32	1.21
PB-USqM6	6.32	1.32	1.28
PA-USqM12	12.65	1.30	1.06
PB-USqM12	12.65	1.43	1.37
PA-UDmL3	6.28	2.10	1.20
PB-UDmL3	6.28	1.44	1.12
PA-UDmL6	12.56	1.69	1.07
PB-UDmL6	12.56	2.06	0.96
PA-UDmM6	6.32	1.67	1.07
PB-UDmM6	6.32	1.35	1.13
PA-UDmM12	12.65	1.67	1.11
PB-UDmM12	12.65	1.32	1.01

Table (5.11) Ratios of Numerical *UCS* to Experimental *UCS* for All Numerical Models

Void Types	Void Size			Average
	Large	Medium	Small	
Circular (Unisize)	1.799	1.652	1.462	1.654
Circular (Mixed)	1.603			1.603
Square	1.428	1.343		1.385
Diamond	1.823	1.503		1.663
All Circular	1.652			
All Voids	1.59			

Table (5.12) Ratios of Numerical *E* to Experimental *E* for All Numerical Models

Void Types	Void Size			Average
	Large	Medium	Small	
Circular (Unisize)	1.216	1.099	1.201	1.195
Circular (Mixed)	1.242			1.242
Square	1.203	1.230		1.216
Diamond	1.088	1.080		1.084
All Circular	1.206			
All Voids	1.196			

5.9 Three-Dimensional versus Two-Dimensional

As mentioned before, in order to evaluate the numerical analysis, the numerical results should be compared to the experimental results obtained from laboratory or/and field tests. Since laboratory or/and field tests, experimental tests, are generally done in three dimensional system, the two-dimensional plane strain, or plane stress, results should be transformed to experimental three-dimensional results. Since the theoretical methods to carry out the transformation are typically very complex, an empirical method through

establishing a relationship between numerical and experimental results might be useful and helpful.

Accordingly, to carry out the comparison, the two-dimensional plane strain mechanical properties given by *UDEC* should be transformed to three-dimensional mechanical properties. Therefore, the relationships between numerical mechanical properties (*UCS* and *E*) given by *UDEC* and the experimental mechanical properties obtained from the laboratory tests carried out on the Hydro-StoneTB[®] cubes are plotted in Figures (5.67) to (5.76). According to the figures, the following conclusions can be drawn:

- 1- The numerical results of uniaxial compressive strength given by the *UDEC* for the models containing circular voids with different size, distribution and uniformity are in decent relationships with experimental results of uniaxial compression tests on the Hydro-StoneTB[®] cubes. The correlation of *UCS* is followed power trend, as shown in Figure (5.67), and can be represented best by the following equation:

$$[UCS(\text{MPa})]_{Exp.} = 0.2635 * [(UCS(\text{MPa}))_{Num.}]^{1.2681} \quad R^2 = 0.7722 \quad \dots (5.17)$$

However, after excluding the results for models containing large unisize circular voids, the numerical results showed better power correlation, as shown in Figure (5.68), and can be represented best by the following equation:

$$[UCS(\text{MPa})]_{Exp.} = 0.1955 * [(UCS(\text{MPa}))_{Num.}]^{1.376} \quad R^2 = 0.888 \quad \dots (5.18)$$

- 2- For the models containing non-circular voids, the numerical results of uniaxial compressive strength given by the *UDEC* showed good relationship with

experimental results of uniaxial compression on the cubes. The correlation of *UCS* is also followed power trend, as shown in Figure (5.69), and can be represented best by the following equation:

$$[UCS(MPa)]_{Exp.} = 0.385 * [(UCS(MPa))_{Num.}]^{1.1655} \quad R^2 = 0.7157 \quad \dots (5.19)$$

- 3- From Figure (5.70) for the merged data, the numerical results of uniaxial compressive strength given by the *UDEC* for the models containing voids with different shape, size, distribution and uniformity (all voids) are in decent relationship with experimental results of uniaxial compression on the cubes. The correlation of *UCS* is followed power trend and can be represented best by the following equation:

$$[UCS(MPa)]_{Exp.} = 0.2613 * [(UCS(MPa))_{Num.}]^{1.2738} \quad R^2 = 0.7809 \quad \dots (5.20)$$

Similarly, after excluding the results for models containing large unisize circular voids, the numerical results showed better correlation, as shown in Figure (5.71), and can be represented best by the following equation:

$$[UCS(MPa)]_{Exp.} = 0.2382 * [(UCS(MPa))_{Num.}]^{1.3125} \quad R^2 = 0.847 \quad \dots (5.21)$$

- 4- The numerical results of *E* given by the *UDEC* for the models containing circular voids with different size, distribution, and uniformity are in moderate relationship with those obtained from the experimental results carried out on the cubes. The correlation of *E* is followed power trend, as shown in Figure (5.72), and can be represented best by the following equation:

$$[E(\text{GPa})]_{Exp.} = 1.0944 * [(E(\text{GPa}))_{Num.}]^{0.894} \quad R^2 = 0.6116 \quad \dots (5.22)$$

However, after excluding the results for models containing large unisize circular voids, the numerical results did not show any change, as shown in Figure (5.73), and the relationship can be represented best by the following equation:

$$[E(\text{GPa})]_{Exp.} = 1.0071 * [(E(\text{GPa}))_{Num.}]^{0.9338} \quad R^2 = 0.6133 \quad \dots (5.23)$$

- 5- For the models containing non-circular voids, the numerical results of Young's modulus given by the UDEC showed poor relationship with those obtained from the experimental results carried out on the cubes. The correlation of Young's modulus is also followed power trend, as shown in Figure (5.74), and can be represented best by the following equation:

$$[E(\text{GPa})]_{Exp.} = 2.5351 * [(E(\text{GPa}))_{Num.}]^{0.5668} \quad R^2 = 0.3219 \quad \dots (5.24)$$

- 6- From Figure (5.75), the numerical results of Young's modulus given by the UDEC for the models containing voids with different shape, size, distribution and uniformity (all voids) are in moderate relationship with those obtained from the experimental results carried out on the cubes. The correlation of Young's modulus is followed power trend and can be represented best by the following equation:

$$[E(\text{GPa})]_{Exp.} = 1.2201 * [(E(\text{GPa}))_{Num.}]^{0.8534} \quad R^2 = 0.5681 \quad \dots (5.25)$$

However, after excluding the results for models containing large unisize circular voids, the numerical results showed a moderate power correlation with smaller R^2 , as shown in Figure (5.76), and can be represented best by the following equation:

$$[E(\text{GPa})]_{Exp.} = 1.2404 * [(E(\text{GPa}))_{Num.}]^{0.8512} \quad R^2 = 0.5471 \quad \dots (5.26)$$

According to the results, the two-dimensional plane strain results gave a good relationship with three-dimensional experimental results. However, the relationship for UCS is stronger than the relationship for E . The correlation can be represented best by power equation as follows:

$$(\text{Experimental Results})_{3D} = a * [(\text{Numerical Results})_{2D}]^b \quad \dots (5.27)$$

Or

$$\text{Three - Dimensional} = a * (\text{Two - Dimensional Plane Strain})^b \quad \dots (5.28)$$

Where a and b are constants. Their values vary depending on void geometry and type of the mechanical properties. Regarding this numerical analysis for Hydro-StoneTB[®] porous cubes using UDEC (version 3.1) with Voronoi tessellation having average block size of 3.5 mm, the value of a and b varied from 0.1955 to 2.5351 and 0.5668 to 1.376 respectively.

For uniaxial compressive strength, the value of a varied from 0.1955 to 0.385. The minimum value, $a = 0.1955$, was for numerical models containing unisize circular voids except those containing large unisize circular void. The maximum value was for the numerical models containing non-circular voids. For numerical models containing voids with different geometry, all voids, the value of a was 0.2613. The value reduced to

0.2382 for numerical models containing voids with different geometry, all voids, except those containing large unisize circular voids. The value of a for Young's modulus varied from 1.0071 to 2.5351. The minimum value, $a = 1.0071$, was for numerical models containing circular voids except those containing large unisize circular void. The maximum value, $a = 2.5351$, was for the numerical models containing non-circular voids. For numerical models containing voids with different geometry (all voids) the value of a was 1.2201. While the value increased to 1.2404 for numerical models containing voids with different geometry (all voids) except those containing large unisize circular void.

Regarding b values, for uniaxial compressive strength, the value of b varied from 1.1655 to 1.378. The minimum value, $b = 1.1655$, was for numerical models containing non-circular voids. The maximum value was for the numerical models containing unisize circular voids except those containing large unisize circular void. For numerical models containing voids with different geometry (all voids) the value of b was 1.2738. The value increased to 1.3125 for numerical models containing voids with different geometry, all voids, except those containing large unisize circular voids. The value of b for Young's modulus varied from 0.5668 to 0.9338. The minimum value, $b = 0.5668$, was for the numerical models containing non-circular voids. The maximum value, $b = 0.9186$, was for numerical models containing circular voids except those containing large unisize circular void. For numerical models containing voids with different geometry (all voids) the value of b was 0.8535. While the value did not change (0.8512) for numerical models containing voids with different geometry, all voids, except those containing large unisize circular void.

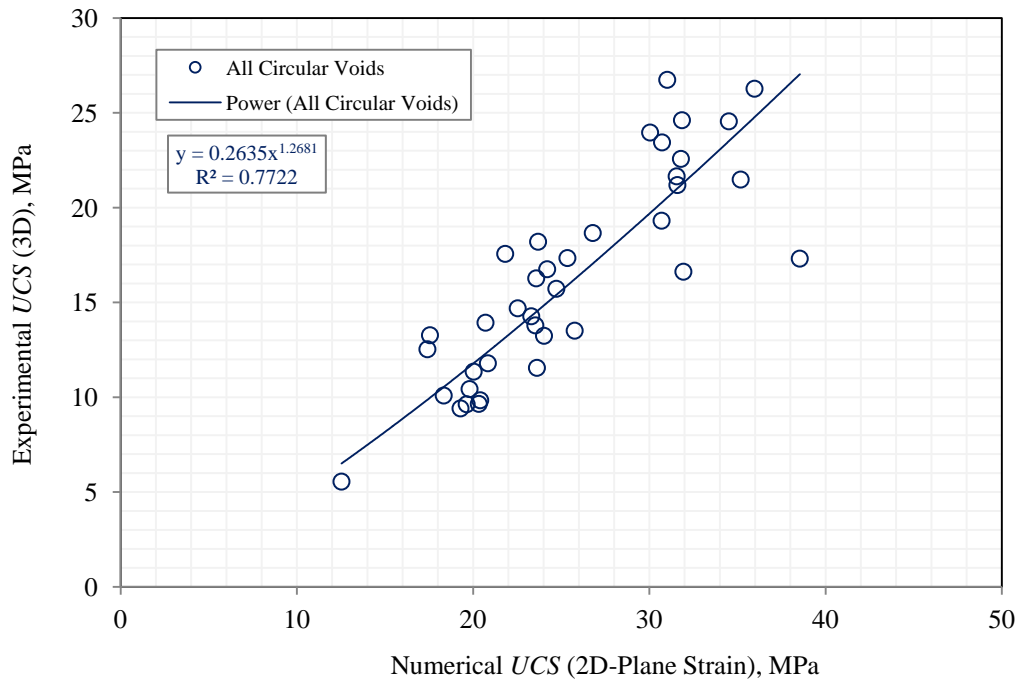


Figure (5.67) Experimental *UCS* versus Numerical *UCS* for Specimens Containing Circular Voids with Different Geometry

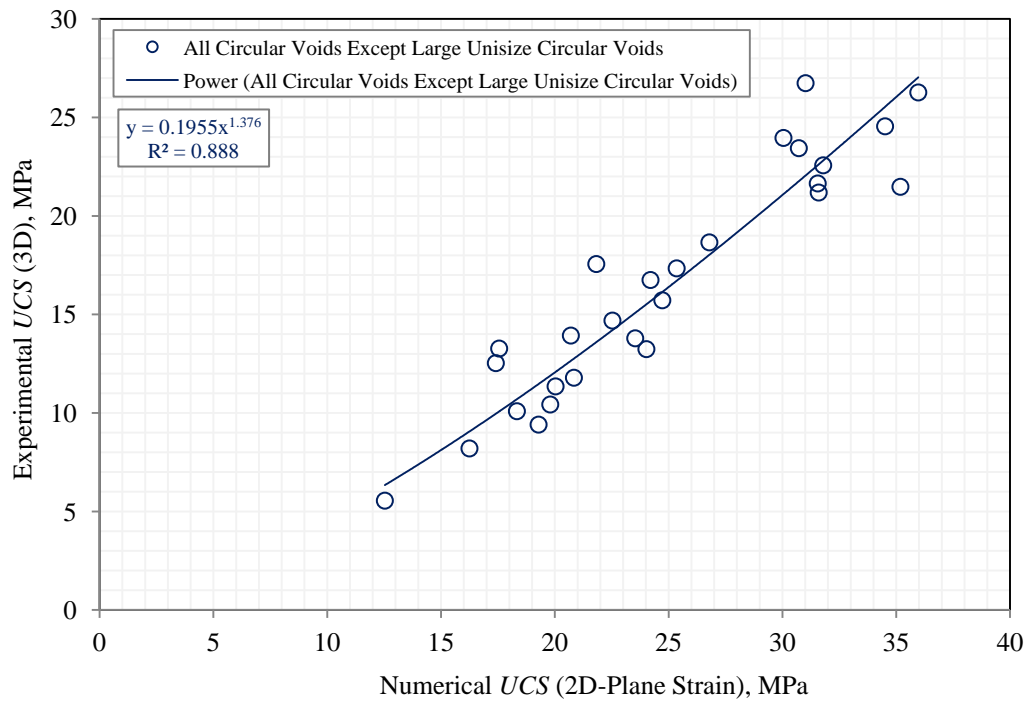


Figure (5.68) Experimental *UCS* versus Numerical *UCS* for Specimens Containing Circular Voids Having Different Geometry

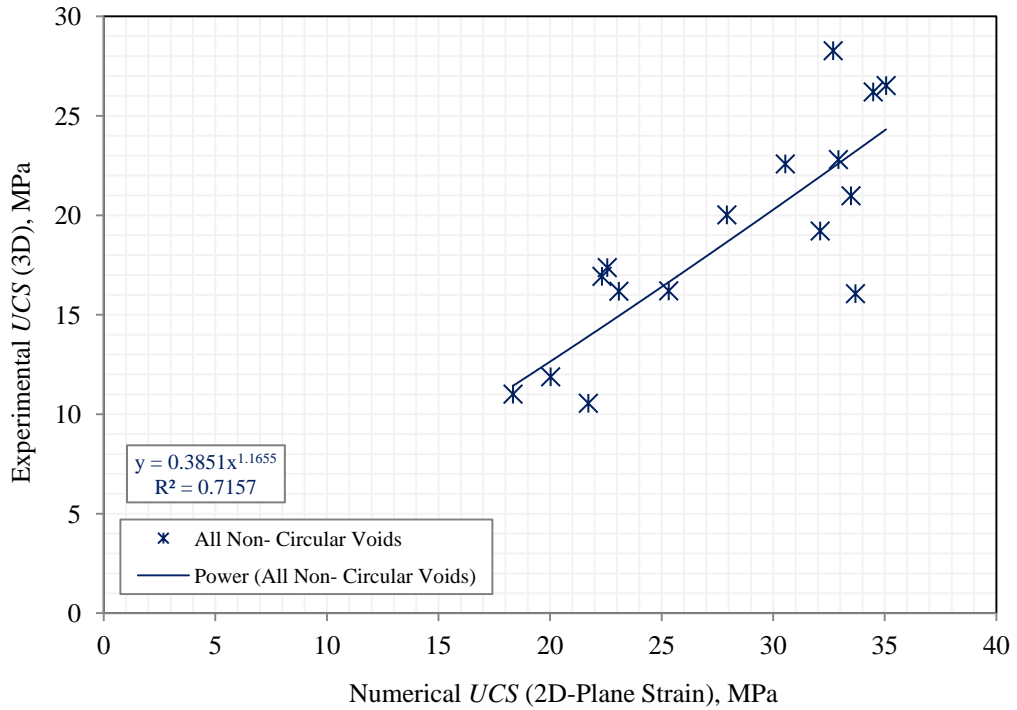


Figure (5.69) Experimental *UCS* versus Numerical *UCS* for Specimens Containing Non-circular Voids Having Different Geometry

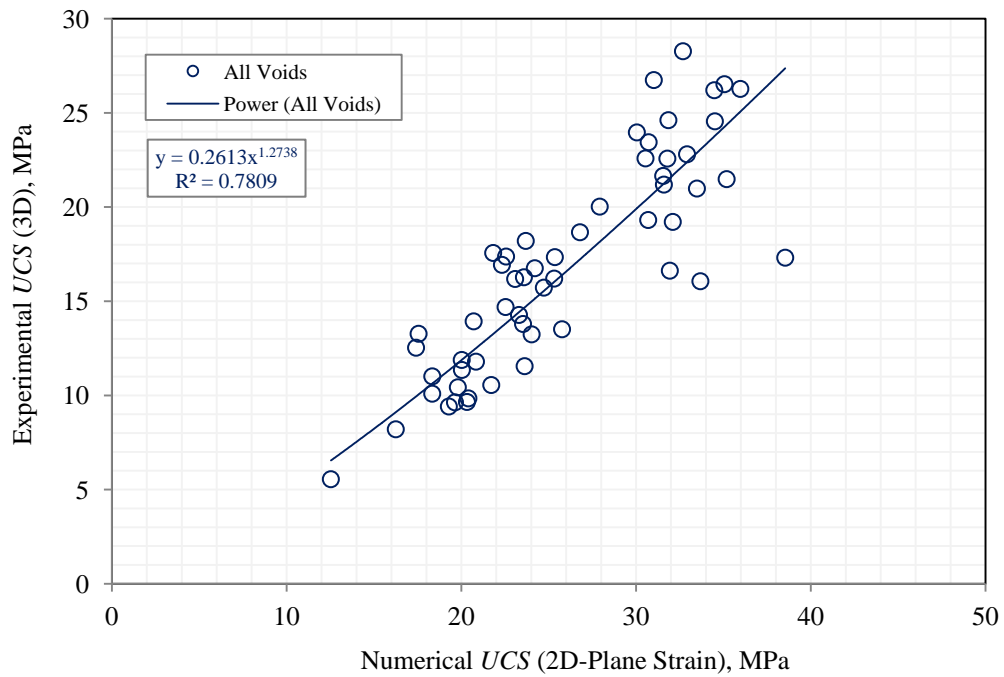


Figure (5.70) Experimental *UCS* versus Numerical *UCS* for Specimens Containing Voids with Different Geometry – All Voids

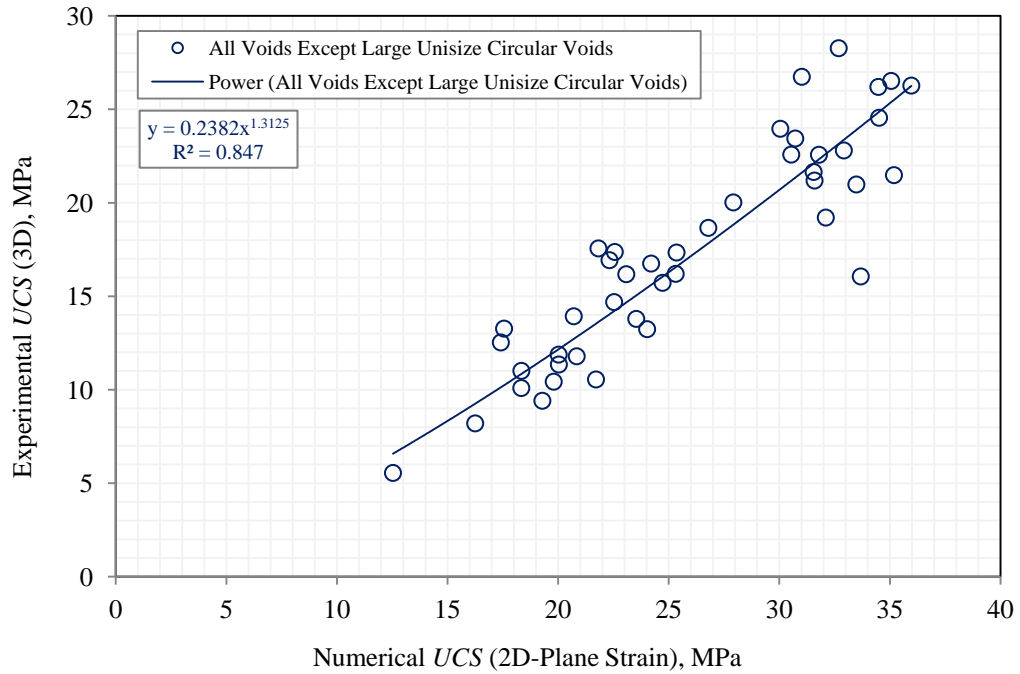


Figure (5.71) Experimental *UCS* versus Numerical *UCS* for Specimens Containing Voids with Different Geometry – All Voids except Large Unisize Circular Voids

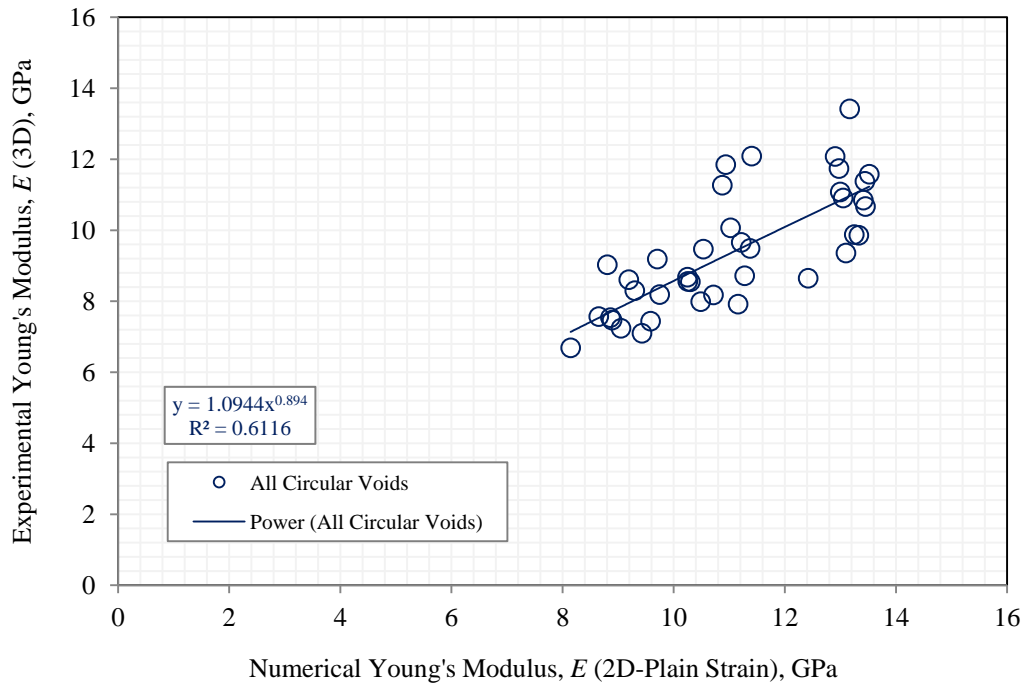


Figure (5.72) Experimental *E* versus Numerical *E* for Specimens Containing Voids with Different Geometry – All Circular Voids

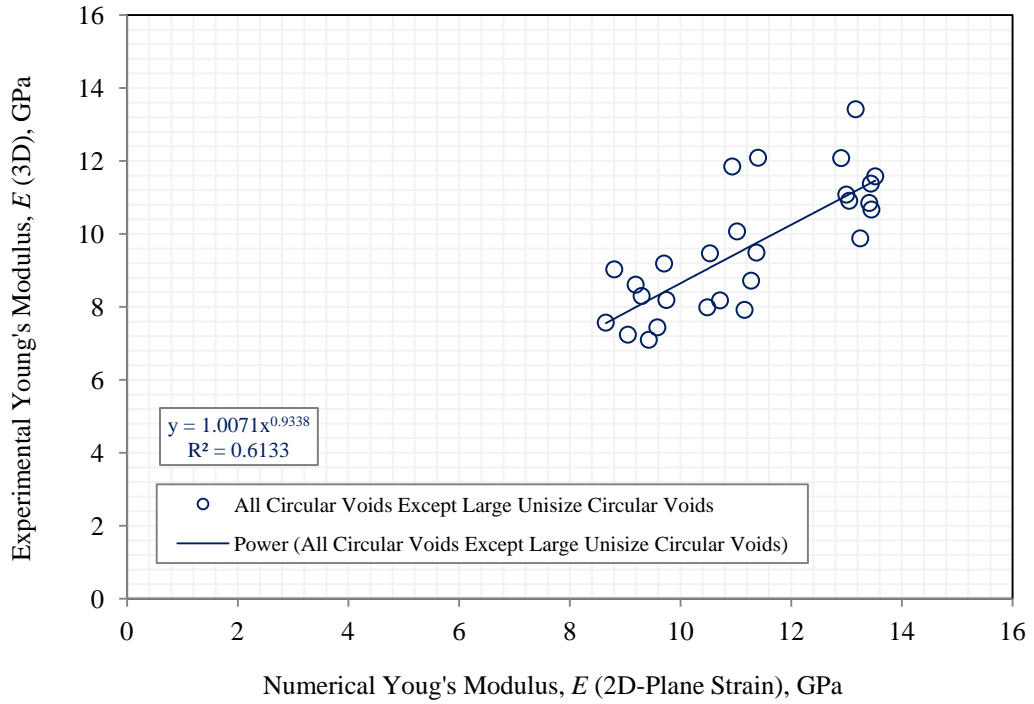


Figure (5.73) Experimental E versus Numerical E for Specimens Containing Voids with Different Geometry – All Voids except Large Unisize Circular Voids

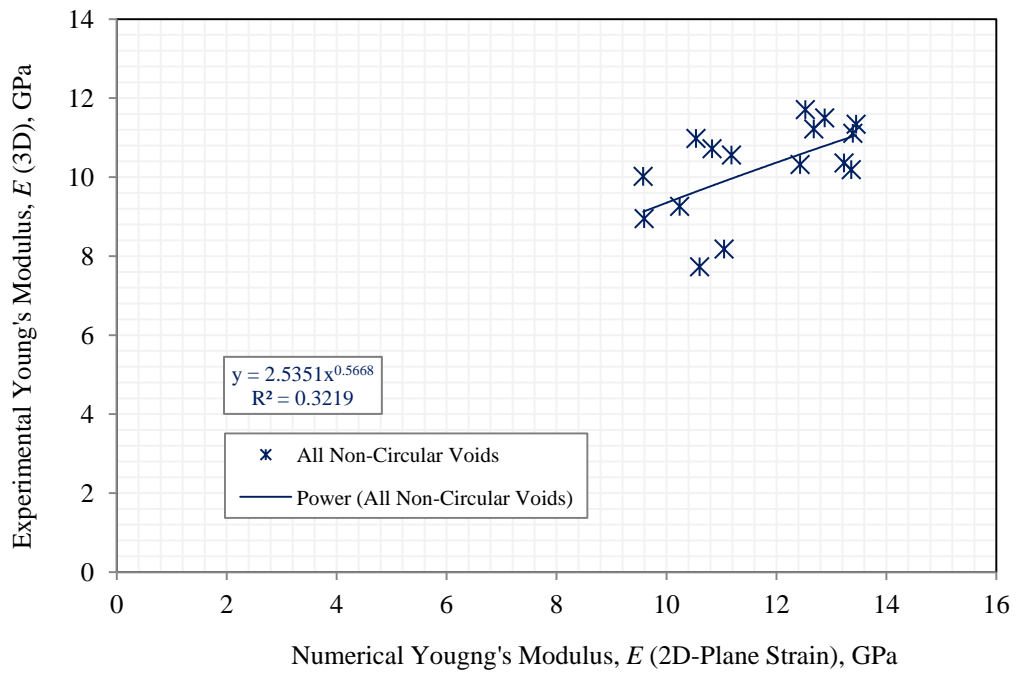


Figure (5.74) Experimental Experimental E versus Numerical E for Specimens Containing Non-Circular Unisize Voids with Different Geometry

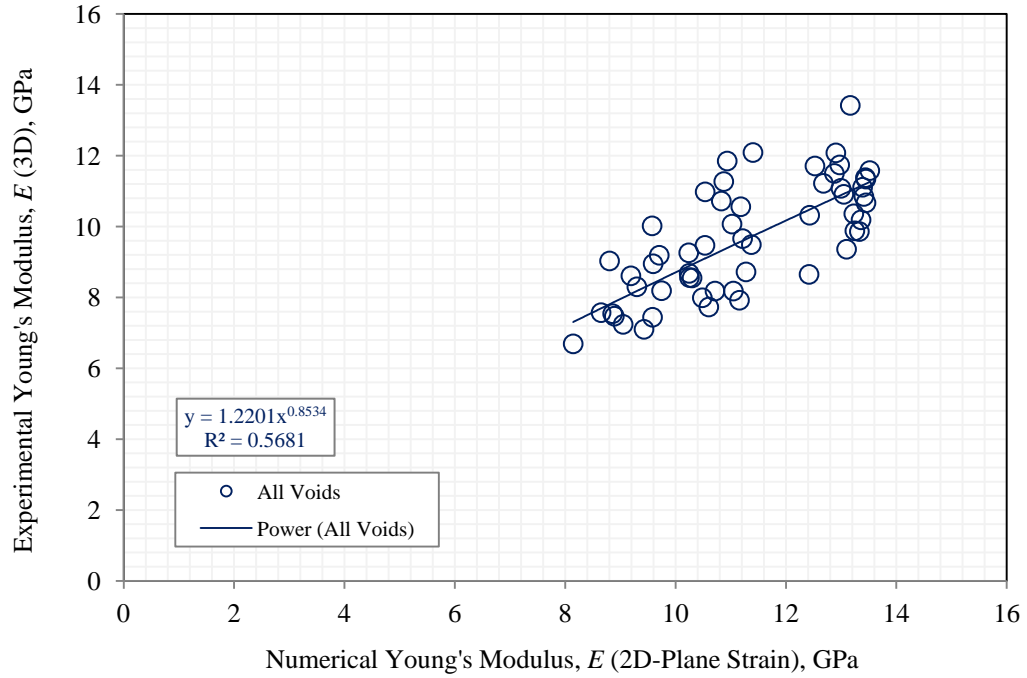


Figure (5.75) Experimental E versus Numerical E for Specimens Containing Voids with Different Geometry – All Voids

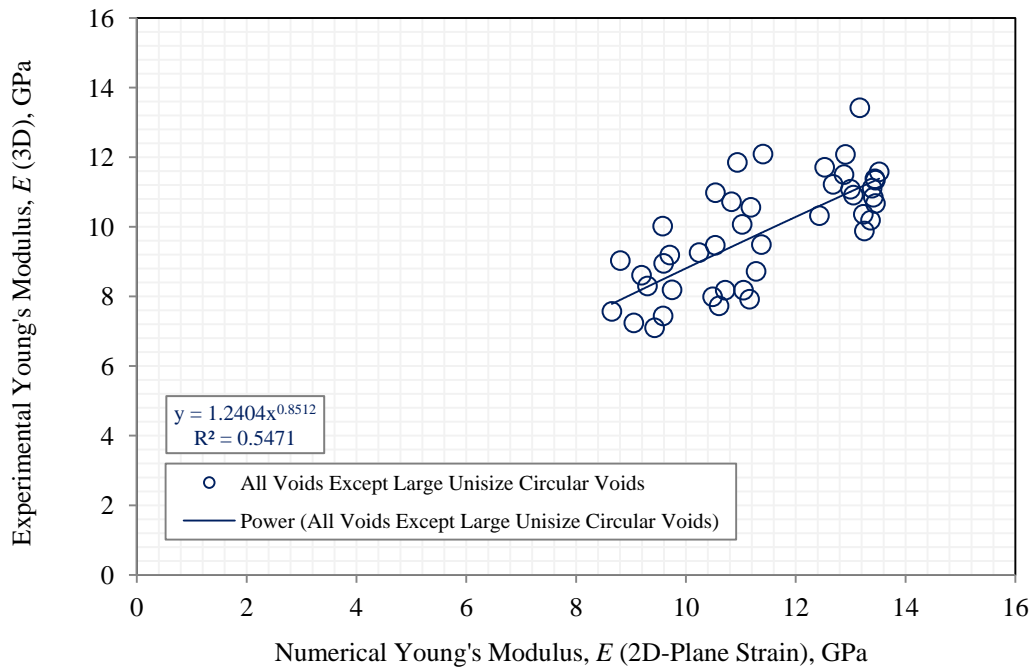


Figure (5.76) Experimental E versus Numerical E for Specimens Containing Voids with Different Geometry – All Voids except Large Unisize Circular Voids

**CHAPTER SIX NUMERICAL SIMULATIONS TO GENERATE NEW MODELS
CONTAINING VOIDS WITH DIFFERENT SHAPES, SIZES, AND DISTRIBUTIONS**

6.1 Introduction

Numerical models are extremely less expensive, not time-consuming, and more controllable compared to experimental tests. Numerical simulations, once created, can be continually changed and modified with extremely less effort. Furthermore, in numerical analysis, material can be simulated at any scales; from the macro-scale, such as simulating the behavior of a tunnel in the abutment of a dam, to micro scale, effects of void porosities on rock mechanical behaviors (Erfourth 2006). For the aforementioned reasons, a new set of numerical models will be created using UDEC to:

- 1- Study the effects of void shapes and their orientations on the mechanical behavior of the rock-like material under uniaxial compression, and
- 2- Validate the hypotheses mentioned in Chapter Four (data analysis); total width of solid column (W) is the second factor which governs the mechanical behavior of rock-like material after void porosity.

6.2 Generate Models to Study the Effects of Void Shape on the Mechanical Properties of Rock-like Material

To explore the effects of void shape exclusively, the other factors such as void porosity, void size, and void distribution, should be kept constant for all the models. To fulfill this requirement, twenty four (24) 152.4 mm porous squares were simulated in UDEC under uniaxial compression. Four different void shapes with two different void

sizes, large (486.1 mm²) and small (244.8 mm²) sizes, and three different porosities (3.2, 6.3, and 12.6%) were studied. The various shapes were circular, square, rectangular (vertical), and triangular (equilateral). Since voids with different sizes and porosities are already leading to different void patterns, only one type of void patterns was studied. The void pattern A as studied in the experimental work, cube, was selected and adopted as the base for comparison purpose with the numerical models. Table (6.1) and Figures (6.1) and (6.2) show the characterizations of model simulated in this section.

Table (6.1) Numerical Models to Simulate the Effects of Void Shapes

Shape of Voids	Size of Voids, (mm)	Number of Voids	Void Porosity, n (%)	Sample Name
Circular	Large, 24.88 mm, (Diameter)	1	3.16	PA-UCL1
		3	6.32	PA-UCL3
		6	12.65	PA-UCL6
	Small, 17.66 mm, (Diameter)	3	3.14	PA-UCS3
		6	6.28	PA-UCS6
		12	12.56	PA-UCS12
Square	Large, 22.05 mm, (Side Length)	1	3.16	PA-USqL1-Vertical
		3	6.32	PA-USqL3-Vertical
		6	12.65	PA-USqL6-Vertical
	Small, 15.65 mm, (Side Length)	3	3.14	PA-USqS3-Vertical
		6	6.28	PA-USqS6-Vertical
		12	12.56	PA-USqS12-Vertical
Rectangular (Vertical)	Large, 15.59 x 31.18 (mm)	1	3.16	PA-URL1-Vertical
		3	6.32	PA-URL3-Vertical
		6	12.65	PA-URL6-Vertical
	Small, 11.06 x 22.13 (mm)	3	3.14	PA-URS3-Vertical
		6	6.28	PA-URS6-Vertical
		12	12.56	PA-URS12-Vertical
Triangular (Equilateral)	Large, 33.5 mm, (Side Length)	1	3.16	PA-TCL1-Straight
		3	6.32	PA-TCL3-Straight
		6	12.65	PA-TCL6-Straight
	Small, 23.78 mm, (Side Length)	3	3.14	PA-TCS3-Straight
		6	6.28	PA-TCS6-Straight
		12	12.56	PA-TCS12-Straight

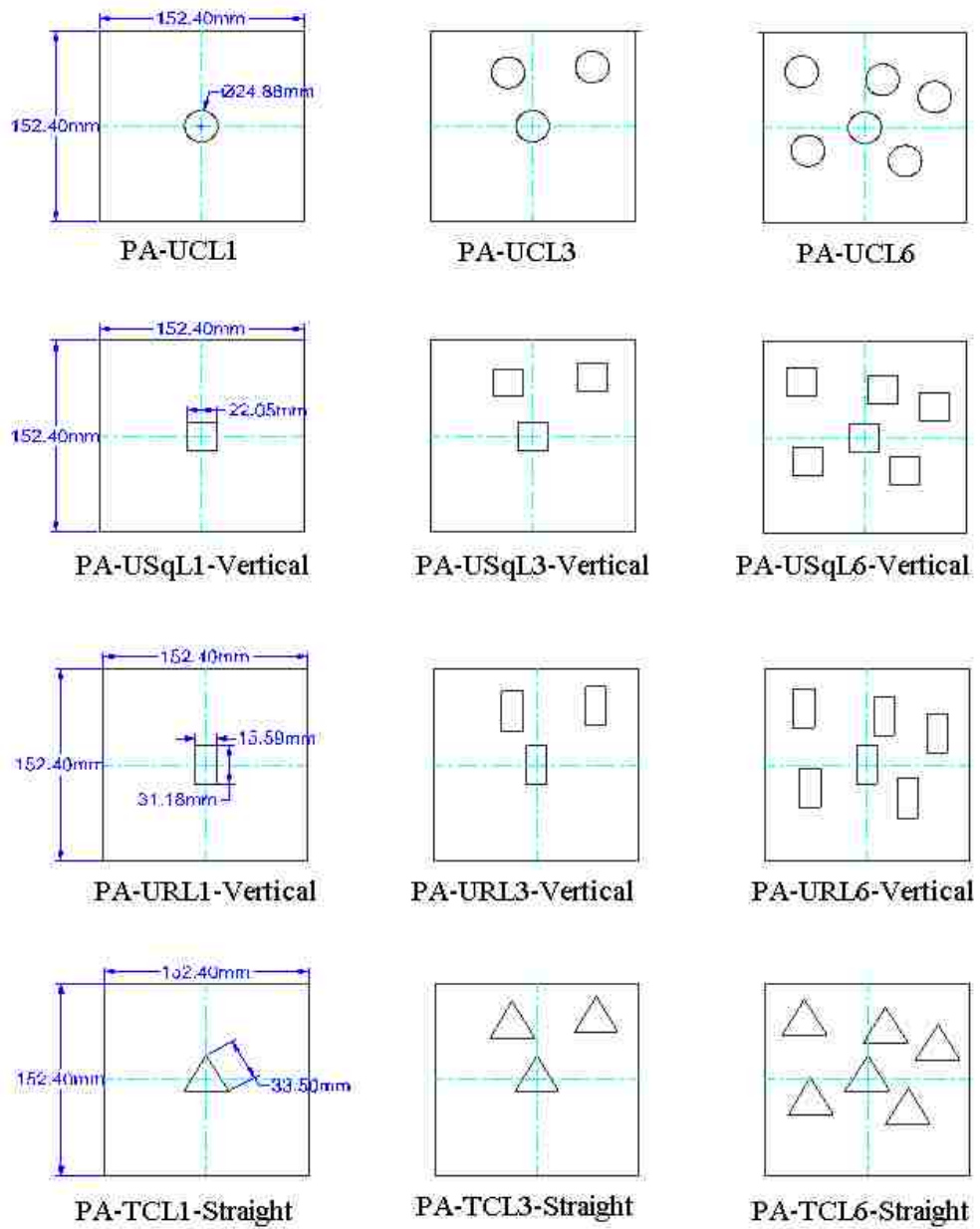


Figure (6.1) Numerical Models to Simulate the Effects of Void Shapes – Large Size

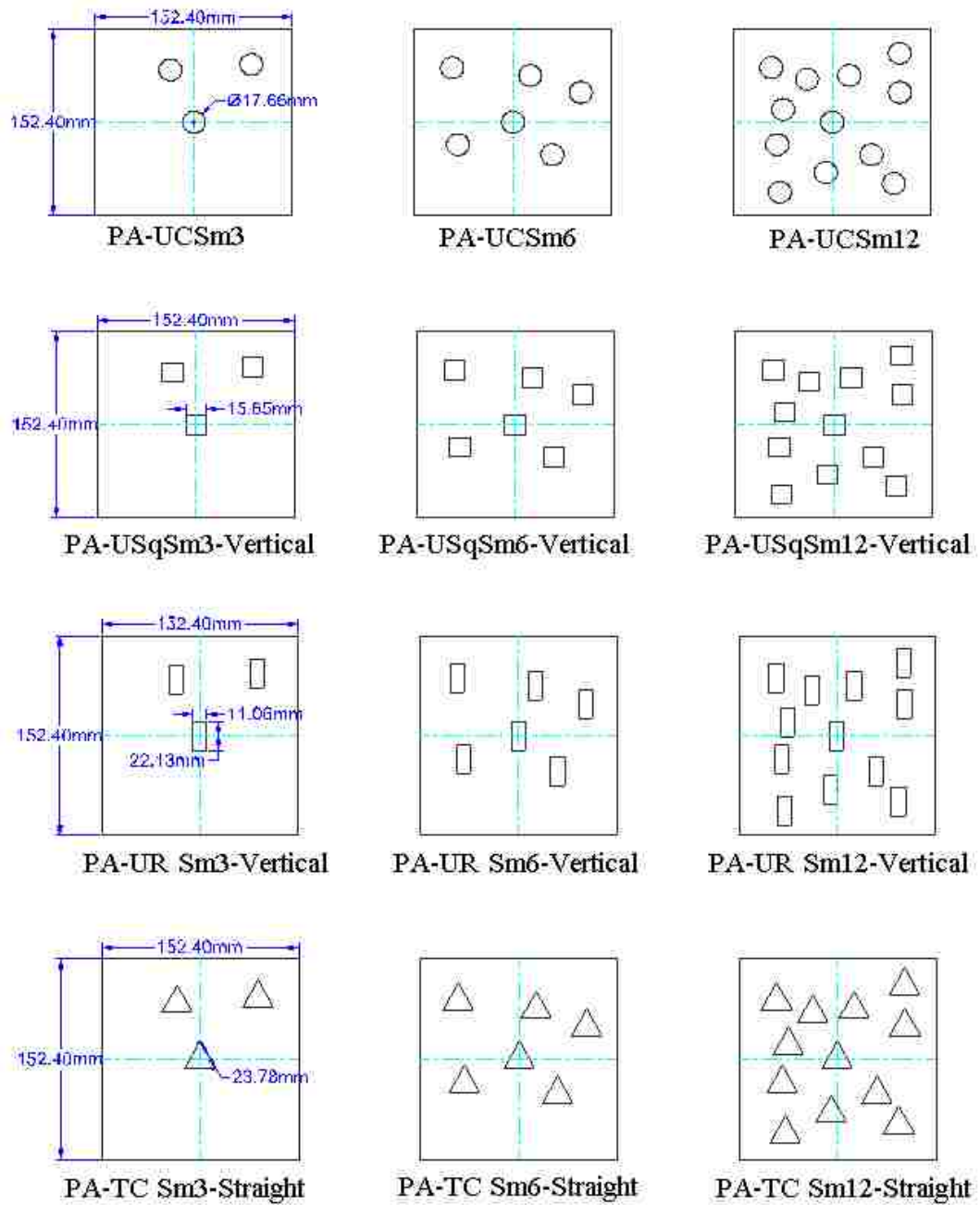


Figure (6.2) Numerical Models to Simulate the Effects of Void Shapes – Small Size

The numerical results, uniaxial compressive strength (*UCS*) and Young's modulus (*E*), for simulated are shown in Table (6.2) and Figures (6.3) to (6.9). According to the results, the following observations can be discussed:

- 1- For the void porosities ranging from 3% to 13%, from Figures (6.3) to (6.6), the numerical results showed decreases in both *UCS* and *E* with increasing void porosity.
- 2- The various void shapes studied in this numerical analysis gave discernible effects on the mechanical properties. For the same void porosity and regardless of the void size, the numerical models containing unisize rectangular (vertical) voids gave the highest compressive strength and modulus of elasticity; while, the numerical models containing unisize triangular (equilateral) voids gave the lowest compressive strength and modulus of elasticity, see Figures (6.3) to (6.6). In other words, regardless of void size, the numerical models with unisize vertical rectangular voids were stronger and stiffer compared to the other models.
- 3- From Figures (6.3) and (6.4), for the same porosity, the models with large square voids are slightly stronger than models with large circular voids. However, for the models with small voids, the results did not follow specific trend; for the void porosities of 3.14% and 6.28%, the models with small square voids were stronger than those with small circular voids, while for the void porosity of 12.56%, the models with small circular voids were stronger than those with small square voids. Regarding Young's modulus, the two different shapes (square and circular voids) did not show any difference; the Young's Moduli for the models

containing unisize square voids were similar to the models containing circular voids regardless the void sizes and void porosity, see Figures (6.5) and (6.6)

- 4- From Figures (6.3) to (6.6), for the same void porosity, the numerical models containing unisize voids gave different values for both *UCS* and *E*. However, the differences in *UCS* are higher than those in *E*.
- 5- The differences in both *UCS* and *E* for different void shapes linearly increased with void porosity increasing as shown in Figures (6.7) and (6.8) and Table (6.3). For models with large voids, the difference in *UCS* for models containing six voids (20.905 MPa) is larger by about four times than the differences in *UCS* for models containing only one void (5.992 MPa), while it is about two times for *E* (3.868 GPa for models containing six voids and 1.550 GPa for models containing one voids). For models with small voids, the difference in *UCS* for models containing twelve voids (12.067 MPa) is about twofold larger than the differences in *UCS* for models containing only three voids (6.888 MPa), while, it is higher by 60% for *E* (1.835 GPa for models containing twelve voids and 1.142 GPa for models containing three voids).
- 6- The relationship between *UCS* and *E* for all numerical models is plotted in Figure (6.9). The results gave a very decent power correlation, and it can be represented best by the following equation:

$$UCS(\text{MPa}) = 0.257 * [E(\text{GPa})]^{1.9047} \quad R^2 = 0.9403 \quad \dots (6.1)$$

Table (6.2) Numerical Models Containing Unisize Large Voids with Different Shapes

Model Name	Void Shape	Porosity (<i>n</i>)	Numerical <i>UCS</i>	Numerical <i>E</i> (25-50%)
		%	MPa	GPa
PA-UCL1	Circular	3.16	41.059	2.566
PA-UCL3		6.32	32.076	2.005
PA-UCL6		12.65	24.762	1.548
PA-UCS3		3.14	42.489	14.615
PA-UCS6		6.28	31.845	13.271
PA-UCS12		12.56	26.566	11.192
PA-USqL1-Vertical	Square	3.16	44.432	15.203
PA-USqL3-Vertical		6.32	33.477	13.358
PA-USqL6-Vertical		12.65	25.315	10.536
PA-USqS3-Vertical		3.14	44.174	14.570
PA-USqS6-Vertical		6.28	34.478	13.390
PA-USqS12-Vertical		12.56	22.562	11.182
PA-URL1-Vertical	Rectangular (Vertical)	3.16	46.723	15.340
PA-URL3-Vertical		6.32	41.722	13.892
PA-URL6-Vertical		12.65	34.656	11.961
PA-URS3-Vertical		3.14	44.592	15.132
PA-URS6-Vertical		6.28	39.360	14.052
PA-URS12-Vertical		12.56	29.974	11.811
PA-TCL1-Straight	Triangular (Equilateral)	3.16	40.731	13.790
PA-TCL3-Straight		6.32	30.186	11.972
PA-TCL6-Straight		12.65	13.751	8.092
PA-TCS3-Straight		3.14	37.705	13.990
PA-TCS6-Straight		6.28	29.974	11.811
PA-TCS12-Straight		12.56	17.907	9.976

Table (6.3) Differences in *UCS* and *E* for Numerical Models Containing Large Voids

Void Porosity, <i>n</i>	Differences in <i>UCS</i> (MPa)		Differences in <i>E</i> (25-50%) (GPa)	
	Large Voids	Small Voids	Large Voids	Small Voids
%				
0.00	0	0	0	0
3.16	5.992	6.888	1.550	1.142
6.32	11.536	9.386	1.921	2.242
12.65	20.905	12.067	3.868	1.835

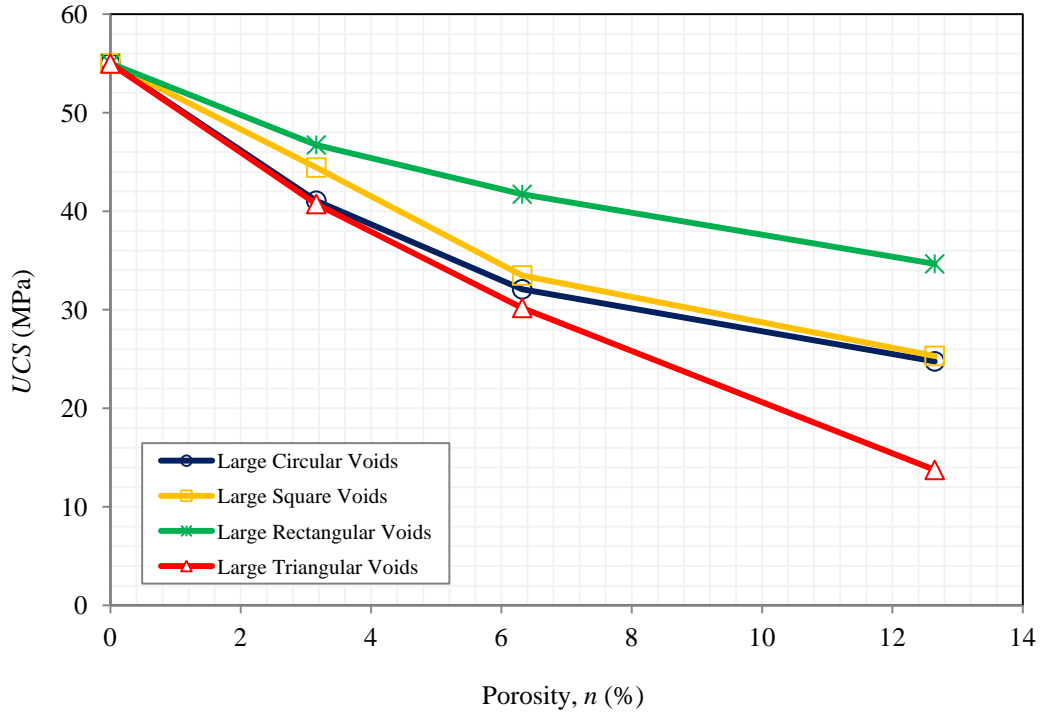


Figure (6.3) Compression Strength versus Void Porosity for Numerical Models Containing Large Unisize Voids

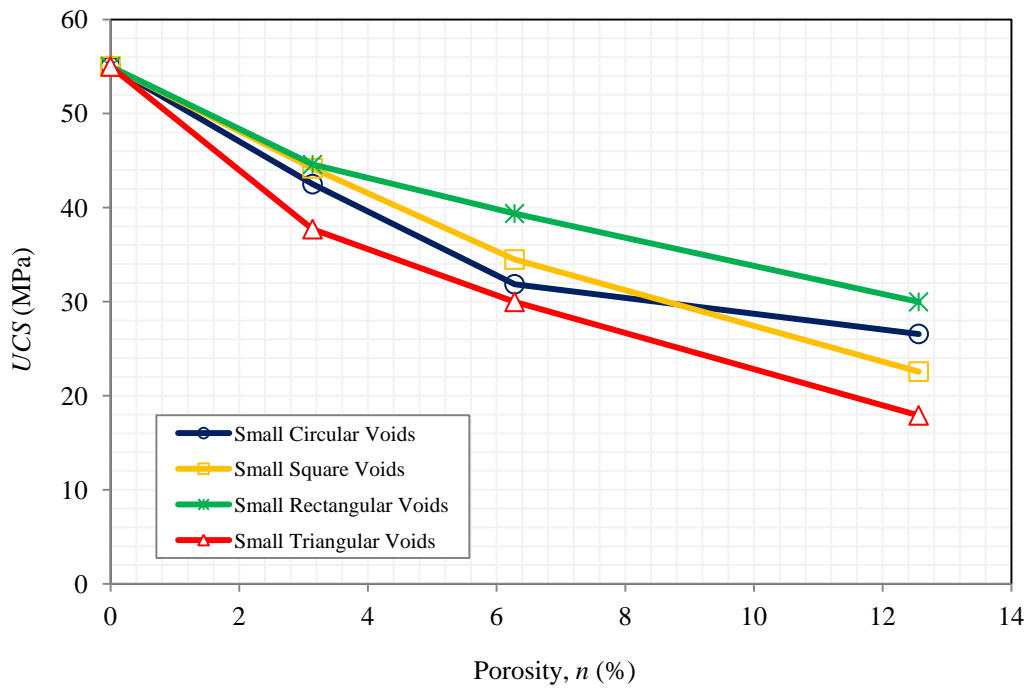


Figure (6.4) Compression Strength versus Void Porosity for Numerical Models Containing Small Unisize Voids

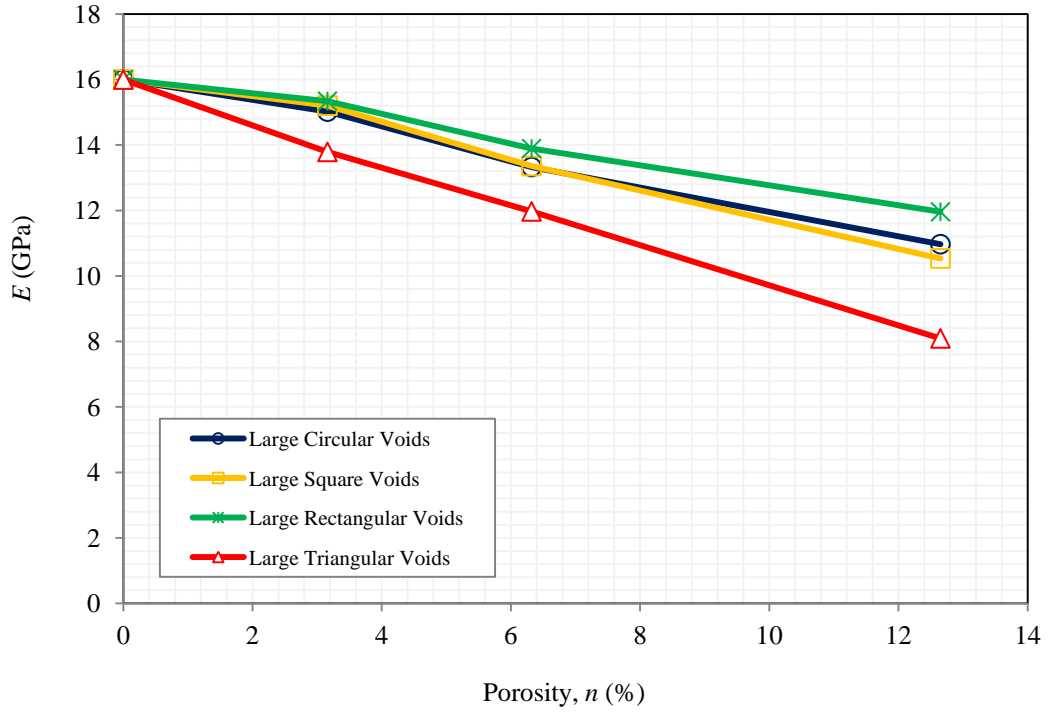


Figure (6.5) Deformation versus Void Porosity for Numerical Models Containing Large Unisize Voids

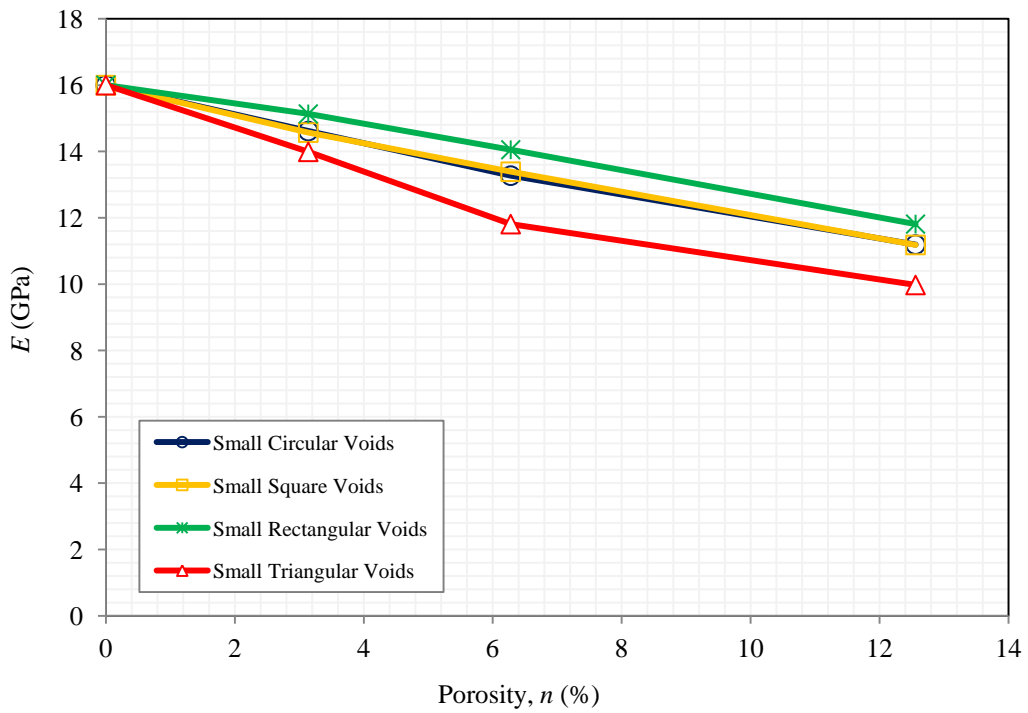


Figure (6.6) Deformation versus Void Porosity for Numerical Models Containing Small Unisize Voids

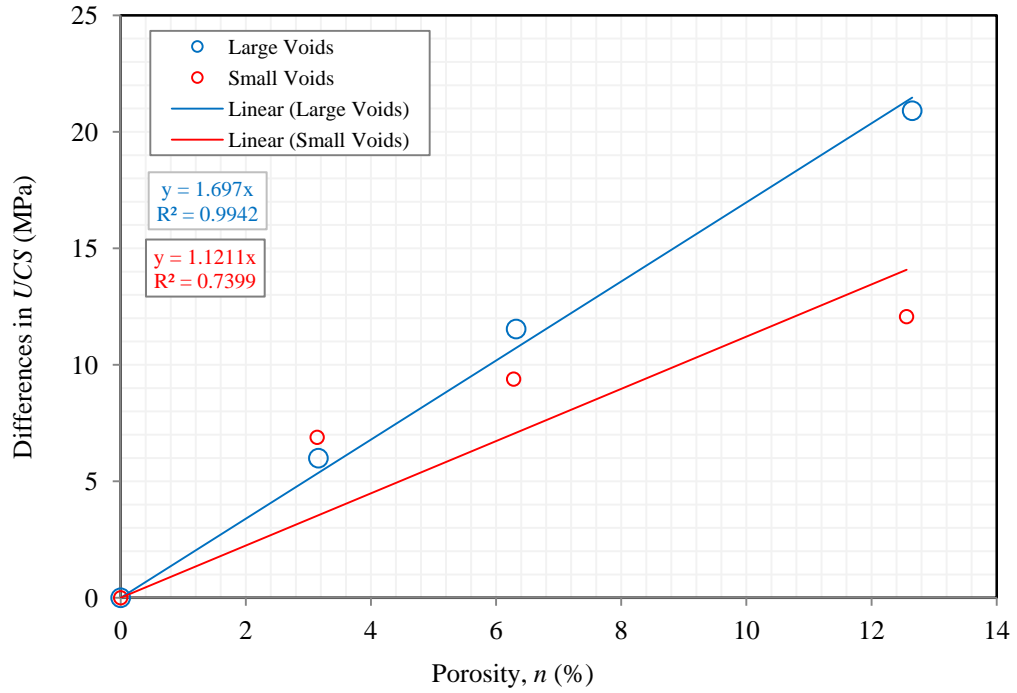


Figure (6.7) Differences in Uniaxial Compression versus Void Porosity for Numerical Models Containing Unisize Voids – Both Large and Small Sizes

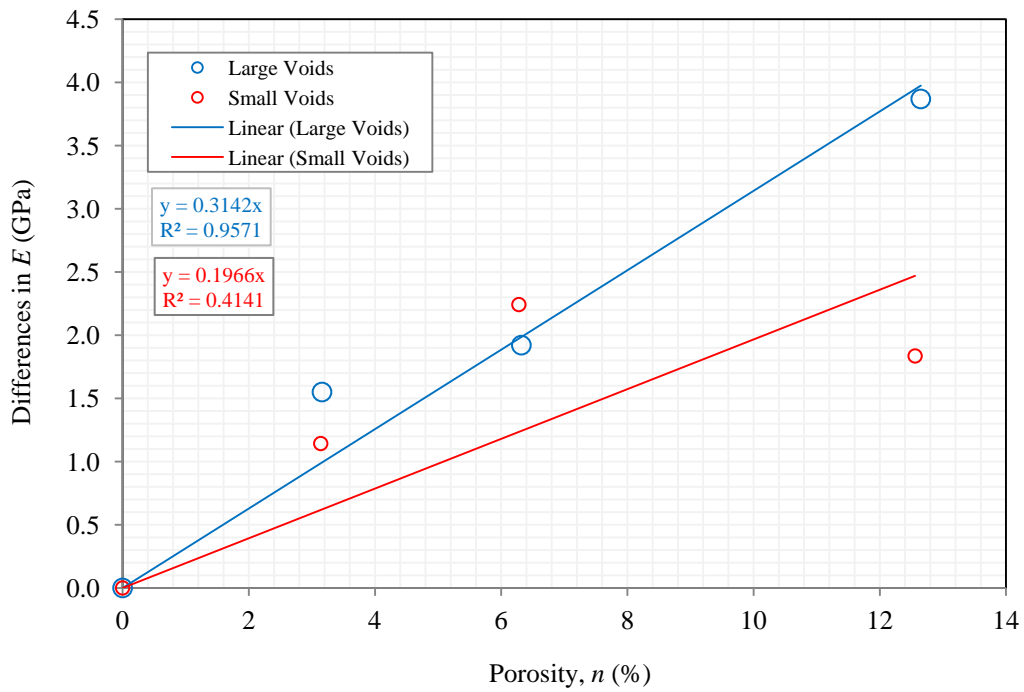


Figure (6.8) Differences in Deformation versus Void Porosity for Numerical Models Containing Unisize Voids – Both Large and Small Sizes

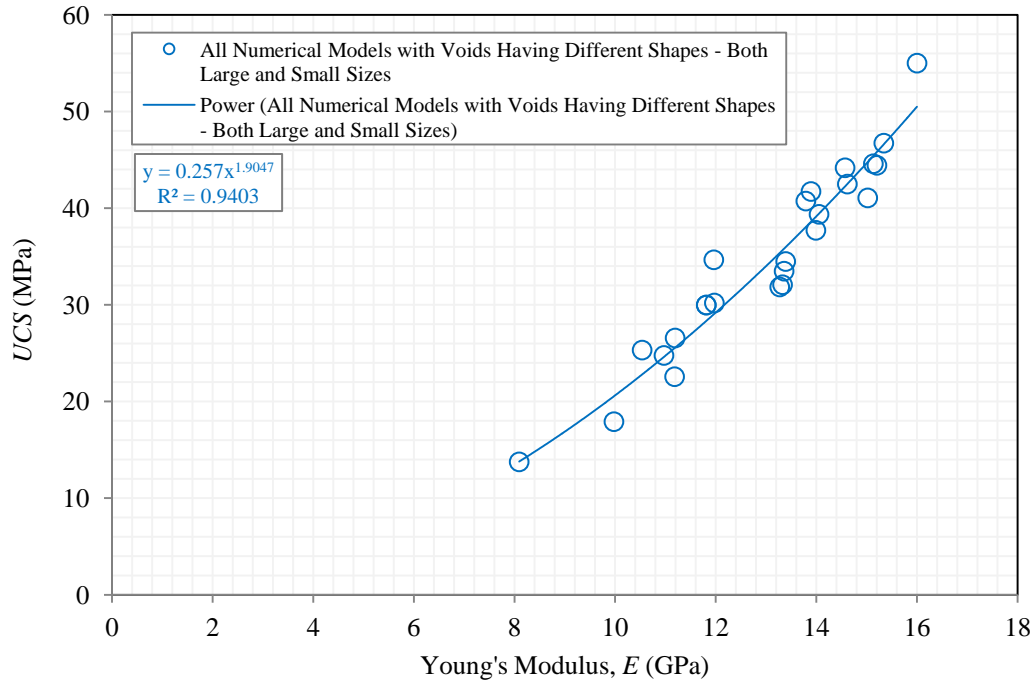


Figure (6.9) Compression Strength versus Deformation for Numerical Models Containing Unisize Voids – Both Large and Small Sizes

6.3 Numerical Simulations to Study the Effects of Void Orientations on the Mechanical Properties of Rock-like Material

Rotating the square voids in the cubes tested in the work of Project Activity Task ORD-FY04-013 by 45 degree to obtain porous cubes with diamond shape voids reduced the uniaxial compressive strength of the cubes by 9% on average. Since both square voids and diamond voids have the same shape and corner sharpness, the void rotation which led to larger void width, (the void dimension perpendicular to the maximum compression stress) might case the decrease in the cube’s strength. Accordingly, to check if the void orientation has effects on the mechanical properties of rock-like materials, 152.4 mm porous squares with the same void porosity, void size, and void distribution, but different orientation were simulated under uniaxial compression in UDEC. The only parameter

changed was void orientation through rotating the voids by either 45 degree or 90 degree or both. Three different void shapes (square, rectangular, and triangular) with two different void sizes (large and small sizes) were studied to check the effects of void orientation on the mechanical properties of the numerical models. For the models with square voids, one void orientation (45 degree to obtain diamond shapes) was studied; while for the models with either rectangular voids or triangular voids two different void orientations (45 degree and 90 degree) were studied. Figure (6.10) and Table (6.4) show the characterizations of the model simulated in this section.

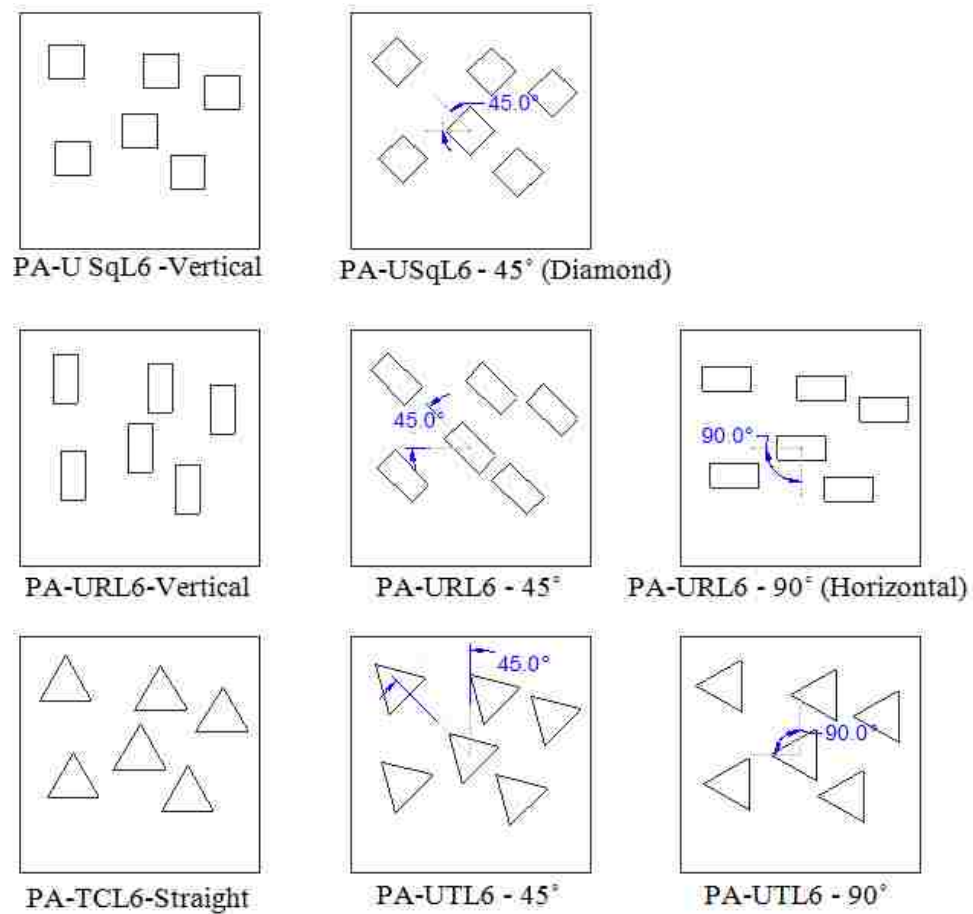


Figure (6.10) Numerical Models to Simulate the Effects of Void Orientation– Large Size

Table (6.4) Numerical Models Containing Unisize Voids with Different Orientations

Shape of Voids	Size of Voids (mm)	Void Rotation	Number of Voids	Void Porosity, n (%)	Sample Name
Square	Large, 22.05 mm, (Side Length)	0-degree (vertical)	1	3.16	PA-USqL1-Vertical
			3	6.32	PA-USqL3-Vertical
			6	12.65	PA-USqL6-Vertical
		45-degree (Diamond)	1	3.16	PA-USqL1- 45° (Diamond)
			3	6.32	PA-USqL3- 45° (Diamond)
			6	12.65	PA-USqL6- 45° (Diamond)
Rectangular	Large, 15.59 x 31.18 (mm)	0-degree (vertical)	1	3.16	PA-URL1-Vertical
			3	6.32	PA-URL3-Vertical
			6	12.65	PA-URL6-Vertical
		45-degree	1	3.16	PA-URL1-45°
			3	6.32	PA-URL3-45°
			6	12.65	PA-URL6-45°
		45-degree (Horizontal)	1	3.16	PA-URL1-90° (Horizontal)
			3	6.32	PA-URL3-90° (Horizontal)
			6	12.65	PA-URL6-90° (Horizontal)
Triangular (Equilateral)	Large, 33.5 mm, (Side Length)	0-degree (vertical)	1	3.16	PA-UTL1-Straight
			3	6.32	PA-UTL3-Straight
			6	12.65	PA-UTL6-Straight
		45-degree	1	3.16	PA-URL1-45°
			3	6.32	PA-URL3-45°
			6	12.65	PA-URL6-45°
		90-degree (Horizontal)	1	3.16	PA-URL1-90°
			3	6.32	PA-URL3-90°
			6	12.65	PA-URL6-90°
Square	Small, 11.0 mm, (Side Length)	0-degree (vertical)	1	3.14	PA-USqS3-Vertical
			3	6.28	PA-USqS6-Vertical
			6	12.56	PA-USqS12-Vertical
		45-degree (Diamond)	1	3.14	PA-USqS3-45° (Diamond)
			3	6.28	PA-USqS6-45° (Diamond)
			6	12.56	PA-USqS12-45° (Diamond)
Rectangular	Small, 11.06 x 22.13 (mm)	0-degree (vertical)	1	3.14	PA-URS3-Vertical
			3	6.28	PA-URS6-Vertical
			6	12.56	PA-URS12-Vertical
		45-degree	1	3.14	PA-URS3-45°
			3	6.28	PA-URS6-45°
			6	12.56	PA-URS12-45°
		45-degree (Horizontal)	1	3.14	PA-URS3-90° (Horizontal)
			3	6.28	PA-URS6-90° (Horizontal)
			6	12.56	PA-URS12-90° (Horizontal)
Triangular (Equilateral)	Small, 23.78 mm, (Side Length)	0-degree (vertical)	1	3.14	PA-UTS3-Straight
			3	6.28	PA-UTS6-Straight
			6	12.56	PA-UTS12-Straight
		45-degree	1	3.14	PA-URS3-45°
			3	6.28	PA-URS6-45°
			6	12.56	PA-URS12-45°
		90-degree (Horizontal)	1	3.14	PA-URS3-90°
			3	6.28	PA-URS6-90°
			6	12.56	PA-URS12-90°

The numerical results, uniaxial compressive strength (*UCS*) and Young's modulus (*E*), for the simulated (models containing unisize voids with different orientations - 0-degree, 45-degree, and 90-degree) are plotted as a function of void porosity as shown in Figures (6.11) to (6.22). The results are also shown in Tables (6.5) and (6.6). According to the results, the following observations can be discussed:

- 1- Void orientations for models containing large square voids gave different values in uniaxial compressive strength as shown in Figure (6.11) However, for models containing small square voids no differences were observed as shown in Figure (6.12). From Figure (6.11), for the same porosity, the models with large square voids (zero rotation) gave slightly higher uniaxial compressive strength compared to the models with rotated square voids (diamond voids). In addition, the differences in the uniaxial compressive strength values increased with void porosity increasing for models with large voids; they are 1.39, 2.76, and 5.29 MPa for void porosities of 3.16, 6.32 and 12.65% respectively. However, the differences in the uniaxial compressive strength values increased with void porosity increasing for models with small voids; they are 5.9, 2.38, and 1.98 MPa for void porosities of 3.14, 6.28 and 12.56% respectively.
- 2- Regarding the values of Young's modulus, the results for models containing square voids (both large and small sizes) showed slightly higher values compared to the models with 45-degree rotated square voids (diamond voids) as shown in Figures (6.12) and (6.14). The differences increased with void porosity increasing as shown in the figures. The differences for the models with large voids are 0.41, 0.56, and 0.94 MPa for void porosities of 3.16, 6.32 and 12.65% respectively. For

the models with small voids, the differences are 0.25, 0.86, and 0.77 MPa for void porosities of 3.16, 6.32 and 12.65% respectively.

- 3- For models with rectangular voids, both large and small void sizes, the void orientations gave different values in both uniaxial compressive strength and Young's modulus as shown in Figures (6.15) to (6.18). From the figures, for the same porosity, the models with vertical rectangular voids gave higher strength and Young's modulus compared to the models with rotated rectangular voids. In addition, the value of uniaxial compressive strength and Young's modulus for models with rectangular voids rotated by 45-degree were higher than those with rectangular voids rotated by 90-degree. The maximum differences in the uniaxial compressive strength values are 4.8, 14.52, and 17.99 MPa for void porosities of 3.15, 6.3 and 12.6% respectively. In other words, regardless of void size, the numerical models with unisize vertical rectangle voids were stronger and stiffer than the models with rotated rectangular voids.
- 4- The different void orientations for models with triangular (equilateral) voids, both large and small void sizes, did not show distinct effects on the mechanical properties of the numerical models as shown in Figures (6.19) to (6.22). From the figures, except the uniaxial compressive strength for models having void porosity of 12.65% (large voids only), similar reduction in both uniaxial compressive strength and Young's modulus with increasing void porosity was observed regardless of the void size and distribution. However, for the void porosity of 12.65% for large voids, see Figure (6.19), the models with straight triangular

voids had lower strength by 6.8 MPa (12.38%) compared to the models containing rotated equilateral triangular voids (both 45 and 90-degree).

Table (6.5) Numerical Results for Models Containing Unisize Large Voids

Model Name	Porosity (<i>n</i>)	Numerical Values		Normalized Numerical Values	
	%	<i>UCS</i> (MPa)	<i>E</i> (GPa)	<i>UCS</i> (MPa)	<i>E</i> (GPa)
PA-UCL1	3.16	41.059	15.020	0.746	0.939
PA-UCL3	6.32	32.076	13.327	0.583	0.833
PA-UCL6	12.65	24.762	10.970	0.450	0.686
PA-USqL1-Vertical	3.16	44.432	15.203	0.808	0.950
PA-USqL3-Vertical	6.32	33.477	13.358	0.609	0.835
PA-USqL6-Vertical	12.65	25.315	10.536	0.460	0.659
PA-USqL1-45° (Diamond)	3.16	43.041	14.793	0.782	0.925
PA-USqL3-45° (Diamond)	6.32	30.713	12.799	0.558	0.800
PA-USqL6-45° (Diamond)	12.65	20.024	9.593	0.364	0.600
PA-URL1-Vertical	3.16	46.723	15.340	0.849	0.959
PA-URL3-Vertical	6.32	41.722	13.892	0.758	0.868
PA-URL6-Vertical	12.65	34.656	11.961	0.630	0.748
PA-URL1-45°	3.16	45.320	14.748	0.824	0.922
PA-URL3-45°	6.32	31.790	11.931	0.578	0.746
PA-URL6-45°	12.65	16.928	9.014	0.308	0.563
PA-URL1-90° (Horizontal)	3.16	41.922	14.318	0.762	0.895
PA-URL3-90° (Horizontal)	6.32	27.203	11.734	0.494	0.733
PA-URL6-90° (Horizontal)	12.65	16.667	7.826	0.303	0.489
PA-UTL1-Straight	3.16	40.731	13.790	0.740	0.862
PA-UTL3-Straight	6.32	30.186	11.972	0.549	0.748
PA-UTL6-Straight	12.65	13.751	8.092	0.250	0.506
PA-UTL1-45°	3.16	44.329	14.570	0.806	0.911
PA-UTL3-45°	6.32	30.541	12.573	0.555	0.786
PA-UTL6-45°	12.65	20.407	8.006	0.371	0.500
PA-UTL1-90°	3.16	43.170	14.783	0.785	0.924
PA-UTL3-90°	6.32	30.541	12.570	0.555	0.786
PA-UTL6-90°	12.65	20.562	8.992	0.374	0.558

Table (6.6) Numerical Results for Models Containing Unisize Small Voids

Sample Name	Porosity (<i>n</i>)	Numerical Values		Normalized Numerical Values	
	%	<i>UCS</i> (MPa)	<i>E</i> (GPa)	<i>UCS</i> (MPa)	<i>E</i> (GPa)
PA-UCSm3	3.14	42.489	14.615	0.772	0.913
PA-UCSm6	6.28	31.845	13.271	0.579	0.829
PA-UCSm12	12.56	26.566	11.192	0.483	0.700
PA-USqSm3-Vertical	3.14	44.174	14.570	0.803	0.911
PA-USqSm6-Vertical	6.28	34.478	13.390	0.627	0.837
PA-USqSm12-Vertical	12.56	22.562	11.182	0.410	0.699
PA-USqSm3-45° (Diamond)	3.14	38.271	14.323	0.696	0.895
PA-USqSm6-45° (Diamond)	6.28	32.102	12.526	0.584	0.783
PA-USqSm12-45° (Diamond)	12.56	20.584	10.411	0.374	0.651
PA-URSm3-Vertical	3.14	44.592	15.132	0.811	0.946
PA-URSm6-Vertical	6.28	39.360	14.052	0.715	0.878
PA-URSm12-Vertical	12.56	29.974	11.811	0.545	0.738
PA-URSm3-45°	3.16	37.114	14.029	0.675	0.877
PA-URSm6-45°	6.32	28.368	12.073	0.516	0.755
PA-URSm12-45°	12.65	21.703	9.791	0.395	0.612
PA-URSm3-90° (Horizontal)	3.14	34.065	13.763	0.619	0.860
PA-URSm6-90° (Horizontal)	6.28	28.771	11.495	0.523	0.718
PA-URSm12-90° (Horizontal)	12.56	15.479	9.308	0.281	0.582
PA-TCSm3-Straight	3.14	37.705	13.990	0.685	0.874
PA-TCSm6-Straight	6.28	29.974	11.811	0.545	0.738
PA-TCSm12-Straight	12.56	17.907	9.976	0.326	0.623
PA-URSm3-45°	3.16	35.704	14.406	0.649	0.900
PA-URSm6 -45°	6.32	29.792	11.817	0.542	0.739
PA-URSm12-45°	12.65	20.055	9.682	0.365	0.605
PA-URSm3-90°	3.14	36.741	13.980	0.668	0.874
PA-URSm6-90°	6.28	31.001	12.044	0.564	0.753
PA-URSm12-90°	12.56	19.863	10.059	0.361	0.629

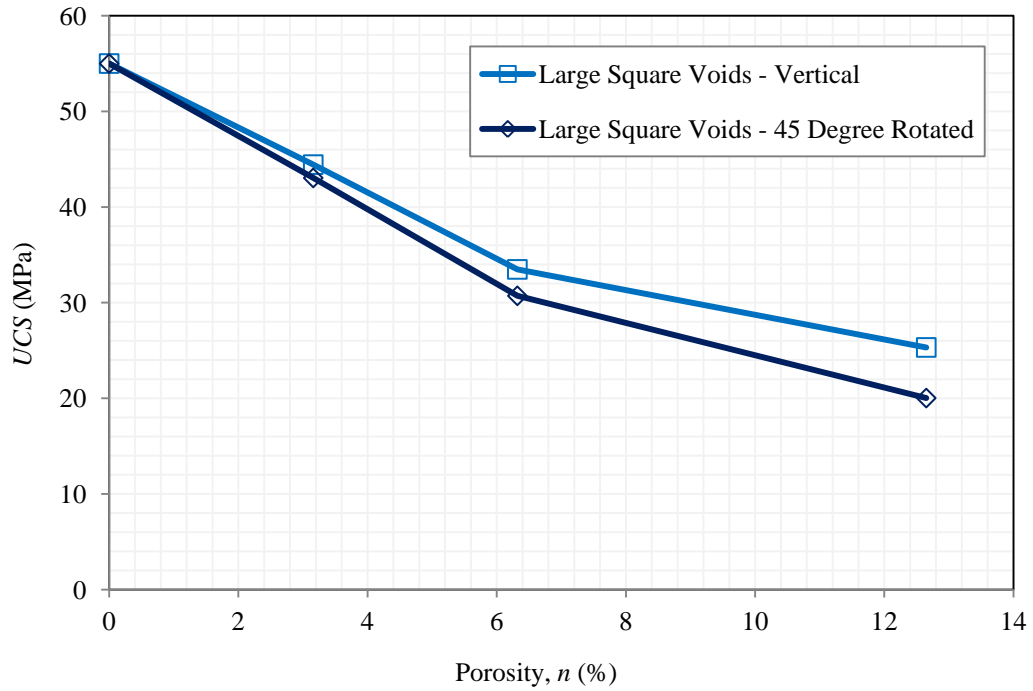


Figure (6.11) Compression Strength versus Void Porosity for Numerical Models Containing Large Unisize Voids – Square Voids

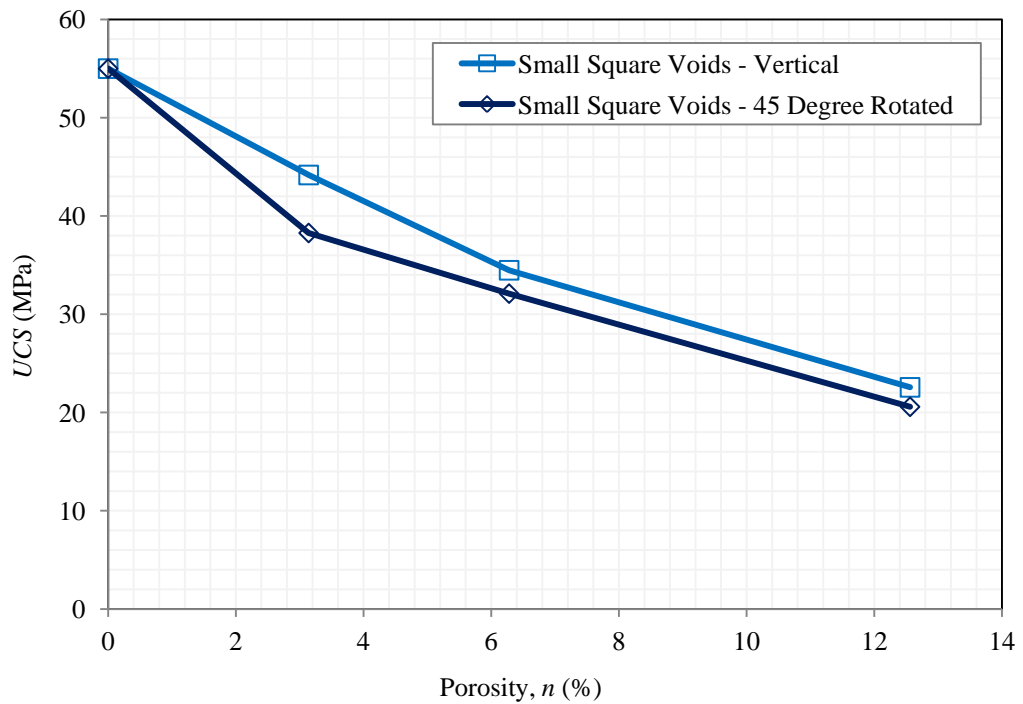


Figure (6.12) Compression Strength versus Void Porosity for Numerical Models Containing Small Unisize Voids – Square Voids

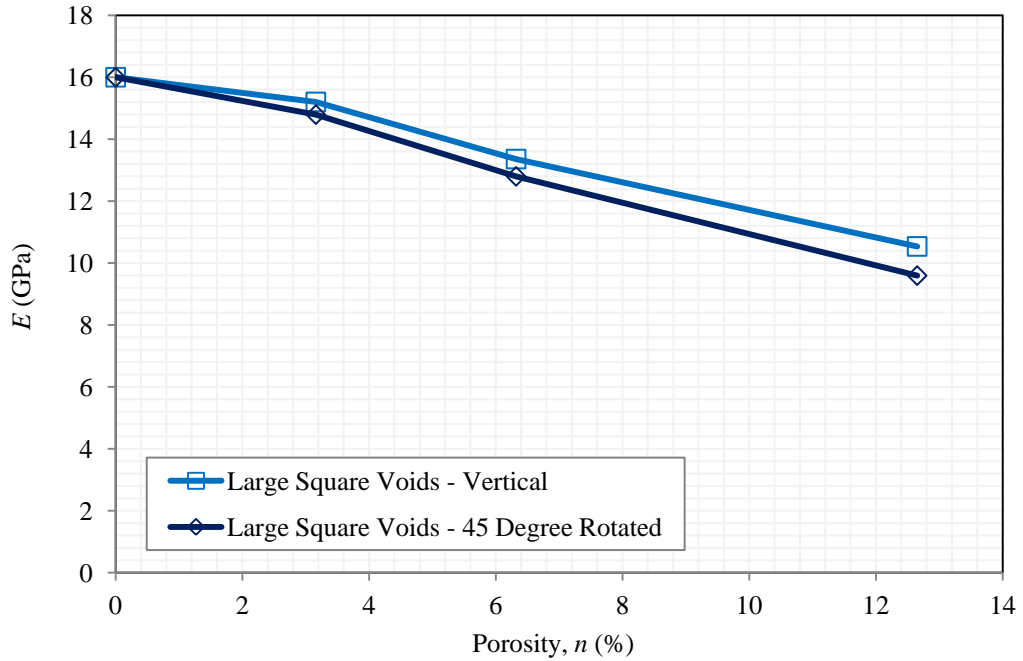


Figure (6.13) Deformation versus Void Porosity for Numerical Models Containing Large Unisize Voids – Square Voids

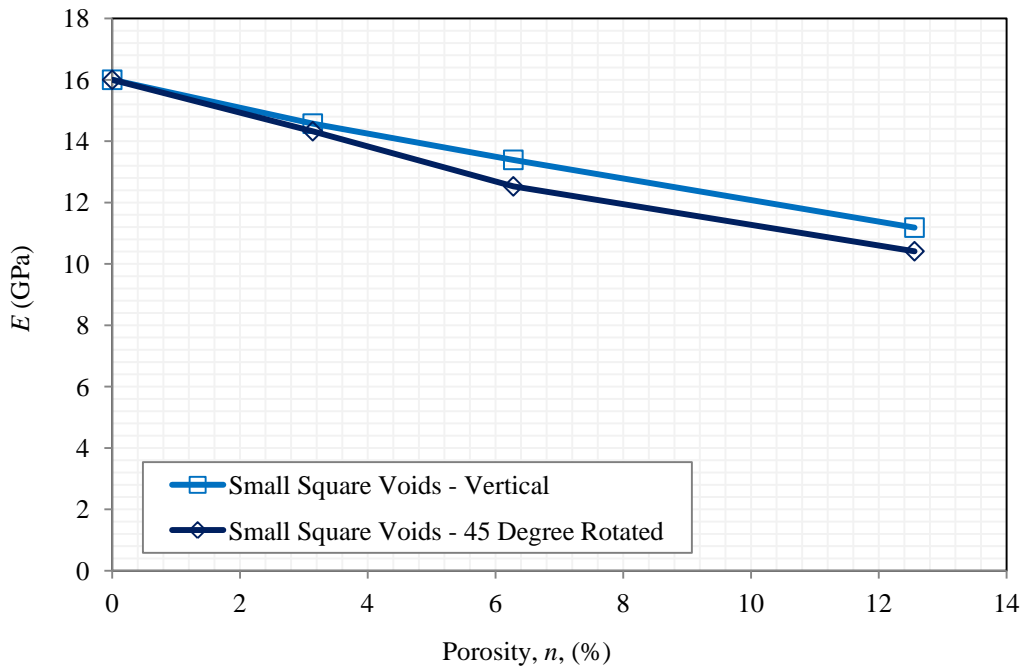


Figure (5.14) Deformation versus Void Porosity for Numerical Models Containing Small Unisize Voids – Square Voids

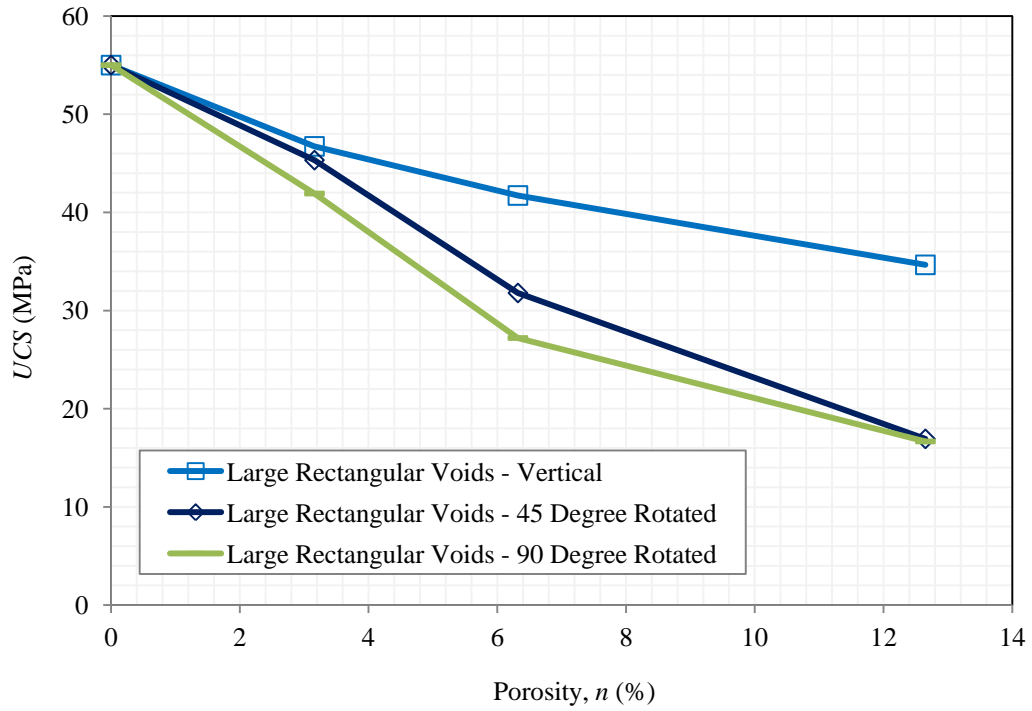


Figure (6.15) Compressive Strength versus Void Porosity for Numerical Models Containing Large Unisize Voids – Rectangular Voids

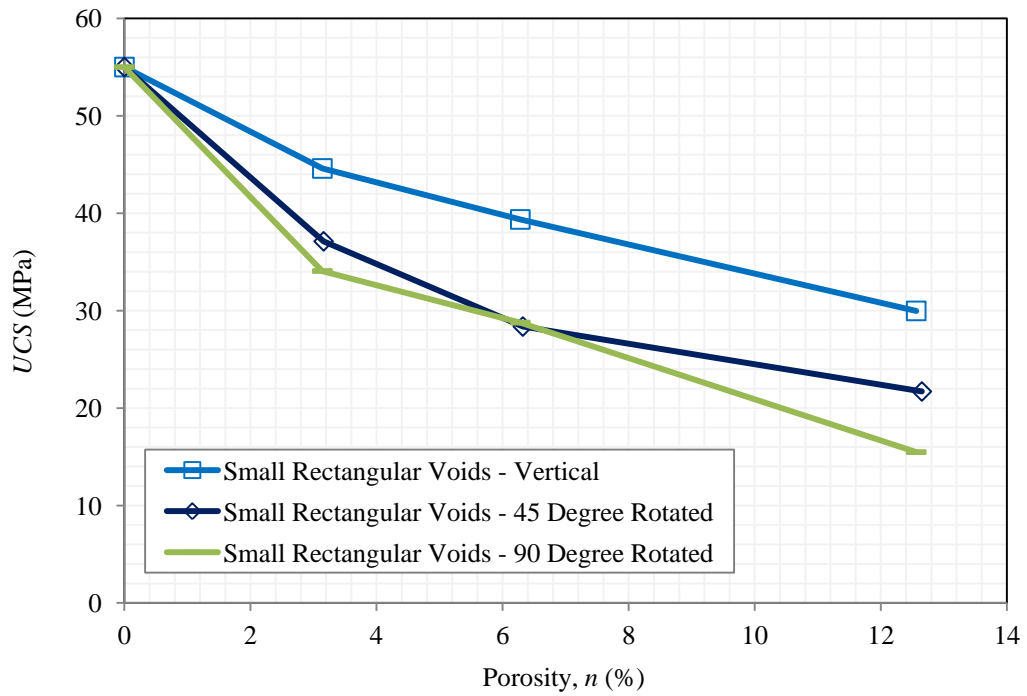


Figure (6.16) Compressive Strength versus Void Porosity for Numerical Models Containing Small Unisize Voids – Rectangular Voids

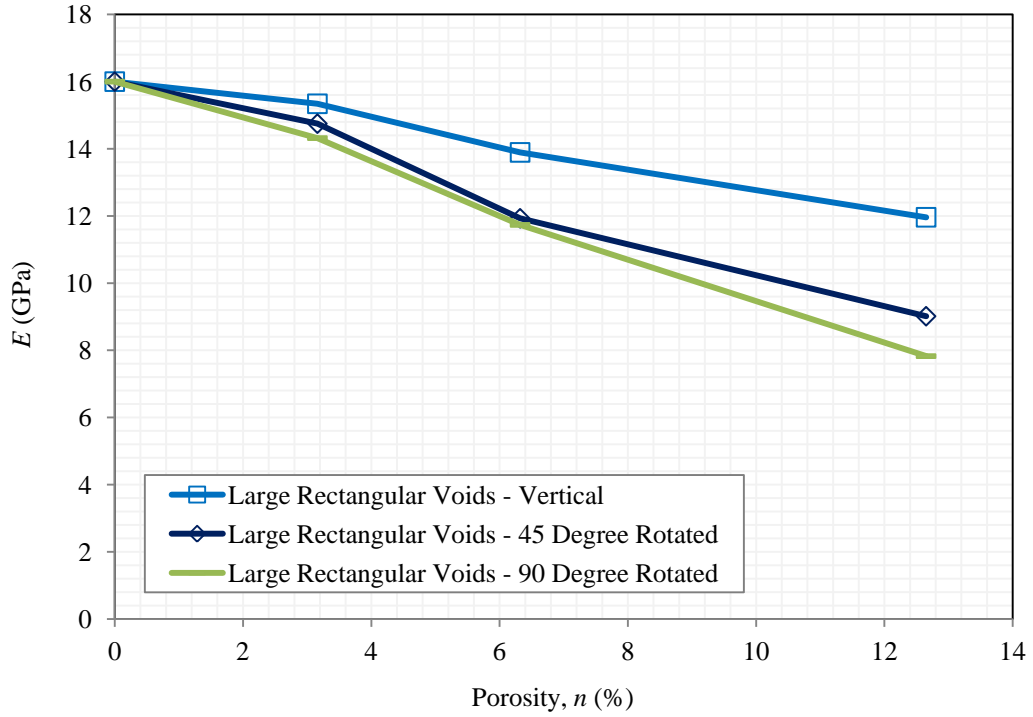


Figure (6.17) Deformation versus Void Porosity for Numerical Models Containing Large Unisize Voids –Rectangular Voids

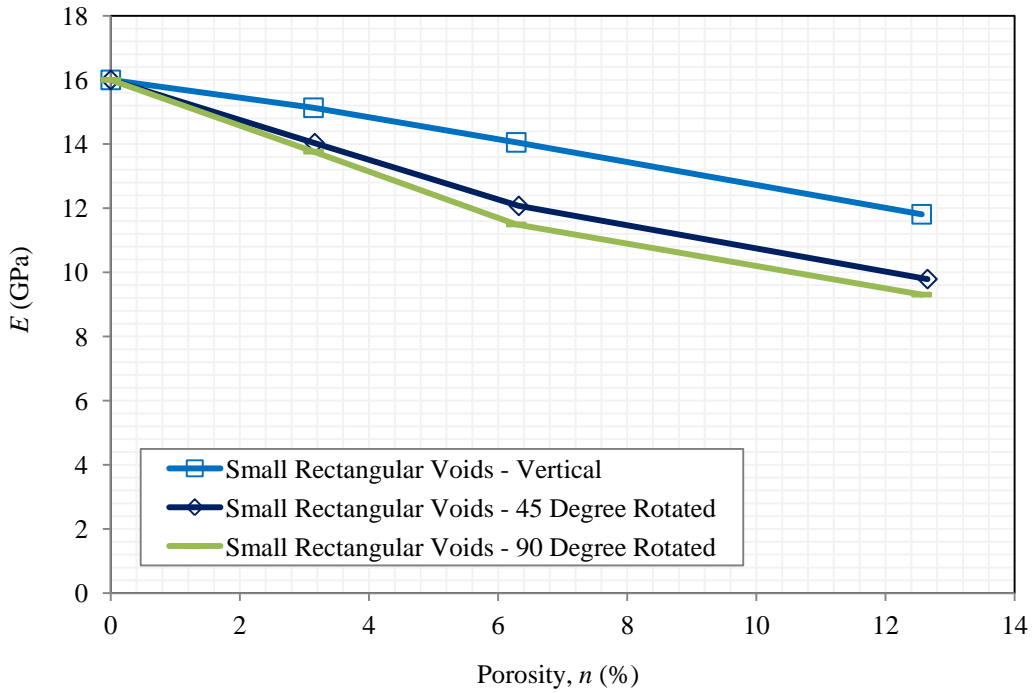


Figure (6.18) Deformation versus Void Porosity for Numerical Models Containing Small Unisize Voids – Rectangular Voids

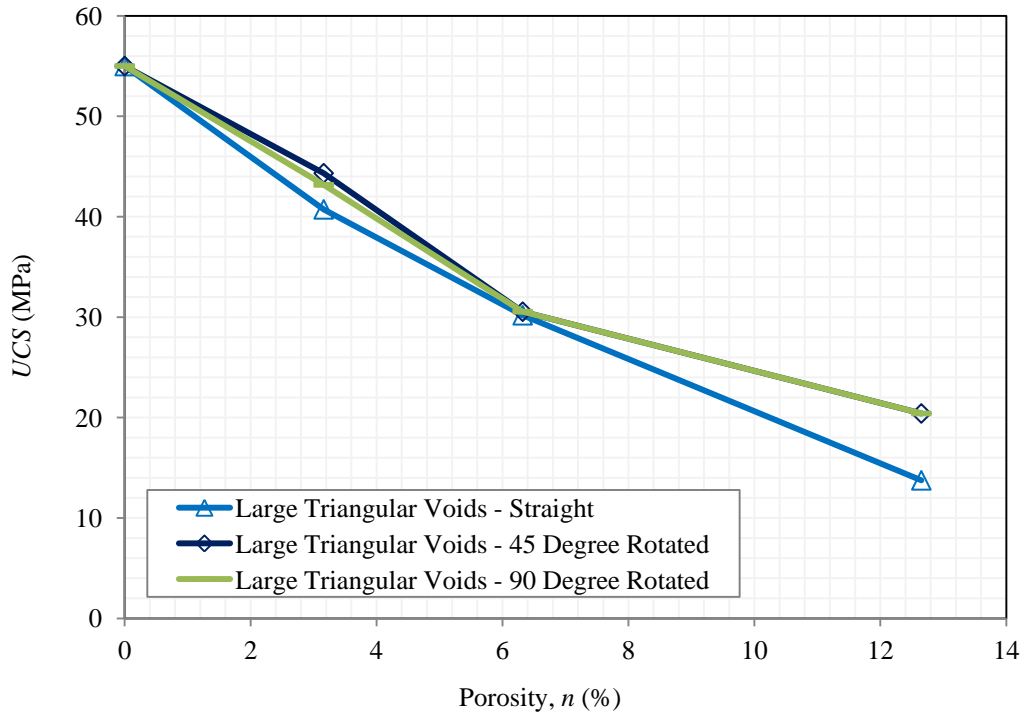


Figure (6.19) Compressive Strength versus Void Porosity for Numerical Containing Large Unisize Voids – Triangular Voids

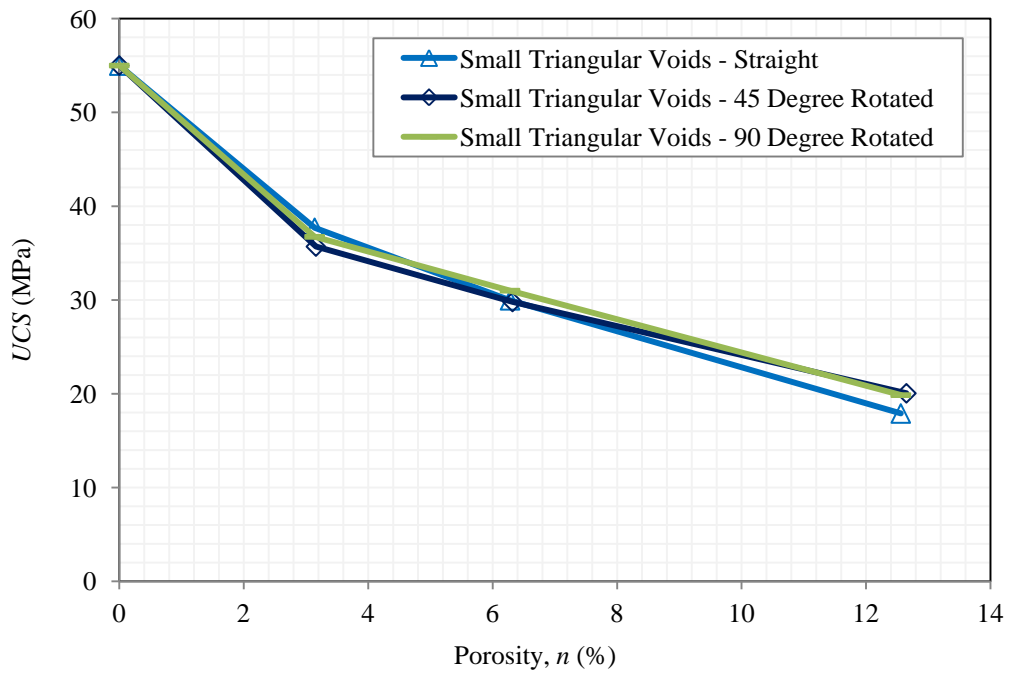


Figure (6.20) Compressive Strength versus Void Porosity for Numerical Containing Small Unisize Voids – Triangular Voids

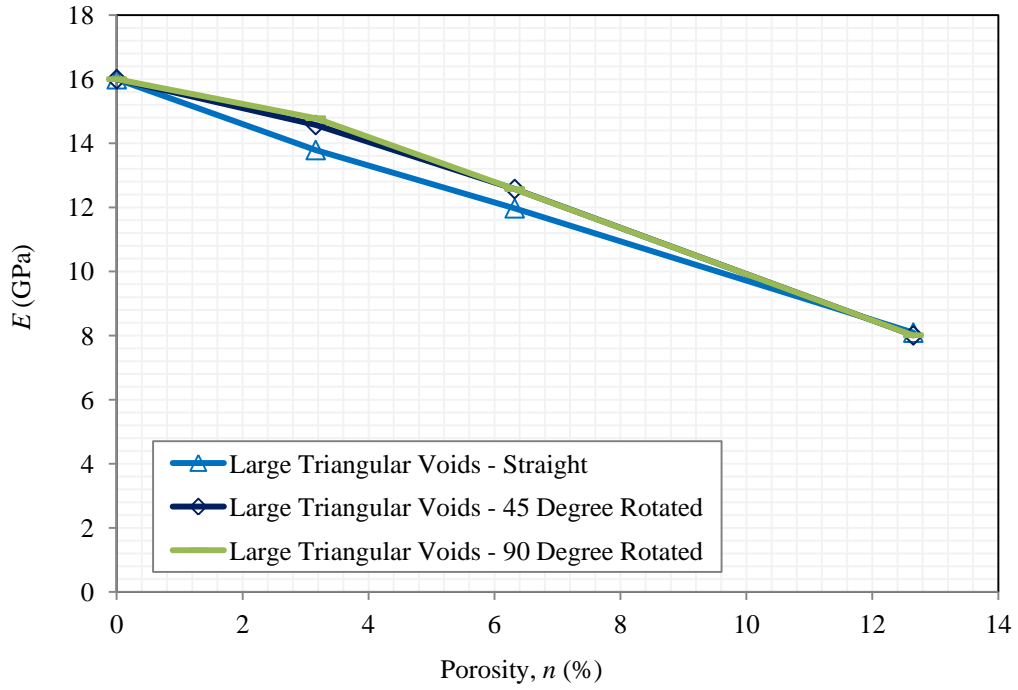


Figure (6.21) Deformation versus Void Porosity for Numerical Models Containing Large Unisize Voids – Triangular Voids

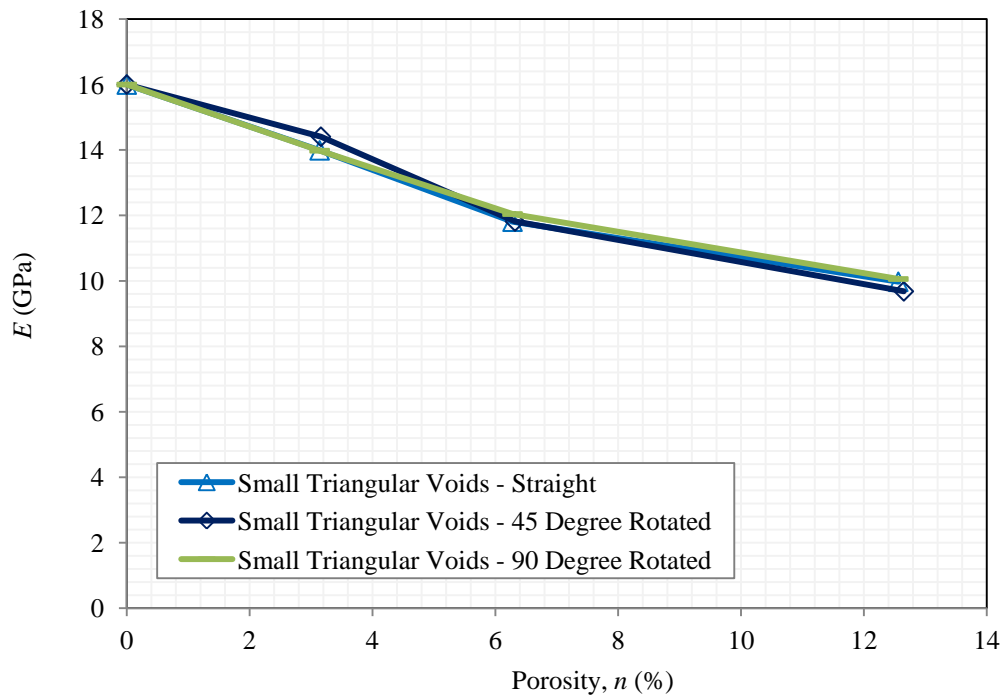


Figure (6.22) Deformation versus Void Porosity for Numerical Models Containing Small Unisize Voids – Triangular Voids

The numerical results showed that the models with either vertical rectangular voids or 45-degree rotated rectangular voids gave the highest value for both UCS and E, while, the models with either horizontal rectangular voids or straight triangular voids gave the lowest values for both UCS and E.

6.4 Numerical Simulations to Validate the Effects of Void Geometry on the Mechanical Properties.

The numerical results from the previous sections, sections 6.2 and 6.3, are used to validate the mathematical expressions in Chapter Four [Eqs. (4.11), (4.12), and (4.16)]. Therefore, the total width of solid columns (W) for each numerical model was measured as shown in Tables (6.7) and (6.8). Figure (6.23) shows examples of solid columns and porous columns for models containing six unisize large voids.

The values of uniaxial compressive strength and Young's modulus for numerical models are plotted as a function of void porosity in Figures (6.24) and (6.25). According to the results, for the void porosity ranging between 3% and 13%, regardless of the void size, void shape, void orientation, and void distribution, the normalized numerical results similar to the experimental results showed increases in both normalized UCS and E with decreasing void porosity. However, on the contrast to the experimental results, the coefficient of determination for uniaxial compressive strength ($R^2 = 0.7902$) is smaller than that for Young's modulus ($R^2 = 0.8182$). The numerical correlations for both strength and deformation followed logarithmic trend with increasing porosity, and they can be represented best by the following equations:

$$\frac{(UCS)_{\text{Porous}}}{(UCS)_{\text{Solid}}} = 0.2577 * \ln((porosity, \%)^{-1}) + 1.048 \quad R^2 = 0.7902 \quad \dots (6.2)$$

$$\frac{(E)_{\text{Porous}}}{(E)_{\text{Solid}}} = 0.208 * \ln((porosity, \%)^{-1}) + 1.1543 \quad R^2 = 0.8182 \quad \dots (6.3)$$

The percentages of the maximum differences in UCS values are 37.3%, 53.3%, and 152% for void porosities 3.15%, 6.3%, and 12.6% respectively. Regarding the deformation, the percentages of the maximum differences in E values are 11.6, 22.2%, and 104% for void porosities 3.15%, 6.3%, and 12.6% respectively. The differences can be attributed to the effects of void geometry and the efficiency of the software used in the numerical analysis. However, since the trend of numerical results in the numerical analysis in Chapter Five were in a good agreement with the trend of the experimental results, the latter cause for the differences can be considered as a secondary cause. Therefore, the main source of the differences in both UCS and E is believed to be the void geometry that can be represented by expressions in Eqs. (4.11), (4.12), and (4.16) as follows:

$$\frac{(UCS)_{\text{Porous}}}{(UCS)_{\text{Solid}}} \propto \left[\frac{\left(\frac{W + 0.01D}{0.01D} \right)}{n} \right] \quad \dots (6.4)$$

$$\frac{(E)_{\text{Porous}}}{(E)_{\text{Solid}}} \propto \left[\frac{\left(\frac{W + 0.01D}{0.01D} \right)}{n} \right] \quad \dots (6.5)$$

$$(UCS)_{\text{Porous}} \propto \left[\frac{E}{n} * \left(\frac{W + 0.01D}{0.01D} \right) \right] \quad \dots (6.6)$$

Accordingly, the numerical values of uniaxial compressive strength and Young's modulus for the numerical models are plotted as a function of void porosity, total width

of solid columns (W), and void size as shown in Figures (6.26) to (6.31). From the results, the following observations can be discussed:

- 1- The relationships of normalized UCS and E with the normalized total width of solid columns (W), shown in Figures (6.26) and (6.27), are in very good agreements. The normalized W was obtained by dividing the total width of solid columns (W) for each numerical model by the model's width, L (152.4 mm). As shown in the figures, both uniaxial compressive strength and Young's modulus increased when the normalized W increasing. The correlations followed very decent power trends and can be represented best by the following equations:

$$\frac{(UCS)_{\text{Porous}}}{(UCS)_{\text{Solid}}} = 0.3171 * \ln(W/L) + 0.8475 \quad R^2 = 0.9216 \quad \dots (6.7)$$

$$\frac{(E)_{\text{Porous}}}{(E)_{\text{Solid}}} = 0.248 * \ln(W/L) + 0.9856 \quad R^2 = 0.896 \quad \dots (6.8)$$

- 2- From Tables (6.7) and (6.8), and Figure (6.23), the numerical models those have the highest strength and stiffness (models containing vertical rectangular voids) gave the largest W compared to the other models; $W = 136.82$ mm. While the numerical models with the lowest strength and stiffness (models containing straight triangular voids) gave the lowest W compared; $W = 118.9$ mm. The total width for solid columns W for models with either circular or square voids were close to each other and accordingly their strength and stiffness were similar; $W = 130.36$ mm for models with square voids, and $W = 127.52$ mm for models with either circular voids.

3- The relationships between the mechanical properties of the numerical models with the void porosity and void geometry expressed by total width of solid columns (W) gave a decent agreement following logarithmic trend as shown in Figures (6.28), (6.29), and (6.31). The mathematical expressions, Eqs. (6.4), (6.5), and (6.6), can be represented best by the following equations:

$$\frac{(UCS)_{\text{Porous}}}{(UCS)_{\text{Solid}}} = 0.1435 * \ln \frac{W + 0.01 * D}{0.01 * D * n} + 0.0304 \quad R^2 = 0.9181 \quad \dots (6.9)$$

$$\frac{(E)_{\text{Porous}}}{(E)_{\text{Solid}}} = 0.1153 * \ln \frac{W + 0.01 * D}{0.01 * D * n} + 0.335 \quad R^2 = 0.9411 \quad \dots (6.10)$$

$$(UCS)_{\text{Porous}} = 6.839 * \ln \left[\frac{E * (W + 0.01 * D)}{0.01 * D * n} \right] - 11.416$$

$$R^2 = 0.9247 \quad \dots (6.11)$$

4- Considering the total width of solid columns (W) to explore the effects of void geometry on the mechanical properties improved the correlations between the mechanical properties of the numerical models and void porosity. From Figures (6.24) and (6.28), the percentages of the maximum differences in UCS values reduced from 152% to 48.4%; up to 68% of the differences are reduced. In addition, the coefficient of determination (R^2) for uniaxial compressive strength increased from 0.7902 to 0.9181. Similarly, the correlations for Young's modulus is improved and the percentages of the maximum differences in E values reduced from 104% to 26.5%; up to 74.5% of the differences are reduced. In addition, the coefficient of determination increased from 0.8182 to 0.9411; see Figures (6.25) and (6.29). Regarding the relationships between the uniaxial compressive strength and Young's modulus as shown in Figures (6.30) and (6.31), the numerical results showed better

correlation, and the coefficient of determination increased from $R^2 = 0.8517$ to $R^2 = 0.9247$.

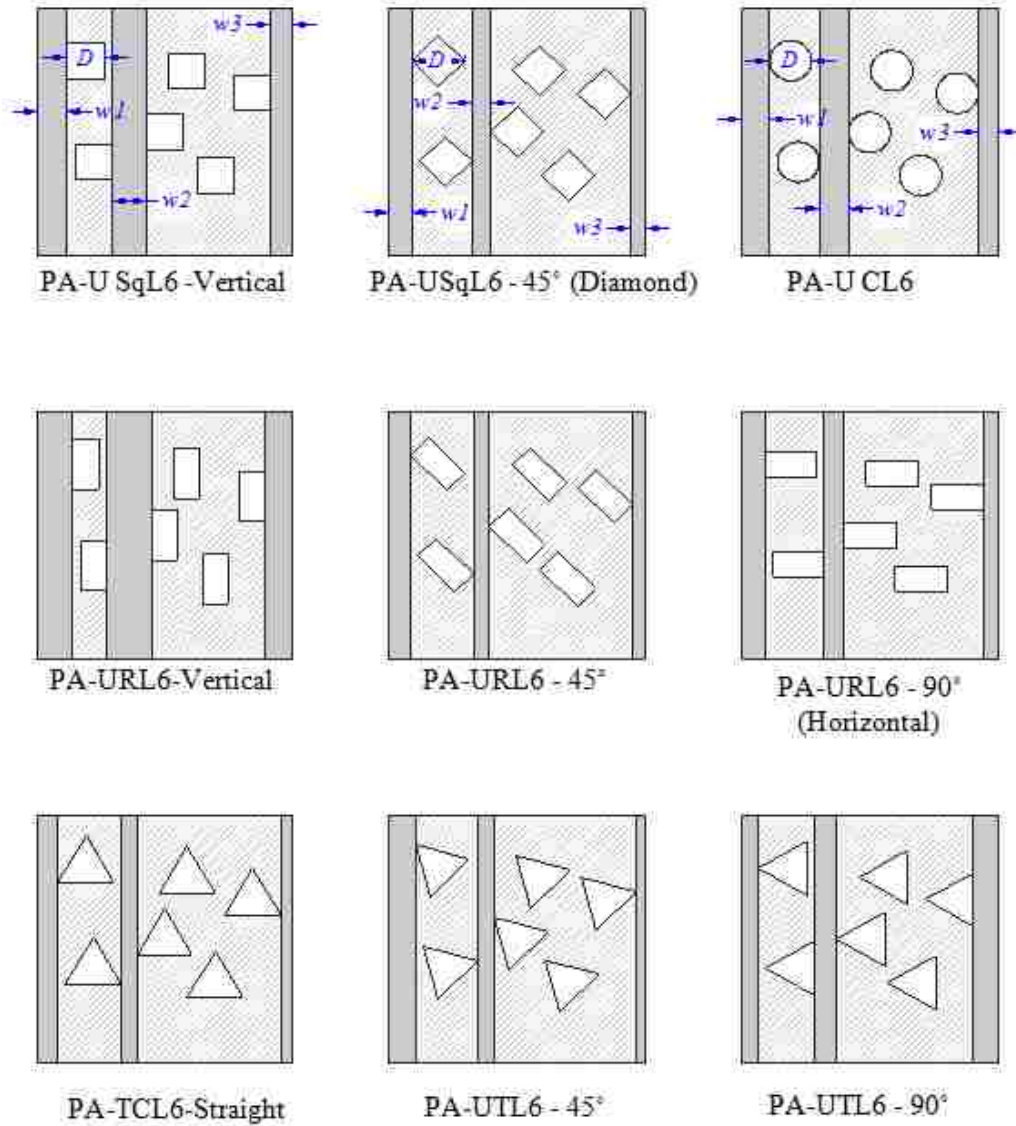


Figure (6.23) Total Width of Solid Columns (W) for Numerical Models Containing Six Large Unisize Voids

Table (6.7) Total Width of Solid Columns for Models Containing Large Unisize Voids

Model Name	Total Width of Solid Columns (mm)					
	w_1	w_2	w_3	w_4	w_5	W
PA-UCL1	63.76	63.76				127.52
PA-UCL3	45.55	19.4	19.48			84.43
PA-UCL6	11.46	16.71	17.72			45.89
PA-USqL1-Vertical	65.18	65.18				130.36
PA-USqL3-Vertical	20.82	46.96	22.31			90.09
PA-USqL6-Vertical	12.88	18.12	20.55			51.55
PA-USqL1-45° (Diamond)	60.61	60.61				121.22
PA-USqL3-45° (Diamond)	42.4	16.25	13.18			71.83
PA-USqL6-45° (Diamond)	13.56	8.31	11.42			33.29
PA-URL1-Vertical	68.41	68.41				136.82
PA-URL3-Vertical	50.18	24.04	2.62	28.77		105.61
PA-URL6-Vertical	21.35	16.11	1.5	6.41	27.01	72.38
PA-URL1-45°	59.66	59.66				119.32
PA-URL3-45°	15.3	41.45	11.29			68.04
PA-URL6-45°	7.37	12.61	9.52			29.5
PA-URL1-90° (Horizontal)	60.61	60.61				121.22
PA-URL3-90° (Horizontal)	42.4	16.25	13.18			71.83
PA-URL6-90° (Horizontal)	8.31	13.56	11.42			33.29
PA-TCL1-Straight	59.45	59.45				118.9
PA-TCL3-Straight	41.24	15.09	10.86			67.19
PA-TCL6-Straight	7.15	12.4	9.09			28.64
PA-URL1-45°	57.52	57.52				115.04
PA-URL3-45°	13.16	44.31	12			69.47
PA-URL6-45°	5.22	15.47	10.23			30.92
PA-URL1-90°	56.55	66.53				123.08
PA-URL3-90°	38.65	22.17	15.35			76.17
PA-URL6-90°	9.8	14.23	13.58			37.61

Table (6.8) Total Width of Solid Columns for Models Containing Unisize Small Voids

Model Name	Total Width of Solid Columns (mm)							
	w_1	w_2	w_3	w_4	w_5	w_6	w_7	W
PA-UCSm3	23.01	49.16	26.71					98.88
PA-UCSm6	4.35	24.94	20.32	15.07				64.68
PA-UCSm12	0.73	20.28	15.07					36.08
PA-USqSm3-Vertical	24.02	50.17	28.71					102.9
PA-USqSm6-Vertical	21.32	16.08	6.35	26.95				70.7
PA-USqSm12-Vertical	21.29	16.08	1.45					38.82
PA-USqSm3-45° (Diamond)	46.92	20.78	22.23					89.93
PA-USqSm6-45° (Diamond)	12.84	18.08	20.47					51.39
PA-USqSm12-45° (Diamond)	12.84	18.04						30.88
PA-URSm13-Vertical	26.51	52.26	33.3	7.15				119.22
PA-URSm6-Vertical	18.57	23.42	6.03	31.53	10.93			90.48
PA-URSm12-Vertical	18.57	23.38	3.52	6.23	6.03	7.33	2.14	67.2
PA-URSm3-45°	20.3	46.06	20.89					87.25
PA-URSm6-45°	12.36	17.21	19.46					49.03
PA-URSm12-45°	12.37	17.18						29.55
PA-URSm3-90° (Horizontal)	20.78	46.92	22.23					89.93
PA-URSm6-90° (Horizontal)	12.84	18.08	20.47					51.39
PA-URSm12-90° (Horizontal)	12.84	18.04						30.88
PA-TCSm3-Straight	19.95	46.1	20.58					86.63
PA-TCSm6-Straight	12.01	17.26	18.82					48.09
PA-TCSm12-Straight	12.01	17.22						29.23
PA-URSm3-45°	18.58	48.28	21.39					88.25
PA-URSm6-45°	10.64	19.44	19.63					49.71
PA-URSm12-45°	10.64	19.4						30.04
PA-URSm3-90°	44.26	24.98	23.77					93.01
PA-URSm6-90°	17.04	15.42	1.4	22				55.86
PA-URSm12-90°	15.38	17.04						32.42

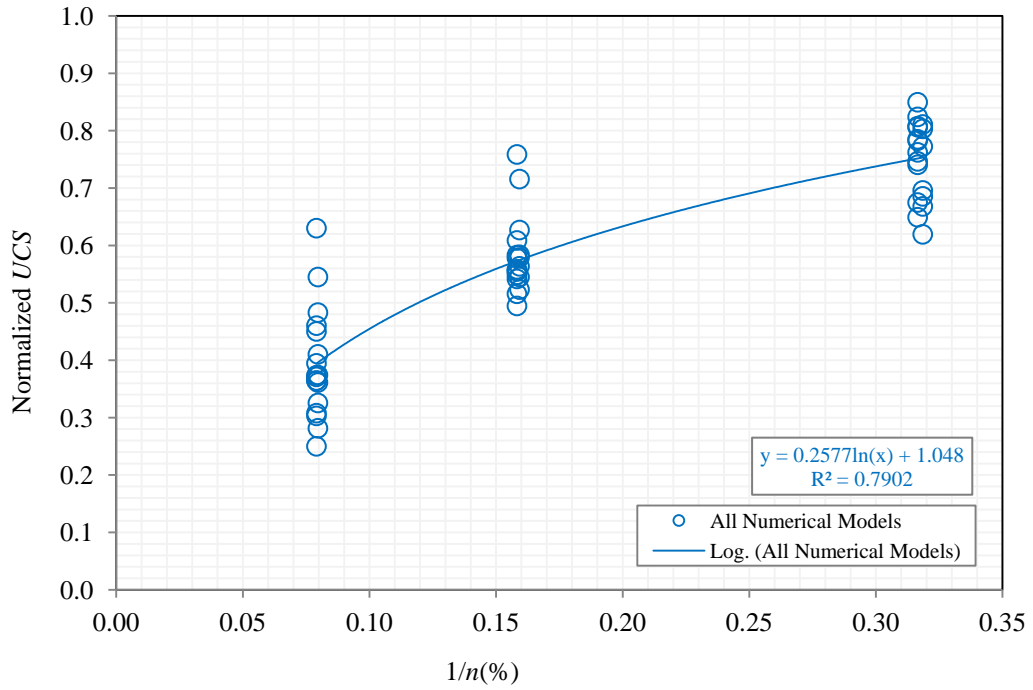


Figure (6.24) Normalized UCS versus Void Porosity for All Numerical Models Containing Unisize Voids with Different Shape, Size, Orientation and Distribution

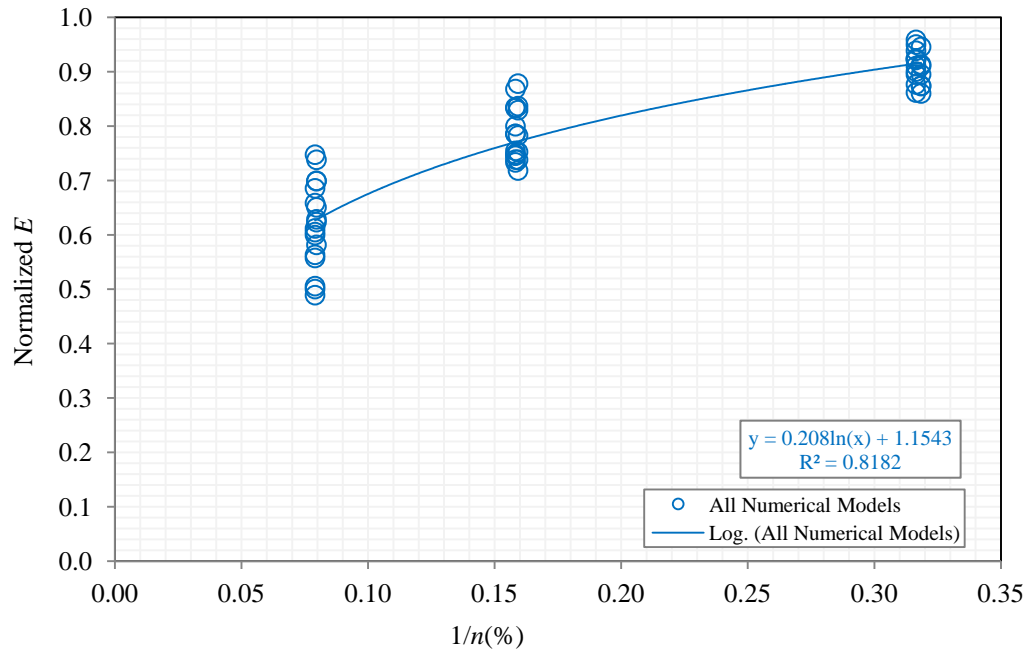


Figure (6.25) Normalized E versus Void Porosity for All Numerical Models Containing Unisize Voids with Different Shape, Size, Orientation and Distribution

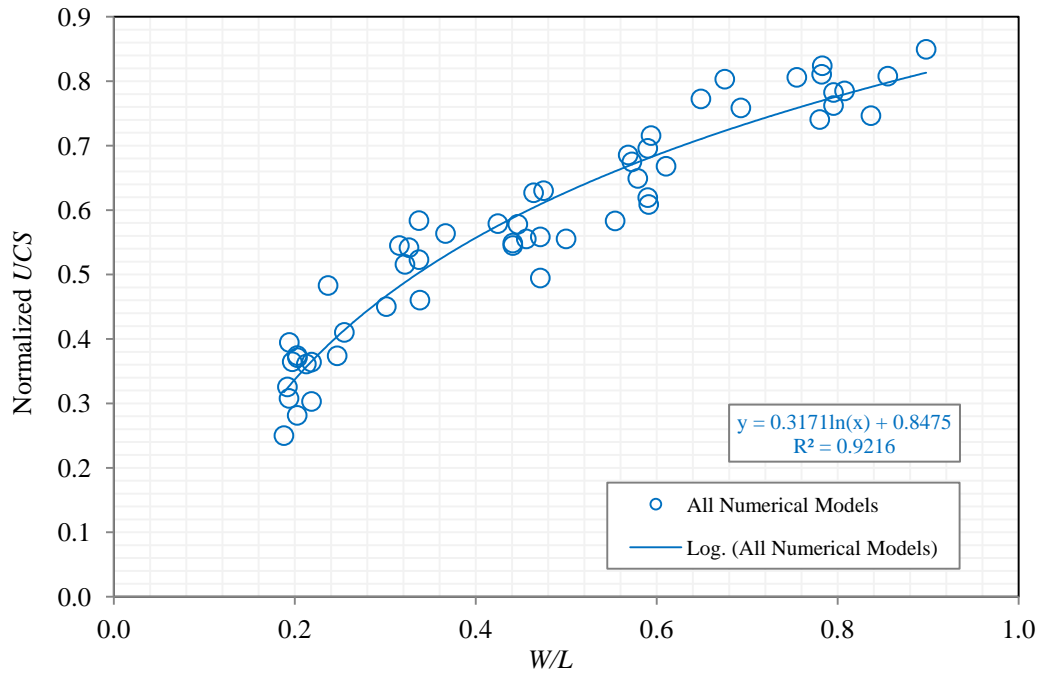


Figure (6.26) Normalized UCS versus Normalized Total Width of Solid Columns (W) for All Numerical Models Containing Unisize Voids with Different Shape, Size, Orientation and Distribution

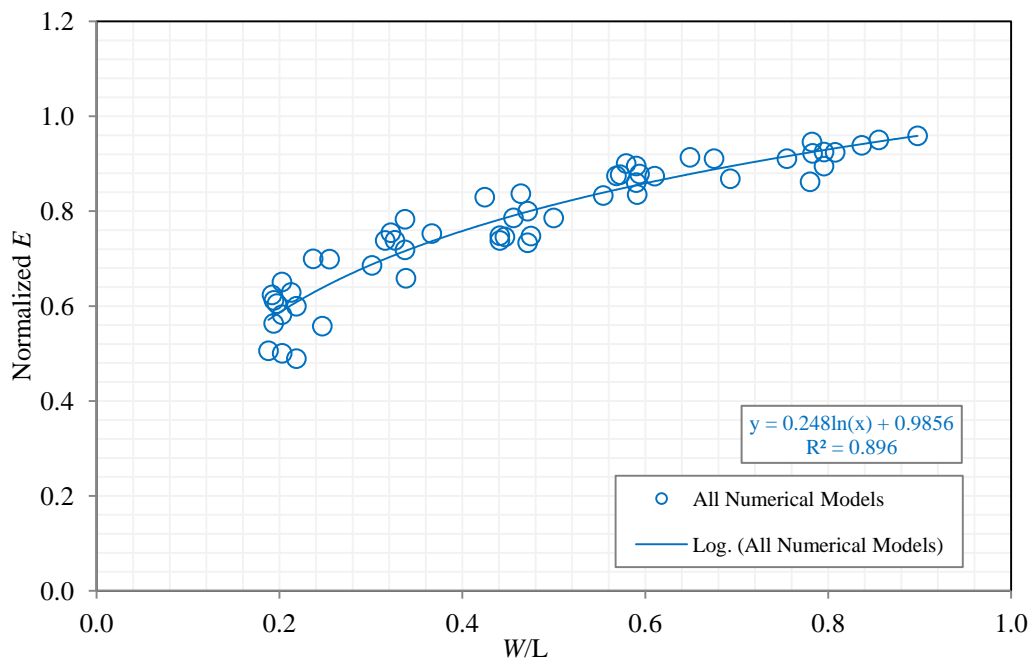


Figure (6.27) Normalized E versus Normalized Total Width of Solid Columns (W) for All Numerical Models Containing Unisize Voids with Different Shape, Size, Orientation and Distribution

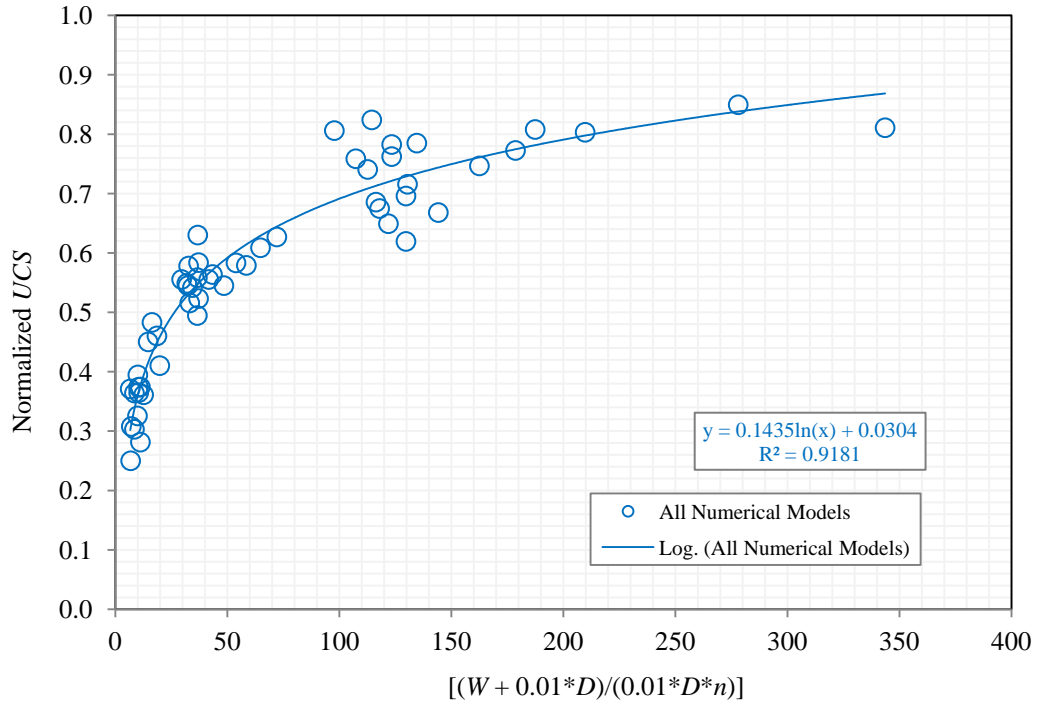


Figure (6.28) Normalized UCS versus Void Porosity versus and Normalized Total Width of Solid Columns (W) for All Numerical Models Containing Unisize Voids with Different Shape, Size, Orientation and Distribution

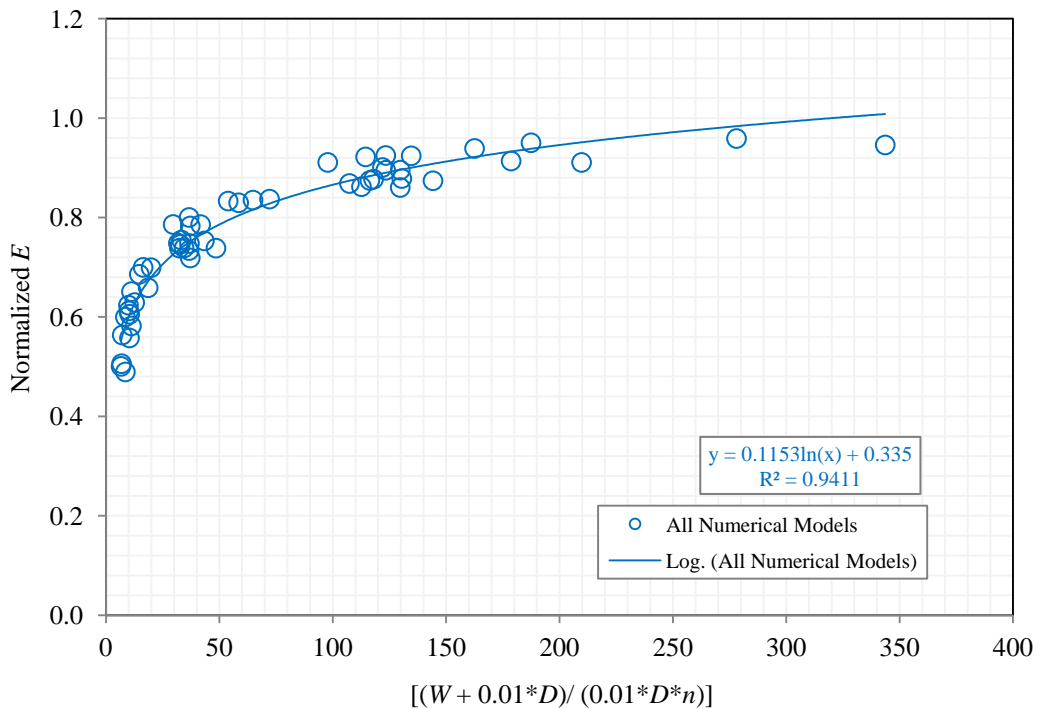


Figure (6.29) Normalized E versus Void Porosity versus and Normalized Total Width of Solid Columns (W) for All Numerical Models Containing Unisize Voids with Different Shape, Size, Orientation and Distribution

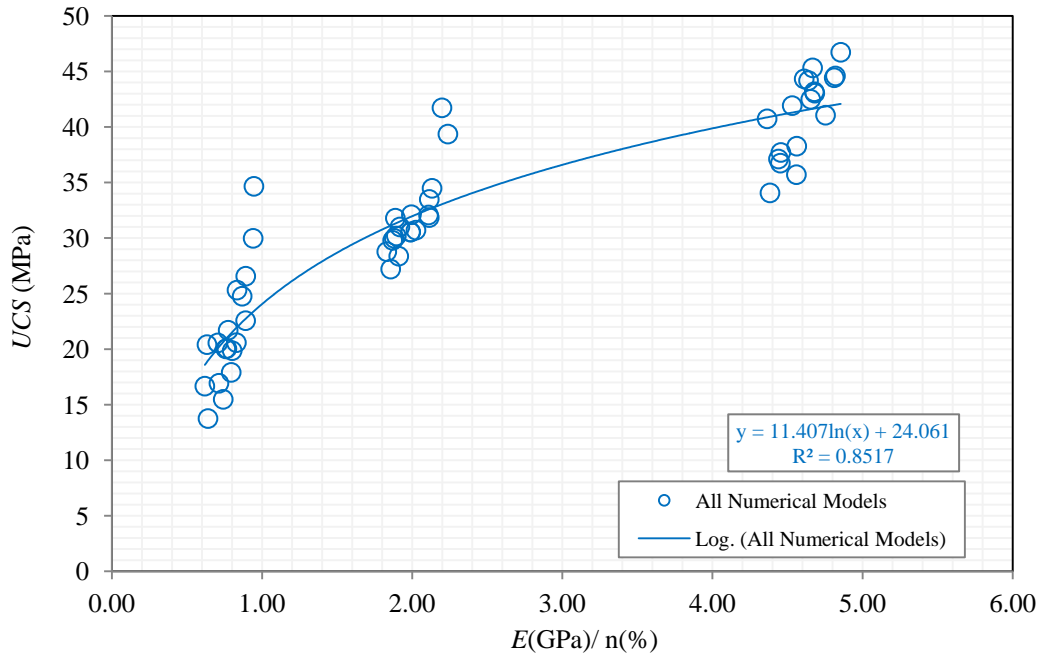


Figure (6.30) Compressive Strength versus Void Porosity and Deformation for Numerical Models Containing Unisize Voids with Different Shape, Size, Orientation and Distribution

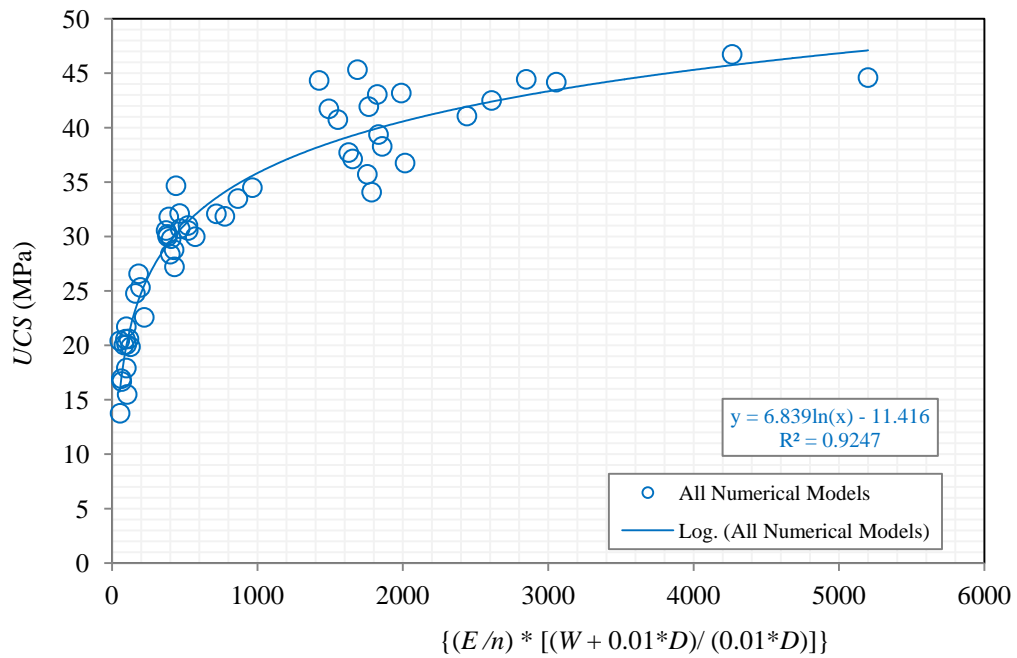


Figure (6.31) Compressive Strength versus Void Porosity, Deformation, and Normalized Total Width of Solid Columns for Numerical Models Containing Unisize Voids with Different Shape, Size, Orientation and Distribution

CHAPTER SEVEN *CONCLUSIONS AND RECOMMENDATIONS*

7.1 Conclusions

This study used both experimental and numerical results to characterize the effects of void porosity and geometry on strength, stiffness and failure modes of rock-like materials. For the experimental program, fifty two porous cubes made of Hydro-Stone TB[®] containing voids with different size, shape and distribution were tested under uniaxial compression. In the numerical works, one hundred twenty seven (127) two-dimensional porous models were simulated under uniaxial compression using UDEC software.

7.1.1 Conclusions for the Experimental Results

From the experimental results, the following conclusions can be drawn:

- 1- For the void porosity ranging from 6% to 20%, the experimental values of uniaxial compressive strength and Young's modulus for Hydro-StoneTB[®] cubes decreased with void porosity increasing. However, the results displayed very high variation, especially with regard to Young's modulus.
- 2- The results in this study showed that it is not-only the porosity but also the void geometry can affect the strength and deformability of rock-like materials. Accordingly, the void geometry is partially responsible for the scattering of the test results.
- 3- The hypothesis of using the bridge distances (B_r), side distances (S), and top distances (T) to express the effects of void geometry on the mechanical properties

of rock-like materials did not improve the correlations between the mechanical properties and void geometry. This may be due to the fact that these factors are interacting with each other and cannot be explored individually.

- 4- The hypothesis of using the total width of solid columns (W) to express the effects of void geometry on the mechanical properties of rock-like materials improved the correlations between the uniaxial compressive strength and void geometry. The percentage of the maximum difference in *UCS* value reduced to less than half. In addition, the coefficient of determination for uniaxial compressive strength increased. However, the Young's modulus did not show any distinct response. The correlations between Young's Modulus and void porosity for rock-like materials are very difficult to be constructed using experimental results obtained from uniaxial compression tests. Therefore, great care must be taken regarding strain measurement for uniaxial compression tests on porous specimens.
- 5- The ratio of specimen size (side length) to void size (void diameter) is important. For the ratio of specimen size to void size equal to and less than 7, both experimental and numerical results showed better correlation with void porosity. In addition, for the same porosity, increasing the void sizes from 12.8 mm in diameter to 31.1 mm in diameter (the ratios of large void sizes to smaller void size were ranging from 1 to about 2.5) did not show discernible effects on the mechanical behaviors of the rock-like material. Accordingly to explore the effect of voids size, larger ratios should be considered.
- 6- The experimental results showed that the dominant failure modes for porous cubes with void porosity ranging from 6% to 20% is axial splitting (tension

fractures or failure). However, in each porous cube there were some shear failure (inclined cracks) depending on the void alignments and bridge distances. In general, the cracked were formed mainly at the void poles (or void tips) and intended to expand approximately parallel to the axial compression load, however, in some cubes cracks were formed between voids horizontally or sub-horizontally depending on the distances between one void and the other voids located at the immediate vicinity of the void. In those cubes, when a crack passes vertically (or sub-vertically) between two voids, a horizontal crack was formed to connect that crack to the void side or the sample side. Finally, the coalescence of those cracks (horizontal (or sub-horizontal) and the vertical (or sub-vertical) cracks) formed an inclined crack that gave a failure mode similar to the shear failure mode.

7.1.2 Conclusions from the Numerical Results

From the numerical results, the following conclusions can be drawn:

- 1- The numerical results from the two-dimensional numerical analysis using discrete element method, UDEC program, showed trend of reduction in the value of the mechanical properties of rock-like materials with void porosity increasing similar to the experimental results. However, the two-dimensional UDEC simulation gave conservative values for both uniaxial compressive strength and Young's modulus compared to the values obtained from the experimental tests. This is because of either modeling a three-dimensional medium in two dimensions plane strain, or inability to model the friction

between the steel platen and the Hydro-StoneTB[®] surfaces (top and bottom faces of the cubes), or both.

- 2- The numerical strength results (numerical *UCS*) showed lesser scattering and larger coefficients of determination (R^2) compared to the experimental strength results. In addition, the differences in *UCS* values reduced by more than half. Accordingly, up to half of the differences in the experimental *UCS* values can be attributed to the uncertainties existing in the experimental uniaxial tests. Similarly, the numerical deformation results (numerical *E*) tremendously reduced the data scattering and greatly increased the coefficients of determination. In addition, the percentages of the maximum differences in *E* values reduced by up to 85%. Therefore, again, great care must be taken regarding strain measurement for uniaxial compression tests on porous specimens.
- 3- The two-dimensional uniaxial compression results can be transferred to three-dimensional results through power relationship; $(\text{Experimental Results})_{3D} = a[(\text{Numerical Results})_{2D}]^b$. UDEC simulations showed that the value of *a* constant is ranging between 0.1955 and 0.385 for uniaxial compressive strength, and between 1.0071 and 2.5351 for Young's modulus. Regarding *b* constant, its value varies from 1.1655 to 1.378 for uniaxial compressive strength, and from 0.5668 to 0.9338 for Young's modulus varied.
- 4- UDEC simulations showed that the void shape has discernible effects on the mechanical properties of the two-dimensional models under uniaxial compression. The numerical simulation displayed that the models containing

vertical rectangular voids were the strongest and stiffest models compared to the models with either, circular voids, or square voids, or straight equilateral triangular voids. While the specimens with straight equilateral triangular voids were the weakest. The porous models with circular void showed similar results to the models with square voids.

- 5- UDEC simulations showed that the void orientation is also having effects on the mechanical properties. The rotation of square voids by 45-degree, to obtain models with voids having diamond shape, gave models with slightly smaller uniaxial compressive strength and Young's Modulus. The rotation of vertical void by 90-degree, to obtain models with horizontal rectangular voids, reduced the strength of the models to less than half. However, the void orientation for triangular voids did not show any effects on the mechanical properties of the two-dimensional models under uniaxial compression.
- 6- UDEC simulations showed that the hypothesis of using the total width of solid columns (W) to express the effects of void geometry on the mechanical properties can improve the correlations between the uniaxial compressive strength and void geometry. From the numerical results, using W to express the effects of void geometry, the percentages of the maximum differences in UCS values reduced from 152% to 49%; up to 68% of the differences are reduced. In addition, the coefficient of determination (R^2) is increased. Similarly, the correlations for Young's modulus is improved and the percentages of the maximum differences in E values reduced from 104% to

27%; up to 74% of the differences are reduced. In addition, the coefficient of determination is increased as well.

7.2 Recommendations

To extend the scope of understanding the effects of void porosity and void geometry on the mechanical properties of porous rock, more researches are needed as follows:

- 1- Three-Dimensional numerical analysis to study the effects of void geometry on the mechanical behavior of rock-like materials.
- 2- Numerical analysis to study the effects of void geometry on the mechanical behavior of rock-like materials using plane stress assumption.
- 3- Numerical analysis to study the effects of void geometry on the crack initiation and propagation using UDEC.
- 4- Numerical analysis to study the effects of void uniformity on the mechanical behavior of rock-like materials; comparing the numerical results for models containing voids with mixed sizes to the numerical results of models containing voids with unisize sizes for the same void porosities.
- 5- In order to see if the block size in the discrete element modeling has effects on the numerical results of UDEC simulations, more numerical study needs with different block sizes.
- 6- To verify the numerical conclusions on the effects of void shape and orientation, more experimental tests are necessary.
- 7- To explore the effects of confining pressure on the mechanical behavior of porous rocks, more numerical simulations with different confining pressure are needed.

- 8- Experimental testing of rock-like material with void porosity less than 6% and more than 20%.
- 9- Since conducting experimental tests to explore the effects of void porosity and geometry on the tensile strength of rocks are semi-impossible, simulating numerical models under uniaxial tension stress can be helpful, and accordingly more research is needed in this area.

APPENDIX (I) LABROTARY TEST DATA

Table (I-A1) EXPERIMENTAL RESULTS OF TESTED CUBES

Sample No.	Sample Name	Porosity (<i>n</i>)	Uniaxial Compressive Strength, <i>UCS</i>	Young's Modulus, <i>E</i> (25 - 50%)
		%	MPa	GPa
1	PA-UCL2-A	6.56	19.24	9.81
2	PA-UCL2-B	6.56	19.37	8.90
3	PA-UCL2-C	6.56	16.62	8.65
4	PB-UCL2-A	6.56	17.17	10.98
5	PB-UCL2-B	6.56	19.99	11.21
6	PB-UCL2-C	6.56	14.75	13.02
7	PC-UCL2-A	6.56	19.17	10.13
8	PC-UCL2-B	6.56	24.27	9.46
9	PC-UCL2-C	6.56	24.96	9.99
10	PA-UCL4-A	13.12	18.20	8.55
11	PA-UCL4-B	13.12	14.27	8.56
12	PA-UCL4-C	13.12	13.51	9.66
13	PB-UCL4-A	13.12	11.45	9.95
14	PB-UCL4-B	13.12	11.65	7.40
15	PB-UCL4-C	13.12	13.24	-
16	PC-UCL4-A	13.12	15.31	11.45
17	PC-UCL4-B	13.12	11.79	11.09
18	PC-UCL4-C	13.12	17.24	8.18
19	PA-UCL6-A	19.68	9.24	6.53
20	PA-UCL6-B	19.68	10.34	6.84
21	PA-UCL6-C	19.68	9.93	7.74
22	PB-UCL6-A	19.68	8.89	13.44
23	PB-UCL6-B	19.68	10.34	5.76
24	PB-UCL6-C	19.68	9.65	9.18
25	PC-UCL6-A	19.68	8.55	7.54
26	PC-UCL6-B	19.68	10.76	15.41
27	PC-UCL6-C	19.68	5.03	-
28	PA-UCM4-A	6.61	21.24	12.2
29	PA-UCM4-B	6.61	24.61	11.95
30	PA-UCM4-C	6.61	21.86	10.29

Table (I-A2) EXPERIMENTAL RESULTS OF TESTED CUBES

Sample No.	Sample Name	Porosity (<i>n</i>)	Uniaxial Compressive Strength, <i>UCS</i>	Young's Modulus, <i>E</i> (25 - 50%)
		%	MPa	GPa
31	PB-UCM4-A	6.61	20.96	10.81
32	PB-UCM4-B	6.61	21.99	11.01
33	PB-UCM4-C	6.61	24.89	11.67
34	PC-UCM4-A	6.61	25.44	13.77
35	PC-UCM4-B	6.61	23.65	12.23
36	PC-UCM4-C	6.61	19.44	14.27
37	PA-UCM8-A	13.21	19.37	7.92
38	PA-UCM8-B	13.21	18.96	-
39	PA-UCM8-C	13.21	17.65	-
40	PB-UCM8-A	13.21	17.72	10.07
41	PB-UCM8-B	13.21	16.96	-
42	PB-UCM8-C	13.21	10.41	-
43	PC-UCM8-A	13.21	15.44	12.78
44	PC-UCM8-B	13.21	13.24	7.60
45	PC-UCM8-C	13.21	13.24	10.91
46	PA-UCM12-A	19.82	12.82	8.23
47	PA-UCM12-B	19.82	12.55	8.80
48	PA-UCM12-C	19.82	12.20	8.80
49	PB-UCM12-A	19.82	7.58	9.52
50	PB-UCM12-B	19.82	9.17	4.10
51	PB-UCM12-C	19.82	9.65	13.46
52	PC-UCM12-A	19.82	5.72	7.80
53	PC-UCM12-B	19.82	2.76	7.34
54	PC-UCM12-C	19.82	5.38	5.72
55	PA-UCS11-A	6.07	26.75	11.95
56	PA-UCS11-B	6.07	27.99	11.20
57	PA-UCS11-C	6.07	24.06	-
58	PB-UCS11-A	6.07	25.41	-
59	PB-UCS11-B	6.07	28.89	10.67
60	PB-UCS11-C	6.07	25.92	10.67
61	PC-UCS11-A	6.07	20.48	11.33
62	PC-UCS11-B	6.07	17.51	11.75
63	PC-UCS11-C	6.07	22.82	11.05
64	PA-UCS22-A	12.14	15.79	11.99

Table (I-A3) EXPERIMENTAL RESULTS OF TESTED CUBES

Sample No.	Sample Name	Porosity (<i>n</i>)	Uniaxial Compressive Strength, <i>UCS</i>	Young's Modulus, <i>E</i> (25 - 50%)
		%	MPa	GPa
65	PA-UCS22-B	12.14	18.89	9.46
66	PA-UCS22-C	12.14	15.65	9.51
67	PB-UCS22-A	12.14	17.31	8.51
68	PB-UCS22-B	12.14	16.96	8.30
69	PB-UCS22-C	12.14	18.41	9.36
70	PC-UCS22-A	12.14	9.93	12.09
71	PC-UCS22-B	12.14	16.75	-
72	PC-UCS22-C	12.14	16.75	-
73	PA-UCS33-A	18.22	10.89	11.02
74	PA-UCS33-B	18.22	10.96	8.34
75	PA-UCS33-C	18.22	12.20	8.04
76	PB-UCS33-A	18.22	11.86	-
77	PB-UCS33-B	18.22	13.24	10.11
78	PB-UCS33-C	18.22	13.31	8.27
79	PC-UCS33-A	18.22	10.41	8.22
80	PC-UCS33-B	18.22	7.65	6.66
81	PC-UCS33-C	18.22	9.77	-
82	PA-USqL3-A	6.28	20.96	10.19
83	PA-USqL3-B	6.28	23.44	-
84	PA-USqL3-C	6.28	18.55	-
85	PB-USqL3-A	6.28	27.79	11.76
86	PB-USqL3-B	6.28	28.96	10.84
87	PB-USqL3-C	6.28	28.06	11.42
88	PA-USqL6-A	12.56	16.96	10.98
89	PA-USqL6-B	12.56	16.55	10.25
90	PA-USqL6-C	12.56	15.10	11.71
91	PB-USqL6-A	12.56	20.34	8.07
92	PB-USqL6-B	12.56	19.24	8.03
93	PB-USqL6-C	12.56	20.48	8.43
94	PA-USqS6-A	6.32	27.17	11.82
95	PA-USqS6-B	6.32	25.17	13.57
96	PA-USqS6-C	6.32	26.27	10.39
97	PB-USqS6-A	6.32	26.20	7.18
98	PB-USqS6-B	6.32	26.54	10.81

Table (I-A4) EXPERIMENTAL RESULTS OF TESTED CUBES

Sample No.	Sample Name	Porosity (<i>n</i>)	Uniaxial Compressive Strength, <i>UCS</i>	Young's Modulus, <i>E</i> (25 - 50%)
		%	MPa	GPa
99	PB-USqS6-C	6.32	26.82	9.91
100	PA-USqM12-A	12.65	16.27	10.31
101	PA-USqS12-B	12.65	17.37	12.77
102	PA-USqS12-C	12.65	18.48	10.80
103	PB-USqS12-A	12.65	17.10	7.67
104	PB-USqS12-B	12.65	15.44	9.76
105	PB-USqS12-C	12.65	16.00	7.78
106	PA-UDmL3-A	6.28	15.38	9.91
107	PA-UDmL3-B	6.28	16.75	10.46
108	PA-UDmL3-C	6.28	16.06	10.58
109	PB-UDmL3-A	6.28	22.41	11.62
110	PB-UDmL3-B	6.28	24.82	11.37
111	PB-UDmL3-C	6.28	21.17	9.83
112	PA-UDmL6-A	12.56	12.00	7.99
113	PA-UDmL6-B	12.56	12.00	4.75
114	PA-UDmL6-C	12.56	11.65	9.90
115	PB-UDmL6-A	12.56	11.17	10.34
116	PB-UDmL6-B	12.56	10.48	7.62
117	PB-UDmL6-C	12.56	10.00	9.69
118	PA-UDmS6-A	6.32	19.17	11.45
119	PA-UDmS6-B	6.32	19.44	11.96
120	PA-UDmS6-C	6.32	19.03	9.64
121	PB-UDmS6-A	6.32	18.68	11.56
122	PB-UDmS6-B	6.32	22.61	10.54
123	PB-UDmS6-C	6.32	22.55	11.57
124	PA-UDmS12-A	12.65	10.27	9.16
125	PA-UDmS12-B	12.65	11.31	7.05
126	PA-UDmS12-C	12.65	11.45	9.35
127	PB-UDmS12-A	12.65	14.41	10.75
128	PB-UDmS12-B	12.65	16.34	12.58
129	PB-UDmS12-C	12.65	17.51	10.69
130	PA-UXCL1M1S3-A	6.59	21.93	11.41
131	PA-UXCL1M1S3-B	6.59	24.55	11.53
132	PA-UXCL1M1S3-C	6.59	23.86	10.29

Table (I-A5) EXPERIMENTAL RESULTS OF TESTED CUBES

Sample No.	Sample Name	Porosity (<i>n</i>)	Uniaxial Compressive Strength, <i>UCS</i>	Young's Modulus, <i>E</i> (25 - 50%)
		%	MPa	GPa
133	PB-UXCL1M1S3-A	6.59	23.03	11.20
134	PB-UXCL1M1S3-B	6.59	18.68	11.77
135	PB-UXCL1M1S3-C	6.59	24.89	10.50
136	PC-UXCL1M1S3-A	6.59	22.61	12.69
137	PC-UXCL1M1S3-B	6.59	19.44	10.45
138	PC-UXCL1M1S3-C	6.59	21.51	9.31
139	PA-UXCL2M3S6-A	14.83	13.17	6.30
140	PA-UXCL2M3S6-B	14.83	14.34	9.68
141	PA-UXCL2M3S6-C	14.83	14.27	7.99
142	PB-UXCL2M3S6-A	14.83	13.86	8.43
143	PB-UXCL2M3S6-B	14.83	13.72	7.93
144	PB-UXCL2M3S6-C	14.83	0.00	4.31
145	PC-UXCL2M3S6-A	14.83	14.69	9.75
146	PC-UXCL2M3S6-B	14.83	0.00	9.20
147	PC-UXCL2M3S6-C	14.83	0.00	9.47
148	PA-UXCL2M5S8-A	19.24	8.96	6.46
149	PA-UXCL2M5S8-B	19.24	12.13	7.03
150	PA-UXCL2M5S8-C	19.24	11.45	7.17
151	PB-UXCL2M5S8-A	19.24	9.93	9.65
152	PB-UXCL2M5S8-B	19.24	10.82	12.64
153	PB-UXCL2M5S8-C	19.24	10.55	6.95
154	PC-UXCL2M5S8-A	19.24	8.96	6.40
155	PC-UXCL2M5S8-B	19.24	7.45	8.07
156	PC-UXCL2M5S8-C	19.24	11.86	-
157	Solid-1	0.00	54.95	16.04
158	Solid-2	0.00	54.80	14.66
159	Solid-3	0.00	53.42	16.01
160	Solid-4	0.00	52.85	16.70
161	Solid-5	0.00	57.31	14.77
162	Solid-6	0.00	55.45	18.13
163	Solid-7	0.00	54.65	15.55
164	Solid-8	0.00	56.94	16.79
165	Solid-9	0.00	56.7	14.91
166	Solid-10	0.00	53.05	16.20

FIGURE (I-1) PHOTOGRAPHS OF TESTED POROUS AND SOLID CUBES

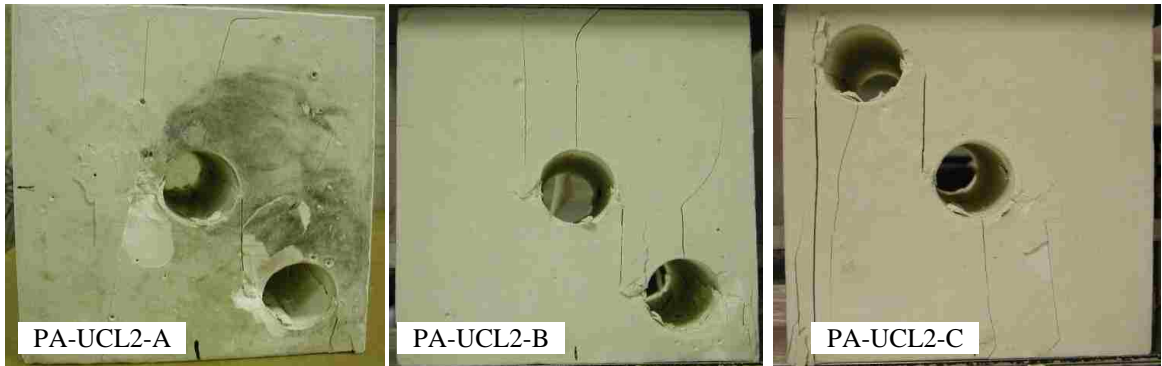
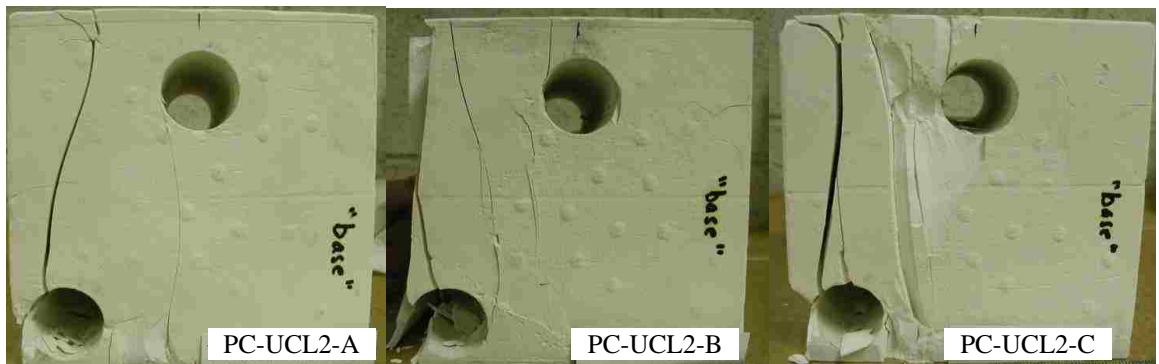
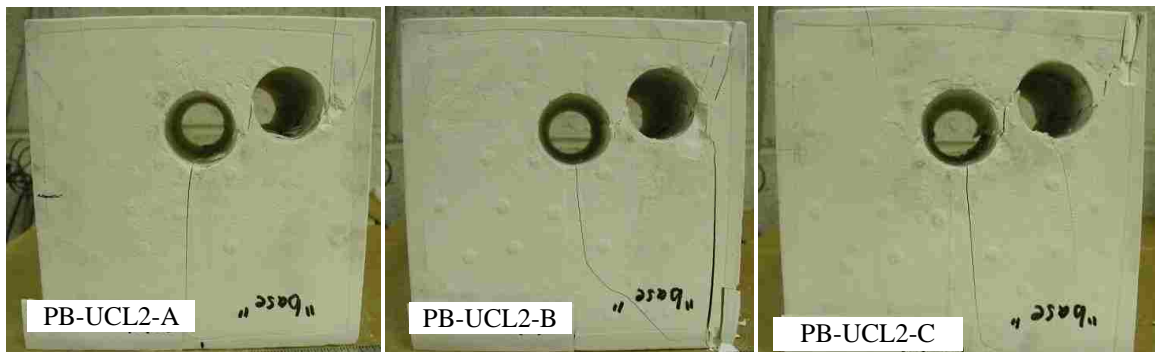
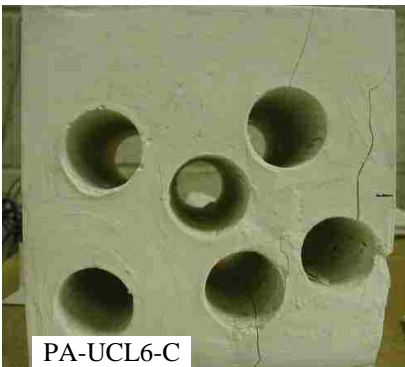
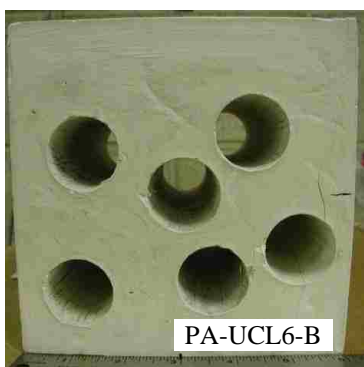
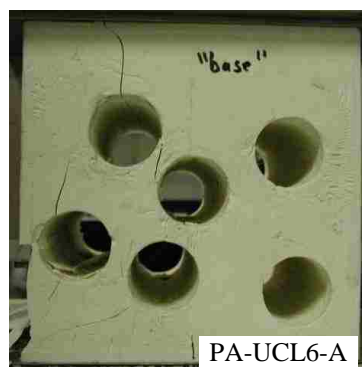
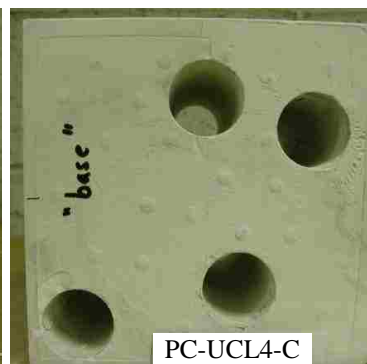
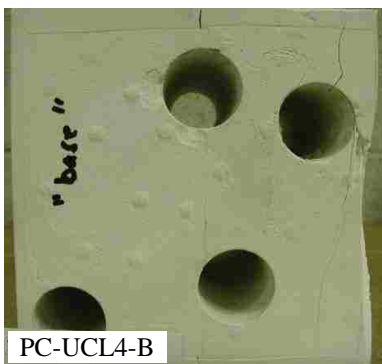
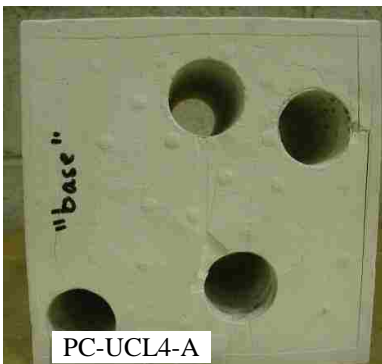
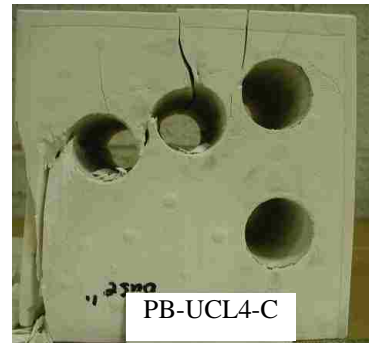
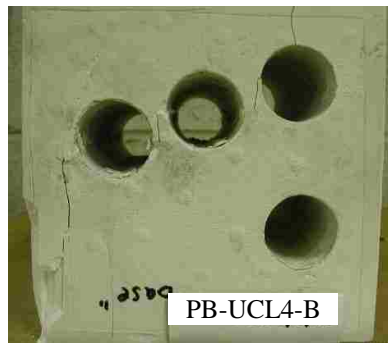
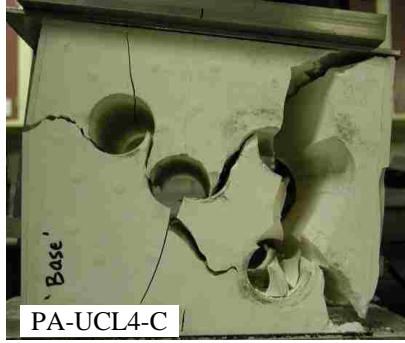
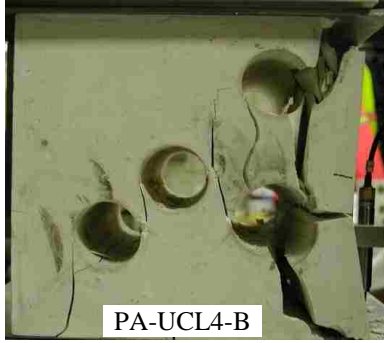
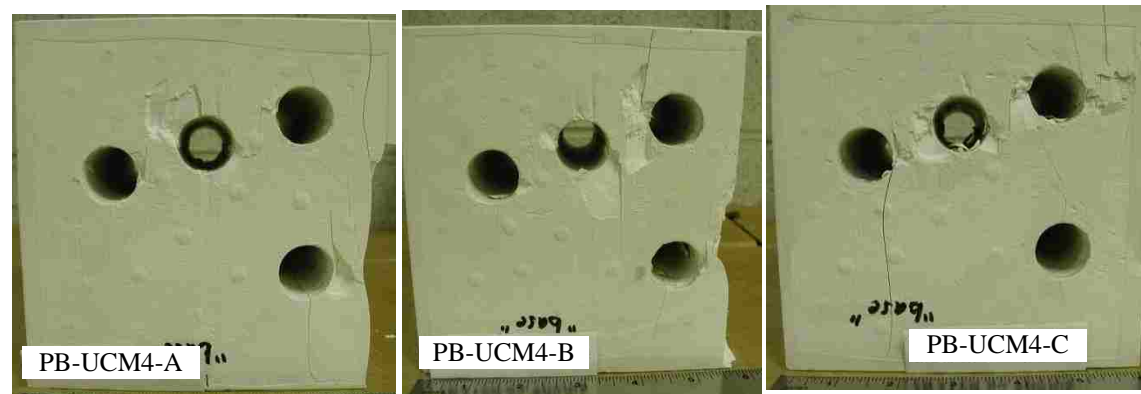
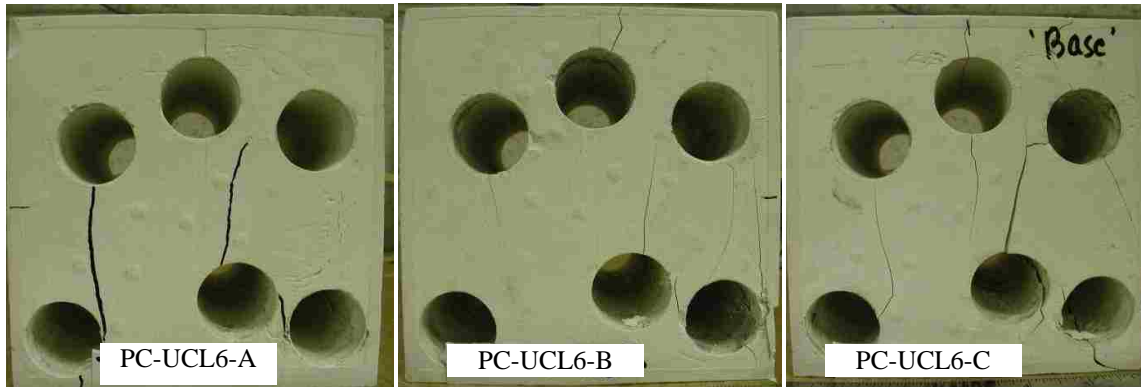
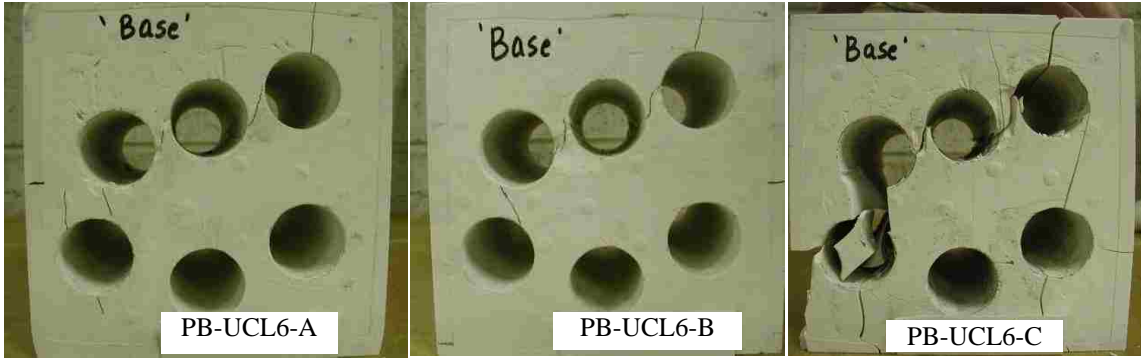
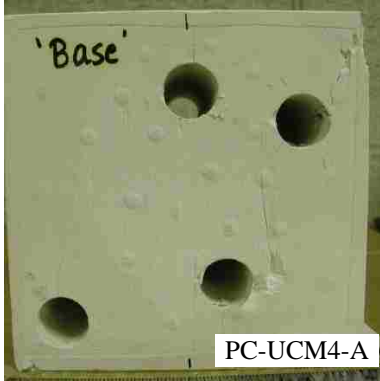


Figure (I.1) Photographs of Tested Porous and Solid Cubes

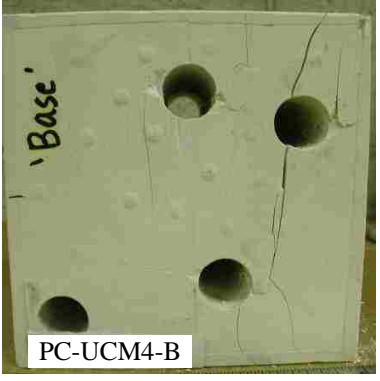




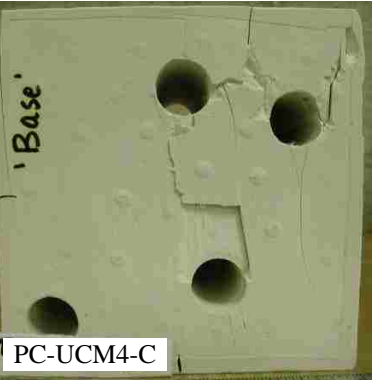




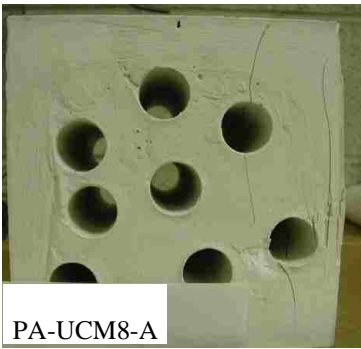
PC-UCM4-A



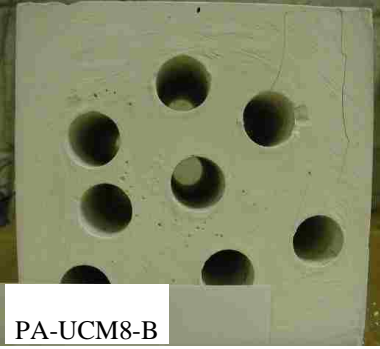
PC-UCM4-B



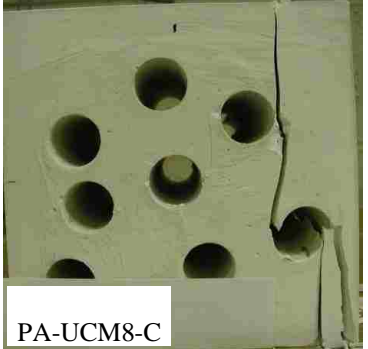
PC-UCM4-C



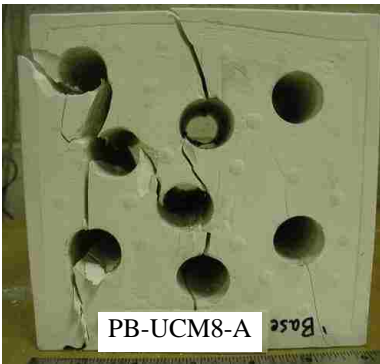
PA-UCM8-A



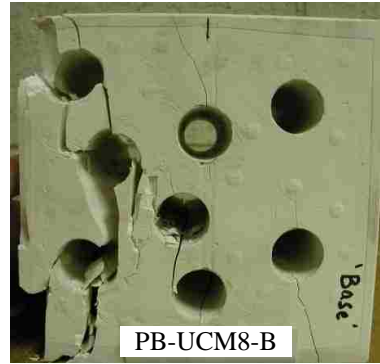
PA-UCM8-B



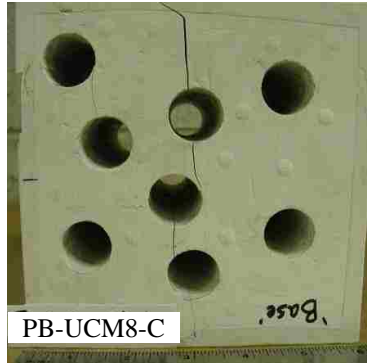
PA-UCM8-C



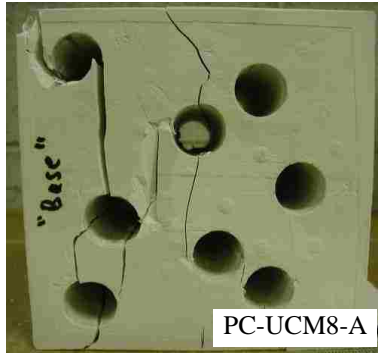
PB-UCM8-A



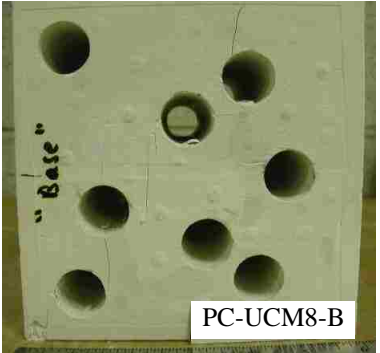
PB-UCM8-B



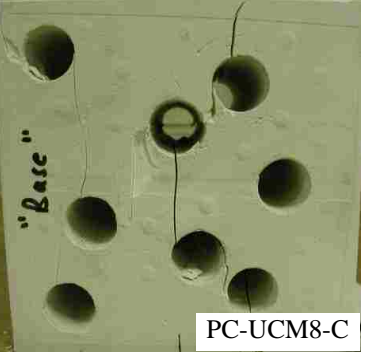
PB-UCM8-C



PC-UCM8-A



PC-UCM8-B



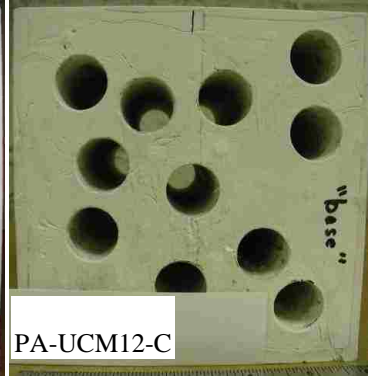
PC-UCM8-C



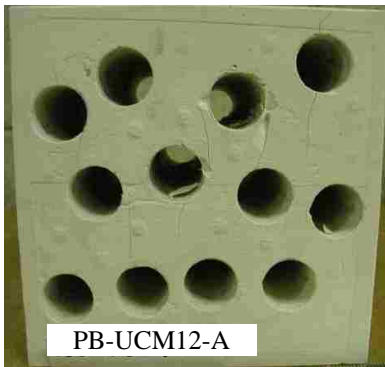
PA-UCM12-A



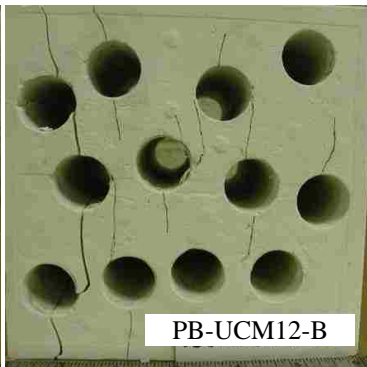
PA-UCM12-B



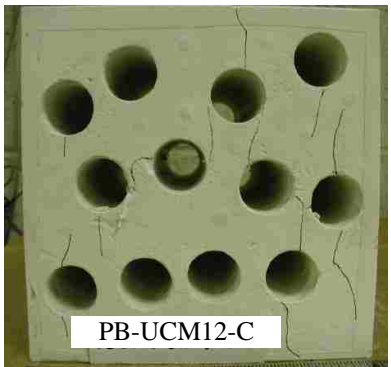
PA-UCM12-C



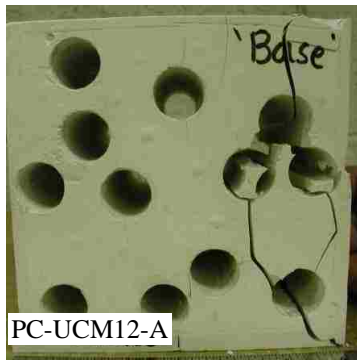
PB-UCM12-A



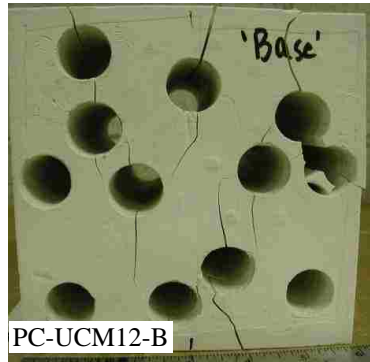
PB-UCM12-B



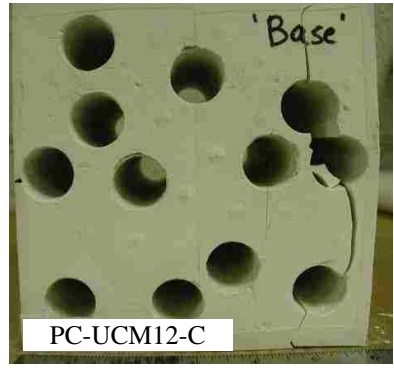
PB-UCM12-C



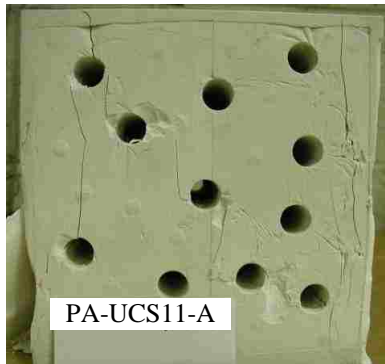
PC-UCM12-A



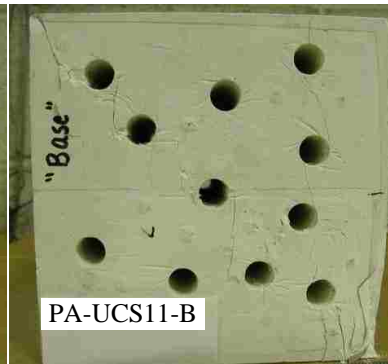
PC-UCM12-B



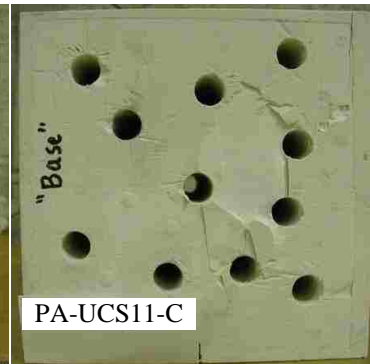
PC-UCM12-C



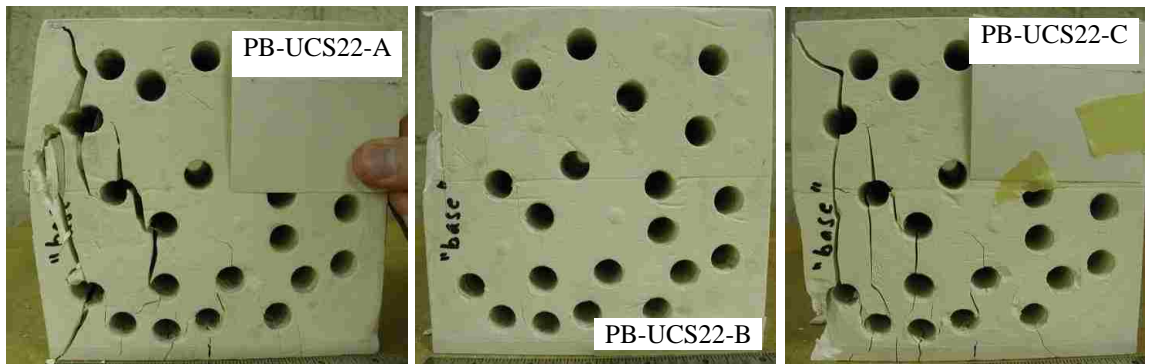
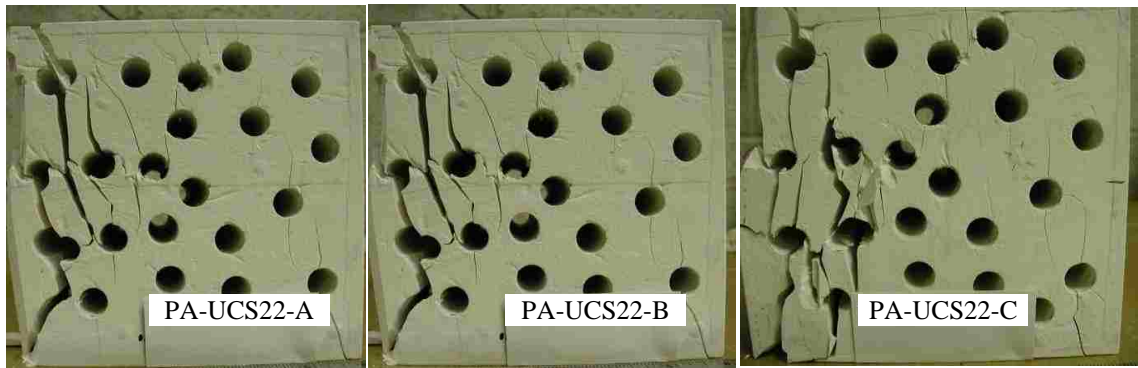
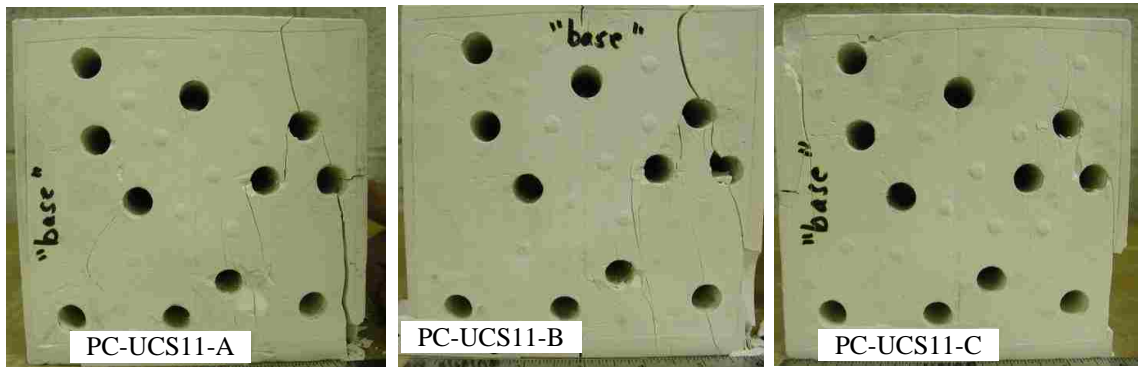
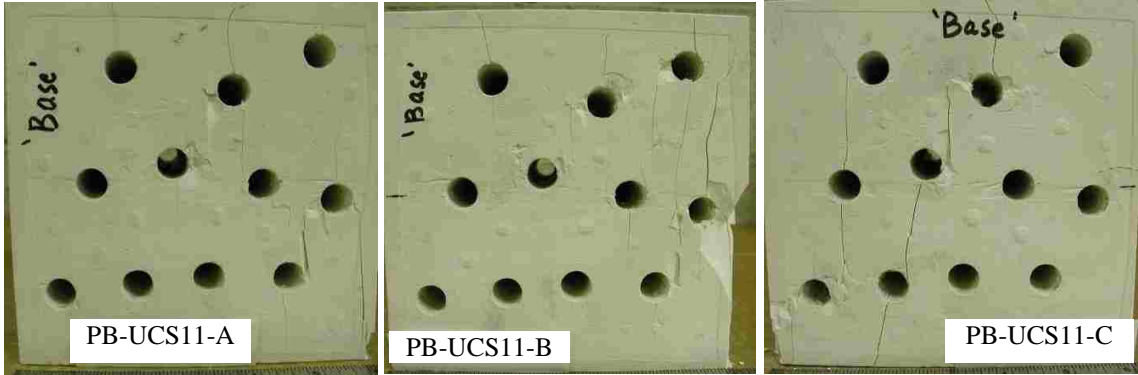
PA-UCS11-A

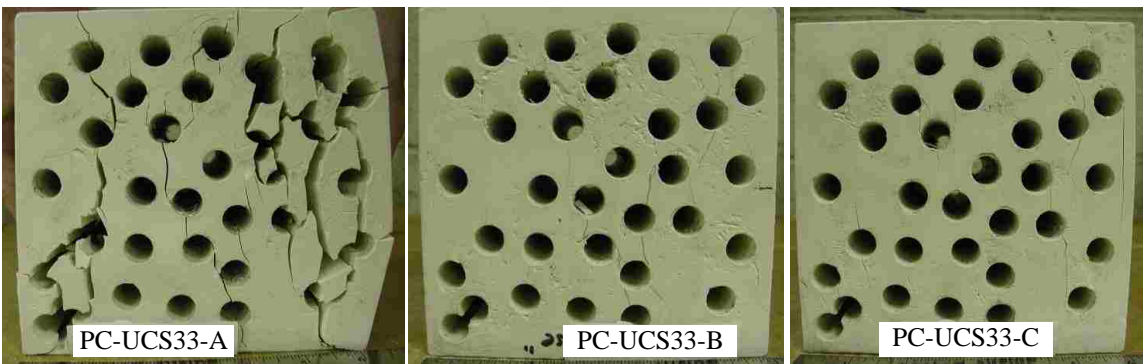
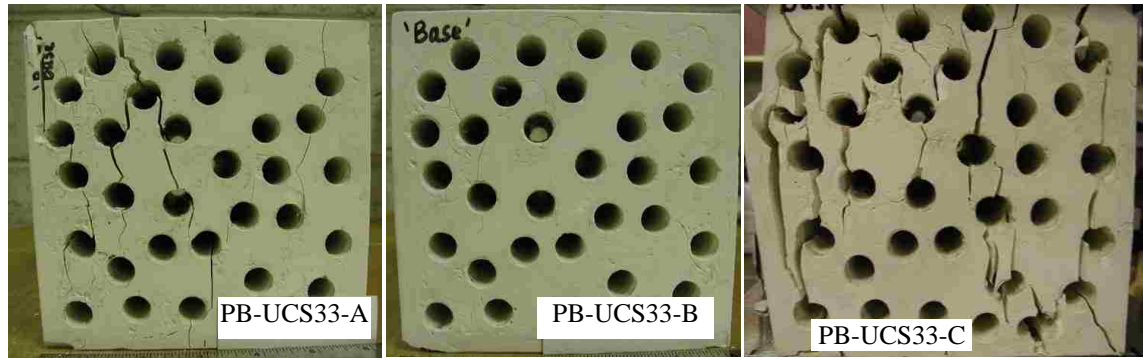
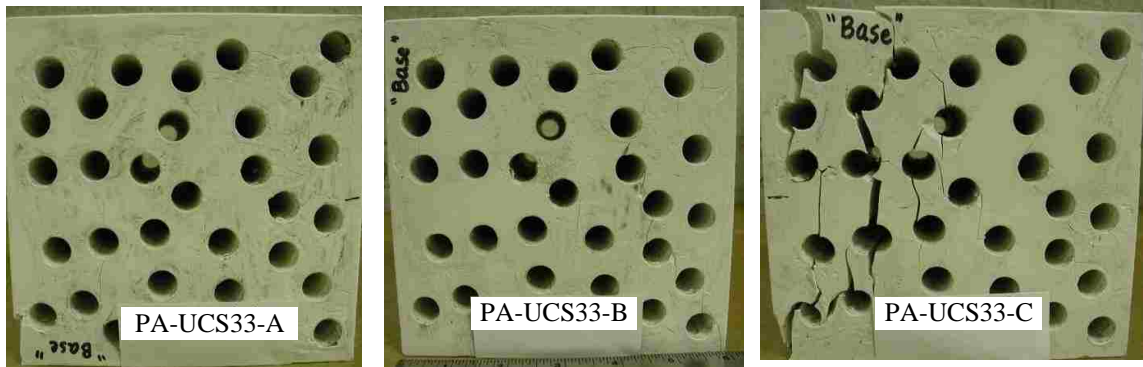
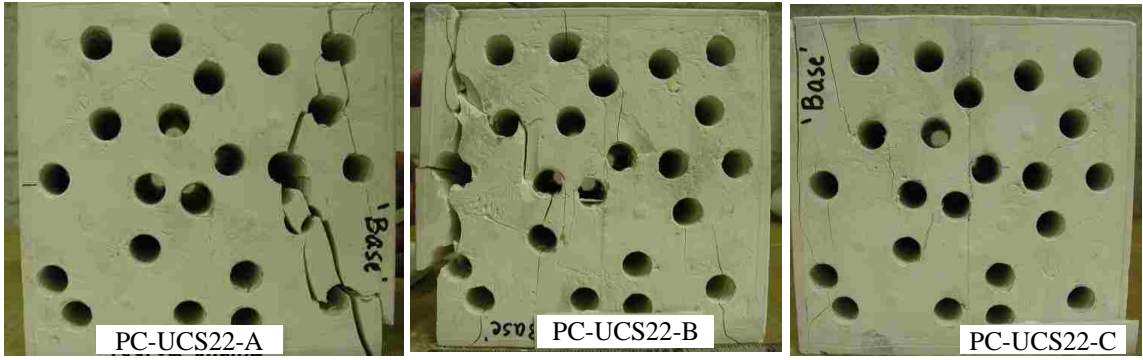


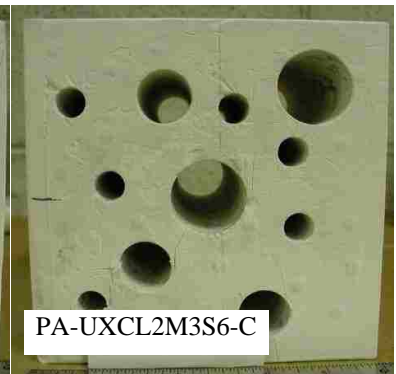
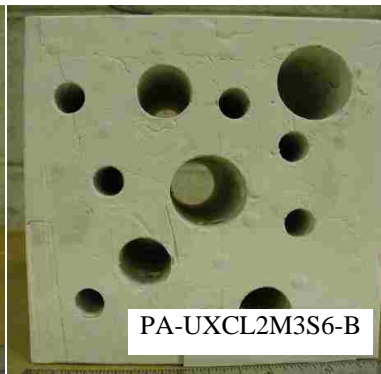
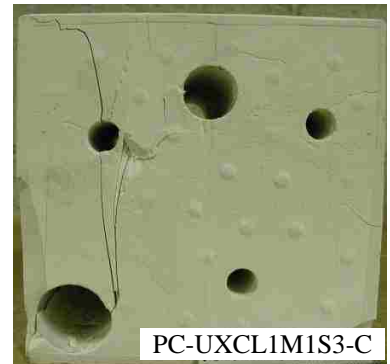
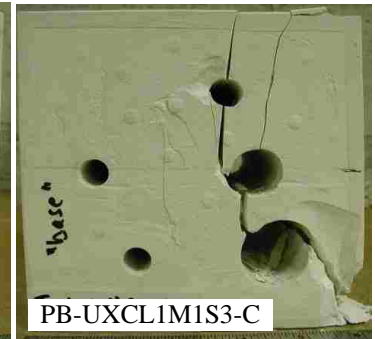
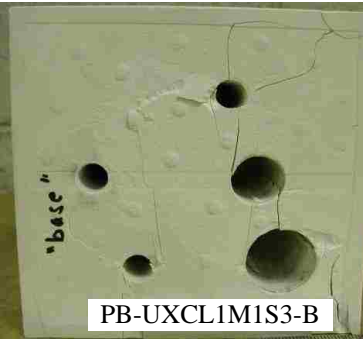
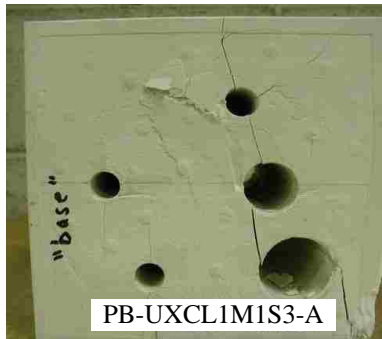
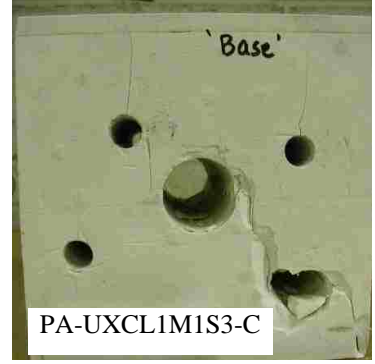
PA-UCS11-B

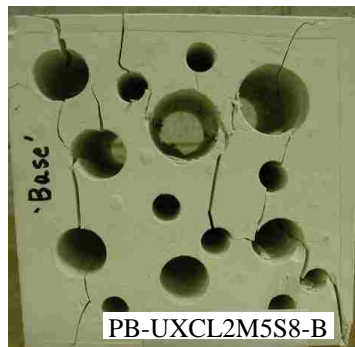
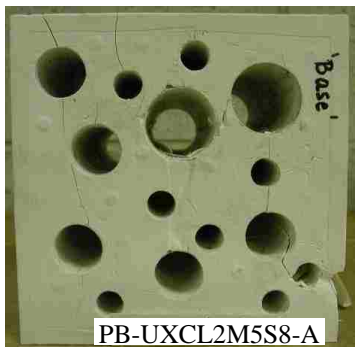
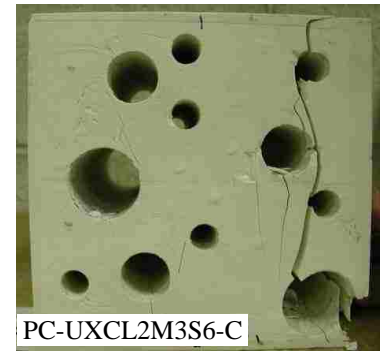
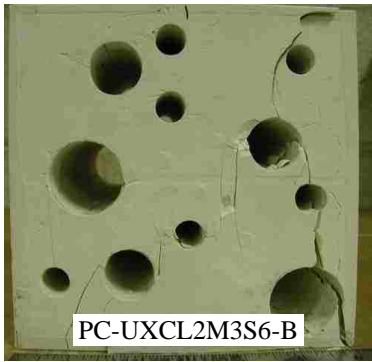
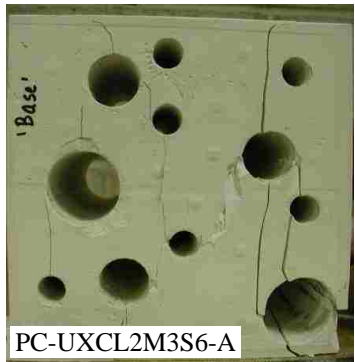
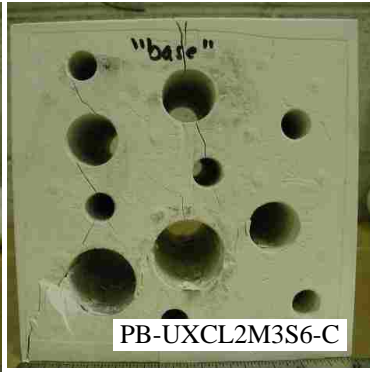


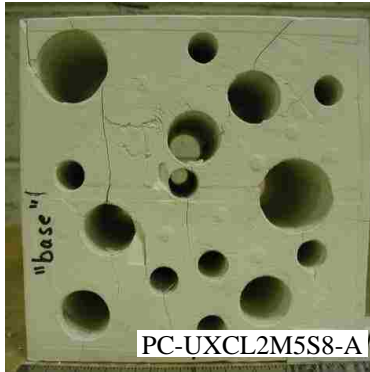
PA-UCS11-C



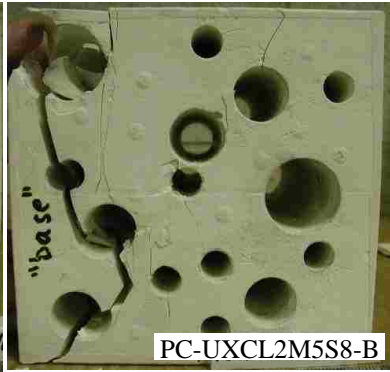




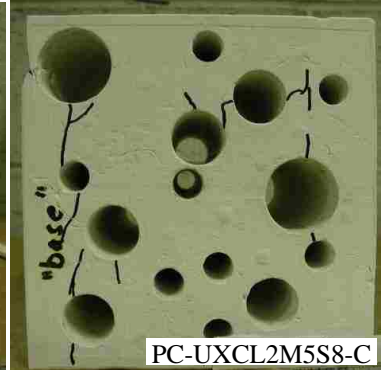




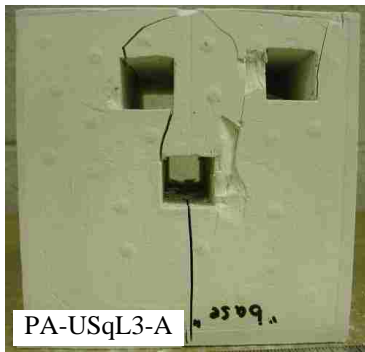
PC-UXCL2M5S8-A



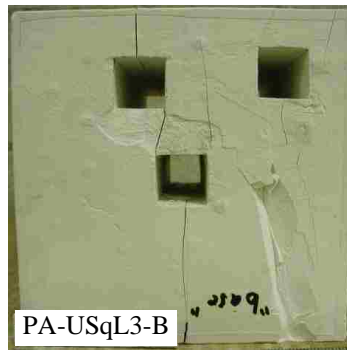
PC-UXCL2M5S8-B



PC-UXCL2M5S8-C



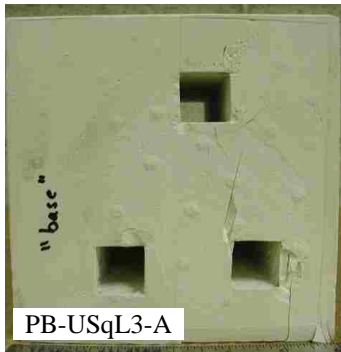
PA-USqL3-A



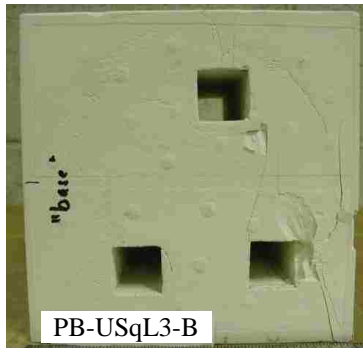
PA-USqL3-B



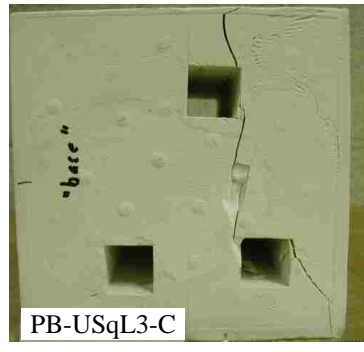
PA-USqL3-C



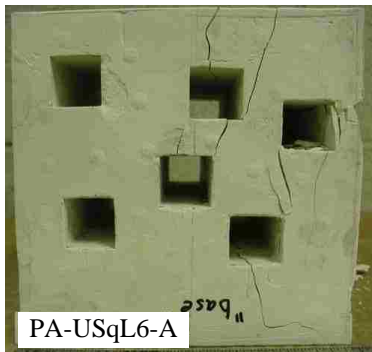
PB-USqL3-A



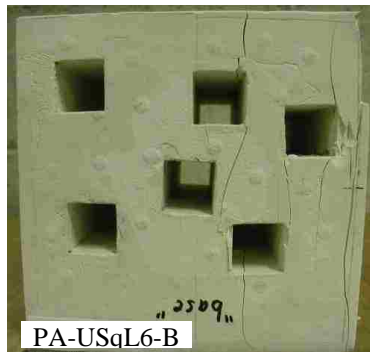
PB-USqL3-B



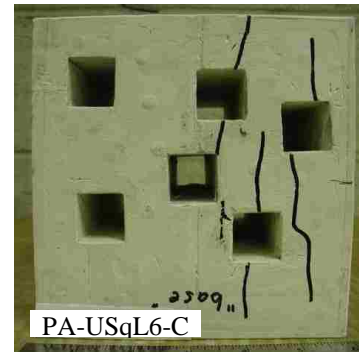
PB-USqL3-C



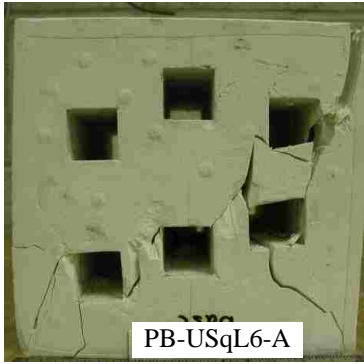
PA-USqL6-A



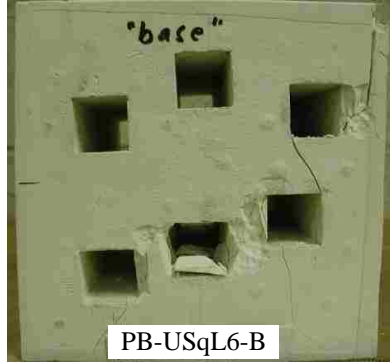
PA-USqL6-B



PA-USqL6-C



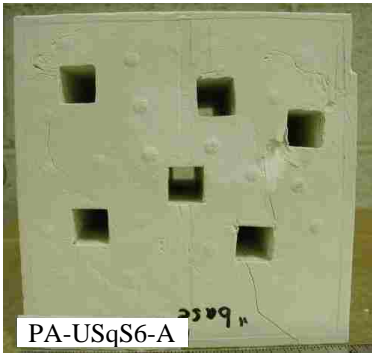
PB-USqL6-A



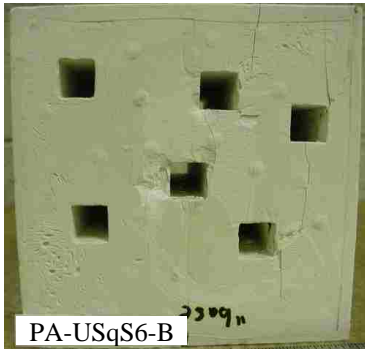
PB-USqL6-B



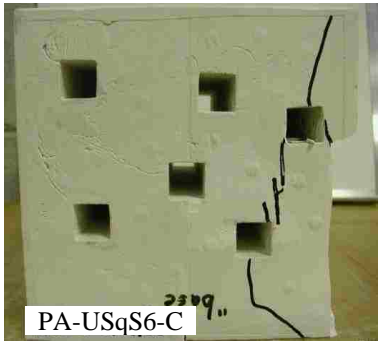
PB-USqL6-C



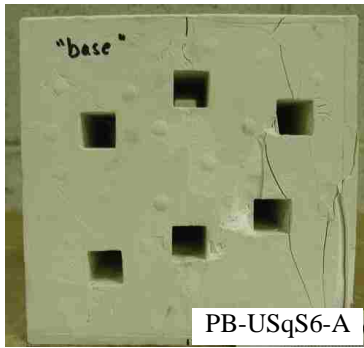
PA-USqS6-A



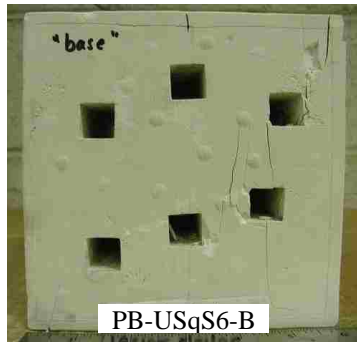
PA-USqS6-B



PA-USqS6-C



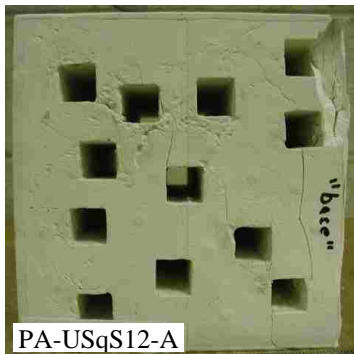
PB-USqS6-A



PB-USqS6-B



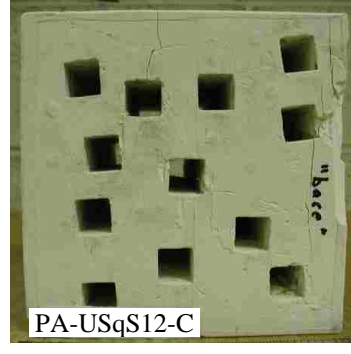
PB-USqS6-C



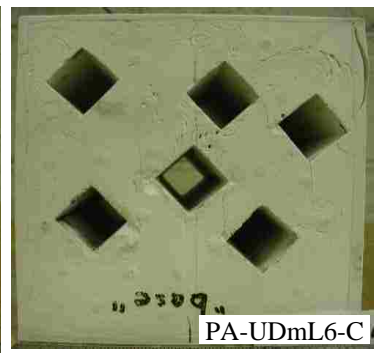
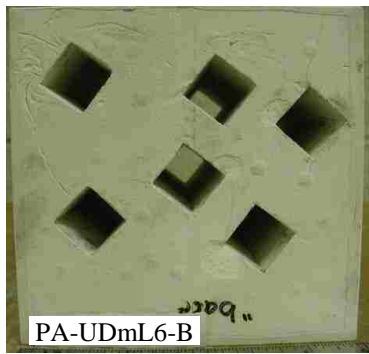
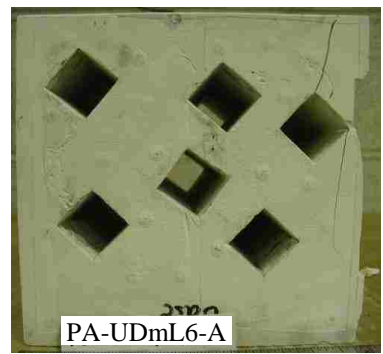
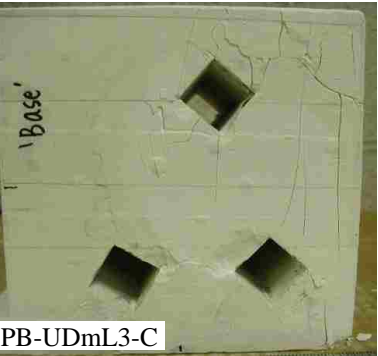
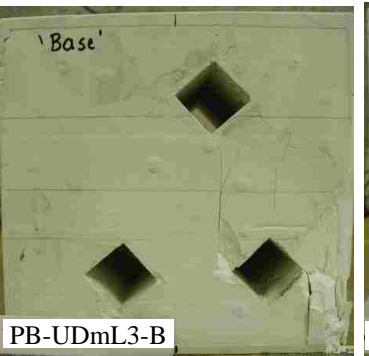
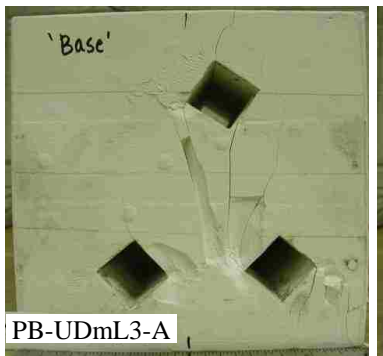
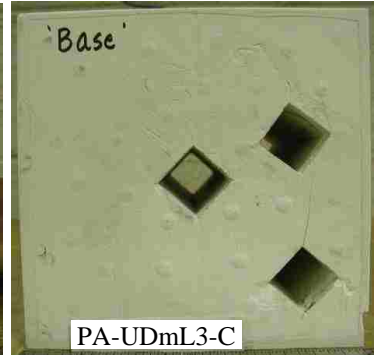
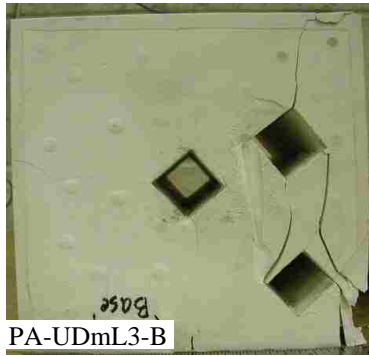
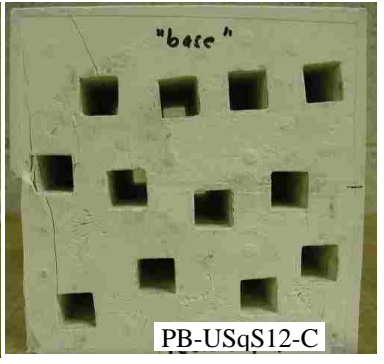
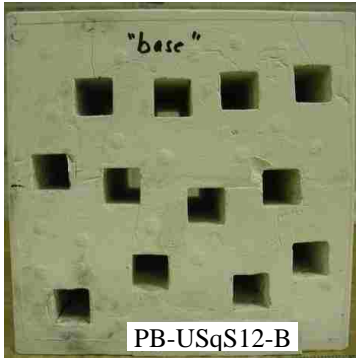
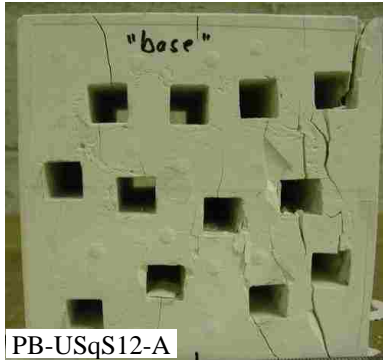
PA-USqS12-A

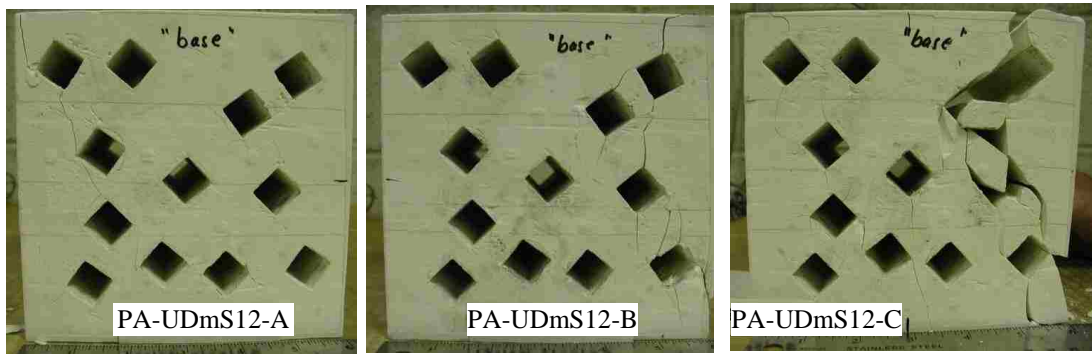
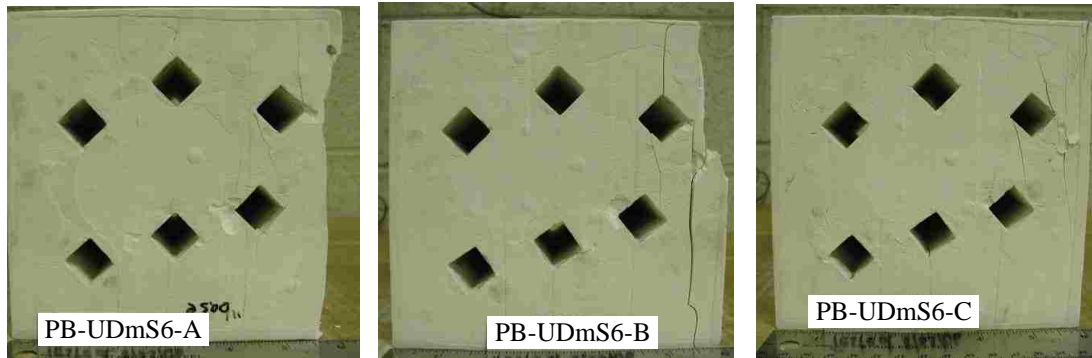
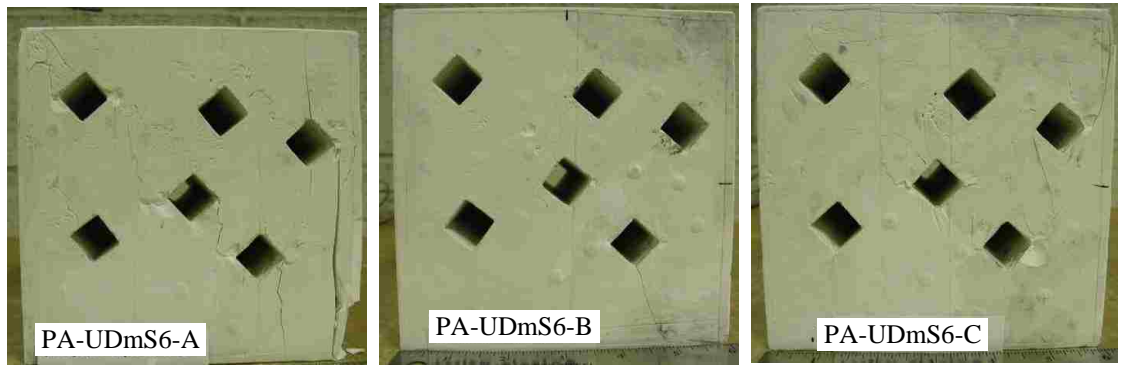
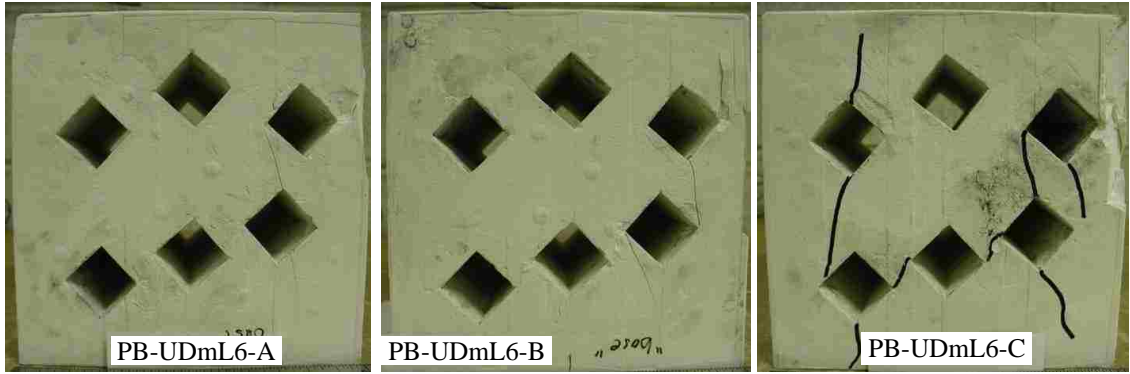


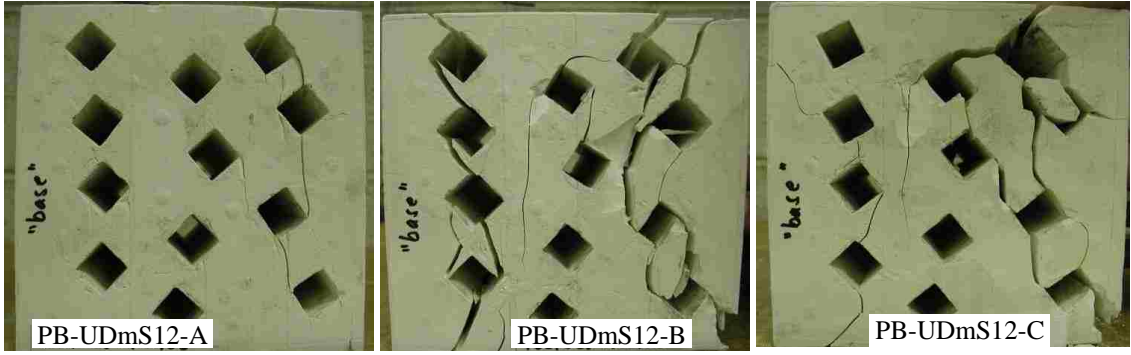
PA-USqS12-B



PA-USqS12-C







PB-UDmS12-A

PB-UDmS12-B

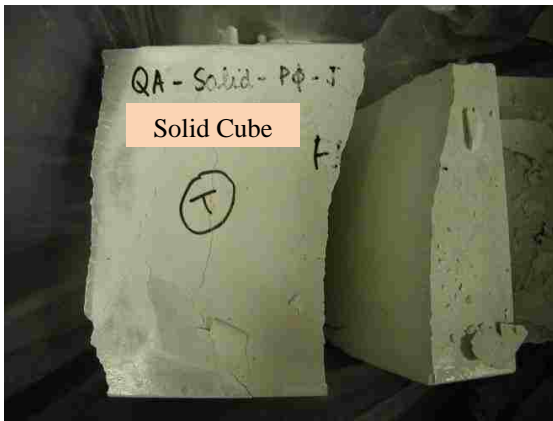
PB-UDmS12-C



Solid Cube During Testing



Tested Solid Cube



Tested Solid Cube



Tested Solid Cube

APPENDIX (II) UDEC CALIBRATION

Table (II-1) MATERIAL PROPERTIES USED IN THE MODEL CALIBRATION

Model Name	Material Properties Used as UDEC Input Data										
	Den	K^m	G^m	\dot{J}_{ten}^m	\dot{J}_{fric}^m	\dot{J}_{coh}^m	res_{Ten}	res_{Fric}	res_{Cohr}	k_n	k_s
	kg/m^3	Pa	Pa	Pa	Degree	Pa	Pa	Degree	Pa	Pa/m	Pa/m
SDSC1	1700	12.11 x10 ⁹	6.24 x10 ⁹	5.516 x10 ⁶	35	12 x10 ⁶	0	15	0	1.211 x 10 ¹²	0.624 x10 ¹²
SDSC2	1700	12.11 x10 ⁹	6.24 x10 ⁹	5.516 x10 ⁶	35	12 x10 ⁶	0	15	0	1.211 x 10 ¹⁴	0.624 x10 ¹⁴
SDSC3	1700	12.11 x10 ⁹	6.24 x10 ⁹	5.516 x10 ⁶	35	24 x10 ⁶	0	15	0	1.211 x 10 ¹⁴	0.624 x10 ¹⁴
SDSC4	1700	12.11 x10 ⁹	6.24 x10 ⁹	5.516 x10 ⁶	35	26 x10 ⁶	0	15	0	1.211 x 10 ¹⁴	0.624 x10 ¹⁴
SDSC5	1700	12.11 x10 ⁹	6.24 x10 ⁹	5.516 x10 ⁶	35	24.5 x10 ⁶	0	15	0	1.1 x 10 ¹⁴	0.55 x10 ¹⁴
SDSC6	1700	12.11 x10 ⁹	6.24 x10 ⁹	5.516 x10 ⁶	35	24.8 x10 ⁶	0	15	0	1.05 x 10 ¹⁴	0.525 x10 ¹⁴
SDSC7	1700	12.11 x10 ⁹	6.24 x10 ⁹	5.516 x10 ⁶	35	25 x10 ⁶	0	15	0	1.05 x 10 ¹⁴	0.525 x10 ¹⁴
SDSC8	1700	12.11 x10 ⁹	6.24 x10 ⁹	5.516 x10 ⁶	35	25.5 x10 ⁶	0	15	0	1.0 x 10 ¹⁴	0.5 x10 ¹⁴
SDSC9	1700	12.11 x10 ⁹	6.24 x10 ⁹	5.516 x10 ⁶	35	25.2 x10 ⁶	0	15	0	1.02 x 10 ¹⁴	0.51 x10 ¹⁴
SDSC10	1700	12.11 x10 ⁹	6.24 x10 ⁹	5.516 x10 ⁶	35	25.2 x10 ⁶	0	15	0	1.03 x 10 ¹⁴	0.515 x10 ¹⁴
SDSC11	1700	12.11 x10 ⁹	6.24 x10 ⁹	5.516 x10 ⁴	35	25.1 x10 ⁶	0	15	0	1.03 x 10 ¹⁴	0.515 x10 ¹⁴
SDSC12	1700	12.11 x10 ⁹	6.24 x10 ⁹	5.516 x10 ⁵	35	25.1 x10 ⁶	0	15	0	1.03 x 10 ¹⁴	0.515 x10 ¹⁴
SDSC13	1700	12.11 x10 ⁹	6.24 x10 ⁹	1.1032 x10 ⁶	35	25.1 x10 ⁶	0	15	0	1.03 x 10 ¹⁴	0.515 x10 ¹⁴
SDSC14	1700	12.11 x10 ⁹	6.24 x10 ⁹	2.758 x10 ⁶	35	25.1 x10 ⁶	0	15	0	1.03 x 10 ¹⁴	0.515 x10 ¹⁴
SDSC15	1700	12.11 x10 ⁹	6.24 x10 ⁹	5.516 x10 ⁶	35	25.1 x10 ⁶	0	15	0	1.03 x 10 ¹⁴	0.515 x10 ¹⁴
SDSC16	1700	12.11 x10 ⁹	6.24 x10 ⁹	11.032 x10 ⁶	35	25.1 x10 ⁶	0	15	0	1.03 x 10 ¹⁴	0.515 x10 ¹⁴
SDSC17	1700	12.11 x10 ⁹	6.24 x10 ⁹	16.548 x10 ⁶	35	25.1 x10 ⁶	0	15	0	1.03 x 10 ¹⁴	0.515 x10 ¹⁴
SDSC18	1700	12.11 x10 ⁹	6.24 x10 ⁹	27.58 x10 ⁶	35	25.1 x10 ⁶	0	15	0	1.03 x 10 ¹⁴	0.515 x10 ¹⁴
SDSC19	1700	12.11 x10 ⁹	6.24 x10 ⁹	5.516 x10 ⁷	35	25.1 x10 ⁶	0	15	0	1.03 x 10 ¹⁴	0.515 x10 ¹⁴
SDSC20	1700	12.11 x10 ⁹	6.24 x10 ⁹	11.032 x10 ⁷	35	25.1 x10 ⁶	0	15	0	1.03 x 10 ¹⁴	0.515 x10 ¹⁴
SDSC21	1700	12.11 x10 ⁹	6.24 x10 ⁹	5.516 x10 ⁸	35	25.1 x10 ⁶	0	15	0	1.03 x 10 ¹⁴	0.515 x10 ¹⁴
SDSC22	1700	12.121 x10 ⁹	6.25 x10 ⁹	16.625 x10 ⁶	21	35.6 x10 ⁶	0	7	0	1.03 x 10 ¹⁴	0.515 x10 ¹⁴
SDSC23	1700	12.121 x10 ⁹	6.25 x10 ⁹	16.625 x10 ⁶	21	36 x10 ⁶	0	7	0	1.03 x 10 ¹⁴	0.515 x10 ¹⁴
SDSC24	1700	12.121 x10 ⁹	6.25 x10 ⁹	16.625 x10 ⁶	21	36.2 x10 ⁶	0	7	0	1.03 x 10 ¹⁴	0.515 x10 ¹⁴
SDSC25	1700	12.121 x10 ⁹	6.25 x10 ⁹	16.625 x10 ⁶	21	36.22 x10 ⁶	0	7	0	1.03 x 10 ¹⁴	0.515 x10 ¹⁴
SDSC26	1700	12.121 x10 ⁹	6.25 x10 ⁹	16.625 x10 ⁶	21	36.22 x10 ⁶	0	3	0	1.03 x 10 ¹⁴	0.515 x10 ¹⁴

Table (II-2) MATERIAL PROPERTIES USED IN THE MODEL CALIBRATION

Model Name	Material Properties Used as UDEC Input Data										
	<i>Den</i>	<i>K^m</i>	<i>G^m</i>	<i>J_{ten}^m</i>	<i>J_{fric}^m</i>	<i>J_{coh}^m</i>	<i>res_{Ten}</i>	<i>res_{Fric}</i>	<i>res_{Cohr}</i>	<i>k_n</i>	<i>k_s</i>
	kg/m ³	Pa	Pa	Pa	Degree	Pa	Pa	Degree	Pa	Pa/m	Pa/m
SDSC27	1700	12.121 2 x10 ⁹	6.25 x10 ⁹	16.625 x10 ⁶	24	33.67 x10 ⁶	0	8	0	1.03 x 10 ¹⁴	0.515 x10 ¹⁴
SDSC28	1700	12.121 2 x10 ⁹	6.25 x10 ⁹	16.625 x10 ⁶	24	33.69 x10 ⁶	0	8	0	1.03 x 10 ¹⁴	0.515 x10 ¹⁴
SDSC29	1700	12.121 2 x10 ⁹	6.25 x10 ⁹	16.625 x10 ⁶	24	33.8x 10 ⁶	0	8	0	1.03 x 10 ¹⁴	0.515 x10 ¹⁴
SDSC30	1700	12.121 2 x10 ⁹	6.25 x10 ⁹	16.625 x10 ⁶	24	33.75 x10 ⁶	0	8	0	1.03 x 10 ¹⁴	0.515 x10 ¹⁴
SDSC31	1700	12.121 2 x10 ⁹	6.25 x10 ⁹	16.625 x10 ⁶	24	33.75 x10 ⁶	0	5	0	1.03 x 10 ¹⁴	0.515 x10 ¹⁴
SDSC32	1700	12.121 2 x10 ⁹	6.25 x10 ⁹	16.625 x10 ⁶	27	27.5 x10 ⁶	0	9	0	1.03 x 10 ¹⁴	0.515 x10 ¹⁴
SDSC33	1700	12.121 2 x10 ⁹	6.25 x10 ⁹	16.625 x10 ⁶	27	32 x10 ⁶	0	9	0	1.03 x 10 ¹⁴	0.515 x10 ¹⁴
SDSC34	1700	12.121 2 x10 ⁹	6.25 x10 ⁹	16.625 x10 ⁶	27	31 x10 ⁶	0	9	0	1.03 x 10 ¹⁴	0.515 x10 ¹⁴
SDSC35	1700	12.121 2 x10 ⁹	6.25 x10 ⁹	16.625 x10 ⁶	27	31.3 x10 ⁶	0	9	0	1.03 x 10 ¹⁴	0.515 x10 ¹⁴
SDSC36	1700	12.121 2 x10 ⁹	6.25 x10 ⁹	16.625 x10 ⁶	27	31.1 x10 ⁶	0	9	0	1.03 x 10 ¹⁴	0.515 x10 ¹⁴
SDSC37	1700	12.121 2 x10 ⁹	6.25 x10 ⁹	16.625 x10 ⁶	27	31.12 x10 ⁶	0	9	0	1.03 x 10 ¹⁴	0.515 x10 ¹⁴
SDSC38	1700	12.121 2 x10 ⁹	6.25 x10 ⁹	16.625 x10 ⁶	27	31.12 x10 ⁶	0	5	0	1.03 x 10 ¹⁴	0.515 x10 ¹⁴
SDSC39	1700	12.121 2 x10 ⁹	6.25 x10 ⁹	16.625 x10 ⁶	27	31.12 x10 ⁶	0	11	0	1.03 x 10 ¹⁴	0.515 x10 ¹⁴
SDSC40	1700	12.121 2 x10 ⁹	6.25 x10 ⁹	16.625 x10 ⁶	31	28 x10 ⁶	0	11	0	1.03 x 10 ¹⁴	0.515 x10 ¹⁴
SDSC41	1700	12.121 2 x10 ⁹	6.25 x10 ⁹	16.625 x10 ⁶	31	27 x10 ⁶	0	11	0	1.03 x 10 ¹⁴	0.515 x10 ¹⁴
SDSC42	1700	12.121 2 x10 ⁹	6.25 x10 ⁹	16.625 x10 ⁶	31	26.7 x10 ⁶	0	11	0	1.03 x 10 ¹⁴	0.515 x10 ¹⁴
SDSC43	1700	12.121 2 x10 ⁹	6.25 x10 ⁹	16.625 x10 ⁶	31	26.66 x10 ⁶	0	11	0	1.03 x 10 ¹⁴	0.515 x10 ¹⁴
SDSC44	1700	12.121 2 x10 ⁹	6.25 x10 ⁹	16.625 x10 ⁶	31	26.65 x10 ⁶	0	11	0	1.03 x 10 ¹⁴	0.515 x10 ¹⁴
SDSC45	1700	12.121 2 x10 ⁹	6.25 x10 ⁹	16.63 x10 ⁶	31	26.55 x10 ⁶	0	11	0	1.03 x 10 ¹⁴	0.515 x10 ¹⁴
SDSC46	1700	12.121 2 x10 ⁹	6.25 x10 ⁹	16.68 x10 ⁶	31	26.5 x10 ⁶	0	11	0	1.03 x 10 ¹⁴	0.515 x10 ¹⁴
SDSC47	1700	12.121 2 x10 ⁹	6.25 x10 ⁹	16.678 x10 ⁶	31	26.48 x10 ⁶	0	11	0	1.03 x 10 ¹⁴	0.515 x10 ¹⁴
SDSC48	1700	12.121 2 x10 ⁹	6.25 x10 ⁹	16.679 x10 ⁶	31	26.46 x10 ⁶	0	11	0	1.03 x 10 ¹⁴	0.515 x10 ¹⁴
SDSC49	1700	12.121 2 x10 ⁹	6.25 x10 ⁹	16.679 x10 ⁶	31	26.44 x10 ⁶	0	11	0	1.03 x 10 ¹⁴	0.515 x10 ¹⁴
SDSC50	1700	12.121 2 x10 ⁹	6.25 x10 ⁹	16.679 x10 ⁶	31	26.45 x10 ⁶	0	11	0	1.03 x 10 ¹⁴	0.515 x10 ¹⁴
SDSC51	1700	12.121 2 x10 ⁹	6.25 x10 ⁹	16.679 x10 ⁶	31	26.45 x10 ⁶	0	5	0	1.03 x 10 ¹⁴	0.515 x10 ¹⁴
SDSC52	1700	12.121 2 x10 ⁹	6.25 x10 ⁹	16.625 x10 ⁶	35	25.2 x10 ⁶	0	15	0	1.03 x 10 ¹⁴	0.515 x10 ¹⁴
SDSC53	1700	12.121 2 x10 ⁹	6.25 x10 ⁹	16.625 x10 ⁶	35	23.2 x10 ⁶	0	15	0	1.03 x 10 ¹⁴	0.515 x10 ¹⁴

Table (II-3) MATERIAL PROPERTIES USED IN THE MODEL CALIBRATION

Model Name	Material Properties Used as UDEC Input Data										
	Den	K^m	G^m	J_{ten}^m	J_{fric}^m	J_{coh}^m	res_{Ten}	res_{Fric}	res_{Cohr}	k_n	k_s
	kg/m^3	Pa	Pa	Pa	$Deg.$	Pa	Pa	$Deg.$	Pa	Pa/m	Pa/m
SDSC54	1700	12.121 2 x10 ⁹	6.25 x10 ⁹	16.625 x10 ⁶	35	23.4 x10 ⁶	0	15	0	1.03 x 10 ¹⁴	0.515x10 ¹⁴ 4
SDSC55	1700	12.121 2 x10 ⁹	6.25 x10 ⁹	16.625 x10 ⁶	35	23.8 x10 ⁶	0	15	0	1.03 x 10 ¹⁴	0.515x10 ¹⁴ 4
SDSC56	1700	12.121 2 x10 ⁹	6.25 x10 ⁹	16.625 x10 ⁶	35	23.6 x10 ⁶	0	15	0	1.03 x 10 ¹⁴	0.515x10 ¹⁴ 4
SDSC57	1700	12.121 2 x10 ⁹	6.25 x10 ⁹	16.625 x10 ⁶	35	23.5x10 ⁶	0	15	0	1.03 x 10 ¹⁴	0.515x10 ¹⁴ 4
SDSC58	1700	12.121 2 x10 ⁹	6.25 x10 ⁹	16.625 x10 ⁶	11	23.5x10 ⁶	0	15	0	1.03 x 10 ¹⁴	0.515x10 ¹⁴ 4
SDSC59	1700	12.121 2 x10 ⁹	6.25 x10 ⁹	16.625 x10 ⁶	5	23.5x10 ⁶	0	15	0	1.03 x 10 ¹⁴	0.515x10 ¹⁴ 4
SDSC60	1700	12.121 2 x10 ⁹	6.25 x10 ⁹	16.670 x10 ⁶	42	20.5 x10 ⁶	0	15	0	1.03 x 10 ¹⁴	0.515x10 ¹⁴ 4
SDSC61	1700	12.121 2 x10 ⁹	6.25 x10 ⁹	17.00 x10 ⁶	42	20.2 x10 ⁶	0	15	0	1.03 x 10 ¹⁴	0.515x10 ¹⁴ 4
SDSC62	1700	12.121 2 x10 ⁹	6.25 x10 ⁹	17.00 x10 ⁶	42	20.25 x10 ⁶	0	15	0	1.03 x 10 ¹⁴	0.515x10 ¹⁴ 4
SDSC63	1700	12.121 2 x10 ⁹	6.25 x10 ⁹	16.7 x10 ⁶	42	20.3 x10 ⁶	0	15	0	1.03 x 10 ¹⁴	0.515x10 ¹⁴ 4
SDSC64	1700	12.121 2 x10 ⁹	6.25 x10 ⁹	17.0 x10 ⁶	42	20.29 x10 ⁶	0	15	0	1.03 x 10 ¹⁴	0.515x10 ¹⁴ 4
SDSC65	1700	12.121 2 x10 ⁹	6.25 x10 ⁹	16.92 x10 ⁶	42	20.32 x10 ⁶	0	15	0	1.03 x 10 ¹⁴	0.515x10 ¹⁴ 4
SDSC66	1700	12.121 2 x10 ⁹	6.25 x10 ⁹	16.92 x10 ⁶	42	20.4 x10 ⁶	0	15	0	1.03 x 10 ¹⁴	0.515x10 ¹⁴ 4
SDSC67	1700	12.121 2 x10 ⁹	6.25 x10 ⁹	16.92 x10 ⁶	42	20.4 5x10 ⁶	0	15	0	1.03 x 10 ¹⁴	0.515x10 ¹⁴ 4
SDSC68	1700	12.121 2 x10 ⁹	6.25 x10 ⁹	16.92 x10 ⁶	42	20.45 5x10 ⁶	0	15	0	1.03 x 10 ¹⁴	0.515x10 ¹⁴ 4
SDSC69	1700	12.121 2 x10 ⁹	6.25 x10 ⁹	16.00 x10 ⁶	31	26.31 x10 ⁶	0	11	0	0.70 x10 ¹⁴	0.35 x10 ¹⁴
SDSC70	1700	12.121 2 x10 ⁹	6.25 x10 ⁹	16.15 x10 ⁶	31	26.24 x10 ⁶	0	11	0	0.71 x10 ¹⁴	0.355 x10 ¹⁴
SDSC71	1700	12.121 2 x10 ⁹	6.25 x10 ⁹	16.12 x10 ⁶	31	26.245 x10 ⁶	0	11	0	0.714 x10 ¹⁴	0.357 x10 ¹⁴
SDSC72	1700	12.121 2 x10 ⁹	6.25 x10 ⁹	16.09 x10 ⁶	31	26.075 x10 ⁶	0	11	0	0.728 x10 ¹⁴	0.364 x10 ¹⁴
SDSC73	1700	12.121 2 x10 ⁹	6.25 x10 ⁹	16.09 x10 ⁶	31	26.068 x10 ⁶	0	11	0	0.7272 x10 ¹⁴	0.3636 x10 ¹⁴
SDSC74	1700	12.121 2 x10 ⁹	6.25 x10 ⁹	16.095 x10 ⁶	31	26.0675 8x10 ⁶	0	11	0	0.7272 x10 ¹⁴	0.3636 x10 ¹⁴
SDSC75	1700	12.121 2 x10 ⁹	6.25 x10 ⁹	16.09 x10 ⁶	31	26.00 x10 ⁶	0	11	0	0.72728 x10 ¹⁴	0.36364x 10 ¹⁴
SDSC76	1700	12.121 2 x10 ⁹	6.25 x10 ⁹	16.077 x10 ⁶	31	26.01 x10 ⁶	0	11	0	0.72728 x10 ¹⁴	0.36364x 10 ¹⁴
SDSC77	1700	12.121 2 x10 ⁹	6.25 x10 ⁹	16.072 x10 ⁶	31	26.0191 5x10 ⁶	0	11	0	0.72728 x10 ¹⁴	0.36364x 10 ¹⁴
SDSC78	1700	12.121 2 x10 ⁹	6.25 x10 ⁹	16.072 x10 ⁶	31	26.0172 5x10 ⁶	0	11	0	0.72728 x10 ¹⁴	0.36364x 10 ¹⁴
SDSC79	1700	12.121 2 x10 ⁹	6.25 x10 ⁹	16.071 x10 ⁶	31	26.0172 x10 ⁶	0	11	0	0.72728 x10 ¹⁴	0.36364x 10 ¹⁴
SDSC80	1700	12.121 2 x10 ⁹	6.25 x10 ⁹	16.072 x10 ⁶	31	26.0173 5x10 ⁶	0	11	0	0.72728 x10 ¹⁴	0.36364x 10 ¹⁴

Table (II-4) NUMERICAL RESULTS FOR SIMULATED MODELS IN THE CALIBRATION PROCESS

Model Name	Uniaxial Compressive Strength, <i>UCS</i>	Young's Modulus, <i>E</i>	Uniaxial Compressive Strength, <i>UCS</i>
	(<i>MPa</i>)	(<i>GPa</i>)	(<i>MPa</i>)
<i>SDSC1</i>	30.281	2.733	-
<i>SDSC2</i>	28.281	15.816	-
<i>SDSC3</i>	52.066	16.123	-
<i>SDSC4</i>	56.660	16.161	-
<i>SDSC5</i>	53.592	16.062	-
<i>SDSC6</i>	54.313	15.999	-
<i>SDSC7</i>	54.480	16.004	-
<i>SDSC8</i>	55.745	15.984	-
<i>SDSC9</i>	55.242	15.984	-
<i>SDSC10</i>	55.039	16.004	-
<i>SDSC11</i>	54.548	15.984	0.011
<i>SDSC12</i>	54.965	16.004	0.073
<i>SDSC13</i>	54.923	15.992	0.155
<i>SDSC14</i>	54.989	15.997	0.521
<i>SDSC15</i>	55.039	16.004	0.000
<i>SDSC16</i>	55.230	16.008	3.424
<i>SDSC17</i>	58.807	16.006	5.507
<i>SDSC18</i>	58.903	16.031	8.383
<i>SDSC19</i>	58.867	16.031	8.390
<i>SDSC20</i>	58.867	16.031	8.390
<i>SDSC21</i>	58.867	16.031	8.390
<i>SDSC22</i>	53.956	16.127	5.510
<i>SDSC23</i>	54.653	16.024	5.508
<i>SDSC24</i>	54.937	16.036	5.506
<i>SDSC25</i>	54.985	16.034	5.510
<i>SDSC26</i>	52.692	16.017	5.510
<i>SDSC27</i>	54.872	16.021	5.506
<i>SDSC28</i>	54.891	16.021	5.506
<i>SDSC29</i>	54.698	16.020	5.506
<i>SDSC30</i>	55.056	16.019	5.506
<i>SDSC31</i>	53.239	16.015	5.506
<i>SDSC32</i>	48.540	15.978	5.492
<i>SDSC33</i>	56.613	16.038	5.492
<i>SDSC34</i>	54.799	16.024	5.492
<i>SDSC35</i>	55.338	16.031	5.492
<i>SDSC36</i>	54.912	16.025	5.492
<i>SDSC37</i>	54.953	16.017	5.492
<i>SDSC38</i>	52.268	16.005	5.492
<i>SDSC39</i>	55.512	16.024	5.492
<i>SDSC40</i>	58.453	16.042	5.446

Table (II-5) NUMERICAL RESULTS FOR SIMULATED MODELS IN THE CALIBRATION PROCESS

Model Name	Uniaxial Compressive Strength, <i>UCS</i>	Young's Modulus, <i>E</i>	Uniaxial Tensile Strength, <i>UTS</i>
	(<i>MPa</i>)	(<i>GPa</i>)	(<i>MPa</i>)
<i>SDSC41</i>	55.761	16.022	5.446
<i>SDSC42</i>	55.220	16.014	5.450
<i>SDSC43</i>	55.325	16.013	5.439
<i>SDSC44</i>	54.819	16.013	5.451
<i>SDSC45</i>	55.401	16.021	5.446
<i>SDSC46</i>	55.231	16.014	5.521
<i>SDSC47</i>	55.120	16.015	5.481
<i>SDSC48</i>	55.145	16.015	5.505
<i>SDSC49</i>	54.744	16.014	5.498
<i>SDSC50</i>	55.064	16.016	5.510
<i>SDSC51</i>	55.049	16.016	5.506
<i>SDSC52</i>	59.069	16.050	5.512
<i>SDSC53</i>	54.323	16.012	5.495
<i>SDSC54</i>	54.762	16.018	5.500
<i>SDSC55</i>	55.710	16.022	5.509
<i>SDSC56</i>	55.225	16.024	5.492
<i>SDSC57</i>	55.026	16.021	5.501
<i>SDSC58</i>	55.007	16.021	5.502
<i>SDSC59</i>	55.014	16.021	5.497
<i>SDSC60</i>	55.296	16.024	5.427
<i>SDSC61</i>	54.534	16.017	5.445
<i>SDSC62</i>	54.559	16.020	5.503
<i>SDSC63</i>	54.498	16.017	5.438
<i>SDSC64</i>	54.638	16.017	5.513
<i>SDSC65</i>	54.462	16.018	5.520
<i>SDSC66</i>	54.662	16.019	5.507
<i>SDSC67</i>	55.048	16.022	5.488
<i>SDSC68</i>	53.134	16.010	5.488
<i>SDSC69</i>	57.553	15.954	5.460
<i>SDSC70</i>	54.985	15.933	5.586
<i>SDSC71</i>	57.491	15.977	5.556
<i>SDSC72</i>	54.471	15.971	5.519
<i>SDSC73</i>	55.240	16.000	5.415
<i>SDSC74</i>	54.520	15.991	5.517
<i>SDSC75</i>	54.194	15.993	5.531
<i>SDSC76</i>	54.146	15.997	5.534
<i>SDSC77</i>	55.123	16.000	5.528
<i>SDSC78</i>	54.147	16.924	5.528
<i>SDSC79</i>	54.272	16.008	5.511
<i>SDSC80</i>	55.026	15.999	5.528

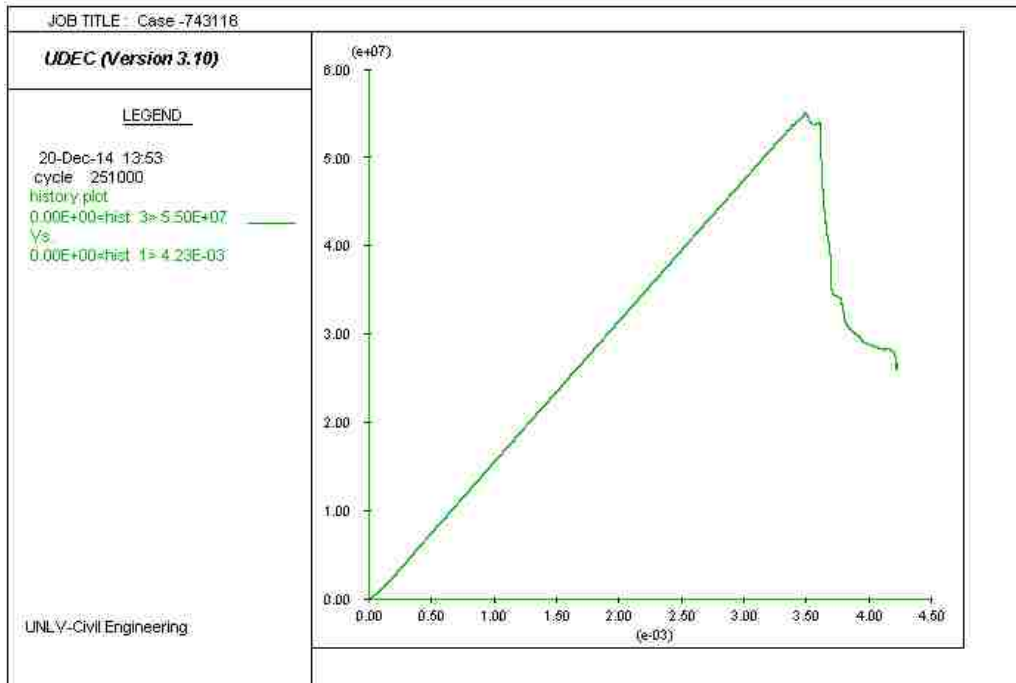


Figure (II.1) COMPRESSION STRESS-STRAIN CURVE FOR THE CALIBRATED MODEL

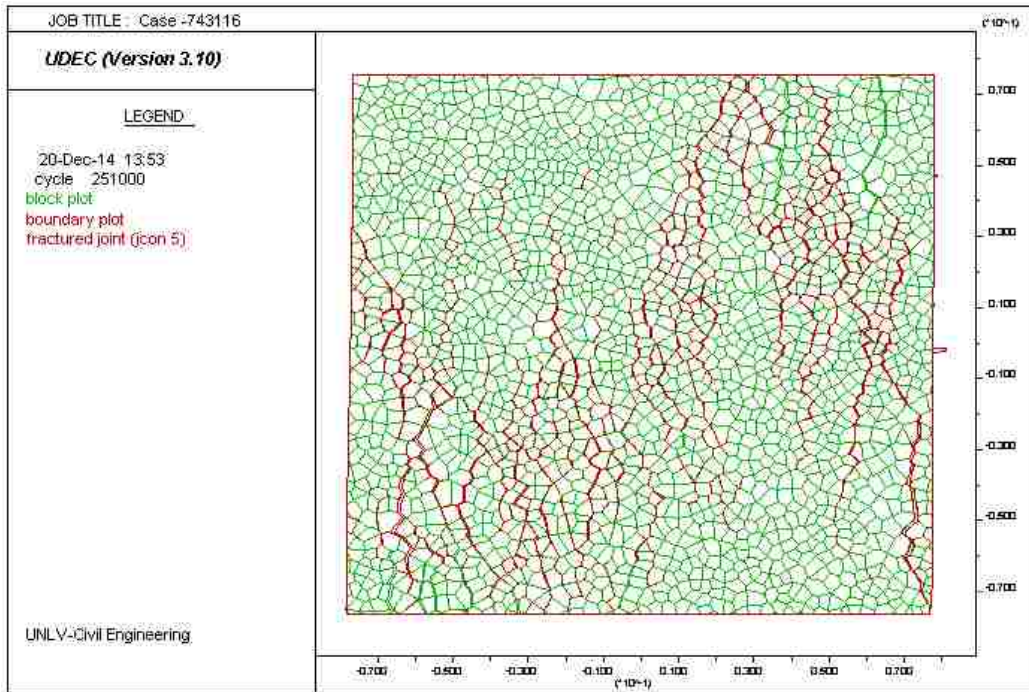
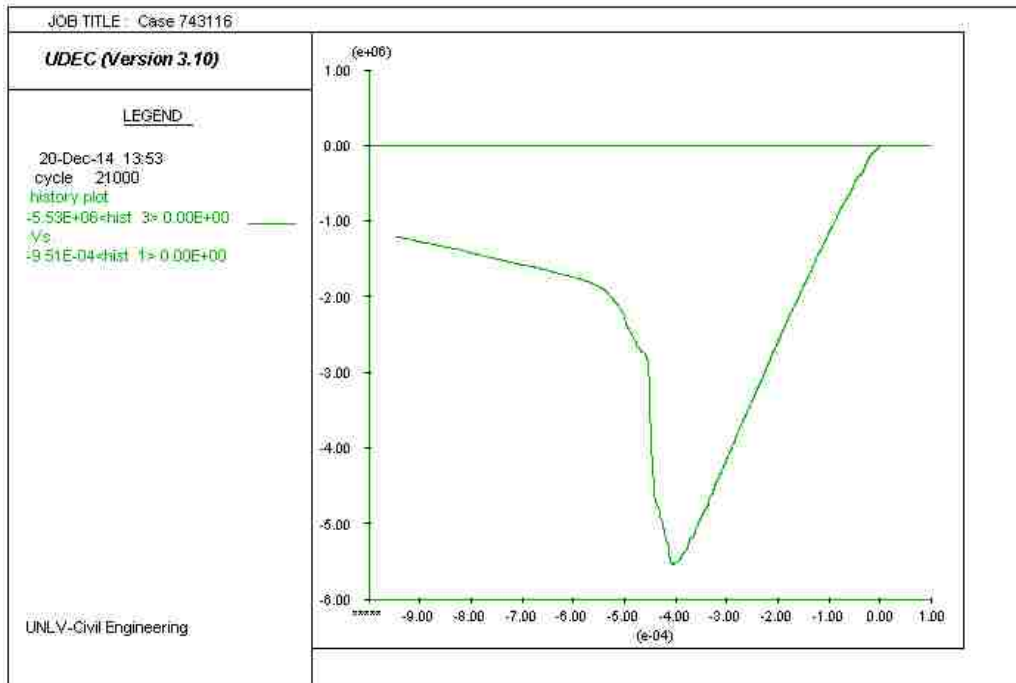


Figure (II.2) POST-FAILURE MODE (IN COMPRESSION) FOR THE CALIBRATED MODEL



Figure(II.3) TENSION STRESS-STRAIN CURVE FOR THE CALIBRATED MODEL

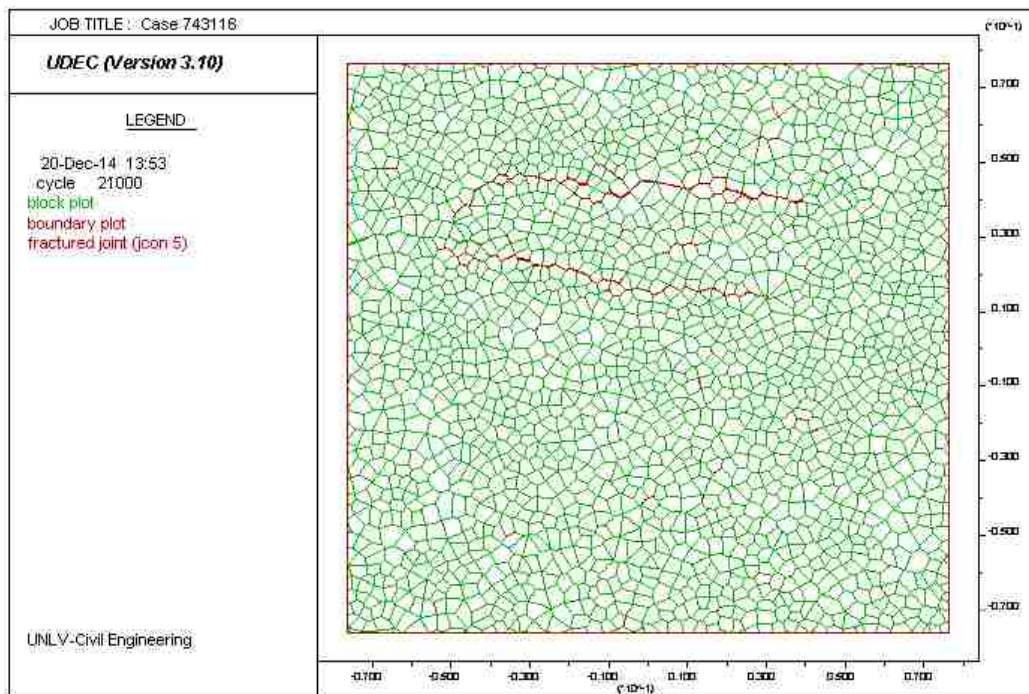
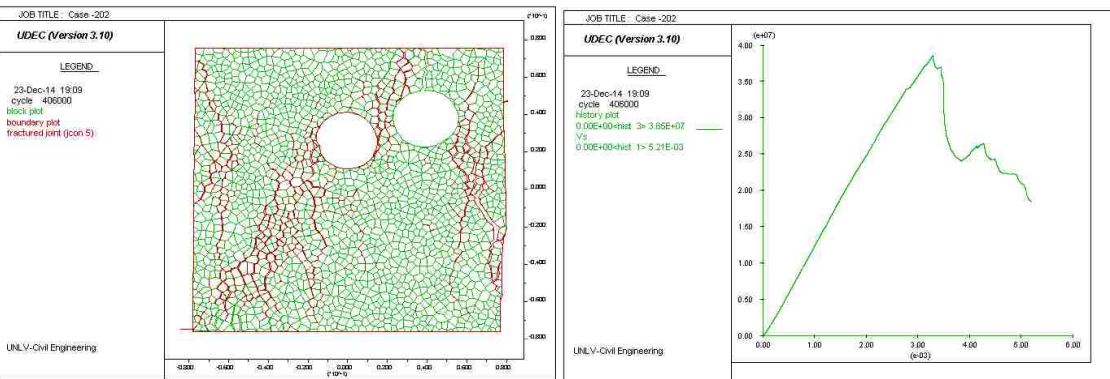
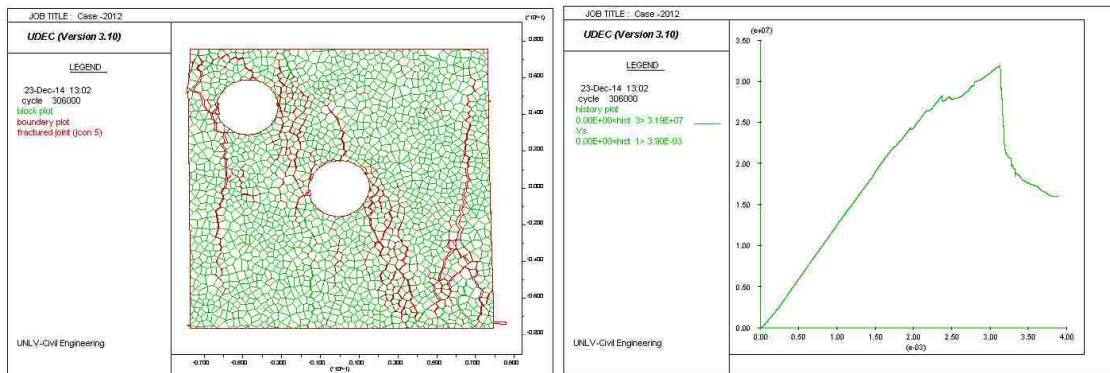
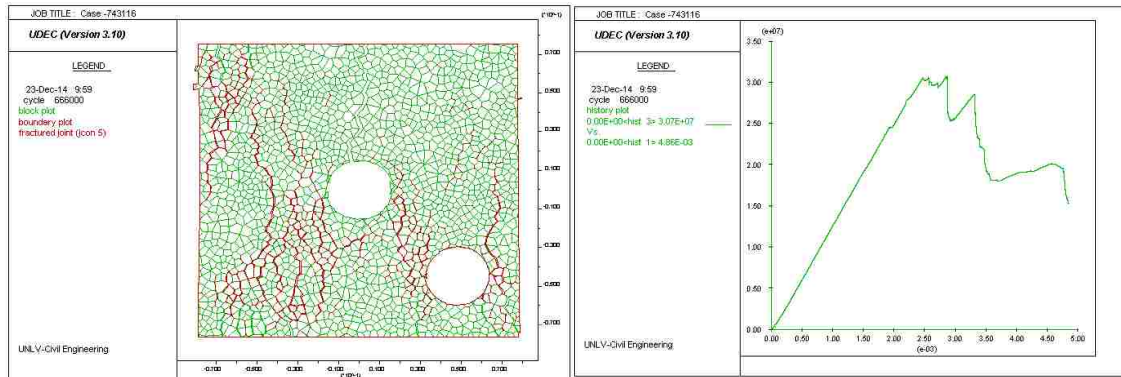
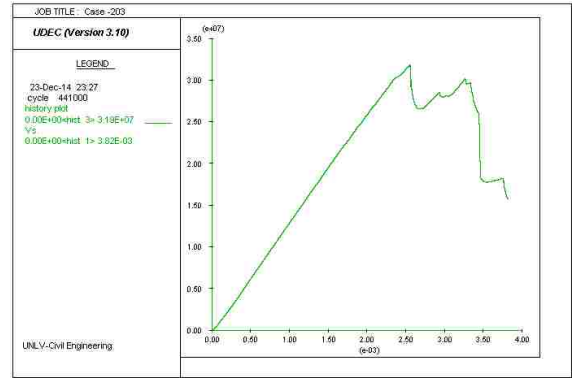
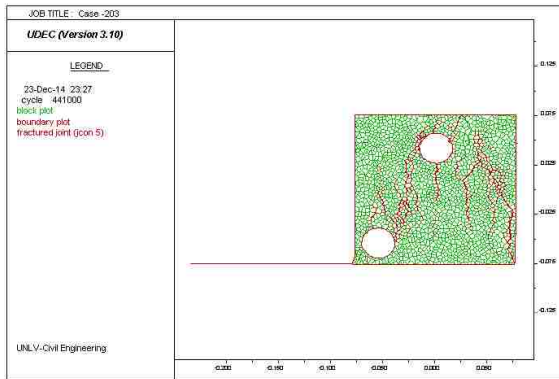


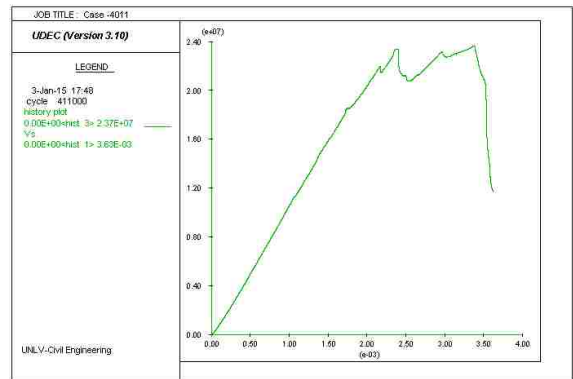
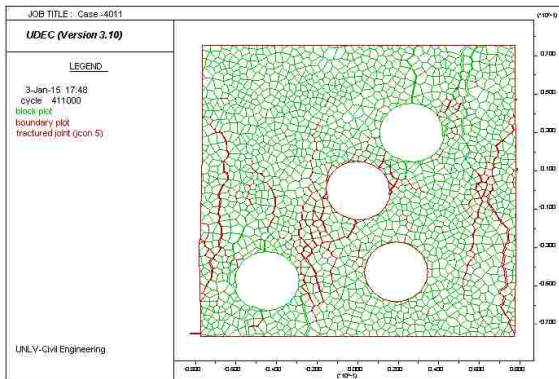
Figure (II.4) POST-FAILURE MODE (IN TENSION) FOR THE CALIBRATED MODEL

**APPENDIX (III) NUMERICAL SIMULATIONS FOR HYDRO-STONETB[®] CUBES
AND THEIR STRESS-STRAIN CURVES**

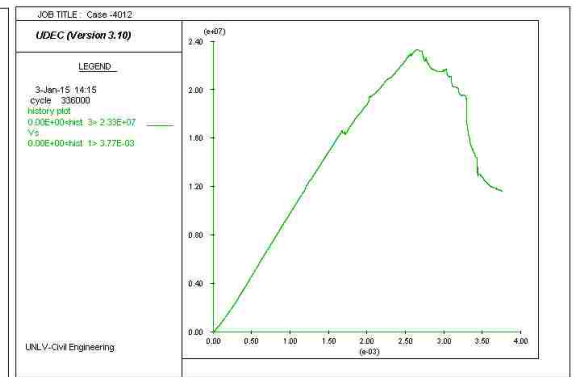
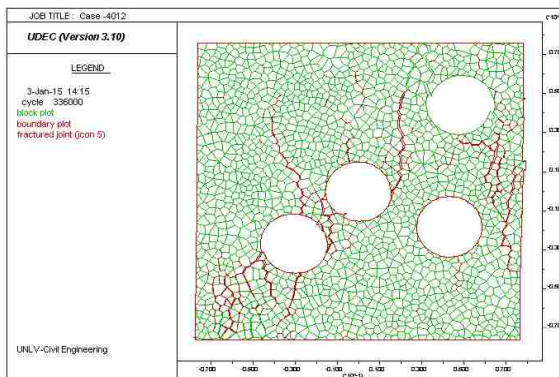




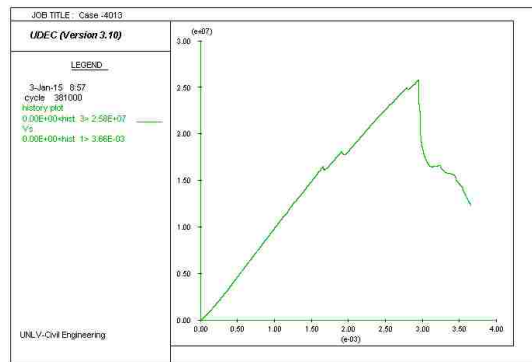
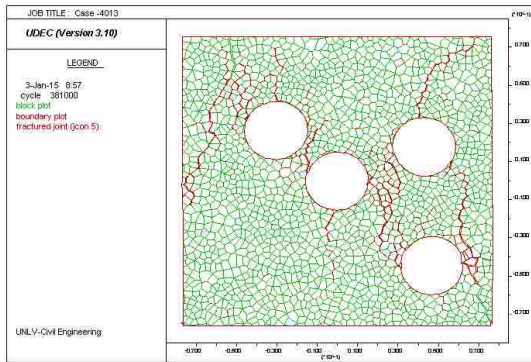
PC-UCL2



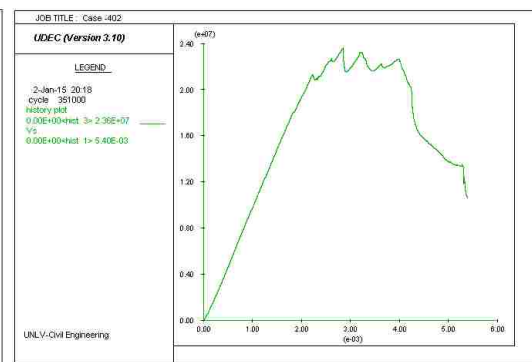
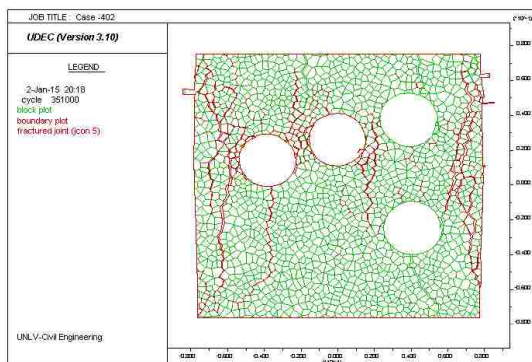
PA-UCL4-1



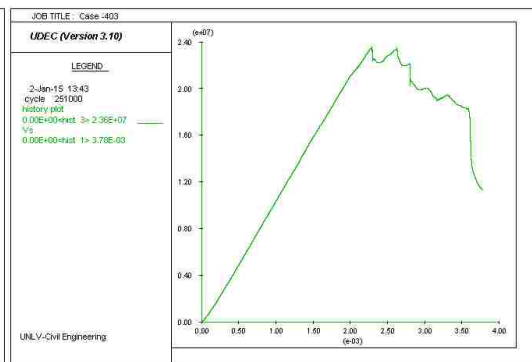
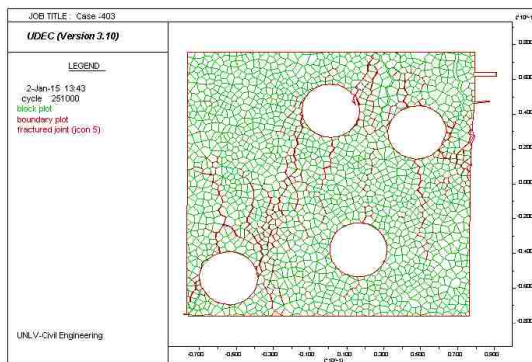
PA-UCL4-2



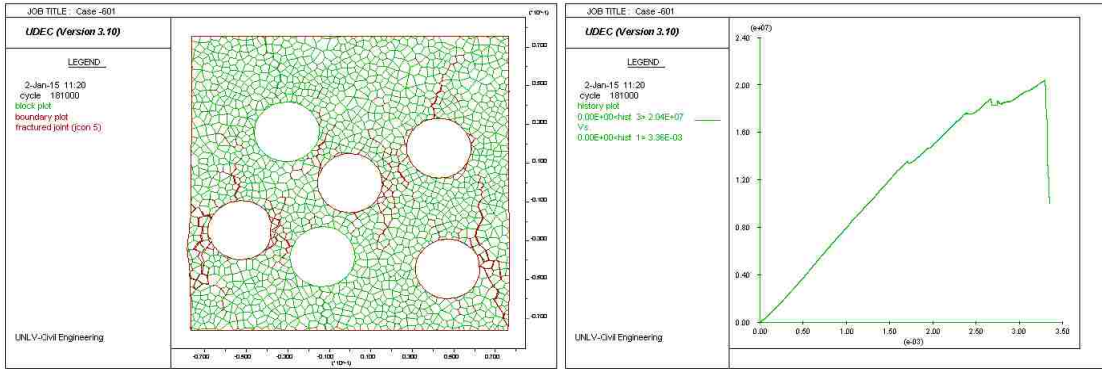
PA-UCL4-3



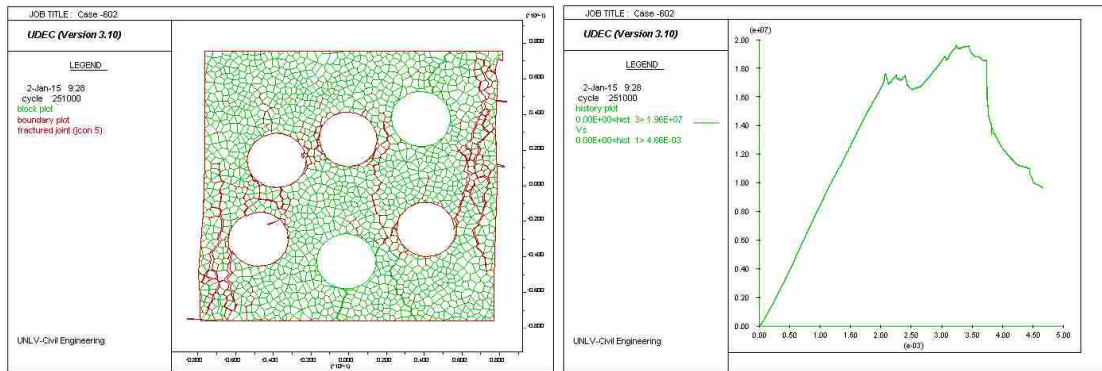
PB-UCL4



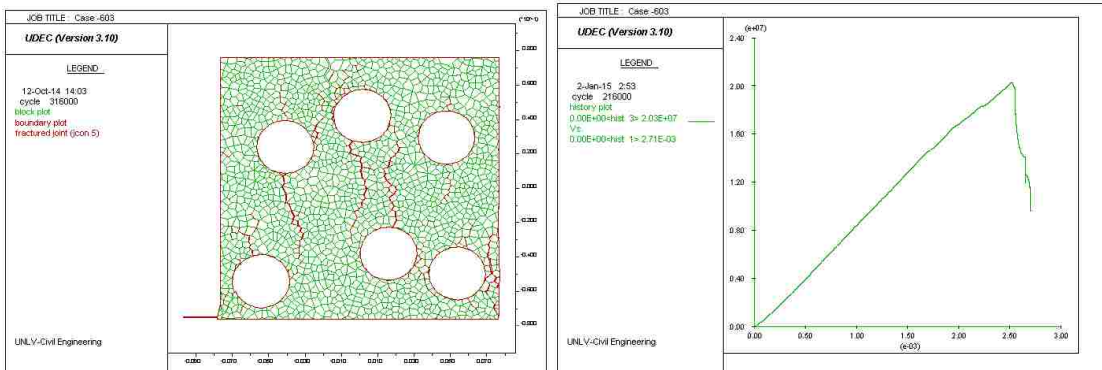
PC-UCL4



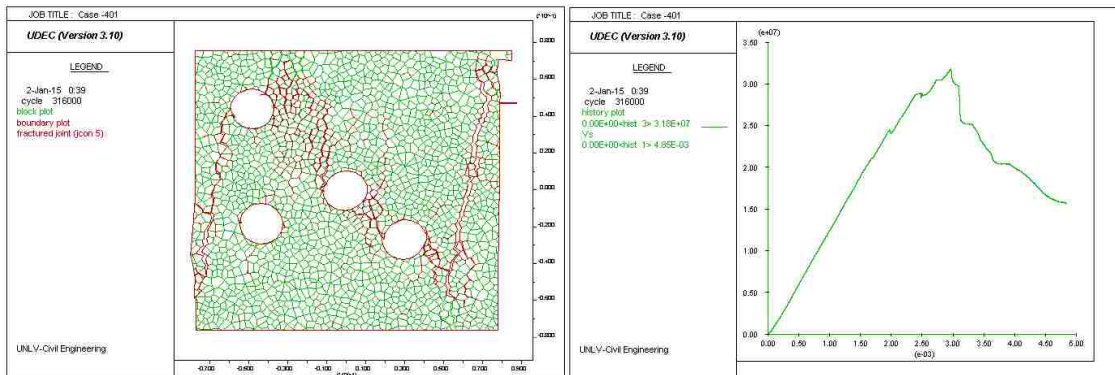
PA-UCL2



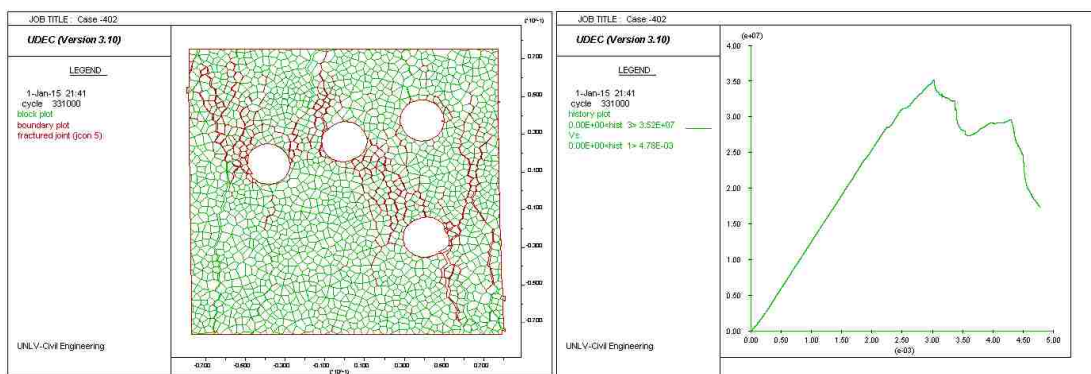
PB-UCL6



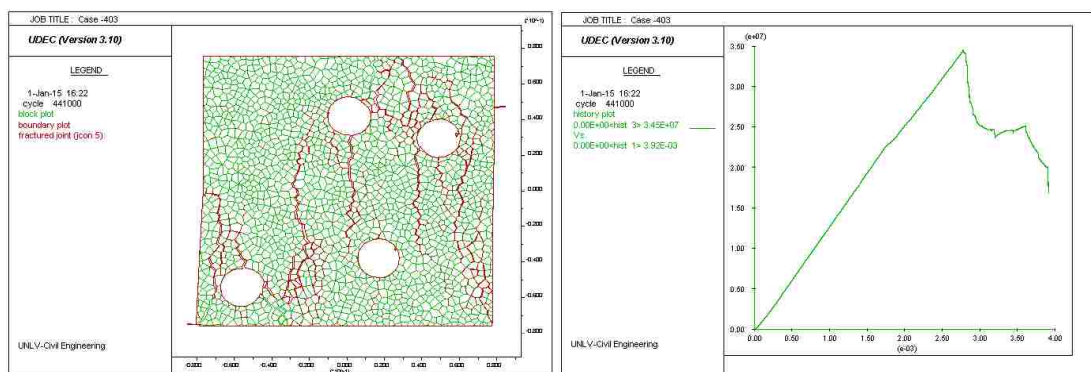
PC-UCL6



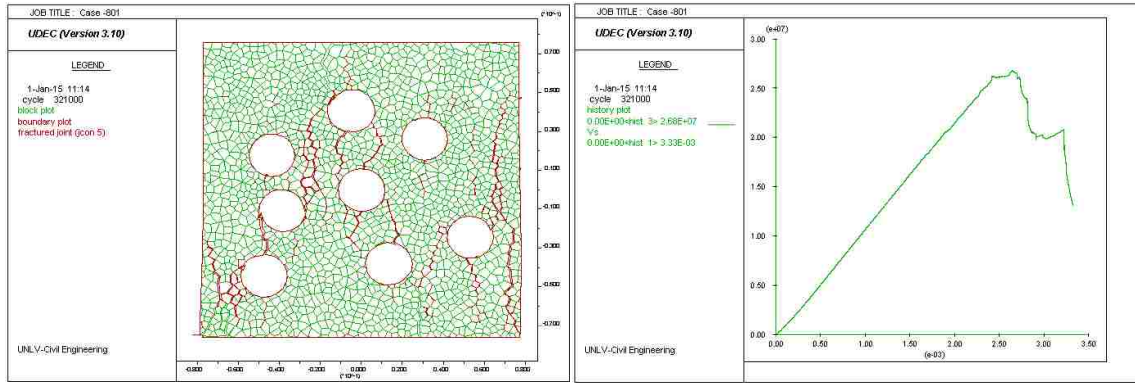
PA-UCM4



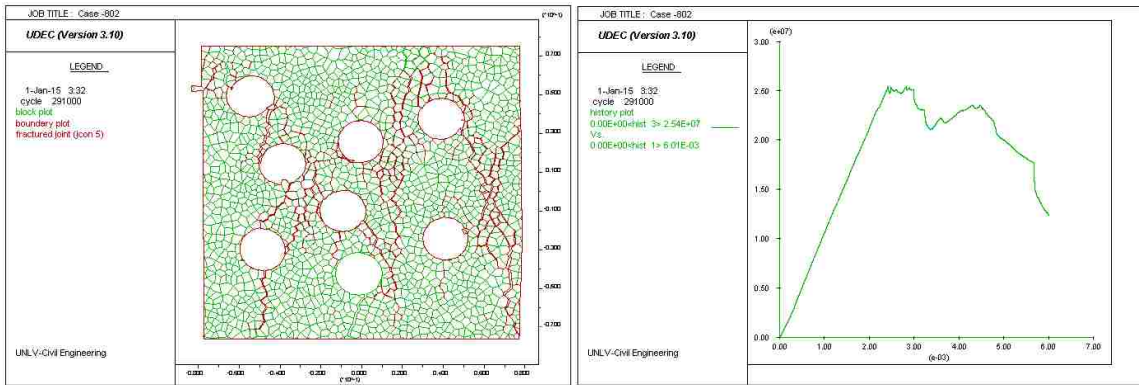
PB-UCM4



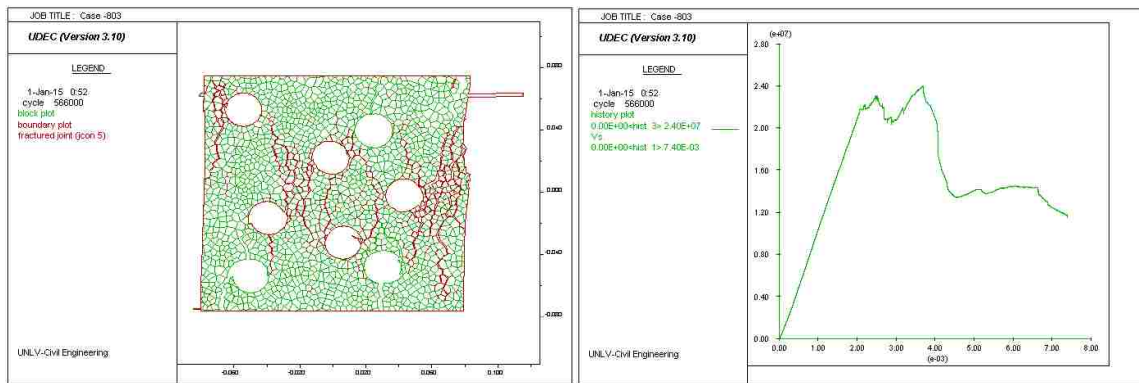
PC-UCM4



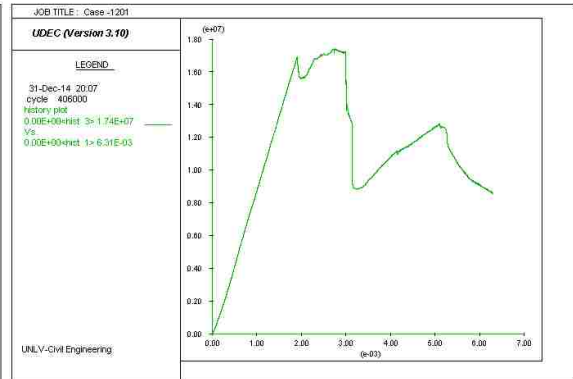
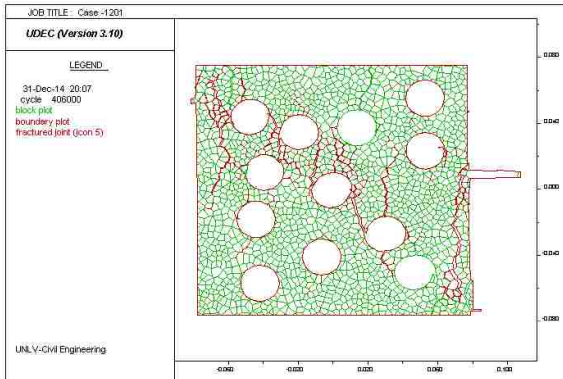
PA-UCM8



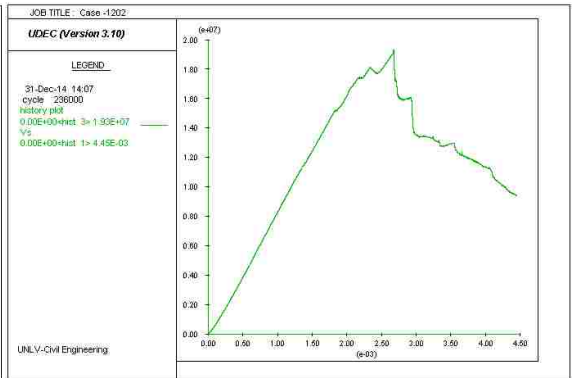
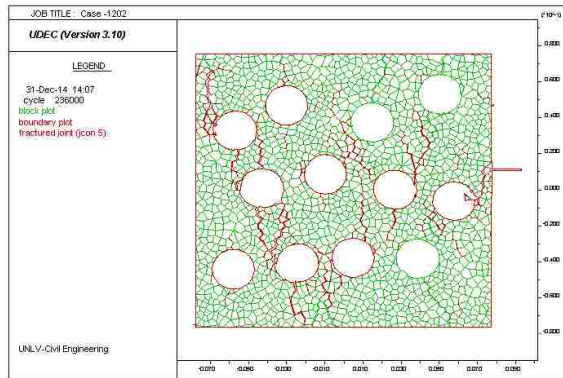
PB-UCM8



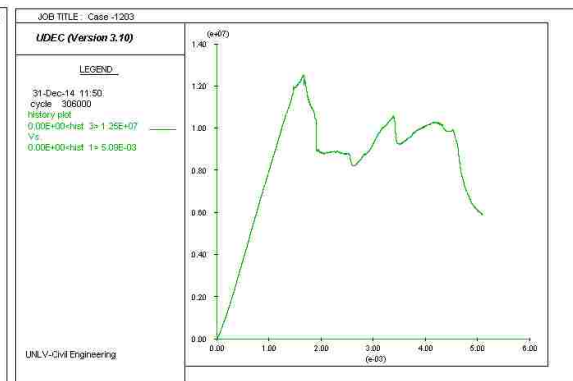
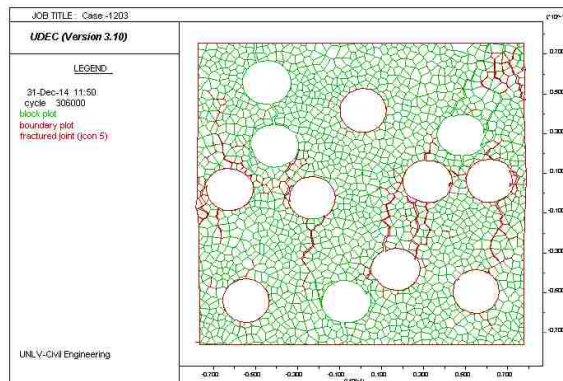
PC-UCM8



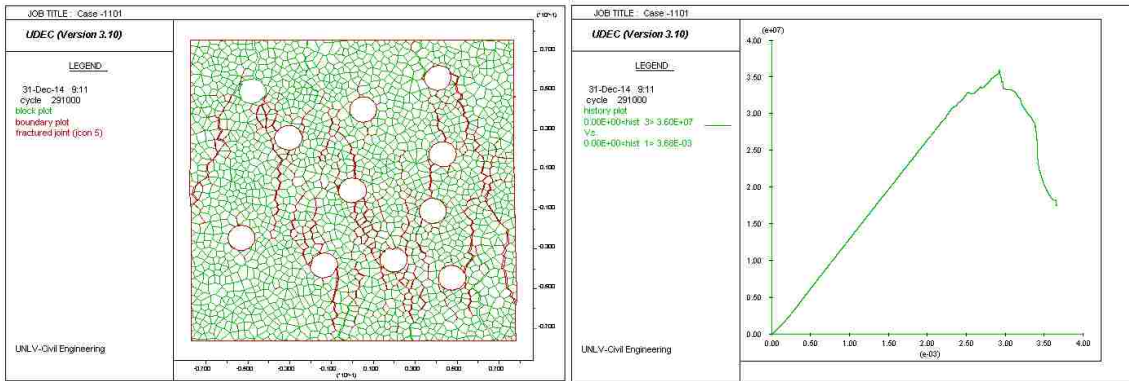
PA-UCLM12



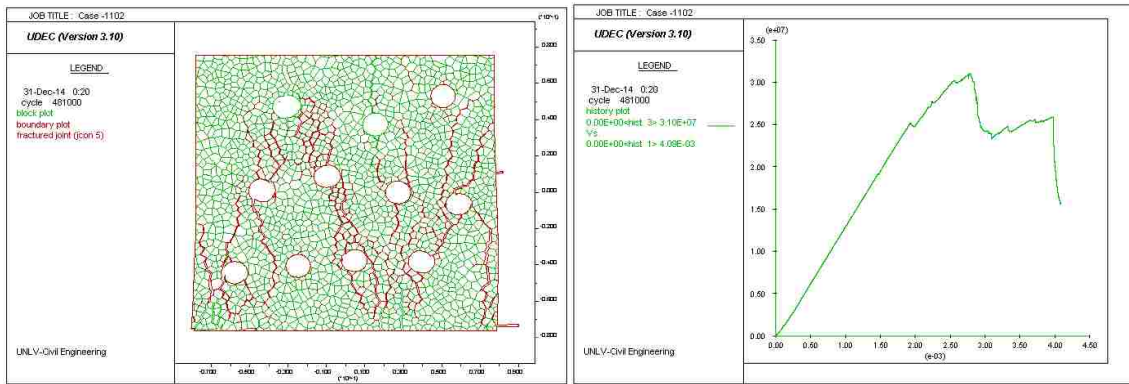
PB-UCM12



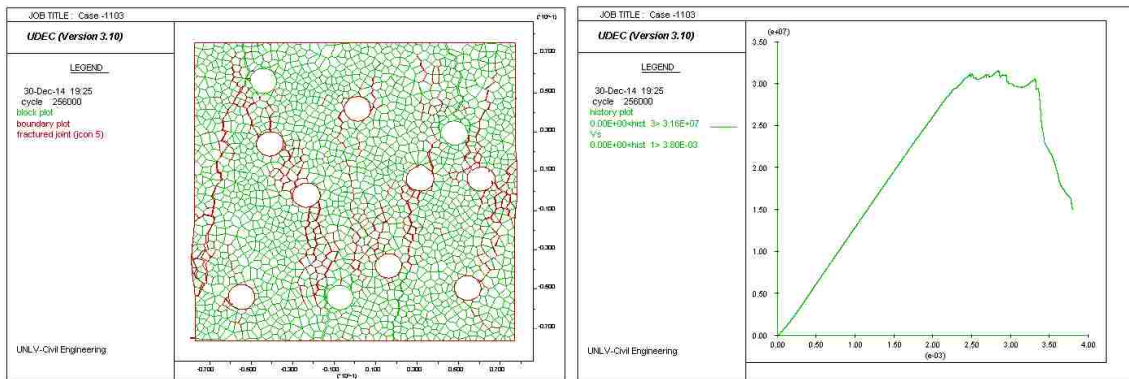
PC-UCM12



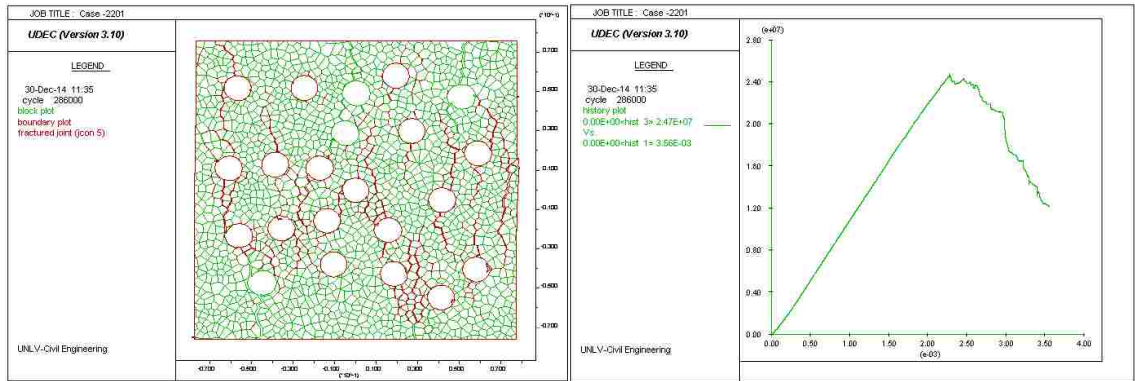
PA-UCS11



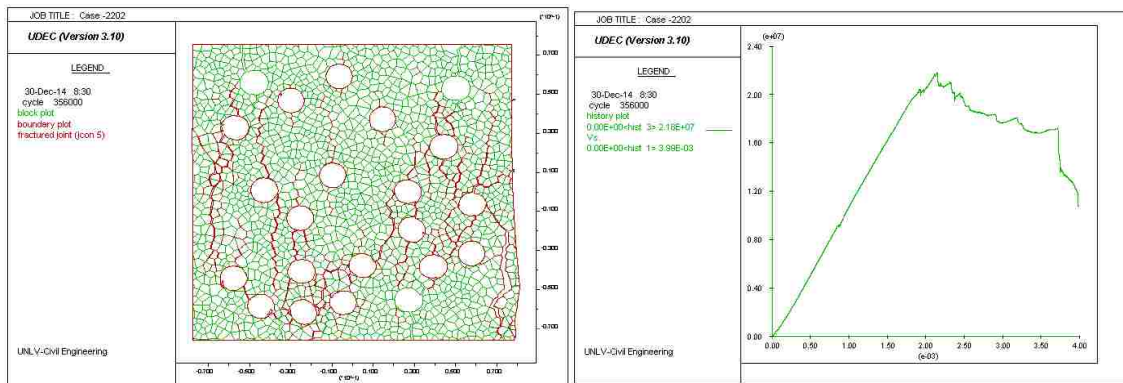
PB-UCS11



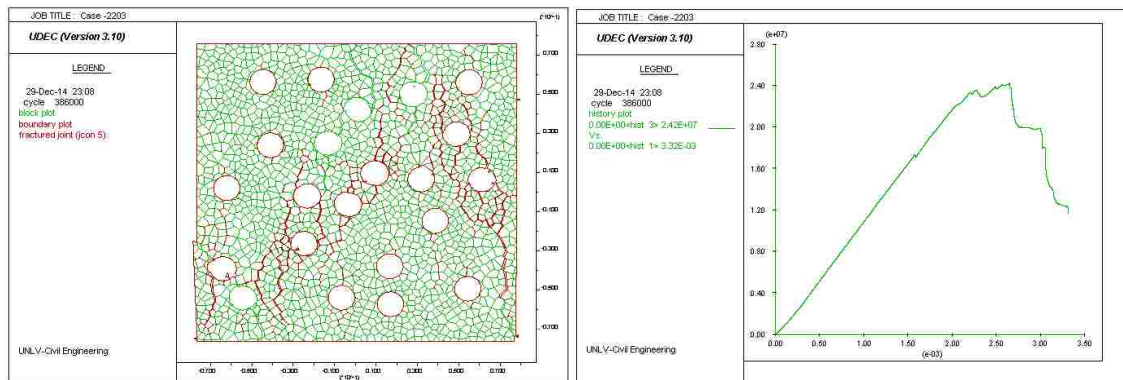
PC-UCS11



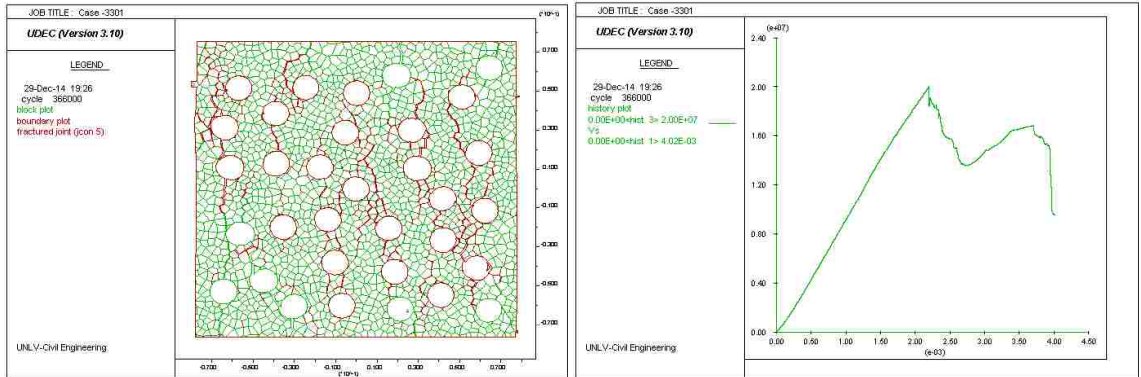
PA-UCS22



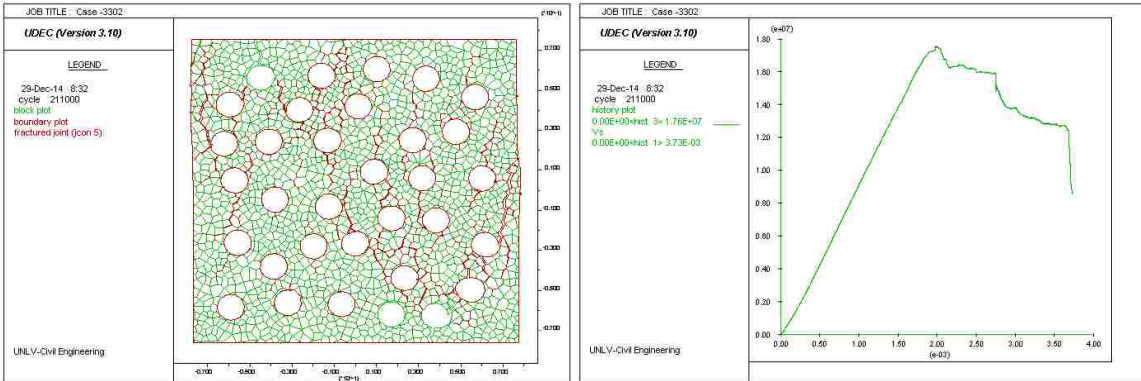
PB-UCS22



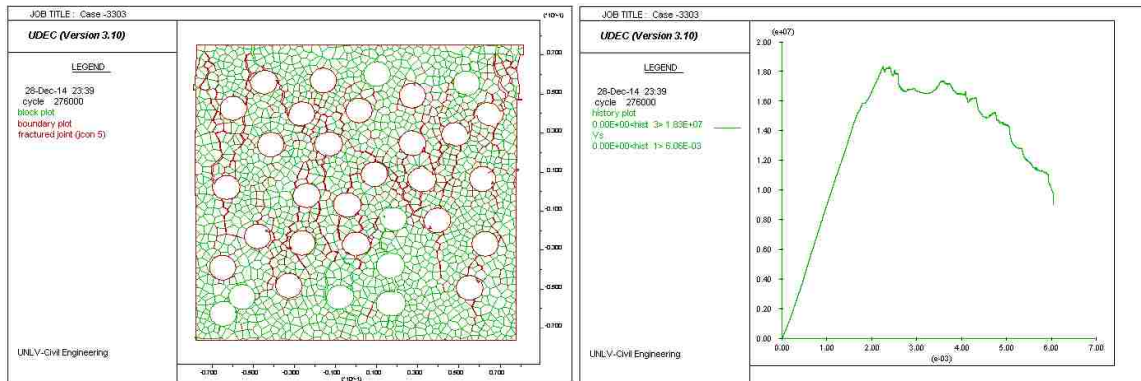
PC-UCS22



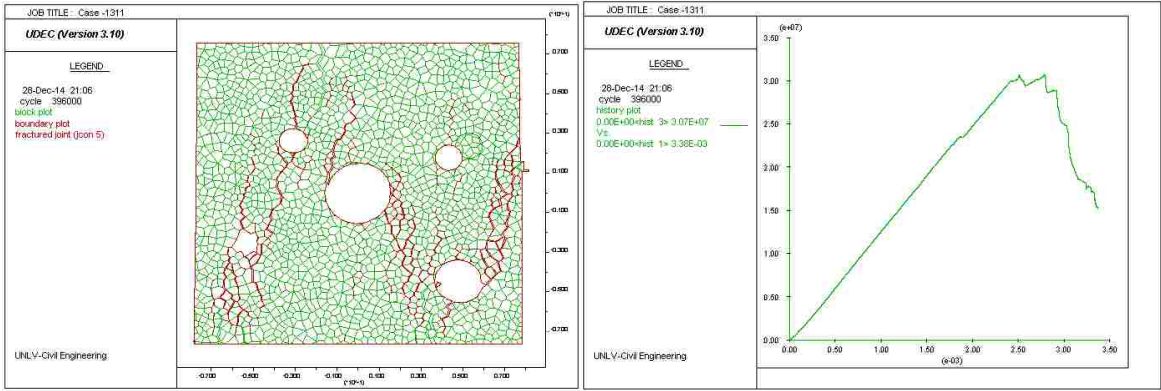
PA-UCS33



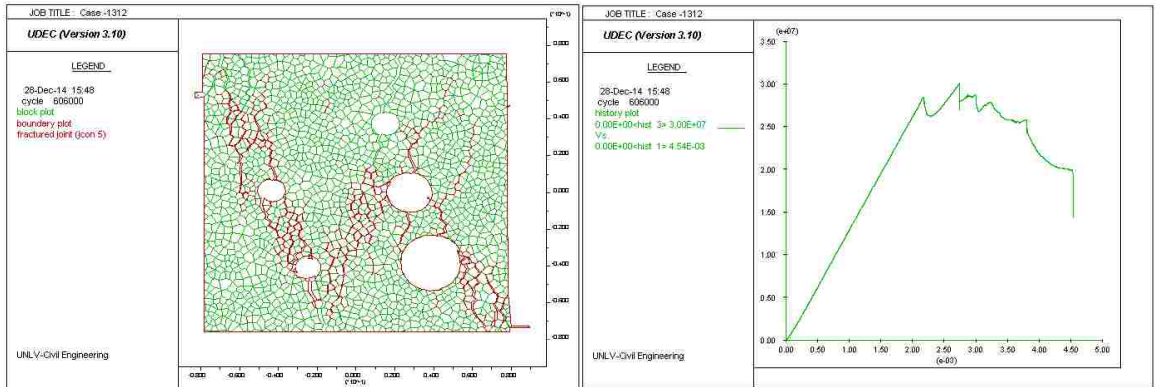
PB-UCS33



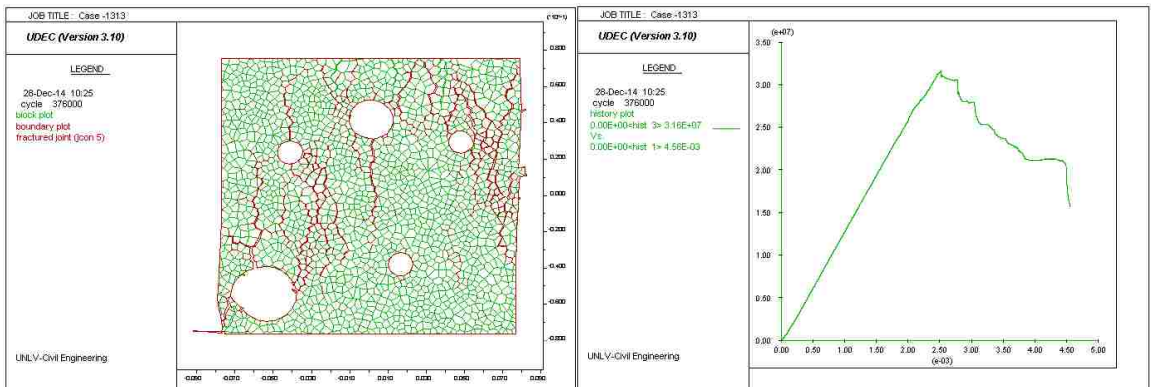
PC-UCS33



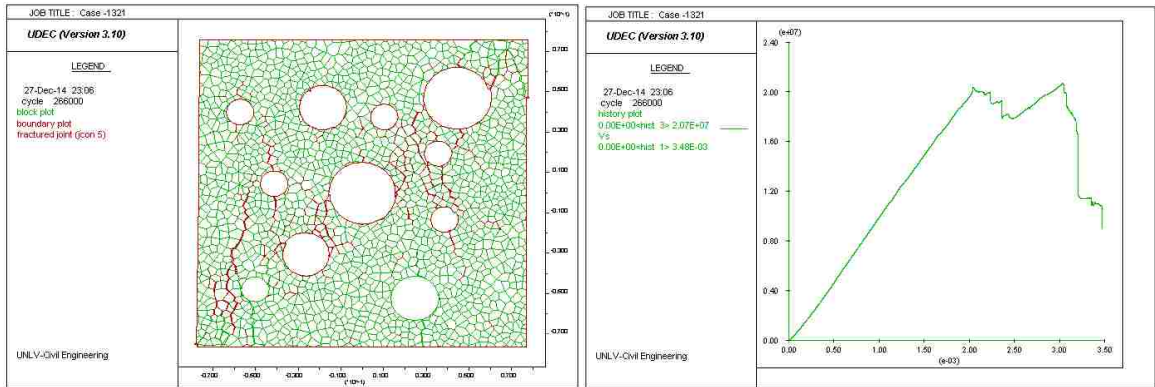
PA-UXCL1M1S3



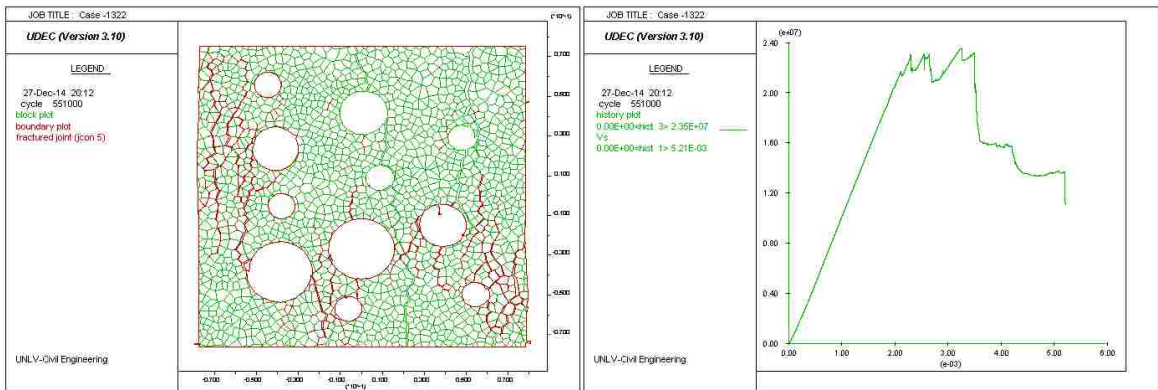
PB-UXCL1M1S3



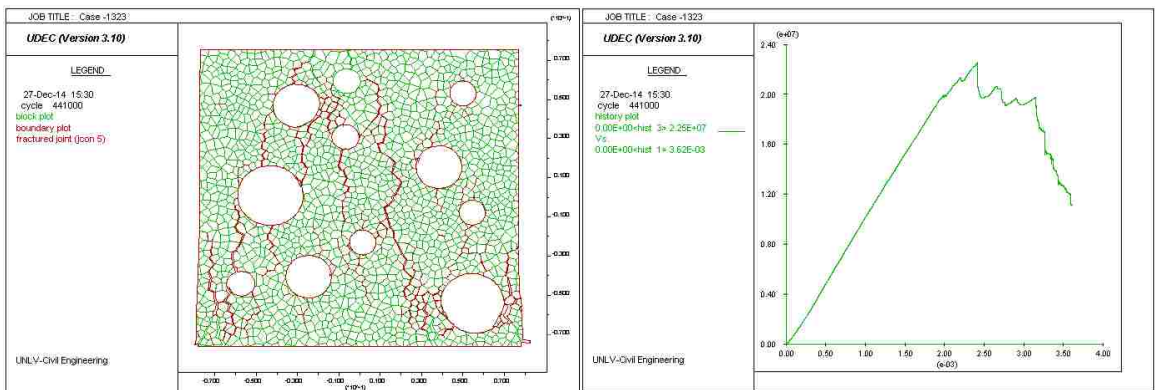
PC-UXCL1M1S3



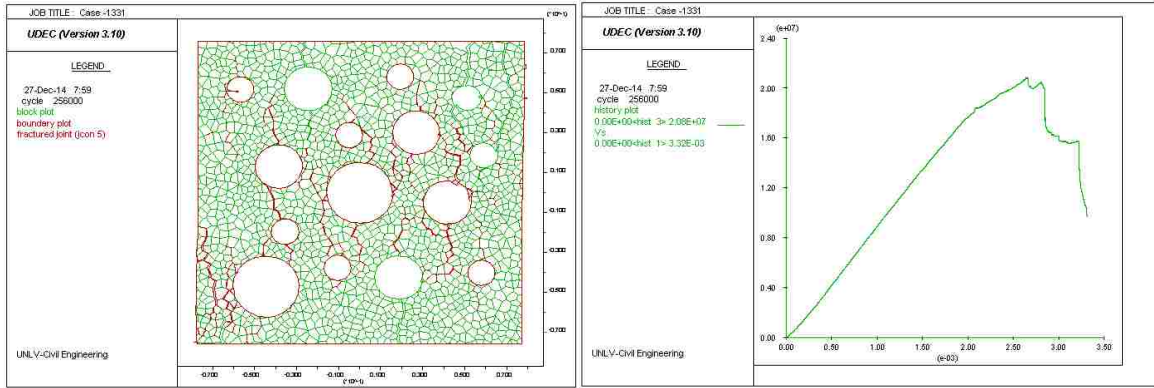
PA-UXCL2M3S6



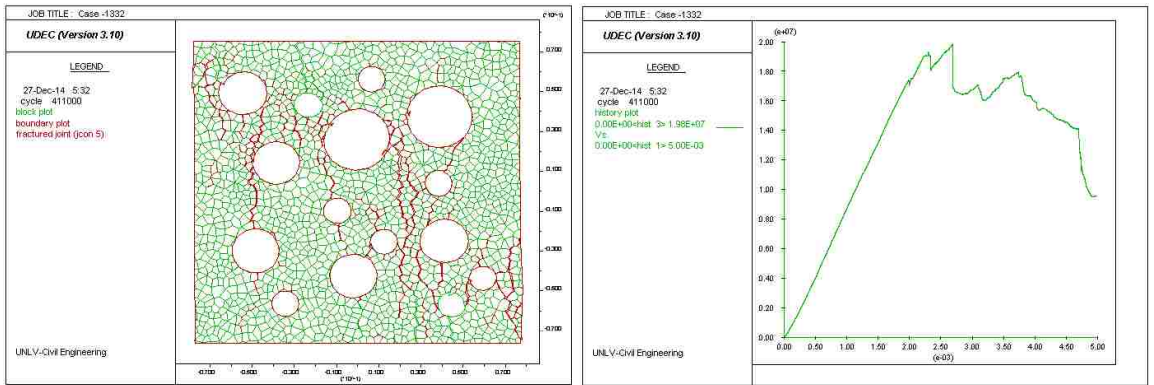
PB-UXCL2M3S6



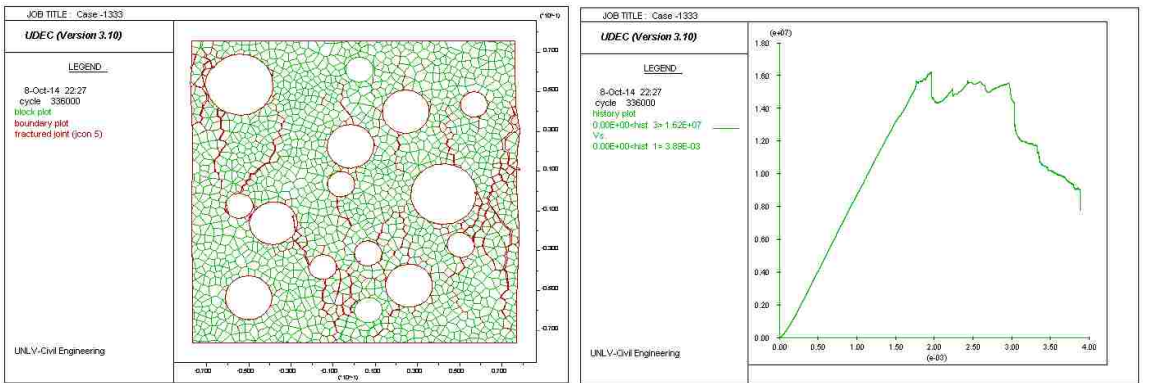
PC-UXCL2M3S6



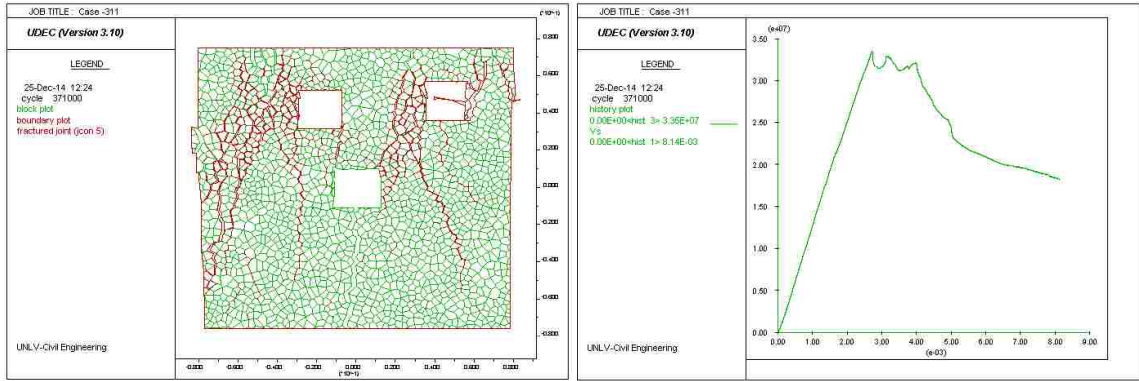
PA-UXCL2M5S8



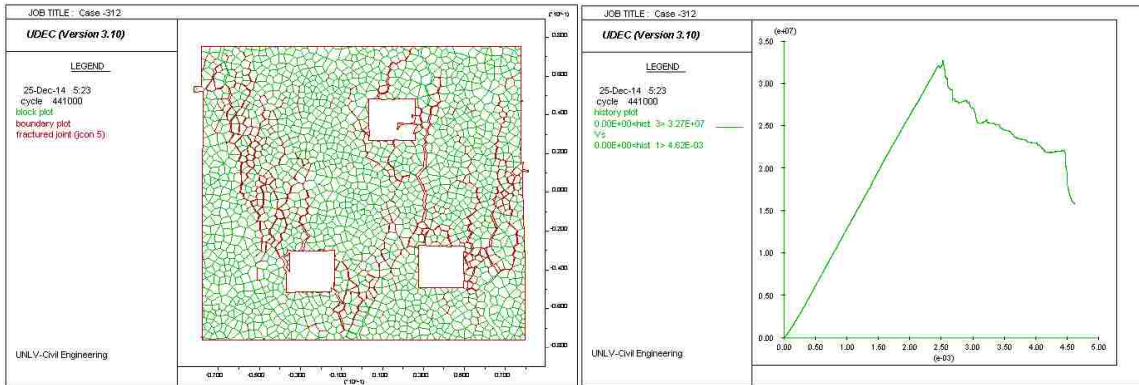
PB-UXCL2M5S8



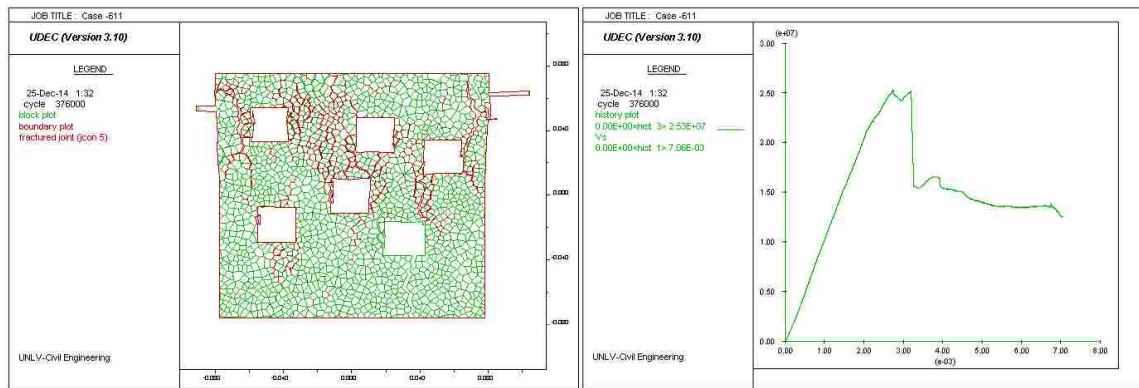
PC-UXCL2M5S8



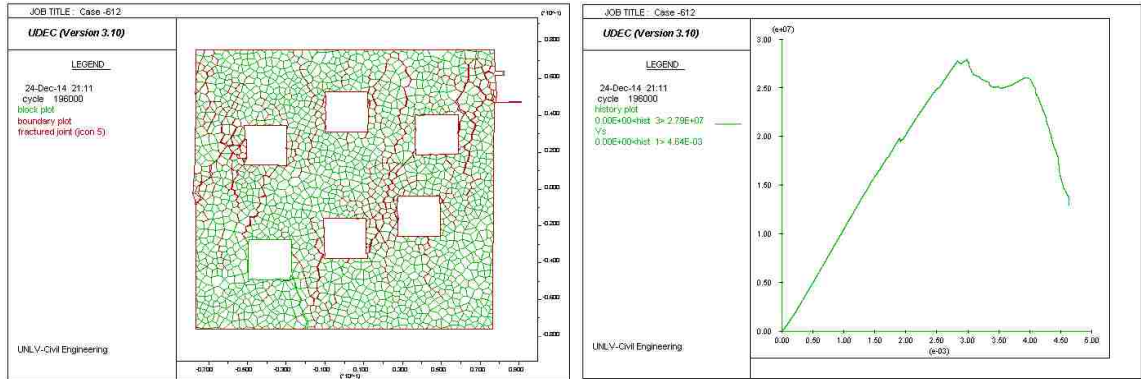
PA-USqL3



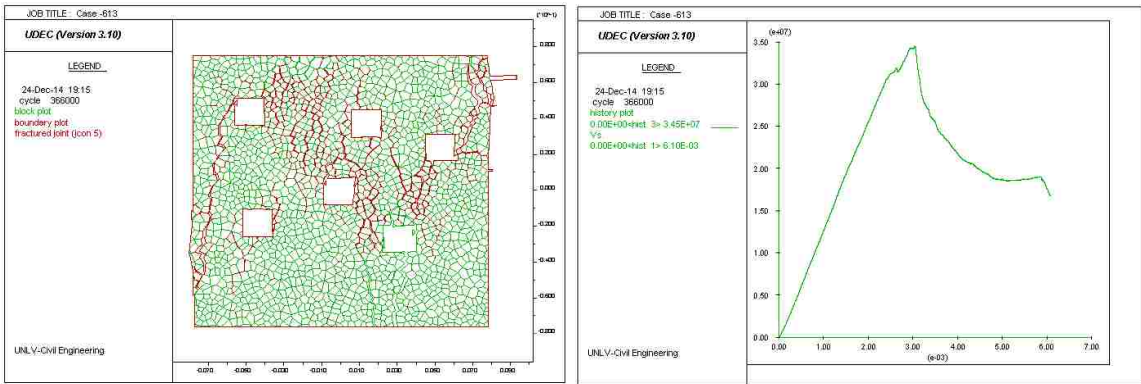
PB-USqL3



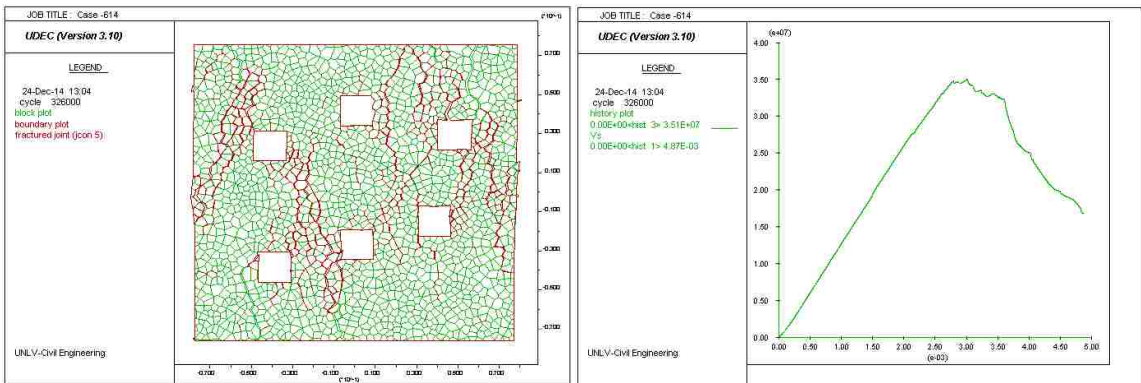
PA-USqL6



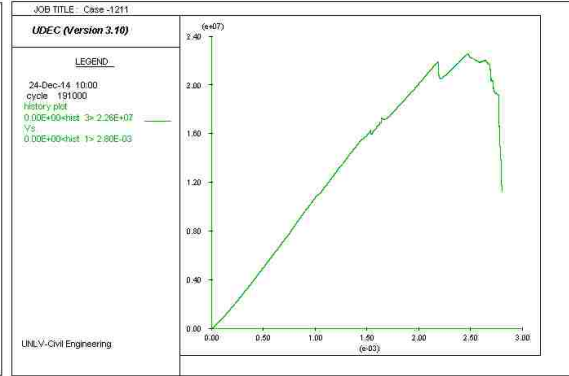
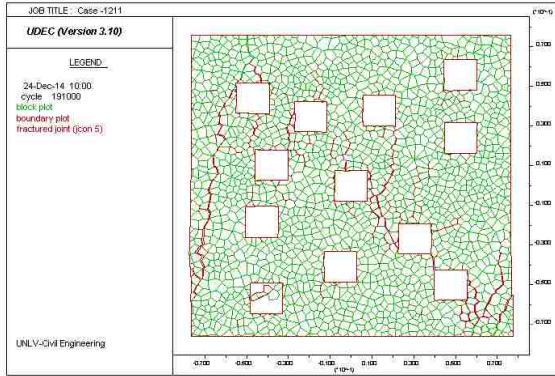
PB-USL6



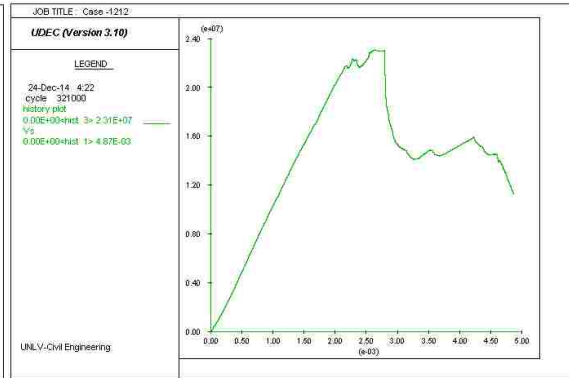
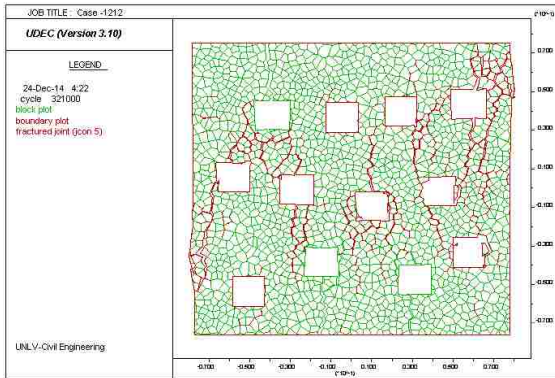
PA-USqS6



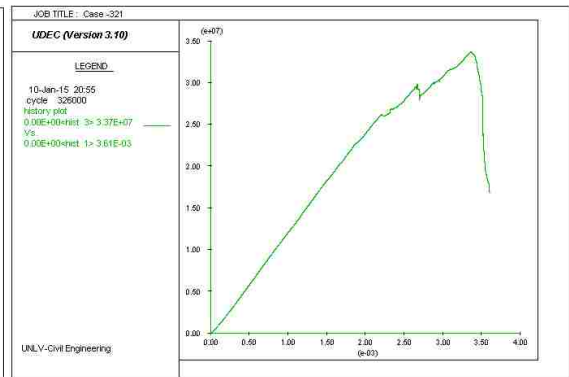
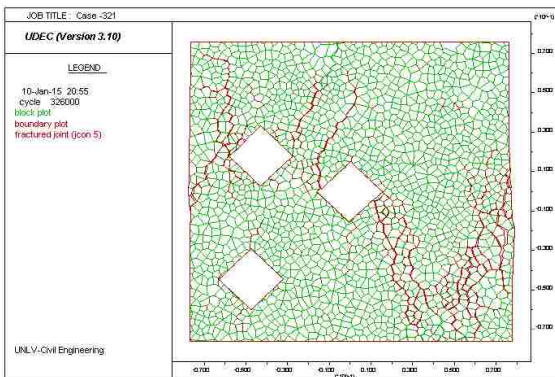
PB-USqS6



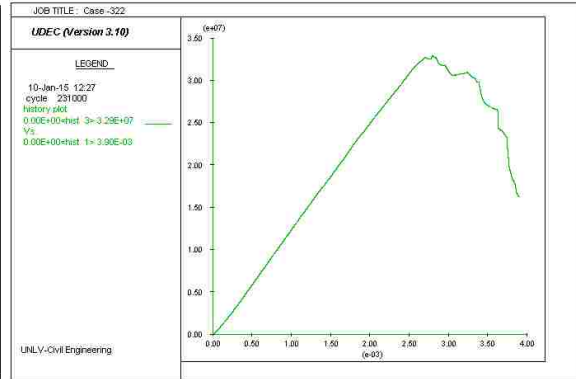
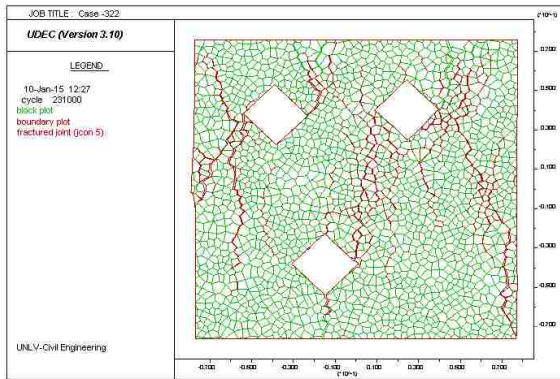
PA-USqS12



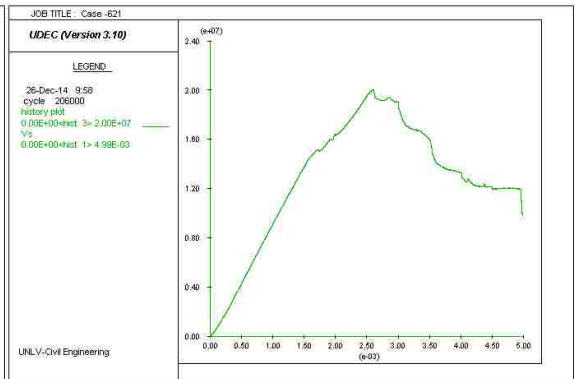
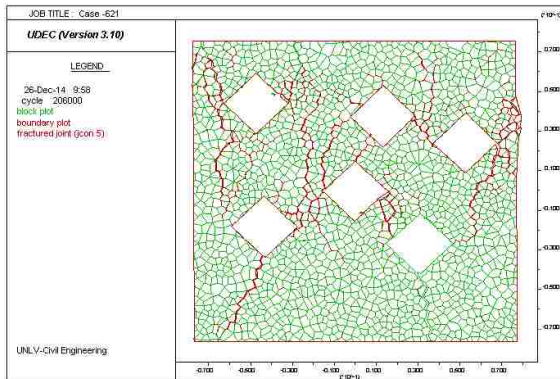
PB-USqS612



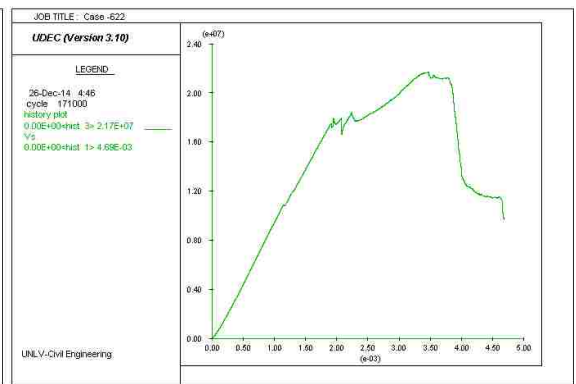
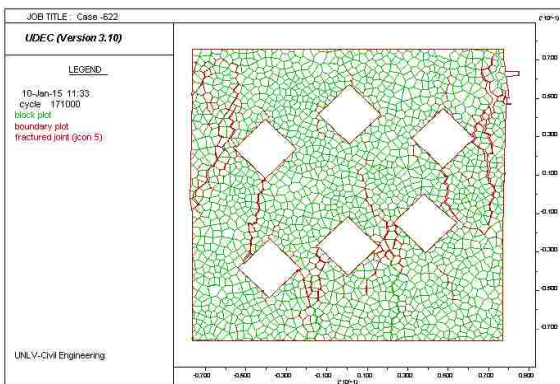
PA-UDmL3



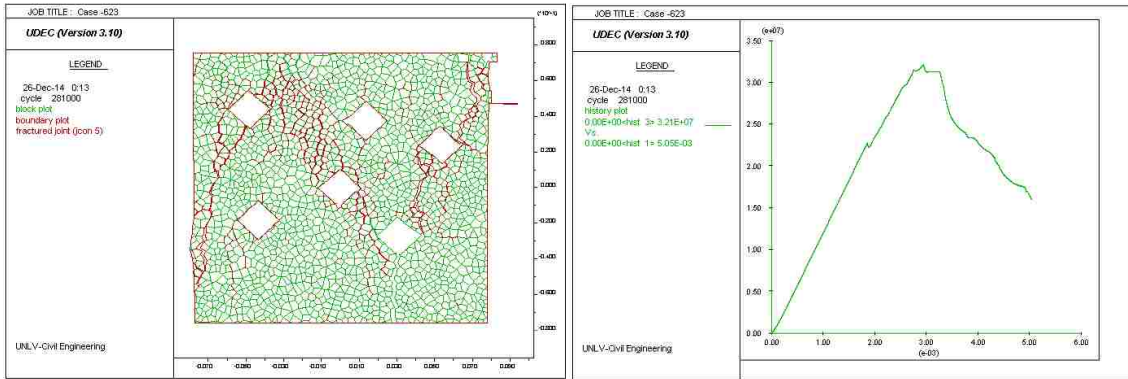
PB-UDmL3



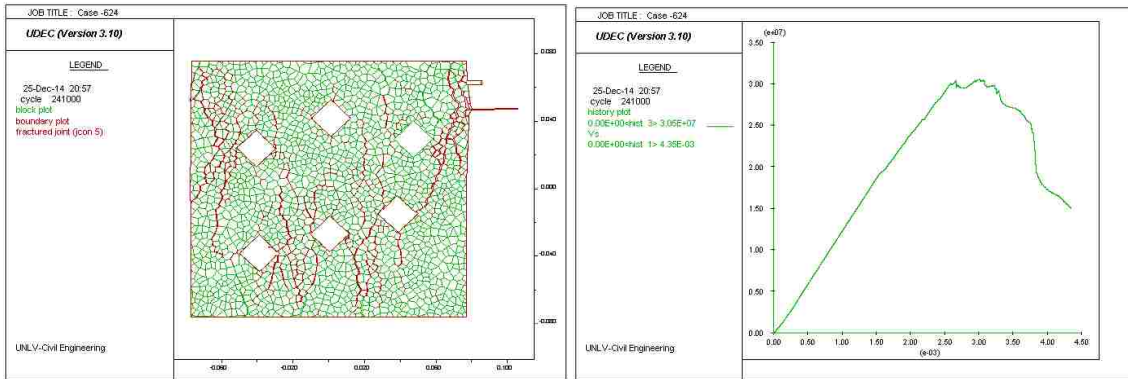
PA-UDmL6



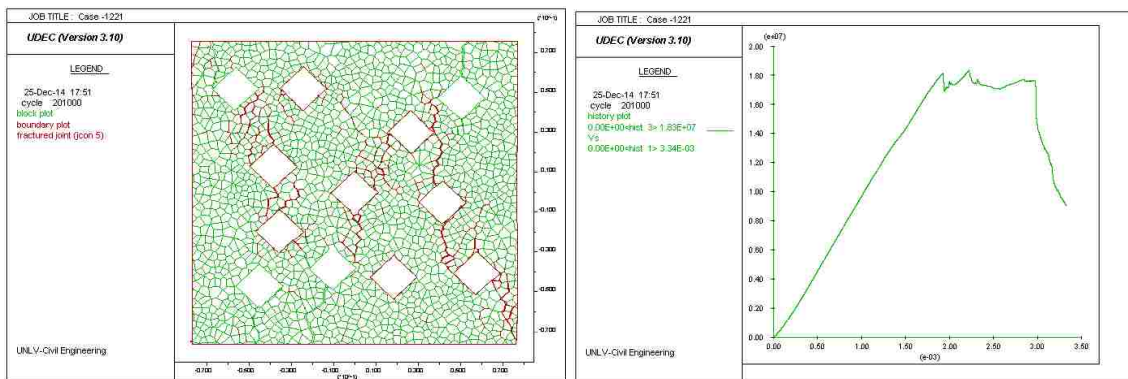
PB-UDmL6



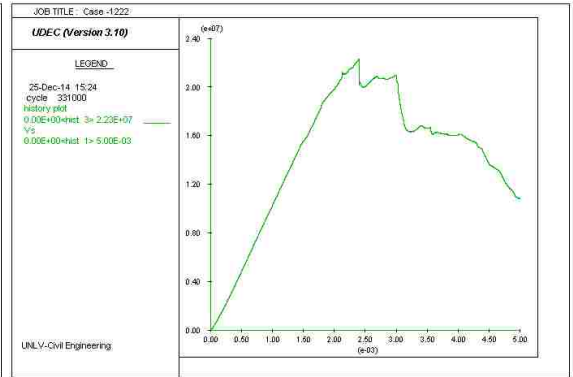
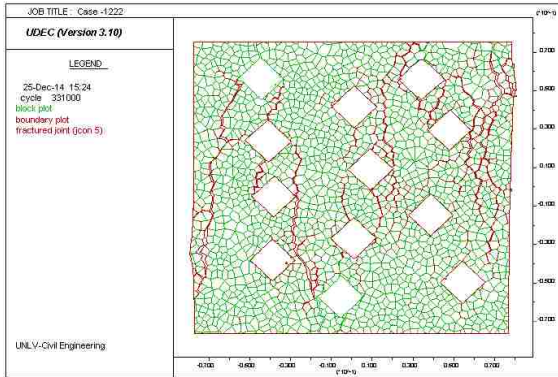
PA-UDmS6



PB-UDmS6



PA-UDmS12



PB-UDmS12

APPENDIX (IV) NUMERICAL MODELS AND THEIR STRESS-STRAIN CURVES

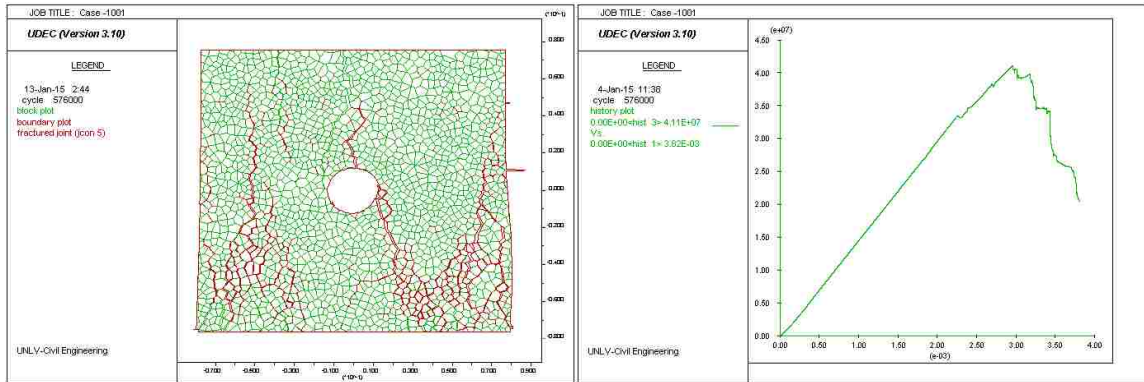
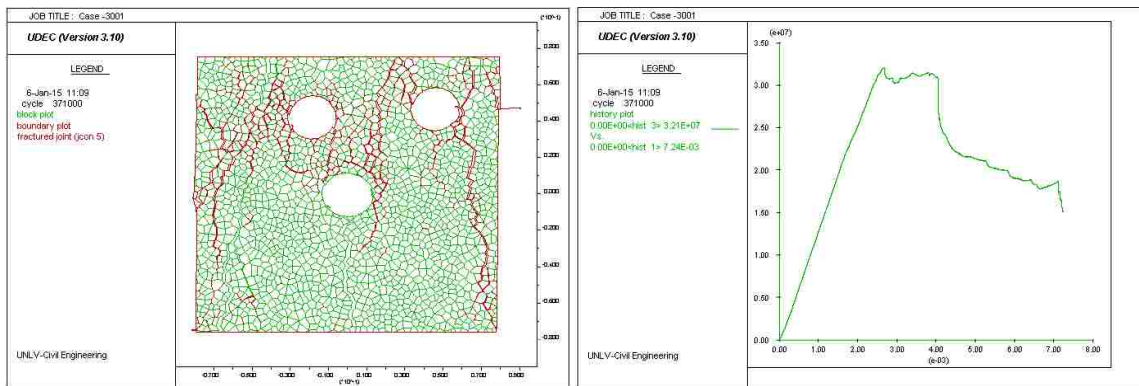
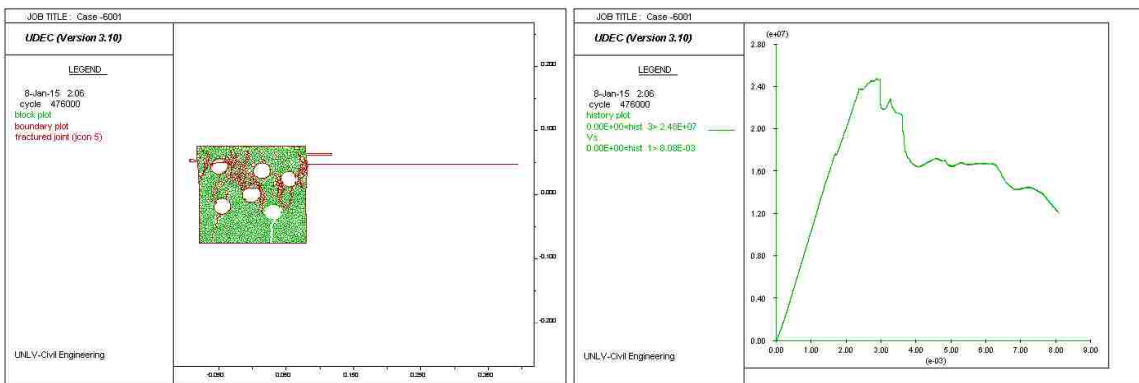


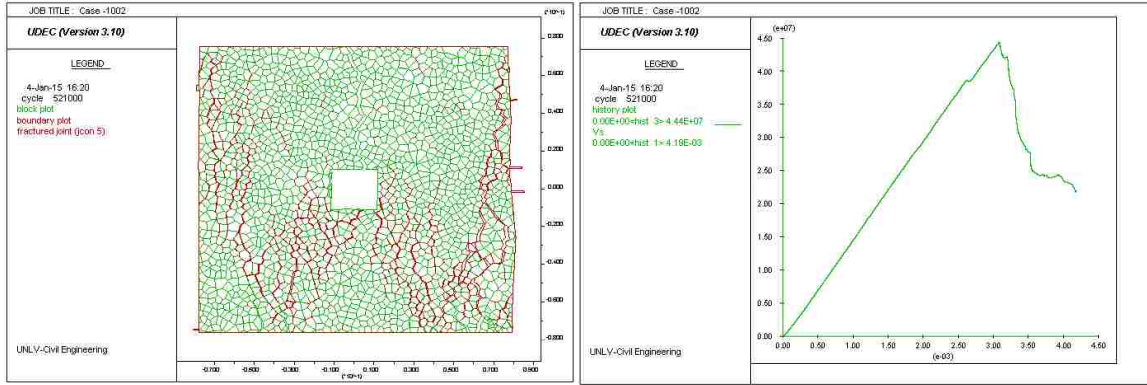
Figure (IV.1) Numerical Models and their Stress-Strain Curves - PA-UCL1



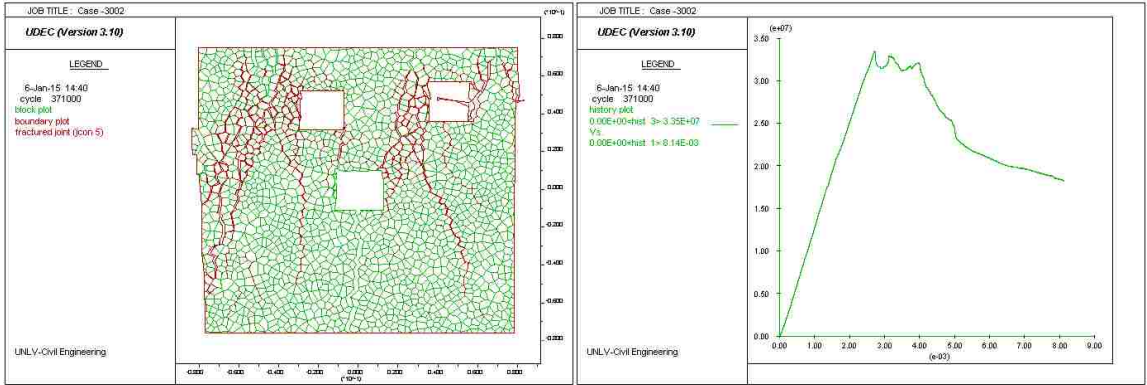
PA-UCL3



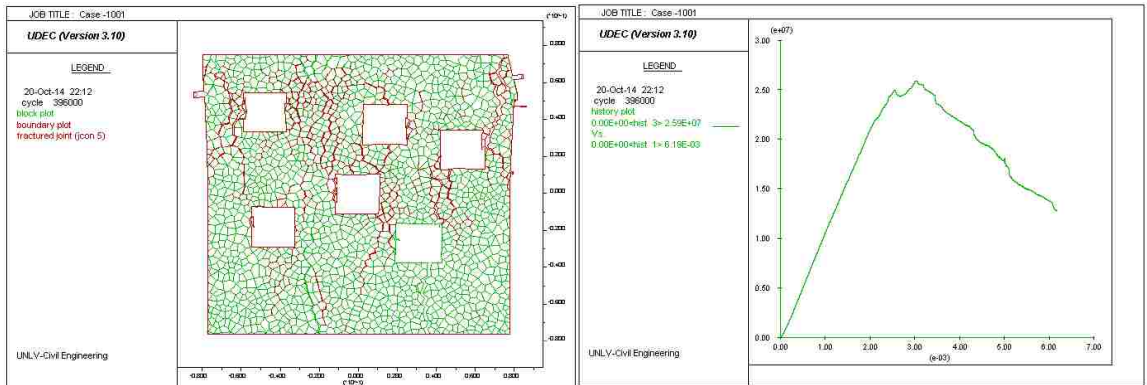
PA-UCL6



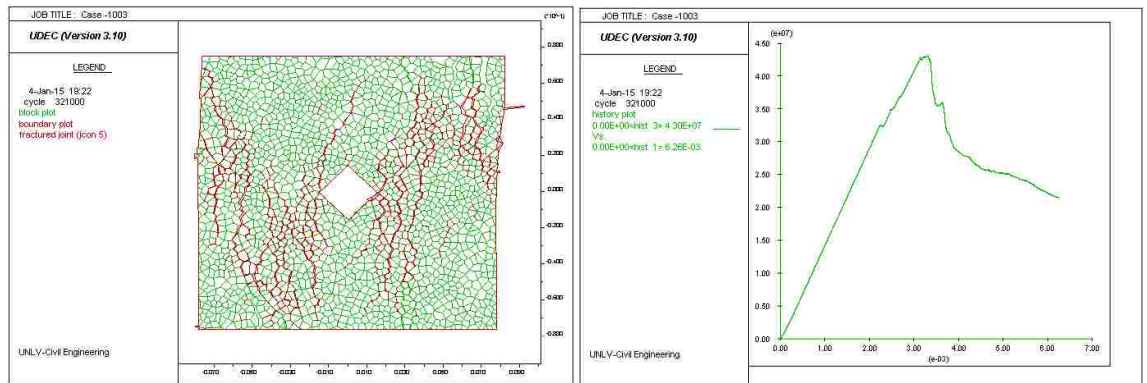
PA-USqL1-Vertical



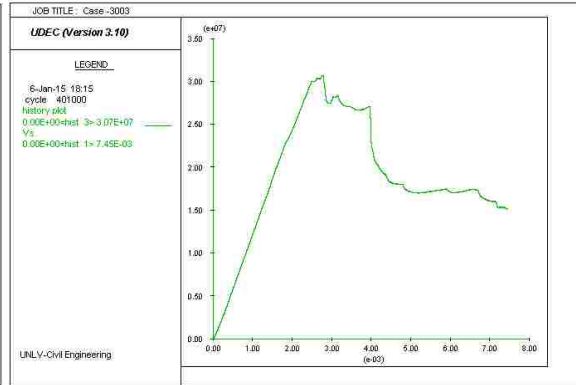
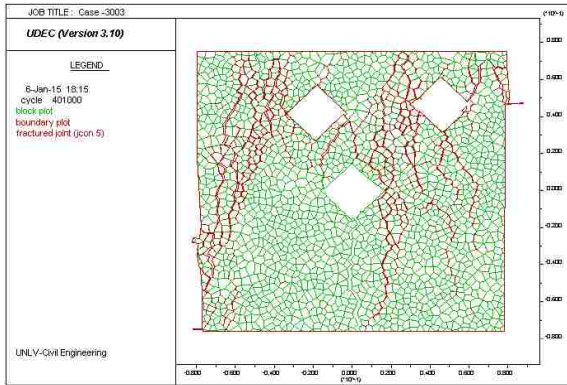
PA-USqL3-Vertical



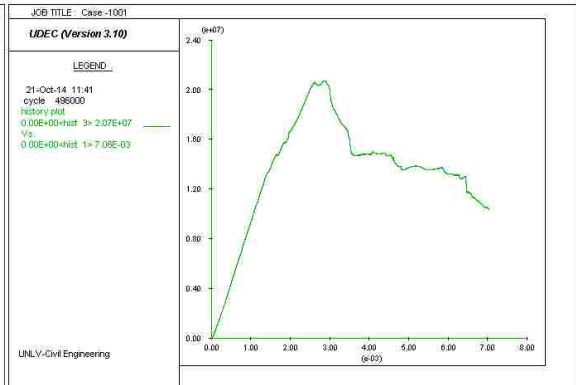
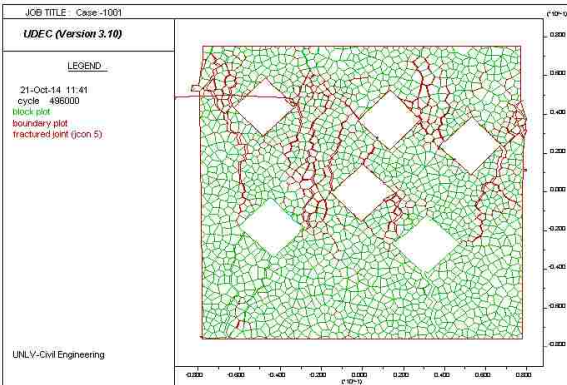
PA-USqL6-Vertical



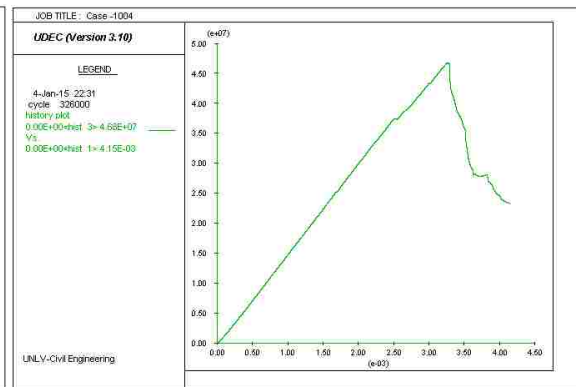
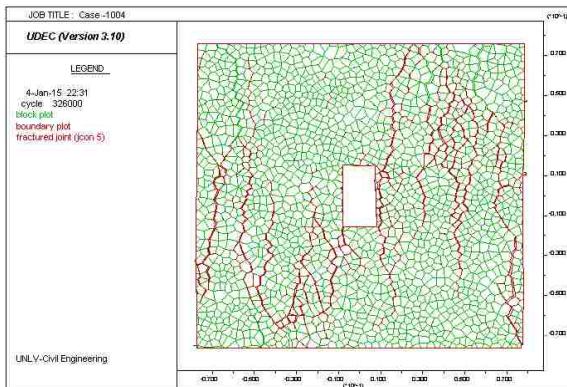
PA-USqL1-45° (Diamond)



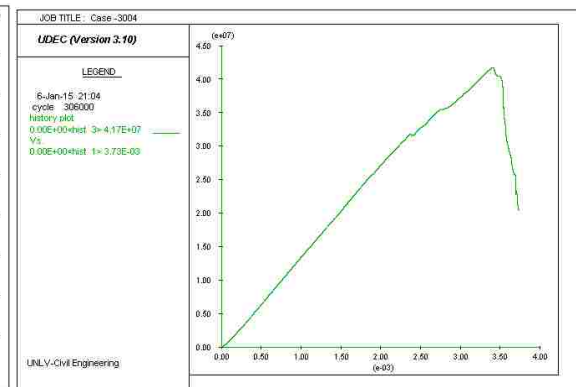
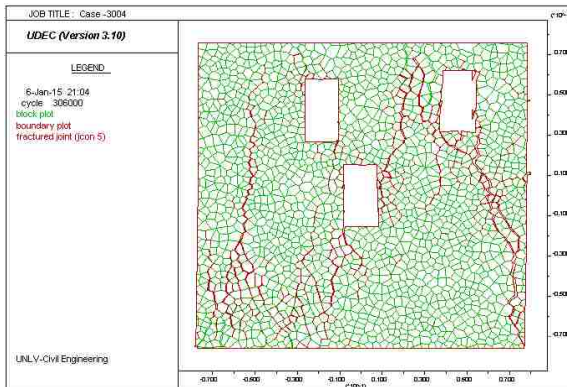
PA-USqL3-45° (Diamond)



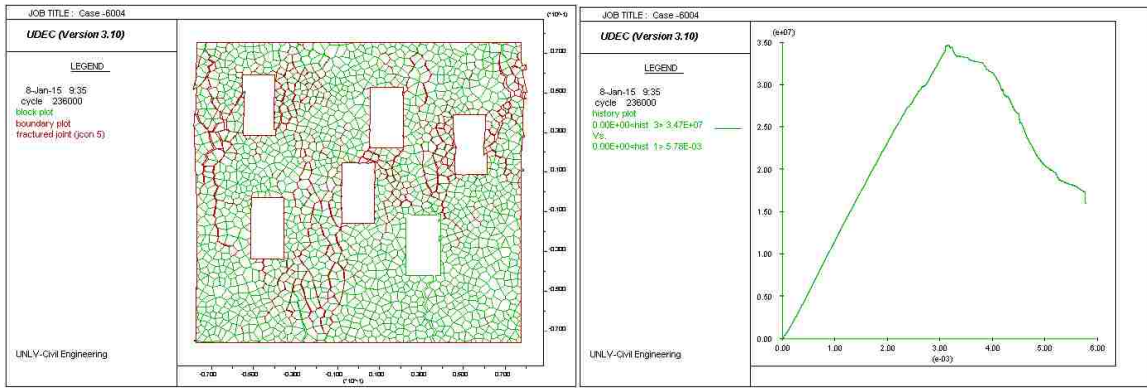
PA-USqL6-45° (Diamond)



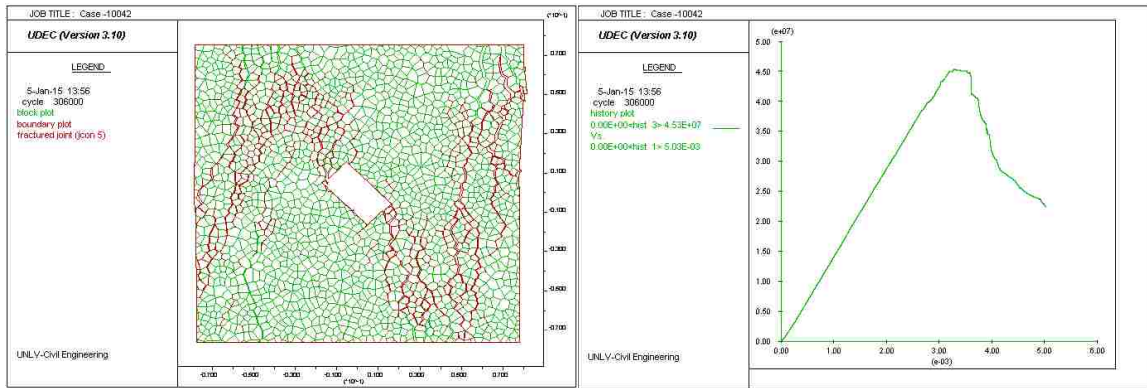
PA-URL1-Vertical



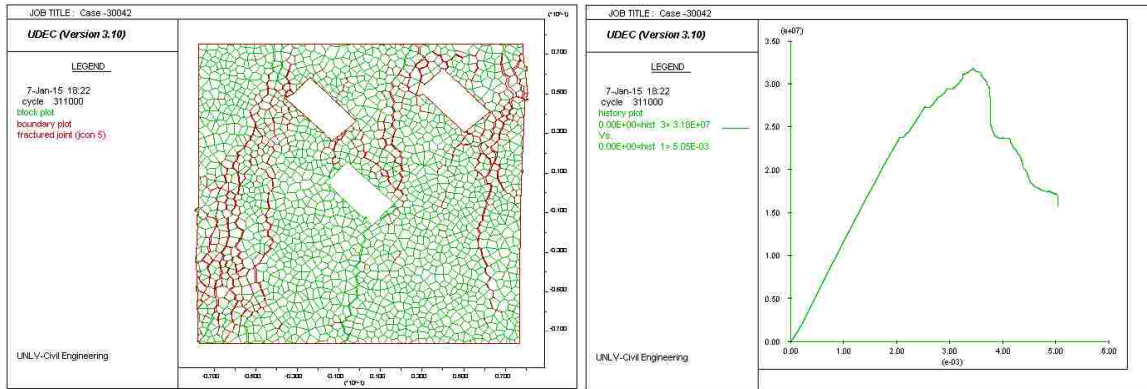
PA-URL3-Vertical



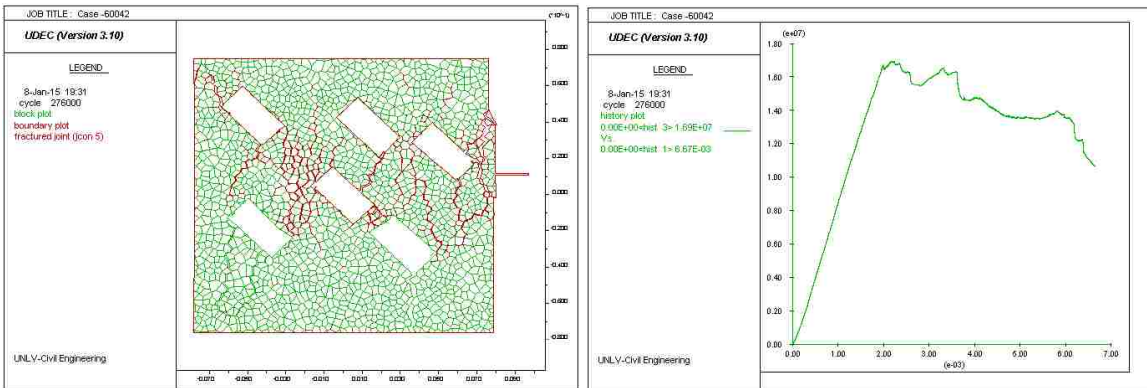
PA-URL6-Vertical



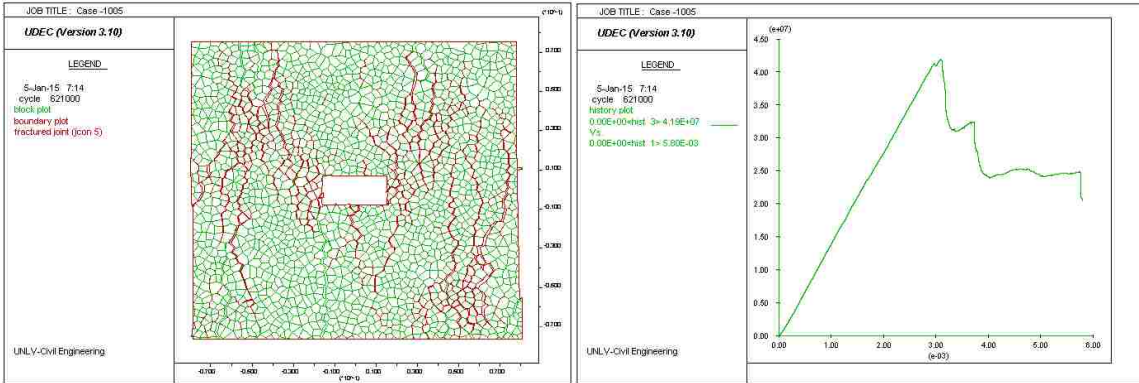
PA-URL1-45°



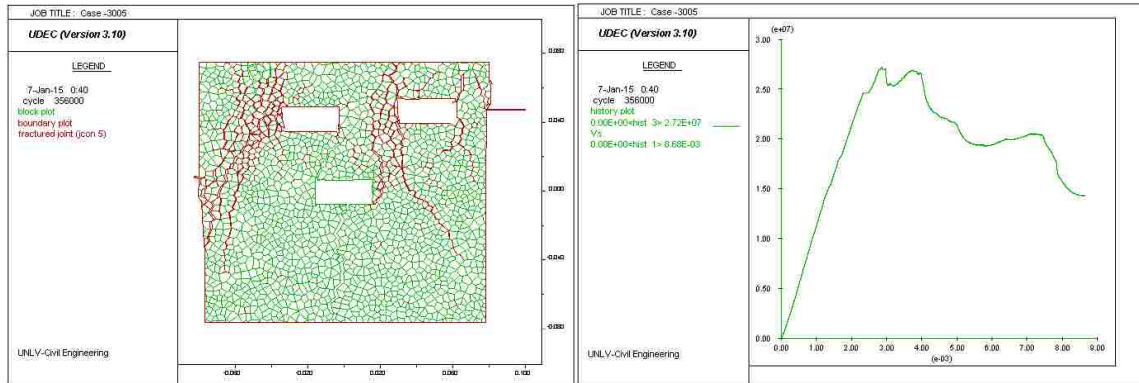
PA-URL3-45°



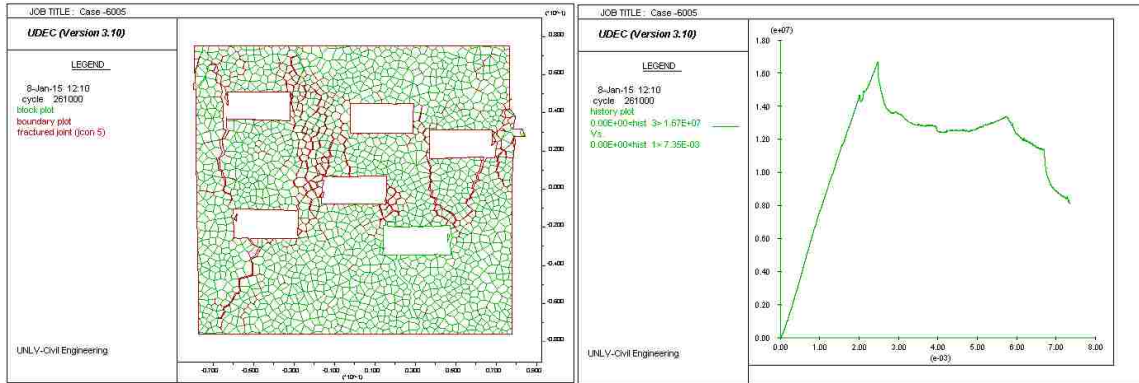
PA-URL6-45°



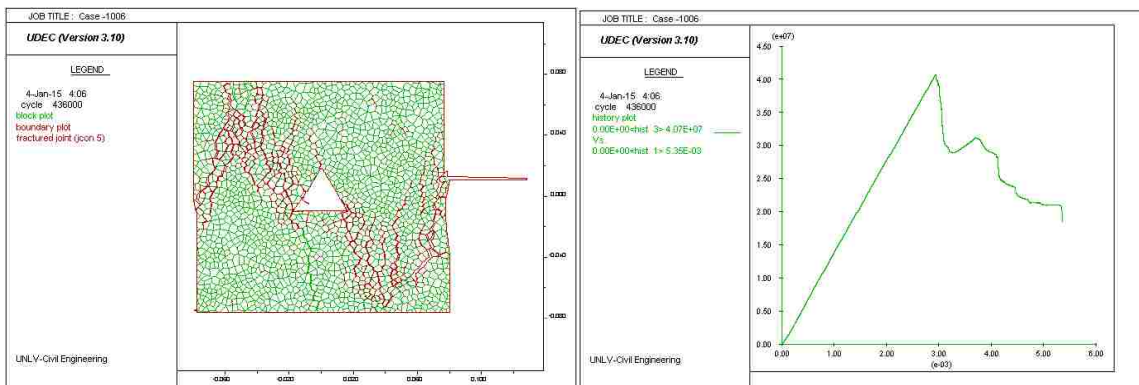
PA-URL1-90° (Horizontal)



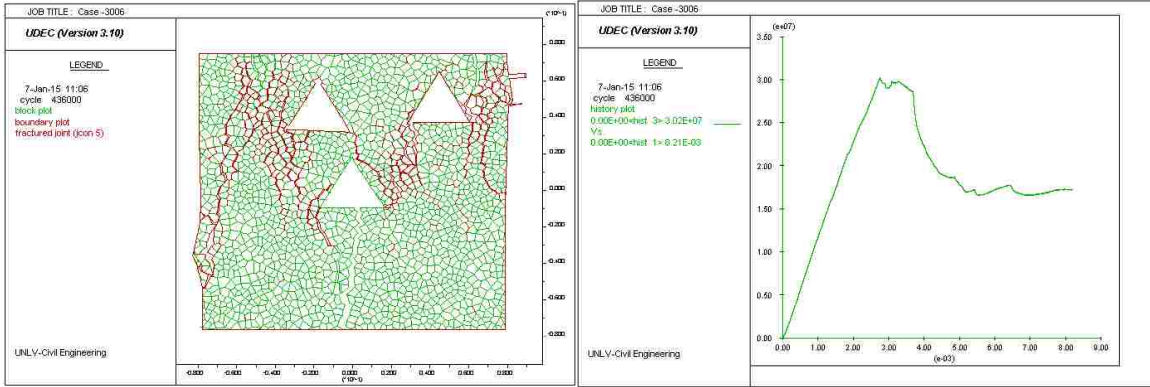
PA-URL3-90° (Horizontal)



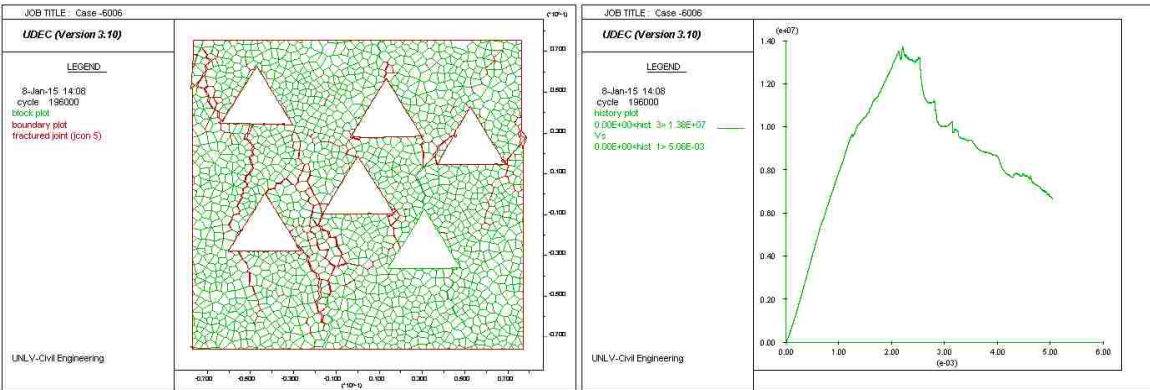
PA-URL6-90° (Horizontal)



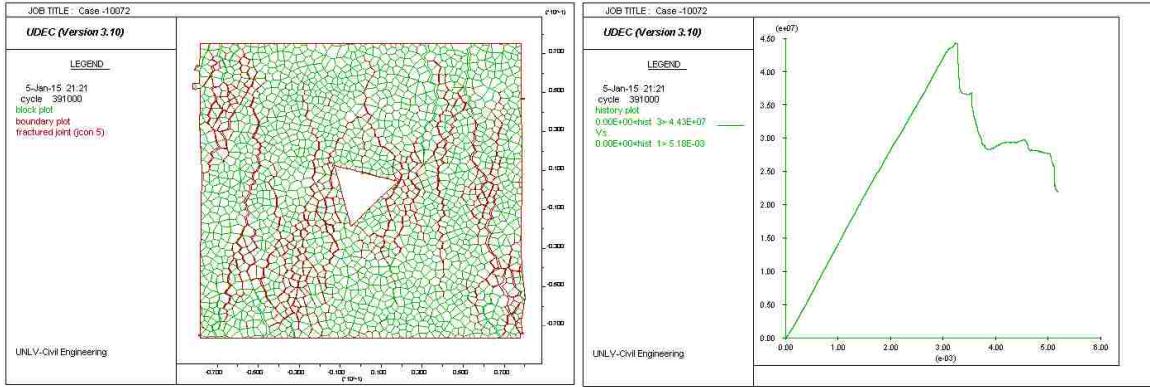
PA-TCL1-Straight



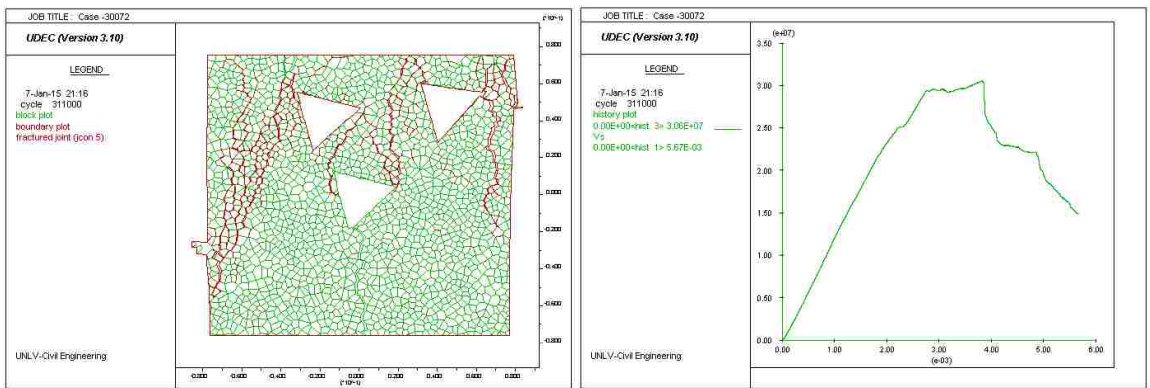
PA-TCL3-Straight



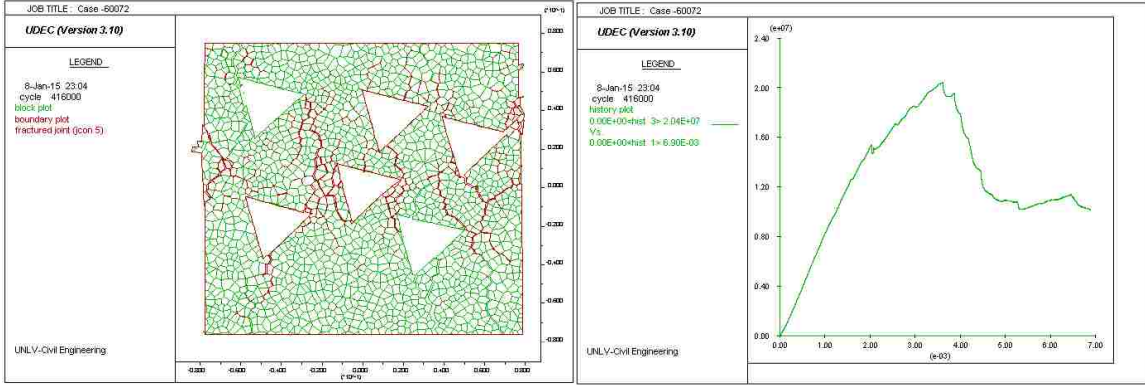
PA-TCL6-Straight



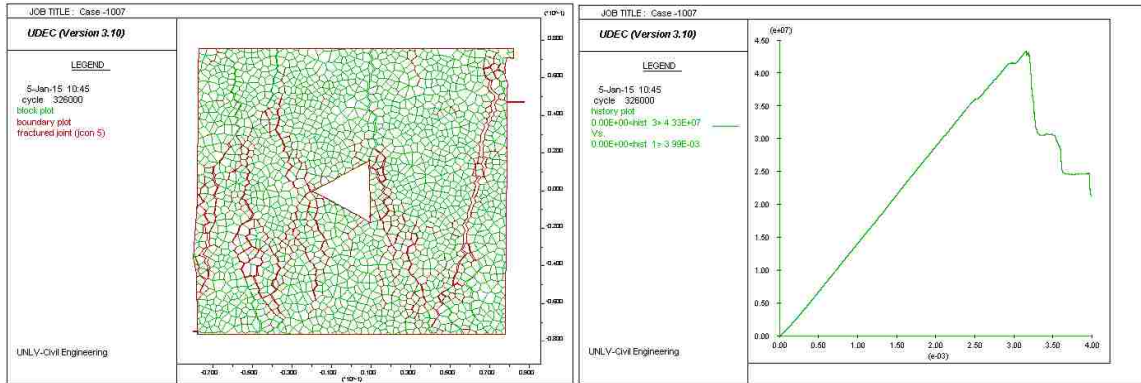
PA-URL1-45°



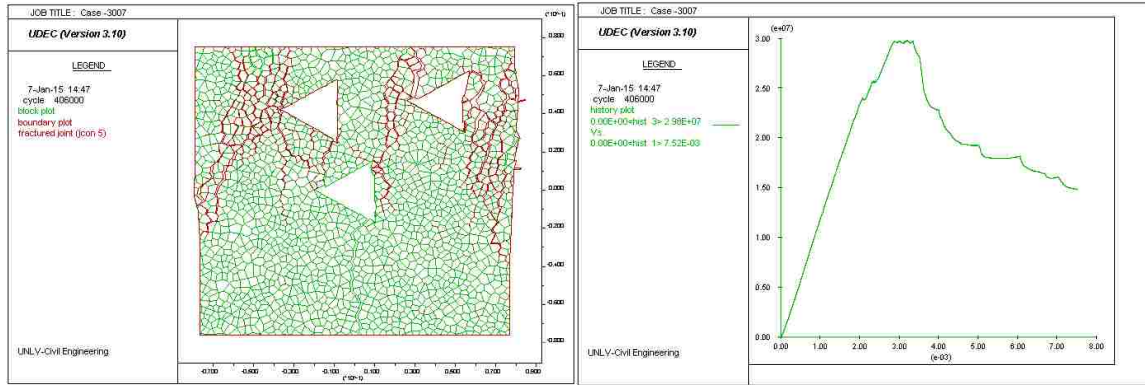
PA-URL3-45°



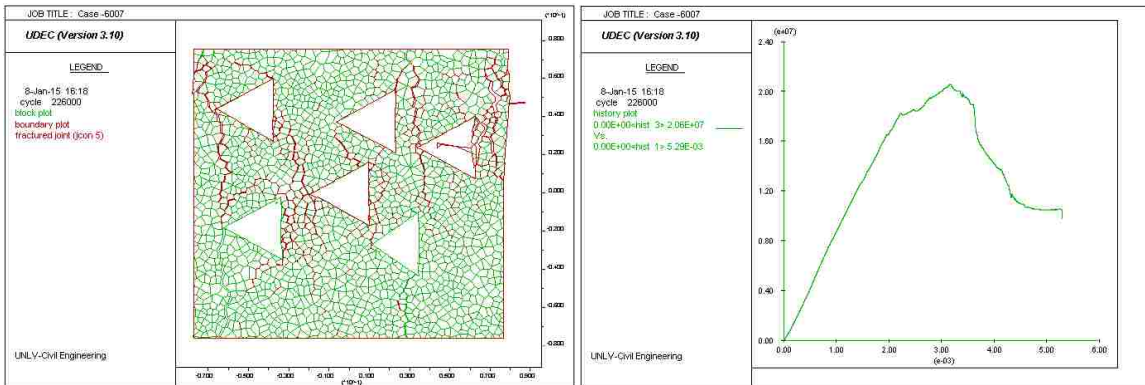
PA-URL6-45°



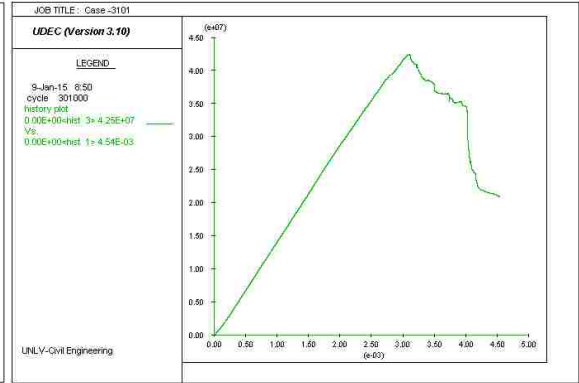
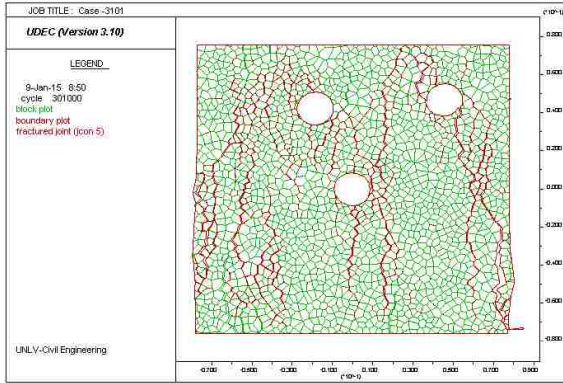
PA-URL1-90°



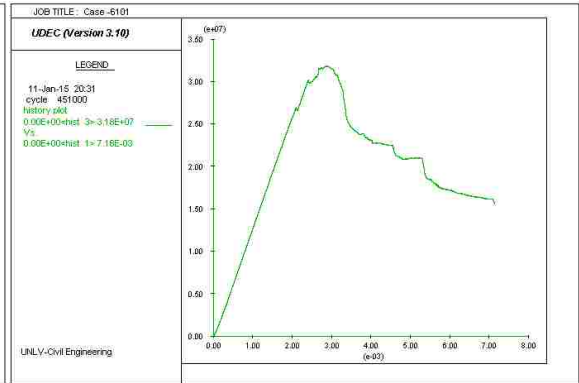
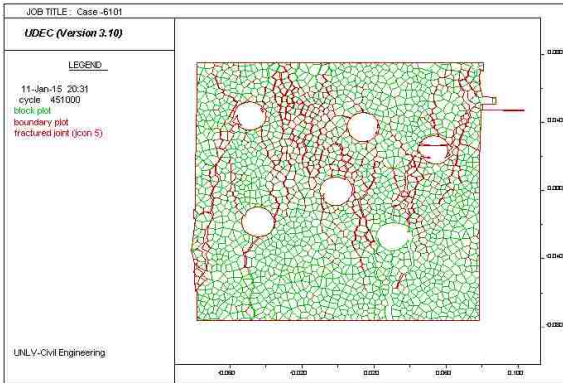
PA-URL3-90°



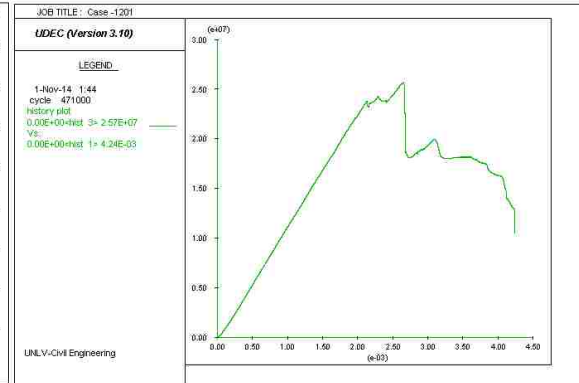
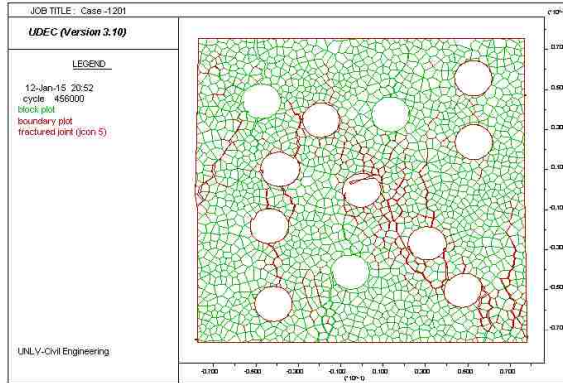
PA-URL6-90°



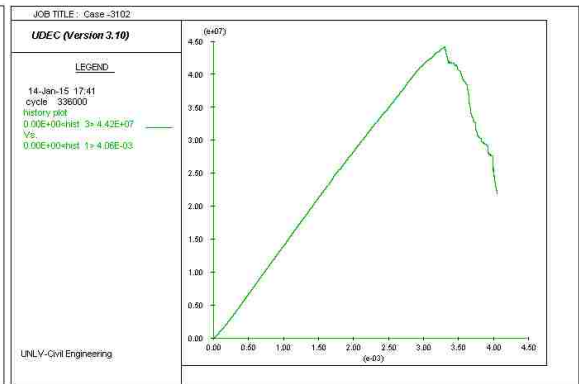
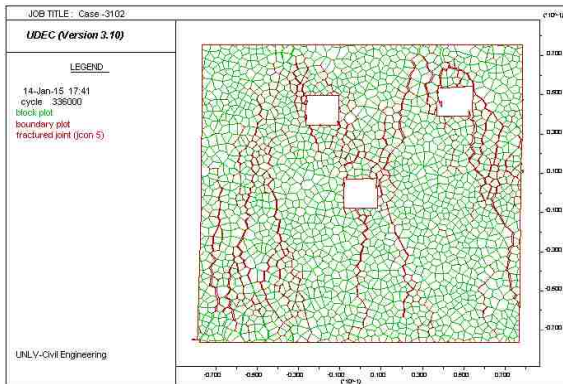
PA-UCS3



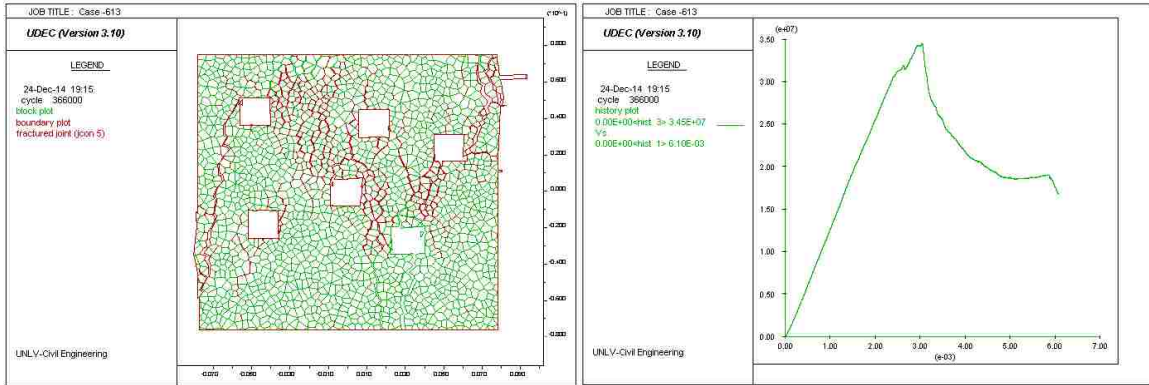
PA-UCS6



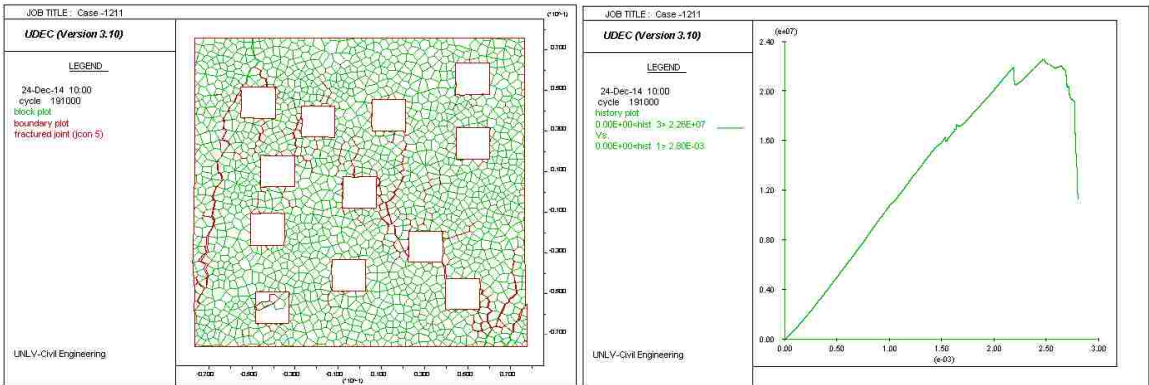
PA-UCS12



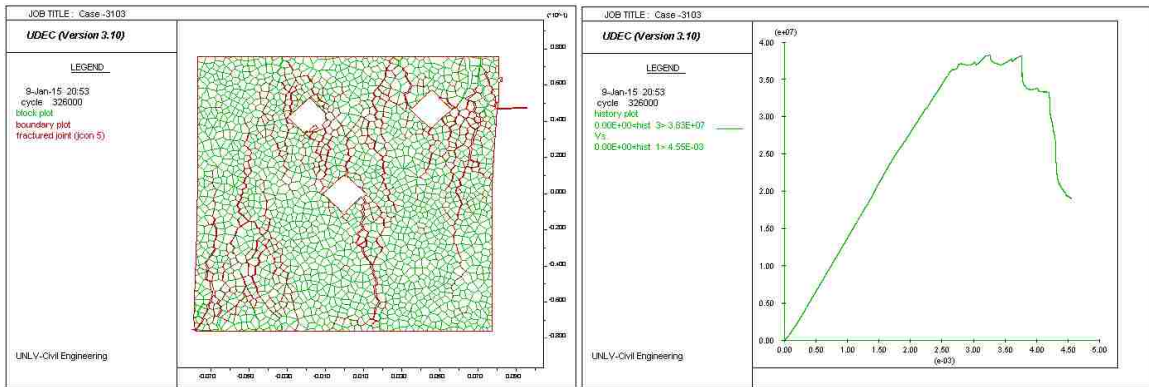
PA-USqS3-Vertical



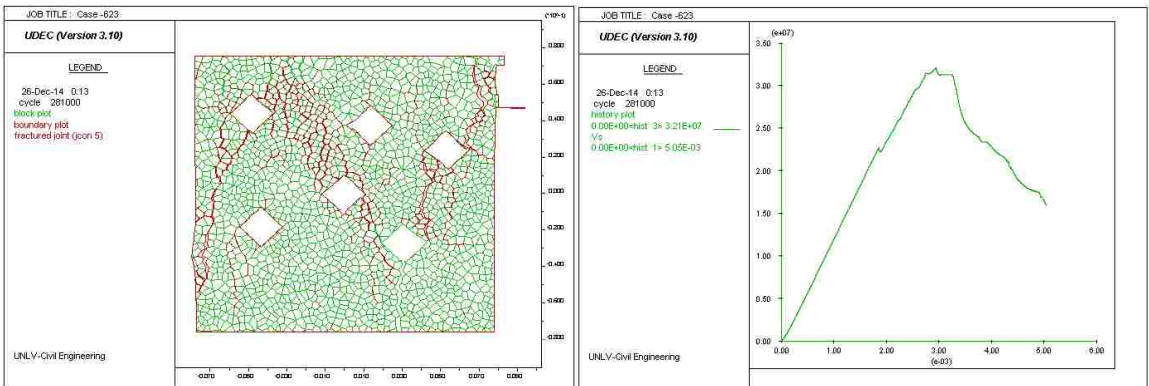
PA-USqS6-Vertical



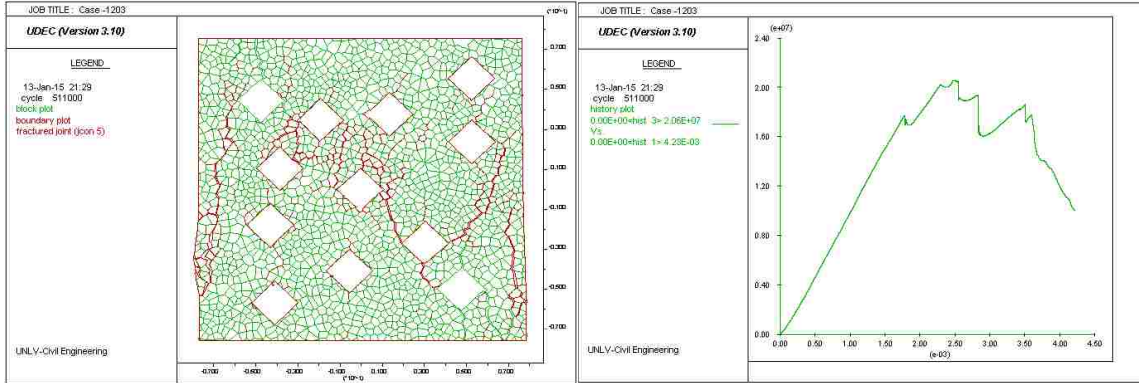
PA-USqS6-Vertical



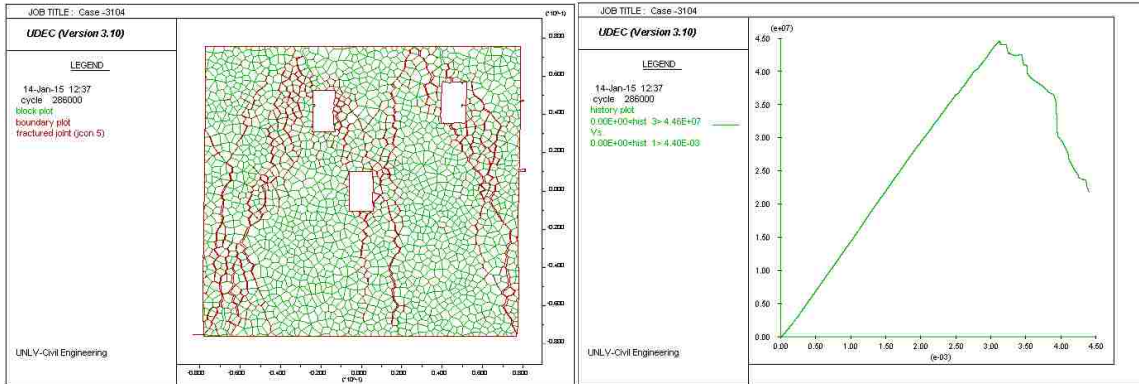
PA-USqS3-45° (Diamond)



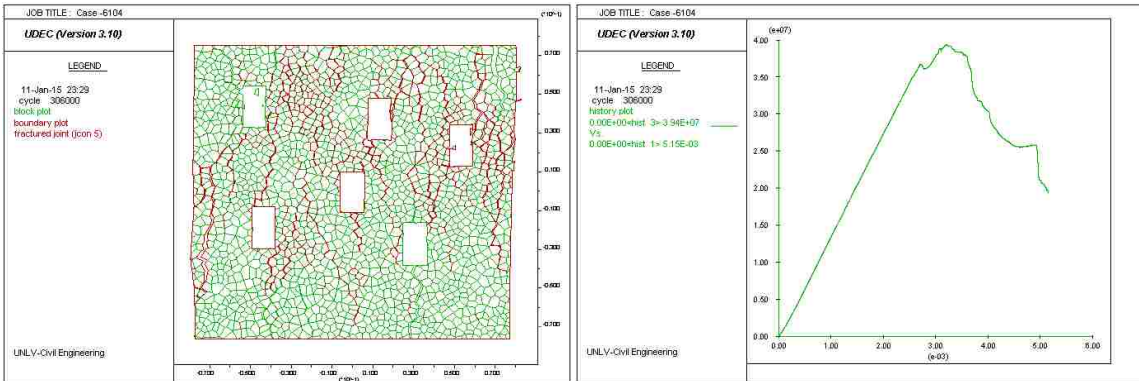
PA-USqS6-45° (Diamond)



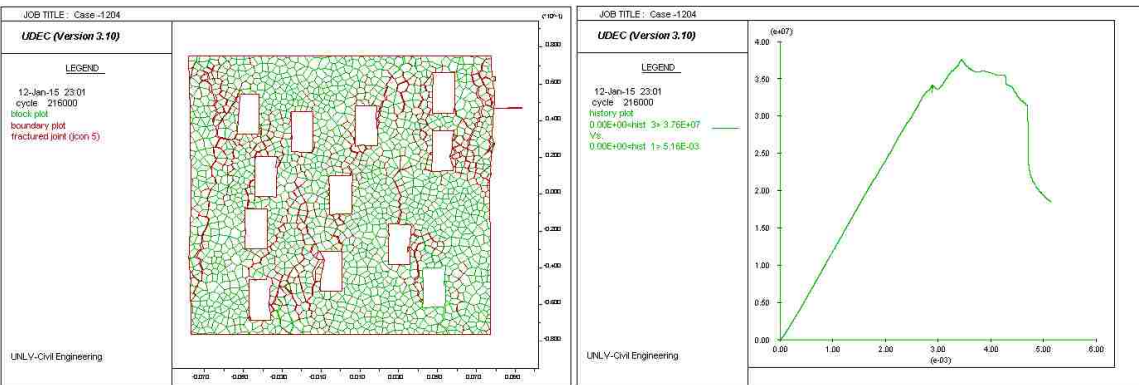
PA-USqS12-45° (Diamond)



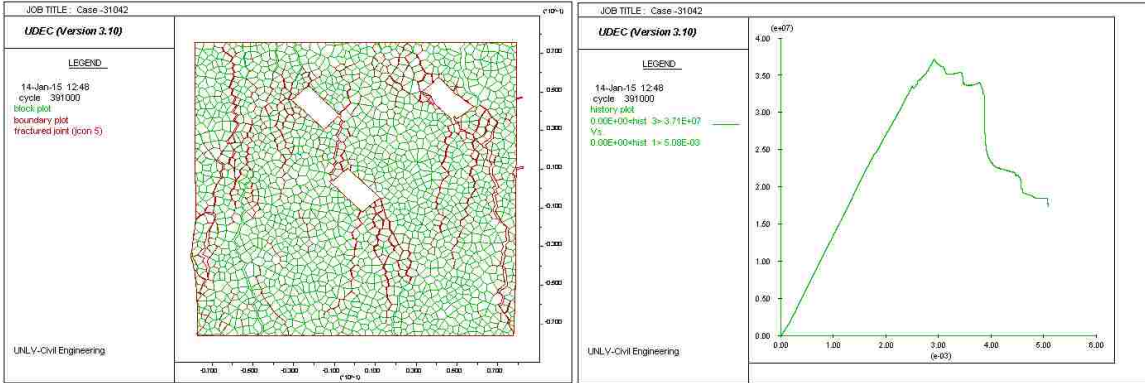
PA-URS3-Vertical



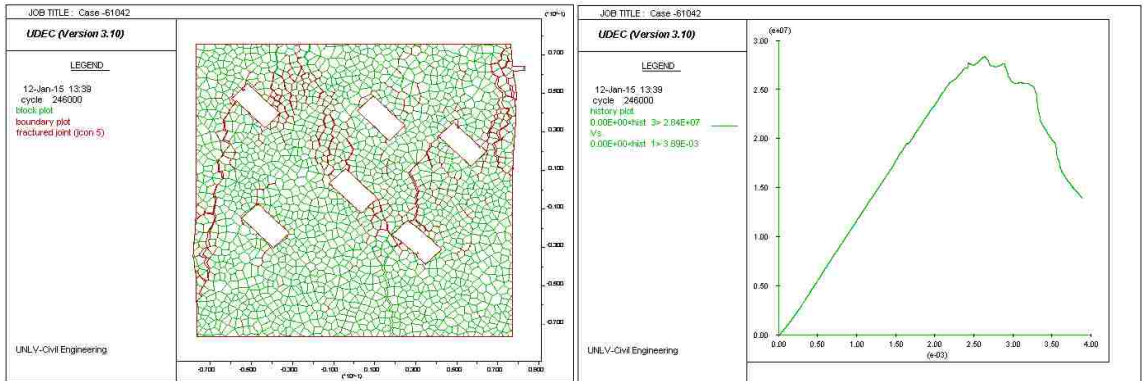
PA-URS6-Vertical



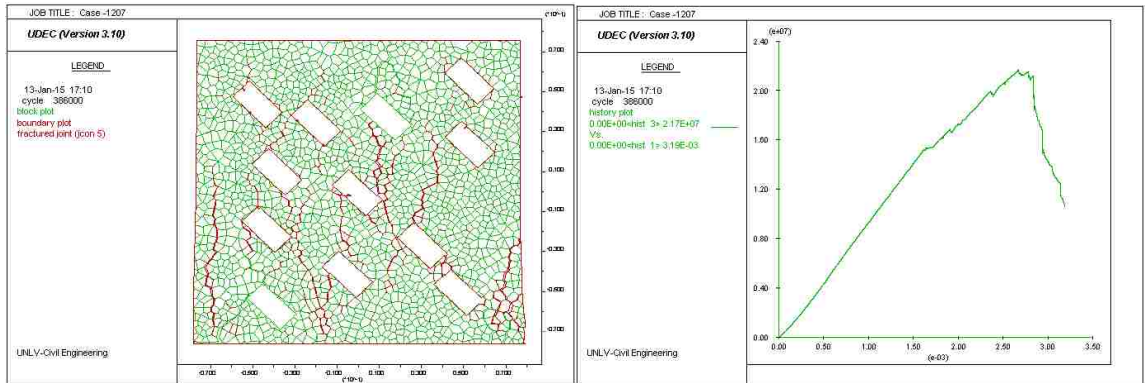
PA-URS12-Vertical



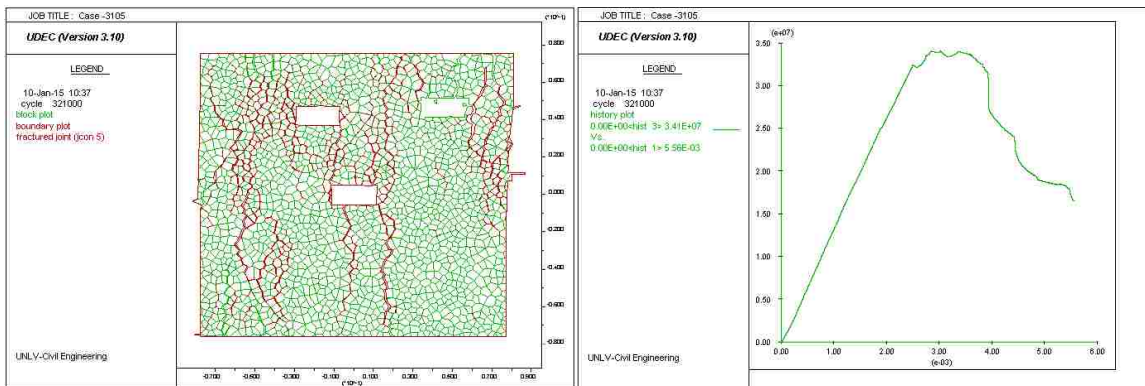
PA-URS3-45°



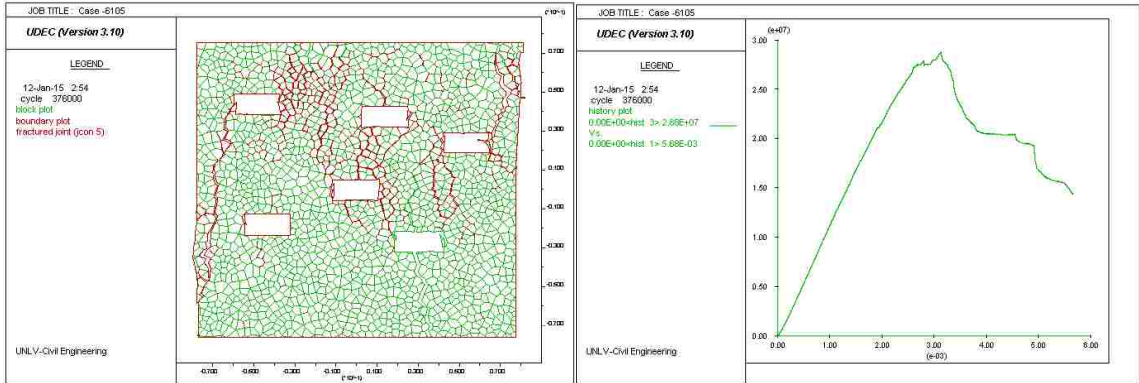
PA-URS6-45°



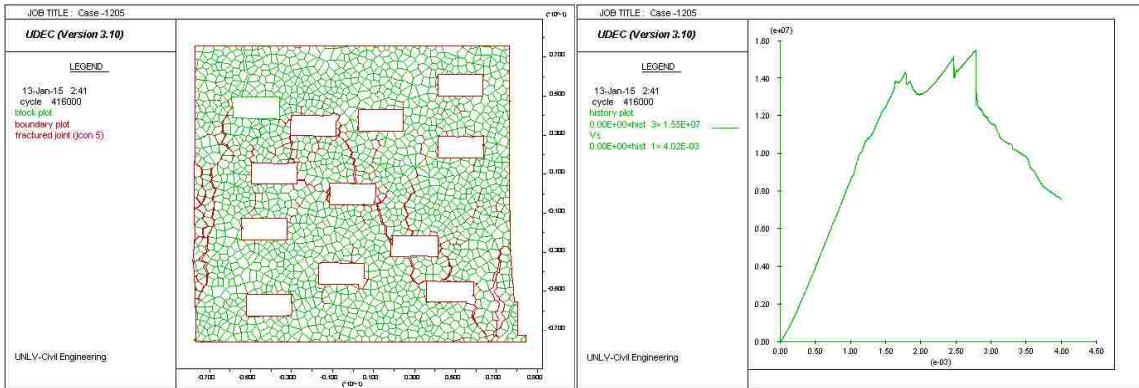
PA-URS12-45°



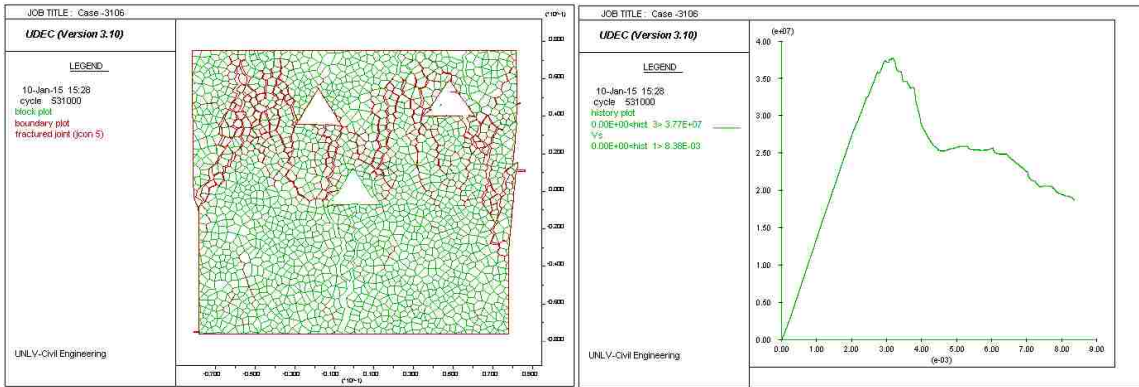
PA-URS3-90° (Horizontal)



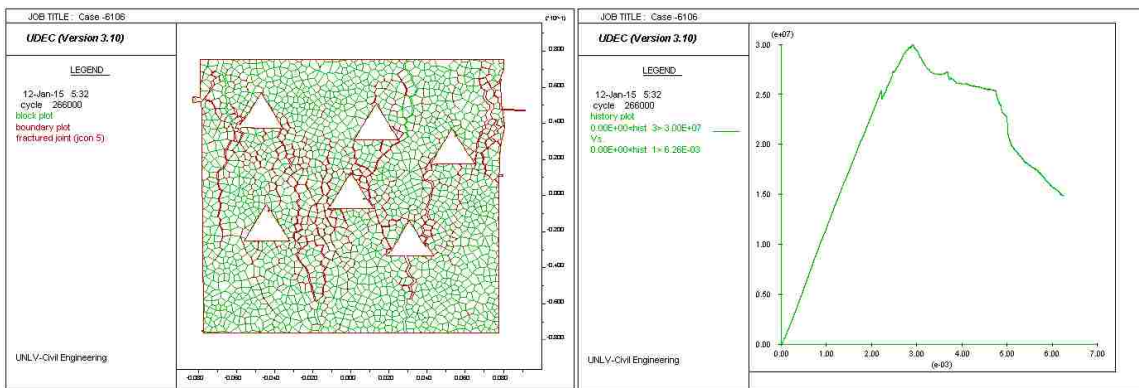
PA-URS6-90° (Horizontal)



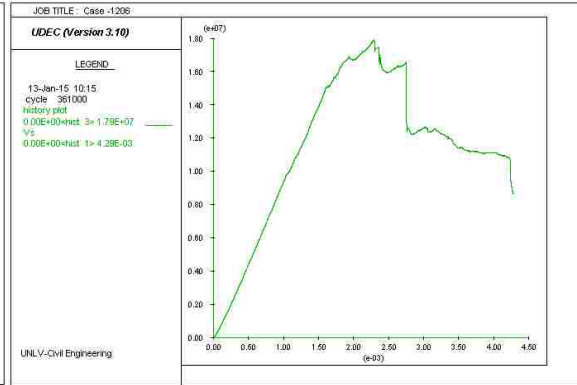
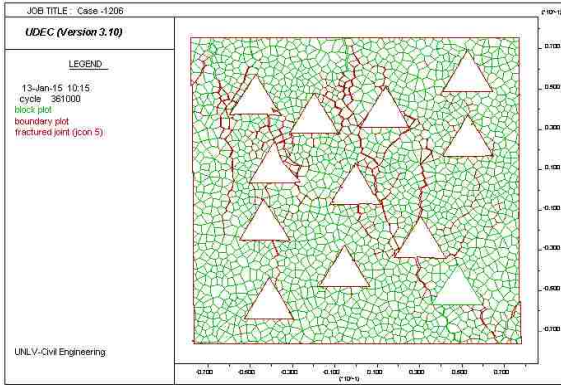
PA-URS12-90° (Horizontal)



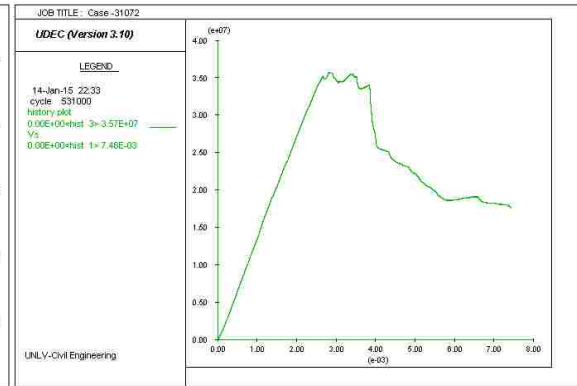
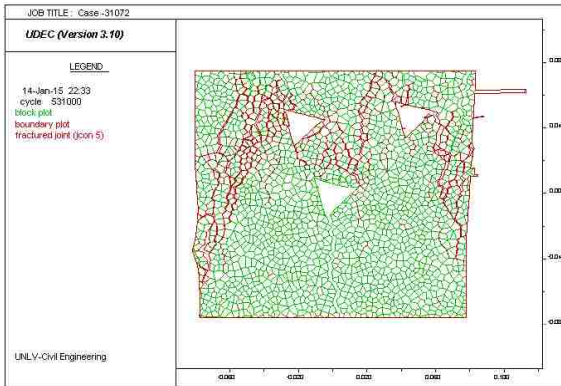
PA-UTS3-Straight



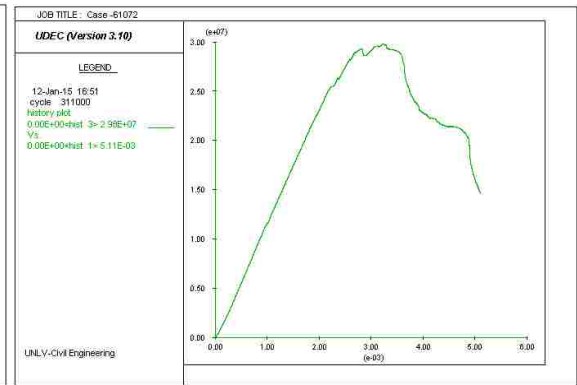
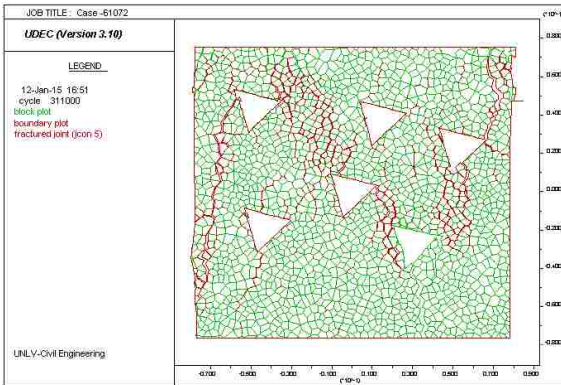
PA-UTS6-Straight



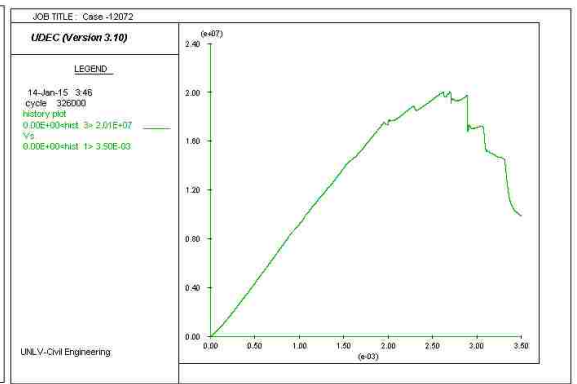
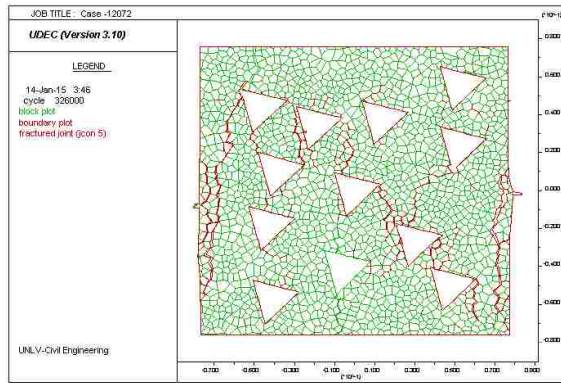
PA-UTS12-Straight



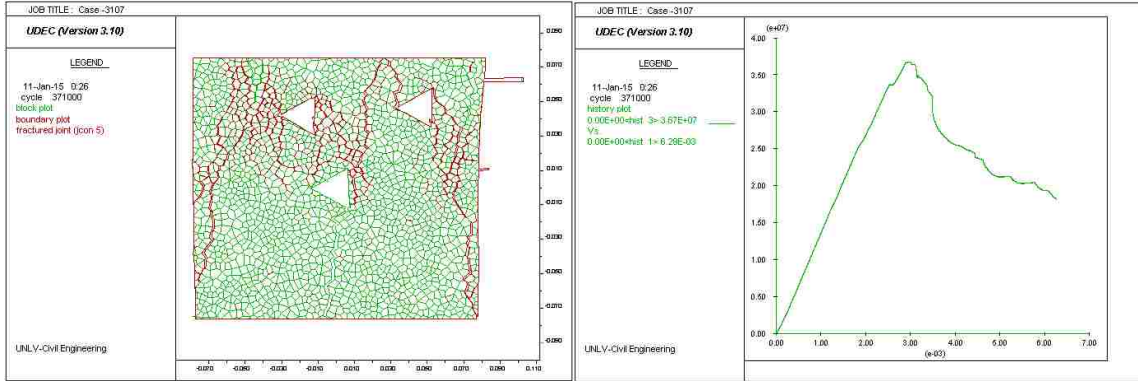
PA-URS3-45°



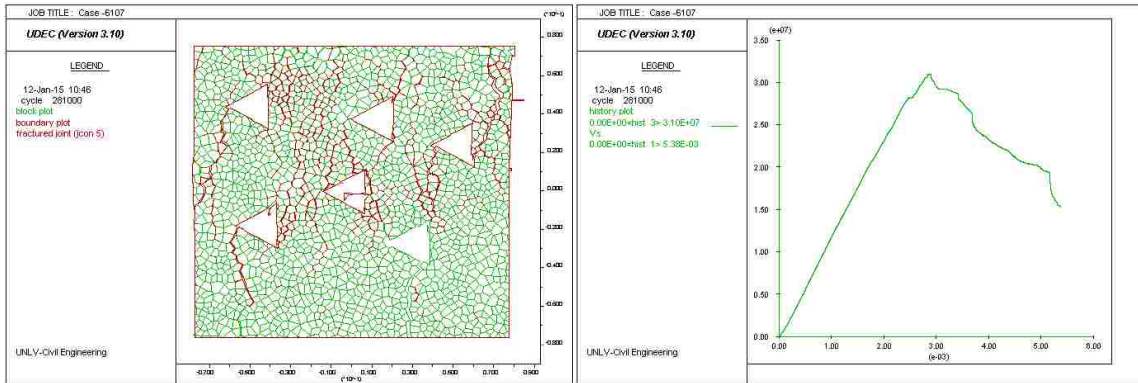
PA-URS6-45°



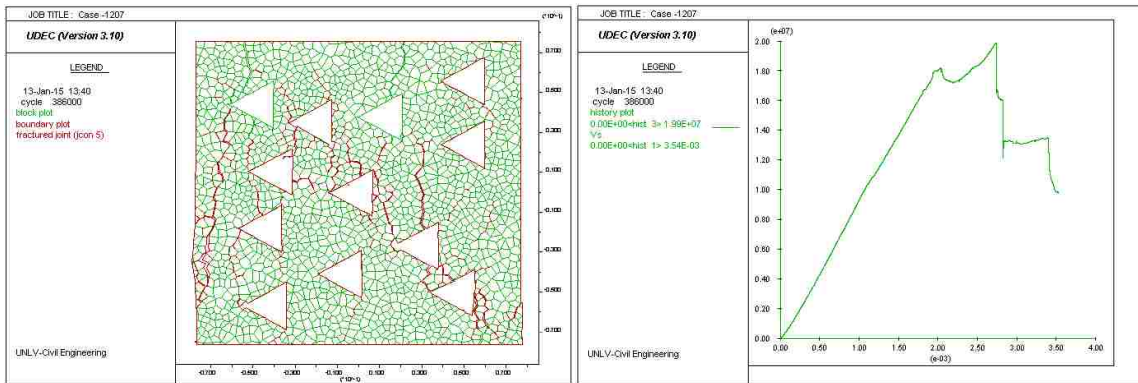
PA-URS12-45°



PA-URS3-90°



PA-URS6-90°



PA-URS12-90°

BIBLIOGRAPHY

- 1- Al-Harhi, A. A., Al-Amri, R. M., and Shehata, W. M. (1999). The porosity and engineering properties of vesicular basalt in Saudi Arabia. *Engineering Geology*, 54, pp. 313–20.
- 2- Altin, L. (1994). *Manufacturing Engineering Processes*, 2nd Edition, Marcel Dekker, 492 pages.
- 3- Anderson T. L. (1995). *Fracture Mechanics*, 2nd Edition, Boca Raton, FL: CRC Press, 680 pages.
- 4- Andreev, G.E. (1995). *Brittle Failure of Rock Materials: Test Results and Constitutive Models*, Balkema, Brookfield, 446 pages.
- 5- ASTM C 109/C 109M – 07. (2007). *Standard Test Method for Compressive Strength of Hydraulic Cement Mortars (Using 2-in. or [50-mm] Cube Specimens)*. American Society for Testing and Materials.
- 6- Avar, B. B. (2002). *Numerical and Experimental Investigation of Formation and Strength Properties of Lithophysae-rich Tuff and Analog Materials*. PhD dissertation, University of Nevada, Las Vegas.
- 7- Avar, B. B., Hudyma, N., and Karakouzian, M. (2003). Porosity Dependence of the Elastic Modulus of Lithophysae-rich Tuff: Numerical and Experimental Investigations. *Int J Rock Mech Min Sci.*, (40): 919–28.
- 8- Bedonyi, J. (1970). Laboratory Tests of Certain Rocks under Axially-symmetrical Loading Conditions. In: *Proceedings of the 2nd international congress on rock mechanics*, Belgrade, 1, pp. 389-397.
- 9- Bieniawski, Z.I., Denkhaus, H.G., and Vogler, U.W. (1969). Failure of Fractured Rock. *Int. J. Rock Mech. Min. Sci.*, vol. 6, (1969), pp. 323-341.
- 10- Bieniawski, Z. T. (1974). Geomechanics Classification of Rock Masses and its Application in Tunneling. In *Proceedings of the 3rd International Congress on Rock Mechanics*, Denver, pp. 27-32.
- 11- Bobet, A. (2010). Numerical Methods in Geomechanics. *The Arabian Journal for Science and Engineering*, 35, pp. 27-48.

- 12- Brady, B. H. G., and Brown, E. T. (2006). *Rock Mechanics: For Underground Mining*, 3rd Edition, *Springer Netherlands*, 628 pages.
- 13- Broek, D. (1986). *Elementary Engineering Fracture Mechanics*, *Springer Science & Business Media*, 1986 - Science - 469 pages.
- 14- BSC (Bechtel SAIC Company) (2003). *Subsurface Geotechnical Parameters Report*. 800-K0C-WIS0-00400-000-00A. *Bechtel SAIC Company*. ACC: ENG.20040108.0001, Las Vegas, Nevada.
- 15- BSC (Bechtel SAIC Company) (2004). *Drift Degradation Analysis*. ANL-EBS-MD-000027 Rev. 03. *Bechtel SAIC Company*. ACC: DOC.20040915.0010, Las Vegas, Nevada.
- 16- BS 1881 (1983). *Testing Concrete. Part 116: Method for Determination of Compressive Strength of Concrete Cubes*. *British Standards Institute*.
- 17- Chawla, M. (2007). *Influence of Lithophysal Geometry on Uniaxial Compression of Tuff-like Rock*. *M.Sc. Thesis*, University of Nevada, Las Vegas.
- 18- Christensen, R. M. (2005). *Exploration of Ductile, Brittle Failure Characteristics Through a Two Parameter Yield/Failure Criterion*. *Mater. Sci. Eng., A*, A374, pp. 417–424.
- 19- Christianson, M., Board, M., and Rigby, D. (2006). *UDEC Simulation of Triaxial Testing of Lithophysal Tuff*. *Golden Rocks 2006- 50 Years of Rock Mechanics*, Colorado School of Mines, June 2006 (Proceedings of the 41st, *U.S. Rock Mechanics Symposium*), Paper No. 06-968. D.P. Yale et al., Eds. ARMA. 2006.
- 20- Costin, L. S., R. H. Price, and Lee, M. Y. (2009). *Characterization of a High Lithophysal Welded Tuff Unit using a Multi-scale Approach*. Paper presented at *International Conference on Rock Joints and Jointed Rock Masses*, Univ. of Ariz., Tucson
- 21- Cundall, P. A. (1971). *A Computer Model for Simulating Progressive Large Scale Movements in Blocky Rock Systems*. In *Proceedings of the Symposium of the International Society for Rock Mechanics* (Nancy, France, 1971), Vol. 1, Paper No. II-8.
- 22- Cundall, P. A., and Hart, R. D. (1992). *Numerical Modelling of Discontinua*. *Engineering Computations*, 9, pp.101–113.

- 23- Deere, D. U., and Miller, R. P. (1966). Engineering Classification and Index Properties for Intact Rock. *Tech. Rep. AFWL-TR-65-116*.
- 24- Dunn, D. E., La Foundation, L. J., and Jackson, R. E. (1973). Porosity Dependence and Mechanism of Brittle Fracture in Sandstone. *Journal of Geophysical Research*, 78, 2403-2417.
- 25- Erfourth, B. S. (2006). Characterization of the Impact of Spherical Voids - Regarding Size, Spatial Distribution, and Porosity - on Engineering Properties of Rock and Rock-like Materials. *M.Sc. Thesis*, Montana Tech of the University of Montana.
- 26- Fairhurst, C. (1964). On the Validity of the "Brazilian" Test for Brittle Materials. *Int. J. Rock Mech. Min.*, 1, pp. 515-546.
- 27- Franklin, J. A., and Dusseault, M. B. (1989). Rock Engineering. *New York: McGraw-Hill*, 600 pages.
- 28- Franklin, J.A. (1971). Triaxial Strength of Rock Material. *Rock Mech.* 3, pp. 86-98.
- 29- Gordon, J. E. (2003). Structures: Or Why Things Don't Fall Down, Reprint Edition, *Da Capo Press*, 424 pages.
- 30- Griffith, A. A. (1921). The Phenomena of Rupture and Flow in Solids. *Phil. Trans Roy. Soc.*, A221, pp. 163-97.
- 31- Griffith, A. A. (1924). Theory of Rupture. *Proceedings, 1st Congr. Appl. Mech.*, Delft, pp. 55-63.
- 32- Hadizadeh, J., and Rutter, E. H. (1983). The Low Temperature Brittle-ductile Transition in Quartzite and Occurrence of Cataclastic Flow in Nature. *Geologische Rundschau (International Journal of Earth Sciences)*, 72, pp. 493-503.
- 33- Hearn, E. J. (2001). Mechanics of Materials I: An Introduction to the Mechanics of Elastic and Plastic Deformation of Solids and Structural Materials, 3rd Edition.
- 34- Hertzberg, R. W. (1996). Deformation and Fracture Mechanics of Engineering Materials, 4th Edition, *New York, NY: John Wiley*, 816 pages.
- 35- Hobbs, D. W. (1970). The Strength and Stress-strain Characteristics of Coal in Triaxial Compression. *J. Geol.* 72 (2), pp. 214-231.

- 36- Hoek, E., and Brown, E.T. (1980). Empirical Strength Criterion for Rock Masses. *J. Geotech. Engng Div., ASCE*, 106 (GT9), 1013-1035.
- 37- Hoek, E., Carranza-Torres, C., and Corkum, B. (2002). Hoek-Brown Failure Criterion-2002 Edition. In: *Proceedings of the 5th North American Rock Mechanics Symposium and 17th Tunneling Association of Canada Conference: NARMS-TAC 2002*, July 7-10, University of Toronto, pp. 267-271.
- 38- Hudyma, N., Avar, B. B., and Karakouzian, M. (2004). Compressive Strength and Failure Modes of Lithophysae-rich Tuff Specimens and Analog Models Containing Cavities. *Engineering Geology*, 73, pp.179–90.
- 39- Hutchinson, J. W. (1983). Fundamentals of the Phenomenological Theory of Nonlinear Fracture Mechanics, *J. Appl. Mechanics*, 50th Anniversary Issue, Vol. 105, pp 1042-1051.
- 40- Itasca Consulting Group (2002). Itasca Software—Cutting Edge Tools for Computational Mechanics. *Itasca Consulting Group*. TIC: 252592, Minneapolis, Minnesota.
- 41- Itasca (2011). Universal Distinct Element Code Constitutive Models. *Itasca Group Consulting Group, Inc.*
- 42- Itasca (2011). Universal Distinct Element Code Creep Material Models. *Itasca Group Consulting Group, Inc.*
- 43- Itasca (2011). Universal Distinct Element Code Theory and Background. *Itasca Group Consulting Group, Inc.*
- 44- Itasca (2011). Universal Distinct Element Code User’s Guide. *Itasca Group Consulting Group, Inc.*
- 45- Jespersen, C., MacLaughlin, M., and Hudyma, N. (2010). Strength, Deformation Modulus and Failure Modes of Cubic Analog Specimens Representing Macroporous Rock. *International Journal of Rock Mechanics & Mining Sciences*, 47, pp. 1349–1356.
- 46- Jing, L., and Stephansson, O. (2007). Fundamentals of Discrete Element Methods for Rock Engineering: Theory and Applications. *Elsevier*, 562 pages.
- 47- Johnston, I. W. (1985). Strength of Intact Geomechanical Materials. *J. Geotech. Eng, ASCE*, 111, pp. 730-749.

- 48- Jumikis, A.R. (1983). *Rock Mechanics*, 2nd Edition, *Gulf Publishing Co.*, 613 pages.
- 49- Kelly, P. (2013). *Solid Mechanics Part I: An Introduction to Solid Mechanics. Solid Mechanics Lecture Notes*.
http://homepages.engineering.auckland.ac.nz/~pkel015/SolidMechanicsBooks/Part_I/index.html.
- 50- Kelsall, P.C., Watters, R.J., and Franzone, J.G. (1986). Engineering Characterization of Fissured Weathered Dolerite and Vesicular Basalt. *Rock Mechanics: Key to Energy Production, Proc. 27th US Symp. on Rock Mechanics*, Tuscaloosa, Alabama.
- 51- Logan, M. J. (1987). Porosity and the Brittle-Ductile Transition in Sedimentary Rocks. *AIP Conference Proceedings* 154, 229 pages.
- 52- Martin, R. J., Price, R. H., Boyd, P. J., and Noel, J. S. (1994). Bulk and Mechanical Properties of the Paintbrush Tuff Recovered from Borehole USW NRG-6: data report. *Sandia National Laboratories*, SAND93-4020. Albuquerque, NM.
- 53- Martin, R. J., Price, R. H., Boyd, P. J., and Noel, J. S. (1995). Bulk and Mechanical Properties of the Paintbrush Tuff Recovered from Borehole USW NRG-7/7A: data report. *Sandia National Laboratories*, SAND94-1996. Albuquerque, NM.
- 54- Meyers, M. A., and Chawla, K. K. (2009). *Mechanical Behavior of Materials*, 2nd Edition, *Cambridge University Press*, 856 pages.
- 55- Moaveni, S. (2008). *Finite Element Analysis: Theory and Application with ANSYS*. *Prentice Hall*, 880 pages.
- 56- Mogi, K. (1972). Fracture and Flow of Rocks. *Tectonophysics*, 13, pp. 541-568.
- 57- Mogi, K. (2007). *Experimental Rock Mechanics*. *Taylor & Francis*. Balkama, London, Uk, 380 pages.
- 58- Nimick, F. B., Price, R. H., Van Buskirk, R. G., and Goodell, J. R. (1985). Uniaxial and Triaxial Compression Test Series on Topopah Spring Tuff from USW G-4, Yucca Mountain, Nevada. *Sandia National Laboratories*, SAND84-1101, Albuquerque, NM.

- 59- Norton, R. L. (1997). *Machine Design: An Integrated Approach*, 1st Edition, *Prentice Hall*, 1048 pp.
- 60- Nott, J. (2009). *Tensile Strength and Failure Criterion of Analog Lithophysal Rock. PhD Dissertation*, University of Nevada, Las Vegas.
- 61- Palchik, V. (1999). Influence of Porosity and Elastic Modulus on Uniaxial compressive Strength in Soft Brittle Porous Sandstones. *Rock Mechanics and Rock Engineering*, 32(4), pp. 303–309.
- 62- Palchik, V., and Hatzor, Y. H. (2004). The Influence of Porosity on Tensile and Compressive Strength of Porous Chalks. *Rock Mechanics and Rock Engineering*, 37 (4), pages 331–341.
- 63- Price, R. H. (1983). Analysis of Rock Mechanics Properties of Volcanic Tuff Units from Yucca Mountain, Nevada Test Site. *Sandia National Laboratories Report*, SAND82-1315. Albuquerque, NM.
- 64- Price, R. H., Nimick, F. B., Connolly, J. R., Keil, K., Schwartz, B. M., and Spence, S. J. (1985). Preliminary Characterization of the Petrologic, Bulk, and Mechanical Properties of a Lithophysal Zone Within the Topopah Spring Member of the Paintbrush Tuff. *Sandia National Laboratories*, SAND84-0860. Albuquerque, NM.
- 65- Price, R. H., Martin III, R. J., Boyd, P. J., and Boitnott, G. N. (1994). Mechanical and Bulk Properties of the Intact Rock Collected in the Laboratory in Support of the Yucca Mountain Site Characterization Project. *Sandia National Laboratories*, SAND94-2243C. Albuquerque, NM.
- 66- Price, R. H. (2004). The Mechanical Properties of Lithophysal Tuff: Laboratory Experiments. TDREBS-MD-000027 Rev. 00. *Bechtel SAIC Company, ACC: DOC.20040506.0001*, Las Vegas, Nevada.
- 67- Pytel, A., and Kiusalaas, J. (2012). *Mechanics of Materials*, 4th Edition, *Stamford: Cengage Learning*, 554 pages.
- 68- Ramamurthy, T., and Arora, V. K. (1993). A Classification for Intact and Jointed Rocks, In: *Geotechnical Engineering of Hard Soils- Soft Rocks. Anagnostopoulos et al., (Eds.), Balkema, Rotterdam. ISBN 90 5410 344 2.*

- 69- Rigby, D. B. (2004). Lithophysal Rock Mass Mechanical Properties of the Repository Host Horizon. *DOE United States Government Identifier*, 800-K0CSS00-00200-000-00A.
- 70- Rigby, D. B. (2007). Influence of Lithophysal Geometry on the Uniaxial Compression of Tuff-like Rock. *Department of Energy Technical Report TR-07-001*, Task ORD- FY04-013.
- 71- Roesler, J., Harders, H., and Baeker, M. (2007). Mechanical Behaviour of Engineering Materials” *Springer Science & Business Media, 2007 - Science*, 534 pages.
- 72- Roylance, D. (2001). Introduction to Fracture Mechanics. <http://web.mit.edu/course/3/3.11/www/modules/frac.pdf>.
- 73- Runesson, K. (2005). Constitutive Modeling of Engineering Materials - Theory and Computation. *Computational Mechanics*, Chalmers University of Technology, Göteborg, 342 pages.
- 74- Sandhu, R. S. (1972). A Survey of Failure Theories of Isotropic and Anisotropic Materials” *Technical Report, AFFDL- TR-72-7 1*.
- 75- Scheldt, T. (2002). Comparison of Continuous and Discontinuous Modelling for Computational Rock Mechanics. *PhD. Thesis, NTNU*, pp 142.
- 76- Schultz, R. A., and Li, Q. (1995). Uniaxial strength testing of non-welded Calico Hills tuff, Yucca, Nevada. *Engineering Geology*, 40, pp. 287-299.
- 77- Sheorey, P. R., Biswas, A. K., and Choubey, V. D. (1989). An Empirical Failure Criterion for Rocks and Jointed Rock Masses. *Engineering Geology*, 26, pp. 141-159.
- 78- Singh, U. K., and Dwivedi, M. (2009). Manufacturing Processes: as Per the New Syllabus, B. Tech. I Year of U. P. Technical University” *New Age International Pvt Ltd Publishers, India*, 292 pages.
- 79- Tillerson, J. R., and Nimick, F. B. (1984). Geoengineering Properties of Potential Repository Units at Yucca Mountain, Southern Nevada. *Sandia National Labs Report*, SAND84-0221.
- 80- Timoshenko, S., and Goodier, J. N. (1951). Theory of Elasticity, 2nd Edition, *New York: McGraw-Hill*, 506 pages.

- 81- Tugrul, A., and Gurpinar, O. (1997). A Proposed Weathering Classification for Basalts and Their Engineering Properties (Turkey). *Bull. Int. Assoc. Eng. Geol.*, 55, 139–149.
- 82- Ugural, A. C. (2004). *Mechanical Design: An Integrated Approach*, New York: McGraw-Hill, 810 pages.
- 83- Ugural, A. C., and Fenster, S. K. (2012). *Advanced Mechanics of Materials and Applied Elasticity*, 5th Edition. *Pearson Education, Inc.*, 680 pages.
- 84- USBR (2001). *Engineering Geology Field Manual*. Volume I, 2nd Edition, 432 pages.
- 85- Vernik, L., Bruno, M., and Boverg, C. (1993). Empirical Relations between Compressive Strength and Porosity of Siliclastic Rocks. *International Journal of Rock Mechanics and Mining Sciences & Geomechanics Abstracts* 30, 677-680.
- 86- Yoshida, N., Morgenstern, N. R., and Chan, D. H. (1990). Failure Criterion for Stiff Soils and Rocks Exhibiting Softening. Author Affiliation: Univ of Alberta Source: *Can. Geotech. J.*, 27 (2), 195-202. ISSN: 0008-3674 CODEN: CGJOAH.
- 87- Yudhbir, Y., Lemanza, W., and Prinzl, F. (1983). An Empirical Failure Criterion for Rock Masses. In: *Proceedings of the 5th International Congress on Rock Mechanics*, Melbourne, Balkema, Rotterdam, 1, B1-B8.
- 88- Zuo, J. P., Li, H. C., Xie, H. P., Ju, Y., and Peng, S. P. (2008). A Nonlinear Strength Criterion for Rock-like Materials Based on Fracture Mechanics. *International Journal of Rock Mechanics and Mining Sciences*, 45, 594–599.

VITA

Omed S. Q. Yousif
yousifo@unlv.nevada.edu

Education:

- **August 2011 - May 2015:** PhD Student, University of Nevada Las Vegas, Department of Civil and Environmental Engineering and Construction, Howard R. Hughes College of Engineering.
- **October 1999 – December 2002:** MSc Student, Hydraulic Engineering, Engineering College, University of Sulaimani, Sulaimani, Iraq.
- **September 1993- July 1997:** Undergraduate Student, Department of Civil Engineering, Salahaddin University, Hawler, Iraq.

Publications:

Rahim, N. O., Rashed, K. A., **Yousif, O. S.** (2007). Effect of Grain Size of Porous Media on Physical Clogging. *Journal of Zankoy Sulaimani*, 10(1), Part A, 59-72.

References:

Dr. Moses Karakouzian, PhD, PE
Professor of Civil Engineering
University of Nevada Las Vegas
Department of Civil and Environmental Engineering
4505 Maryland Parkway, Box 454015
Las Vegas, NV 89154-4015
Tel: 702-895-0959
Fax: 702-895-3936
email: mkar@unlv.nevada.edu